

Damian Mazur
Marek Gołębiowski
Mariusz Korkosz
Editors

Analysis and Simulation of Electrical and Computer Systems

Lecture Notes in Electrical Engineering

Volume 452

Board of Series editors

Leopoldo Angrisani, Napoli, Italy
Marco Arteaga, Coyoacán, México
Samarjit Chakraborty, München, Germany
Jiming Chen, Hangzhou, P.R. China
Tan Kay Chen, Singapore, Singapore
Rüdiger Dillmann, Karlsruhe, Germany
Haibin Duan, Beijing, China
Gianluigi Ferrari, Parma, Italy
Manuel Ferre, Madrid, Spain
Sandra Hirche, München, Germany
Faryar Jabbari, Irvine, USA
Janusz Kacprzyk, Warsaw, Poland
Alaa Khamis, New Cairo City, Egypt
Torsten Kroeger, Stanford, USA
Tan Cher Ming, Singapore, Singapore
Wolfgang Minker, Ulm, Germany
Pradeep Misra, Dayton, USA
Sebastian Möller, Berlin, Germany
Subhas Mukhopadhyay, Palmerston, New Zealand
Cun-Zheng Ning, Tempe, USA
Toyoaki Nishida, Sakyo-ku, Japan
Bijaya Ketan Panigrahi, New Delhi, India
Federica Pascucci, Roma, Italy
Tariq Samad, Minneapolis, USA
Gan Woon Seng, Nanyang Avenue, Singapore
Germano Veiga, Porto, Portugal
Haitao Wu, Beijing, China
Junjie James Zhang, Charlotte, USA

“Lecture Notes in Electrical Engineering (LNEE)” is a book series which reports the latest research and developments in Electrical Engineering, namely:

- Communication, Networks, and Information Theory
- Computer Engineering
- Signal, Image, Speech and Information Processing
- Circuits and Systems
- Bioengineering

LNEE publishes authored monographs and contributed volumes which present cutting edge research information as well as new perspectives on classical fields, while maintaining Springer’s high standards of academic excellence. Also considered for publication are lecture materials, proceedings, and other related materials of exceptionally high quality and interest. The subject matter should be original and timely, reporting the latest research and developments in all areas of electrical engineering.

The audience for the books in LNEE consists of advanced level students, researchers, and industry professionals working at the forefront of their fields. Much like Springer’s other Lecture Notes series, LNEE will be distributed through Springer’s print and electronic publishing channels.

More information about this series at <http://www.springer.com/series/7818>

Damian Mazur · Marek Gołębiowski
Mariusz Korkosz
Editors

Analysis and Simulation of Electrical and Computer Systems

 Springer

Editors

Damian Mazur
Department of Electrical and Computer
Engineering Fundamentals
Rzeszów University of Technology
Rzeszów
Poland

Mariusz Korkosz
Department of Electrical and Computer
Engineering Fundamentals
Rzeszów University of Technology
Rzeszów
Poland

Marek Gołębiowski
Department of Electrical and Computer
Engineering Fundamentals
Rzeszów University of Technology
Rzeszów
Poland

ISSN 1876-1100 ISSN 1876-1119 (electronic)
Lecture Notes in Electrical Engineering
ISBN 978-3-319-63948-2 ISBN 978-3-319-63949-9 (eBook)
<https://doi.org/10.1007/978-3-319-63949-9>

Library of Congress Control Number: 2017948224

© Springer International Publishing AG 2018

This work is subject to copyright. All rights are reserved by the Publisher, whether the whole or part of the material is concerned, specifically the rights of translation, reprinting, reuse of illustrations, recitation, broadcasting, reproduction on microfilms or in any other physical way, and transmission or information storage and retrieval, electronic adaptation, computer software, or by similar or dissimilar methodology now known or hereafter developed.

The use of general descriptive names, registered names, trademarks, service marks, etc. in this publication does not imply, even in the absence of a specific statement, that such names are exempt from the relevant protective laws and regulations and therefore free for general use.

The publisher, the authors and the editors are safe to assume that the advice and information in this book are believed to be true and accurate at the date of publication. Neither the publisher nor the authors or the editors give a warranty, express or implied, with respect to the material contained herein or for any errors or omissions that may have been made. The publisher remains neutral with regard to jurisdictional claims in published maps and institutional affiliations.

Printed on acid-free paper

This Springer imprint is published by Springer Nature
The registered company is Springer International Publishing AG
The registered company address is: Gewerbestrasse 11, 6330 Cham, Switzerland

Preface

This book reports on selected results from the XIII Scientific Conference on Selected Issues of Electrical Engineering and Electronics (WZEE 2016), held on May 04–08, 2016, in Rzeszów, Poland. The Conference was organized by the Rzeszów Division of Polish Association of Theoretical and Applied Electrical Engineering (PTETiS) in cooperation with the Faculty of Electrical and Computer Engineering of the Rzeszów University of Technology.

It presents selected aspects of electrical engineering, electronics and mechatronics, the analysis, synthesis, and applications of which have increasingly become a real challenge for various research communities, ranging from scientists to engineers.

The main aim of the book was to enable the academic community to discuss and present the latest technological advantages and research results, as well as to integrate new interdisciplinary scientific circles in the field of electrical engineering, electronics and mechatronics.

The presented papers cover a wide range of topics:

- Mathematical models of electronic components and systems;
- Methods and tools for modeling and simulation of selected electrical systems;
- New solutions in the field of construction, technology and metrology of electrical engineering;
- Processing, optimization and signal processing;
- Automation and control of electric machines;
- Calculation methods of electromagnetic fields;
- Impact of electromagnetic fields on organisms and the environment;
- New developments in the field of electrical engineering, electronics and related areas;
- Protection of devices against electromagnetic surge; and
- Practical implementations and applications of systems and components.

On the basis of a strict peer review process, 30 papers were selected for this publication (WZEE, May 04–08, 2016). The authors deserve a full appreciation for their high quality and inspiring contributions.

Rzeszów, Poland

Damian Mazur
Marek Gołębiowski
Mariusz Korkosz

Contents

Applications of SiC MOSFETs in AC–DC Converters Dedicated for Distributed Generation Systems	1
S. Piasecki and M.P. Kazmierkowski	
Magnetic Composites in Electric Motors	15
Mariusz Najgebauer, Jan Szczygłowski, Barbara Ślusarek, Marek Przybylski, Andrzej Kapłon and Jarosław Rolek	
Brushless DC Motor with Permanent Magnets for Unmanned Aerial Vehicle Hybrid Drive	29
P. Bogusz, M. Korkosz, J. Prokop and P. Wygonik	
Electromagnetic Review of Rotor/Stator Misalignment in Permanent Magnet Axial Flux Motor	53
Adrian Mlot, Adam C. Malloy, Mariusz Korkosz and Michael Lamperth	
Field-Based Analysis and Optimal Shape Synthesis of Switched Reluctance Motors	71
Paolo Di Barba, Maria Evelina Mognaschi, Marek Przybylski, Najmeh Rezaei, Barbara Slusarek and Sławomir Wiak	
An Analytical Model of an Electrical Machine with Internal Permanent Magnets	87
Tomasz Drabek and Jerzy Skwarczyński	
Analysis and Synthesis of Intelligent System for Electric Mode Control in Electric Arc Furnace	111
Orest Lozynskyy, Andriy Lozynskyy, Yaroslav Paranchuk, Roman Paranchuk, Yaroslav Marushchak and Andriy Malyar	
Passive Stall Control Systems of Power Limitation Modes for Vertical Axis Wind Turbines (VAWT)	131
Ihor Shchur, Andrii Lozynskyy, Bohdan Kopchak, Yurii Biletskyi and Vsevolod Shchur	

Multithreading Analysis of Properties and Electromagnetic Interference in Inductive Contactless Power Supply System with Bidirectional Energy Flow—Part 1: Topology System for Electric Vehicles	161
R.M. Miśkiewicz, A.J. Moradewicz, P. Chudzik and D. Stando	
Review of Structural Solutions in High-Voltage Overhead Power Lines and Possibilities of Reducing Emission of Electromagnetic Fields	173
Zbigniew Wróblewski, Dariusz Sztafrowski and Jacek Gumiela	
Active Power Flow Control on Cross-Border Connections	185
L. Beňa, K. Buczek, P. Ryzd and H. Wachta	
Wind Farm Fluctuation Suppression Using Energy Storage	207
Bartosz Waśkiewicz	
Simulations and Experimental Investigations of an Impulse System for Battery Charging in Electric Bike	219
Krzysztof Ludwinek, Jan Staszak, Roman Nadolski, Zbigniew Gawecki, Jarosław Kurkiewicz and Tomasz Bekier	
Powers Balances in the AC Circuit with Nonlinear Load and Reactive Power Compensation	229
M. Wciślik	
The Analysis of Wind Turbine with Horizontal Rotation Axis with the Use of Numerical Fluid Mechanics	241
Damian Mazur, Mariusz Trojnar and Andrzej Smoleń	
Electrical Circuits of Non-integer Order: Introduction to an Emerging Interdisciplinary Area with Examples	251
Jordan Hristov	
The Electromagnetic Compatibility in Researches of Railway Traffic Control Devices	275
Zofia Wróbel	
The Horn Gap Arresters Modelling in a Lightning Discharge Analysis	289
Zofia Wróbel	
Evaluating the Level of Waveform Distortion	305
Jacek Bartman	
Digital Processing of Frequency–Pulse Signal in Measurement System	319
D. Świsulski, E. Pawłowski and M. Dorozhovets	

Time Analysis of Data Exchange in Distributed Control Systems Based on Wireless Network Model 333
 B. Twaróg, Z. Gomółka and E. Żesławska

Non-Invasive Thermal Methods for the Research and Diagnosis of Electromechanical Objects 343
 B. Twaróg, Z. Gomółka, E. Żesławska and A. Lewicki

Mutual Forces Acting on Chains of Particles 355
 Eugeniusz Kurgan and Piotr Gas

The S_{11} -parameter Analysis of Multi-slot Coaxial Antenna with Periodic Slots 367
 Piotr Gas

The Reliability of Critical Systems in Railway Transport Based on the Track Rail Circuit 377
 Ryszard Mielnik, Maciej Sulowicz, Krzysztof Ludwinek and Marek Jaskiewicz

Research of Cohesion Principle in Illuminations of Monumental Objects 395
 D. Mazur, H. Wachta and K. Leśko

Analysis and Simulation of Internal Transport in the High Storage Warehouse 407
 J. Krystek and S. Alszer

Effectiveness Analysis of Small Hybrid Power Plant with Energy Storage 421
 Andrzej Smolen and Marek Golebiowski

Application for Contactless Objects' Identification by NFC Chips Embedded in Mobile Devices 429
 Bartosz Pawłowicz and Anna Pitera

Applications of SiC MOSFETs in AC–DC Converters Dedicated for Distributed Generation Systems

S. Piasecki and M.P. Kazmierkowski

Abstract This chapter briefly describes possibilities and benefits offered by silicon carbide power transistors, especially SiC MOSFETs, implemented in AC–DC converters dedicated for distributed generation systems. Particular features provided by the wide band gap devices, as high efficiency or high power density, are illustrated by several laboratory prototypes. The chapter presents design parameters of the analyzed demonstrators where different types of SiC MOSFETs are considered. Moreover, experimentally measured efficiency characteristics and current–voltage waveforms are presented for each prototype.

Keywords Silicon Carbide · SiC applications · SiC MOSFETs · Distributed generation · Power converters

1 Introduction

An AC–DC and DC–AC energy conversion is main functionality expected from the power electronic grid interface in distributed generation systems (DGSs). The interfaces mostly the AC–DC converters, e.g., voltage source converters (VSCs), are used. Increasing number of DGSs connected to the grid results in increasing number of power converters [1–4]. Installed AC–DC converters are expected to minimize the cost and volume as well as the reliability and functionality improvement. Introduction of silicon carbide (SiC) power transistors provides new possibilities in this kind of applications [5]. Lower on-state resistances and achieved higher switching frequencies lead to the development of high-efficient and more compact converters [6–10]. Moreover, according to the higher dynamic of the

S. Piasecki (✉) · M.P. Kazmierkowski
Institute of Control and Ind. Electronics, Warsaw University of Technology,
Warsaw, Poland
e-mail: szymon.piasecki@ee.pw.edu.pl

M.P. Kazmierkowski
e-mail: mpk@isep.pw.edu.pl

converter, some additional functionalities realized by control algorithm may be introduced [11]. These benefits have been confirmed by several SiC-based converter prototypes and demonstrators presented last years [12, 13].

Recently many types of SiC transistors have been introduced on the market [5], while parameters of the devices are continuously improved, e.g., increasing nominal current and blocking voltage (3.3 kV transistors are available) of the transistors is observed. For low-voltage, low- and medium-power applications (several kVA), a 1200 V class silicon carbide MOSFETs seems to be very attractive alternative to traditional, Si-based devices. For AC–DC converters in these applications, discrete packages (with 80, 40 or 25 m Ω devices), as well as single and three-phase modules may be considered. Transistors in discrete packages allow to achieve low switching energies. However, despite higher switching energies, single- and three-phase modules are also interesting solution due to better thermal performance and simple mounting.

The discussed chapter presents three different designs of AC–DC converters dedicated for DSGs, utilizing different SiC MOSFET transistors and different packages. Design objectives and strategy, as well as properties of each laboratory demonstrator, are listed and described. Grid-connected operation and efficiency of each prototype are illustrated by selected characteristics and experimental results.

2 SiC-Based AC–DC Converters

2.1 High Efficiency

The first of the analyzed switching devices are 25 m Ω SiC MOSFETs integrated in a three-phase SiC MOSFET module CCS050M12CM2 from Cree. Due to high inductance of the leads, a 16 kHz switching frequency has been selected for nominal operation. The module was implemented for a 10 kVA two-level voltage source converter (VSC) in order to achieve high efficiency and minimized noise generated by magnetic components. To minimize the power losses natural convection cooling system with 220 mm, SK92-type heatsink was applied ($R_{TH} = 0.9$ K/W). The module was attached on the top of the heatsink and equipped with double-sided power board. Two 80 μ F/700 V capacitors provide necessary DC side capacitance, additional fast 1 μ F/1 kV and 150 nF/1 kV capacitors are applied to improve switching performance of SiC MOSFETs. On the top of the power board, six gate drivers are mounted, while additional Zener diodes and damping resistors can be found close to gate–source outputs of the module [10, 14]. Total dimensions of the converter’s power section (221 \times 100 \times 106 mm) lead to the 2.3 dm³ volume and weight equal 2.0 kg. View of the power section (semiconductors with gate drivers, heatsink, and DC-link capacitors) of the converter prototype is presented in Fig. 1.

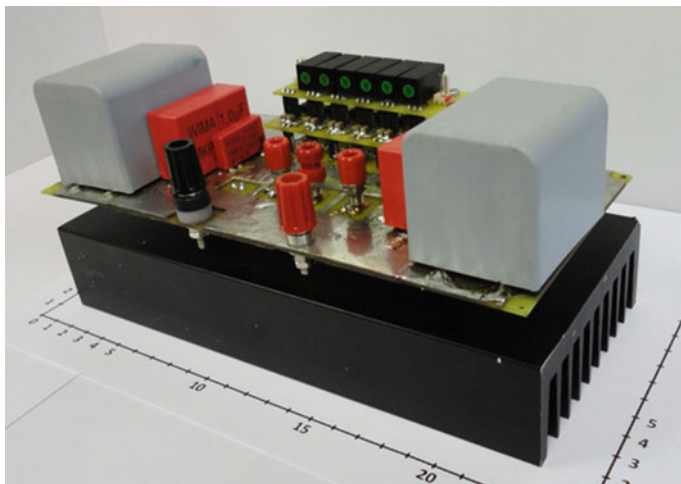


Fig. 1 10 kVA AC–DC converter based on 25 mΩ SiC MOSFET module-view of the laboratory prototype (power section)

Table 1 Parameters of the high efficient AC–DC converter

Parameter		Value	
Rated power	P_N	10	kVA
AC nominal voltage	U_{AC}	230	V
AC nominal current	I_{AC}	14.5	A
DC nominal voltage	U_{DC}	580–700	V
DC nominal current	I_{DC}	14.3–17.3	A
Switching frequency	f_{sw}	16	kHz
Parameters of LCL filter			
Converter side inductor	L_C	1.5	mH
Grid side inductor	L_G	0.1	mH
Filter capacitance	C_{LCL}	5	μF
DC-link capacitance	C_{DC}	162	μF

To assure sufficient power quality of processed energy, the converter is connected to the grid through an LCL filter. Parameters of the filter have been selected for nominal conditions: power equals 10 kVA, 16 kHz switching frequency and $U_{DC} = 700$ V, according to methodology presented in [14, 15]. Parameters of the converter have been collected in Table 1.

The proposed prototype has been connected to the 3×230 V AC grid and verified through series of experimental measurements. Efficiency characteristics of the converter (with LCL filter), for active rectifier and inverter operation modes, have been presented in Fig. 2. Laboratory tests have been performed with usage of Yokogawa WT1806 power analyzer, what assures desired precision of the measurement. In Fig. 2, it can be observed that analyzed design (converter with filter)

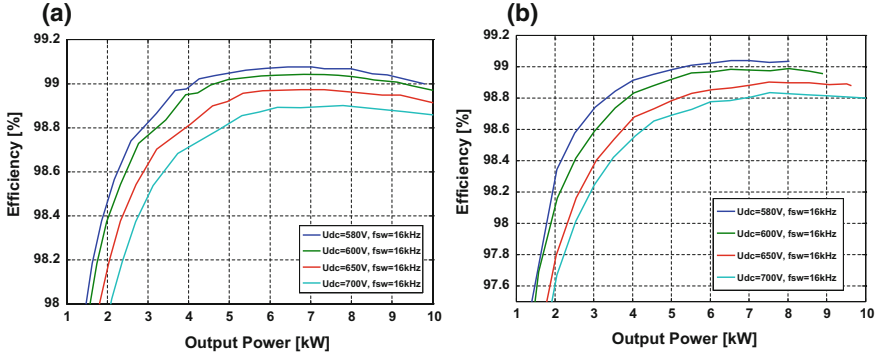


Fig. 2 Efficiency characteristics of the AC–DC converter based on 25 mΩ SiC MOSFET module for: **a** Active rectifier operation. **b** Inverter operation, both with $f_{sw} = 16$ kHz and different values of U_{DC}

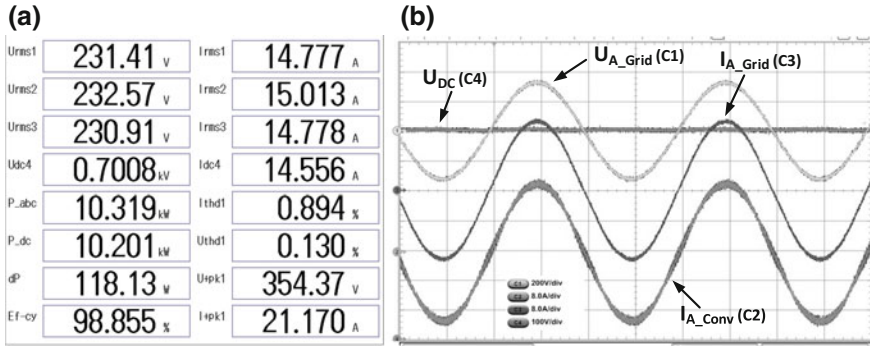


Fig. 3 Active rectifying operation of the AC–DC converter based on 25 mΩ SiC MOSFET module during steady state. Operation conditions: $U_{DC} = 700$ V, $f_{sw} = 16$ kHz, $P_{OUT} = 10.2$ kW. **a** Screen from the Yokogawa power analyzer. **b** Current and voltage waveforms, from the top: grid voltage of phase A (U_{A_Grid}), DC-link voltage (U_{DC}), grid side current of the phase A (I_{A_Grid}), converter side current of the phase A (I_{A_Conv})

reaches efficiency around 99% for nominal power, for both: active rectifier and inverter operation modes. Current and voltage waveforms recorded during experimental investigation, as well as main parameters of the system, have been presented in Figs. 3 and 4. In Fig. 3, active rectifier operation under nominal load is presented, while Fig. 4 shows inverter operation under the same conditions.

To control the grid-connected operation of the AC–DC converter, the direct power control with space vector modulation (DPC-SVM) method is used. More details related to the control method can be found in [11, 14]. It should be stressed that for selected switching frequency (16 kHz), the converter achieves high

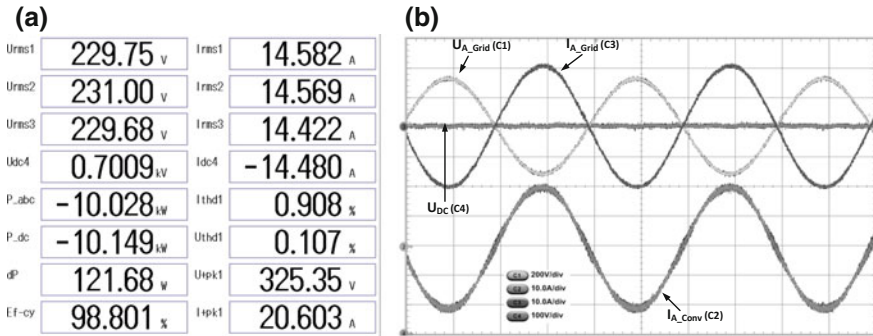


Fig. 4 Inverting operation of the AC–DC converter based on 25 m Ω SiC MOSFET module during steady state. Operation conditions: $U_{DC} = 700$ V, $f_{sw} = 16$ kHz, $P_{OUT} = 10$ kW. **a** Screen from the Yokogawa power analyzer. **b** Current and voltage waveforms, from the top: grid voltage of phase A (U_{A_Grid}), grid side current of the phase A (I_{A_Grid}), DC-link voltage (U_{DC}), converter side current of the phase A (I_{A_Conv})

efficiency and quality of processed energy (current THD on the grid side is below 1%), what were main goals of presented design.

2.2 High Power Density

Other analyzed switching devices were SiC MOSFETs in discrete TO-247 package and 80 m Ω on-state resistance (C2M0080120D from Cree). According to relatively low switching energies of the devices and possible to achieve high switching frequency, these transistors have been implemented for a 20 kVA high power density design. To increase the current of the single device, two power semiconductors have been connected in parallel and controlled as the one switch. Moreover, to improve switching performance of the converter, C4D20120A SiC Schottky diodes have been used as reverse diodes. Power devices are mounted on two heatsinks LAM-5-150 from Fischer Elektronik with forced cooling. Devices of the positive and negative groups are mounted on separated heatsinks to reduce coupling capacitance. All power devices are mounted on the top of the heatsinks and connected to the power board (busbar) that contains positive and negative poles. Middle points of all phases are prepared on separate PCB and wire connections to the filter inductors are placed between the heatsinks. On the top of the busbars, DC-snubbers and DC-link capacitors are mounted (3×100 nF/1000 V, 6×3 μ F/900 V), while main part of the DC-link capacitance is placed close to the input connectors. Other items mounted on the top of the busbars are gate drivers, each of them is designed to control two C2M0080120D transistors at once. The control signal from the external controller is delivered via fiber optics in order to ensure isolation from the power circuit. Driving voltages are 24 and -10 V,

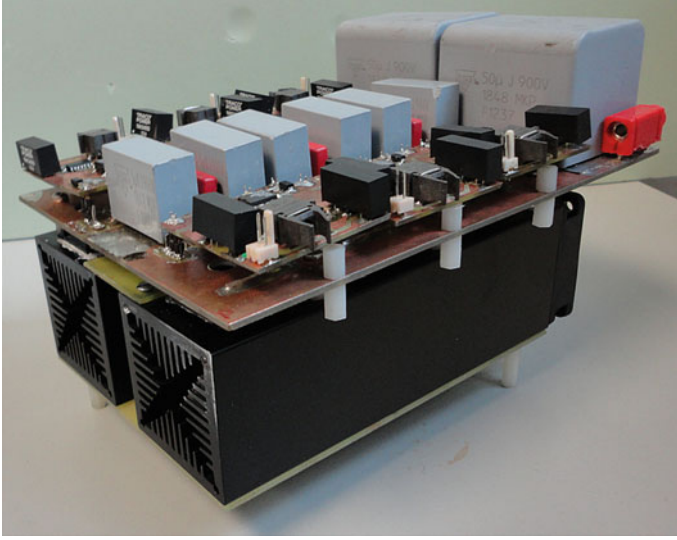


Fig. 5 20 kVA AC–DC converter based on $2 \times 80 \text{ m}\Omega$ SiC MOSFETs in TO-247 package-view of the laboratory prototype

Table 2 Parameters of AC–DC converter with high power density

Parameter		Value	
Rated power	P_N	20	kVA
AC nominal voltage	U_{AC}	230	V
AC nominal current	I_{AC}	28.5	A
DC nominal voltage	U_{DC}	580–700	V
DC nominal current	I_{DC}	28.5	A
Switching frequency	f_{sw}	80	kHz
Parameters of LCL filter			
Converter side inductor	L_C	250	μH
Grid side inductor	L_G	100	μH
Filter capacitance	C_{LCL}	5	μF
DC-link capacitance	C_{DC}	118	μF

respectively, while the receiver and the logic block operate on the voltage levels $-5/-10 \text{ V}$ (with respect to MOSFET source potential). Due to asymmetric supply turn-on and turn-off resistors are selected to be 20 and 6.8Ω , respectively.

The total dimensions of presented power section (without the LCL filter and controller) are $135 \times 200 \times 100 \text{ mm}$ (2.7 dm^3 , power density of power section: 7.40 kW/dm^3), weight is 2.01 kg . View of the prototype is presented in Fig. 5, while main parameters are collected in Table 2.

As in the previous case, to assure sufficient power quality of processed energy and to minimize the distortion of 80 kHz switching, the converter is connected to

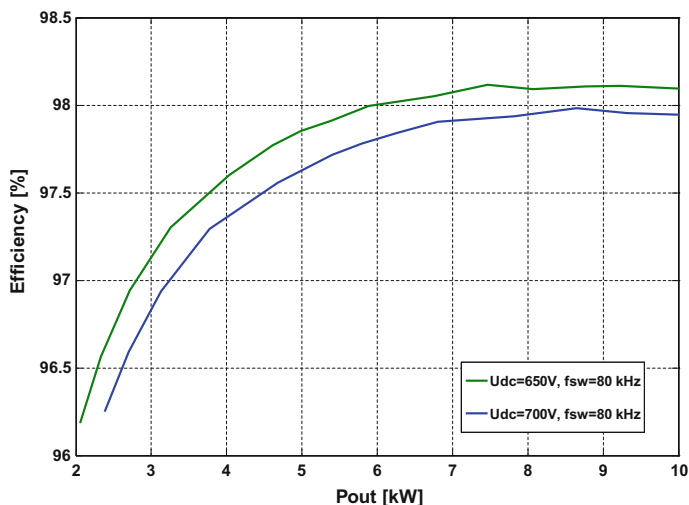


Fig. 6 Efficiency characteristics of the AC–DC converter based on 2×80 m Ω SiC MOSFETs in discrete package; for active rectifier operation with $f_{sw} = 80$ kHz and $U_{DC} = 650$ V, and $U_{DC} = 700$ V

the grid converter through a LCL filter. Parameters of the filter have been selected for nominal conditions: power equals 20 kVA, 80 kHz switching frequency and $U_{DC} = 700$ V, according to methodology presented in [14]. Here, also a direct power control with space vector modulation (DPC-SVM) is used as a control method [11, 14].

The prototype has been connected to the 3×230 V AC grid and verified through series of experimental measurements. Efficiency characteristic of the converter (with LCL filter), for active rectifier operation, has been presented in Fig. 6 (also with usage of Yokogawa WT1806 power analyzer). Due to parallel connection of C2M0080120D transistors, even at 80 kHz switching frequency, the converter achieves high performance with experimentally measured efficiency around 98%. Current and voltage waveforms with main parameters of the operating systems recorded by Yokogawa analyzer, for a 10 kW load and different values DC-link voltage (700 and 650 V), are shown in Fig. 7.

2.3 Universality

The last analyzed switching devices were SiC MOSFETs in discrete TO-247 package and 25 m Ω on-state resistance (C2M0025120D from Cree). These devices provide low on-state resistance and due to discrete package relatively low inductance of the leads, therefore, have been implemented for a 10 kVA AC–DC converter designed as a compromise between high efficiency and high power density.

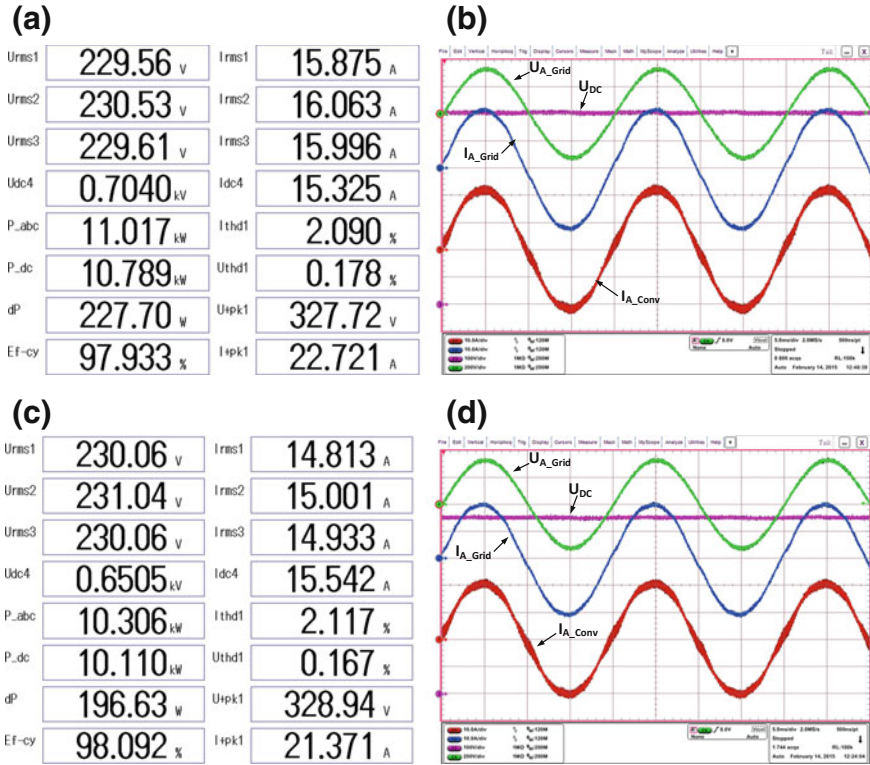


Fig. 7 Active rectifying operation of the AC–DC converter based on 2×80 mΩ SiC MOSFETs during steady state. Operation conditions: **(a, b)** $U_{DC} = 700$ V, $f_{sw} = 80$ kHz, $P_{OUT} = 10.7$ kW; **(c, d)** $U_{DC} = 650$ V, $f_{sw} = 80$ kHz, $P_{OUT} = 10.1$ kW. **(a, c)** Screens from the Yokogawa power analyzer; **(b, d)** current and voltage waveforms, from the *top*: grid voltage of phase A (U_{A_Grid}), DC-link voltage (U_{DC}), grid side current of the phase A (I_{A_Grid}), converter side current of the phase A (I_{A_Conv})

Here also, to improve switching performance of the converter, C4D20120D SiC Schottky diodes have been used as reverse diodes. These features allow the converter to operate with a wide range of switching frequencies, which leads to universality of applications in DGSS.

As in the previous case, the power devices are mounted in two heatsinks LAM-5-150 with air forced cooling. Devices of the positive and negative groups are mounted on separate heatsinks to reduce coupling capacitance. All power devices are mounted on the top of the heatsinks, on the top of the busbars, the DC-snubbers (6×470 nF/1000 V, WIMA MKP4) are mounted, while main part of the DC-link capacitance (2×50 μF/900 V, Vishay 1848 MKP) is placed close to the input connectors. On the top of the power board, 2 PCB bars with gate drivers (for negative and positive groups of the transistors separately) are mounted with additional Zener diodes and damping resistors for each device driver. Each gate driver is supplied from

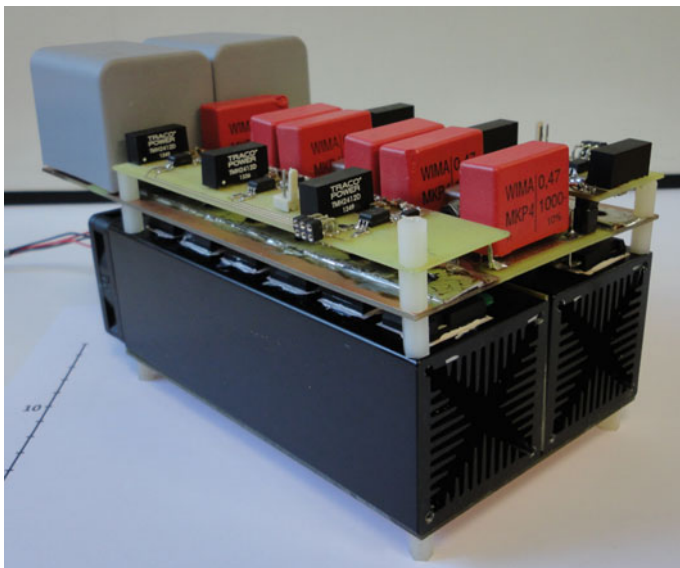


Fig. 8 10 kVA AC–DC converter based on 25 mΩ SiC MOSFETs in discrete TO-247 package-view of the laboratory prototype

Table 3 Parameters of AC–DC converter based on 25 mΩ SiC MOSFETs in TO-247 package

Parameter	Value		
Rated power	P_N	10	kVA
AC nominal voltage	U_{AC}	230	V
AC nominal current	I_{AC}	14.5	A
DC nominal voltage	U_{DC}	580–700	V
DC nominal current	I_{DC}	14.4–17.3	A
Switching frequency	f_{sw}	40	kHz
Parameters of LCL filter			
Converter side inductor	L_C	250	μH
Grid side inductor	L_G	100	μH
Filter capacitance	C_{LCL}	5	μF
DC-link capacitance	C_{DC}	118	μF

the Traco TMH2412D, driving voltages are equal 19 and -5 V. The total dimensions of the power section ($200 \times 101 \times 100$ mm) lead to volume of 2.02 dm^3 (power density of power section: 4.95 kW/dm^3) and weight equals 1.8 kg. The view of the power section of designed prototype is presented in Fig. 8, while main parameters are collected in Table 3. A 40 kHz switching frequency has been selected to provide a compromise between high efficiency and high power density. The converter is connected to the grid through an LCL filter with the same parameters as in case of high power density design. Here also, a direct power control with space vector modulation (DPC-SVM) is used as a control method [14] for grid operation of the converter.

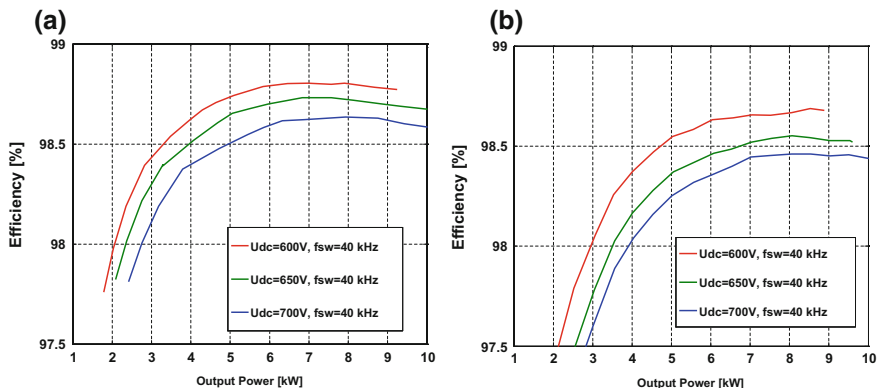


Fig. 9 Efficiency characteristics of the AC–DC converter based on 25 mΩ SiC MOSFET in discrete package, switched at 40 kHz for: **a** Active rectifier operation. **b** Inverter operation both with different values of U_{DC}

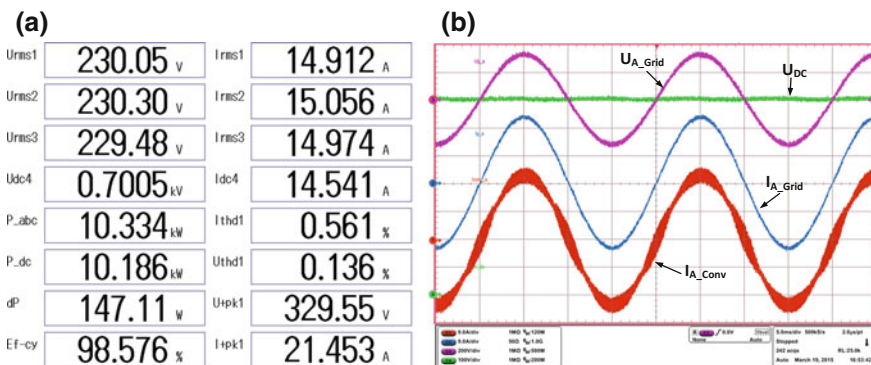


Fig. 10 Active rectifying operation of the AC–DC converter based on 25 mΩ SiC MOSFETs in discrete package during steady state. Operation conditions: $U_{DC} = 700$ V, $f_{sw} = 40$ kHz, $P_{OUT} = 10.1$ kW. **a** Screen from the Yokogawa power analyzer. **b** Current and voltage waveforms, from the *top*: grid voltage of phase A (U_{A_Grid}), DC-link voltage (U_{DC}), grid side current of the phase A (I_{A_Grid}), converter side current of the phase A (I_{A_Conv})

As in previous cases, the prototype has been connected to the 3×230 V AC grid and verified through series of experimental measurements. Efficiency characteristic of the converter including LCL filter, for active rectifier and inverter operation modes, has been presented in Fig. 9 (measurements with Yokogawa WT1806 power analyzer). Due to low on-state resistance of the transistors, even at 40 kHz of switching frequency, the converter achieves high performance with experimentally measured efficiency around 98.7%.

Current and voltage waveforms with main parameters of the operating converter recorded by Yokogawa Analyzer are presented in Figs. 10 and 11. Figure 10 shows

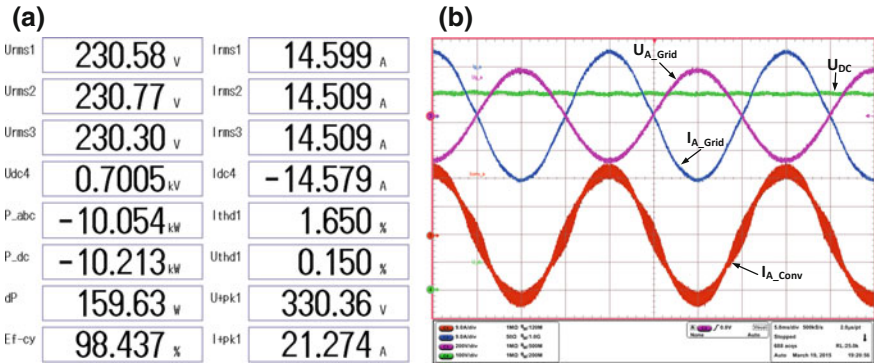


Fig. 11 Inverting operation of the AC-DC converter based on 25 mΩ SiC MOSFETs in discrete package during steady state. Operation conditions: $U_{DC} = 700$ V, $f_{sw} = 40$ kHz, $P_{OUT} = 10$ kW. **a** Screen from the Yokogawa power analyzer. **b** Current and voltage waveforms, from the top: grid voltage of phase A (U_{A_Grid}), DC-link voltage (U_{DC}), grid side current of the phase A (I_{A_Grid}), converter side current of the phase A (I_{A_Conv})

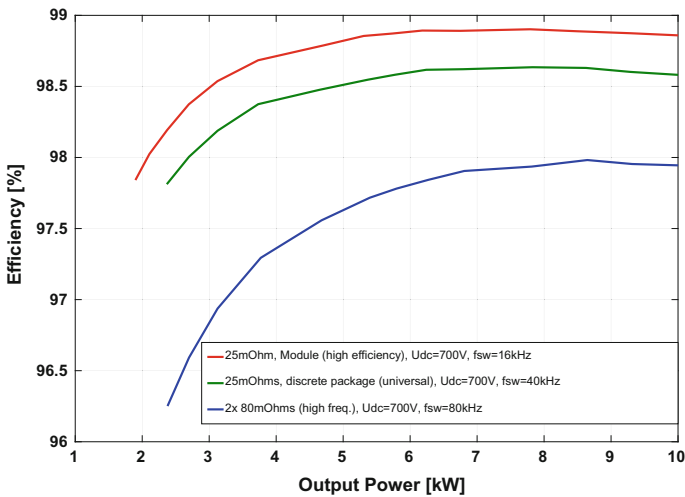
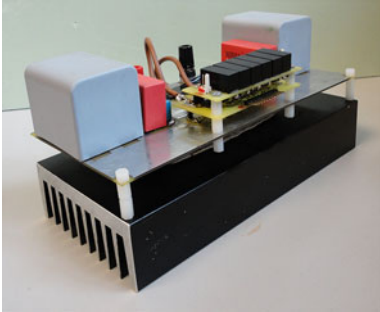




Fig. 12 Efficiency versus output power characteristics of analyzed prototypes. Converters operate as the active rectifiers under nominal conditions with $U_{DC} = 700$ V

operation under nominal load as active rectifier with $U_{DC} = 700$ V and 40 kHz switching frequency. Figure 11 illustrates the same operation conditions but for inverting operation.

Table 4 The main features of the investigated prototypes (with grid side LCL filter) and view of the power sections of particular designs

Parameters of power section	Picture
<p>25 mΩ 3 phase module (high efficiency) Volume: 10.6 (dm³) Power density: 0.94 (kW/dm³) Weight: 15.7 (kg) Cost: 946 (€) Peak efficiency: 99.1% Switching frequency: 16 kHz</p>	
<p>2 \times 80 mΩ discrete package (high power density) Volume: 3.82 (dm³) Power density: 5.23 (kW/dm³) Weight: 5.45 (kg) Cost: 953 (€) Peak efficiency: 98.2% Switching frequency: 80 kHz</p>	
<p>25 mΩ discrete package (universality) Volume: 3.16 (dm³) Power density: 3.16 (kW/dm³) Weight: 5.24 (kg) Cost: 1093 (€) Peak efficiency: 98.8% Switching frequency: 40 kHz</p>	

3 Conclusions

The chapter presents experimental investigation and benefits offered by silicon carbide (SiC) MOSFETs applied in power electronic converters for distributed generation systems. Properties of SiC devices are illustrated by three different prototypes of AC–DC converters. Each converter uses other types of SiC MOSFETs, achieving different features related to efficiency and power density. The experimentally achieved efficiency characteristics and current–voltage waveforms

for all discussed converters operating with 3×230 V AC grid are presented. Each converter is connected to the grid through an LCL filter, and parameters of the filters are selected according to established operation conditions of the converter. Common efficiency characteristics of analyzed converters, for similar operation conditions, are presented in Fig. 12. As it can be observed, according to used type of transistors and value of switching frequency, the high improvement of overall system efficiency may be achieved. However, to achieve higher power density, the switching frequency needs to be increased, what can be observed in Table 4, which presents experimentally obtained parameters and features of the analyzed prototypes (with included parameters of the LCL filters). Analysis of the three different designs, dedicated for different applications with different properties: high efficiency, high power density, universality allow to illustrate and verify potential of SiC power MOSFETs implemented in low-power converters for DGSS.

Acknowledgements This work has been supported by the National Science Center, Poland, based on decision DEC-2012/05/B/ST7/01183.

References

1. Teodorescu, R., Liserre, M., Rodriguez, P.: Grid Converters for Photovoltaic and Wind Power Systems. Wiley, London (2011)
2. Benysek, G., Kazmierkowski, M.P., Popczyk, J., Strzelecki, R.: Power electronic systems as a crucial part of smart grid infrastructure—a survey. Bull. Polish Acad. Sci. Techn. Sci. **59**(4), 455–473 (2011)
3. Teichmann, R., Malinowski, M., Bernet, S.: Evaluation of three-level rectifiers for low-voltage utility applications. IEEE Trans. Ind. Electron. **52**(2), 471–481 (2005)
4. Kolar, J.W., Biela, J., Waffler, S., Friedli, T., Badstuebner, U.: Performance trends and limitations of power electronic systems. In: Proceedings of 6th International Conference on Integrated Power Electronics Systems (CIPS), pp. 1–20 (2010)
5. Rabkowski, J., Pefitsis, D., Nee, H.P.: Silicon carbide power transistors: a new era in power electronics is initiated. IEEE Ind. Electron. Mag. **6**(2), 17–26 (2012)
6. Rabkowski, J., Pefitsis, D., Nee, H.P.: Design steps toward a 40-kVA SiC JFET inverter with natural-convection cooling and an efficiency exceeding 99.5%. IEEE Trans. Ind. Appl. **49**(4), 1589–1598 (2013)
7. Hayashi, Y.: Power density design of SiC and GaN DC-DC converters for 380 V DC distribution system based on series–parallel circuit topology. In: Proceedings of IEEE Applied Power Electronics Conference and Exposition (APEC), pp. 1601–1606 (2013)
8. Zdanowski, M., Pefitsis, D., Piasecki, S., Rabkowski, J.: On the design process of a 6-kVA Quasi-Z-inverter employing SiC power devices. IEEE Trans. Pow. Electron. **31**(11), 7499–7508 (2016)
9. Piasecki, S., Rabkowski, J., Kazmierkowski, M.P.: Application of 25mΩ SiC MOSFETs in a 10kVA grid-connected AC/DC converter. In: Proceedings of 16th International Conference on Silicon Carbide and Related Materials (ICSCRM) (2015)
10. Piasecki, S., Rabkowski, J.: Experimental investigations on the grid-connected AC/DC converter based on three-phase SiC MOSFET module. In: Proceedings of 17th European Conference on Power Electronics and Applications (EPE ECCE Europe), pp. 1–10 (2015)
11. Jasiński, M., Wrona, G., Piasecki, S.: Chapter 3: Control of grid connected converter (GCC) under grid voltage disturbances. In: Orłowska-Kowalska, T., Blaabjerg, F., Rodriguez,

- J. (eds.) *Advanced and Intelligent Control in Power Electronics and Drives*, pp. 91–142. Springer, Switzerland (2014)
12. Piasecki, S., Rąbkowski, J., Wrona, G., Platek, T.: SiC-based support converter for passive front-end AC drive applications. In: *Proceedings of 39th Annual Conference of the IEEE Industrial Electronics Society (IECON)*, pp. 6010–6015 (2013)
 13. Rąbkowski, J., Piasecki, S., Kazmierkowski, M.P.: Design of a three-phase AC/DC converter with paralleled SiC MOSFETs. In: *Proceedings of 6th International Power Electronics and Motion Control Conference and Exposition (PEMC)*, pp. 621–627 (2014)
 14. Piasecki, S.: Research and development of multi-objective optimization procedures for AC–DC grid converters in particular for renewable/distributed energy systems. Ph.D. Thesis, Warsaw University of Technology, pp. 1–229 (2016)
 15. Piasecki, S.: High order line filters for grid connected AC–DC converter—parameters selection and optimization. In: *Proceedings of 23rd IEEE International Symposium on Industrial Electronics (ISIE)*, pp. 2687–2692 (2014)

Magnetic Composites in Electric Motors

Mariusz Najgebauer, Jan Szczygłowski, Barbara Ślusarek,
Marek Przybylski, Andrzej Kapłon and Jarosław Rolek

Abstract Magnetic composites are manufactured as magnetic powder bonded by dielectric material, which bond and insulate powder grains. Magnetic composites are applied in electric machines due to their favorable magnetic and mechanical properties as well as possibility of tailoring their physical properties. The paper is a review of soft and hard magnetic composites, their internal structure, properties, and advantages resulted from their application on magnetic circuits of electric motors.

Keywords Magnetic composites · Magnetic and mechanical properties · Electric motors

1 Introduction

Electric motors are devices with relatively high conversion efficiency of electrical energy into mechanical. Further increase of electric motors efficiency could be obtained by an appropriate selection of materials for magnetic circuits, what results

M. Najgebauer (✉) · J. Szczygłowski
Częstochowa University of Technology, Częstochowa, Poland
e-mail: najgebauer@el.pcz.czest.pl

J. Szczygłowski
e-mail: jszczyg@gmail.com

B. Ślusarek · M. Przybylski
Tele and Radio Research Institute, Warsaw, Poland
e-mail: barbara.slusarek@itr.org.pl

M. Przybylski
e-mail: marek.przybylski@itr.org.pl

A. Kapłon · J. Rolek
Kielce University of Technology, Kielce, Poland
e-mail: akaplon@tu.kielce.pl

J. Rolek
e-mail: jrolek@tu.kielce.pl

in a reduction of power losses. In previous paper [1], the impact of the application of modern soft magnetic materials, such as 6.5% Si-Fe steels or amorphous alloys, on power losses generated in electric motors has been analyzed. The anisotropy of magnetic properties, which determines usefulness of the material for construction of magnetic circuits in electric motors, was also discussed. However, it should be noted that despite the favorable magnetic properties of analyzed materials, these have a complicated and expensive production technology.

Designers of electric motors are still looking for new materials that allow them to design electric devices with new structures of magnetic circuits. Such types of materials are magnetic composites, which are produced by bonding magnetic powder by a dielectric material. Magnetic composites have a lot of advantages such as good magnetic and mechanical properties, high resistivity as well as abilities: to tailor physical properties of composites, to produce elements with complicated shapes with high dimensional accuracy, to produce isotropic magnetic circuits with three-dimensional distribution of magnetic flux, to magnetize isotropic permanent magnets in all direction and multipolarly, to produce hybrid elements (i.e., elements with at least two areas having different physical properties), to mechanical forming in the case of prototyping devices and finally—easy recycling and small powder waste.

The use of magnetic composites allows often reducing the volume of magnetic circuits of electric machines, their appropriate shaping and it improves the efficiency of electric units working at a frequency above 300 Hz.

The present paper is focused on production technology of soft and hard magnetic composites, their chosen magnetic and mechanical properties as well as advantages resulted from their application in new construction of electric motors.

2 Technology Production of Magnetic Composites

The main component of magnetic composites is magnetic powder that could be obtained by mechanical or physicochemical methods, such as, e.g., milling of magnetic alloys or by atomization of materials from liquid phase [2–4]. Soft magnetic powders are generally produced by atomization of liquid metal or its alloy. Hard magnetic powders are usually produced by the ingot crushing method, mechanical synthesis or hydrogenation methods. In the case of Nd-Fe-B powders, the most commonly used method is based on the milling of magnetic ribbons obtained by rapid solidification of melt alloy (Melt spun ribbon).

Magnetic powder grains could be coated with a binder during the powder preparing process or alternatively—a mixture of magnetic powder, a binder, and a lubricant are prepared. Binders are used in the preparing of magnetic composites in order to bond powder grains. Binders are dielectrics and create an insulating layer on a surface of powder grains. Photographs of metallographic structures of magnetic composites are depicted in Fig. 1.

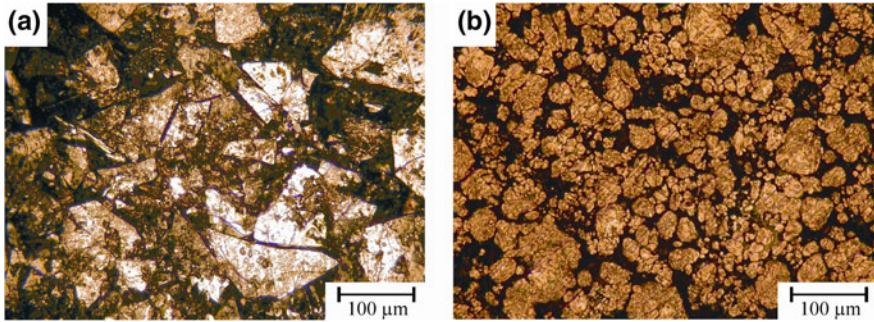


Fig. 1 Metallographic structure of Nd-Fe-B hard magnetic composite (a) and iron powder based soft magnetic composite (b), zoom 100 \times [19]

3 Physical Properties of Magnetic Composites

Magnetic, electrical, and mechanical properties of magnetic composites depend on many factors, of which the most important are magnetic properties of powder, size of powder grains, amount, and type of the binder and admixtures, manufacturing technology, and parameters of process (pressure and temperature) [4–21].

Referring to magnetic properties of the powder, two main types of composites can be specified: soft magnetic composites or dielectromagnetics (manufactured from powders of pure iron, soft ferrites and Fe-P, Fe-Si and Fe-Ni alloys) and hard magnetic composites, known as bonded magnets or dielectromagnets (manufactured from powders of Ba- and Sr-based ferrites, Al-Ni-Co, Sm-Co alloys or nanocrystalline Nd-Fe-B alloys) [2, 5, 6, 9, 22, 23].

3.1 Soft Magnetic Composites

Soft magnetic composites are usually manufactured by pressing grains of soft magnetic powder and dielectric binder [6, 19, 23]. The magnetic parameters of soft magnetic composites made of Somaloy 500 powder are shown in Fig. 2 as an example.

A dielectric binder is used in magnetic composites for bonding powder grains and for creating an insulating layer on their surfaces. Powder grains are insulated from each other, what affects significantly physical properties of the material. Dielectric layers are responsible for an increase in resistivity of the magnetic composite and—due to a limitation of eddy current flows—for power losses reduction, especially at higher frequencies. An increase of a dielectric content in the composite makes its magnetic properties worse (lower saturation induction and maximum magnetic permeability), but at the same time, it improves its mechanical properties [3, 6, 11–14, 17, 18, 23–25]. The influence of dielectric volume content

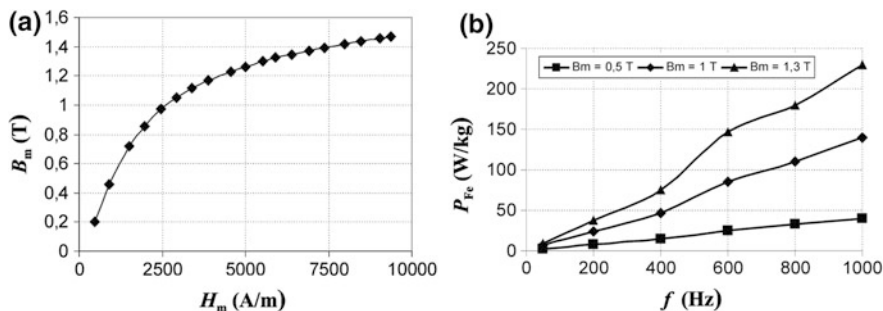


Fig. 2 Magnetic properties of the Somaloy 500 + 0.5% Kenolube composite: magnetization curve at 50 Hz (a), frequency dependence of losses at different values of induction (b) [19]

Table 1 Chosen magnetic properties of the Silame-type composite [3]

Magnetic parameter	Volume content of dielectric				
	14 vol.%	17 vol.%	20 vol.%	25 vol.%	33 vol.%
B_S (T)	0.72	0.60	0.54	0.51	0.50
μ_{max} (-)	34.7	30.8	33.4	24.3	16.1

on chosen magnetic properties of composite from Silame to nanocrystalline iron-based alloy powder is presented in Table 1.

Physical properties of magnetic composites also depend on the technological parameters, associated with the preparation of magnetic powder (size of grains) as well as the element forming (e.g., pressure and curing temperature) [3, 18–20, 25]. The grains size has a significant impact on the density of compacts. Fine powders have a high internal friction coefficient, which causes losses of the compression pressure and the lower density of a compact. In the case of larger grains, the number of air gaps is lower. Thus, the best physical properties of composites are obtained for magnetic powder with relatively high distribution of grain size.

The properties of magnetic composites manufactured in the pressing process strongly depend on the compacting pressure. The higher compacting pressure causes the lower number and volume of air gaps, what improves magnetic and mechanical properties of the composite. Physical properties of composites also depend on the curing temperature, which is determined by the type of binding materials. If the curing temperature is too high, the insulating layers of grains can be damaged, what causes higher power losses [6, 11–16, 19, 24, 25]. Exemplary influences of the technological parameters on magnetic and mechanical properties of the soft magnetic composite made of the Somaloy 500 powder + 0.6% LB1 are depicted in Figs. 3 and 4.

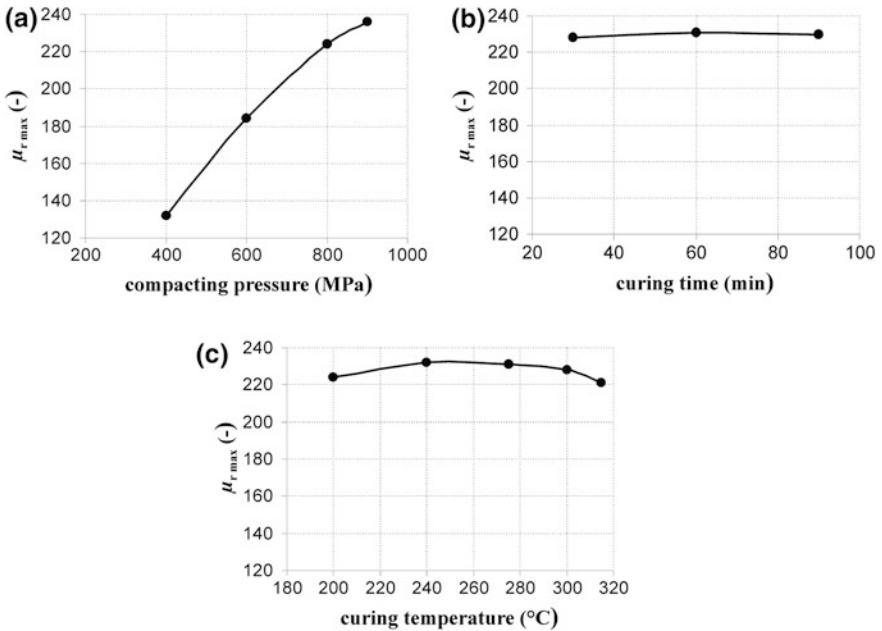


Fig. 3 The influence of technological parameters on maximum magnetic permeability for the soft magnetic composite made of the Somaloy 500 powder + 0.6% LB1: as a function of the compacting pressure (a), as a function of the curing time (b) and as a function of the curing temperature at 50 Hz (c) [19]

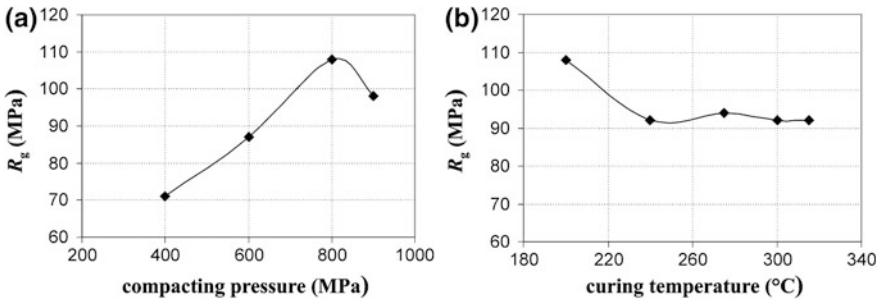


Fig. 4 The influence of the compacting pressure (a) and the curing temperature (b) on the bending strength for the soft magnetic composite made of the Somaloy 500 powder + 0.6% LB1 [19]

3.2 Hard Magnetic Composites

Hard magnetic composites (bonded magnets, dielectromagnets) are obtained by bonding of hard magnetic powder with dielectric, for example with epoxy resin or a polyamide. The final products are mostly manufactured in the pressing or the

injection moulding technologies. As in the case of soft magnetic composites, parameters of the technological process have significant influence on physical properties of bonded magnets. The properties of bonded magnets can be also tailored by appropriate doping of their composition with different types of magnetic and/or nonmagnetic powders as well as by changing the manufacturing parameters [2, 5, 9, 20–22, 26–28].

The bonded magnets are mainly manufactured from powdered Nd–Fe–B nanocrystalline ribbons. The Nd–Fe–B composites have for some applications insufficient mechanical properties as well as a negative temperature coefficient of coercivity TK (H_{cJ}). Mechanical properties of Nd–Fe–B composites can be improved by increasing the binder content or by doping their composition with the other metallic powders, e.g., iron powder.

Basic parameters of the bonded magnets manufacture are compacting pressure and curing temperature—for the pressing technology, and injection pressure and temperature—for the injection technology. In the case of pressing composites, the mixture of magnetic powder, binders, and admixtures is formed in the matrix under the pressure of 700–900 MPa. Next, the obtained compact is cured at temperature, which depends on the binder type. Using epoxy resin, the curing temperature ranges from 160 up to 200 °C, whereas in the case of injection composites, the curing temperature for polyamide is about 270 °C. The manufacturing parameters have a crucial influence both on magnetic and mechanical properties of bonded magnets, what is shown in Fig. 5 [19].

The injection temperature has a major impact on their mechanical properties (e.g., bending and compression strengths) of bonded magnets manufactured in the injection technology [20].

In the case of Nd–Fe–B pressing composites, an increase in the epoxy resin content improves their mechanical properties, but at the same time, it causes deterioration of magnetic ones and an increase in materials resistivity. Example of influence of content of epoxy resin is shown in Fig. 6 [19, 20].

The doping of the composition of Nd–Fe–B magnets with iron powder results in their higher hardness, as well as bending strength and compression strength.

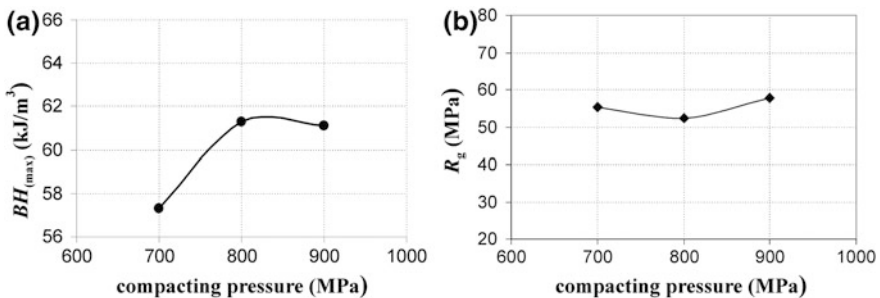


Fig. 5 The influence of the compacting pressure on the maximum magnetic energy product (a) and the bending strength (b) for the Nd–Fe–B bonded magnet [19]

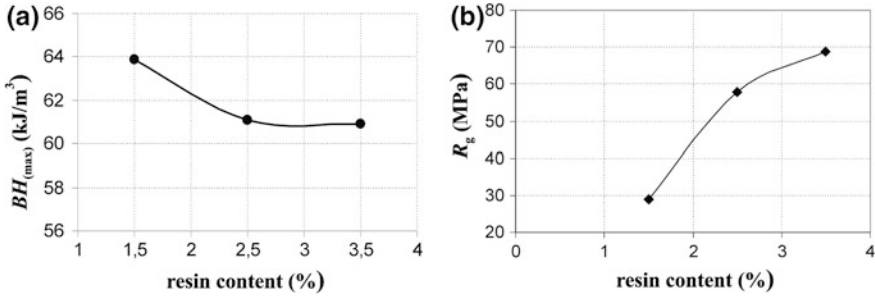


Fig. 6 The influence of the epoxy resin content on the maximum magnetic energy product (a) and the bending strength (b) for the Nd-Fe-B bonded magnet [19]

Table 2 The influence of iron doping on magnetic and mechanical properties of the Nd-Fe-B composite [28]

Iron powder content (wt.%)	Magnetic and mechanical properties				
	B_r (T)	H_{cB} (kA/m)	$(BH)_{max}$ (kJ/m ³)	R_C (MPa)	HBW (-)
0	0.724	448.5	84.6	112.1	35.0
5	0.694	385.9	66.1	118.8	36.6
10	0.690	349.8	62.6	130.6	37.1
15	0.684	314.0	51.8	136.2	37.7

HBW Brinell hardness, R_C bending strength

However, it worsens magnetic properties of the magnets. In particular, it makes magnetic coercivity significantly lower [9, 20, 28]. The influence of the iron doping on properties of the Nd-Fe-B composite is presented in Table 2.

The iron doping of Nd-Fe-B magnets composition reduces the production costs. It should be noted that Nd-Fe-B composites doped by iron powder are placed between cheap ferrite magnets with weak magnetic properties and more expensive pure Nd-Fe-B composites. The appropriate doping of the bonded magnet composition allows tailoring their properties in order to adopting them to requirements of electric machine constructions.

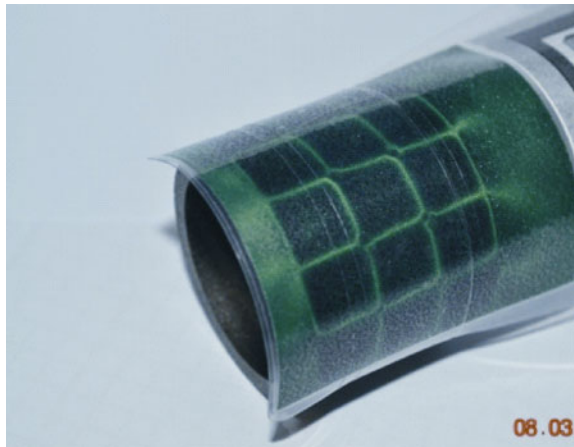
A temperature coefficient of coercivity TK (H_{cJ}) has a major impact on working conditions of permanent magnets at high temperatures. A negative value of the TK (H_{cJ}) coefficient indicates that magnetic parameters become worse with increase of temperature. This property limits the use of bonded magnets at higher temperatures. The TK (H_{cJ}) coefficient can be improved by doping the composite composition with ferrite or AlNiCo powders, which have positive values of the TK (H_{cJ}) coefficient. However, a higher content of these powders causes significant deterioration of magnetic properties of bonded magnets [20, 21, 26–28].

The powder metallurgy, in particular, the bonding method, makes it possible to produce hybrid elements, i.e., elements having areas of different physical properties. These elements can be made from soft, hard or nonmagnetic powders.



Fig. 7 Samples of hybrid elements [20]

Fig. 8 Multipolar bonded magnets manufactured by Tele and Radio Research Institute



The manufacturing of hybrid elements in a single technological process allows the electric motors constructors to design new structures of magnetic circuits [20]. Exemplary hybrid elements made of soft (iron) and hard (Nd–Fe–B) magnetic powders are depicted in Fig. 7.

Hard magnetic composites might exhibit isotropic or anisotropic properties. Commercially produced composites are usually isotropic ones. These can be magnetized in all direction or/and even multipolarly. The sample of multipolar bonded magnet is depicted in Fig. 8.

4 Examples of Magnetic Composites Application

Soft magnetic composites are alternative core materials, comparing to soft ferrites and electrical steel sheets. Soft ferrites have lower power losses at higher frequency, but also lower values of saturation induction, what causes large dimension of

Fig. 9 Application areas of soft magnetic composites [29]

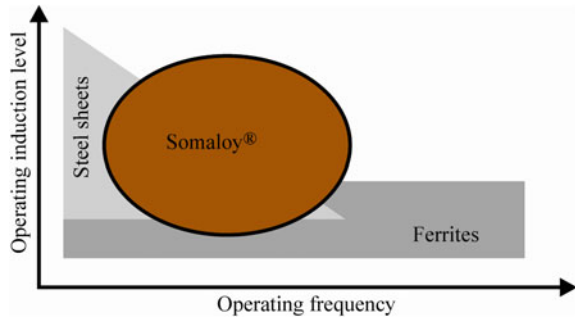


Table 3 Parameters of synchronous motors [32]

Parameters	Materials of stator cores		
	Fe–Si steel	Somaloy 500	Somaloy 500 (optimized core)
P_n (W)	10.66	10.66	10.66
M_n (mN m)	34	34	34
P_{Fe} (W)	3.72	6.78	4.57
η (%)	41	37	40.5

magnetic cores. On the other hand, electrical steel sheets have high values of saturation induction (about 2 T), but their application at higher frequency is restricted due to high values of power losses related to eddy currents. Soft magnetic composites due to unique combination of magnetic properties can be used in application areas restricted for conventional soft magnetic materials, what is depicted in Fig. 9 [29–31].

Direct replacement of a magnetic core made of conventional materials (soft ferrites or electrical steels) by a composite core is not effective, due to worse properties of magnetic composites comparing to conventional materials. The effective use of magnetic composites requires redesign of the electric devices, taking advantages and limitations of these materials into consideration [5, 7, 12, 23, 30–32]. In the case of a single-phase synchronous motor, a direct replacement of the stator core made of electrical steel by the composite core (Somaloy 500) of the same dimensions results in higher power losses and lower efficiency. The optimizing design of the stator core allows reducing power losses and increasing the motor efficiency [32]. Parameters of synchronous motors with different materials of a stator core are compared in Table 3.

Another example of soft magnetic composite applications is the yokeless stator of the disk motor with permanent magnets type YASA (Yokeless And Segmented Armature). In this construction, a stator yoke is replacement by the coils with cores made of Somaloy 3P. The motor bars can carry a no-load flux of 1.5 T and a peak-load flux of 1.8 T, which are under the saturation limit of the Somaloy 3P composite (about 2 T). This construction allows reducing the stator mass of 50% and obtaining the motor efficiency above 94% for a wide speed range. Moreover, the YASA motors

have about 20% higher electromagnetic torque density, compared to typical constructions of disk motors with permanent magnets [33].

The optimized design of magnetic circuit constructions with the use of magnetic composites allows reduction in weight and volume of electric devices as well as for significant reduction of the number of used parts—only a few elements are required [6, 23, 25, 29–31], as depicted schematically in Fig. 10 [34].

Hard magnetic composites are generally used as permanent magnets in small electric motors. The main advantage of these composites is the ability to tailor their properties by doping the composition or by appropriate selection of manufacturing parameters. It can be presented for the 5 W DC motor with permanent magnet excitation, produced commercially by MIKROMA S.A. The motor body was equipped with the bonded magnets made of Nd–Fe–B powder and Nd–Fe–B powder doped with strontium ferrite powder. The magnetic properties of these bonded magnets are presented in Table 4. Each of the DC motors has different bonded magnets and rotor windings. An impact of the bonded magnet type on the motor operating parameters is presented in Table 5. The motor with permanent magnets made of the pure Nd–Fe–B powder and the 75 wt.% Nd–Fe–B + 25 wt.%

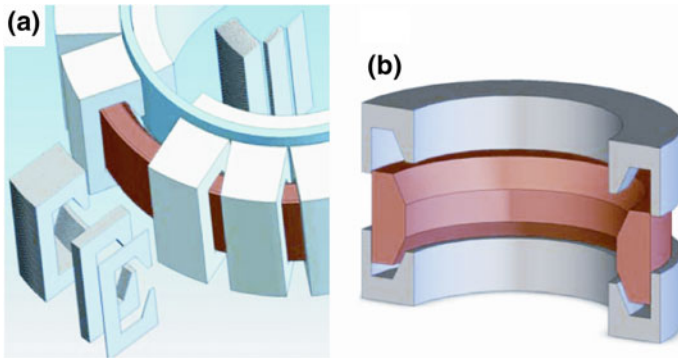


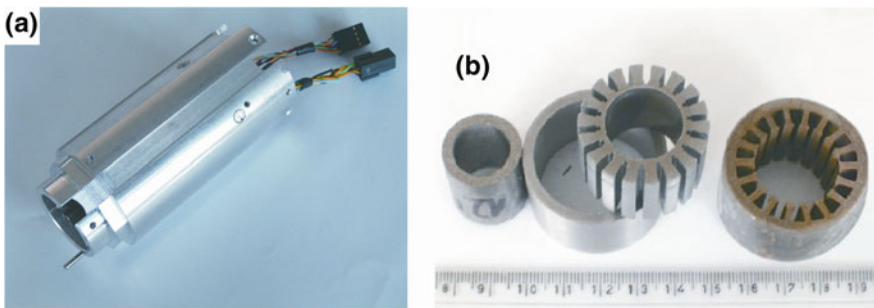
Fig. 10 Parts used in the tubular linear synchronous motor for magnetic circuits: made of electrical steels (a) and made of soft magnetic composites (b) [34]

Table 4 Magnetic properties of ferrite and composite magnets [27]

Magnet materials	Magnetic properties		
	B_r (T)	H_{cB} (kA/m)	$(BH)_{max}$ (kJ/m ³)
Sintered strontium ferrite	0.36	278	26.3
50 wt.% Nd–Fe–B + 50 wt.% strontium ferrite	0.30	192	15.7
75 wt.% Nd–Fe–B + 25 wt.% strontium ferrite	0.44	304	35.2
100% Nd–Fe–B	0.62	456	72.0

Table 5 Chosen operating parameters of the DC motors [27]

Magnet materials	Operating parameters					
	U (V)	I (A)	Torque (N m)	Rotation speed (rpm)	P (W)	η (%)
Sintered strontium ferrite	12	0.800	0.01	5000	5.00	52.0
50 wt.% Nd–Fe–B + 50 wt.% strontium ferrite	24	0.930	0.03	2911	8.93	40.0
75 wt.% Nd–Fe–B + 25 wt.% strontium ferrite	24	0.846	0.03	3700	11.38	57.0
100% Nd–Fe–B	24	0.750	0.03	3693	11.36	63.2

**Fig. 11** The body of a DC brushless motor for electro-tools (a) and its soft and hard magnetic composites (b) [20]

strontium ferrite powder have the motor power higher than 11 W, whereas for the 50 wt.% Nd–Fe–B + 50 wt.% strontium ferrite powder—the motor power is about 9 W. In all cases, the achieved powers are comparable to the power of the commercial 10 W DC motor of larger dimensions. Thus, the appropriate selection of the bonded magnet composition and the rotor windings allows producing DC motors of the same body and different powers [27].

Summarizing, the research on properties and applications of soft and hard magnetic composites demonstrate that these can be successfully applied in electric motors for the automotive industry, electro-tools, household devices or battery operated trucks [19, 20]. Figures 11 and 12 show the exemplary brushless motors with elements made of magnetic composites. Both motors have passed operational tests.

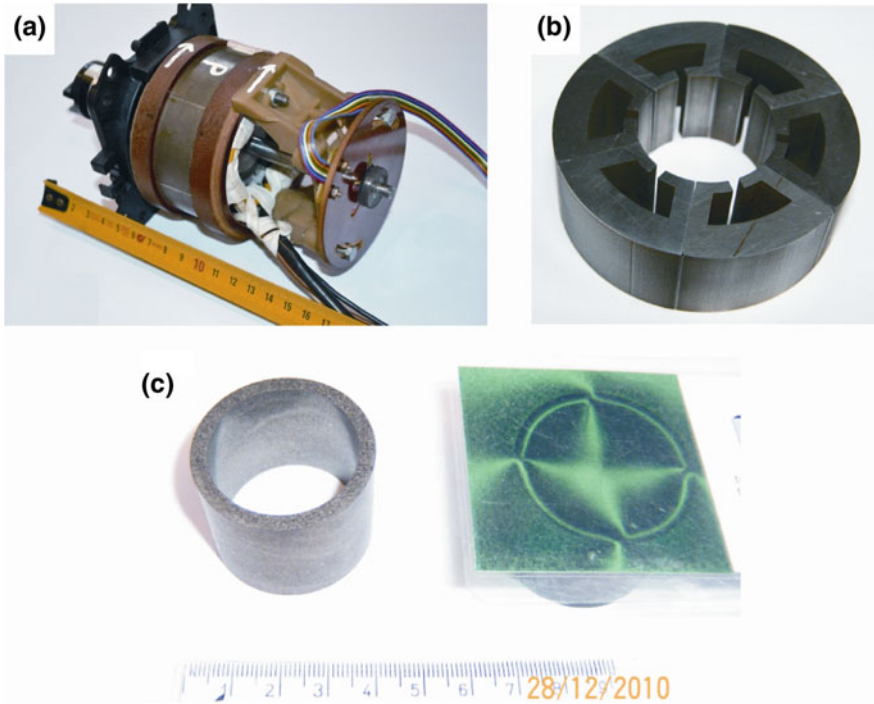


Fig. 12 A DC brushless motor for household devices (a), soft magnetic composites (b), four-pole permanent magnet made of Nd-Fe-B composite [19]

5 Conclusions

The paper shows properties of soft and hard magnetic composites as well as their advantages from applications in electric motors. Magnetic composites have a unique combination of magnetic and mechanical properties. Moreover, these properties can be tailored by the appropriate selection of the composition and the manufacturing parameters. The properties of magnetic composites allow the constructors to design new structures of their magnetic circuits, which are better adapted to the customer requirements and can allow reducing a size and weight of electric motors. The review of soft and hard magnetic composites shows designers of electric motors possibilities of applications of new types of soft and hard magnetic materials in future constructions of electric machines.

References

1. Najgebauer, M., Szczygłowski, J., Kaplon, A.: Soft magnetic materials for energy-efficient electric motors. In: 12th Conference on Selected Problems of Electrical Engineering and Electronics WZEE'2015, pp. 115–118. Kielce. <http://ieeexplore.ieee.org> (2015)
2. Ślusarek, B.: Powder magnetic materials. *Prz. Elektrotechniczn.* **4**, 16–19 (2010)
3. Konieczny, J., Dobrzański, L.A., Wysłocki, J.J., Przybył, A.: Magnetycznie miękkie materiały kompozytowe polimer-cząstki proszku stopu $\text{Co}_{68}\text{Fe}_4\text{Mo}_1\text{Si}_{13,5}\text{B}_{13,5}$ (Soft magnetic composite materials polymer-particles powder $\text{Co}_{68}\text{Fe}_4\text{Mo}_1\text{Si}_{13,5}\text{B}_{13,5}$ alloy). *Composites* **6**, 81–84 (2006)
4. Biało, D.: Wytwarzanie kompozytów w procesach metalurgii proszków (Manufacturing of composites by the powder metallurgy route). *Composites* **1**, 89–92 (2001)
5. Węgliński, B.: Rozwój magnetycznych kompozytów proszkowych w Politechnice Wrocławskiej (Development of magnetic powder composites at Wrocław University of Technology). *Stud. Mater.* **58**, 89–98 (2005)
6. Dobrzański, L.A., Drak, M., Ziębowicz, B.: Manufacturing, properties and application of composite materials with specific magnetic properties. *Arch. Mater. Sci.* **29**, 159–167 (2008)
7. Website of Höganäs, Sweden. <http://www.hoganas.com>
8. Drak, M., Ziębowicz, B., Dobrzański, L.A.: Manufacturing of hard magnetic composite materials Nd–Fe–B. *JAMME* **31**, 91–95 (2008)
9. Dobrzański, L.A., Drak, M.: Hard magnetic composite materials Nd–Fe–B with additions of iron and X2CrNiMo-17-12-2 steel. *J. Alloys Compd.* **449**, 88–92 (2008)
10. Pang, Y.X., Hodgson, S.N.B., Koniarek, J., Węgliński, B.: The influence of the dielectric on the properties of dielectromagnetic soft magnetic components. Investigations with silica and silica hybrid sol–gel derived model dielectric. *J. Magn. Magn. Mater.* **301**, 83–91 (2007)
11. Jansson, P.: SMC materials—including present and future applications. In: World Congress on Powder Metallurgy and Particulate Materials PM2TEC'2000. New York, USA. <http://www.hoganas.com> (2000)
12. Hultman, L.O., Jack, A.G.: Soft magnetic composites—motor design issues and applications. In: World Congress on Powder Metallurgy and Particulate Materials PM2TEC'2004. Chicago, USA. <http://www.hoganas.com> (2004)
13. Zhou, Y., Hultman, L.O., Kjellén, L.: Production aspects of SMC components. In: World Congress of Powder Metallurgy PM 2004. Vienna, Austria. <http://www.hoganas.com> (2004)
14. Hultman, L.O., Persson, M., Engdahl, P.: Soft magnetic composites for advanced machine design. In: Promoting Powder Metallurgy in Asia PMAAsia'2005. Shanghai, China. <http://www.hoganas.com> (2005)
15. Andersson, O.: Iron powder in electrical machines, possibilities and limitations. In: World Congress on Powder Metallurgy and Particulate Materials PM2TEC'2001. New Orleans, USA. <http://www.hoganas.com> (2001)
16. Pennander, L.-O., Jack, A.G.: Soft magnetic iron powder materials. AC properties and their applications in electrical machines. In: International Congress and Exhibition EUROPM'2000. Valencia, Spain. www.hoganas.com (2000)
17. Ślusarek, B., Przybylski, M.: The influence of kind of powder on physical properties of soft magnetic composites. In: International Powder Metallurgy Congress and Exhibition EUROPM'2009. Copenhagen, Denmark (2009)
18. Nowosielski, R., Wysłocki, J.J., Wnuk, I., Gramatyka, P.: Nanocrystalline soft magnetic cores. *J. Mater. Process. Technol.* **175**, 324–329 (2006)
19. Przybylski, M.: Zastosowanie proszkowych materiałów magnetycznych w maszynach elektrycznych (Application of powder magnetic materials in electric machines). Ph.D. dissertation (2012)
20. Ślusarek, B.: Nowoczesne proszkowe kompozyty magnetyczne w zastosowaniu do maszyn i urządzeń elektrycznych (New powder magnetic composites in application to electric machines and devices). Tele and Radio Research Institute, Warsaw (2012)

21. Ślusarek, B.: Dielektromagnes prasowany (Compacted dielectromagnet for use in electric engineering). Patent PL 197344 B1 (2008)
22. Ślusarek, B., Gawryś, P., Przybylski, M.: New PM magnetic developments. *Met. Powder Rep.* **64**, 18–24 (2009)
23. Shokrollahi, H., Janghorban, K.: Soft magnetic composite materials (SMCs). *J. Process. Technol.* **189**, 1–12 (2007)
24. Dobrzański, L.A., Ziębowicz, B., Drak, M.: Mechanical properties and the structure of magnetic composite materials. *JAMME* **18**, 79–82 (2006)
25. Ziębowicz, B., Szewieczek, D., Dobrzański, L.A.: New possibilities of application of composite materials with soft magnetic properties. *JAMME* **20**, 207–210 (2007)
26. Ślusarek, B., Kordecki, A.: Zastosowanie domieszkowanych dielektromagnesów NdFeB w silnikach prądu stałego (Applying of dielectromagnets NdFeB with metallic additions in DC Motors). *Prace Naukowe Instytutu Maszyn, Napędów i Pomiarów Elektrycznych Politechniki Wrocławskiej*, 48/20, 192–197, Wrocław (2000)
27. Ślusarek, B., Dudzikowski, I.: Application of permanent magnets made from NdFeB powder and from mixtures of powders in DC motors. *J. Magn. Magn. Mater.* **239**, 597–599 (2002)
28. Dobrzański, L.A., Drak, M.: Properties of composite materials with polymer matrix reinforces with Nd–Fe–B hard magnetic particles. *J. Process. Technol.* **175**, 149–156 (2006)
29. Brochure 1/2009: Somaloy[®] Technology. Compact, light and cost-efficient solutions. Höganäs AB, Sweden. <http://www.hoganas.com> (2009)
30. Andersson, O., Hofecker, P.: Advances in soft magnetic composites—materials and applications. In: *The International Conference on Powder Metallurgy and Particulate Materials PowderMet'2009*. Las Vegas, USA. <http://www.hoganas.com> (2009)
31. Hultman, L.O., Andersson, O.: Advances in SMC technology—materials and applications. In: *International Congress and Exhibition EUROPM'2009*. Copenhagen, Denmark. <http://www.hoganas.com> (2009)
32. Petkovska, L., Cvetkovski, G.: Soft magnetic composite core—a new prospective for small AC motors design. In: *EuroCon'2009*. Saint Petersburg, Russia. <http://www.docstoc.com> (2009)
33. Woolmer, T.J., McCulloch M.D.: Analysis of the yokeless and segmented armature machine. In: *IEEE International Electric Machines and Drives Conference*, pp. 704–708. Antalya, Turkey (2007)
34. Pennander, L.-O., Nord, G., Maezawa, K., Saito, M., Berchowitz, D.: Design of soft magnetic composite components for tubular linear motors. In: *Motor and Drive System Conference*. Miami, USA. www.hoganas.com (2006)

Brushless DC Motor with Permanent Magnets for Unmanned Aerial Vehicle Hybrid Drive

P. Bogusz, M. Korkosz, J. Prokop and P. Wygonik

Abstract Hybrid drive for a small unmanned aerial vehicle (UAV) must fulfil specified requirements. Parallel hybrid drive system is preferred in UAVs. Requirements for electrical machine used in a hybrid drive can be different because of variety of tasks which UAVs can realize. In the analysed case, the electric machine was predicted to operate as a combustion engine starter, a motor and a generator. Brushless DC motor 24/20 with permanent magnets was designed to be used in the hybrid drive. In the paper, original circuit-based mathematical model of brushless DC motor with permanent magnets known as the flux model which takes into account the nonlinearity of the magnetic circuit was presented. Waveforms of chosen parameters of the machine in different operation modes (starter, motor and generator) were determined based on the simulation model. In the motoring operation, dynamic variation of one control parameter (i.e. dynamic change of commutation point) was used to increase generated electromagnetic torque.

Keywords Brushless DC motor with permanent magnet • Unmanned aerial vehicle hybrid drive • Motor mode • Generator mode

P. Bogusz · M. Korkosz (✉) · J. Prokop
The Faculty of Electrical and Computer Engineering, Rzeszow University
of Technology, Rzeszow, Poland
e-mail: mkosz@prz.edu.pl

P. Bogusz
e-mail: pbogu@prz.edu.edu

J. Prokop
e-mail: jprokop@prz.edu.pl

P. Wygonik
The Faculty of Mechanical Engineering and Aeronautics, Rzeszow University
of Technology, Rzeszow, Poland
e-mail: piowyg@prz.edu.pl

1 Introduction

Unmanned aerial vehicles become more and more popular in recent years. Combustion engines are mostly used to drive unmanned aerial vehicles in contrast to electric machines. Appearance of commercial solutions of hybrid drives in automotive industry was the beginning of research on using them also in the aviation industry. The research carried out currently is mainly focused on very small or small unmanned aerial vehicles [1–9]. The hybrid drive represents an attempt to combine advantages of a combustion engine drive with a typical electric drive. The main advantage of a combustion engine is high energetic density of fuel which allows long flights. On the other hand, an electric motor has higher efficiency of energy conversion and the electric motor is significantly quieter than a combustion engine [8–10].

In the paper, results of studies of the brushless DC motor with permanent magnets for a hybrid drive of a small UAV were presented. Due to made requirements, designed structure of the electric machine should operate as a combustion engine starter, a motor or a generator. The concept of a hybrid drive and specified requirements for the electric machine were presented in part II. In part III, the designed structure of the electric machine and used configuration of stator windings connection were discussed. The original mathematical model of brushless DC motor with permanent magnets was discussed in part IV. The simulation model was presented in part V. Analysis of the combustion engine start-up during a flight of an aerial vehicle was conducted based on the simulation model (part VI). Influence of commutation point variation on the motor properties at maximum speed of the hybrid drive was analysed in part VII. The machine behaviour under generating operation with simultaneous control of charging current of batteries was discussed in part VIII.

2 The Concept of UAV Hybrid Drive

An exemplary set of forces, which was shown in Fig. 1, acts on an airplane during a steady level flight.

For an un-accelerated level flight, thrust equilibrates drag, whereas, lift equals weight of the airplane. Drag and lift are forces which depend on aerodynamic coefficients, wing area and square of a flight speed. Thrust is forced by a drive system to obtain specific flight parameters (speed, altitude). Lift-to-drag ratio is defined as a relation of lift force coefficient to aerodynamic drag force coefficient. The drag is composed from two separate origins: induced drag and parasite drag. In Fig. 2, exemplary drag characteristic was shown.

By taking into account drag characteristic, it is possible to determine so-called airframe required power, which is necessary for steady flight of an aerial vehicle, as a function of flight speed. Thrust is produced by the propeller, which is driven by

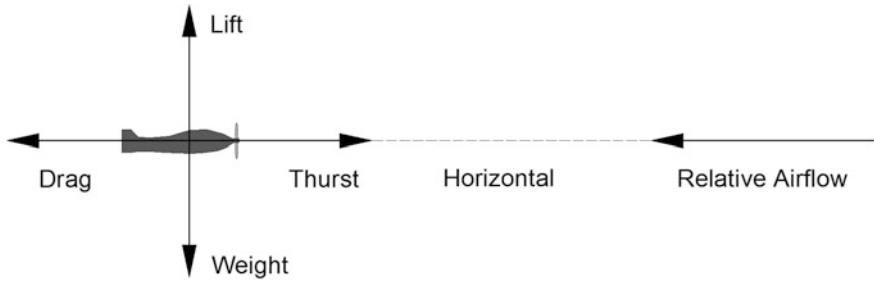
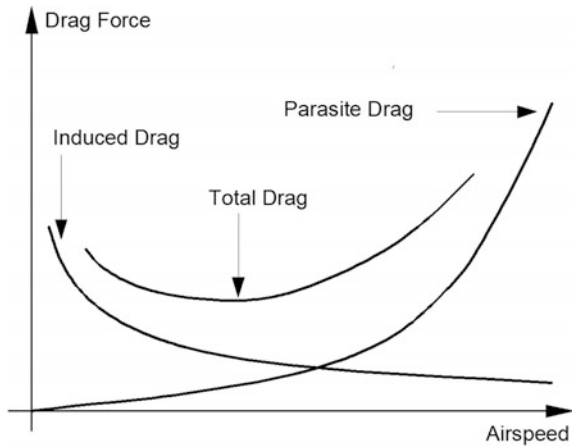


Fig. 1 Basic airplane forces [11]

Fig. 2 Drag characteristics [11]



the combustion engine. The engine must have so-called propulsion available power to produce thrust which in turn allows obtaining required flight speed in order to balance forces set which acts on the airplane. In Fig. 3, the available propulsion power of a drive as a function of the airspeed was shown.

Curves of the propulsion power available and the airframe power required cross in two points. In these two points, an airplane will be on specified altitude but with different speeds. The difference between the power required and the power available is a reserve power. With the reserve power, it is possible to increase a flight speed without changing altitude or only change altitude of an airplane. The airspeed at which maximum reserve power occurs is the airspeed at which maximum climb rate can occur.

The required power curve has a clear minimum. The example of required power characteristic was shown in Fig. 4 with marked two characteristic speeds, i.e. maximum endurance speed and speed when lift-to-drag ratio is maximal.

Fig. 3 Airframe and propulsion power characteristics [11]

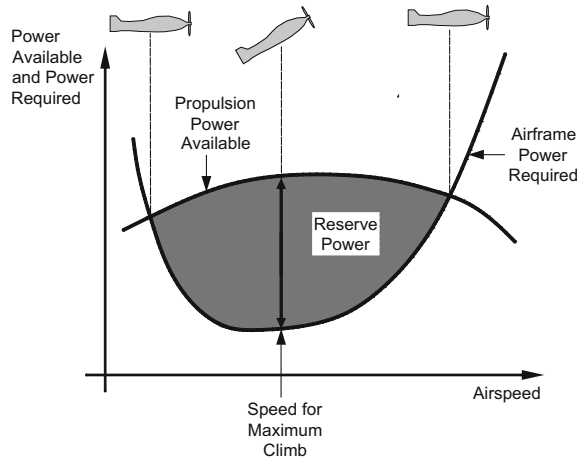
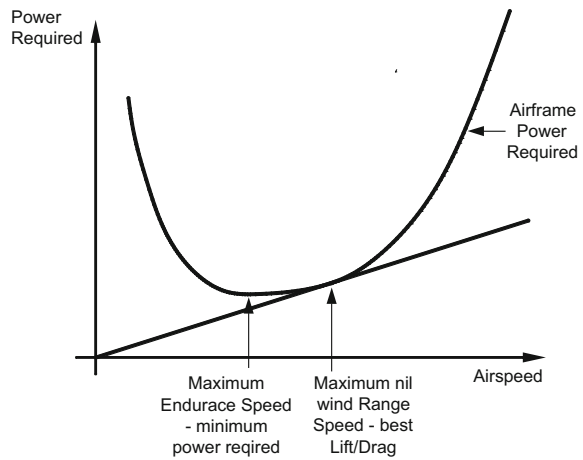


Fig. 4 Range and endurance characteristics [11]



To drive an aerial vehicle, a combustion engine or an electric motor can be used. Both drives have advantages and disadvantages. Figure 5 shows the example of combustion engine characteristics.

All types of combustion engines have low efficiency of energy conversion. Additionally, minimal fuel consumption occurs only in narrow range of speed. An operation with maximum power is connected with significant increase in fuel consumption. In drives with electric machines, brushless DC motors with permanent magnets (BLDCM) are mostly used. In Fig. 6, characteristics of brushless DC motor with permanent magnets were shown.

An electric motor ensures operation with constant torque on the shaft up to the rated speed. It is possible to increase temporarily electromagnetic torque (and thus power) by increasing phase currents. In Fig. 6, the area of temporary operation of a

Fig. 5 Engine torque, power and specific fuel consumption (SFC) characteristic

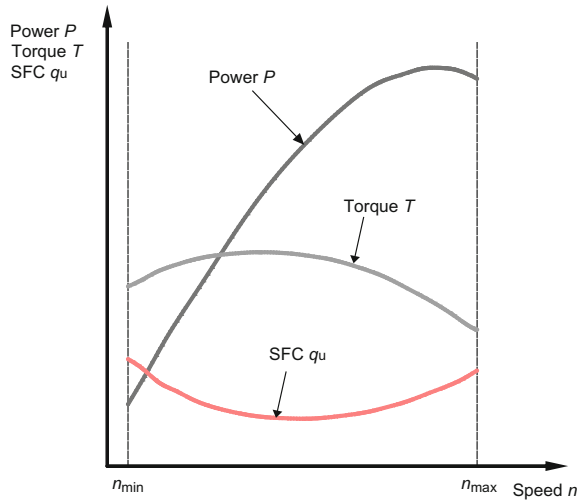
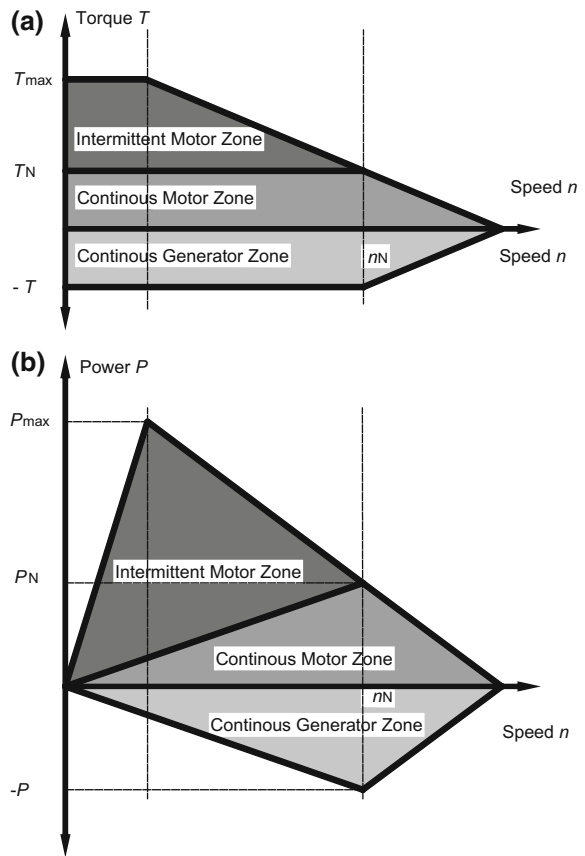


Fig. 6 BLDCM torque (a) and power (b) characteristics



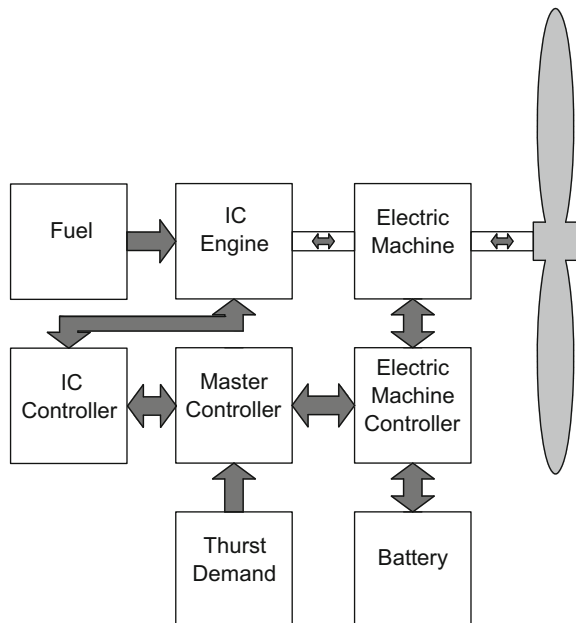
motor was marked. An efficiency of energy conversion in BLDCM can exceed 90%. Additionally, high value of efficiency is available in a significantly wider range of speeds than for a combustion engine.

A hybrid drive represents an attempt to combine advantages of a combustion engine drive with an electric motor drive. In a hybrid drive, it is possible to limit disadvantages of above-mentioned drives. Hybrid drives can be configured as serial, parallel or mixed systems. A parallel system is the best solution in small hybrid drive systems. However, in the parallel system, two variants are possible, i.e. coupling of a combustion engine and an electric machine by gear or connecting them on common shaft. Both solutions have advantages and disadvantages. It is hard to point which solution is better. In many cases, only design or functional considerations can decide which solution should be used.

Because of design requirements, a parallel hybrid drive system with machines on common shaft was used in the analysed system (Fig. 7).

Based on curves shown in Figs. 2, 3 and 4, preliminary calculations were conducted for the designed UAV. Thus, general requirements for whole drive system and for particular components, i.e. the combustion engine and the electric motor were specified. Requirements made for the combustion engine and the electric motor connected with required power in specified working point are slightly different. The electric machine must operate in three modes, i.e. combustion engine starter, motoring operation and generating operation. Due to generating operation, the combustion engine must dispose enough power to drive the propeller and the generator (about 20% more than rated power of the electric motor). Theoretically,

Fig. 7 A schematic diagram of a parallel hybrid drive system



an electric machine can generate comparable value of power in generating operation as rated power for motoring operation (Fig. 6). In practise, this power is slightly lower. In the analysed case, the electric machine (in generating operation) should provide sufficient value of charging current of batteries (Li-Po). The value of this current cannot exceed 0.1 C. Thus, demand for power to drive the generator will equal about 1 kW. Necessity of batteries charging during a flight at a specific altitude with a combustion engine drive results from necessity of limiting their capacity (and thus their weight). An amount of remaining energy and energy obtained during a flight must be sufficient to perform two planned functions, i.e. for a silent flight only with the electric drive and for restarting the combustion engine after a silent flight. For this reason, the electric motor will be a starter for the combustion engine. Therefore, a value of maximum generated electromagnetic torque T_{\max} (Fig. 6) is very important for this mode. Maximum value of torque will be limited by permissible value of batteries unloading current I_{\max} . Minimum value of generated electromagnetic torque should be sufficient to restart the combustion engine.

The following design requirements have been adopted for the electric motor to be used in a hybrid drive:

- supply voltage—52 V,
- required motor output power at aircraft cruising speed for independent operation—3500 W,
- maximum speed in the hybrid operation mode—8000 rpm,
- minimum starting torque—8 Nm,
- maximum supply current amplitude—200 Å,
- overall efficiency as high as possible,
- weight as small as possible,
- maximum outer diameter of the motor—105 mm.

Due to above-mentioned requirements, it was necessary to design brushless DC motor with permanent magnets. Additionally, the designed electric machine should be structurally adjusted to be used in the parallel hybrid drive system shown in Fig. 7.

Preliminary studies of designed motor to be used in a hybrid drive of the UAV were presented in [12]. The structure of the BLDC motor was shown in Fig. 8.

Laboratory tests conducted for the 12/14 motor with delta-connected windings showed 20% increase in produced torque in comparison to the same structure but with star-connected windings. Therefore, delta-connected windings were planned to be mounted in the designed 24/20 motor. Additionally, four parallel branches were intended in each phase. Figure 9 shows an electric diagram of the designed motor.

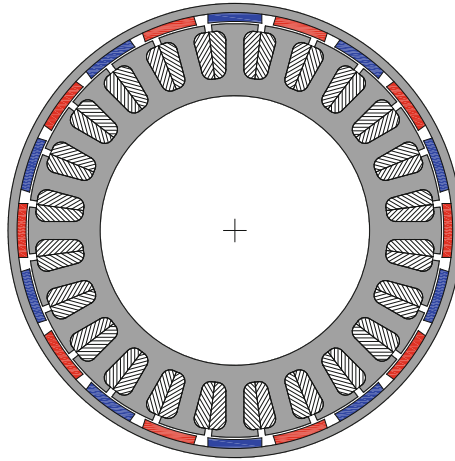


Fig. 8 A designed structure of the 24/20 BLDC motor

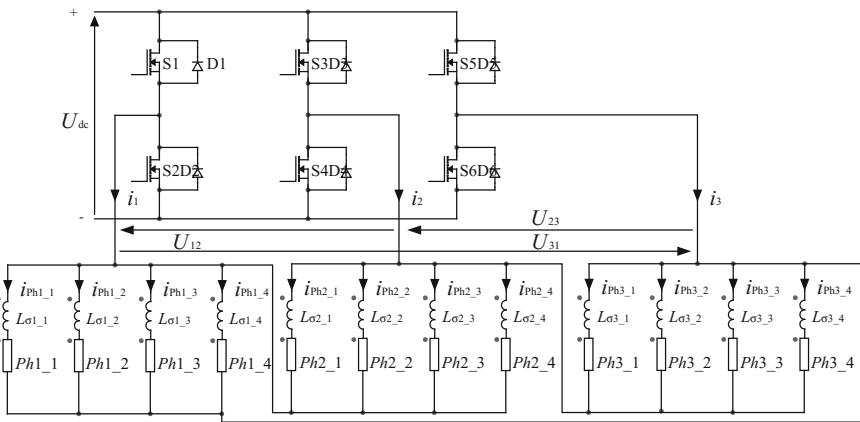


Fig. 9 An electric diagram of the designed 24/20 BLDC motor

3 A Mathematical Model of the BLDC Motor

The subject of the study is a three-phase 24/20 BLDC machine. An electric diagram of the machine, including the supply circuit and delta-connected stator windings, was shown in Fig. 9. Four parallel branches per each phase were provided in the designed motor. A circuit-based mathematical model known as the flux model which takes into account the nonlinearity of the magnetic circuit has been proposed for the discussed BLDC machine. Functional dependencies of fluxes on the rotor position and phase currents were determined by means of 2D field methods, and

next, the obtained set of relationships was used in the circuit model. The main assumption of the mathematical modelling is taking equality of magnetic co-energy of 2D field model with co-energy of the discussed field model. The following simplifying assumptions have been adopted:

- symmetry of the magnetic circuit structure of both stator and rotor,
- omitting phenomena relating to eddy currents and magnetic hysteresis, in particular, assuming zero losses in stator and rotor cores,
- omitting the influence of temperature on fluxes generated by permanent magnets,
- constancy in time of permanent magnets parameters.

Decomposition of phase fluxes into the sum of fluxes induced by phase currents (leakage and main fluxes) and fluxes from permanent magnets was also assumed.

The voltage–current equation, the equation of rotational motion torques, and the formula expressing angular velocity for the BLDC motor model from Fig. 9 can be written down in the form [12]:

$$\mathbf{u} = \mathbf{R}\mathbf{i} + \frac{d}{dt}\boldsymbol{\psi}(\theta, \mathbf{i}, i^{\text{PM}}) \quad (1)$$

$$J \frac{d\omega}{dt} + D\omega + T_L = T_e(\theta, \mathbf{i}, i^{\text{PM}}) \quad (2)$$

$$\frac{d\theta}{dt} = \omega \quad (3)$$

where vectors representing voltages \mathbf{u} , currents \mathbf{i} , and associated winding fluxes induced by winding currents and generated by permanent magnets $\boldsymbol{\psi}(\theta, \mathbf{i}, i^{\text{PM}})$, as well as the matrix of resistances \mathbf{R} are defined as follows:

$$\mathbf{u} = \begin{bmatrix} \mathbf{u}^1 \\ \mathbf{u}^2 \\ \mathbf{u}^3 \\ \mathbf{u}^4 \end{bmatrix} \quad \mathbf{i} = \begin{bmatrix} \mathbf{i}^1 \\ \mathbf{i}^2 \\ \mathbf{i}^3 \\ \mathbf{i}^4 \end{bmatrix} \quad \boldsymbol{\psi}(\theta, \mathbf{i}, i^{\text{PM}}) = \begin{bmatrix} \boldsymbol{\psi}^1(\theta, \mathbf{i}, i^{\text{PM}}) \\ \boldsymbol{\psi}^2(\theta, \mathbf{i}, i^{\text{PM}}) \\ \boldsymbol{\psi}^3(\theta, \mathbf{i}, i^{\text{PM}}) \\ \boldsymbol{\psi}^4(\theta, \mathbf{i}, i^{\text{PM}}) \end{bmatrix} \quad (4)$$

$$\mathbf{R} = \begin{bmatrix} \mathbf{R}^1 & \mathbf{0} & \mathbf{0} & \mathbf{0} \\ \mathbf{0} & \mathbf{R}^2 & \mathbf{0} & \mathbf{0} \\ \mathbf{0} & \mathbf{0} & \mathbf{R}^3 & \mathbf{0} \\ \mathbf{0} & \mathbf{0} & \mathbf{0} & \mathbf{R}^4 \end{bmatrix} \quad (5)$$

In Eqs. (4) and (5) for $k = 1, 2, 3, 4$, vectors of voltages \mathbf{u}^k , currents \mathbf{i}^k , fluxes $\boldsymbol{\psi}^k(\theta, \mathbf{i}, i^{\text{PM}})$ and matrices of resistances \mathbf{R}^k are defined as:

$$\mathbf{u}^k = \begin{bmatrix} u_1^k \\ u_2^k \\ u_3^k \end{bmatrix} \quad \mathbf{i}^k = \begin{bmatrix} i_1^k \\ i_2^k \\ i_3^k \end{bmatrix} \quad \Psi^k(\theta, \mathbf{i}, i^{\text{PM}}) = \begin{bmatrix} \psi_1^k(\theta, \mathbf{i}, i^{\text{PM}}) \\ \psi_2^k(\theta, \mathbf{i}, i^{\text{PM}}) \\ \psi_3^k(\theta, \mathbf{i}, i^{\text{PM}}) \end{bmatrix} \quad (6)$$

$$\mathbf{R}^k = \begin{bmatrix} R_1^k & 0 & 0 \\ 0 & R_2^k & 0 \\ 0 & 0 & R_3^k \end{bmatrix} \quad (7)$$

Moreover, the following symbols are used in (1)–(3): θ —the rotor position; i^{PM} —the permanent magnet magnetization equivalent current, J —the rotor moment of inertia; D —the coefficient of viscous friction; ω —the angular velocity; T_L —the load torque; $T_e(\theta, \mathbf{i}, i^{\text{PM}})$ —the electromagnetic torque of machine.

For the discussed model described by the Eq. (1), it is assumed that the fluxes from individual phases for four parallel branches, which depend on the rotor position θ , are sums of fluxes induced by currents in individual windings (end winding leakage fluxes and main fluxes) and fluxes generated by permanent magnets according to the definition:

$$\Psi(\theta, \mathbf{i}, i^{\text{PM}}) = \mathbf{L}_\sigma \mathbf{i} + \Psi^{\text{curr}}(\theta, \mathbf{i}, i^{\text{PM}}) + \Psi^{\text{PM}}(\theta, i^{\text{PM}}), \quad (8)$$

where the matrix of leakage fluxes \mathbf{L}_σ and vectors of fluxes from currents $\Psi^{\text{curr}}(\theta, \mathbf{i}, i^{\text{PM}})$ and magnets $\Psi^{\text{PM}}(\theta, i^{\text{PM}})$ are defined as follows:

$$\mathbf{L}_\sigma = \begin{bmatrix} \mathbf{L}_\sigma^{11} & \mathbf{0} & \mathbf{0} & \mathbf{0} \\ \mathbf{0} & \mathbf{L}_\sigma^{22} & \mathbf{0} & \mathbf{0} \\ \mathbf{0} & \mathbf{0} & \mathbf{L}_\sigma^{33} & \mathbf{0} \\ \mathbf{0} & \mathbf{0} & \mathbf{0} & \mathbf{L}_\sigma^{44} \end{bmatrix} \quad (9)$$

$$\Psi^{\text{curr}}(\theta, \mathbf{i}, i^{\text{PM}}) = \sum_{l=1}^4 \begin{bmatrix} \Psi^{1l}(\theta, \mathbf{i}^l, i^{\text{PM}}) \\ \Psi^{2l}(\theta, \mathbf{i}^l, i^{\text{PM}}) \\ \Psi^{3l}(\theta, \mathbf{i}^l, i^{\text{PM}}) \\ \Psi^{4l}(\theta, \mathbf{i}^l, i^{\text{PM}}) \end{bmatrix} \quad (10)$$

$$\Psi^{\text{PM}}(\theta, i^{\text{PM}}) = \begin{bmatrix} \Psi^{1\text{PM}}(\theta, i^{\text{PM}}) \\ \Psi^{2\text{PM}}(\theta, i^{\text{PM}}) \\ \Psi^{3\text{PM}}(\theta, i^{\text{PM}}) \\ \Psi^{4\text{PM}}(\theta, i^{\text{PM}}) \end{bmatrix} \quad (11)$$

In Eqs. (9)–(11), matrices of end winding self-inductances coefficients and vectors of other fluxes are defined as (for $k, l = 1, 2, 3, 4$):

$$\mathbf{L}_\sigma^{\text{kk}} = \begin{bmatrix} L_{1\sigma}^{\text{kk}} & 0 & 0 \\ 0 & L_{2\sigma}^{\text{kk}} & 0 \\ 0 & 0 & L_{3\sigma}^{\text{kk}} \end{bmatrix} \quad (12)$$

$$\Psi^{kl}(\theta, \mathbf{i}^l, i^{PM}) = \sum_{j=1}^3 \begin{bmatrix} \Psi_{1j}^{kl}(\theta, i_j^l, i^{PM}) \\ \Psi_{2j}^{kl}(\theta, i_j^l, i^{PM}) \\ \Psi_{3j}^{kl}(\theta, i_j^l, i^{PM}) \end{bmatrix} \quad (13)$$

$$\Psi^{kPM}(\theta, i^{PM}) = \begin{bmatrix} \psi_1^{kPM}(\theta, i^{PM}) \\ \psi_2^{kPM}(\theta, i^{PM}) \\ \psi_3^{kPM}(\theta, i^{PM}) \end{bmatrix} \quad (14)$$

The vector of fluxes (14), which are generated by permanent magnets, as a function of rotor θ can be presented for $k = 1, 2, 3, 4$ as series:

$$\Psi^{kPM}(\theta, i^{PM}) = \begin{bmatrix} \sum_{v=1}^{\infty} \psi_{1v}^{kPM}(i^{PM}) \sin(v\theta) \\ \sum_{v=1}^{\infty} \psi_{2v}^{kPM}(i^{PM}) \sin(v\theta - \alpha) \\ \sum_{v=1}^{\infty} \psi_{3v}^{kPM}(i^{PM}) \sin(v\theta - \beta) \end{bmatrix}, \quad (15)$$

where $\psi_{iv}^{kPM}(i^{PM})$ are amplitudes of v th flux harmonic.

Expression for the electromagnetic torque in the Eq. (2) can be written down in the form:

$$T_e(\theta, \mathbf{i}, i^{PM}) = \frac{\partial W_c^*(\theta, \mathbf{i}, i^{PM})}{\partial \theta}, \quad (16)$$

where $W_c^*(\theta, \mathbf{i}, i^{PM})$ is a total co-energy of a magnetic field in the motor air gap. The magnetic co-energy from Eq. (16) can be expressed in the form of two addends, one is dependent $W_c'(\theta, \mathbf{i}, i^{PM})$ and the other is independent $W_c''(\theta, i^{PM})$ on the winding currents, so expression for the electromagnetic torque can be written down in the form:

$$T_e(\theta, \mathbf{i}, i^{PM}) = \frac{\partial W_c'(\theta, \mathbf{i}, i^{PM})}{\partial \theta} + \frac{\partial W_c''(\theta, i^{PM})}{\partial \theta} \quad (17)$$

In Eq. (17), the first component of the r.h.s. represents the main torque, and the second—the so-called cogging torque in de-energized state of the machine.

With the definition (8) taken into account, the resulting torque (17) can be expressed in the form:

$$T_e(\theta, \mathbf{i}, i^{PM}) = T_{PM}(\theta, \mathbf{i}, i^{PM}) + T_{cur}(\theta, \mathbf{i}, i^{PM}) + T_{cog}(\theta, i^{PM}) \quad (18)$$

Individual terms of the r.h.s. in (18) represent, respectively:

- the torque from the flux of permanent magnets and phase currents T_{PM}

$$T_{\text{PM}}(\theta, \mathbf{i}, i^{\text{PM}}) = \sum_{i=1}^3 \sum_{k=1}^4 i_i^k \frac{\partial \psi_i^{k\text{PM}}(\theta, i^{\text{PM}})}{\partial \theta} \quad (19)$$

- the torque from fluxes induced by phase currents T_{phase}

$$T_{\text{cur}}(\theta, \mathbf{i}, i^{\text{PM}}) = \sum_{i=1}^3 \sum_{k=1}^4 \frac{\partial}{\partial \theta} \int_0^{i_i^k} \psi_i^k(\theta, i_1^1, \dots, \bar{i}_i^k, 0, \dots, 0, i^{\text{PM}}) d\bar{i}_i^k \quad (20)$$

- the cogging torque resulting from fluxes connected only with magnets T_{cog} , i.e. in de-energized state of the machine. It can be expanded into a Fourier series:

$$T_{\text{cog}} = \sum_{v=1}^{\infty} T_v \cos(vq\theta), \quad (21)$$

where T_v is the amplitude of v -th harmonic and q is the number of slots.

Additional constraints on voltages and currents are imposed by the assumption that motor windings are delta-connected. In such case, the relationship between currents in individual parallel phase branches and the phase currents is described by the following equation of constraints:

$$\begin{bmatrix} i_{\text{ph1}} \\ i_{\text{ph2}} \\ i_{\text{ph3}} \end{bmatrix} = \begin{bmatrix} 1 & -1 & 0 \\ 0 & 1 & -1 \\ -1 & 0 & 1 \end{bmatrix} \begin{bmatrix} \sum_{k=1}^4 i_1^k \\ \sum_{k=1}^4 i_2^k \\ \sum_{k=1}^4 i_3^k \end{bmatrix} \quad (22)$$

Equations (1)–(3) together with (8) and (18) constitute circuit-based mathematical model of the three-phase BLDC machine with four parallel branches per each phase which allow analysing both static and dynamic states.

4 A Simulation Model of the BLDC Motor

The resultant BLDC motor simulation model comprises the following components: the model of electromagnetic system; the model of rotating mechanical structure; and the model of the motor supplying converter together with the control system.

For the purpose of construction of the BLDC motor simulation model, fluxes vector (10) can be separated to the sum of self-inductance fluxes (denoted with subscript ‘phase’) and mutual coupling fluxes (marked with subscript ‘mutual’) is defined as:

$$\Psi^{\text{curr}}(\theta, \mathbf{i}, i^{\text{PM}}) = \Psi_{\text{phase}}^{\text{curr}}(\theta, \mathbf{i}, i^{\text{PM}}) + \Psi_{\text{mutual}}^{\text{curr}}(\theta, \mathbf{i}, i^{\text{PM}}) \quad (23)$$

The vector of self-inductance fluxes $\Psi_{\text{phase}}^{\text{curr}}(\theta, \mathbf{i}, i^{\text{PM}})$ is defined as:

$$\Psi_{\text{phase}}^{\text{curr}}(\theta, \mathbf{i}, i^{\text{PM}}) = \begin{bmatrix} \Psi_{\text{phase}}^{11}(\theta, \mathbf{i}^1, i^{\text{PM}}) \\ \Psi_{\text{phase}}^{22}(\theta, \mathbf{i}^2, i^{\text{PM}}) \\ \Psi_{\text{phase}}^{33}(\theta, \mathbf{i}^3, i^{\text{PM}}) \\ \Psi_{\text{phase}}^{44}(\theta, \mathbf{i}^4, i^{\text{PM}}) \end{bmatrix}, \quad (24)$$

where vectors $\Psi_{\text{phase}}^{\text{kk}}(\theta, \mathbf{i}^k, i^{\text{PM}})$ for $k = 1, 2, 3, 4$ are defined:

$$\Psi_{\text{phase}}^{\text{kk}}(\theta, \mathbf{i}^k, i^{\text{PM}}) = \begin{bmatrix} \psi_{11}^{\text{kk}}(\theta, i_1^k, i^{\text{PM}}) \\ \psi_{22}^{\text{kk}}(\theta, i_2^k, i^{\text{PM}}) \\ \psi_{33}^{\text{kk}}(\theta, i_3^k, i^{\text{PM}}) \end{bmatrix} \quad (25)$$

The vector of mutual coupling fluxes $\Psi_{\text{mutual}}^{\text{curr}}(\theta, \mathbf{i}, i^{\text{PM}})$ contains all remaining mutual fluxes both between different phases and between branches in a given phase.

On the grounds of assumption that there is one-to-one correspondence between involved currents and fluxes, it is necessary to determine reverse characteristics, i.e. establish relationships between phase currents and their self-inductance fluxes. The relationships determine the circuit current functions which can be written down in the form (for $k = 1, 2, 3, 4$):

$$\mathbf{i} = \mathbf{i}(\theta, \Psi_{\text{phase}}^{\text{curr}}, i^{\text{PM}}) \quad (26)$$

or based on (10)

$$\begin{bmatrix} \mathbf{i}^1 \\ \mathbf{i}^2 \\ \mathbf{i}^3 \\ \mathbf{i}^4 \end{bmatrix} = \begin{bmatrix} \mathbf{i}^1(\theta, \Psi_{\text{phase}}^{11}, i^{\text{PM}}) \\ \mathbf{i}^2(\theta, \Psi_{\text{phase}}^{22}, i^{\text{PM}}) \\ \mathbf{i}^3(\theta, \Psi_{\text{phase}}^{33}, i^{\text{PM}}) \\ \mathbf{i}^4(\theta, \Psi_{\text{phase}}^{44}, i^{\text{PM}}) \end{bmatrix}, \quad (27)$$

where for $k = 1, 2, 3, 4$

$$\begin{bmatrix} i_1^k \\ i_2^k \\ i_3^k \end{bmatrix} = \begin{bmatrix} i_1^k(\theta, \psi_{11}^{\text{kk}}, i^{\text{PM}}) \\ i_2^k(\theta, \psi_{22}^{\text{kk}}, i^{\text{PM}}) \\ i_3^k(\theta, \psi_{33}^{\text{kk}}, i^{\text{PM}}) \end{bmatrix} \quad (28)$$

Figure 10 shows a schematic diagram of a structure of the BLDC motor simulation model taking into account mutual couplings between phases and based on the voltage–current relationship (1) with definitions (8) and (23) taken into account.

A schematic diagram of electromagnetic torque calculation T_e of the BLDC machine from the Eq. (18) was presented in Fig. 11.

Particular blocks in the diagram in Fig. 11 represent particular components of electromagnetic torque described in Eqs. (19)–(21).

In a steady-state analysis at constant rotor velocity ω , rotor position equals $\theta = \omega t + \theta_0$, while in dynamic states, the torques Eq. (2) should be included in the simulation model. Figure 12 shows a block diagram of the equation of rotational motion corresponding to (2).

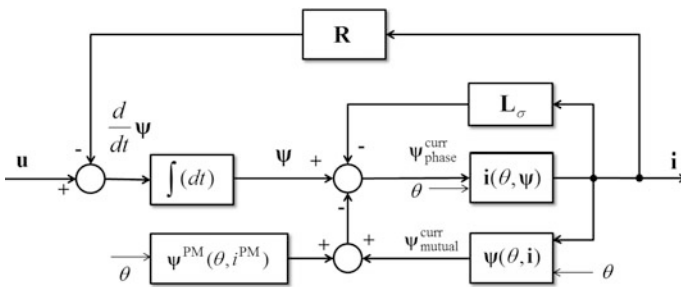


Fig. 10 A schematic diagram of the simulation model based on voltage–current equations of the BLDC machine [12]

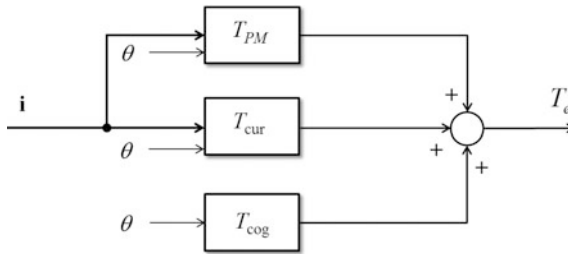


Fig. 11 A schematic diagram of electromagnetic torque calculation T_e of the BLDC machine [12]

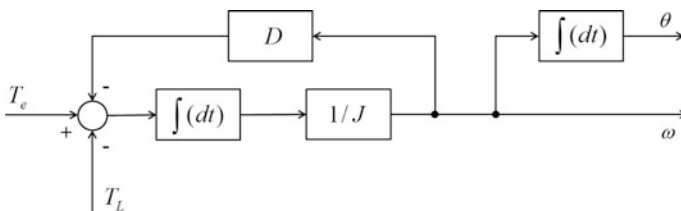


Fig. 12 A block diagram of the simulation model for mechanical structure of the three-phase BLDC machine

The block diagrams in Figs. 10, 11 and 12 are the base of a full simulation model of the analysed BLDC motor which takes into account the nonlinearity of magnetic circuit and couplings between phases.

The simulation model of the BLDC machine was developed in MATLAB/Simulink environment [13]. The BLDC machine will operate under hard start-ups as well as in motor-generator operation at higher range of rotor speed. A schematic diagram of the simulation model of a drive with the BLDCM supplied from battery was shown in Fig. 13 [14].

The presented model is capable to simulate the BLDC machine in both motoring operation (start-up, autonomous operation) and generating operation focused on battery charging. For determining the machine operation mode and entering appropriate pre-assumed values (e.g. speed, maximum start-up current), the block named 'Reference signals' is used. The block containing logic, which implements control algorithms of both motoring and generating operations, is denoted as the 'Hybrid Drive Control Unit'. This block is also used to control the combustion engine (after module expansion).

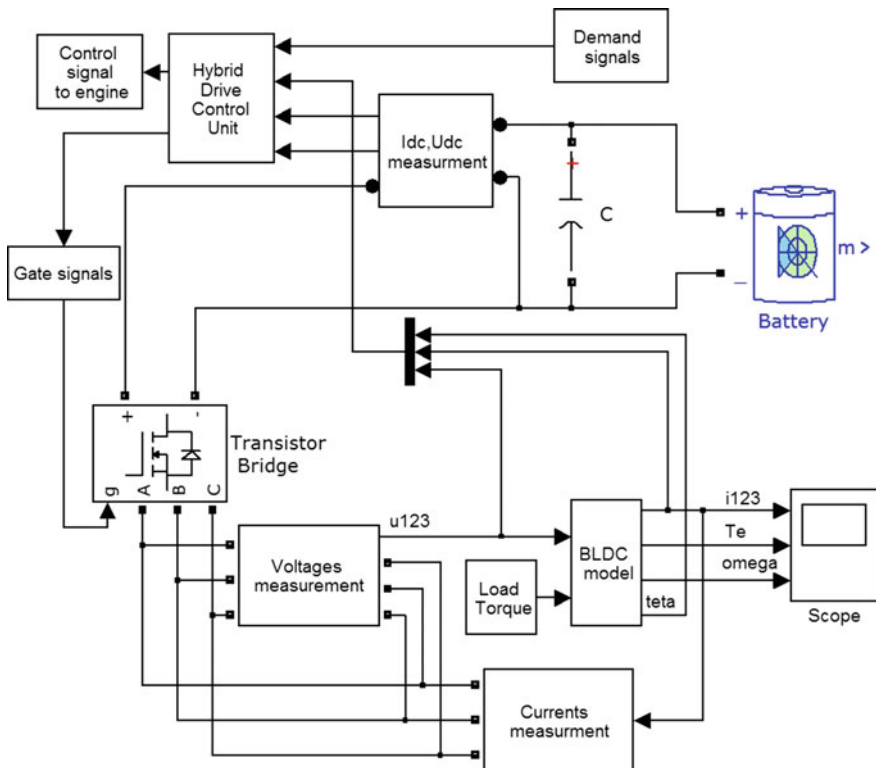


Fig. 13 An electric diagram of the designed 24/20 BLDC motor [14]

5 Waveforms of Currents and Starting Torque During Combustion Engine Start-up

In the hybrid drive, the designed motor is expected also to operate as the combustion engine starter. The electric drive alone is used in the course of the so-called silent flight. When batteries are discharged to a predefined level, the combustion engine must be restarted. In view of technical restrictions, the engine starting action must occur at a reduced speed of the electric motor. The following figures show plots of phase currents i_{ph} (Fig. 14) and the electromagnetic torque T_e (Fig. 15) as a function of the rotor position θ obtained at motor speed $n = 2000$ rpm and the starting current value limited to $190 \text{ A} \pm 10 \text{ A}$.

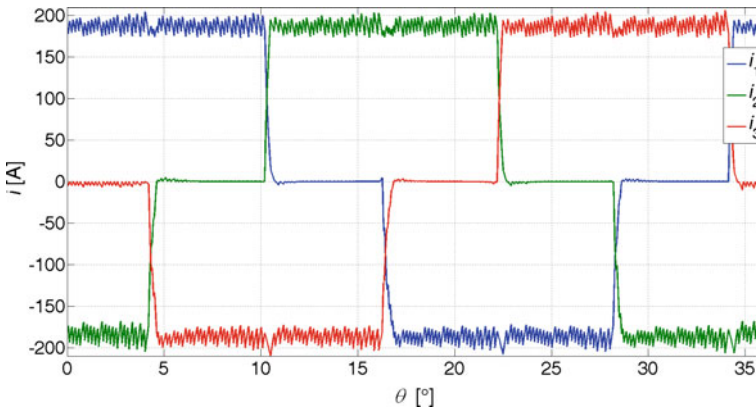


Fig. 14 Phase currents i_{ph} as a function of the rotor position θ at $n = 2000$ rpm

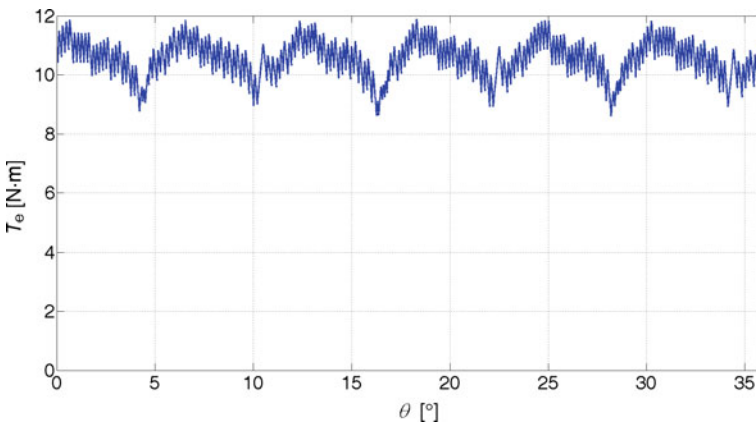


Fig. 15 The electromagnetic torque T_e as a function of the rotor position θ at $n = 2000$ rpm

As it can be seen, the required minimum starting torque exceeding 8 N m (8.6 N m) is generated at the maximum supply current value of 200 A.

6 Increasing the Output Power During Motoring Operation

Preliminary simulation studies showed that designed motor do not reach assumed working point [12]. To obtain the required output power of 3500 W at the maximum speed of 8000 rpm, it is necessary to apply a dynamical change of the phase currents commutation point. Authors of [8] discuss the possibility to maintain the required output power by changing a turn-on angle value. It was adopted in the analysis that zero value of the turn-on angle occurs at the point where plots of phase voltages cross each other. Using a negative value of the turn-on angle θ_{on} for individual transistors accelerates commutation of motor currents. The following figures show plots of the average electromagnetic torque T_{eav} (Fig. 16), the motor output power P_{out} (Fig. 17), the overall efficiency η (Fig. 18) and the phase current rms value I_{phrms} (Fig. 19) as a function of the turn-on angle θ_{on} obtained at speed $n = 8000$ rpm and supply voltage $U_{dc} = 52$ V.

At the turn-on angle value $\theta_{on} = -0.75^\circ$, the motor achieves the required output power of 3500 W with increased ripples of the electromagnetic torque T_e . By changing value of the turn-on angle θ_{on} , it is also possible to temporarily increase the output power. By increasing the turn-on angle, a small increase of the total efficiency has been obtained.

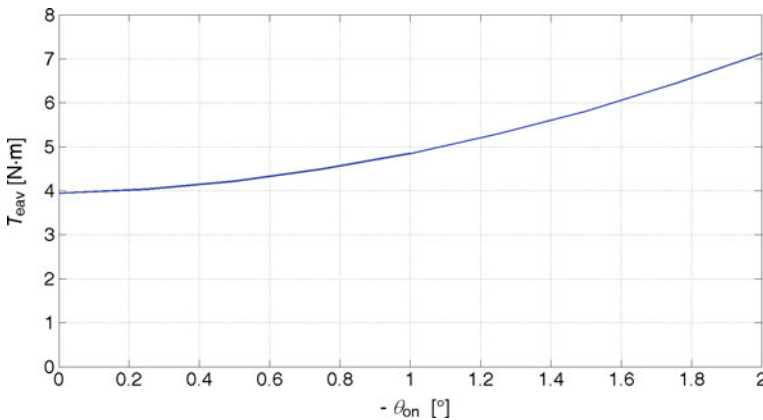


Fig. 16 The average electromagnetic torque T_{eav} as a function of the turn-on angle θ_{on}

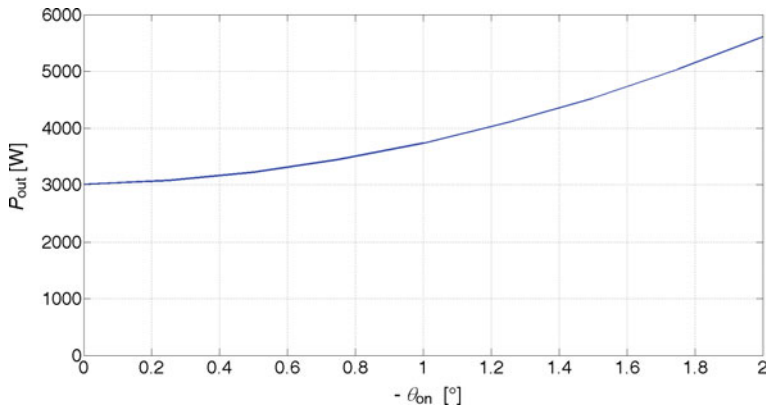


Fig. 17 The output power P_{out} as a function of the turn-on angle θ_{on}

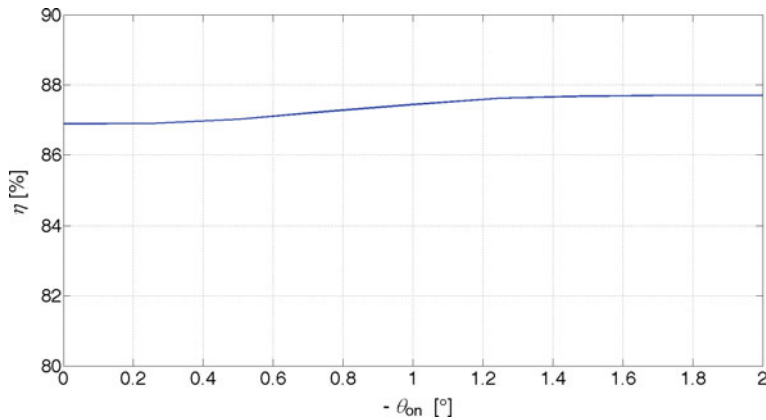


Fig. 18 The overall efficiency torque η as a function of the turn-on angle θ_{on}

The following figures show plots of: phase currents i_{ph} (Fig. 20), current in one of phase branches i_{ph1_1} (Fig. 21), phase voltages u (Fig. 22), supply current i_{dc} (Fig. 23), and electromagnetic torque T_e (Fig. 24) as a function of the rotor position θ at constant motor speed $n = 8000$ rpm, supply voltage $U_{dc} = 52$ V, and $\theta_{on} = -0.75^\circ$.

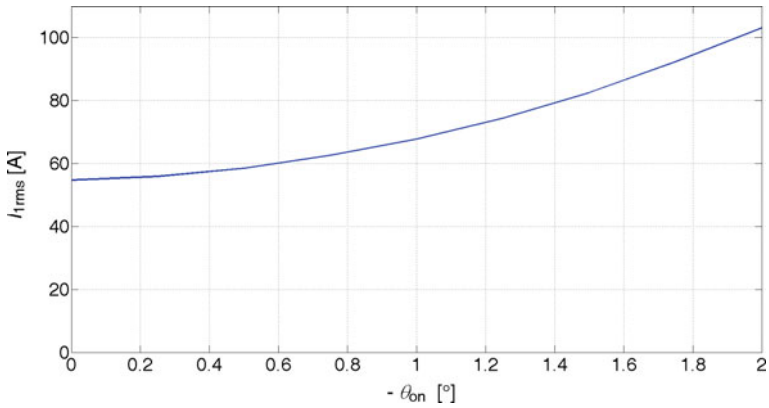


Fig. 19 The phase current rms value I_{phrms} as a function of the turn-on angle θ_{on}

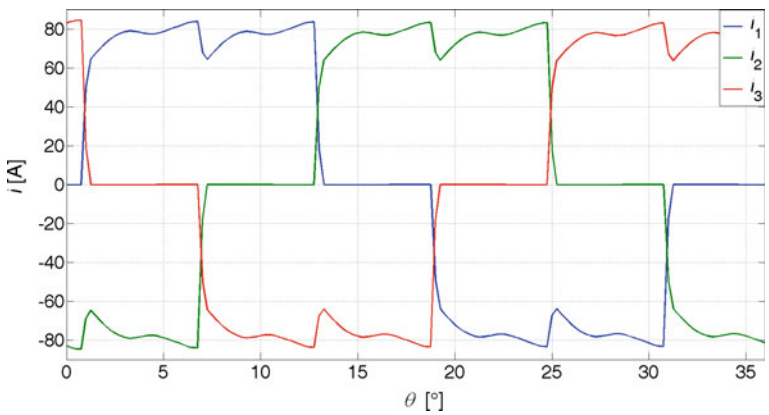


Fig. 20 Phase currents i_{ph} as a function of the rotor position θ at $n = 8000$ rpm and $\theta_{on} = -0.75^\circ$

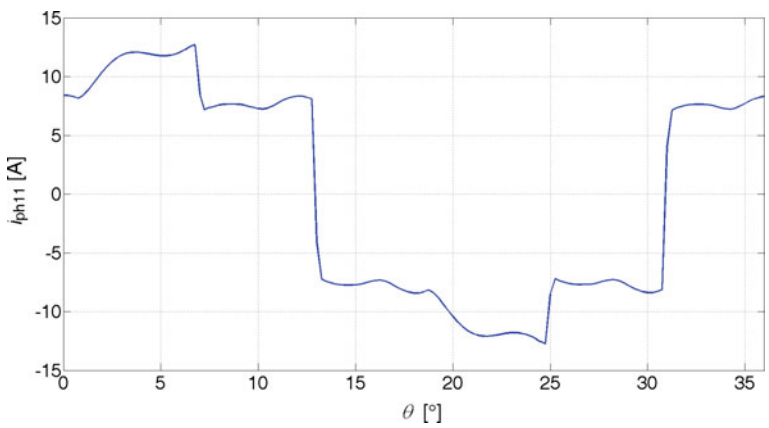


Fig. 21 The current i_{ph1_1} in one of phase Ph1 branches as a function of the rotor position θ at $n = 8000$ rpm and $\theta_{on} = -0.75^\circ$

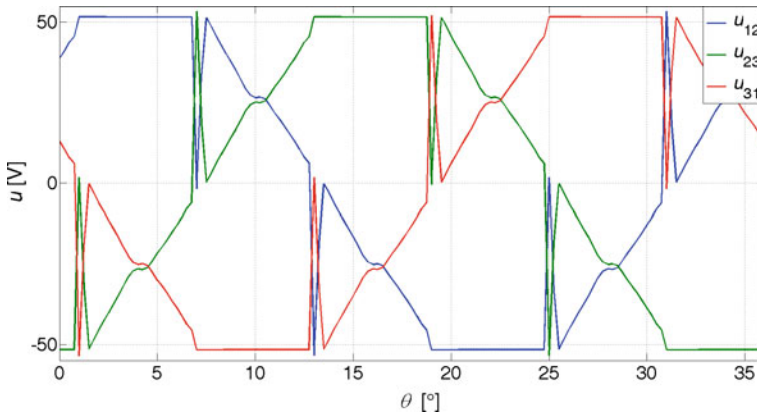


Fig. 22 Line-to-line voltage u as a function of the rotor position θ at $n = 8000$ rpm and $\theta_{\text{on}} = -0.75^\circ$

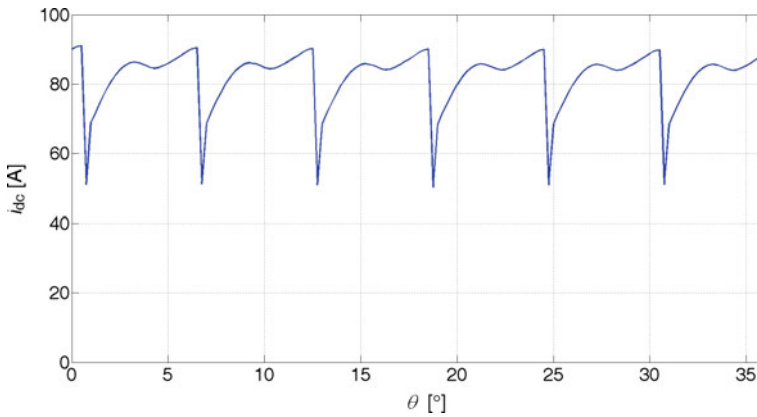


Fig. 23 The supply current i_{dc} as a function of the rotor position θ at $n = 8000$ rpm and $\theta_{\text{on}} = -0.75^\circ$

7 Waveforms of Currents and Starting Torque During Battery Charging

To ensure battery charging, the electric machine should operate in generating operation. In the scientific literature, there are articles which deal with control of generating operation of brushless DC motors with permanent magnets [15–17].

In the designed hybrid drive, there is an option to charge batteries during a flight at the specified altitude. Dedicated combustion engine disposes enough reserve of power which can be used to drive the electric machine. The BLDCM controller changes operation mode of the electric machine after receiving information about

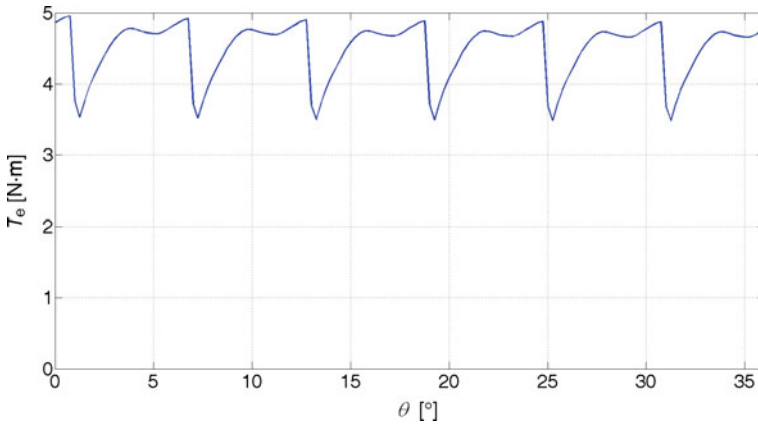


Fig. 24 The electromagnetic torque T_e as a function of the rotor position θ at $n = 8000$ rpm and $\theta_{on} = -0.75^\circ$

reached specified altitude. A battery charging process occurs after changing the control strategy by the power electronic system. To make regulation of battery charging current possible (it is especially important for Li–Po batteries), the maximum value of voltage induced by the generator must be lower than the battery voltage ($e_{max} < U_{dc}$). The machine controller operates then in the boost mode increasing the voltage up to the value resulted from charging current of the battery.

Figure 25 shows waveforms of phase currents, phase-to-phase voltages and battery charging current obtained as a result of simulations at speed $n = 4000$ rpm, $I_{ref} = 25$ A and battery charging current $I_{dc} = -16$ A. To control phase currents, digital delta-type regulators were used.

The process of charging Li–Po batteries requires stabilization of the current, while voltage stabilization is required when charging is close to the end. The main task of the control system is stabilization of charging current of batteries (i_{dc}) at assumed reference value (I_{dcref}) regardless of a drive speed changes. Figure 26 shows waveforms of phase currents (i_1, i_2, i_3), charging current of batteries (i_{dc}), reference current (I_{dcref}) and speed changes (n).

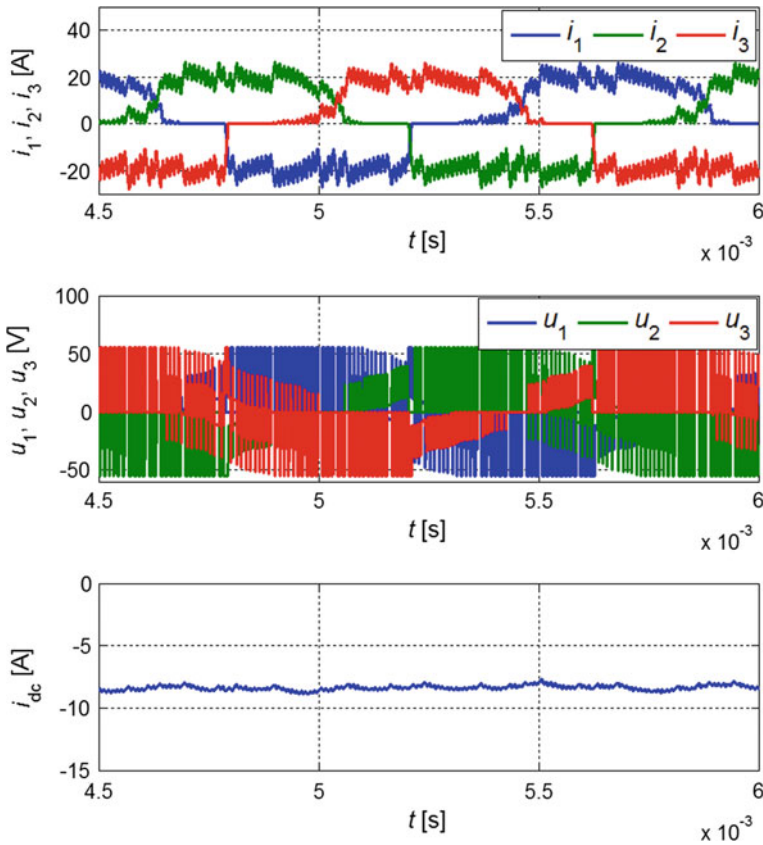


Fig. 25 Waveforms of (a) phase currents i_1, i_2, i_3 , (b) phase voltages u_1, u_2, u_3 , (c) battery charging current i_{dc} in generating operation

8 Conclusions

The paper presents results of studies connected with three-phase brushless DC motor with permanent magnets designed for a hybrid drive of a small unmanned aerial vehicle. Developed simulation model allows simulating the BLDCM in all operation modes of electrical part of the hybrid drive. In the starter operation mode, motor produces required minimal starting torque, which is sufficient to restart the combustion engine during the flight. The control algorithm of motoring operation was complimented by dynamic variation of commutation angle. The commutation angle variation (earlier turn-on) allows obtaining required power on the shaft of the hybrid drive at maximum speed $n = 8000$ rpm. In the generating operation, the controller operates in the boost mode which allows controlling charging current of the battery in the wide range of combustion engine speed. It is especially important

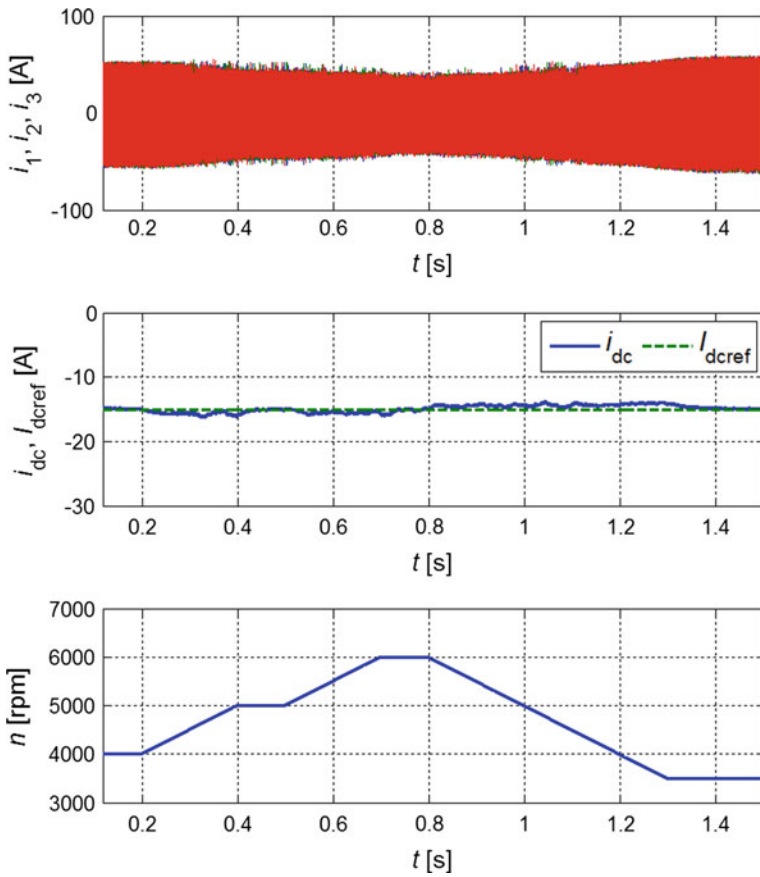


Fig. 26 Waveforms of phase currents i_1, i_2, i_3 , the battery charging current i_{dc} , the reference current I_{dcref} and speed changes (n)

for Li-Po batteries. Adopted coupling of both machines allows turning on and turning off the combustion engine during the flight.

Acknowledgements The research work was supported in part by The National Centre for Research and Development Project DZP/INNOLOT-1/2020/2013 of Poland and in part by the statutory funds of the Department of Electrodynamics and Electrical Machine Systems, Rzeszow University of Technology.

References

1. Harmon, F.G., Frank, A.A., Joshi, S.S.: The control of a parallel hybrid-electric propulsion system for a small unmanned aerial vehicle using a CMAC neural network. *Neural Netw.* **18**(2005), 772–780 (2005)
2. Harmon, F.G., Frank, A.A., Chattot, J.J.: Conceptual design and simulation of a small hybrid-electric unmanned aerial vehicle. *J. Aircr.* **43**(5), 1490–1498 (2006)
3. Glasscock, R.R., Hung, J.Y., Gonzalez, L.F., Walker, R.A.: Multimodal hybrid powerplant for unmanned aerial systems (UAS) Robotics. In: Twenty-Fourth Bristol International Unmanned Air Vehicle Systems Conference, March 30th to April 1st 2009, Bristol, UK
4. Lieh, J., Spahr, E.: Design of hybrid propulsion systems for unmanned aerial vehicles. In: 47th AIAA/ASME/SAE/ASEE Joint Propulsion Conference and Exhibit, 31 July–03 August 2011, San Diego, CA, AIAA 2011-6146
5. Lee, B., Park, P., Kim, C., Yang, S., Ahn, S.: Power managements of a hybrid electric propulsion system for UAVs. *J. Mech. Sci. Technol.* **26**(8), 2291–2299 (2012)
6. Li, Y.P., Liu, L., Zhang, X.H., Shi, S.T., Guo, C.W.: Ground tests of hybrid electric power system for UAVs. *Appl. Mech. Mater.* **448–453**, 2326–2334 (2014)
7. Friedrich, C., Robertson, P.A.: Hybrid-electric propulsion for aircraft. *J. Aircr.* **52**(1), 176–189 (2015)
8. Bogusz, P., Korkosz, M., Prokop, J.: A study of design process of BLDC motor for aircraft hybrid drive. In: IEEE International Symposium on Industrial Electronics (ISIE), pp. 508–513 (2011)
9. Gabriel, D.L., Meyer, J., Du Plessis, F.: Brushless DC motor characterisation and selection for a fixed wing UAV. In: AFRICON, pp. 1–6 (2011)
10. Gieras, J.F.: Permanent magnet motor technology: design and applications, 3rd edn. CRC Press, London (2009)
11. Glasscock, R.R.: Design, modelling and measurement of hybrid powerplant for unmanned aerial vehicles (UAVs). Queensland University of Technology (2012)
12. Bogusz, P., Korkosz, M., Powrózek, A., Prokop, J., Wygonik, P.: An analysis of properties of the BLDC motor for unmanned aerial vehicle hybrid drive. In: 2015 International Conference on Electrical Drives and Power Electronics (EDPE), pp. 458–464 (2015)
13. Matlab Documentation
14. Bogusz, P., Korkosz, M., Powrózek, A., Prokop, J., Wygonik, P.: An analysis of operation of brushless DC machine used in unmanned aerial vehicle hybrid drive. In: 2015 International Conference on Electrical Drives and Power Electronics (EDPE), pp. 402–408 (2015)
15. Becerra, R.C., Ehsani, M., Jahns, T.M.: Four-quadrant brushless ECM drive with integrated current regulation. *IEEE Trans. Ind. Appl.* **28**(4), 833–841 (1992)
16. Hasan, S.M.N., Husain, I., Veillette, R.J., Carletta, J.E.: A PM brushless DC starter/generator system for a series–parallel 2×2 hybrid electric vehicle. In: 42nd IAS Annual Meeting IEEE Industry Applications Conference, pp. 1686–1693 (2007)
17. Renken, F., Wolf, J.: Power electronics for hybrid-drive systems. In: European Conference on Power Electronics and Applications, pp. 1–10 (2007)

Electromagnetic Review of Rotor/Stator Misalignment in Permanent Magnet Axial Flux Motor

Adrian Mlot, Adam C. Malloy, Mariusz Korkosz
and Michael Lamperth

Abstract This paper presents the findings of a finite element analysis (FEA) investigation into the effect of rotor/stator misalignment on motor performance in a single rotor, dual stator, axial flux electric motor (AFM). Results obtained from the FEA are in good agreement with experimental measurements giving confidence in the use of the model. The results are useful to machine designers who wish to determine the sensitivity of rotor/stator misalignment, due to assembly errors or tolerance stack on machine performance. Axial offset of the rotor in the air gap is found to cause unbalanced axial forces on the rotor of up to 1400 N. The difference in iron loss between stators increased by 17 and 40% at high speed under open- and short-circuit conditions, respectively. Conversely, angular offset between the two stators was found to have little impact on unbalanced rotor forces and iron loss but a relatively large impact on recirculating currents within the machine which lead to uneven heating of the two stators. For an angular offset of 10 elec. deg. a recirculating current of 93 A was found for a phase current of 175 A. Torque ripple was found to decrease from 8 to 6%.

Keywords Air gap misalignment • Stator misalignment • Unbalanced axial force • Current/voltage imbalance • Axial flux PM motor

A. Mlot (✉) · A.C. Malloy
GKN-EVO EDrive Systems Ltd, Woking, UK
e-mail: adrian.mlot@gkn-evo.com

A.C. Malloy
e-mail: adam.malloy@gkn-evo.com

M. Korkosz
Faculty of Electrical and Computer Engineering, Rzeszow University of Technology,
Rzeszow, Poland
e-mail: mkosz@prz.edu.pl

M. Lamperth
HSR Hochschule Für Technik Rapperswil, Rapperswil-Jona, Switzerland
e-mail: michael.lamperth@hsr.ch

1 Introduction

Rotating machines are susceptible to manufacturing and assembly variations which can lead to unbalanced forces and reduced performance. Study of the performance of the machines with misalignment will be useful in the diagnosis of manufacturers' inaccuracies and in defining tolerance stack limits for mechanical designers. Differences between electrical machine topologies (e.g. induction, reluctance, permanent magnet) mean that each machine type can experience manufacturing and assembly errors which are unique to its design [1–6]. An axial flux permanent magnet synchronous machine (PMSM) with double stator topology has been considered in this paper. In earlier works, the authors have analysed AFM machines without misalignment effects utilizing 2-D/3-D FEM and analytical models to design a three-phase PM motor to deliver very high torque and power density in a compact and lightweight unit [7, 8]. This makes it particularly suitable for use in electric and hybrid vehicles where low weight and compact packing are important in delivering optimum efficiency in performance and design. The disk shape of the motor consists of a single rotor sandwiched between two stators where the two sets of three-phase windings are connected in parallel (Fig. 1).

This paper extends the author's previous research [9] to give insight into the machine performance including effect on iron loss and axial force due to the magnetic attraction in the air gap between the magnet and the stator.

Rotor/stator misalignments may cause an unbalanced magnetic pull due to asymmetric magnetic flux distribution in the air gap. The resulting unbalanced force on the rotor can cause lower bearing life, extra noise, increased shaft stress, vibrations, increased torque ripple and cogging torque [10, 11]. Asymmetric magnetic flux distribution can also cause imbalanced phase voltages and consequently affect the three-phase coil current waveforms [12]. It is crucial to monitor the current imbalance between stators because this imbalance causes uneven

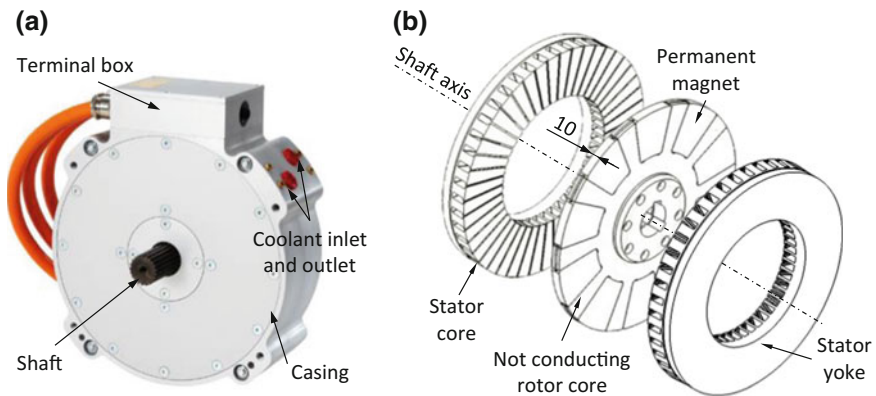


Fig. 1 Prototype of AFM (a) and the topology (b)

thermal loading in the topology investigated here. This means that one stator reaches maximum operating temperature and limits further power being extracted from the machine while the other stator still has some thermal headroom. Asymmetrical magnetic field distribution in the air gaps and current imbalance between stators may also cause unequal iron loss between stators (discussed in Sects. 4.5 and 5.5). At high speed in both no-load and load operation, there is a risk that proximity effects in the winding may increase copper loss.

The analysis of rotor/stator eccentricity or misalignment in radial flux PM motors and in axial flux single-sided motors has been the subject of many previous investigations [4, 6, 12–17]. Misalignment faults can be static or dynamic, which are widely explained in [5, 13, 18]. They can be also classified as having mixed eccentricity [6].

Less attention has been paid to the analysis of unbalanced axial force and machine characteristics in axial flux machines with a central rotor sandwiched between two stators. Section 2 presents two common types of uniform static misalignment which may occur in AFM. It also presents a comparison between the measured and predicted machine parameters of a machine without misalignment effects in order to validate the FEA model for the misalignment study. Results of the 3-D FEA predictions of AFM performance with rotor and stator misalignment are presented in Sects. 3 and 4, respectively. Discussion and conclusions are given in Sect. 5.

2 Mathematical Model of Rotor/Stator Misalignment

Two potential machine faults, rotor misalignment and stator misalignment are demonstrated in Fig. 2. These defects lead to geometry asymmetry in the AFM. In this study, the rotor rotates on its own axis and in the centre of the stator core.

Rotor misalignment is characterized by unequal mechanical air gap lengths δ_1 and δ_2 , with uniform eccentricity as shown in Fig. 2a [14, 18, 19]. Rotor misalignment is due to manufacturing tolerances and compliances in the bearing system that support the rotor between the two stators. In this work, the rotor misalignment has been normalized and is defined by $|\delta + \delta_1|/\delta$, where δ is the designed air gap.

Stator misalignment is characterized by an angular offset between the two stators. This assembly defect is illustrated in Fig. 2b. The offset angle β (in elec. deg.) between the two stators is investigated at 1.25°, 2.5°, 5°, 7.5° and 10° when the slot pitch is 40 elec. degrees.

Analysis of the unbalanced axial force and motor characteristics has been carried out using magneto-static and transient FE methods with 3-D formulations based on Maxwell's equations. Figure 2 presents the mathematical model and mesh discretization of the AFM with rotor and stator misalignment included in the modelled

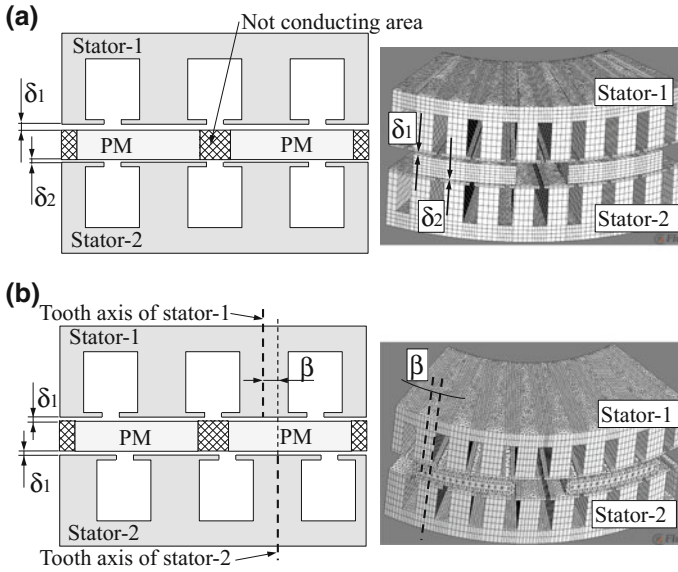


Fig. 2 Schematic representation and 3-D FE models with chosen mesh sizes of rotor misalignment (a) and stator misalignment (b)

geometry. Due to the periodic nature of the motor design, the study domain is reduced to 1/5 of the machine. The 3-D model includes a periodic boundary condition imposing identical values of each variable on corresponding nodes.

3 Experimental Validation

In order to validate the FE model for use, its predictions of machines with no misalignment have been compared with experimental values. The measured values were carried out on GKN-EVO's test rig, and its arrangement is shown in Fig. 3a. The AFM under test (no misalignment) is coupled to the torque transducer and operates in torque control mode. The 3-D FEA results are compared against measured machine parameters with very good agreement. The predicted and measured values of line-to-line voltage constant k_e and synchronous inductance L_s are 0.6162 and 0.62 V s/rad, and 210 and 231 μH , respectively. Figure 3b presents a comparison between predicted and measured torque constant of the prototype machine without misalignment. The agreement is good, validating the model for use. The discrepancy between measured and predicted values may be due to imperfect inverter control, magnet temperature varying during the measurements, or geometry and material property uncertainties.

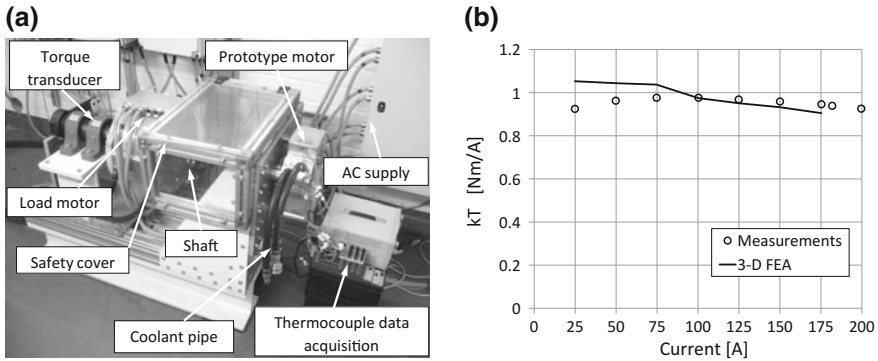


Fig. 3 Test-rig with prototype AFM without misalignment on test for measuring machine performance (a) and comparison between predicted and measured k_T at different RMS currents at 500 rpm (b)

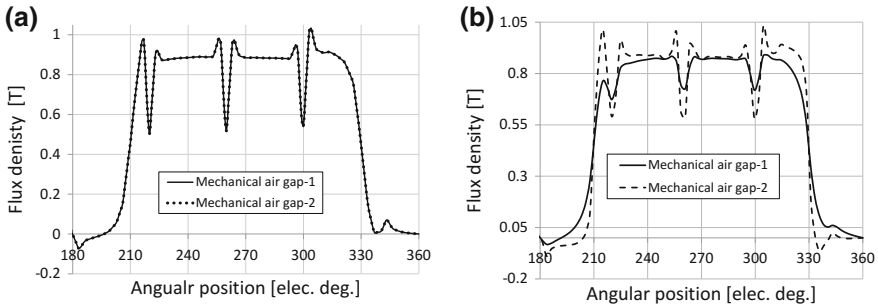


Fig. 4 No-load air gap flux density distribution, z -component. Machine without misalignment effects (a) and with 1.533 normalized air gap offset

4 Rotor Misalignment Results

4.1 Flux Density in the Air Gap

The air gap size changes lead to a change in the flux present between the stator and rotor. This has an impact on the flux linked by the phases [15, 16, 20, 21]. Figure 4 shows the z -component of the flux density in the middle of mechanical air gap of the machine with normalized 1.533 air gap offset compared with a ‘healthy’ machine.

It can be seen that the mechanical air gap (between stator and PM) length plays a significant role in the distribution of the magnetic field. The flux density in the machine with air gap offset has a more pronounced peak than the machine with equal air gap. When comparing the flux density in both air gaps (δ_1 and δ_2) in Fig. 4b, it is clear that the smallest air gap has significantly increased local

minimums and maximums. Also, due to unequal leakage flux, the total amount of the flux is unequal between the air gaps leading to unbalance axial force on the rotor.

4.2 Analysis of Back-EMF and Current Waveforms

The results of the back-EMF voltage waveform and RMS current waveform at 350 Å load with 1.533 normalized air gap offset are summarized in Fig. 5. It can be concluded that the rotor misalignment leads to a very small imbalance of voltage and current due to the differences in flux within each air gap.

Current imbalance I_{imb} and back-EMF voltage U_{imb} imbalance are defined using (1) and (2), respectively.

$$I_{imb} = \frac{I_{I1} - I_{I2}}{I_{ref}} \times 100 \quad (1)$$

$$U_{imb} = \frac{U_{U1} - U_{U2}}{U_{ref}} \times 100, \quad (2)$$

where I_{ref} is phase current, U_{ref} is back-EMF voltage and both are for the machine without any stator/rotor misalignments, and I_{I1} , I_{I2} , U_{U1} , U_{U2} are amplitudes of current at load condition and line-to-neutral voltage at open circuit, respectively (see Fig. 5), in the U phase of stator-1 and stator-2.

In the case of the 1.533 normalized air gap offset, the current imbalance at full load condition is 2.78% while the back-EMF voltage imbalance at open circuit is 3.22% (Fig. 6a, b). Increasing air gap offset leads to an increase in the current phase shift of up to 3.55 and 10 electrical degrees at high and low load current, respectively. However, back-EMF phase shift is 0 at any rotor offset, and the phase current induced in each stator is also not shifted at open circuit. Short-circuit current

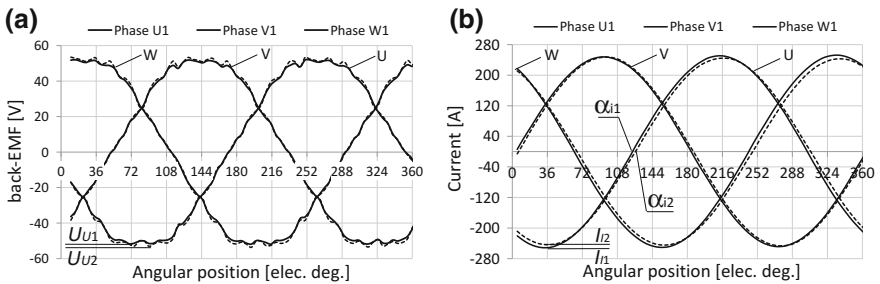


Fig. 5 Back-EMF at 1000 rpm (a) and current waveforms at full load operation (b) with 1.533 normalized rotor air gap offset

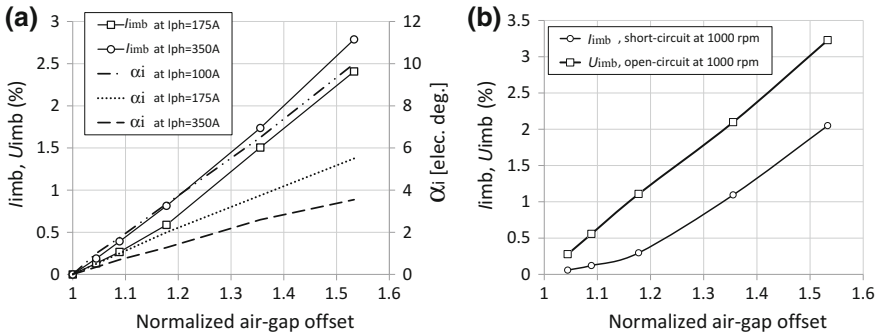


Fig. 6 Imbalance amplitude of current and current phase shift (a), and voltage (open circuit) and short-circuit current (b) versus normalized air gap offset for difference RMS phase load current

is less affected by air gap offset than current at load operation. The imbalance short-circuit current was not higher than 2.1% (Fig. 6b).

4.3 Analysis of Axial Force

The virtual work method [22] is adopted here to calculate the axial force on each stator at each angular position of the rotor. The axial force on the rotor is computed as the difference between both waveforms of axial force on stator-1 and stator-2 [23].

Axial misalignment of the rotor has a significant effect on axial force variations and low influence on electromagnetic torque (see Sect. 4.4). At high current in the q -axis, it will be seen that the effect of rotor offset leads to increased axial force in stator-1 from 5957 N up to 6756 N and to decreased axial force in stator-2 from -5957 N to -5589 N (Fig. 7a). At high d-axis current, axial force acting on stator-1 increases from 8110 N to 9047 N and decreases from -8110 N to -7655 N in stator-2 (Fig. 7b). In non-offset machine (normalized air gap offset equals 1), the force on the stator-1 and stator-2 is equal but not in the same direction (negative values). For comparison in Fig. 7a, b, the force acting in stator-2 is presented as an absolute value.

Figure 8 shows the z -component of the axial unbalanced force. Increasing the load current in the machine has only a small effect on the axial unbalanced force. A 1.533 normalized air gap offset gives rise to an unbalanced force of over 1400 N at full current load.

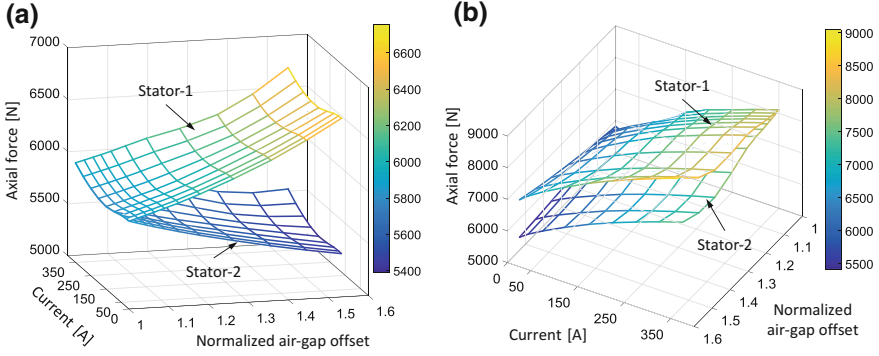


Fig. 7 Axial force in q -axis (a) and d -axis (b) versus RMS current for different rotor misalignment

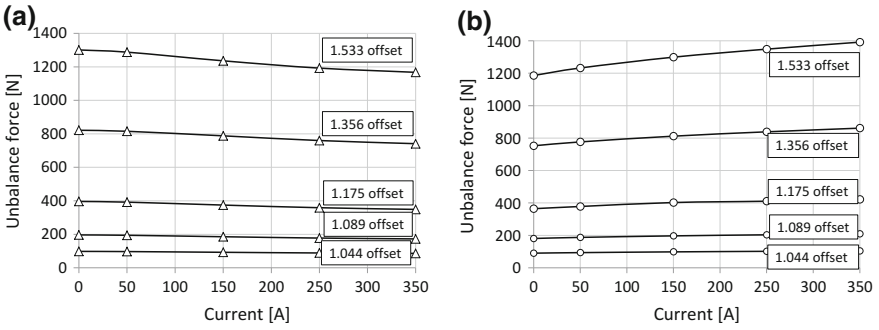


Fig. 8 Axial unbalanced force in q -axis (a) and d -axis (b) versus RMS current for different rotor misalignment

4.4 Analysis of Electromagnetic Torque and Torque Ripple

The electromagnetic torque is calculated using the virtual work method [22]. Cogging torque is generated due to the interaction between the permanent magnets and the geometry of the stator teeth [24]. The offset of the dual air gap configuration increases cogging torque T_{cogg} from 1.3 N m when the machine is free of any misalignments to 3.4 N·m when the normalized rotor offset is 1.533. Nevertheless, the electromagnetic average torque T_{av} , torque ripple coefficient ε and torque constant k_T are not affected by rotor misalignment, Figs. 9 and 10. The torque ripple coefficient defined by Nakate et al. [25] is shown in (3).

$$\varepsilon = \frac{T_{\text{max}} - T_{\text{min}}}{T_{\text{av}}} \times 100, \quad (3)$$

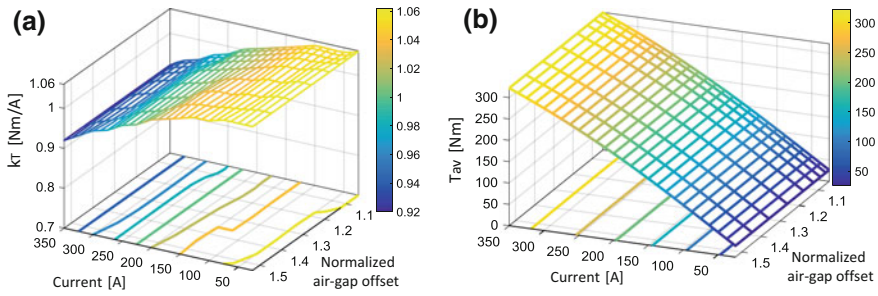


Fig. 9 Torque constant (a) and electromagnetic torque (b) with normalized rotor offset for different RMS current

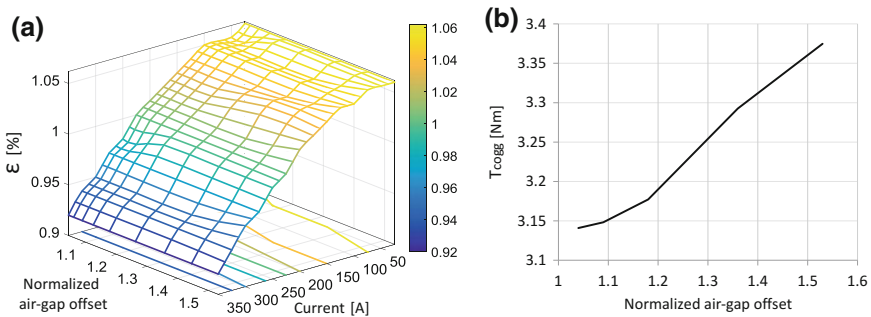


Fig. 10 Torque ripple for different RMS current (a) and cogging torque at 1 k rpm (b) with normalized rotor offset

where T_{\min} , T_{\max} and T_{av} are the minimum, maximum and average values of the electromagnetic torque.

4.5 Analysis of Iron Loss

As it was shown in Figs. 4 and 6, any rotor/stator offset in the machine geometry can affect the flux density in air gap and consequently the current/voltage waveform and the power loss. Here, the magnet losses and copper loss including proximity effect are neglected. Nevertheless, it can be concluded from earlier authors’ investigations [26–28] that proximity loss in wires placed in the slot near the air gap can be affected by any change to the magnetic field distribution in the air gap. From Fig. 4b, it is clear that the flux density in the air gap was affected by air gap offset, consequently, the authors expect proximity losses to be affected.

To quantify iron loss in the machine with air gap offset, the stator iron loss was evaluated for different speeds at open- and short-circuit operation. The stator iron

power loss was estimated from the separate components of hysteresis, classical Joule eddy current and excess loss [29]. These magnetic losses as an average power over a period were computed using the model described in Fig. 2 and can be expressed as a function of the frequency f and of the peak value of the magnetic flux density B_{mag} as shown in (4).

$$W_{\text{Fe}} = k_h B_{\text{mag}}^2 f k_f + \frac{1}{T} \int_0^T \left[\sigma \frac{d^2}{12} \left(\frac{dB}{dt}(t) \right)^2 + k_{\text{excess}} \left(\frac{dB}{dt} \right)^{1.5} \right] k_f dt, \quad (4)$$

where k_h is the coefficient by hysteresis, k_{excess} is the coefficient of losses in excess, σ is the conductivity of the material, k_f is the coefficient of filling close to 1 and d is the thickness of the lamination. The material coefficients used in this FEA are listed in Table 1.

The overall iron loss in both cores versus normalized air gap offset for different speed is shown in Fig. 11a. The iron loss in each stator core is shown in Fig. 11b. A 17 and 40% difference in iron loss can be seen in each stator at open and short circuit, respectively, at high speed and high air gap offset. Total iron loss (in both stators) compared with the machine without any misalignment effects is increased by 2 and 6.8% at open- and short-circuit operation, respectively, at high speed.

Table 1 Material coefficient for lamination

Hysteresis coefficient	k_h	$\text{W s/T}^2/\text{m}^3$	385
Electric conductivity	σ	$(\Omega \text{ m})^{-1}$	2.38e6
Lamination sheet thickness	d	m	3.5e-4
Excess loss coefficient	k_{excess}	$\text{W}/(\text{T s}^{-1})^{1.5}/\text{m}^3$	0
Packing factor	k_f	–	0.98
Mass density	ρ	kg/m^3	7650

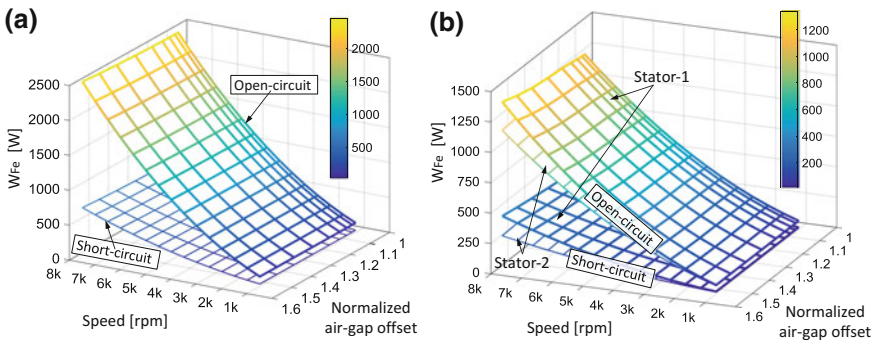


Fig. 11 Iron loss versus normalized air gap offset for different speed at open circuit and short circuit. Total iron loss (a), and iron loss separately computed in each stator core (b)

5 Stator Misalignment Results

5.1 Flux Density in the Air Gap

The flux density in the middle of the mechanical air gaps for both sides of the rotor disk without and with 10 elec. degrees stator offset is shown in Fig. 12.

Looking at the z -component of the flux density field through the mechanical air gap, it can be seen that local minimums and maximums caused by slotting effects are marginally changed by stator offset and are shifted when the stator offset is increased.

5.2 Analysis of Back-EMF and Current Waveforms

The stator misalignment case shows a greater imbalance in load current waveform and in back-EMF waveform compared with the rotor misalignment case. Distortion of back-EMF and phase current waveforms due to the misaligned stator can significantly affect the torque ripple and torque constant [11, 24]. Figure 13 shows that the stator misalignment defect leads to the phase shift of phase current and back-EMF voltage in the winding.

The phase shift is due to unsymmetrical armature reaction field related to both stators. Also due to stator offset, we can observe the current amplitude increases of the three phases related to stator-1, while decreasing of the three phase of the stator-2 (Fig. 13b).

Figure 14a shows the current amplitude imbalance and phase shift changes of current α_1 at load operation.

The imbalanced current is significant and can create unequal heating of the stator winding. The heat may increase the winding temperature and dangerously affect the insulation of the conductors in the armature and reduce the life expectancy of the

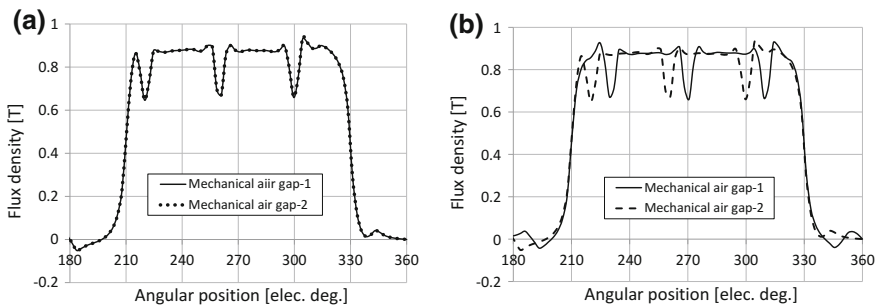


Fig. 12 No-load air gap flux density distribution. Machine without (a) and with 10 electrical degrees stator offset (b)

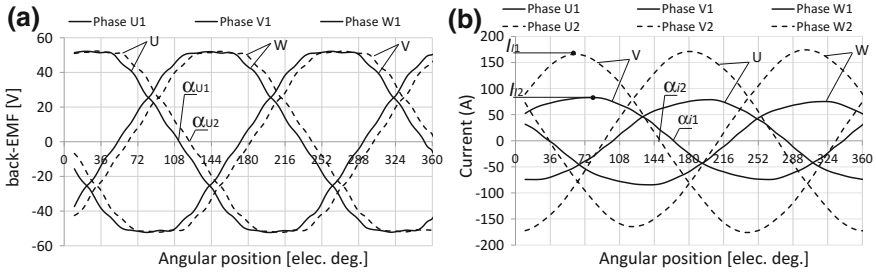


Fig. 13 Back-EMF at 1000 rpm (a) and current waveforms at full load operation (b) with 10 elec. degrees stator offset

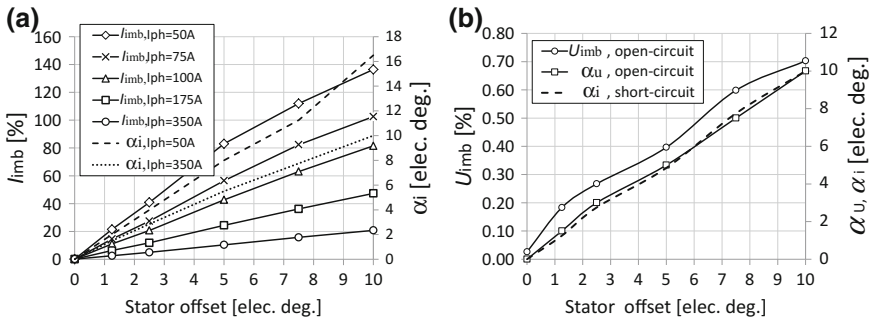


Fig. 14 Imbalance amplitude and phase shift of current for different phase currents (a), and imbalance amplitude of voltage and its phase shift at open-circuit and short-circuit current phase shift (b) versus stator offset at 1 k rpm

winding. The amplitude of back-EMF and its phase shift α_U are also affected (Fig. 14b). The amplitude of short-circuit currents was unchanged and its phase shift was similar to the voltage phase shift (Fig. 14b).

5.3 Analysis of Axial Force

The analysis predicted that axial force variations were negligible. In both cases, with and without stator offset, the axial force is not higher than 8000 N and 6200 N at full load operation in d -axis and q -axis, respectively (Fig. 15).

The effect on unbalanced axial force is much smaller when compared with the rotor misalignment case. In this study, it is found that the unbalanced force on the rotor is never higher than 50 N.

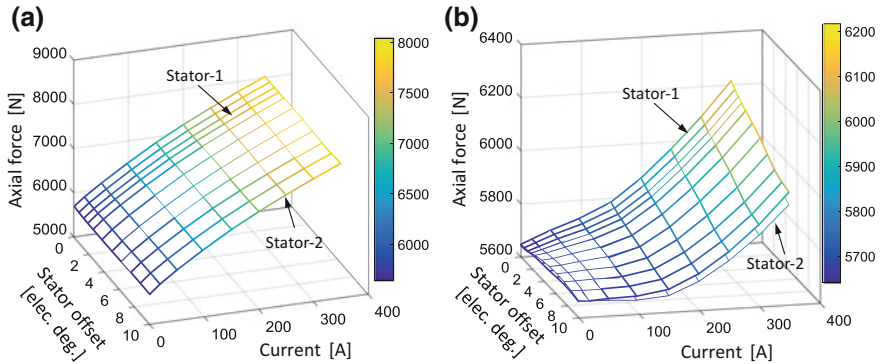


Fig. 15 Axial force versus stator offset for different phase RMS current in d -axis (a) and q -axis (b)

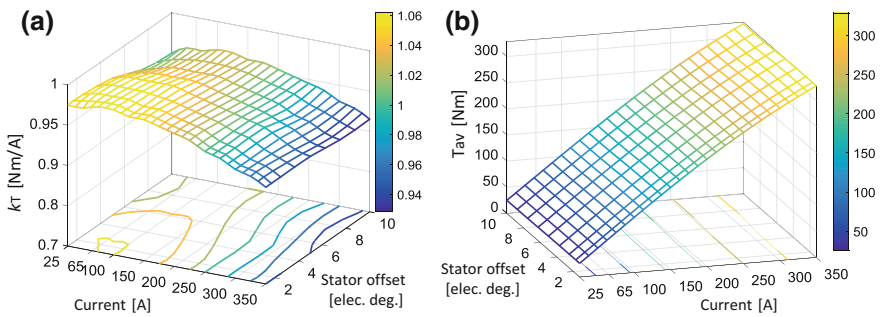


Fig. 16 Torque constant (a) and electromagnetic average torque (b), for a machine with stator offset misalignment

5.4 Analysis of Electromagnetic Torque and Torque Ripple

The most important machine parameters were not significantly affected by stator misalignment (Fig. 16). The torque constant k_T is slightly reduced at high current load when the stators are significantly shifted. It can be observed that the machine performance decreases when the stator offset is higher than 7.5 electrical degrees (Fig. 16a).

Stator misalignment reduces the cogging torque T_{cogg} by up to 78%, and the torque ripple factor ε is decreased when stator misalignment ranges between 2 and 8 electrical degrees (Fig. 17a). ε is not higher than 6% at 175 A load for the machine with any stators misaligned, whilst the ε for the machine without stator misalignment is 7.8%.

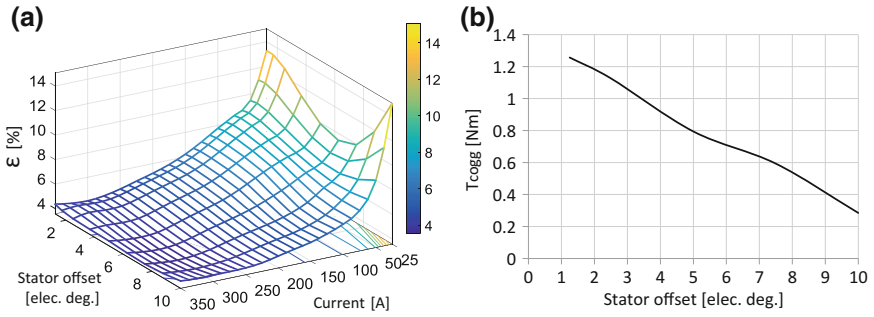


Fig. 17 Torque ripple for different RMS current (a) and cogging torque at 1 k rpm (b) for a machine with stator offset misalignment

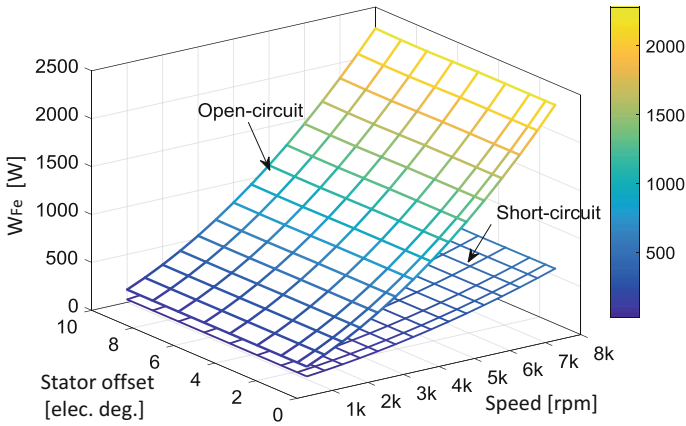


Fig. 18 Iron loss versus stator offset for different speed at open circuit and short circuit

5.5 Analysis of Iron Loss

The overall iron loss in both cores versus stator offset for different speed at open and short-circuit operation is shown in Fig. 18. It can be seen that the stator misalignment has not affected the power iron loss, and the losses in each stator core were roughly equal (the difference of iron loss between both stators was lower than 0.05%).

6 Discussion and Conclusions

In this work, the effects of rotor and stator misalignment on AFM performance were investigated using an experimentally validated 3-D FEA model. It was found that rotor misalignment caused large axial forces (1400 N for a 1.533 normalized offset) to act on the rotor. This was caused by unequal leakage flux, resulting in unequal amounts of flux in the air gaps either side of the rotor. This is an important characterization as this axial force must be accommodated for in the mechanical design of the machine. This misalignment case also caused the cogging torque to increase from 1.3 to 3.4 N m. All other machine parameters remained relatively unchanged. Iron loss in the stator cores has also been investigated and it was found that the total iron loss in the machine with 1.533 normalized rotor offset was increased by 2% compared with a ‘healthy’ machine at high speed under no-load operation. The difference in iron losses between both stator cores was 17%, which may lead to unequal heating.

It was found that stator misalignment caused large phase current imbalances (135% for 50 Å with a 10 elec. deg. misalignment). This was caused by the phase offset in the back-EMF which was a direct result of the stator misalignment. It can be concluded that any small difference between voltages will result in circulating current. This is an important characterization as imbalanced currents can cause unequal heating of the stator windings, leading one stator to reach its thermal limit before the other. This happens when recirculating current adds to current in one stator and subtracts from current in other stator. Stator misalignment leads to decreases of the cogging torque and ripple torque factor from 1.3 N m to 0.28 N m and from 7.77 to 6.04%, respectively. Iron loss in each stator core at short-circuit and open-circuit operation is not affected by stator misalignment.

References

1. Burakov, A., Arkkio, A.: Comparison of the unbalanced magnetic pull mitigation by the parallel paths in the stator and rotor winding. *IEEE Trans. Magn.* **43**, 4083–4088 (2007)
2. Li, Y., Zhou, G., Wan, S., Li, H.: Analysis of unbalanced magnetic pull on turbo-generator rotor under air-gap eccentric fault and rotor short circuit fault. *Int. J. Adv. Comput. Technol.* **5**, 523–530 (2013)
3. Wu, L.J., Zhu, Z.Q., Chen, J.T., Xia, Z.P.: An analytical model of unbalanced magnetic force in fractional-slot surface-mounted permanent magnet machines. *IEEE Trans. Magn.* **46**, 2686–2700 (2010)
4. Li, J.T., Liu, Z.J., Nay, L.H.: Effect of radial magnetic force in permanent magnet motors with rotor eccentricity. *IEEE Trans. Magn.* **43**, 2525–2527 (2007)
5. Shek, J.K.H., Dorrell, D.G., Hsieh, M., Lin, H., Mostafa, K.: Unbalanced forces in electrical generators for wave and tidal devices. In: *European Wave and Tidal Energy Conference*, pp. 1–6 (2013)
6. Ebrahimi, B.M., Faiz, J., Roshtkhari, M.J.: Static-, Dynamic-, and Mixed-Eccentricity Fault Diagnoses in Permanent-Magnet Synchronous Motor, vol. 56, pp. 4727–4739 (2009)

7. Malloy, A.C., Mlot, A., Cordner, M.J., Lamperth, M.: Axial flux machines for hybrid module applications. In: IEEE International Electric Vehicle conference, pp. 1–8 (2014)
8. Malloy, A.C.: Thermal Management of the Permanent Magnet in the Totally Enclosed Axial Flux Permanent Magnet Synchronous Machine, pp. 1–225. Ph.D. dissertation. Imperial College London, London (2014)
9. Mlot, A., Malloy, A.C., Lamperth, M.U.: Effect of rotor/stator on the performance of a permanent magnet axial-flux motor. In: 8th IET International Conference on Power Electronics, Machines and Drives (PEMD), pp. 1–6 (2016)
10. Kim, J.M., Sung, S.J., Jang, G.H.: Characterization and experimental verification of the axial unbalanced magnetic force in brushless DC motors. *IEEE Trans. Magn.* 3001–3004. (2012)
11. Faiz, J., Ebrahimi, B.M., Akin, B., Toliyat, H.A.: Finite-element transient analysis of induction motors under mixed eccentricity fault. *IEEE Trans. Magn.* **44**, 66–74 (2008)
12. Takahata, R., Wakui, S., Miyata, K., Noma, K., Senoo, M.: Analysis of rotor eccentricity on permanent magnet synchronous characteristics. In: The 2010 International Power Electronics Conference, pp. 1306–1311 (2010)
13. Mirimani, S.M., Vahedi, A., Marignetti, F.: Effect of inclined static eccentricity fault in single stator-rotor axial flux permanent magnet machines. *IEEE Trans. Magn.* **48**, 143–149 (2012)
14. Dorrell, D.G., Hsieh, M.F., Guo, Y.G.: Unbalanced magnet pull in large brushless rare-earth permanent magnet motors with rotor eccentricity. *IEEE Trans. Magn.* **45**, 4586–4589 (2009)
15. Mirimani, S.M., Vahedi, A.: Effects of static eccentricity in axial flux permanent magnet machines. In: IEEE Power Electronic & Drive Systems & Technologies Conference, pp. 311–315 (2010)
16. Jang, S.M., Lee, S.H., Cho, H.W., Cho, S.K.: Analysis of unbalanced force for high-speed slotless permanent magnet machine with Halbach array. *IEEE Trans. Magn.* **39**, 3265–3267 (2003)
17. Cho, C.P., Fussel, B.K.: Detent torque and axial force effects in a dual air-gap axial-field brushless motor. *IEEE Trans. Magn.* **29**, 2416–2418 (1993)
18. Tenhunen A.: Finite-element calculation of unbalanced magnetic pull and circulating current between parallel winding in induction motor with non-uniform eccentric rotor. In: Proceedings of Electromotion'01, pp. 19–24 (2001)
19. Kelk, H.M., Eghbali, H.A., Toliyat, H.A.: Modelling and analysis of cage induction motors under rotor misalignment and air gap eccentricity. In: IEEE Industry Applications Conference, vol. 2, pp. 1324–1328 (2005)
20. Ghoggal, A., Zouzou, S.E., Sahraoui, M., Derghal H., Hadri-Hamida, A.: A winding function-based model of air-gap eccentricity in saturated induction motors. In: XXth International Conference on Electrical Machines, pp. 2739–2745 (2012)
21. Faiz, J., Pakdelian, S.: Diagnosis of static eccentricity in switched reluctance motors based on mutually induced voltages. *IEEE Trans. Magn.* **44**, 2029–2034 (2008)
22. Benhama, A., Willoamson, A.C., Reece, A.B.J.: Force and torque computation from 2-D and 3-D finite element field solution. *IEEE Electron. Power Appl.* 25–31 (1999)
23. Sobora, J., Byrtus, M., Kindl, V., Hruska K.: Analysis of rotor's eccentricity influence on bearing load of induction machine. In: 16th International Conference on Mechatronics-Mechatronica, pp. 71–78 (2014)
24. Hwang, S.M., Kim, K.T.: Comparison of vibration sources between symmetric and asymmetric HDD spindle motors with rotor eccentricity. *IEEE Trans. Ind. Appl.* **37**, 1727–1731 (2001)
25. Nakata, T., Takahashi, N., Uehara, K.: Analysis of magnetic characteristics of brushless DC motor taking into account the distribution of magnetization. *IEEE Trans. Magn.* **22**, 1084–1086 (1986)

26. Mlot, A., Lukaszyn, M., Korkosz, M.: Influence of an end-winding size on proximity losses in a high-speed PM synchronous motor. In: Selected Problems of Electrical Engineering and Electronics (WZEE), pp. 1–6 (2015)
27. Mlot, A., Korkosz, M., Lukaszyn, M.: Investigation of end winding proximity losses in a high-speed PM machine. In: Lecture Notes in Electrical Engineering 324, Analysis and Simulation of Electrical and Computer Systems, pp. 171–186. Springer, Berlin (2015)
28. Mlot, A., Korkosz, M., Grodzki, P., Lukaszyn, M.: Analysis of the proximity and skin effects on copper loss in a stator core. Arch. Electr. Eng. **63**(2), 211–225 (2014)
29. Cedrat: Flux3D, User's Guide. (2008)

Field-Based Analysis and Optimal Shape Synthesis of Switched Reluctance Motors

Paolo Di Barba, Maria Evelina Mognaschi, Marek Przybylski,
Najmeh Rezaei, Barbara Slusarek and Slawomir Wiak

Abstract This study focuses on a class of a three-phase switched reluctance motor. The aim of the paper is to optimize torque and iron loss as a function of the geometry. To enhance the efficiency of the motor, a procedure of automated optimal design is adopted. The analysis model of the motor is based on 2D finite element method simulation, while the design optimization is based on evolutionary computing.

Keywords Finite elements methods · Genetic algorithm · Multi-objective optimization · Switched reluctance motor

1 Introduction

Switched reluctance motors (SRM) have inherent advantages such as simple structure with non-winding construction in rotor side, fail-safe because of high tolerances, robustness, low cost with no permanent magnet in the structure, and also

P. Di Barba (✉) · M.E. Mognaschi · N. Rezaei
Department of Electrical, Computer and Biomedical Engineering,
University of Pavia, Pavia, Italy
e-mail: paolo.dibarba@unipv.it

M.E. Mognaschi
e-mail: eve.mognaschi@unipv.it

N. Rezaei
e-mail: najmeh.rezaei01@ateneopv.it

M. Przybylski · B. Slusarek
Tele and Radio Research Institute, Warsaw, Poland
e-mail: marek.przybylski@itr.org.pl

B. Slusarek
e-mail: barbara.slusarek@itr.org.pl

S. Wiak
Institute of Mechatronics and Information Systems,
Lodz University of Technology, Lodz, Poland
e-mail: swiak@wp.pl

possible operation at high temperatures or under strong temperature variations [1]. With these advantages, the SRM recently are increasingly used in a broad range of applications. The fundamental theory, design procedure, modeling, and analysis of SRM have been presented in the literature [2–4]. In recent years, machine designers have focused greatly on evolutionary computation based design optimization techniques to fulfill the desired performance requirements under various constraints such as converter rating, winding configuration, and outline dimensions [5]. Automated optimal design of motors has been applied since the 90s [6] and nowadays it is still being used successfully [7]. Multi-objective optimization methodology has been used in various optimization problems in different areas of engineering considering the aspect multi-physics of the electrical devices and MEMS actuator like those proposed in [8, 9]. From the literature [10–12], it is also evident that computational intelligence techniques like genetic algorithm (GA) has been effectively implemented for design optimization of SRM.

As the design of SRM for a particular application is a compromise between various performance criteria, improvement of a performance parameter may result in the degradation of other important features. Consequently, the designer has to search for solutions that are feasible with respect to all performance parameters. To deal with this trade-off and achieve efficient design, multi-objective optimization based design techniques seem to be the most suitable approach. Hence, there is growing interest towards the application of multi-objective optimization techniques for solving a wide variety of SRM design optimization problems [13].

Shape design of electromagnetic devices usually demands that multiple criteria be fulfilled concurrently. The most general solution is represented by the front of nondominated solutions [14]. The aim of this study is to optimize geometrical parameters of a 12/8 SRM to improve the maximum torque and also to reduce the total iron losses. The machine then is analyzed through finite element model (FEM) due to its accuracy in modeling complex geometry and considering physical phenomena like saturation. Genetic algorithm (GA) optimization code was carried out under MATLAB software coupled to FEM.

2 Motor Model and Field Analysis

The proposed structure of the 12/8 SRM, characterized by nominal power 450 W, 14,000 rpm and supply voltage of whole drive of 230 V, 50 Hz is shown in Fig. 1. It can be used as the drive of house appliances like washing machines [15]. The values of physical sizes of motor are reported in Table 1.

The stator and the rotor are assumed to be made of “M27: USS Motor - 26 Gage (M330-50-A5 according to IEC 60404-8-4 standard)” 0.5 mm thick electrical steel which the B–H curve is shown in Fig. 2 and loss curve is shown in Fig. 3. An advanced design procedure is needed in view of the design optimization in terms of geometry properties.

Fig. 1 Geometry, design variables, flux lines

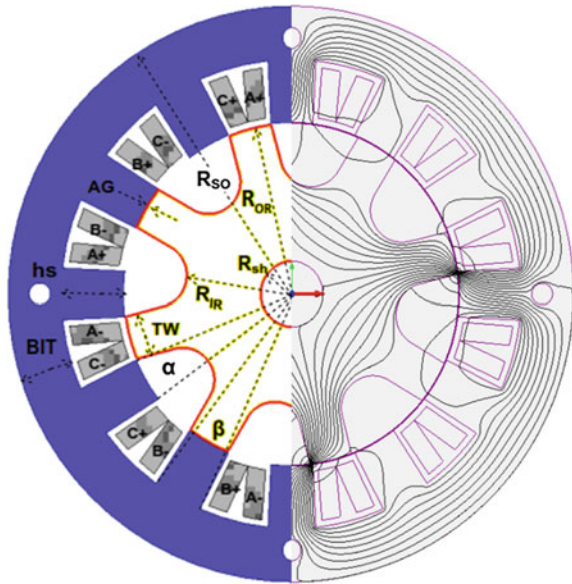


Table 1 Size of switched reluctance motor

Parameters	Value	Symbol
Stator outer radius	70 mm	R_{SO}
Stator inner radius	41.75 mm	R_{SI}
Shaft radius	8 mm	R_{Sh}
Air gap length	0.25 mm	AG
Rotor outer radius	41.5 mm	R_{OR}
Rotor pole width	11 mm	TW
Rotor inner radius	26.5 mm	R_{IR}
Stator pole height	15.25 mm	h_s
Back iron thickness	13 mm	BIT
Stator tooth outer span	15.14 ($^{\circ}$)	α
Stator tooth inner span	12.58 ($^{\circ}$)	β
Number turns of a coil winding	140	N
Axial length of a magnetic core	46.6 mm	

Since the motor exhibits a four-pole magnetic field which is shown in Fig. 1; currents in the motor windings have been set to simulate one-phase control mode ($i_a \neq 0, i_b = 0, i_c = 0$). Each phase incorporates four coils; phase “a” is driven by unipolar current with a constant value of 1 A. The two-dimensional finite element model of the motor is implemented using MagNet code by Infolytica [16]. The mesh with maximum element size of 0.5 mm with a detail of which is shown in Fig. 4 is considered. In simulation, the axial stack length has been set equal to 1 m.

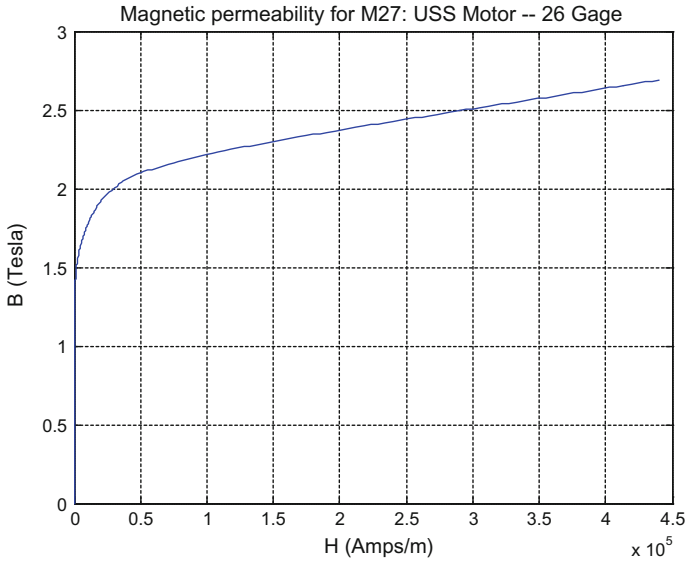


Fig. 2 Specific B-H curve for M27 material

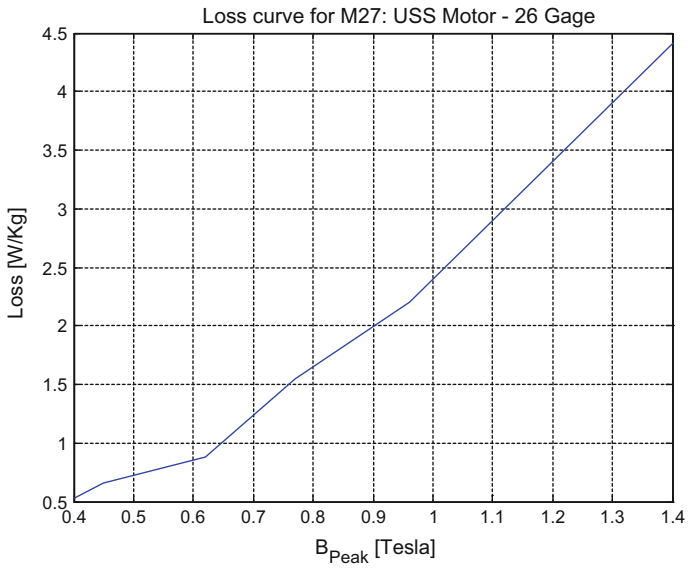
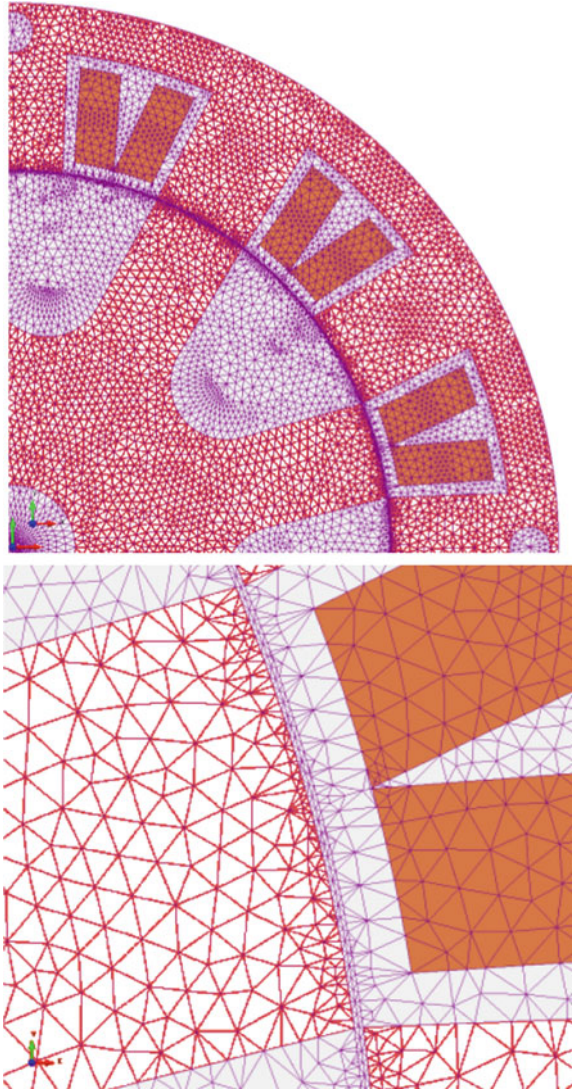


Fig. 3 Loss curve for M27 material at a frequency = 60 Hz

Fig. 4 Detail of the mesh

A typical solution for the field analysis of prototype model is shown in Fig. 1. The torque versus rotor position over 45° is shown in Fig. 5. Moreover, total losses were calculated by assuming supplying phase A with 1 A current with 60 Hz frequency and is also shown in Fig. 5. Additionally, magnetic induction along the air gap midline is shown in Figs. 6 and 7.

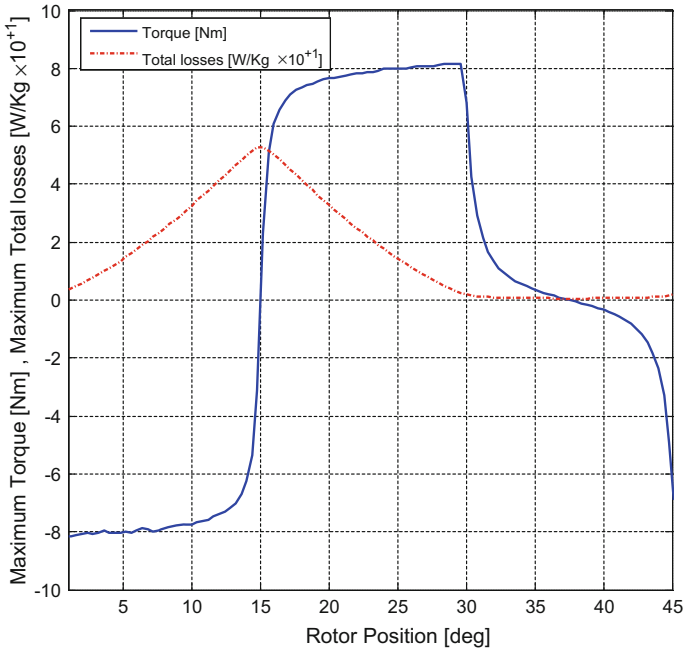


Fig. 5 Motor torque and iron losses versus rotor position for prototype

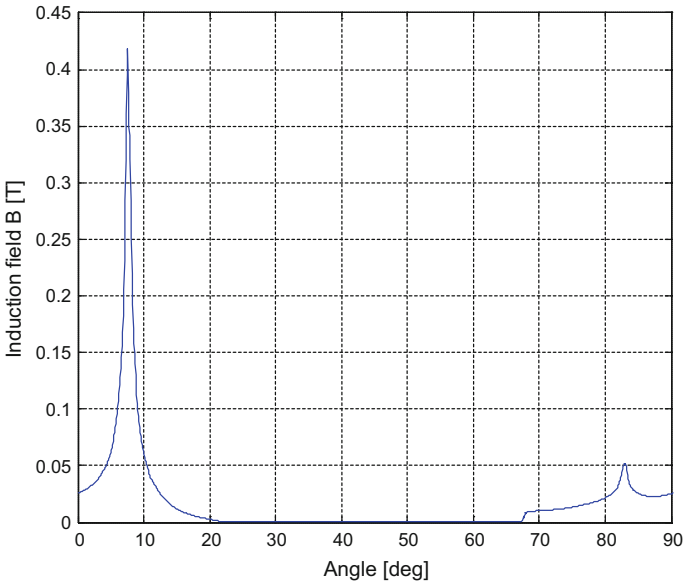


Fig. 6 Magnetic induction along the air gap midline at rotor initial position (see Fig. 1)

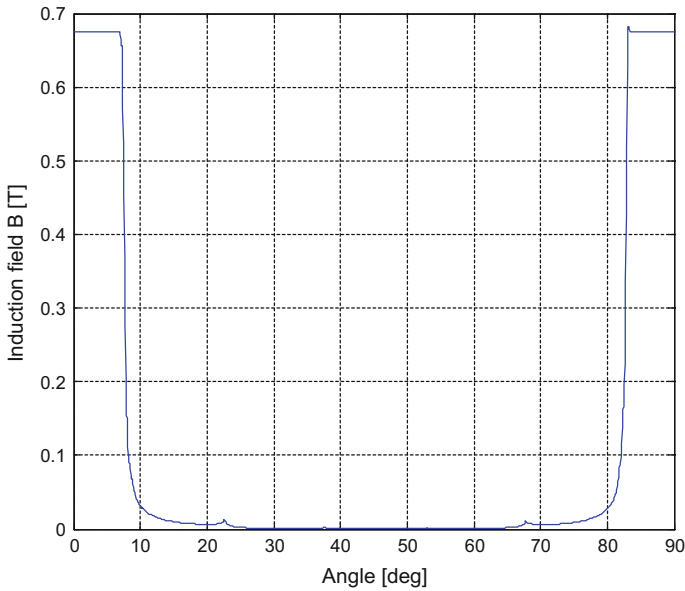


Fig. 7 Magnetic induction along the air gap midline with rotor aligned with stator poles

3 Inverse Problem: Optimal Shape Synthesis

Geometric sizes of machine are considered as unknown parameters for the optimization procedure. Specifically, the rotor outer radius, rotor inner radius, and back iron thickness are considered as design variables while the remaining parameters are considered as fixed.

X_1 = rotor outer radius (R_{OR})

X_2 = rotor inner radius (R_{IR})

X_3 = back iron thickness (BIT)

The following inverse problem is considered:

given the material properties (i.e., B–H magnetization curve, P–B loss curve) and the power supply (one phase on, equal to 1 A), find the optimal values of geometric variables such that the maximum torque is maximized and the iron loss is minimized, subject to the problem constraints.

3.1 Design the Problem

A vector $X = \{X_i\}$, $i = 1, 2, 3$ of design variables is shown in Fig. 8. To satisfy variable bound as one of constraints, the overall diameter of the switched reluctance

Fig. 8 Prototype geometry, design variables

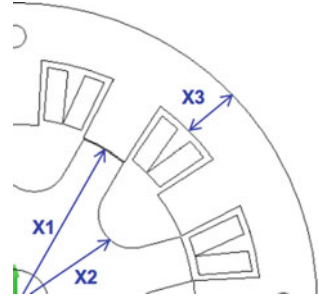


Table 2 Variation range of the design variables

Design variables X (mm)	X_1	X_2	X_3
Min	30.5	17	6
Max	46.6 mm	30.97	24

motor must not exceed 70 mm; and the air gap width is kept constant equal to 0.25 mm. The range of continuous-valued variables is reported in Table 2.

Overall, the constraints define the feasible design space of $\Omega \in \mathbb{R}^3$. The problem of determining optimal value for these parameters is formulated to provide trade-off solutions between torque density and power loss in the iron core. The objective functions are defined as:

$$f_1(x) = \text{Minimization of total iron losses}$$

$$f_2(x) = \text{Maximization of the maximum value of torque.}$$

The above criteria are defined by:

$$f_1(x) = \int_{S(x)} P[B(x)]^2 ds, x \in \Omega$$

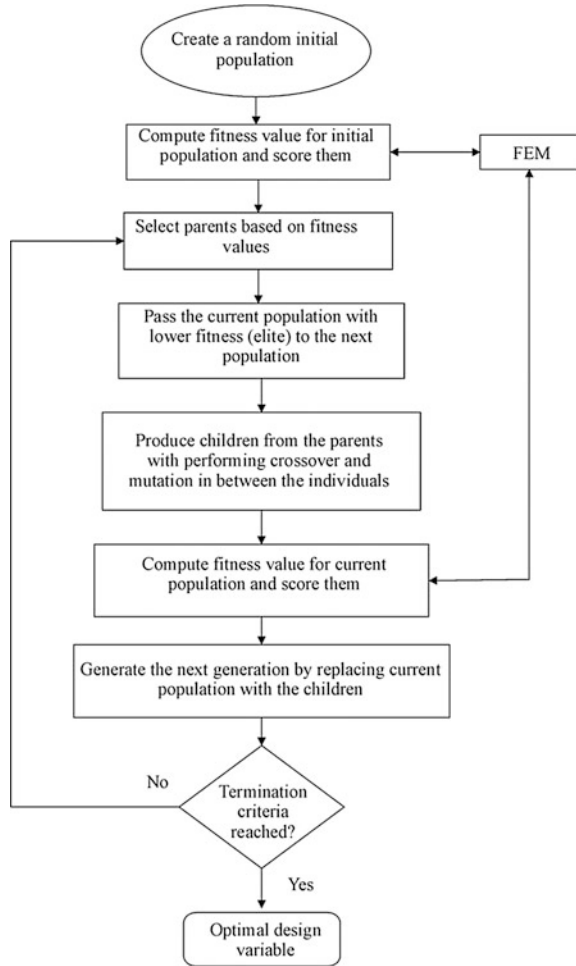
$$f_2(x) = \int r_0 \times f dv,$$

$$f = \int_{\Omega} \nabla \cdot \overline{\overline{T}} d\Omega = \int_{\Gamma} \overline{\overline{T}} \cdot \overline{\overline{n}} d\Gamma$$

where P is the specific power loss in the ferromagnetic material subject to induction B , S is iron volume, r_0 is the vector going from the origin to an element of volume in the body, V is the volume of the body, f is the force on body calculated by $\overline{\overline{T}}$ the Maxwell's stress Tensor, Γ is a closed surface enclosing the body and $\overline{\overline{n}}$ is the outward normal versor, respectively. Due to this fact that the induction, iron volume, and force values are dependent on x (the design variables), thus the inverse problem should be investigated for finding optimal values of geometric parameters for a given material to satisfy problem criteria.

In this study, a multi-objective genetic algorithm optimization method based on Pareto-optimal solutions is implemented for solving the problem. Figure 9 shows the flowchart diagram that is used for multi-objective optimal design of an SR motor in MATLAB [17].

Fig. 9 Optimal design of SR motor by GA in MATLAB



3.2 Optimization Process and Problem Formulation

Genetic algorithm (GA) is one kind of direct search algorithms, based on the developing mechanism from genetic evolution and natural selection. It begins by randomly creating its population. Each individual of the population represents a search point in the space of potential solutions of the given optimization problem. Candidate solutions are combined by a crossover operator to produce offspring, which expands the current population of solutions. Thus, the individuals in the population are evaluated via the fitness function. Meanwhile, a mutation operator is performed at a certain probability level to increase variation in the search space. By favoring the mating of the more fit individuals, the more promising areas of the search space are explored. The process of evaluation, selection, crossover and

mutation is repeated until a predetermined number of generations are reached or a satisfied solution has been found. The following sections describe each of the components of our GA method [18].

Multi-objective optimization involves minimizing or maximizing multiple objective functions subject to a set of constraints that are often contradictory, as the minimization of an objective leads to an increase of another goal, so the solution we seek is always a compromise between these objectives. The general multi-objective optimization problem (MOOP) can be stated as finding the n -dimensional vector, x , which

$$\text{Min or Max } f(x) = f_1(x), f_2(x), f_3(x), \dots, f_n(x) \quad (1)$$

$$x \in F$$

where $x \in R^n, f_i : R^n \rightarrow R$ and F is the feasible set of problem including inequality, equality and/or variable bounds to be satisfied such as:

$$F = \{x \in R^n : g_i(x) \leq 0 \ \& \ h_i(x) = 0 \ \& \ a x_{lb} \leq x_i \leq x_{ub} \quad i = 1, 2, \dots, n \quad (2)$$

The vector $f(x)$ includes several objective functions. An ideal solution of (1) introduced as Pareto-optimal solution (nondominated set) would be a point $x^* \in F$ such that (Table 3):

$$f_i(x^*) \leq f_i(x), \forall x \in F, \forall i \in \{1, 2, \dots, k\}$$

Population size is the number of individuals in each generation.

Selection function defines the selection method of parents for the next generation. ‘‘Tournament’’ selection chooses each parent by choosing tournament size players at random and then choosing the best individual out of that set to be a parent.

Crossover function is a genetic operator that combines two individuals, or parents to produce a new child for the next generation. The ‘‘Intermediate’’ crossover function creates children by taking a weighted average of the parents. Intermediate crossover (IC) is controlled by a single parameter ratio which can be a scalar or a row vector of length number of variables.

Table 3 Genetic optimization parameters

Parameters	Value/type
Population size	20
Selection function	Tournament
Crossover function	Intermediate
Mutation function	Adaptive feasible
Elite count	1
Crossover fraction	0.8
Pareto fraction	1
Stopping criterion	50 generations

$$\text{child} = \text{parent1} + \text{rand} * \text{Ratio} * (\text{parent2} - \text{parent1})$$

The ratio parameter in this study is set to 1.

Mutation function is used by genetic algorithm to make small random changes in the individuals in the population in order to create mutation children that provides genetic diversity. Thus, mutation enables the genetic algorithm to search a broader space. “Adaptive Feasible” mutation function is used so that mutation satisfied constraints and bounds.

Elite count specifies the number of individuals that are guaranteed to survive to the next generation.

Crossover fraction sets the fraction of the next generation, other than elite children, that are produced by crossover.

Pareto fraction defines the fraction of individuals to keep on the first Pareto front while the solver selects individuals from higher fronts.

Stopping criterion determines what causes the algorithm to terminate [17].

4 Results

The results of the optimization (solution of a Pareto-optimal set in objective space) and the objective function space of the synthesis problem are shown in Fig. 10. The solutions (marked by circles) are examples of best compromise solution between conflicting design criteria, i.e., torque and losses [19].

To illustrate the specific improvements obtained from optimization, two solutions are selected and their comparison with initial design (prototype) is presented in Table 4. The comparison of the results shows that solution B has best maximum torque but higher iron loss, whereas solution A has low iron loss and poor torque. The comparison of the results verified that each objective gets improved at the cost of the other and there is a clear trade-off between maximum torque and total losses. Notice that there is no clear best design, therefore the design can be selected based on the preferences of the designer, for a given specific application.

Flux and field distributions of the two optimal designs in the nominal condition are carried out by Magnet. The geometry and field results are shown in Figs. 11 and 12.

With respect to the optimal solutions obtained on Pareto front (circles in Fig. 9), the trend of varying design variables along Pareto front is shown in Fig. 12. By analyzing Figs. 9 and 12, the contribution of each design variables to performance of the model is defined. It shows that as rotor outer radius is increased, the maximum torque and consequently maximum iron losses are increased too. In contrary, as back iron thickness is increased, the maximum torque and maximum losses are decreased. It is worth highlighting that rotor inner radius makes nondominant contribution to quality characteristics. Additionally, it is also interesting to note that the prototype is one of the solutions on the front (Fig. 13).

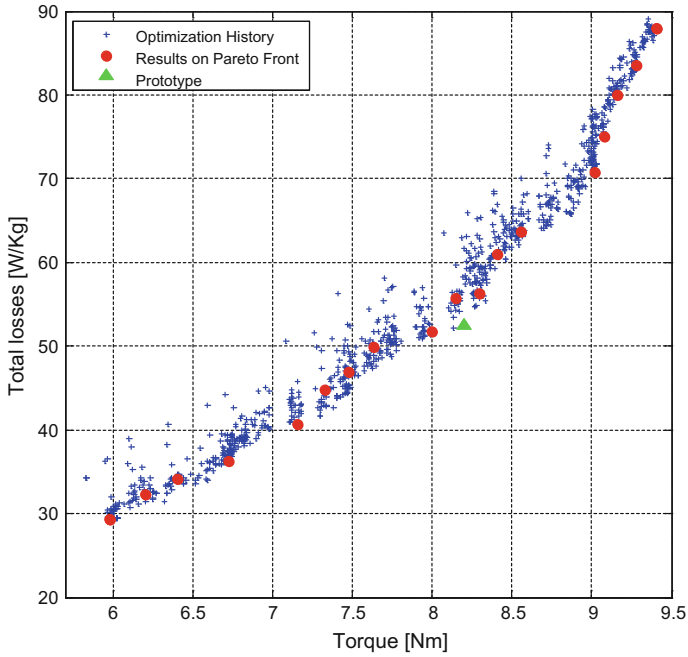


Fig. 10 Objective space, prototype (*triangle*), nondominated solutions (*circle*)

Table 4 Compared solutions obtained for objective functions

Performance parameters	Rotor outer radius (mm)	Rotor inner radius (mm)	Back iron thickness (mm)	Torque (Nm)	Total losses (W/kg)
Solution A	48.37	17.54	6.13	9.41	87.90
Solution B	30.50	18.87	24.00	5.98	29.25
Prototype	41.50	26.50	13.00	8.20	52.46

Fig. 11 Geometry and flux lines for solution A

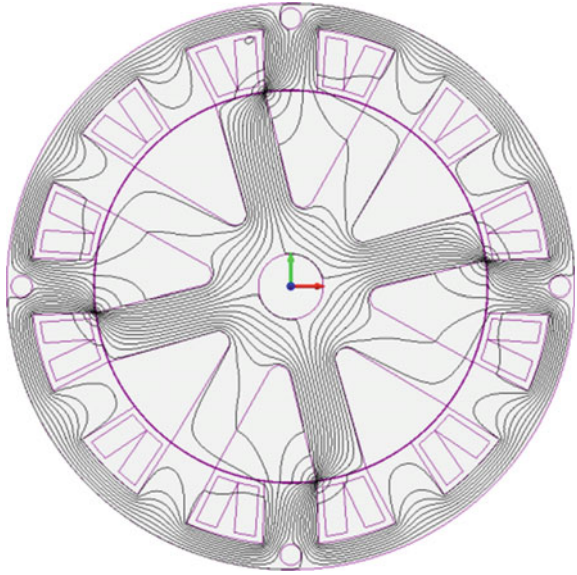
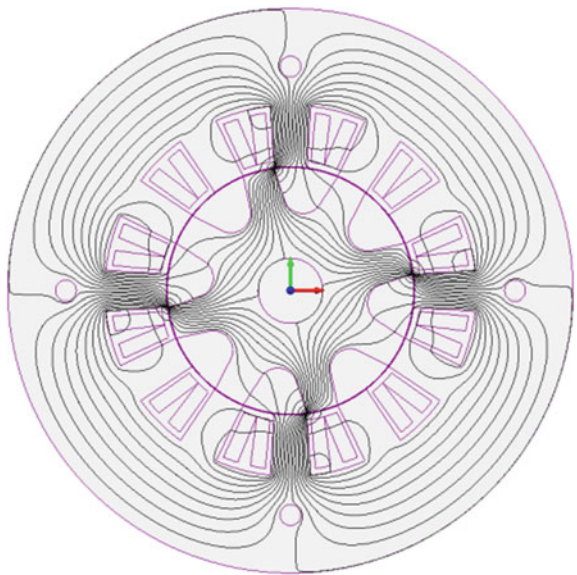


Fig. 12 Geometry and flux lines for solution B



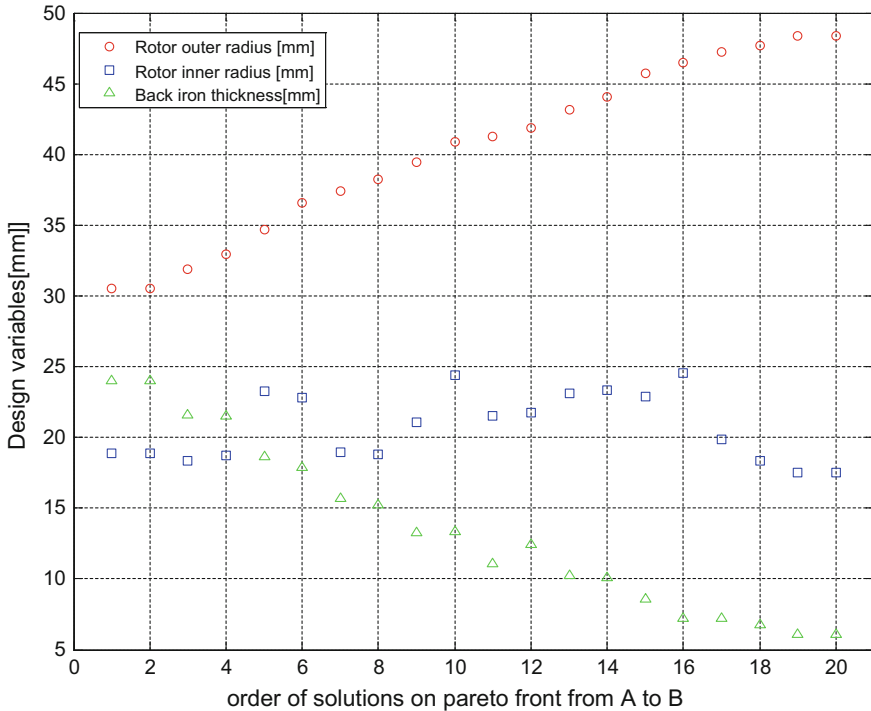


Fig. 13 Pareto front solutions comparison as a function of design variables

5 Conclusion

The optimization approach used in this work has proved that the optimal shape design problem is well posed because it has achieved its objectives, namely improving the performance of a 12/8 SRM prototype through the optimization of geometrical parameters under constraints. According to the results, it is possible to identify solutions which improved both torque and total iron losses.

References

1. Ahn, J.W.: Switched Reluctance Motor, Torque Control. InTech, Croatia (2011)
2. Stephenson, J.M., Blenkinsop, P.T., Corda, J., Fulton, N.N.: Variable-speed switched reluctance motors. *IEE Proc. Electr. Power Appl.* **127**, 253–265 (1980)
3. Krishnan, R.: Switched Reluctance Motor Drives: Modeling, Simulation, Analysis, Design, and Applications. CRC Press, Boca Raton (2001)
4. Miller, T.J.E.: Optimal design of switched reluctance motors. *IEEE Trans. Ind. Electron.* **49**, 15–27 (2002)

5. Uler, G.F., Mohammed, O.A., Koh, C.S.: Utilizing genetic algorithms for the optimal design of electromagnetic devices. *IEEE Trans. Magn.* **30**, 4296–4298 (1994)
6. Palka, R.: Synthesis of magnetic fields by optimization of the shape of areas and source distributions. *Archiv für Elektrotechnik* **75**, 1–7 (1991)
7. Di Barba, P., Mognaschi, M.E., Palka, R., Paplicki, P., Szkolny, S.: Design optimization of a permanent-magnet excited synchronous machine for electrical automobiles. *Int. J. Appl. Electromagn. Mech.* **39**, 889–895 (2012)
8. Di Barba, P., Dolezel, I., Mognaschi, M.E., Savini, A., Karban, P.: Non-linear multi-physics analysis and multi-objective optimization in electroheating applications. *IEEE Trans. Magn.* **50**, 673–676 (2014)
9. Di Barba, P., Dughiero, F., Mognaschi, M.E., Savini, A., Wiak, S.: Biogeography-inspired multiobjective optimization and MEMS design. *IEEE Trans. Magn.* **52**, 1–4 (2016)
10. Mirzaeian, B., Moallem, M.: Multiobjective optimization method based on a genetic algorithm for switched reluctance motor design. *IEEE Trans. Magn.* **38**, 1524–1527 (2002)
11. Raminosa, T., Blunier, B., Fodorean, D., Miraoui, A.: Design and optimization of a switched reluctance motor driving a compressor for a PEM fuel-cell system for automotive applications. *IEEE Trans. Ind. Electron.* **57**, 2988–2997 (2010)
12. Goldberg, D.E.: *Genetic Algorithms in Search, Optimization and Machine Learning*. Addison Wesley Longman Publishing, Boston (1989)
13. Balaji, M., Kamaraj, V.: Evolutionary computation based multi-objective pole shape optimization of switched reluctance machine. *Int. J. Electr. Power Energy Syst.* **43**, 63–69 (2012)
14. Di Barba, P., Mognaschi, M.E.: Recent experiences of multiobjective optimization in electromagnetic: a comparison of methods. *Int. J. Comput. Math. Electr. Electron. Eng.* **24**, 921–930 (2005)
15. Jankowski, B., Kapelski, D., Karbowski, M., Przybylski, M., Ślusarek, B.: Analysis of static characteristics of a switched reluctance motor. In: Gołębiowski, L., Mazur, D. (eds.) *LNEE*, vol. 324, pp. 289–304. Springer, Heidelberg (2015)
16. MagNet, Infolytica Corporation. <http://www.infolytica.com>
17. MATLAB Genetic Algorithm, The MathWorks, Inc., Natick, USA (2013)
18. Xu, J.X., Panda, S.K., Zheng, Q.: Multiobjective optimization of current waveforms for switched reluctance motors by genetic algorithm. *Int. J. Model. Simul.* **24**, 1860–1865 (2002)
19. Di Barba, P., Mognaschi, M.E.: Sorting Pareto solutions: a principle of optimal design for electrical machines. *Int. J. Comput. Math. Electr. Electron. Eng.* **28**, 1227–1235 (2009)

An Analytical Model of an Electrical Machine with Internal Permanent Magnets

Part II. The Work of Electric Generator Under an Unbalanced Load: Simulations and Measurement Verification

Tomasz Drabek and Jerzy Skwarczyński

Abstract This paper presents an analytical, circuit model of three-phase electrical machine with permanent magnets submerged in ferromagnetic rotor, modified in relation to the model presented in the first part of the study. This modification involves taking account of armature reaction, what required changes in the structure of the model. The model takes into account a strong, local saturation of the magnetic circuit of the rotor that depends also on the armature currents. Of course, the model also includes a voltage–current equations of the armature on the stator. The paper presents the results of the measurement verification of this model. The range of the control tests contains electrical waveforms in steady states only, since he had to check the overall usefulness of mathematical formalism, which was not used yet. The verification of the model was performed for the machine operating as a generator, with a single-phase resistive load. The verification results are positive.

Keywords Electrical machine with magnets · Circuit model of the machine · Local saturations · Permeability of the air gap

T. Drabek (✉) · J. Skwarczyński
Department of Power Electronics and Energy Control Systems,
Faculty of Electrical Engineering, Automatics, Computer Science
and Biomedical Engineering, AGH University of Science
and Technology, Krakow, Poland
e-mail: drabek@agh.edu.pl

J. Skwarczyński
e-mail: jskw@agh.edu.pl

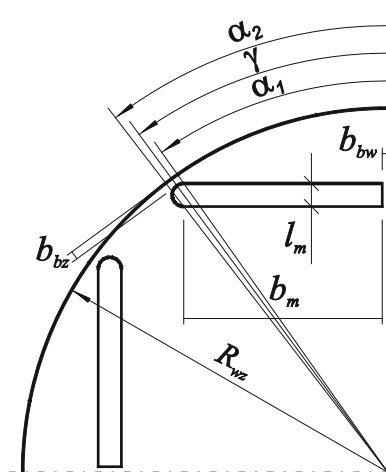
1 The Aim and Scope of the Study

In the first part of our work has been formulated mathematical model of synchronous machine with internal permanent magnets [1]. The model was formulated based on [2–7]. An initial measurement verification of the model was in [1]. It was based on a comparison of the calculated waveforms of electromotive forces (EMF), induced in the open armature winding, with the waveforms measured on the real machine (in generator operation, with the open armature winding). The object of the study was a three-phase synchronous machine, with rated data: $P_N = 4$ kW, $U_N = 400$ V, $I_N = 7.3$ A, $n_N = 1500$ rot/min. Armature winding is symmetrical, in the 36 half-open stator slots. Neodymium magnets of the excitation are embedded in the core of the cylindrical rotor. Figure 1 shows the cross section of the machine (as in [1]).

Comparison of the results of calculations and measurements shows the small adjustments needed to the parameters of the mathematical model, initially determined on the basis of the technical documentation of the machine. Because after the corrections were obtained waveforms fully in line with measured waveforms [1], it was necessary to check whether the adjusted parameters will get similarly good simulation results for the loaded machine. However, it required additions to theory and to prepare appropriate programs of digital computation. Therefore, these actions have been moved to this stage of work.

Verification of the mathematical model of a synchronous machine with internal permanent magnets in load conditions should be based on a comparison of selected waveforms measured on the modeled machine with obtained computationally, based on the equations of the model. This may be performed under various conditions, of which the most characteristic ones should be considered: work of the machine in power grid and work of generator with inactive load. Work of the machine in power grid is troublesome for modeling, due to the difficulties in identification evolving parameters of the grid and its voltage waveforms.

Fig. 1 The cross section of one pole of the rotor



Much easier to model is a generator operation with a separate load. It can be carried at a load either balanced or unbalanced, in the extreme case for loaded single phase only. It appears that the armature reaction of the one phase generator load can be considered as a sufficiently general case to start the verification process.

2 The Mathematical Model of a Loaded Generator

The range of tests covered electrical waveforms in steady state only, because he had to check the overall usefulness of new mathematical formalism. Therefore, computer simulations were performed assuming a constant rotational speed of the rotor. Circuit model of the machine is described by ordinary differential equations. Due to the nonlinearity of the magnetic circuit, the numerical method integration of the equations is chosen.

Each of the three symmetrical armature windings (phase) is described by the equation:

$$u_{zk} = (R_s + R_{zk})i_{sk} + (L_{\sigma s} + L_{zk})\frac{di_{sk}}{dt} + \frac{d}{dt}\psi_{sk} \quad k = 1, 2, 3, \quad (1)$$

where u_{zk} —a voltage source connected to the circuit of the stator phase in series, i_{sk} —current of stator phase k ($k = 1, 2, 3$), R_s —resistance of phase, $L_{\sigma s}$ —leakage inductance of phase, R_{zk} , L_{zk} —resistance and inductance connected to the phase in series (as a load), ψ_{sk} —magnetic flux coupled to the phase, derived from the permanent magnets ψ_{smk} and from armature currents ψ_{ssk} :

$$\psi_{sk} = \psi_{smk} + \psi_{ssk} \quad (2)$$

For numerical integration of Eq. (1), equations were described in the form:

$$\frac{d}{dt}\psi_k = u_{zk} + e_{smk} - (R_s + R_{zk})i_{sk}, \quad (3)$$

where

$$e_{smk} = -\frac{d}{dt}\psi_{smk} \quad (4)$$

$$\psi_k = (L_z + L_{\sigma s})i_{sk} + \psi_{ssk}(i_1, i_2, i_3, \varphi) \quad (5)$$

φ —the angle of the rotor position.

3 Armature Reaction

In order to analytically determine the magnetic flux coupled to the armature is necessary to determine the magnetic field in the air gap between the rotor and stator (in “main air gap” of the machine). Magnetic field distribution in the air gap, determined by the armature currents and by the permanent magnets of the rotor, may be represented by the formula [1]:

$$B_g(\alpha) = -\frac{\mu_0}{\delta_z} \{U_{bz_m}(\alpha) + \Theta_{z_m}(\alpha)\}, \quad (6)$$

where $\theta_{z_m}(\alpha)$ —angular distribution of the armature ampere-turns, $U_{bz_m}(\alpha)$ —angular distribution of magnetic tension across external magnetic bridges of the rotor [1], δ_z —radial dimension of the substitute air gap, α —angle coordinate of the rotor, measured from the magnetic axis one of the magnets.

Angular distribution of the armature ampere-turns (without average value) can be represented by the formula:

$$\Theta_{z_m}(\beta) = \sum_{v=1,3,5\dots}^{\infty} \Theta_{mv} \cos v p_b (\beta - \chi_t), \quad (7)$$

where

$$\Theta_{mv} = \left\{ -\frac{4}{\pi} z_{ip} \frac{\sin v p_b \vartheta}{v p_b} \frac{\sin v p_b \zeta}{v p_b \zeta} \frac{\sin v p_b q \xi}{q \sin v p_b \xi} \right\} i_t(t) = \Theta_{mjv} i_t(t) \quad (8)$$

$i_t(t)$ —momentary value of armature current (phase), β —angle coordinate of the stator ($\beta = \alpha + \varphi$), measured from the magnetic axis of phase 1 ($k = 1$), v —one half of the angular size of a single coil of the armature, ζ —one half of the angular size of the opening of the armature slot, ξ —one half of the angle between the axes of adjacent coils of the armature, χ_t —position of the magnetic axis of the phase winding, p_b —number of pole pairs, q —number of coils in a polar group of phase winding, z_{ip} —number of turns of phase for one pair of poles; for single layer winding: $z_{ip} = q \cdot z_z$, z_z —number of turns of one coil.

Distribution of magnetic tension of external magnetic bridges of the rotor can be represented by the formula:

$$U_{bz_m}(\alpha) = U_{bz1} \cdot u_{z_m1}(\alpha) + U_{bz2} \cdot u_{z_m2}(\alpha) \quad (9)$$

If the ampere-turns of the symmetrical winding affect the magnetic field in the air gap, then for external magnetic bridges it can only be assumed that $U_{bz1} = -U_{bz3}$, $U_{bz2} = -U_{bz4}$. Generally, it can be assumed:

$$(\alpha_2 - \alpha_1) = 2\kappa_1 \neq (\alpha_4 - \alpha_3) = 2\kappa_2 \quad (10)$$

Functions $u_{zm1}(\alpha)$, $u_{zm2}(\alpha)$, presented as Fourier series, have the form:

$$u_{zm1}(\alpha) = \sum_{\rho=1,3,5,\dots}^{\infty} U_{m1\rho} \sin(\rho p_b(\alpha - \gamma)),$$

$$U_{m1\rho} = \frac{2\pi}{\rho} \cdot \frac{\cos p_b \rho \kappa_1}{\pi^2 - (2p_b \rho \kappa_1)^2} \quad (11)$$

$$u_{zm2}(\alpha) = \sum_{\rho=1,3,5,\dots}^{\infty} U_{m2\rho} \sin(\rho p_b(\alpha - (\frac{\pi}{p_b} - \gamma)))$$

$$U_{m2\rho} = \frac{2\pi}{\rho} \cdot \frac{\cos p_b \rho \kappa_2}{\pi^2 - (2p_b \rho \kappa_2)^2} \quad (12)$$

For $\rho = 1, 3, 5, \dots$ is:

$$\begin{aligned} \sin(\rho p_b(\alpha - (\frac{\pi}{p_b} - \gamma))) &= \sin(\rho p_b(\alpha + \gamma)) \cdot \cos(\rho\pi) - \cos(\rho p_b(\alpha + \gamma)) \cdot \sin(\rho\pi) \\ &= -\sin(\rho p_b(\alpha + \gamma)) \end{aligned}$$

Distribution of magnetic tension can be described by Fourier series:

$$U_{bz m}(\alpha) = \sum_{\rho}^{\infty} \{U_{bz1} U_{m1\rho} \sin \rho p_b(\alpha - \gamma) - U_{bz2} U_{m2\rho} \sin \rho p_b(\alpha + \gamma)\} \quad (13)$$

Not only magnets affect U_{bz1} , U_{bz2} values, but also the momentary value of the armature ampere-turns, and therefore they depend on the currents of the stator winding. They are the products of equivalent magnetic strength [A/m] in external bridges and length of external bridges:

$$U_{bz1} = H_{bz1} \cdot l_{bz1} \quad (14)$$

$$U_{bz2} = H_{bz2} \cdot l_{bz2} \quad (15)$$

The field strengths H_{bz1} , H_{bz2} are calculated from the equations:

$$-W_m + W_{s1} - c_1 H_{bz1} - c_2 H_{bz2} = B_{bz1}(H_{bz1}) \quad (16)$$

$$-W_m + W_{s2} - c_2 H_{bz1} - c_1 H_{bz2} = B_{bz2}(H_{bz2}), \quad (17)$$

where

$$W_m = \frac{b_m}{b_{bc}} B_r \quad (18)$$

$$W_{s1} = \frac{\mu_o R_{sw}}{b_{bc} \delta_z} i_t(t) \sum_{v=1,3,5\dots}^{\infty} \frac{\Theta_{mjv}}{p_b v} \left\{ \begin{array}{l} [\sin p_b v \alpha_1] \cdot \cos p_b v \varphi + \\ [\sin v \frac{\pi}{2} \sin p_b v \frac{1}{2} (\alpha_4 - \alpha_1)] \\ \cdot \sin p_b v \varphi \end{array} \right\} \quad (19)$$

$$W_{s2} = \frac{\mu_o R_{sw}}{b_{bc} \delta_z} i_t(t) \sum_{v=1,3,5\dots}^{\infty} \frac{\Theta_{mjv}}{p_b v} \left\{ \begin{array}{l} [\sin p_b v \alpha_1] \cdot \cos p_b v \varphi - \\ [\sin v \frac{\pi}{2} \sin p_b v \frac{1}{2} (\alpha_4 - \alpha_1)] \\ \cdot \sin p_b v \varphi \end{array} \right\} \quad (20)$$

$$c_1 = \frac{\mu_o}{b_{bc}} \left\{ (\alpha_1 + \frac{1}{2}(\alpha_4 - \alpha_2)) \frac{R_{sw}}{2\delta_z} + \mu_{mr} \frac{b_m}{l_m} \right\} l_{bz1} \quad (21)$$

$$c_2 = \frac{\mu_o R_{sw}}{b_{bc} 2\delta_z} (\alpha_1 - \frac{1}{2}(\alpha_3 - \alpha_1)) l_{bz2} \quad (22)$$

Equations (16)–(22) were obtained [1] by assuming similar angular sizes of bridges:

$$(\alpha_4 - \alpha_2) \approx (\alpha_3 - \alpha_1) \quad (23)$$

Magnetic tensions of bridges U_{bz1} , U_{bz2} depend on the armature current and theoretically may vary in wide limits. However, the armature current smaller than rated current can be regarded as the sum of the fixed component U_{bz0} , determined by the permanent magnets, and the varying component, derived from armature currents. Initially, it was assumed that this component is so small that the magnetization characteristic of bridges in the range of changes in the operating point can be approximated by a straight line:

$$B_{bz} = B_{b0} + \mu_b H_{bz} \quad (24)$$

The assumption (23) of similar angular size of bridges, i.e., $l_{bz1} \approx l_{bz2} = l_{bz}$ and $\kappa_1 = \kappa_2 = \kappa$, seems reasonable in these conditions. Angles $\alpha_1 \div \alpha_4$ can now be expressed using angles γ and κ :

$$\alpha_1 = \gamma - \kappa, \alpha_2 = \gamma + \kappa, \alpha_3 = \frac{\pi}{p_b} - \gamma - \kappa, \alpha_4 = \frac{\pi}{p_b} - \gamma + \kappa \quad (25)$$

The values W_{s1} , W_{s2} by (19) and (20), depending on armature currents and rotor position, taking into account (25), are equal:¹

$$W_{s1} = i_t(t) \frac{\mu_o R_{sw}}{b_{bc} \delta_z} \sum_{v=1,3,5,\dots}^{\infty} \frac{\Theta_{mjv}}{p_b v} \sin p_b v(\varphi + \alpha_1) =$$

$$i_t(t) \sum_{v=1,3,5,\dots}^{\infty} W_{mjv} \sin p_b v(\varphi + \alpha_1) = i_t(t) W_{s1j}(\varphi) \quad (26)$$

$$W_{s2} = -i_t(t) \frac{\mu_o R_{sw}}{b_{bc} \delta_z} \sum_{v=1,3,5,\dots}^{\infty} \frac{\Theta_{mjv}}{p_b v} \sin p_b v(\varphi - \alpha_1) =$$

$$i_t(t) \sum_{v=1,3,5,\dots}^{\infty} W_{mjv} \sin p_b v(\varphi - \alpha_1) = i_t(t) W_{s2j}(\varphi) \quad (27)$$

The values W_{s1j} , W_{s2j} are periodic functions of the rotor position φ . Taking into account (25) can also be different and described as c_1 and c_2 :

$$c_1 = \mu_o \frac{l_{bz}}{b_{bc}} \left\{ \frac{R_{sw}}{2\delta_z} \left(\frac{\pi}{2p_b} - \kappa \right) + \mu_{mr} \frac{b_m}{l_m} \right\} \quad (28)$$

$$c_2 = \mu_o \frac{l_{bz}}{b_{bc}} \frac{R_{sw}}{2\delta_z} \left(2\gamma - \kappa - \frac{\pi}{2p_b} \right) \quad (29)$$

The system of Eqs. (16) and (17), after taking into account (24), assumes the form:

$$-W_m + W_{s1} - c_1 H_{bz1} - c_2 H_{bz2} = B_{bo} + \mu_b H_{bz1} \quad (30)$$

$$-W_m + W_{s2} - c_2 H_{bz1} - c_1 H_{bz2} = B_{bo} + \mu_b H_{bz2} \quad (31)$$

In matrix notation:

$$\begin{bmatrix} H_{bz1} \\ H_{bz2} \end{bmatrix} = -\frac{1}{\Delta} \begin{bmatrix} c'_1 & -c_2 \\ -c_2 & c'_1 \end{bmatrix} \begin{bmatrix} B_{bo} + W_m - W_{s1} \\ B_{bo} + W_m - W_{s2} \end{bmatrix} \quad (32)$$

¹

$$\begin{aligned} \sin\left(\frac{v\pi}{2}\right) \sin p_b v \frac{1}{2}(\alpha_4 - \alpha_1) &= \sin\left(\frac{v\pi}{2}\right) \sin\left(\frac{\pi}{2}v - p_b v(\gamma - \kappa)\right) \\ &= \sin\left(\frac{v\pi}{2}\right) \left\{ \sin\left(\frac{\pi}{2}\right) \cos p_b v(\gamma - \kappa) - \cos\left(\frac{v\pi}{2}\right) \sin p_b v(\gamma - \kappa) \right\} \\ &= \cos p_b v(\gamma - \kappa) = \cos p_b v \alpha_1 \{ [\sin p_b v \alpha_1] \cos p_b v \varphi \\ &\quad \pm [\sin v \frac{\pi}{2} \sin p_b v \frac{1}{2}(\alpha_4 - \alpha_1)] \sin p_b v \varphi \} \\ &= \pm \sin p_b v(\varphi - \alpha_1) \end{aligned}$$

$$\Delta = (c'_1)^2 - c_2^2 \quad (33)$$

$$c'_1 = c_1 + \mu_b \quad (34)$$

Finally,

$$U_{bz1} = H_{bz1} l_{bz1} = -\frac{l_{bz1}}{\Delta} \{ (c'_1 - c_2)(B_{bo} + W_m) - c'_1 W_{s1} + c_2 W_{s2} \} \quad (35)$$

$$U_{bz2} = H_{bz2} l_{bz2} = -\frac{l_{bz2}}{\Delta} \{ (c'_1 - c_2)(B_{bo} + W_m) - c'_1 W_{s2} + c_2 W_{s1} \} \quad (36)$$

For $l_{bz1} \approx l_{bz2} = l_{bz}$, expressions for magnetic tensions (35) and (36) can be formulated as:

$$\begin{aligned} U_{bz1} &= -(B_{bo} + \frac{b_m}{b_{bc}} B_r) \frac{l_{bz}}{c'_1 + c_2} + \frac{l_{bz}}{\Delta} (c'_1 W_{s1j} + c_2 W_{s2j}) i_t(t) \\ &= U_{bz0} + a_1(\varphi) i_t(t) \end{aligned} \quad (37)$$

$$\begin{aligned} U_{bz2} &= -(B_{bo} + \frac{b_m}{b_{bc}} B_r) \frac{l_{bz}}{c'_1 + c_2} - \frac{l_{bz}}{\Delta} (c'_1 W_{s2j} + c_2 W_{s1j}) i_t(t) \\ &= U_{bz0} - a_2(\varphi) i_t(t), \end{aligned} \quad (38)$$

where

$$U_{bz0} = -(B_{bo} + \frac{b_m}{b_{bc}} B_r) \frac{l_{bz}}{c'_1 + c_2} \quad (39)$$

$$a_1(\varphi) = \frac{l_{bz}}{\Delta} (c'_1 W_{s1j}(\varphi) + c_2 W_{s2j}(\varphi)) \quad (40)$$

$$a_2(\varphi) = \frac{l_{bz}}{\Delta} (c'_1 W_{s2j}(\varphi) + c_2 W_{s1j}(\varphi)) \quad (41)$$

The coefficients a_1 , a_2 are unitless, with values dependent on the position of the rotor. Magnetic field distribution in the air gap (6), dependent on the armature currents according to (7), (37), (38) and (9), can be used to calculate the flux coupled with the stator winding as a function of rotor position.

4 The Magnetic Flux Coupled with the Stator Winding

When calculating the magnetic flux coupled with symmetrical stator winding, derived from the radial component of the flux density in the air gap, winding coefficients $k_{w\zeta}$ are generally used. They reduce the impact of individual ζ -harmonic of the flux density $B_\zeta(\beta)$ on the magnetic flux coupled with phase winding:

$$\psi_s(t) = z_t R_{sw} l_{Fe} \sum_{\zeta}^{\infty} k_{w\zeta} \int_{-\frac{\pi}{2}}^{\frac{\pi}{2}} B_\zeta(\beta, t) d\beta \quad (42)$$

The use of this approach in the present case, however, does not lead to satisfactory results. The curve EMF of this machine, derived from the permanent magnets, draws attention to a significant level of harmonic with frequencies corresponding to speeds of movement slots of the armature relative to the permanent magnets. In the test machine, slot harmonics can come only from highly saturated magnetic bridges in the rotor. The mechanism of deformations of EMF explains the registration EMF in coil wound around a single tooth of armature.

The magnetic flux ψ_s passing through the section surface of the stator, which includes a winding of one pole of the armature, can be regarded as the sum of the magnetic fluxes Φ_z of individual teeth, covered by this winding. It is considered that the magnetic flux passing the tooth is equal to the magnetic flux coupled to a coil wound on this tooth (for one-turn coil). One can also say that the value of the magnetic flux coupled with the stator winding always changes by the value of the magnetic flux coupled with the tooth-coil. The winding of one pole includes 11 teeth in this case, therefore it can be written as:

$$\psi_s(\varphi) = \sum_{l=1}^{11} z_l \phi_{z_l}(\varphi) = \sum_{l=1}^{11} z_l \psi_{cl}(\varphi), \quad (43)$$

where $\Phi_{z_l} \approx \psi_{cl}$ is magnetic flux of l -tooth, z_l is the total number of coils per tooth pitch in accordance with the winding diagram.

According to this approach, the waveform EMF induced in the winding phase can be considered as the sum waveforms EMF of tooth-coils, shifted by an angle corresponding to the slot pitch. The measurements and calculations have confirmed this conclusion. Taking into account the teeth of the stator complicates the model significantly, above all making it less transparent. Without taking into account the changes in the radial dimension of the air gap, the only way to obtain the required waveform of EMF is treated magnetic flux coupled with the winding phase as the sum of the magnetic fluxes of teeth. Consequently, this approach was also used in the calculation of the armature reaction.

The magnetic flux derived from the magnetic field (6), coupled with a tooth-coil with angular size $2\nu_c$ is:

$$\begin{aligned}
\psi_c(\varphi) &= z_c R_{sw} l_{Fe} \int_{(\xi_c - \vartheta_c)}^{(\xi_c + \vartheta_c)} B_g(\beta) d\beta \\
&= -z_c R_{sw} l_{Fe} \frac{\mu_o}{\delta_z} \times \int_{(\xi_c - \vartheta_c)}^{(\xi_c + \vartheta_c)} \sum_{\rho=1,3,5,\dots}^{\infty} \left\{ \begin{array}{l} U_{bz1} U_{m1\rho} \sin \rho p_b (\beta - \varphi - \gamma) \\ -U_{bz2} U_{m2\rho} \sin \rho p_b (\beta - \varphi + \gamma) \\ + \Theta_{m\rho} \cos \rho p_b \beta \end{array} \right\} d\beta \\
&= z_c \Lambda \sum_{\rho=1,3,5,\dots}^{\infty} \frac{\sin \rho p_b \vartheta_c}{\rho p_b \vartheta_c} \left\{ \begin{array}{l} U_{bz1} U_{m1\rho} \sin \rho p_b (\varphi + \gamma - \xi_c) - \\ U_{bz2} U_{m2\rho} \sin \rho p_b (\varphi - \gamma - \xi_c) - \\ \Theta_{m\rho} \cos \rho p_b \xi_c \end{array} \right\}
\end{aligned} \tag{44}$$

The symbol Λ designated value which can be regarded as a permeance of a segment of the air gap:

$$\Lambda = \mu_o \frac{2\vartheta_c R_{sw} l_{Fe}}{\delta_z} [H] \tag{45}$$

According to (43) and taking into account the number of pole groups, here equal to the number of pole pairs, equations of the motion will be:

$$\begin{aligned}
\psi_s(\varphi) &= p_b \sum_{l=1}^{11} z_l \psi_{cl}(\varphi) \\
&= p_b \sum_{l=1}^{11} z_l \Lambda \sum_{\rho=1,3,5}^{\infty} \frac{\sin \rho p_b \vartheta_c}{\rho p_b \vartheta_c} \times \left\{ \begin{array}{l} [U_{bz0} + a_1 i_l(t)] U_{m1\rho} \sin \rho p_b (\varphi + \gamma - \xi_{cl}) \\ -[U_{bz0} - a_2 i_l(t)] U_{m2\rho} \sin \rho p_b (\varphi - \gamma - \xi_{cl}) \\ -\Theta_{mj\rho} i_l(t) \cos \rho p_b \xi_{cl} \end{array} \right\} \\
&= p_b \Lambda \sum_{\rho=1,3,5,\dots}^{\infty} \frac{\sin \rho p_b \vartheta_c}{\rho p_b \vartheta_c} \times \left\{ \begin{array}{l} U_{bz0} U_{m1\rho} \sum_{l=1}^{11} z_l \sin \rho p_b (\varphi + \gamma - \xi_{cl}) \\ -U_{bz0} U_{m2\rho} \sum_{l=1}^{11} z_l \sin \rho p_b (\varphi - \gamma - \xi_{cl}) \\ \left[\begin{array}{l} a_1 U_{m1\rho} \sum_{l=1}^{11} z_l \sin \rho p_b (\varphi + \gamma - \xi_{cl}) \\ + a_2 U_{m2\rho} \sum_{l=1}^{11} z_l \sin \rho p_b (\varphi - \gamma - \xi_{cl}) \\ -\Theta_{mj\rho} \sum_{l=1}^{11} z_l \cos \rho p_b \xi_{cl} \end{array} \right] \end{array} \right\} + i_l(t)
\end{aligned} \tag{46}$$

In the magnetic flux ψ_s , components can be identified from different sources:

$$\psi_s = \psi_{sm} + \psi_{ss} = \psi_{sm} + \psi_{s\delta} + \Delta\psi_{sb} \quad (47)$$

In the magnetic flux ψ_{ss} , the separated component $\psi_{s\delta}$ depends on the permeance of the air gap and a component $\Delta\psi_{sb}$, related to the magnetic tensions of magnetic bridges. The formulas for these components take into account the equality harmonics $U_{m1\rho} = U_{m2\rho} = U_{m\rho}$ resulting from Eq. (23).

$$\psi_{sm} = 2p_b \Lambda U_{bz0} \sum_{\rho=1,3,5\dots}^{\infty} U_{m\rho} \frac{\sin(\rho p_b \vartheta_c)}{\rho p_b \vartheta_c} \sin(\rho p_b \gamma) \cdot \sum_{l=1}^{11} z_l \cos(\rho p_b (\phi - \xi_{cl})) \quad (48)$$

$$\psi_{s\delta} = -i_t(t) p_b \Lambda \sum_{\rho=1,3,5\dots}^{\infty} \frac{\sin(\rho p_b \vartheta_c)}{\rho p_b \vartheta_c} \cdot \Theta_{mj\rho} \sum_{l=1}^{11} z_l \cos(\rho p_b \xi_{cl}) \quad (49)$$

$$\begin{aligned} \Delta\psi_{sb} &= i_t(t) p_b \Lambda \sum_{\rho=1,3,5\dots}^{\infty} \frac{\sin(\rho p_b \vartheta_c)}{\rho p_b \vartheta_c} U_{m\rho} \cdot \sum_{l=1}^{11} z_l (a_1 \sin \rho p_b (\varphi + \gamma - \xi_{cl}) + a_2 \sin \rho p_b (\varphi - \gamma - \xi_{cl})) \\ &= i_t(t) p_b \Lambda \sum_{\rho=1,3,5\dots}^{\infty} \frac{\sin(\rho p_b \vartheta_c)}{\rho p_b \vartheta_c} U_{m\rho} \cdot \left\{ \begin{array}{l} \left(\begin{array}{l} a_1(\varphi) \sin \rho p_b (\varphi + \gamma) + \\ a_2(\varphi) \sin \rho p_b (\varphi - \gamma) \end{array} \right) \cdot \\ \sum_{l=1}^{11} z_l \cos \rho p_b \xi_{cl} - \\ \left(\begin{array}{l} a_1(\varphi) \cos \rho p_b (\varphi + \gamma) + \\ a_2(\varphi) \cos \rho p_b (\varphi - \gamma) \end{array} \right) \cdot \\ \sum_{l=1}^{11} z_l \sin \rho p_b \xi_{cl} \end{array} \right\} \end{aligned} \quad (50)$$

In the tested machine, one pole of each phase winding is created by 3 identical, diametrical coils, with a pitch 9 and axes shifted through one slot pitch. If the teeth numbering starts from one side, the subsequent positions of the axis of the teeth to the axis of the middle tooth (6-th in group) are:

- for teeth covered by the first pole group, in the first phase winding:

$$\xi_{cl} = \pi(l - 6)/18 \quad (51)$$

- for teeth covered by the first pole group, in the k -th phase winding:

$$\xi_{ckl} = (k-1)\frac{\pi}{3} + \pi(l-6)/18 = (k-1)\frac{\pi}{3} + \xi_{c1l} \quad k = 1, 2, 3 \quad (52)$$

Among the coils placed on the teeth of the pole group, one can extract pairs, which, from the flux component ψ_{sm} (48), will correspond the components:

$$\begin{aligned} C_\rho \cos \rho p_b \left(\varphi - (k-1)\frac{\pi}{3} - |\xi_{c1l}| \right) + C_\rho \cos \rho p_b \left(\varphi - (k-1)\frac{\pi}{3} + |\xi_{c1l}| \right) \\ = 2C_\rho \cos \rho p_b \xi_{c1l} \cos \rho p_b \left(\varphi - (k-1)\frac{\pi}{3} \right), \quad l = 1..5 \end{aligned} \quad (53)$$

Analyzing the winding diagram of the tested machine, it can be concluded that the magnetic flux of the coil of the central tooth (6) and magnetic fluxes of three pairs of teeth (5–7, 4–8, 3–9) are coupled with three coils of phase winding, the magnetic flux of pair 2–10 is coupled with the two coils and the magnetic flux of pairs 1–11 is coupled with the one coil. In this case, the flux ψ_{sm} from the (48), coupled to the k -th phase, can be represented as:

$$\begin{aligned} \psi_{smk} = 2p_b z_z \Lambda U_{bz0} \cdot \\ \sum_{\rho=1,3,5\dots}^{\infty} U_{m\rho} \frac{\sin(\rho p_b \vartheta_c)}{\rho p_b \vartheta_c} \sin(\rho p_b \gamma) \cos(\rho p_b \left(\varphi - (k-1)\frac{\pi}{3} \right)) \times \\ \left\{ 3 + 2 \left(3 \left(\cos \rho p_b \frac{3\pi}{18} + \cos \rho p_b \frac{2\pi}{18} + \cos \rho p_b \frac{\pi}{18} \right) + \right. \right. \\ \left. \left. 2 \cos \rho p_b \frac{4\pi}{18} + \cos \rho p_b \frac{5\pi}{18} \right) \right\} \end{aligned} \quad (54)$$

and in a shorter form:

$$\begin{aligned} \psi_{smk} = 2p_b z_z \Lambda U_{bz0} \cdot \\ \sum_{\rho=1,3,5\dots}^{\infty} U_{m\rho} d_{c\rho} \frac{\sin(\rho p_b \vartheta_c)}{\rho p_b \vartheta_c} \sin(\rho p_b \gamma) \cos(\rho p_b \left(\varphi - (k-1)\frac{\pi}{3} \right)), \end{aligned} \quad (55)$$

where

$$\begin{aligned} d_{c\rho} = z_6 + 2 \sum_{l=1}^5 z_l \cos \rho p_b |\xi_{cl}| \\ = 3 + 2 \left(3 \left(\cos \rho p_b \frac{3\pi}{18} + \cos \rho p_b \frac{2\pi}{18} + \cos \rho p_b \frac{\pi}{18} \right) + \right. \\ \left. 2 \cos \rho p_b \frac{4\pi}{18} + \cos \rho p_b \frac{5\pi}{18} \right) \end{aligned} \quad (56)$$

The coefficients $d_{c\rho}$ are specific to a particular winding, whose scheme is necessary to determine them. A comparison of the equations (55) and (48) for $l = 1$

shows that the particular harmonics differ only by the ratio $d_{c\rho}$ and the number of turns.²

For the flux component $\psi_{s\delta k}$ (49) will be:

$$\psi_{s\delta k} = -i_t(t)p_b\Lambda \cdot \sum_{\rho=1,3,5,\dots}^{\infty} \frac{\sin(\rho p_b \vartheta_c)}{\rho p_b \vartheta_c} \Theta_{mj\rho} \sum_{l=1}^{11} z_l \cos \rho p_b \left((k-1)\frac{\pi}{3} + \xi_{c1l} \right) \quad (57)$$

Among the components of the second series in (57), there are pairs of similar, as (53), but $\varphi = 0$, so we can write:

$$\psi_{s\delta k} = -i_t(t)p_b z_z \Lambda \cdot \sum_{\rho=1,3,5,\dots}^{\infty} d_{c\rho} \frac{\sin(\rho p_b \vartheta_c)}{\rho p_b \vartheta_c} \Theta_{mj\rho} \cos(\rho p_b (k-1)\frac{\pi}{3}), \quad k = 1, 2, 3 \quad (58)$$

In the first part of Eq. (50) (for the component $\Delta\psi_{sb}$), in all arguments of the sine and cosine functions, are differences of angles φ and ξ_{c1} , so the substitution $\varphi - \xi_{c1} = \varphi - (k-1)\cdot\pi/3 - \xi_{c1l} = \varphi' - \xi_{c1l}$ yields the second part of the expression (50), as the angle φ' replaces the angle φ . Then the sum $\sum z_l \sin(\rho p_b \cdot \xi_{c1l})$ (for $l = 1 \dots 11$) is equal to zero because the odd nature of the sine function resets the components within each pair. As a result, the expression for the flux component $\Delta\psi_{sb}$ takes the form:

$$\Delta\psi_{sbk} = i_t(t)p_b z_z \Lambda \cdot \sum_{\rho=1,3,5,\dots}^{\infty} U_{m\rho} d_{c\rho} \frac{\sin(\rho p_b \vartheta_c)}{\rho p_b \vartheta_c} \times \left(a_1(\varphi) \sin \rho p_b \left(\varphi - (n-1)\frac{\pi}{3} + \gamma \right) + a_2(\varphi) \sin \rho p_b \left(\varphi - (n-1)\frac{\pi}{3} - \gamma \right) \right) \quad (59)$$

Equations (55), (58) and (59) represent the magnetic fluxes coupled with the stator winding, due to the permanent magnet and the armature current of one phase.

²When the rotor of the generator has a constant rotational speed, the magnetic flux coupled with the windings and the magnetic flux coupled with the coil are a periodic functions of time, capable of being represented by Fourier series. Coefficients $d_{c\rho}$ express the relationship between the harmonics of both waveforms. At unladen generator, the coefficients $d_{c\rho}$ allow to separate components of individual teeth in the magnetic flux coupled to the phase winding.

5 Parameters of Magnetic Bridges

The properties of the magnetic bridges of the rotor, through the circumferential magnetic tension values of the bridges, affect both the value of the EMF derived from the permanent magnets and reaction of the armature.

Value of the magnetic tension in external magnetic bridge U_{bz} is defined [1] as the product of substitute magnetic field strength in the bridge H_{bz} and a representative length of the bridge l_{bz} :

$$U_{bz} = \int_{l_b} \overline{H}_b \overline{dl} = H_{bz} l_{bz} \quad (60)$$

Path integration in the expression (60) is a circle with a radius $R_{oc} = R_{rz} - b_{bz}/2$, concentric with the rotor.

Determining the value of the magnetic field and the substitute length of the bridge requires additional conditions. Provided that one applies the Gauss's law for magnetism, wherein it is necessary to calculate the value of flux, value of density of magnetic flux is linked to the strength of magnetic field by the magnetization characteristics of the bridges.

The assumption of a constant magnetic flux density in the bridge and infinite magnetic permeability of iron outside the bridge corresponds to the step change in the magnetic field strength at the ends of the bridge. The results of measurements and simulations indicate the desirability of assumptions of sinusoidal changes of the field strength within the bridge, with a maximum field strength in the middle and minimum (0) at its edges, and the corresponding changes of magnetic tension within the bridge:

$$H_{bz}(\alpha) \approx H_{bz\max} \sin \frac{\pi}{2\kappa}(\alpha + \kappa - \gamma) \quad (61)$$

$$\begin{aligned} U_{bz}(\alpha) &= R_{oc} \int H_{bz}(\alpha) d\alpha + U_p \\ &= U_p - \frac{2\kappa}{\pi} R_{oc} H_{bz\max} \cos \frac{\pi}{2\kappa}(\alpha + \kappa - \gamma) \end{aligned} \quad (62)$$

Unfortunately, the assumption of the changes of magnetic field strength in the bridge and the constant cross section of the bridge is associated with changes in magnetic flux along the length of the bridge. Having faced difficulties in meeting all the requirements with one simple geometric structure, it was decided that for the applications of model, the substitute bridge would represent only specific properties of the required structure:

- magnetic tension changing along the circumferential dimension of the bridge, according to the formula:

$$U_{bz}(\alpha) = \frac{1}{2}\Delta U_{bz}\left(1 - \cos\frac{\pi}{2\kappa}(\alpha + \kappa - \gamma)\right) + U_p \tag{63}$$

- the smallest (structural) cross section of the bridge $s_{bz} = b_{bz} l_{Fe}$ and the magnetic flux Φ_{bz} through the surface of the induction vector $B_{bz\max}$, corresponding (by the characteristics of magnetization) the maximum field strength $H_{bz\max}$:

$$\Phi_{bz} = s_{bz}B_{bz\max}(H_{bz\max}) \tag{64}$$

$$\begin{aligned} H_{bz\max} = H_{bz}(\alpha = \gamma) &= \frac{1}{R_{oc}}\left(\frac{d}{d\alpha}U_{bz}(\alpha)\right)_{\alpha=\gamma} \\ &= \frac{\pi}{4\kappa R_{oc}}\Delta U_{bz}\left(\sin\frac{\pi}{2\kappa}(\alpha + \kappa - \gamma)\right)_{\alpha=\gamma} = \frac{\pi}{4}\frac{\Delta U_{bz}}{\kappa R_{oc}} \end{aligned} \tag{65}$$

- substituting circumferential length of the bridge l_{bz}' , with the value resulting from the formula:

$$\begin{aligned} \Delta U_{bz} &= R_{oc} \int_{\gamma-\kappa}^{\gamma+\kappa} H_{bz}(\alpha) d\alpha = R_{oc}H_{bz\max} \int_{\gamma-\kappa}^{\gamma+\kappa} \sin\frac{\pi}{2\kappa}(\alpha + \kappa - \gamma) d\alpha \\ &= \frac{4}{\pi}\kappa R_{oc}H_{bz\max} = H_{bz\max}l'_{bz} \end{aligned} \tag{66}$$

$$l'_{bz} = \frac{4}{\pi}\kappa R_{oc} \tag{67}$$

When the magnetic field is derived from permanent magnets only, the values B_{bz} and H_{bz} called “operating point of the bridge” can be determined by applying the Gauss’s law for magnetism and the Eqs. (16) and (17) resulting from it, which at opened stator windings can be reduced to a single equation:

$$\frac{b_m}{b_{bc}}B_r - (c_1 + c_2)H_{bz} = B_{bz}(H_{bz}), \tag{68}$$

where c_1, c_2 are in (28) and (29).

Calculated in this way, B_{bz} and H_{bz} are maximum values of flux density and magnetic field strength in cross section s_{bz} , in the middle of the substitute circumferential length of the bridge l_{bz}' . With the approximation of the characteristics of magnetization, a straight line $B_{bz} = B_{b0} + \mu_b H_{bz}$ is obtained:

$$H_{bz\max} = \frac{1}{c_1 + \mu_b + c_2} \left(\frac{b_m}{b_{bc}} B_r - B_{bo} \right) \quad (69)$$

Parameters of a line (or other curve used) are, in this way, the parameters of the bridges and affecting the properties of the machine. Among parameters, particularly important ones that should be considered, there are the circumferential length of bridges $l_{bz}' (\equiv \kappa)$ and the position of the axis of the bridge (the angle γ).

Analytical determination of these values is not possible. When formulating a mathematical model of the machine with internal magnets, it was assumed that the parameters of the bridges would be chosen experimentally or by FEM calculations. This approach makes sense when the parameters chosen for the easy-to-implement operating state (or for calculations of the operating state) can be used to simulate many important static and dynamic processes. The curve of EMF, induced in the windings of the armature by the permanent magnets, was considered as fundamental to the identification process. The curve of EMF of tooth-coil was also useful for the identification, under the same conditions. The best option is to make a direct registration of the EMF-curve. The curve may also be computationally determined from the measured waveform of EMF of phase winding, using the formulas (48), (55) and (56). Harmonics of EMF induced in the tooth-coils and in phase windings are linked by coefficients d_{cp} (56). After analyzing the harmonics of EMF of phase winding, d_{cp} coefficients can be used to calculate components of EMF, derived from the magnetic fluxes of individual teeth. Figure 2 shows a comparison of waveform resulting from the calculation and measurement. Differences are due to the small deformations of the EMF components, derived from imperfect symmetry of the machine.

Decomposition of EMF of phase winding into components does not yet specify the limits of integration of the magnetic field in air gap when obtaining the components of the magnetic flux. If, however, EMF induced in the tooth-coils is equal

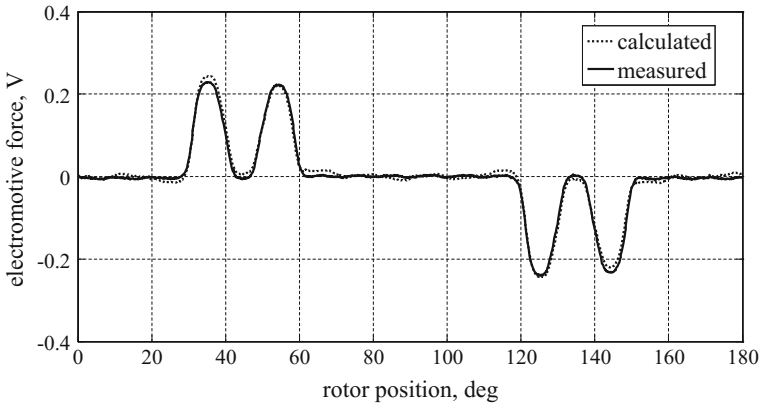


Fig. 2 The EMF of tooth-coil

to the corresponding component of the winding EMF, it can be concluded that the position of the coil sides corresponds to the boundaries of integration of the magnetic field.

The dimensions of the coil with several turns, wound with a thin wire, are intentionally minimized, but at the opening of the slot in the present machine 3 mm (2.6°), and so will be comparable to the width of the opening. Angular size of the coil for the calculation is therefore difficult to estimate and can only be assumed that it falls in the range of 7.4° – 10° . Figure 3 shows that waveforms of EMF for tooth-coil and for phase winding calculated for the angular size of the coil equal to 7.6° , 8.2° , 8.8° , and 10° . For the angular size of the coil equal to slot pitch (10°), slots harmonics in EMF of winding disappear and the simulated waveform is identical to that obtained using the formula (56). Waveforms in Fig. 3 allow for a conclusion that the angular size in the range of 8° – 8.4° provides the best approximation of real waveforms. It is representative of real dimensions of the tooth-coil.

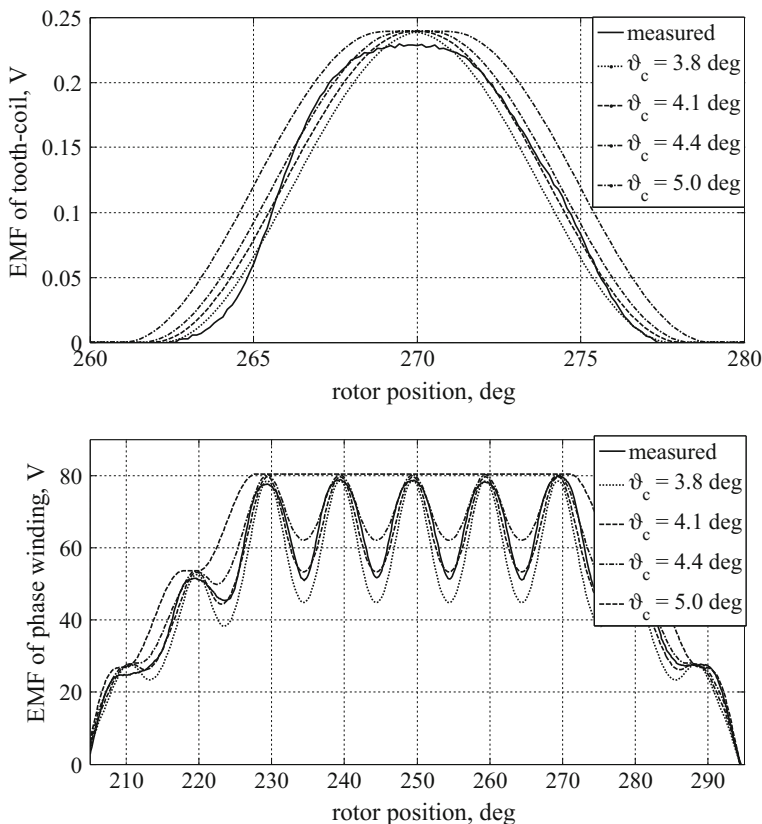


Fig. 3 The impact of changes of the limits of integration to the calculated curves of EMF

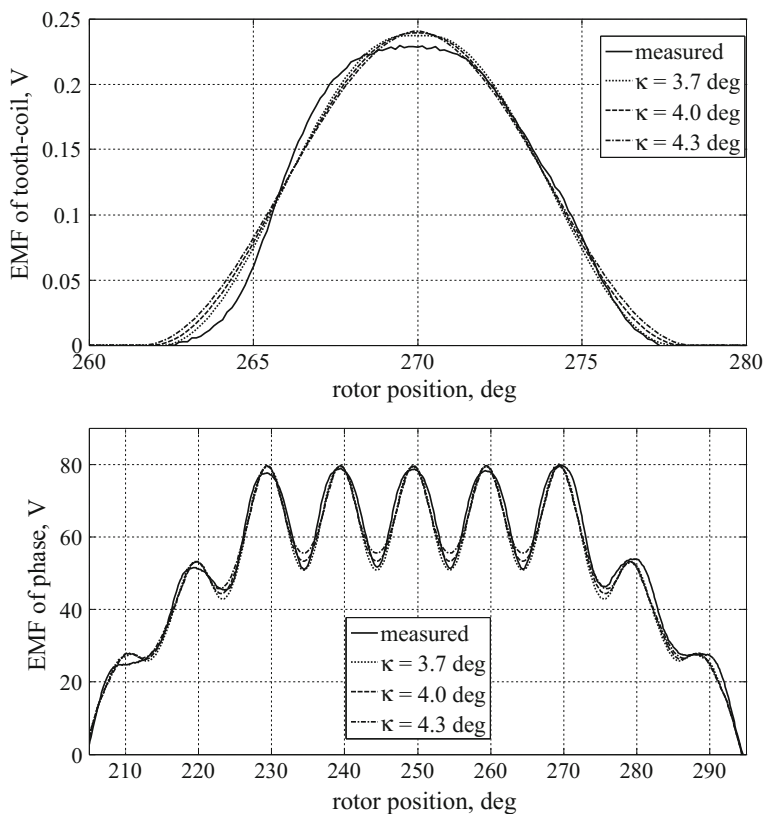


Fig. 4 The impact of changes of the angular size of bridges to the calculated curves of EMF

The calculations were performed for the angular size of magnetic bridges $2\kappa = 8^\circ$. Waveforms in Fig. 4 allow to evaluate the impact of the substitute angular size of bridges on curves of EMF in tooth-coils and in phase winding.

The calculation result for the angle $\kappa = 4^\circ$ is the nearest to the measured curve. This calculation does not take into account the existence of stator slots—the air gap is treated as smooth, taking the minimum radial dimension of gap as the substitute air gap. Although the validated model of the machine is not based on the assumption of a smooth air gap, however, the slots of the stator complicate the model significantly and, above all, make it less explanatory. If changes in the radial dimension of the air gap are not taken into account, the only way to obtain the required waveform of EMF is to treat the magnetic flux coupled with the phase winding as a sum of the magnetic fluxes of teeth.

On the basis of simulation calculations for generator without a load, in further calculations, the angle size of the magnetic bridges was assumed to be $2\kappa = 8^\circ$ and the angle size of tooth-coil was $2\upsilon_z = 8.2^\circ$. Approximation of parts of characteristic of magnetizing by sections of straight line leads to the illustrative model equations

but requires in calculations controls of field strength in bridges because armature currents changes depending on operating points of bridges. The maximum value of the magnetic field strength can be calculated from the formulas (37) and (38). Obviously, this is a function of the rotor position. Magnetic field strength in the bridges is equal only in certain positions of the rotor (for $\varphi = n \cdot \pi/4$). In the case of an unbalanced load, the extreme values of magnetic field strength in the bridges 1 and 4 are different as in 2 and 3.

6 Measuring Verification of the Model

The measurements were performed at the Laboratory of Electrical Machines KEiASPE AGH, on a test synchronous machine SMwsg 132S4, driven by a DC motor. Only one phase of the generator was loaded, with the resistance of 18 Ω. Measured (recorded) values were: current of the loaded phase, the voltage at all phases (relative to the star point of the stator winding), and EMF of one tooth-coil.

From relatively simple mathematical formalism proposed for the object with complicated and non-linear magnetic circuit, high accuracy calculations should not be expected, especially for an unbalanced load. The basic assumption in the formulation of the model was the omission of magnetic tensions in the magnetic yoke and one can expect that this will be the main cause of quantitative errors. The only possibility to take these magnetic tensions into account is the enlarged air gap between the rotor and stator. Table 1 shows the errors calculated RMS values of EMF, the current and magnetic flux coupled with the load phase, corresponding to the enlarged air gap according to the Carter ratio (13%), and 20, and 40%. This allows for an evaluation of the impact size of the air gap on the simulation results and the reasonability of these tests. In the first case, the calculation of the magnetic fluxes was made for tooth pitch equal 10°, in other cases—8.2°. Size of the magnetic bridges was 8°.

The integration of the magnetic field in the range of 10°, equivalent to the traditional calculation of flux coupled with the coil, leads to a large quantity and quality errors. For the range reduced to 8.2°, waveforms are similar, and a several-percent enlargement of the radial dimension of the air gap reduces the RMS values error below 10%. The measured RMS value of EMF was 54.7 V, the value calculated as the sum of EMF of the coils with angle size 8.2° was 63 V, the value calculated as EMF of phase winding was 75 V (error 34%).

Table 1 Errors calculated RMS values of EMF of phase, current of phase and magnetic flux coupled with the load phase

Measured value	$\delta_z = k_{cs} \cdot \delta$ $v_z = 5^\circ$	$\delta_z = \delta$ $v_z = 4.1^\circ$	$\delta_z = 1.2\delta$ $v_z = 4.1^\circ$	$\delta_z = 1.4\delta$ $v_z = 4.1^\circ$
$E_{smRMS} = 54.7 \text{ V}$	-15.4%	2.2%	5.25%	8.1%
$I_{sRMS} = 2.85\text{A}$	-18.6%	0.34%	3.8%	6.8%
$\psi_{sRMS} = 0.115\text{Wb}$	-57.6%	-22.7%	-5.3%	8.2%

Figure 5 shows the calculated and measured waveforms of current generator armature loaded by 18 Ω resistance in single phase. The level of load generator allowed to use characteristics of magnetization of magnetic bridges as a straight line: $B = 2.0737 + 1.57 \mu_o H$. The calculations assume that the air gap increased by 20%. This decreased the RMS value of EMF without changes in the shape of EMF.

Figure 6 shows the waveform of the magnetic flux coupled to the load phase. Measuring waveform of the magnetic flux was obtained on the basis of the Eq. (3):

$$\psi_k(t) = \int (e_{smk}(t) - (R_s + R_{zk})i_{sk}(t))dt \tag{70}$$

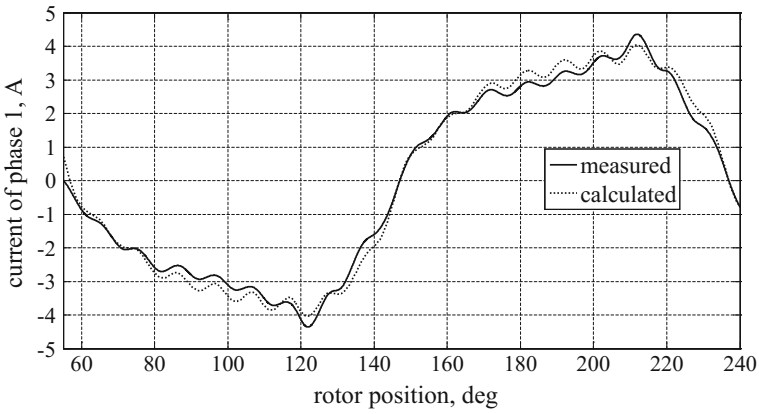


Fig. 5 The waveform of current of phase 1

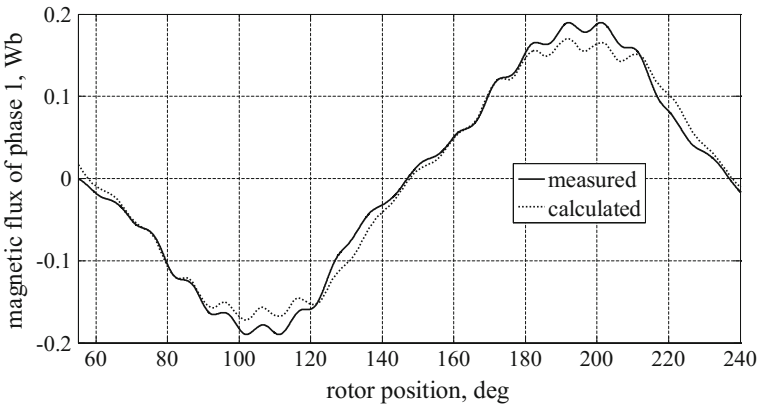


Fig. 6 The waveform of magnetic flux of phase 1

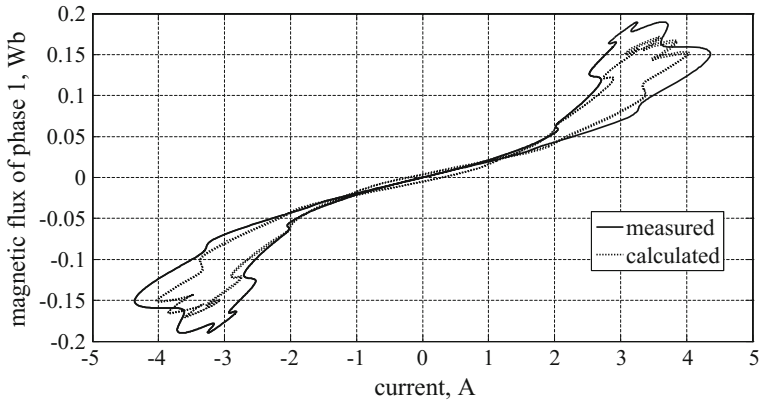


Fig. 7 The relationship $\psi_1(i_{s1})$

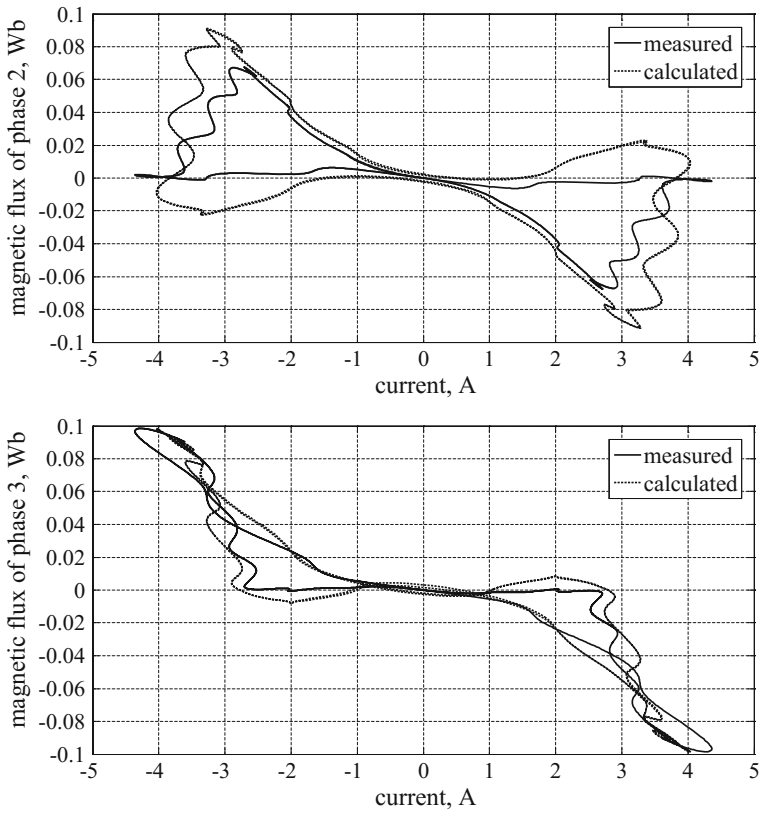


Fig. 8 The relationship $\psi_k(i_{sk})$ for unladen phases ($k = 2, 3$)

Figure 7 shows the relationship $\psi_1(i_{s1})$ measured and calculated. This corresponds to the self-inductance of the phase of a synchronous machine in traditional design, i.e., without permanent magnets and without the highly saturated magnetic bridges. Nonlinearity and ambiguity of this relationship indicate the scale of error assumption of full saturation of bridges (i.e., the level of μ_0).

Figure 8 shows the relationships of magnetic fluxes coupled with unladen phases of the armature current, which in traditional synchronous machines correspond with mutual inductance. Waveforms of these magnetic fluxes were obtained using the relationship for the EMF, induced in each unladen phase:

$$e_k(t) = -\frac{d}{dt}\psi_k(t) = -\frac{d}{dt}(\psi_{sm} + \psi_{k1}(i_1)) = e_{smk}(t) - \frac{d}{dt}\psi_{k1}(i_1), k = 2, 3 \quad (71)$$

$$\psi_{k1}(i_1) = \int (e_{smk}(t) - e_k(t)) dt \quad (72)$$

7 Summary and Conclusions

Comparing the results of calculations and measurements, one can find their significant qualitative similarity. It is expressed in the presence of most specific features of the nonlinear objects in the calculated waveforms with significant influence of harmonic magnetic field in the air gap on the voltage and current waveforms. The properties of the formulated model, such as the impact of various parameters on the obtained results, are not well known because this model exists not long enough. It seems that the further exploration of the properties of the model will improve the accuracy of the simulation results and simultaneously will expand the knowledge of the machines with internal magnets. The authors hope that the simplicity of the model will make it useful in the analysis of dynamic behavior of electric drives, as well as generator sets with electrical machines with internal magnets.

References

1. Drabek, T., Matras, A., Skwarczyński, J.: An analytical model of an electric machine with internal permanent magnets. Lecture Notes in Electrical Engineering 324, Springer International Publishing, Switzerland (2015)
2. Hanselman, D.: Brushless Permanent Magnet Motor Design. Magna Physics Publishing, Madison (2006)
3. Gieras, J.: Permanent Magnet Motor Technology, Design and Applications. CRC Press, Boca Raton (2010)
4. Bajek, M.: Property Analysis and synthesis design of a synchronous motor with permanent magnets for direct starting (LSPMSM) using field methods and optimization. The doctoral dissertation, supervisor W. Jażdżyński, AGH, Kraków (2012)

5. Honsinger, V.B.: The fields and parameters of interior type ac permanent magnet machines. *IEEE Trans. Power Appar. Syst.* **101**(4), 867–876 (1982)
6. Skwarczyński, J.: Internal asymmetries synchronous machines with poles. *Elektrotechnika, zeszyt 16, nr 1350*, Wydawnictwa AGH, Kraków (1990)
7. Drabek, T.: Determination of parameters of mathematical models of electromechanical, reluctance actuators. The doctoral dissertation, AGH, Kraków (1999)

Analysis and Synthesis of Intelligent System for Electric Mode Control in Electric Arc Furnace

Orest Lozynskyy, Andriy Lozynskyy, Yaroslav Paranchuk,
Roman Paranchuk, Yaroslav Marushchak and Andriy Malyar

Abstract The hierarchical structure of the adaptive optimal control system for electric mode (EM) of the electric arc furnace is proposed. Components of the systemic control vector and a technique of its synthesis for complex criterion of minimum dispersion and maximum arc power is substantiated. The model of adapting the control vector to change of technological stages and stochastic characteristics of perturbations was developed. Systemic solutions for recognition of technological stages of steel melting and identification of moments of their change based on a neural network were studied. Circuit design solutions for operational measurement of informative parameters of the steel-melting process using wavelet transform are proposed. Results of the experimental study of the neural network melting stage recognition system for electric arc furnace DSP-3 are presented.

Keywords Electric arc furnace · Optimization · Adaptation · Regulation · Synthesis · Neural network · Criterion · Wavelet transform

1 Introduction

Electric arc furnaces (EAF) as objects of control belong to the class of complex systems. The modern tendency towards scaling-up of single capacity of contemporary EAF and specific installed capacity of electric power equipment and their electric mode (EM) intensification significantly change the characteristics of the electric arc furnace as an electric technology unit and piece of electricity-powered equipment [1]. These trends and specificities of the modes put new stringent requirements to indices of EAF electric and technological efficiency and

O. Lozynskyy (✉) · A. Lozynskyy · Y. Paranchuk · R. Paranchuk
Y. Marushchak · A. Malyar
National University “Lviv Polytechnic”, Lviv, Ukraine
e-mail: lozynsky@polynet.lviv.ua

Y. Paranchuk
e-mail: yparanchuk@yahoo.com

electromagnetic compatibility of modes, which are to be implemented in new EAF or already operating ones during their modernization.

2 Analysis of the Existing Solutions

Electric and technological efficiency of steel making in EAF is characterized by specific consumption of energy. First of all, this concerns electric power losses in the low-voltage circuit (LVC), heat losses, intensity of furnace lining wear and tear, as well as electromagnetic compatibility with the power supply network and with other power-consuming equipment.

Reequipment of EAF operating on three-phase current requires complex solution of problems of synthesizing the multi-criteria optimal control vector, high-accuracy stabilization of EM coordinates, automated recognition of technological stages of steel melting and quality information support of the steel-making mode control system at different levels [2].

This strategy can only be implemented on the basis of using high-efficiency technical algorithmic and organizational solutions which are fulfilled by bringing up-to-date power supply systems, automatic control systems (ACS) and automatic regulation system (ARS) of the operating electrometallurgical units. EAF power layouts must be designed using special high-efficiency high-capacity controlled power supplies, such as electric power thyristor converters with minimum non-linear properties [3, 4].

To increase the speed of arc current regulation, Danieli Group (Italy) proposed a three-phase current system of power supply through a self-saturating reactor [5]. The system offsets arc current deviation on one period of voltage, the regulation causing, however, significant distortion of sinusoidal waveform of arc current, i.e., it generates higher-order harmonics into the power supply grid. This requires a large installed capacity of the reactor (1.4 times as large as the capacity of the furnace transformer), as well as connecting the windings of the grid and furnace transformers (FT) according to star-delta wiring diagram, and during automatic regulation of reactor resistance in the open loop system there is restricted functionality in terms of synthesis of optimal control.

This drawback is not featured by the proposed double-loop EM control system which consists of the electrode positioning circuit used in the existing ACS with electromechanical or electrohydraulic drive. The other circuit is solely an electric high-speed circuit for regulating a certain electric coordinate—that of current, arc power, furnace reactive power, etc., the speed of which is a 70–100 times higher than speed of the mechanical circuit [6]. The high-speed circuit functions on the basis of the original [4] magnetic thyristor voltage converter (MTVC). The main specificity of this circuit is a functionality enabling formation and operational implementation of the required external characteristic $I_a(U_a)$ of the electric arc furnace—artificial external characteristic (AEC). Formation of the AEC according to the control criterion makes it possible to implement the respective strategy of

single-criterion or multi-criteria optimization and, at the same time, to considerably improve dynamic accuracy of stabilization of the above-specified EM coordinates, i.e. to reduce their dispersion 20–50-fold, which adds to increasing the efficacy of the selected strategy of optimal control [5–10].

One of the conditions of high-quality stabilization of EM coordinates and accuracy of extreme optimal control of melting modes is continuous monitoring of parameters of EAF LVC and measurement of arc voltage. Solution of this task is complicated by dynamic and static asymmetry of load modes in each phase, stochastic non-stationarity of coordinate and parametric perturbations in the power supply circuit of the three-phase arc system without a zero conductor. Taking into account the above-discussed specificities of the modes, authors in [11, 12] substantiate the feasibility of solving this problem on the basis of neural network principles of identification and prediction. These studies developed system and circuit solutions for the neural network system of monitoring (identification) of the parameters of the power circuit elements and operational control (measurement) of arc voltage.

While eliminating EM perturbations, synthesis and implementation of electrodes positioning law, which is optimal from the point of view of dynamics indices, is one of the major approaches to energy-effective control of melting modes. Dynamic performance criterion is a compromise solution between speed of travel and the overshoot whose integral control quality index is dispersion of arc length and EM coordinates. Taking on board the complexity of EAF mode models, significant non-linearities, gap clearance, backlash, elasticity, etc., wide application of fuzzy set theory for fulfilment of problems of optimal control of modes and electric coordinates regulation is a practicable approach to implementing optimal dynamics, which was developed and substantiated in studies [8, 13–17]. As another option of implementing optimal dynamics (i.e. the electrode positioning law) for the above-specified conditions of coordinate and parametric non-stationarity, studies [18–21] research and provide grounds for viability of using neural controller in the electromechanical electrode position control system.

3 Discussion of the Results

Stochastic nature of processes running in the electric power circuit and melting circuit of the electric arc furnace, lack of their precise mathematical description and need for optimal control implementation under continuous variation of the parameters of the characteristics of external influences, as well as change of operative requirements to integral performance indices of the arc furnace complex make it imperative that the techniques (models) of EAF electric mode optimal control synthesis being developed should be based upon the principle of adaptation of control action formation to the specificities of a current technological stage of melting [22–25]. This principle must rely on stochastic models of recognising a current technological stage and identifying the moments of its change (start and end) and implementation of the optimal control vector components corresponding

to the mode of this stage. As informative parameters, recognition models use arc current frequency responses, including wavelet spectrum parameters [26].

The hierarchical structure of adaptive optimal arc power control system of three-phase EAF developed on the basis of such approach is shown in Fig. 1. Arc power control subsystem (APCSS) is represented by electrode position control circuit (EPCC) whose control action is arc length increment Δl_a , which is implemented based on off-the-shelf arc power controller (for instance, ARDM-T), and high-speed arc power stabilization circuit (APSC) comprising the developed MTVC. Control action of this circuit is increments of equivalent inductance x_{ic} of the controlled impedance coil (IC).

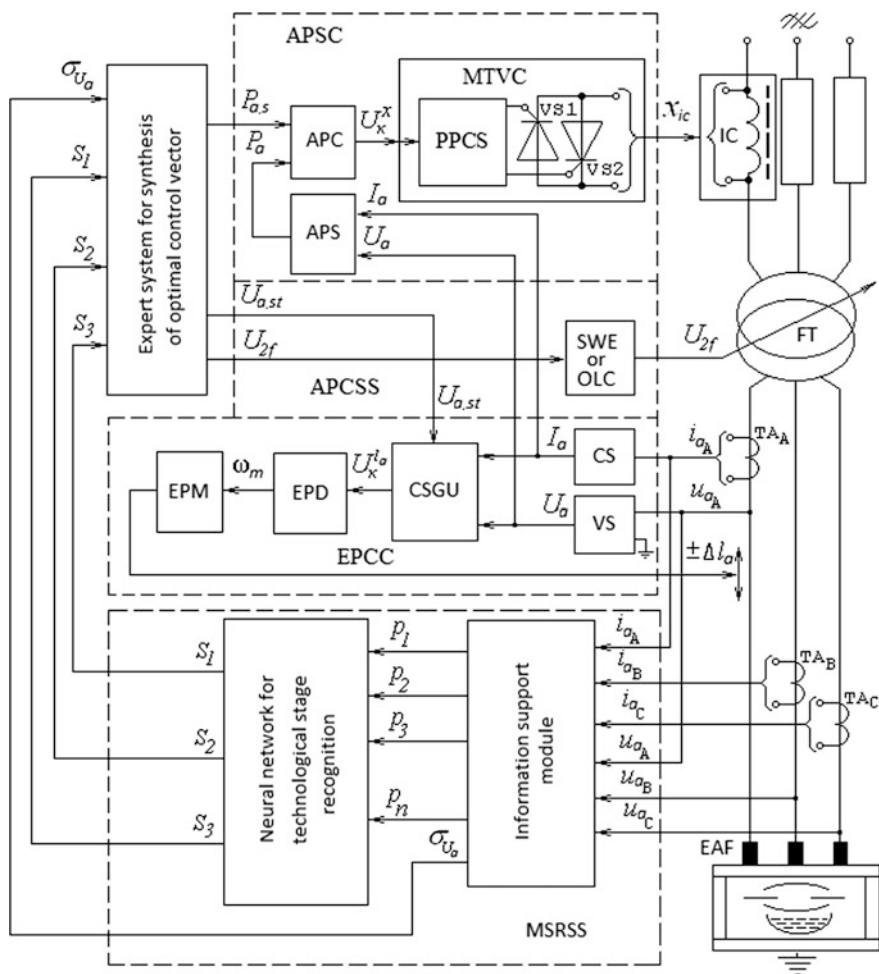


Fig. 1 Functional diagram of the hierarchical adaptive optimal arc power control system for EAF

Melting stage recognition subsystem (MSRSS) is implemented on the basis of the Kohonen complex neural network, whose input signals vector is formed in the information support module. Systemic control vector $\vec{x}(P_{a.s}, U_{a.st}, U_{2f})$ is synthesized by the upper-level (expert system). Steel melting control is fulfilled via channel of arc length l_a (voltage U_a), control channel of secondary voltage U_{2f} of the electric arc FT using typical devices for on-load control (OLC) or switching without excitation (SWE) and control channel of inductance x_{ic} of IC.

It was proposed that for parametric optimization of this hierarchical structure a decentralized approach should be used, according to which parametric optimization of individual local sub-systems (EPCC, APSC) is implemented relying on certain partial criteria of optimality which are in line with the general goal of mode control at electric steel-melting complex.

The systemic control vector is presented by stabilization level setting signal for arc power $P_{a.s}$, set value of arc voltage $U_{a.st}$ of EPCC and voltage U_{2f} of the secondary winding of the FT.

The main function of EPCC is reliable arc-striking and autonomous regulation of arc length (voltage) in each phase. It is performed in accordance with the differential law $U_k^{l_a} = aU_a - bI_a$ in modes of operational short circuits, arc extinctions and similar modes and according to the law of departure of arc voltage U_a from the set value $U_{a.st}$ $U_k^{l_a} = k_u(U_a - U_{a.st})$ in arcing modes. For this, signals of averaged value of arc voltage U_a and current I_a at the outputs of arc voltage sensor VS and arc current sensor CS are fed onto the inputs of control signal generation unit CSGU. In the function of output signal $U_k^{l_a}$ of this unit, output control signal Δl_a for re-positioning of the electrode in order to eliminate the departure of arc length value from the set (steady-state) value is generated by electrode positioning drive (EPD) and electrode positioning mechanism (EPM). However, taking into consideration significant response time of EPM and EPD and restricted rigidity and strength of some EPM elements, gap clearances and backlashes in the mechanical transmissions and insensitive zone with respect to control signal $U_k^{l_a}$, this circuit does not allow obtaining proper dynamic and static precision of control of arc power and other EM coordinates.

To eliminate this drawback, the structure of the proposed system was supplied with an additional high-speed electric APSC, whose major function is quality stabilization of arc power at the level of set value $P_{a.s}$ in modes with $P_a > P_{a.a}$. A unique feature of the APSC is the capacity for change of external characteristic $I_a(U_a)$ of the arc furnace and operative generation of desired AEC, which correspond to arc power plots with a horizontal section of arc power stabilization shown in Fig. 2.

It is implemented by using PI arc power controller for which input signal is the signal of the set value of arc power $P_{a.s}$ and its current value P_a generated at the output of the arc power sensor APS. Both circuits function concurrently and independently. Owing to over ten-fold speed of APSC as compared to EPCC speed, elimination of perturbations based on arc length is performed by EPCC for quasi-static process of regulation (stabilization) of arc power $P_a \cong P_{a.s}$. Organic combination of the specified functional capacities of APSC and EPCC enable

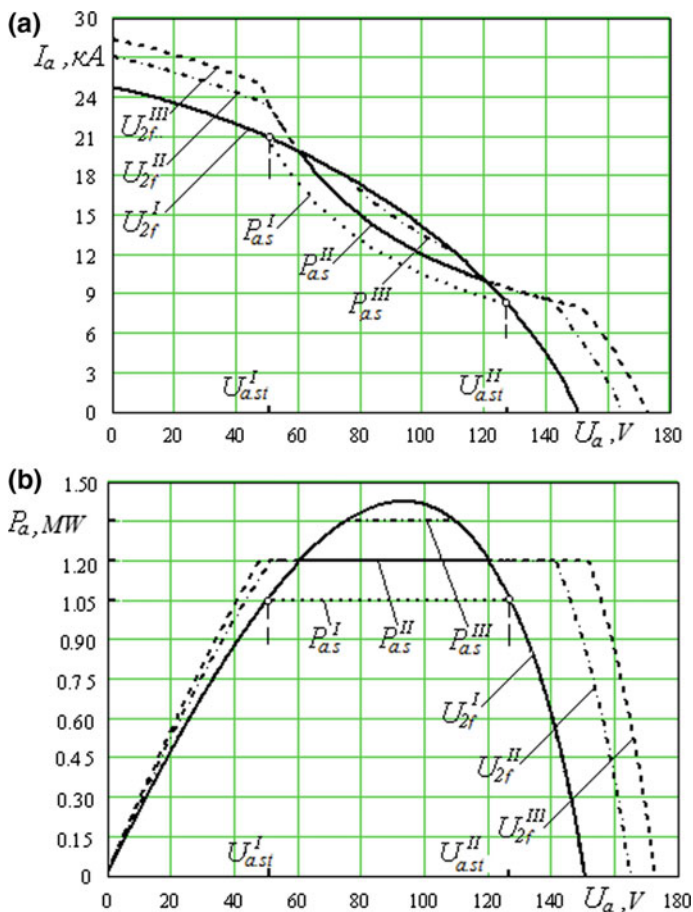


Fig. 2 External characteristics of electric arc furnace of DSP-6 type $I_a(U_a)$ (a) and corresponding plots of arc power $P_a(U_a)$ (b) for optimal control implementation according to criterion $D_{P_a} \Rightarrow \min$

reliable arc-striking and quality arc power stabilization at the set level in modes with $P_a > P_{a,s}$ under the influence of real dynamic perturbations at various technological stages of melting which differ in integral stochastic characteristics and parameters.

However, as Fig. 2 shows, dynamic and static accuracy of arc power stabilization, which is evaluated by dispersion D_{P_a} and value of $\bar{P}_a - P_{a,s}$ (\bar{P}_a is mean value on stationarity interval $P_a(t)$), will substantially depend on dispersion D_{U_a} (or standard deviation σ_{U_a}) of the process of arc voltage (arc length) fluctuation set for a given technological stage of arc power stabilization level $P_{a,s}$, set value of arc voltage $U_{a,st}$ of EPCC and secondary voltage U_{2f} of the FT.

The two latter control (setting) actions, namely value of $U_{a.st}$ and U_{2f} , are implemented on the existing EM ACS for each stage or period of melting a particular steel grade according to the a priori developed directive melting schedule for each EAF. Other conditions being the same, these two setting actions indirectly and explicitly determine arc power average \bar{P}_a .

However, taking into account continuous and random variation of external influences and perturbations of the melting process, in particular using different grades of melting feed, its different stowing density, different ambient temperature, initial temperature of the melting feed, temperature of the walls and the melting space at the start of the process, etc., melting at different stages will be accompanied by different values of arc voltage dispersion σ_{U_a} , this causing respective change of predicted average arc power \bar{P}_a and its dispersion D_{P_a} at each stage of melting. This, in turn, results in departure of the actual melting mode from the set one, changes in physical and chemical transformations of the melting feed and the melt, as well as in respective departure of integral indices of electric and technological efficiency from the values set by the directive melting schedule. Particularly noticeable these features become in modern high-impedance EAF with installed capacity of electric power equipment increased from 0.5–0.7 to 0.9–1.1 MVA/t, in which long arcs are used for melting ($U_{2f} \in [700, 1000]$ V).

In the proposed double-loop structure of coordinate-parametric regulation of arc power, this drawback is eliminated by using corresponding functionalities of EAF APSC. The study shows that the most significant improvement of electric and technological efficiency is achieved due to synthesis and implementation of the optimal control vector appropriate to the set requirements which ensures high-performance arc power stabilization. This is attained first of all by applying a principally new setting action on formation of AEC corresponding to the set criterion and the respective EAF arc power characteristic (Fig. 2). For control based on this criterion, a model of synthesis of systemic optimal control vector $\bar{x}(P_{a.s}, U_{a.st}, U_{2f})$ was obtained for each technological stage or period of melting in the proposed hierarchical structure of EM ACS:

$$D_{P_a}(U_{2f}, U_{a.st}, P_{a.s}) = \int_0^{U_{2f}} \{ (P_a(U_a, U_{2f}, P_{a.s}) - \bar{P}_a(U_{2f}, U_{a.st}, P_{a.s}))^2 \times f(U_a, \bar{U}_a, \sigma_{U_a}) \} dU_a \leq D_{P_a}^{\max} \Rightarrow \min \tag{1}$$

$$\text{for } \bar{P}_a(U_{2f}, U_{a.st}, P_{a.s}) = \int_0^{U_{2f}} P_a(U_a, U_{2f}, P_{a.s}) \cdot f(U_a, \bar{U}_a, \sigma_{U_a}) dU_a \Rightarrow \bar{P}_a;$$

$$U_{a.st}^I \leq U_{a.st} \leq U_{a.st}^{II}; \quad U_{2f}^I \leq U_{2f} \leq U_{2f}^{II},$$

where

$$P_a(U_a, U_{2f}, P_{a.s}) = \begin{cases} P_{a.s} & \text{for } U_{a.st}^I \leq U_{\partial} \leq U_{a.st}^{II}; \\ \frac{U_a \cdot (\sqrt{(U_{\partial} \cdot r)^2 + (r^2 + x^2)(U_{2f}^2 - U_a^2)} - U_a \cdot r)}{r^2 + x^2} & \\ \text{for all other } U_a, & \end{cases}$$

$f(U_a, \bar{U}_a, \sigma_{U_a})$ is function of distribution density of arc voltage oscillation $U_a(t)$ at a certain technological stage (period) of steel melting;

σ_{U_a} is standard deviation of the process $U_{\partial}(t)$;

$\bar{U}_{\partial} \cong U_{\partial,ycm}$ is mean value of the process $U_a(t)$;

\bar{P}_a is directive (desired) value of average arc power at a certain technological stage (period) of steel melting;

$D_{P_a}^{\max}$ is maximum allowable arc power value at a certain melting stage; $U_{a.st}^I, U_{a.st}^{II}, U_{2f}^I, U_{2f}^{II}$ are directive boundary values which set the region of allowable solutions for $U_{a.st}^*$ and U_{2f}^* for each technological stage (period) of steel melting, respectively.

Efficiency of action on values of \bar{P}_a and D_{P_a} of the setting action $U_{a.st}$ and perturbing action σ_{U_a} is illustrated by surface plots shown in Fig. 3 computed on the basis of the obtained model (1) for parameters of the electric steel furnace of the DSP-6 type.

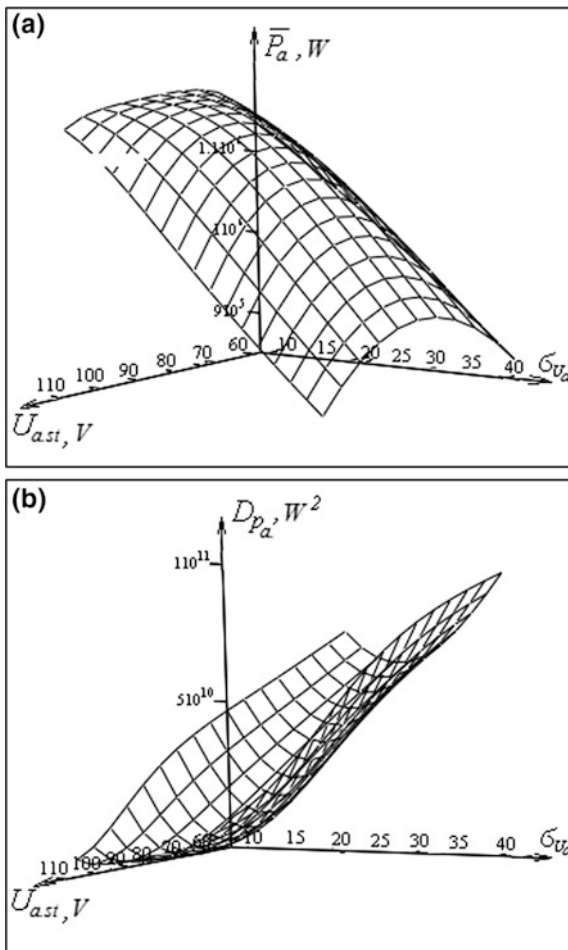
According to this model, for each technological stage of melting a certain steel grade, taking into account a priori average value of σ_{U_a} specific for it, an optimal control vector $\vec{x}(P_{a.s}, U_{a.st}, U_{2f})$ of the system is synthesized pursuant to the criterion of arc power dispersion minimization $D_{P_a} \leq D_{P_a}^{\max} \Rightarrow \min$ sub on condition of obtaining the directive average value of arc power \bar{P}_a and keeping the restrictions on the values of $U_{a.st}^*$ and U_{2f}^* . These restrictions are dictated by operative technological, electric, production, economic or other requirements at the current stage (period) of steel melting.

Therefore, for such optimal system to function, an important role is performed by the sub-system of recognizing steel-melting stages and identifying the moments of their change. This system is based on data from the set of parameters bearing information about modes, stages and decision making algorithm.

As the research showed, the set of information-bearing parameters that we studied (2nd, 4th and 6th arc current harmonics, consumed electricity) should also include parameters of wavelet spectrum of arc current signals from the range 200–300 Hz.

Wavelet transform is a specific type of linear transformation of signals. Basis of proper functions serving as the basis for signal decomposition possesses a number of special properties and capacities allowing focusing on these or those specificities

Fig. 3 Plots of dispersion D_{P_a} (a) and average arc power \bar{P}_a (b) in the plane of change of the setting action $U_{a,st}$ and perturbing action σ_{U_a} of the developed EM ACS for DSP-6 EAF



of the signal being analysed which cannot be identified using conventional Fourier or Laplace transforms. From the mathematical standpoint, any localized R-functions $\Psi(t) \in L^2(R)$ can be used for wavelet basis, i.e. any functions which have a double function (dual functions). With regard to time-frequency localization, wavelet functions occupy an intermediary position between harmonic (sinusoidal) functions localized in frequency and non-localized in time and Dirac delta function which is time-localized but fuzzy across the whole of the frequency domain.

Wavelet functions enable a continuous wavelet transform which is done using the expression

$$W_{a,b} = \int_{-\infty}^{\infty} \Psi_{a,b}(t) \cdot i_a(t) \cdot dt,$$

which is a convolution of arc current signal $i_a(t)$ with function $\Psi_{a,b}(t)$ for which this signal is transferred from time domain into wavelet domain with basis functions

$$\Psi_{a,b}(t) = \frac{1}{\sqrt{|a|}} \cdot \Psi\left(\frac{t-b}{a}\right)$$

where parameters a and b represent extension (compression) and shift of one function $\Psi\left(\frac{t-b}{a}\right)$ (functions of parent wavelets, the main of which are shown in Fig. 4 (at the top)). Inverse wavelet transform is determined as

$$i_a(t) = \frac{1}{C_\Psi} \cdot \int_{-\infty}^{\infty} \int_{-\infty}^{\infty} \frac{da \cdot db}{a^2} \cdot W_{a,b} \cdot \Psi_{a,b},$$

where $C_\Psi = \int_{-\infty}^{\infty} \frac{1}{|\omega|} \cdot \left| \hat{\Psi} \right|^2 \cdot d\omega$. Parameter a is referred to as scale parameter, and parameter b as shift parameter.

Experience shows that it is advisable to obtain bases of functions for arc current wavelet analysis from functions going to zero in infinity. The faster the function goes to zero, the more suitable it is to be used as wavelets-basis in analysis of real forms of arc current.

Choice of functions for wavelet-basis is determined by parameters and nature of information which need to be obtained for input signal description. This said, as basis functions, for analysis of EAF arc current forms it is practicable to use functions obtained by differentiating Gaussian functions to the 4th order derivatives with various values of their scale a (Fig. 4). These functions are localized along the axis of argument (independent variable of time) $b = 0$, invariant under shift and linear under scaling (compression/extension).

Coefficients of discrete wavelet transform of the arc current signal $i_a(t)$ are estimated as described below. First, a constant component of the signal $i_a(t)$ is isolated. Then, signal convolution with the parent wavelet extended along the whole time axis is performed. After that, the parent wavelet is compressed two-fold, and coefficients of its convolution with one and the other halves of the signal $i_a(t)$ are computed. Then, the parent wavelet is again compressed two-fold and another four coefficients are computed. The first two steps result in one coefficient, while each following step produces twice as many coefficients as the previous one. By further compression, the parent wavelet identifies higher and higher frequencies in the spectrum of the signal $i_a(t)$, and its location on the time axis shows the moment at which a respective frequency appears.

Based on the above-described procedure of computing the coefficients of the discrete wavelet transform, shapes of arc current curves obtained at different technological stages of melting in the EAF of the DSP-100H3A type (Donetsk Steel Works) were analysed (Fig. 5), namely at the stage of the pit melt-through and

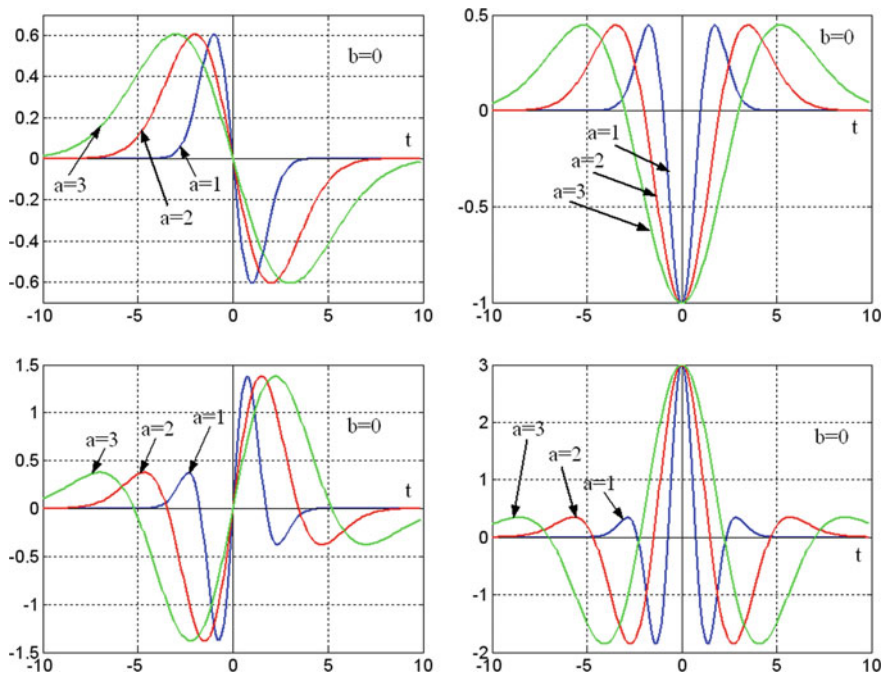


Fig. 4 Wavelet functions advisable for harmonic analysis of arc current

furnace feed downslide, stage of completing the melting of the solid feed (arcing at the liquid melts), tranquil mode (oxidation period, arcing in the bulk of the slag). The number of steps of analysis (detailing levels) of arc current curve shape was adopted to be 7.

The analysis conducted according to the above-described algorithm of analysing the shape of arc current curves presented in Fig. 5 results in the coefficients of the discrete wavelet transform. Having these coefficients, we can also perform an inverse wavelet transform. The arc current curves obtained using the inverse wavelet transform for 5 levels of composition are shown in the respective time dependencies of $i_a(t)$ in Fig. 5.

If we take that, when doing wavelet transform, time and scale are inversely proportional according to $\omega = k/a$, then, similarly to Fourier transform, one can use the notion of harmonics, where ω is frequency, a is scale and k is conversion factor that can be computed either by simple superposition of a harmonic with a known frequency on the wavelet spectrum of this harmonic or it can be selected from the table of proportionality factors. For instance, for the parental wavelet obtained by 1st order differentiation of the Gaussian function (Fig. 4), $k = \sqrt{3}/2$. The wavelet transform unit (WTU) computes coefficients of arc current wavelet transforms, which form the vector of input information-bearing parameters of the neural network system of melting stage recognition in the electric arc furnace (Fig. 6).

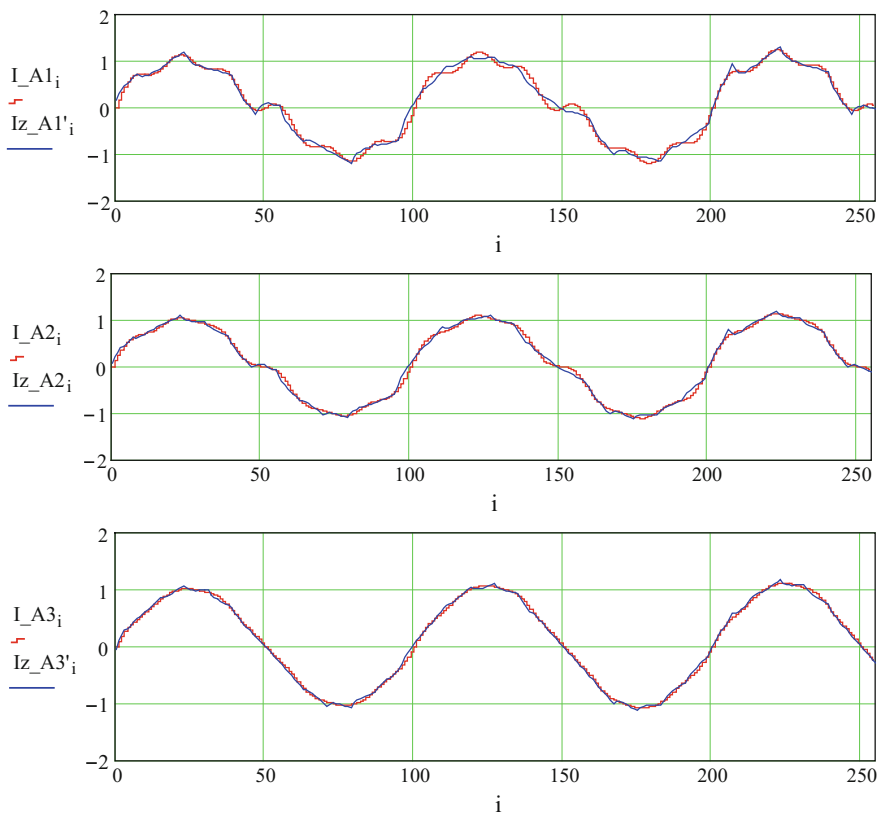


Fig. 5 Time dependencies of experimental arc current curves for EAF DSP-3 at different melting stages obtained by inverse wavelet tranfrom

Solution of the problem of technological melting stages recognition and identification of moments of their change according to EM (Fig. 1) using the developed ACS structure can be implemented by applying a complex neural network with the Kohonen layer.

Let us assume that the characteristics which most comprehensively reflect the technological situation in the melting space of EAF and indirectly provide the numerical estimation of physical and chemical condition of the furnace feed and the melt include dispersion of the envelope curve of half-period average arc current, 2nd, 4th and 6th higher harmonics of arc current. The listed characteristics form the vector of information-bearing parameters or input pattern, which for the three phases of EAF will be denoted as $X = \{x_1, x_2, \dots, x_{12}\}$.

In the process of steel making this vector changes, which results in a set of vectors X used for functioning of the Kohonen neural network [3]. The basic structure is a mono-dimensional neural network structure whose diagram is shown in Fig. 7.

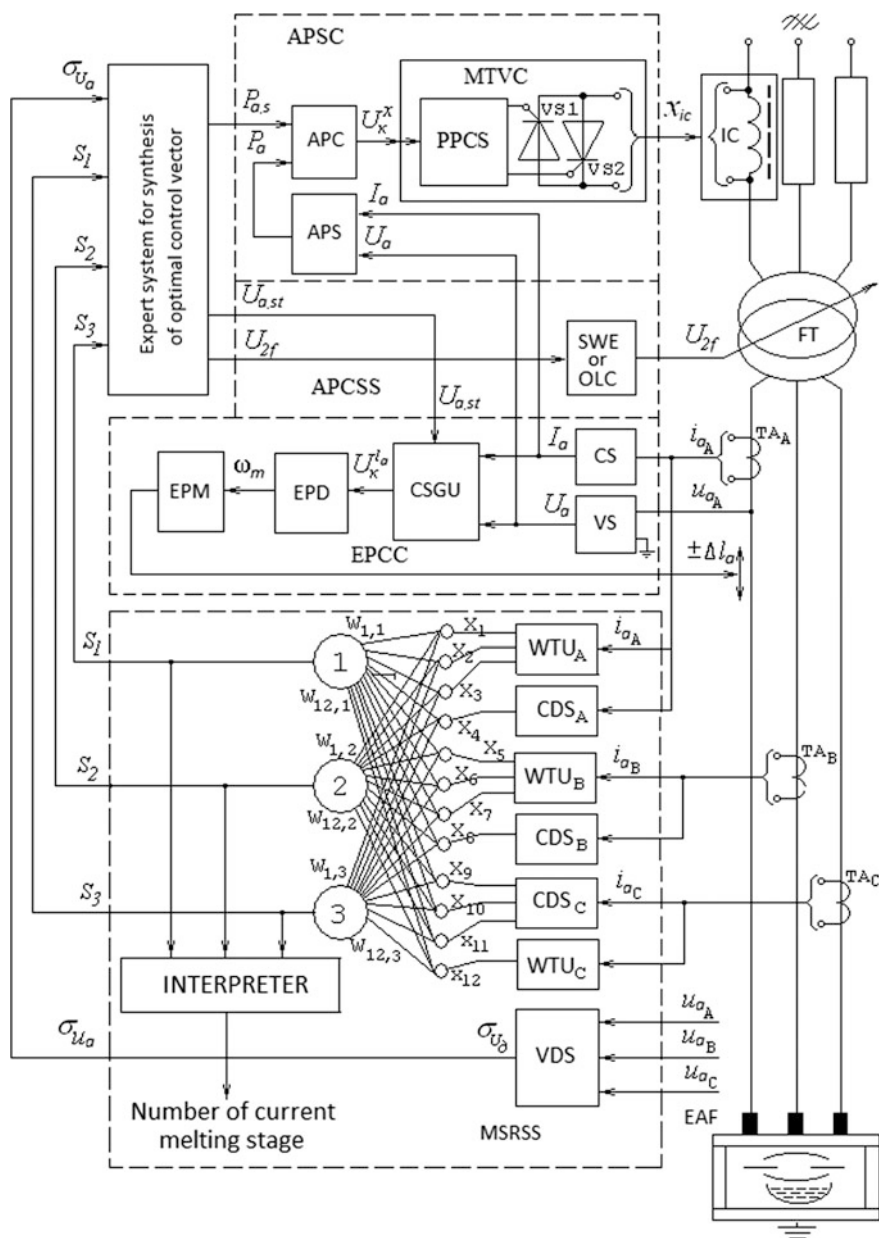
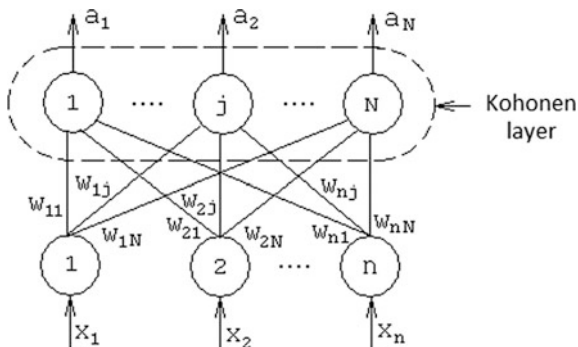


Fig. 6 Functional diagram of the neural network system of melting stages recognition and electric mode control of the electric arc furnace, where *CDS* current dispersion sensor, *VDS* voltage dispersion sensor

Fig. 7 Structural diagram of the artificial neural network



In the presented neural network structure, the Kohonen layer consists of N neurons each of which receives n (12 in our case) input signals from the layer below whose function is to distribute input signals according to their value.

At its input each j th neuron of the Kohonen layer forms intensity I_j by the expression:

$$I_j = D(W_j, X),$$

where $W_j = (w_{1j}, w_{2j}, \dots, w_{nj},)$ is weight vector;

$D(W_j, X)$ is a certain measure (metrics) of the distance or relationship between W_j, X .

For function $D(W_j, X)$ the following relationships are used:

- (1) Euclidean distance:

$$D(W_j, X) = \sqrt{\sum_{i=1}^n (X_i - W_{i,j})^2}$$

- (2) squared Euclidean distance:

$$D(W_j, X) = \sum_{i=1}^n (X_i - W_{i,j})^2$$

(3) correlation coefficient (degree of relationship):

$$D(W_j, X) = \sum_{i=1}^n \frac{(X_i - M_x) \cdot (W_{ij} - M_{W_j})}{\sigma_x \cdot \sigma_{W_j}},$$

where $M_x = \frac{1}{n} \sum_{i=1}^n X_i$; $M_{W_j} = \frac{1}{n} \sum_{i=1}^n W_{ij}$;

$$\sigma_x = \sqrt{\frac{1}{n} \sum_{i=1}^n (X_i - M_x)^2}; \quad \sigma_{W_j} = \sqrt{\frac{1}{n} \sum_{i=1}^n (W_{ij} - M_{W_j})^2}$$

The degree of relationship differs from the distance measure in that the higher it is, the more similar the vectors are.

In the process of the network algorithm functioning, each Kohonen layer neuron computes function I_j . Then the element with the lowest value of I_j for distance measure or with the highest value of I_j for degree of relationship is found. When the neuron with the extreme value of I_j is found, values of weights of this neuron are corrected using the expression:

$$W_{ij}^H = W_{ij}^C + \alpha \cdot (X_i - W_{ij}^C)$$

where W_{ij}^H , W_{ij}^C are new and previous value of weight (when initializing the network, W_{ij}^C is assigned a random value or its value is obtained using other methods); α is learning rate factor.

After correcting the weights, the network is input with sequential vectors of input reference signals, and when a sufficient number of reference signals have been input, neuron synapses (weights) are grouped according to the trend identified by the neural network on the basis of all the inputs.

Learning process in the Kohonen network occurs as self-learning, i.e. without a “teacher”. Thus, it is difficult to predict which neuron of the Kohonen layer will be activated for the set input vector, or, in other words, inform of this or that stage of melting, and there is no need to do that. It should be only guaranteed that the learning will result in distinguishing dissimilar input vectors X.

In order to check the effectiveness of using the Kohonen network, recognition of vectors X obtained with the operating furnace of the DSP-100H3A type at Donetsk Metal Works was done at two stages: A1—pit melt-through; A2—arcing in the pool of molten metal. For identifying the current stage, a neural network with two neurons in the Kohonen layer was built. The network was trained in MatLab 6.5. As function $D(W_j, X)$, Euclidean distance (dist) was taken. To verify that the network operates correctly, identification of stages for this same vector X was performed using Bayesian method. The results obtained for the two melting stages are presented in the table below.

	X1	X2	X3	X4	X5	X6	X7	X8	X9
Stage 1	1	1	1	0	0	0	1	1	1
Stage 2	0	0	0	1	1	1	0	0	0
Neuron 1	0	0	0	1	1	1	0	0	0
Neuron 2	1	1	1	0	0	0	1	1	1

It can be seen from the presented data that the network clearly distinguishes input forms of X_i , i.e. the moment when one stage is replaced by a sequential one, but there is no clear definition which neuron is responsible for this or that stage.

The developed Kohonen neural network with sufficient accuracy identifies one of the two technological stages of melting in EAF. The result of identification coincides with that obtained by applying Bayesian method.

Similar studies of the technological stage recognition system using the above-discussed neural network were carried out on the basis of the DSP-3 furnace.

To obtain information on characteristics of change of formal features—information-bearing parameters of the electric and technological modes closely correlating with the process of change of technological stages of electric steel-melting, changes of instantaneous values of arc current and voltage and active energy were digitally recorded for 10 experimental meltings.

Change of technological stages which were identified in the studied melting processes in this furnace is illustrated with the graph in Fig. 8.

The results of processing the data showed that the highest informative value is offered by harmonic components of arc current, namely 2nd, 4th and 6th harmonics, evaluations of the components of the wavelet spectrum of arc current signals in the range 200–300 Hz and consumed active electric energy. The set of the listed features x_j describes the object $I(\omega) = \{x_1, x_2, \dots, x_N\}$. Therefore, if there is a specified set of M-objects $\{\omega_i\}$ on which there is a breaking-up into a finite number of classes Ω_k , $k = \overline{1, m}$, $\bigcup_{k=1}^m \Omega_k = M$, the problem of recognizing the stages consists in computing the values of predicates $P(\omega \in \Omega_k)$, $k = \overline{1, m}$ for a given object ω and set of classes Ω_k , $k = \overline{1, m}$ according to $I(\omega)$ and in consequent solution of the objects grouping problem.

The structure of the obtained Kohonen neural network for recognizing the above-mentioned melting stages based on the input state vector which comprises current integral values of the 2nd, 4th and 6th harmonics of arc current of each phase and active electric energy consumed since the start of the melting process is shown in Fig. 9.

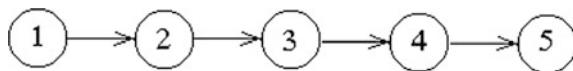
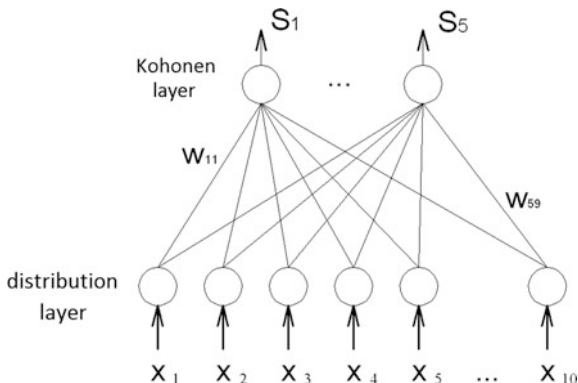


Fig. 8 Graph of the technological process status in the electric arc furnace of the DSP-3 type: 1, 3—pit melt-through; 2, 4—furnace feed downslide and arcing in the pool of the molten metal; 5—oxidation of the melt (1, 2—main charge; 3, 4—additional charge)

Fig. 9 Kohonen neural network for recognizing technological stages of melting in the DSP-3 furnace



The neural network contains five output neurons in the Kohonen layer, each of which receives ten input signals x_1, x_2, \dots, x_{10} from the input (distribution) layer which is a direct transmitter of signals. Input i with respective j -th output is assigned weight $w_{j,i}$. As a result, we obtained a matrix of synaptic relations W . The function of the neuron of the output Kohonen layer consists in computing intensity I_j using the formula $I_j = D(W_j, X)$, where $D(W_j, X)$ is a certain measure of distance or degree of relationship between W_j and X .

In the process of training such a neural network, the matrix of synaptic relations W was defined by the expression

$$W_j^{k+1} = W_j^k + \eta_j^k \cdot G^k(j, x^k) \cdot (x^k - W_j^k),$$

where $0 < \eta_j^k < 1$ is a network learning factor declining during training as k increases;

$G^k(j, x^k)$ is neighbourhood function which was defined by the Gaussian formula:

$$G^k(j, x^k) = \exp\left(-\frac{d^2(j, x^k)}{2 \cdot (\sigma^k)^2}\right),$$

where $d(j, x^k)$ is distance from the j -th neuron to the winning neuron with index w^k in the k -th training cycle, σ^k is parameter of Gaussian function width.

Based on the obtained values of intensity I_j of the output Kohonen layer neuron, the element with the extreme value of I_j is determined. The output signal of this neuron is assigned 1, all the other 0.

Training and testing samples for the neural network were formed based on the results of processing the outcomes of the studies of the DSP-3 furnace. The results of simulating the operation of the trained Kohonen neural network are shown in Fig. 10.

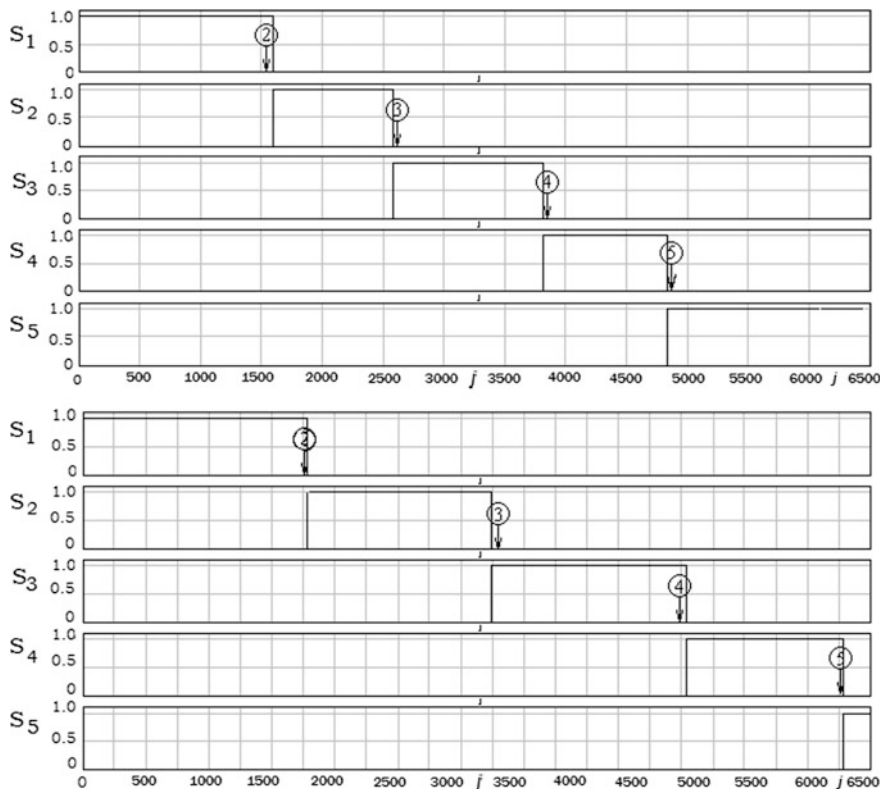


Fig. 10 Change of activity of output neurons of the Kohonen neural network and actual change of melting stages according to the expert assessment on the interval of two meltings

To assess the accuracy of melting stage identification synthesized by the Kohonen neural network, experts in the field (technologists) were engaged. The precise moments of melting stage change were computed using expert techniques. In the diagrams in Fig. 10 the arrow marks show the moments of technological melting stage change. Analysis of the results of the synthesized Kohonen neural network testing shows fairly high adequacy of recognition of the output neurons activity change when compared with the moments of the real change of melting stage identified by the experts (technologists).

This proves a sufficient level of correspondence between the changes of parameters of the Kohonen neural network input signals and change of technological stages of melting in the electric arc furnace. The maximum error of identification of the moment of melting stage change by the neural network did not exceed $\pm 5\%$ of the duration of a current technological stage, the end moment of which is being identified

4 Conclusions

1. The developed hierarchical structure of the electric arc furnace EM control system, which includes the electromechanical circuit of electrode positioning, high-speed electric circuit which forms different types of external characteristics of the furnace and technological stage recognition sub-system as the top level enables synthesis of multi-criteria EM control vector with adaptation of its elements to the current requirements and characteristics of the steel melting process perturbations.
2. The model studies and computations of characteristics and indices of the optimal control system based on the complex criterion of maximizing arc power showed that average arc power can be increased with simultaneous reduction of its dispersion, which enhances furnace efficiency and accuracy of heat mode control in the melting space.
3. Application of the neural network principles of identification and the developed wavelet transform circuitry for operative computation of informative parameters of steel melting is an effective means of high-accuracy recognition of technological stages of melting in EAF and on this basis implementation of adaptive models of multi-criteria optimal control of EAF EM.
4. The experimental study of the developed neural network system of technological stages recognition revealed high accuracy of identification of stage change moments which were determined by the experts—the absolute error of identification did not exceed 30–50 s in relation to the reference values.

References

1. Kudrin, B.I.: Retrospective and perspective views on electric power consumption in electrometallurgy. Part 1. *Electrometall. J.* **10**, 2–13 (2003)
2. Balan, R., Maties, V., Hancu, O., Stan, S., Ciprian, L.: Modeling and control of an electric arc furnace. In: *Mediterranean Conference on Control and Automation, MED '07*, pp. 1–6 (2007)
3. UA Patent No. 53074 A. Ukraine. Device for regulation of electrical mode of multi-phase electric arc furnace. O. Yu. Lozynskyy, A. O. Lozynskyy, Ya.S. Paranchuk, R.Ya. Paranchuk. - Published 15/01/03.- Bulletin No. 1
4. Paranchuk, Y.S.: Harmonic analysis of current of magnetic thyristor voltage converter. *Tekhnichna Electrodynamic J. Power Electron. Energy Effic.* **2**, 37–40 (2002)
5. Bedyne, M., Romano, M.: Electric arc furnace powered by self-saturating reactor. *Electrometall. J.* **4**, 15–20 (2004)
6. Lozynskyy, O.Y., Paranchuk, Y.S.: System for the optimum control of the electrical conditions of an arc furnace powered through a controlled reactor. *Russ Metall (Metally) (English Translation of Elektrometallurgiya)* **8**, 737–743 (2007)
7. Lozynskyy, O., Paranchuk, Y., Paranchuk, R.: Multicriterion intelligent control system and optimal stabilization of arc steel-melting furnace electrical regimes coordinates. *Comput. Probl. Electr. Eng.* **1**(1), 35–44 (2011)

8. Lozynskyy, O.Y., Paranchuk, Y.S.: Hierarchical system of multi criteria optimal control of electric arc furnace modes with fuzzy adaptation. *Tekhnichna Elektrodynamika J.* **3**, 103–104 (2012)
9. Lozynskyy, O.Y., Paranchuk, Y.S.: Optimization of modes control system for electric steel-melting in electric arc furnaces. *Electrotekhnikha J.* **6**, 50–54 (2004)
10. Gomes, A.A., Durango, J.J.M., Mejia, A.E.: Electric arc furnace modeling for power quality analysis. In: ANDESCON, IEEE, pp. 1–6 (2010)
11. Paranchuk, Y.S., Paranchuk, R.Y.: Neutral network system for continuous voltage monitoring in electric arc furnace. *Sci. Bull. Natl. Min. Univ.* **2**(152), 74–80 (2016)
12. Schlang, M., Poppe, T., Gramckow, O.: Neural networks for steel manufacturing. *IEEE Expert Intell. Syst.* **11**(4), 8–9 (1996)
13. Lozynskyy, O.Y., Marushchak, Y.Y.: Some aspects of control actions formation in electromechanical systems. *Electrotekhnikha J.* **5**, 52–56 (1999)
14. Lozynskyy, O., Paranchuk, Y., Paranchuk, R.: Modelling of power control of arc steel melting furnace with fuzzy correction of regulation signal. *Przegląd Electrotechniczny* **3a**, 265–267 (2013)
15. Lozynskyy, A.O., Paranchuk, Y.S., Demkiv, L.I.: Study of the electrode positioning system of electric arc furnace with fuzzy controller. *Tekhnichna Elektrodynamika J.* **2**, 73–76 (2014)
16. Lozynskyy, O., Paranchuk, Y., Paranchuk, R.: Fuzzy control law of electrode travel in arc steelmaking furnace. In: Proceedings of the 16th International Conference on Computational Problems of Electrical Engineering, pp. 103–106. Lviv, Ukraine (2015)
17. Sadeghian, A., Lavers, J.D.: Nonlinear black-box modelling of electric arc furnace: an application of fuzzy logic systems. In: Fuzzy Systems Conference Proceedings, 1999. FUZZ-IEEE'99, 1999 IEEE International, Vol. 1, pp. 234–239 (1999)
18. Zhao, H.: NN-based approximate model control for the EAF electrode regulator system. Hindawi Publishing Corporation *Mathematical Problems in Engineering* Volume 2013, Article ID 874890, p 11 (2013)
19. Liand, L., Mao, Z.: A direct adaptive controller for EAF electrode regulator system using neural networks. *Neurocomputing* **82**, 91–98 (2012)
20. Paranchuk, Y., Matsyhin, A.: The system of arc lengths regulation of an electric arc furnace with a neuro-controller. *Przegląd Electrotechniczny* **3a**, 271–273 (2013)
21. Malyar, A.V., Andreishyn, A.S.: Selection of a neural network for computing filling factor of the deep well pump. *Probl. Autom. Electr. Drive Theory Pract. Special issue of Elektromekhanichni ta Eletrozberigaiyuchi Systemy Journal. Kremenchuk* **3**(19), 543–545 (2012)
22. Lozynskyy, A.O., Kostyniuk, L.D., Paranchuk, Y.S., Perevozniuk, V.Y., Smetaniuk, Y.V.: Automated recognition of technological stages of furnace feed melting. *Electrotekhnikha J.* **9**, 39–42 (1986)
23. Denys, B.D., Lozynskyy, O.Y., Kostyniuk, L.D., Perevozniuk, V.Y.: Method of identification of technological melting stages and process end moment recognition in electric arc furnaces. *Electrotekhnikha J.* **2**, 8–10 (1985)
24. Lozynskyy, O.Y., Kostyniuk, L.D., Perevozniuk, V.Y.: Automated system of recognition of melting stages in EAF. *Electrotekhnikha J.* **3**, 23–24 (1987)
25. Chang, G.W., Shih, M.-F., Chen, Y.-Y., Liang, Y.-J.: A hybrid wavelet transform and neural-networks-based approach for modelling dynamic voltage-current characteristics of electric arc furnace. *IEEE Trans. Power Deliv.* **29**, 815–824 (2014)
26. Li, D.-M., Yu, X.-Y., Wang, X., Tang, T.-Q.: Power quality disturbances fuzzy identification based on DQ conversion and wavelet energy distribution. In: Instrumentation, Measurement, Computer, Communication and Control (*IMCCC*), 2012 Second International Conference, pp. 1403–1407 (2012)

Passive Stall Control Systems of Power Limitation Modes for Vertical Axis Wind Turbines (VAWT)

Ihor Shchur, Andrii Lozinskyi, Bohdan Kopchak, Yurii Biletskyi
and Vsevolod Shchur

Abstract Vertical axis wind turbines (VAWT) with direct drive permanent magnet synchronous generator operate with the greatest energy efficiency and reliability in low-power wind energy conversion systems (WECS). This article offers a classification of optimal control methods of such WECS. Special attention is also given to an unexplored area—the development of control systems of power limitation mode when VAWT work at high wind speeds—passive stall and feathering control. In particular, the structures of control systems were developed, the parameters of power regulators were obtained, and these regimes were compared by means of computer simulation. The fractional order control method was also used for this mode and the parameters of fractional order PID power regulator were found by the method of Particle Swarm Optimization (PSO). The article also demonstrates how to realize the mode of passive stall control in the energy-shaping control system (ESCS) previously developed by the authors.

Keywords VAWT · PMSG · Optimum control · Power limitation modes · Passive stall regulation · Fractional order control · Energy-shaping control

I. Shchur (✉) · A. Lozinskyi · B. Kopchak · Y. Biletskyi · V. Shchur
National University „Lviv Polytechnic“, Lviv, Ukraine
e-mail: i_shchur@meta.ua

A. Lozinskyi
e-mail: addriy.o.lozynskyy@lpnu.ua

B. Kopchak
e-mail: kopchakb@gmail.com

Y. Biletskyi
e-mail: shadovv00@gmail.com

V. Shchur
e-mail: lesyk_shchur@yahoo.com

1 Introduction

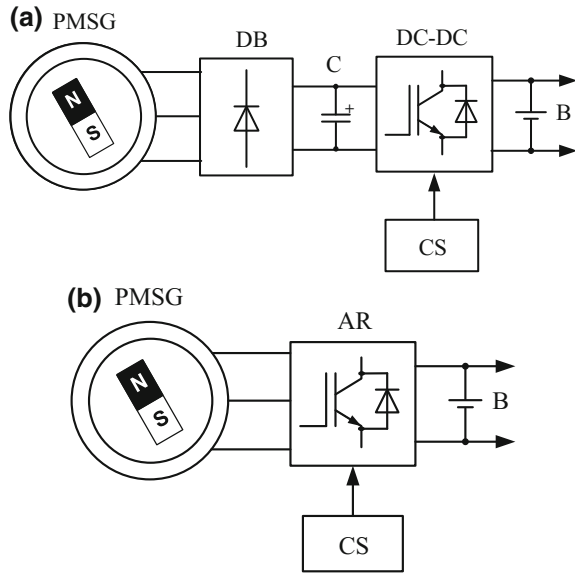
In many countries, especially in highly developed countries, the rate of renewable energy is increasing. Prominent in this process is the wind energy that is represented by high power wind turbines (WT) with the horizontal axis of rotation (HAWT), which are often combined in wind farms [1]. Along with this, low-power (up to 10 kW) wind energy conversion systems (WECS) recently are becoming more and more common [2]. They are used by individual consumers for power supply in case of lack of centralized power grids, or if the availability of the latter for additional power supply to reduce power consumption from the grid, increase energy efficiency, ensuring uninterrupted power supply, etc. [3]. Specific work conditions of low-power WECS cause significant differences from powerful HAWT in design and tasks of automatic control of their work in different modes.

Low-power WECS are installed directly at consumers, where the wind is mostly characterized by low average speeds, frequent gusts, changes in direction and high turbulence. Features of location and specific characteristics of wind determine the benefits of the application of WT with a vertical axis of rotation (VAWT). These turbines operate efficiently with gusty winds, constantly perceive the wind from any directions, and start at low wind speeds thanks to low-speed gearless drive of the multipolar synchronous generator with permanent magnets (PMSG) [4]. The vertical design of VAWT makes it possible to place a relatively large PMSG under WT, which will not affect the aerodynamic characteristics of the latter. The absence of mechanical multiplier reduces the starting wind speed of VAWT.

Unlike HAWT, which is based on the traditional pattern and differ mainly in the number of blades, in VAWT there is a huge variety, which due to the current elevated interest in wind power is growing. VAWT may differ by the following features: prevailing principle of operation (the drag or lift) and accordingly the value of tip speed ratio (TSR); passive or active design (rigidly mounted or rotary blades); the number of WT working on a generator; using power augmentation-guide-vane and more [5].

The specific (on a unit of power) cost of low-power VAWT is much higher than powerful HAWT. Therefore, to reduce the payback period, the low-power WECS must produce maximum energy efficiency in all modes of operation, especially at low wind speeds, because in these conditions these WT are the vast majority of the time. The practice of VAWT application allows selecting the most efficient configuration. Thus, the WT of passive construction have the lowest cost and highest reliability. The straight-blade VAWT (SB-VAWT) with corresponding aerodynamic profile NACA excel by the highest power density due to high TSR and low cost [6]. However, lack of opportunity to adjust the aerodynamic characteristics of passive VAWT leaves you to make automatic control of WECS only by changing of generator electrical load. To this end, there are two most commonly used configurations of power electronic control systems, with cheaper passive diode rectifier DB and DC/DC converter and more expensive with a voltage active rectifier (AR) (Fig. 1) [7]. As loading in both systems used the battery B, which is

Fig. 1 Common controlled electromechanical systems for WECS with VAWT and PMSG: **a** based on a DC/DC converter, **b** based on an AR



connected to the electrical consumers via direct current or through voltage inverter —AC. Apart from cost, these systems differ also a number of other indicators, but allow you to provide the desired load regulation of PMSG, so a type of electronic system is not essential for the building of control system. Automatic control of these WECS made respective control systems CS.

Much more energy efficiency and safety of WECS with VAWT depends on the approaches to the design of control systems and therefore the quality of their work.

The main objective of this paper is to analyze approaches to creating automatic control systems (ACS) for WECS with VAWT and research of control systems for power limitation of passive VAWT at its work on the winds at a speed higher than the nominal.

The paper is organized as follows: Sect. 2, under the basic laws of VAWT operation, introduces the classification of control systems of optimal loading of PMSG in partial-load operating mode and shows how VAWT power can be limited in the full-load operating mode when wind speed is higher than the nominal. Section 3 is devoted to the creation and research by computer simulation of systems to VAWT power limitation using classic controllers. Section 4 shows how you can improve the system power limitation using fractional order PID power regulator. In Sect. 5 we researched and developed the subsystem of VAWT power limitation for developed previously by the authors the energy-shaping control system (ESCS), designed for optimal control of WECS describing as a port-controlled Hamiltonian system (PCHs). Finally, some conclusions are discussed.

2 The Main Patterns of VAWT Work in Different Modes and Control Systems Review

At any moment WECS is at a certain operating point, which depends on a number of factors: wind speed V , the angular velocity ω of VAWT, the power of electrical loads of PMSG, the efficiency of the generator at this point, the nature of work (transient or steady state mode).

The output power of the VAWT shaft, which creates by wind flow, described by the known expression

$$P_{WT} = \frac{1}{2} \rho A C_P(\lambda) V^3, \quad (1)$$

where ρ is the air density, $A = 2rh$ is the washing area of SB-VAWT with the radius r and the height of blade h , C_P is the power coefficient, and $\lambda = \omega r/V$ is the TSR.

Power coefficient function $C_P(\lambda)$ is the main dimensionless characteristic of the VAWT aerodynamic properties, which is generally considered to be stable (for aerodynamically passive VAWT) and independent of WT working conditions [8].

The mechanical torque on the VAWT shaft is equal

$$T_{WT} = \frac{P_{WT}}{\omega} = \frac{1}{2} \rho A r \frac{C_P(\lambda)}{\lambda} V^2. \quad (2)$$

According to expressions (1) and (2), power coefficient function $C_P(\lambda)$ determines the nature of power and torque of the VAWT. These characteristics for specific WT can be obtained by calculation or by modeling of aerodynamic processes during WT work by finite element method in CFD (Computation Fluid Dynamics) [9], or experimentally in wind tunnels. In further studies we will use the dependence, which is typical for 3-blads low-power SB-VAWT (Fig. 2):

$$C_P(\lambda) = 1.14 \left(\frac{9.47}{\lambda} - 1 \right) e^{\frac{-6}{\lambda}}. \quad (3)$$

Dependence $C_P(\lambda)$, as shown in Fig. 2, provides the maximum value of power coefficient $C_{P_{\max}} = 0.3514$ for the optimal value of TSR $\lambda_{\text{opt}} = 3.675$. The point $C_{P_{\max}}(\lambda_{\text{opt}})$ is called maximum power point (MPP). To support the work of VAWT at this point, its angular velocity must be maintained at an optimum value, which should be directly proportional to the wind speed:

$$\omega_{\text{opt}} = \frac{\lambda_{\text{opt}}}{r} V. \quad (4)$$

Based on $C_P(\lambda)$, from (1) and (2) basic dependences can be calculated for particular VAWT, which characterize its work. Figures 3 and 4 show the calculated

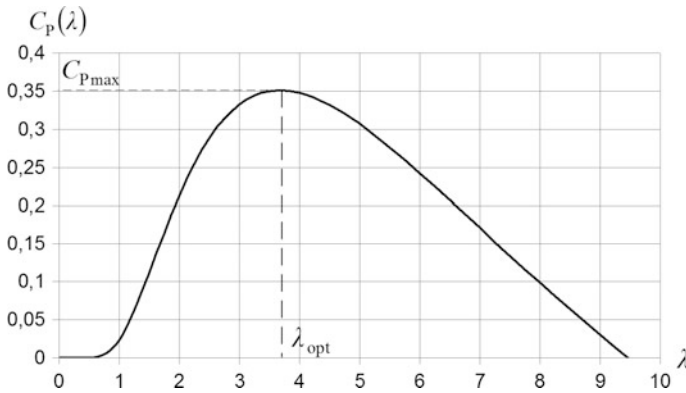


Fig. 2 Power coefficient function of SB-VAWT adopted in this paper

curves, respectively, torque and mechanical power on a shaft of VAWT vs its angular velocity at constant values of wind speed for WT with aerodynamic characteristic (3) and the rated power of 1 kW, which obtains at the wind speed of 10 m/s. The curve of VAWT optimal torque values T_{opt} , shown in Fig. 3, corresponds to the curve of maximum power P_{max} , connecting the extremes of the curves in Fig. 4.

One of the most important characteristics of WECS is its power curve—a dependence of output electrical power P_{WECS} versus wind speed. Functions of this type (Fig. 5) usually are served graphically in passports of specific WECS by manufacturers [10].

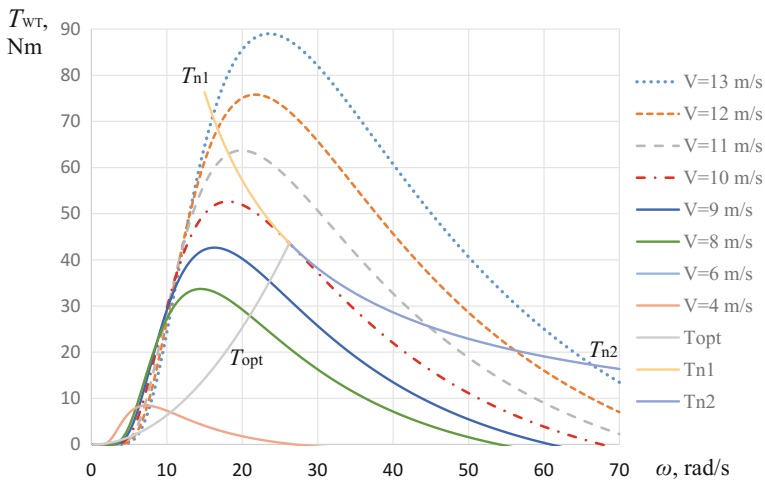


Fig. 3 Mechanical torque on the VAWT shaft versus its angular velocity for WT with rated power of 1 kW at different wind speeds

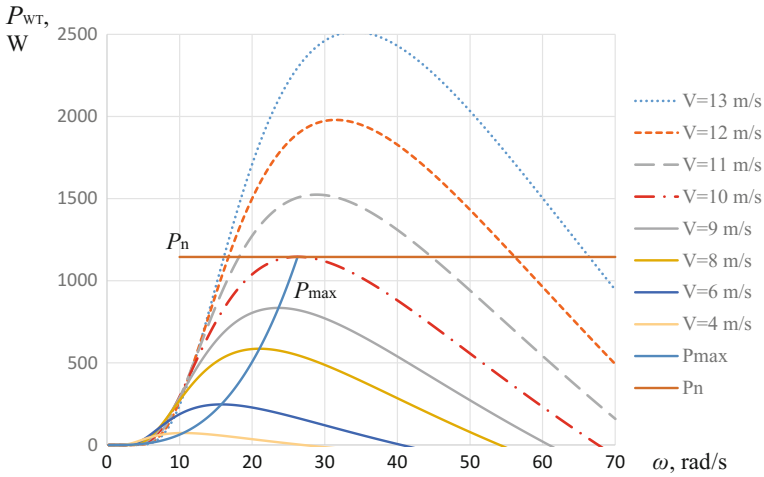


Fig. 4 Output mechanical power on the VAWT shaft vs its angular velocity for WT with rated power of 1 kW at different wind speeds

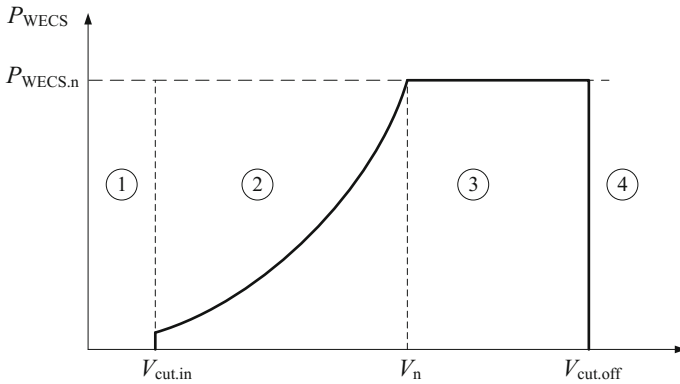


Fig. 5 Typical power curve of WECS

Figure 5 highlight 4 zones. WT will not start in zone 1 because of the low wind speed and starts generating the output electricity from the wind speed $V_{cut.in}$, known as the cutting speed and, usually between 3 and 4 m/s. In the range of wind speeds from $V_{cut.in}$ to the rated wind speed V_n (control zone 2) WT work with partial-load, and only at wind speed, V_n output power of WT reaches its nominal value $P_{WECS,n}$, for which an electric generator is designed. In the range of wind speed from V_n to $V_{cut.off}$, called cutting speed, (control zone 3) the electric output power of WT must be limited at rated level by one of the possible ways. With increasing of wind speed over $V_{cut.off}$ braking system works, VAWT ceases to rotate, and therefore process of generating electricity stops (zone 4).

The most task of automatic control of WECT with aerodynamically passive VAWT (fixed blades) with partial-power at low and average wind speeds is ensuring optimal electrical load of PMSG that VAWT always moved with optimum proportional to wind speed angular velocity according to (4) and worked in MPP—Maximum Power Point Tracking (MPPT) [11]. Substituting in (2) the value of the wind speed from Eq. (4), we obtain the following relationship:

$$T_{\text{opt}} = \frac{0.5\rho AC_{\text{Pmax}} r^3}{\lambda_{\text{opt}}^3} \omega_{\text{opt}}^2 = K_{\text{T}} \omega_{\text{opt}}^2, \quad (5)$$

where $K_{\text{T}} = \frac{0.5\rho r^3 A C_{\text{Pmax}}}{\lambda_{\text{opt}}^3}$.

The law on the formation of the reference mechanical torque $T_{\text{WT}}^* = K_{\text{T}} \omega^2$ by the mean of PMSG load is the most common for optimal sensorless control providing asymptotic movement of VAWT operating point to the MPP.

Maximum output power of VAWT is not a goal in contrast to the power of electricity at WECT output. That value depends also on the loss of a channel, power transformation, and transmission. Therefore, the goal of optimal control at the site of partial-power WT must be the maximum approaching power curve in static and dynamic modes (Fig. 5), which is applied in several studies [12, 13].

In the partial-load operating mode (control zone 2) WECT is an overwhelming amount of time, thus generating electricity from small power. The extremely high requirements to quality of control systems work, providing optimal control in order to obtain maximum power from the wind. Based on the analysis of scientific publications on this subject we identified the following classification criteria of optimal control systems for WECS with VAWT:

- (a) type of control—passive [14], active [15], active–passive [16];
- (b) availability of wind speed sensors—sensors and sensorless [11, 15];
- (c) availability of information about the performance of the components of WECS—VAWT (characteristic $C_{\text{P}}(\lambda)$, the point of maximum power $C_{\text{Pmax}}(\lambda_{\text{opt}})$, optimal TSR λ_{opt} , generator (the dependence of efficiency from power and angular velocity), whole WECS (power curve $P_{\text{WECS}}(V)$), without the need of any data [11, 15];
- (d) principle of automatic control—as to disturbance (optimal torque control—OTC) [11], as to deviation (TSR-control, optimal power control—OPC) [11], intelligent (fuzzy-logic control—FLC, artificial neural network—ANN) [17, 18], search control (perturbation and observation—P&O, hill-climb searching—HCS) [11, 19, 20];
- (e) mathematical description and corresponding methods of control—linearized [11], nonlinear (adaptive control [21], sliding mode control—SMC [22], feedback linearization control [23]), control based on energy approach (passive-based control—PBC, energy-shaping control—ESC) [24].

The task of automatic control of WECS operation in large wind speeds (zone 3 in Fig. 5) is to limit the electrical power output at rated value, especially for PMSG

that eliminates overheating. Limitations are also associated with acceptable mechanical loads on VAWT. In powerful HAWT for this purpose active pitch-control unfolding blades are used for their interaction with a smaller airflow [8]. In some low-power VAWT also, pitch-controlled blades or special additional plates that rise on high VAWT angular velocity are used and create additional aerodynamic resistance [18]. However, it significantly complicates WECS and reduces the reliability of its work in adverse weather conditions.

In WECS with SB-VAWT, we can achieve a similar effect by the special control system, which, through appropriate regulation of generator load speed and, respectively, VAWT angular velocity, shifts the operating point of VAWT so that it captured less power from wind flow. Herewith, there are two areas of regulation, which correspond to two flat parts of the curve $C_p(\lambda)$ (Fig. 2), which lie on opposite sides of λ_{opt} . If at increasing of wind speed the angular velocity of VAWT decreases, the λ decline, reducing the value of power coefficient CP. This is so-called passive stall regulation [25]. With appropriate work of control system, we can stabilize VAWT power by reducing its angular velocity and increasing mechanical torque. If at increasing of wind speed VAWT rotates at a much higher angular velocity so that it substantially exceeded λ_{opt} , it is also possible to stabilize power, but on the contrary—by reducing the mechanical torque of VAWT. This mode is called feathering regulation [25].

If we limit the power of research VAWT at the rated level $P_{WT,n} = 1145$ W, as shown in Fig. 4, that for this power get the dependences of VAWT torque from its angular velocity in the areas of stall regulation T_{n1} and feathering regulation T_{n2} (Fig. 3). As seen in the last, in the area of stall regulation the VAWT torque considerably increases, which should be provided in its design. According to the torque and the current of PMSG increase too that causes additional losses in the armature winding of the generator. In the area of feathering regulation, rather—the torque and the loss of copper in the generator decrease, but significantly increase the angular velocity of VAWT and generator, which also must be provided in the construction of WECS.

Unfortunately, passive stall and feathering regulation do not find proper coverage in special scientific literature. Automatic control mode that provides passive stall regulation of VAWT devoted some attention in papers [26, 27].

Control of small VAWT in the work [26] carried out by adjusting the DC voltage U_{DC} in the output of diode bridge, by which PMSG is loaded. In electrical power limiting mode, the fast PI controller comes into work. It reduces the reference on U_{DC} , which, in turn, is regulated in a closed system by varying the electrical load of PMSG using DC/DC converter. For reduction of dynamic loads on VAWT during the transition from zone 2 to zone 3 and vice versa, the authors used a small transition zone, where the voltage U_{DC} is maintained at its maximum level.

In work [27] automatic control in zone 3 is held in the open-loop system—if the current in the DC link in excess of the acceptable value, the reference on the optimal angular velocity of VAWT decreases.

Thus, the development of effective control systems for small WECS with VAWT at large winds are still not sufficiently solved the problem. As shown in

Figs. 3 and 4 in power limitation modes, especially in the stall regulation, the control object is characterized by significant nonlinearity. Therefore, for the automatic control of VAWT in these modes is topical application of modern control methods of nonlinear systems.

3 Creation and Research of Power Limitation Systems of WECS by Classical Methods

General computer model of WECS has been developed in Matlab/Simulink environment to conduct research by computer simulation. It consists of the following subsystems: wind flow speed (test and turbulent), high-speed passive VAWT with aerodynamic characteristic (3), PMSG from SimPowerSystem library, AR operation imitator, in which transistors working with PWM have been replaced by controllable voltage sources for the purpose of faster simulation, PMSG optimal load control system, which works in accordance with principle (5). VAWT and PMSG parameters have been presented in the Appendix.

3.1 Development of Control Systems for Stall Regulation

Transition of WT in stall regulation mode is carried out by increasing VAWT load torque using PMSG. However, as shown in Fig. 3, VAWT angular velocity will decrease and its mechanical torque will also increase at wind speeds that are slightly higher than the nominal value for WT. With further increase of wind speed, VAWT torque will reach a maximum and then will start to fall because the operating WT point will move to decreasing area of $T_{WT}(\omega)$ characteristic. The analysis shows that for a generator pre-set load torque this area of the characteristic is statically unstable for WT operation. Stability can be achieved only by the automatic control in closed ACS.

Research studies conducted by computer simulation have shown that for stabilizing the operating VAWT point at a pre-set stabilizing power characteristic $P_{WT,n}$ (Fig. 4), the latter in such static unstable and nonlinear ACS cannot automatically adjust with required speed for the electric power, measured at the output of PMSG. It is necessary to carry out directly automatic adjustment of VAWT mechanical power. As it appears impossible to be measured, its value should be calculated, and it is not accurate computation, but the speed of obtaining at least an approximate value of P_{WT} . It can be easily done by the help of measured values of wind speed V and the generator angular velocity ω according to the expressions (1) and (3). On the structural scheme of developed ACS for stall regulation (Fig. 6) it is done by power estimator (PE). Obtained current value of the VAWT power \hat{P}_{WT} at its output is compared with the nominal value $P_{WT,n}$. Their difference comes to power

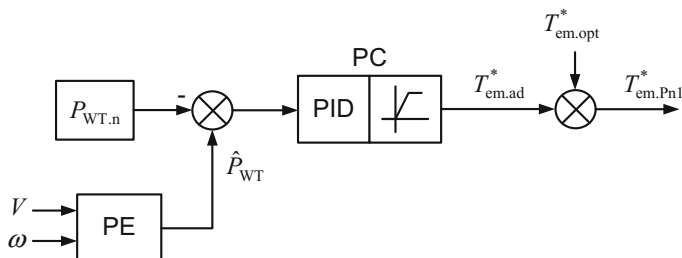


Fig. 6 Block diagram of the ACS, which provides passive stall regulation mode of VAWT

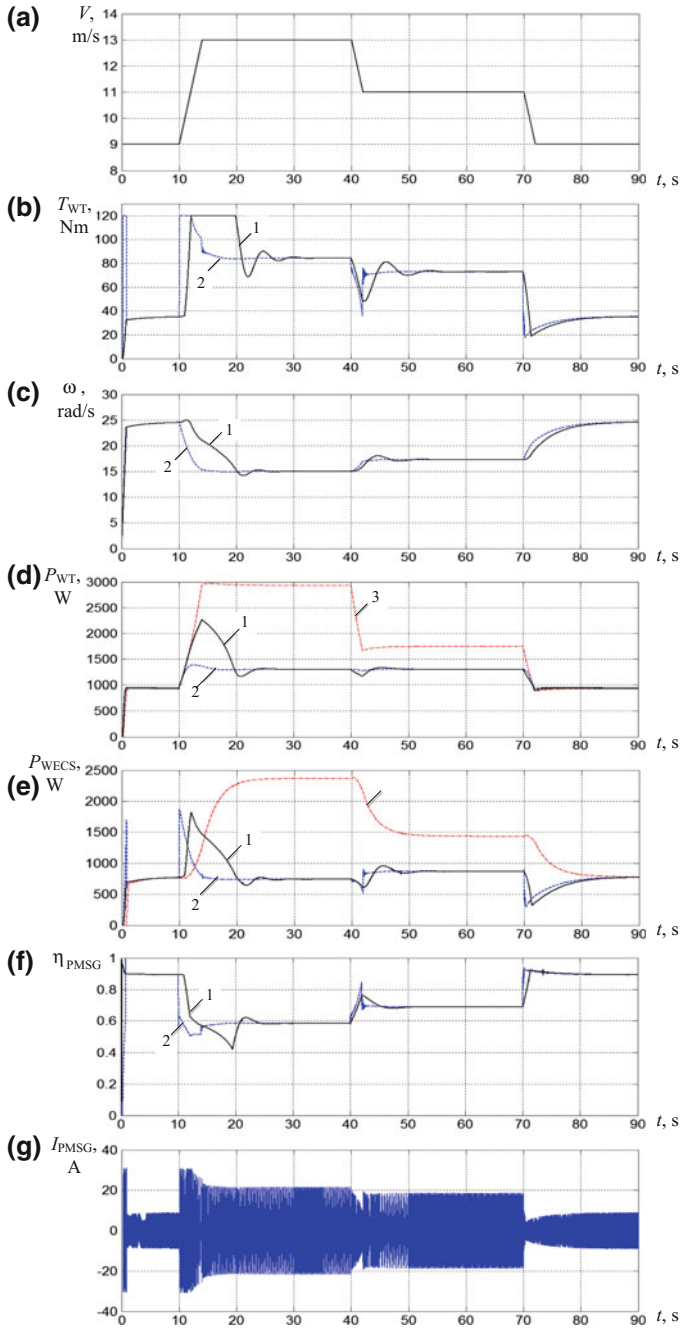
controller PC, which creates the reference for additional electromagnetic torque $T_{em.ad}^*$. It is added to the reference for electromagnetic torque $T_{em.opt}^*$ of PMSG formed by control system in case of partial-load of WECS.

Power limitation system works in the following way. In the partial-load mode of WECS $P_{WT} < P_{WT,n}$, that is why the output of the PC will be a negative signal, which is limited at 0. Therefore, the limitation system is not working. With increasing wind speed above nominal value there occurs condition $P_{WT} > P_{WT,n}$, which leads to the appearance of the reference $T_{em.ad}^*$ at the output of PC. It is added to $T_{em.opt}^*$, in resulting in forming a new reference $T_{em.Pn1}^*$ for electromagnetic torque, which will provide power limitation of VAWT on the nominal level with decreasing ω .

Mechanical power for simulations is limited at 1300 W. Power limitation system with PI and PID controllers has been researched. The best coefficients for these controllers as determined by computer simulation are as follows: PI controller— $k_p = 0.15$, $k_i = 0.10$; PID controller— $k_p = 0.75$, $k_i = 0.35$, $k_d = 1.10$.

Figure 7 shows the waveforms of computer simulation to illustrate the work of the power limitation system of VAWT by means of stall regulation. Test wind speed has been formed as follows (Fig. 7a): to 10 s $V = 9$ m/s, which is lower than the nominal, equal to 10 m/s, at 10 s wind speed is rapidly growing to 13 m/s, at 40 s it plummets to 11 m/s, and at 70 s goes back to 9 m/s. Thus, one can see the entry of WECS in power limitation mode and its exit from this mode. As a result of the formation of signal $T_{em.ad}^*$ at the PC output at high wind speeds there increases electromagnetic torque of PMSG (Fig. 7b) and the WT angular velocity decreases (Fig. 7c). This leads to the stabilization of VAWT mechanical power at a pre-set level of 1300 W (curves 1 and 2 in Fig. 7d), while in the case without limitation VAWT mechanical power increases significantly (curve 3 in Fig. 7d). Accordingly, the electric power at the output of WECS will also be limited at 750–850 W (curves

Fig. 7 Time dependencies of main coordinates of WECS, illustrating the entry and exit of it in power limitation mode by stall regulation: **a** test wind speed, **b** PMSG electromagnetic torque, **c** VAWT angular speed, **d** VAWT mechanical power, **f** electrical power at the output of WECS, **e** efficiency of PMSG, **g** linear armature current at phase of PMSG (1—PI controller, 2—PID controller, 3—without power limitation)



1 and 2 in Fig. 7e.), while without limitation it will increase to 2000 W (curve 3 in Fig. 7e). Decreasing the level of electrical power below the nominal one is due to the decrease in the efficiency of the generator η_{PMSG} (Fig. 7f) due to the growth of its electromagnetic torque and armature currents accordingly (Fig. 7g).

The obtained results of simulation have shown the different speed of regulation of power limitation systems of VAWT with PI and PID controllers. Unlike PI controller, PID controller enables the system to more quickly react to the increase in wind speeds above nominal value. This eliminates overshoot of VAWT mechanical power (Fig. 7d), due to the faster growth of PMSG electrical power (Fig. 7f), though. Thus, a system with PID controller has a less dynamic load on the mechanical part of WECS, and the system with the PI controller provides a less dynamic load on the electrical part. It is also possible to make settings of PID controller with compromising indices on mechanical and electrical parts of the WECS.

3.2 *Development of Control Systems for Feathering Regulation*

Transition of WT in feathering regulation operation mode is carried out by reducing the load torque of WT using PMSG. However, as shown in Fig. 2, the angular velocity of VAWT will be on the increase. Automatic control enables to easily stabilize VAWT mechanical power or output electrical power of WECS. Since the work of WT in this mode occurs on a stable area of its characteristics $T_{\text{WT}}(\omega)$, the possibility of automatic control is greatly enhanced compared to stall regulation.

The analysis shows that for reliable operation in strong wind it is essentially important to limit electrical power in PMSG output because it will not lead to its overheating and consequent failure. Mechanical overload in VAWT shaft can be permissible if they are projected in the construction of WECS. The same applies to the angular speed of both WT and the generator. Therefore, it is necessary to implement control system similar to stall regulation, with regulatory impact through electromagnetic torque of the generator in order to stabilize the output electrical power of WECS.

However, as confirmed by the research studies carried out by computer simulation, stabilization of the PMSG output power is difficult because of the unpredictable influence of electromagnetic torque: its increase is accomplished by increasing the armature current, resulting in lower output voltage because of losses in the windings. This can be accompanied by both increase and decrease in output power of the generator. To address this controversy, it has been decided to stabilize not the output power but electromagnetic power of PMSG instead, or the reference for this power, which is a bit easier.

All abovementioned solutions have been presented on the developed block diagram of the designed control system for feathering regulation (Fig. 8).

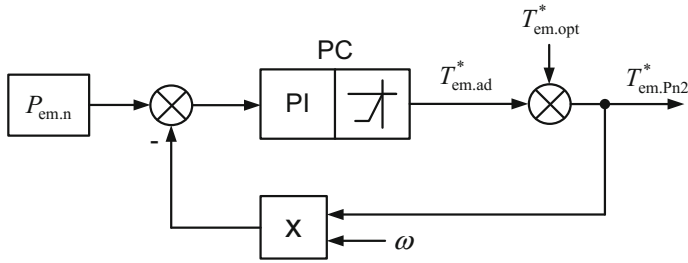


Fig. 8 Block diagram of the control system, which provides feathering regulation of VAWT

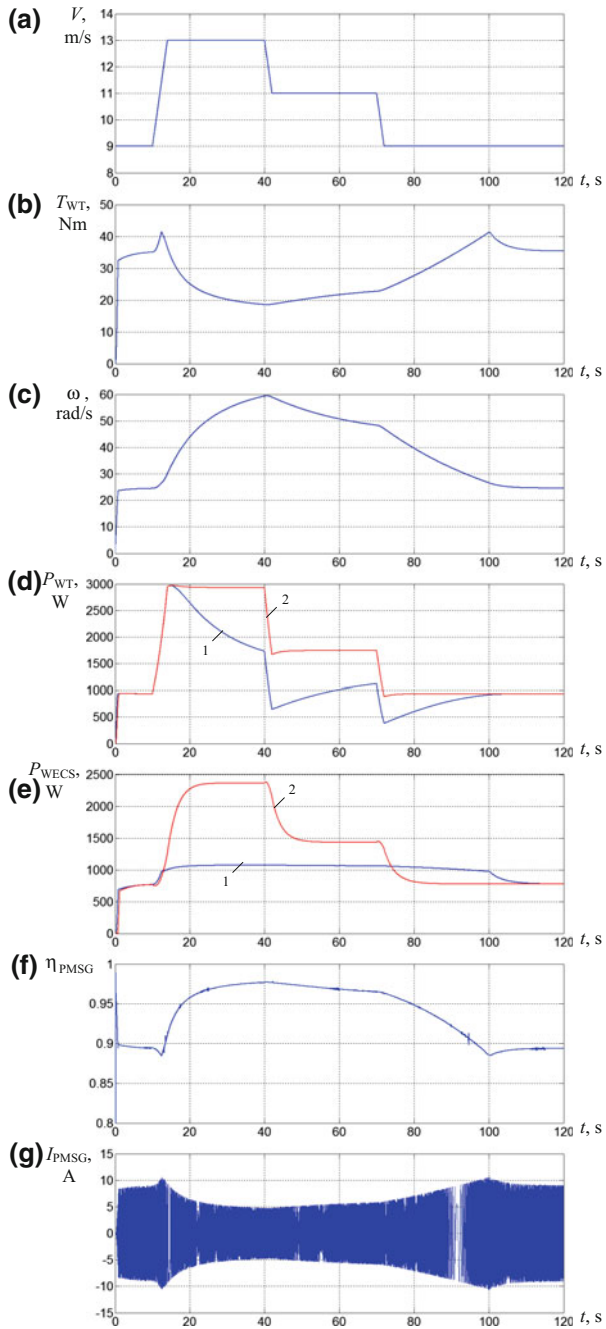
Power limitation system works in the following way. In the mode of partial-load of WECS electromagnetic power of wind turbine, P_{em} is lower than the nominal value $P_{em.n}$, because at the output of PC there will be zero signal provided by the limitation of PC. Thus, the power limitation system does not work. With increasing wind speed above nominal value there occurs condition $P_{em} > P_{em.n}$, which leads to the reference for additional negative electromagnetic torque $T_{em.ad}^*$, which reduces the value $T_{em.opt}^*$ at the output of the PC. It result in forming a new task for electromagnetic torque $T_{em.Pn2}^*$, which may provide limitation of the electromagnetic power of PMSG at nominal levels with increasing ω .

It is enough to use PI controller to limit pre-set electromagnetic power in this mode. $P_{em.n}$ is pre-set as the value of 1100 W, which provides electrical power limitation for WT at the level close to the nominal one. PI controller coefficients as determined by computer simulation are as follows: $k_p = 5.0$, $k_i = 2.0$.

Figure 9 shows the waveforms of computer simulation to illustrate the work of power limitation system of WECS by feathering regulation. Test wind speed (Fig. 9a) is the same as in the stall regulation. The output signal of the PC in power limitation modes provides the decrease of electromagnetic torque of PMSG (Fig. 9b) and the increase of VAWT angular velocity (Fig. 9c). This leads to the decrease in VAWT mechanical power (curve 1 in Fig. 9d) compared to the system without limiting power (curve 2 in Fig. 9d). Accordingly, the electric power at the output of WECS will be stabilized at 1050 W (curve 1 in Fig. 9e compared to curve 2 with no limitation). The efficiency of generator η_{CTPM} in this mode increases (Fig. 9f) because of its electromagnetic torque and armature current reduce, accordingly (Fig. 9g).

3.3 Comparative Analysis of VAWT Power Limitation Methods at High Wind Speed

The analysis of developed control systems structures and the results of simulation of WECS work on the test wind profile with the transition to high-speed wind and the return to slack wind have enabled to draw the following conclusions.



◀**Fig. 9** Time dependencies of main coordinates of WECS, illustrating the entry and exit of it in power limitation mode by feathering regulation: **a** test wind speed, **b** PMSG electromagnetic torque, **c** VAWT angular speed, **d** VAWT mechanical power, **f** electrical power at the output of WECS, **e** efficiency of PMSG, **g** linear armature current at phase of PMSG (*I*—with power limitation, 2—without power limitation)

1. Stall regulation is characterized by a high degree of nonlinearity of the object related to the maximum of characteristics $T_{WT}(\omega)$, thus the satisfactory operation of the control system can be achieved only by VAWT mechanical power control, the value of which has to be calculated online using the measured approximate value of wind speed.
Feathering regulation is characterized by significantly lower nonlinearity, which allows direct control of PMSG electromagnetic power and enables to build a simpler control system of this power.
2. The mechanical torque on the shaft of VAWT considerably increases in the stall regulation mode, but its angular velocity decreases, whereas in the feathering regulation mode, by contrast, mechanical torque decreases and the angular velocity increases. Therefore, implementation of such WECS power limitation modes requires different approaches to the design of mechanical parts of VAWT.
3. PMSG losses in copper are on the increase in the stall regulation mode as a result of a significant increase in electromagnetic torque, leading to a significant decrease in the efficiency of PMSG and, thus, electrical power at the output of WECS. By contrast, in feathering regulation mode losses in copper are reduced, although iron losses slightly increase because of increased frequency of electric move force, but they do not play a significant value in PMSG. This allows ensuring high value of generator efficiency in feathering regulation mode and to obtain more electric energy at the output of WECS in strong wind in comparison with the stall regulation.
4. Due to the direct control of PMSG electromagnetic power in feathering regulation mode its value can be stabilized at a pre-set nominal level regardless of changes in wind speed in the range of high speeds. Excess energy is going to accumulate as kinetic energy of the rotating parts of VAWT and PMSG, and then it will be eliminated by further nominal generator load. This provides much better smoothness of WECS generated electrical power in feathering regulation compared with the stall regulation.

The conducted analysis has shown a number of advantages of feathering regulation to limit the power of VAWT in high-speed wind operation. However, it eliminates one major drawback, i.e., a significant increase in VAWT angular velocity compared with the nominal one, which greatly complicates the design of VAWT and mechanical transmission and reduces the reliability of WECS. Therefore, further studies focus on improving stall regulation by applying new approaches to design ACS.

4 Fractional Order Control of Power Limitation of VAWT

4.1 *Intelligent Methods of Electromechanical Systems Synthesis with the Use of Fractional Order Controllers*

Nowadays it is evident that increasing the adequacy of traditional models, including electromechanical systems (EMS) units, is impossible by means of classical mathematics apparatus and approaches in integer order differential space. It is known that many physical phenomena, processes, and elements of EMS are described as dynamic systems by fractional order derivatives, i.e., they are characterized by fractality [28]. The perspective of applying fractional order derivatives (operators) and integrals in EMS is based on the following:

- the necessity to take into account peculiarities of fractality of EMS technological processes and elements in the creation of their models by using equations with fractional order derivatives or integrals;
- the advantages of fractional order controllers compared to classical ones in terms of robust control of fractal nature objects, as well as nonlinearity, multi-massive scale, backlash objects, etc.

A series of research studies has been devoted to the evaluation of fractality degree of natural phenomena that affect technological processes related to EMS functioning and their control objects in particular [29, 30]. Fractal phenomena include kinetic energy turbulence of air flows linked to wind fractal structure and changing temperatures of atmosphere layers [31], which is important for the WT operation. Their consideration has a significant impact on the “wind flow—wind wheel” model adequacy.

One way of solving the problem of dynamic stability and quality of power as generated by WT has been presented in [32]. Applied ACS implements the strategy of SMC using fractional order controllers in control loop by DC/DC converter. The system has significant advantages, viz. stability and robustness to parametric uncertainties of wind wheel and generator, as well as insensitivity to disturbances in the electrical network.

The synthesis results of various systems described by fractional order transfer functions (TF) have made it possible to obtain appropriate fractional order controllers. Reliable sources [33, 34] show much interest in fractional order PID controllers ($PI^{\nu}D^{\mu}$) with TF

$$W_R(s) = K_p + K_i s^{-\nu} + K_d s^{\mu}, \quad (6)$$

where K_p , K_i , K_d are the transfer coefficients under the proportional, integral and differential fractional components of the controller; ν and μ stand for fractional orders under integral and differential components of the controller.

The use of TF controller (6) is justified because its fractional integral and differential components provide more opportunities in the synthesis of ACS loops. Nevertheless, the search for $[K_p, K_i, K_d, \nu, \mu]$ vector to optimize synthesis results requires conducting the research in a 5-dimensional space. Thus, when using such controller structure it is necessary to set five parameters, i.e., two parameters more than in the case of conventional PID controller when $\nu = 1$ and $\mu = 1$. However, this extends the functionality of the controller in the process of optimizing EMS circuits compared to integer order controllers and therefore provides better flexibility in setting and quality of dynamic performance, which, accordingly, enables the solution to the problem of synthesis of EMS with more complex requirements, including robust synthesis.

EMS synthesis under the conditions of stability, quality, robustness, and insensitivity to disturbances with a certain frequency band requires a rational choice of fractional controller adjustment settings that allow taking into account the abovementioned conditions. The most effective approaches with the aim of finding optimal or suboptimal solutions to multi-dimensional purpose functions appear to be the intellectual methods, viz. Particle Swarm Optimization (PSO) and Genetic Algorithm (GA) as online methods which can be applied in the design of self-tuning systems.

For the purpose of parametric EMS optimization in the online mode an innovative approach has been offered which is based on the modification of two methods: the method of technological readjustment of closed systems [35], designed to detect required readjustment and calculate controller parameters by the reaction of closed EMS to pre-set disturbance, and the adaptive method with the use of EMS transition function [36]. The originality of the proposed approach lies in the application of the reference model of standard fractional order forms and intelligent methods. This method involves all kinds of transformations, including the ones with a preliminary definition of the model parameters as well as those with the direct transition from test transient process characteristics to optimal parameters adjustment. The required disturbance is introduced only into a closed system. The advantage of this approach can be obvious from the fact that it does not require to set EMS equipment in a special debug mode, which reduces its adjustment time.

The algorithm for selecting $PI^{\nu}D^{\mu}$ controller parameters to optimize a loop with a specific control object using PSO [37] and the transition function with the desired parameters is as follows.

1. The transition function with the desired parameters, pre-set time, sampling time and the number of calculation points is introduced into computer memory.
2. Five-dimensional swarm space (according to the number of varied controller parameters) for $PI^{\nu}D^{\mu}$ controller is built [37]).
3. At each iteration for each particle swarm element (the coordinate of controller parameters in 5-dimensional space) and its acquired parameters in the space motion, there is a transition function of the optimized loop which is compared

with the reference transition function in online mode. The particle whose parameters provide the lowest absolute standard deviation and lower than the previous iteration will be determined as the best one in this iteration, and its parameters will determine the trajectory of the other particles motion in the next iteration. The number of iterations can be set manually, or, alternatively, the procedure of iterative process termination can be introduced when the absolute standard deviation of the reference transition function from optimized loop transition functions is lower than the set one.

PI^νD^μ controller parameters search can be conducted with regard to the following typical transition functions points: time of the first achievement of 95% of transition default value t_{095} , the maximum deviation of the coordinate y_{\max} or overshoot σ , time of achieving maximum deviation of the coordinate t_{\max} . According to the abovementioned algorithm, comparison of transition function with the reference one occurs only in certain specific points of the transition process, viz. t_{095} , y_{\max} and t_{\max} .

4.2 Fractional Order Control of Stall Regulation of VAWT Power

The proposed method has enabled synthesis of control loop for WT power limitation in stall regulation mode, where instead of obtained (Sect. 3.1) PID controller

$$W_{PC}(s) = 0.75 + 0.35s^{-1} + 1.1s^1 \quad (7)$$

fractional order PI^νD^μ controller has been applied.

PI^νD^μ controller has been synthesized by the above-proposed approach by means of using specific points of fractional order transition function for $\omega_{oc} = 2 \text{ c}^{-1}$: $t_{095} = 1.1 \text{ s}$, $\sigma = 7.32\%$, $t_{\max} = 2.8 \text{ s}$. The criterion for the completion of the synthesis is the achievement of the desired quality of the transition process with a pre-set standard deviation from the pre-set points of standard transition function. The optimization has resulted in obtaining fractional order controller with the following TF:

$$W_{PC}(s) = 0.2 + 0.2s^{-0.9} + 1.0s^{0.5}. \quad (8)$$

Figure 10 shows basic waveforms of test wind speed reproduction with WT, similar to test wind speed shown in Fig. 7. Transition processes by means of using classical PID controller have been also displayed (7) for the purpose of comparison. It can be seen from the obtained results that the use of fractional order PI^νD^μ controller (8) makes it possible to slightly accelerate transition processes of entering WT power limitation mode and virtually eliminate their oscillation, which will have a positive impact on WT operation.

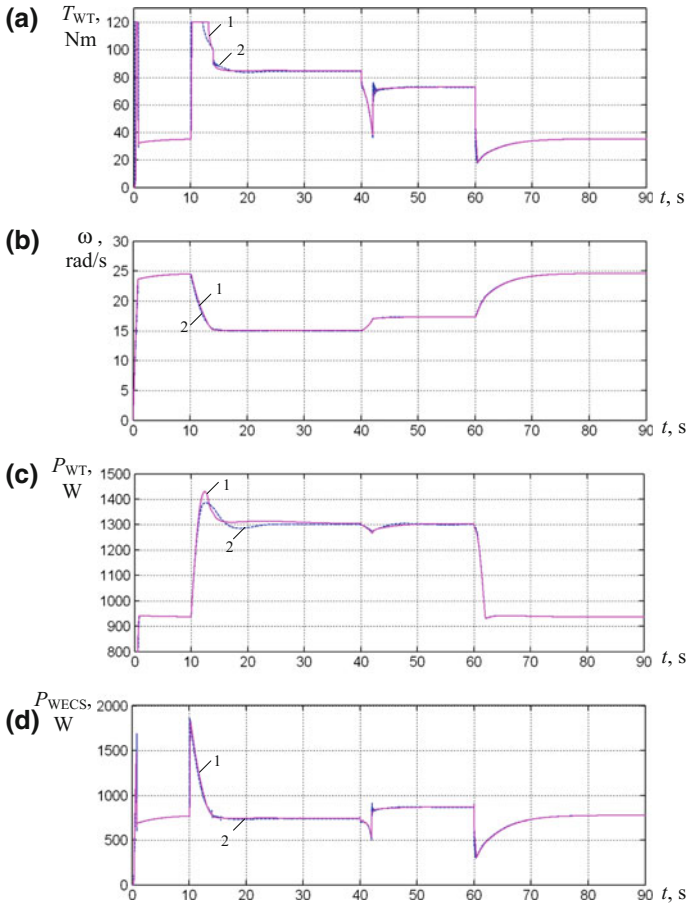


Fig. 10 Comparison of computer simulation results illustrating input and output of wind turbines in power limitation mode by stall regulation using conventional PID controller (curves 2) and fractional order $PI^\lambda D^\mu$ controller (curves 1): **a** PMSG electromagnetic torque, **b** VAWT angular velocity, **c** VAWT mechanical power, **d** output electrical power of WECS

5 Power Limitation of VAWT by Passive Stall Control in Energy-Shaping Control System (ESCS)

5.1 Energy-Shaping Control

Among the most promising methods of ACS synthesis of complex objects are those based on energy approaches [38], which allow design ESCS. Such energy-shaping control consists in the ACS assuring the passivity of the whole system. This allows

operating in the desired equilibrium point \mathbf{x}_0 since passivity itself provides oscillation damping in the system and its stable operation in the selected point [38].

In general, ESCS synthesis procedure consists in decomposing a system into simpler subsystems interlinked in some way [39], and finding such additional subsystems and interconnections that the total energy of the closed-loop system would attain a minimum in the equilibrium point \mathbf{x}_0 [40]. This equilibrium point is the control aim and is defined by the reference signal. In ESCS synthesis procedure both control object and ACS can be represented as an Euler–Lagrange system (ELs) [38] or the port-controlled Hamiltonian system (PCHs) [40]. System representation as PCHs makes it possible to consider the physical structure of the control object, which, in turn, greatly simplifies the part-differential equations to which the synthesis procedure is reduced; it also allows to simplify and make more transparent the stability analysis. PCHs model is as follows [40]:

$$\begin{cases} \dot{\mathbf{x}}(t) = [\mathbf{J}(\mathbf{x}) - \mathbf{R}(\mathbf{x})] \frac{\partial H}{\partial \mathbf{x}} + \mathbf{G}(\mathbf{x}) \cdot \mathbf{u}(t) \\ \mathbf{y}(t) = \mathbf{G}^T(\mathbf{x}) \frac{\partial H}{\partial \mathbf{x}} \end{cases}, \quad (9)$$

where $\mathbf{x}(t)$ is the state vector of the controlled system (the object), $\mathbf{J}(\mathbf{x}) = -\mathbf{J}^T(\mathbf{x})$ is a skew-symmetric matrix which reflects the interconnection structure of the system, $\mathbf{R}(\mathbf{x}) = \mathbf{R}^T(\mathbf{x}) \geq 0$ is a symmetric positive semi-definite matrix which reflects the dissipation in the system, $H(\mathbf{x}) = 0.5 \mathbf{x}^T \mathbf{D}^{-1} \mathbf{x}$ is the energy function of the controlled system, \mathbf{D} is the diagonal matrix of inertias, $\mathbf{G}(\mathbf{x})$ is the port matrix, and $\mathbf{u}(t)$ and $\mathbf{y}(t)$ are vectors of input and output system energy variables.

According to [41], ESCS synthesis procedure is reduced to the writing of the mathematical model of the object in the PCHs form (9), the selection of a matrix of the control system ($\mathbf{J}_a(\mathbf{x})$ and $\mathbf{R}_a(\mathbf{x})$) and, thanks to the energy-shaping principles, interconnection and damping assignment, to the solving of the following matrix equation:

$$\begin{aligned} & [\mathbf{J}(\mathbf{x}) + \mathbf{J}_a(\mathbf{x}) - (\mathbf{R}(\mathbf{x}) + \mathbf{R}_a(\mathbf{x}))] \frac{\partial(H_d - H)}{\partial \mathbf{x}} \\ & = [\mathbf{J}_a(\mathbf{x}) - \mathbf{R}_a(\mathbf{x})] \frac{\partial H}{\partial \mathbf{x}} + \mathbf{G}(\mathbf{x}) \cdot \mathbf{b}(\mathbf{x}) \end{aligned}, \quad (10)$$

where H_d is the desired energy function, which attain a minimum in the equilibrium point x_0 , and $\mathbf{b}(\mathbf{x}) = \mathbf{u}$ is the vector of input system energy variables, formed through feedback.

The results of synthesis are the elements of regulator matrix $\mathbf{J}_a(\mathbf{x})$ that were found and the final equations of ESCS regulators [41–43]. However, during synthesis some elements of regulator matrices ($\mathbf{J}_a(\mathbf{x})$ and $\mathbf{R}_a(\mathbf{x})$) could be “free” [41–43], they are intended for ACS setting up and can be selected manually or calculated with parametrical synthesis procedure.

5.2 ESCS of WECS with VAWT

There already exist several variants of ACS of WECS, based on energy-shaping [24, 44–46]. In most cases, during the synthesis of ESCS of WECS authors consider the control object in simplified form—as a mechanical system. This approach is caused by the fact that electromagnetic time constants are much smaller than the mechanical ones, and that is why at mechanical systems ACS synthesis the inertia of the current circuit is usually not taken into account. However, in the WECS case, the current loop effect is quite important, as it should also provide a minimization of losses in the generator—in order to produce maximum WECS output power. That is why it's important to synthesize ESCS of WECS while taking into account electromagnetic part (Generator—Power converter—Load or Grid) [24]. Proposed in literature ESCS of WECS are synthesized for optimal power extraction mode and require additional adaptation for power limitation mode.

We synthesized ESCS of WECS while taking into account electromagnetic part (PMSG and power converter). PMSG is described in rotation coordinates d - q [47]. ESCS regulators, obtained by the described above approach, are as follows [24]:

$$\begin{cases} u_{dc}\mu_d^* = -k(i_q - i_{q0}) + R_s i_{d0} - pL_d i_{q0}(\omega - \omega_0) \\ \quad - pL_q i_q \omega_0 \\ u_{dc}\mu_q^* = k(i_d - i_{d0}) + R_s i_{q0} + pL_q i_{d0}(\omega - \omega_0) \\ \quad + p(\Phi + L_d i_d)\omega_0 \\ T_{em}^* = T_{WT} - r_3(\omega - \omega_0) \end{cases}, \quad (11)$$

where u_{dc} is a constant voltage in DC output circuit of power converter, μ_d^* and μ_q^* are the reference duty ratio functions in d - q frame, r_3 is the damping coefficients, which express mechanical damping of the control system, k is the decoupling coefficient, which compensates the cross-links between d -axes and q -axes voltage control channels, i_d and i_q are d -axes and q -axes projections of the stator current vector, respectively, i_{d0} and i_{q0} are, respectively, d -axes and q -axes reference signals of the projections of current vector, L_d and L_q are d -axes and q -axes stator inductances, respectively, R_s is the stator resistance per phase, p is the number of rotor pole pairs, Φ is the rotor flux linkage, ω_0 is the reference VAWT speed, T_{em}^* is the signal of reference torque and TWT is the VAWT torque.

By correcting procedure of reference values forming [24] the expressions of new WECS of PMSG load without a wind speed sensor can be obtained:

$$\begin{cases} u_{dc}\mu_d^* = -r_1(i_d - i_{d0}) - k(i_q - i_{q0}) + R_s i_{d0} \\ \quad - pL_d i_{q0}(\omega_z - \omega_0) - pL_q i_q \omega_0 \\ u_{dc}\mu_q^* = -r_2(i_q - i_{q0}) + k(i_d - i_{d0}) + R_s i_{q0} \\ \quad + pL_q i_{d0}(\omega_z - \omega_0) + p(\Phi + L_d i_d)\omega_0 \\ T_{em}^* = T_{WT} - r_3(\omega_z - \omega_0) \end{cases}, \quad (12)$$

where ω_z is the angular speed signal with delay.

In the obtained ACS (12) $\omega_z = \omega / (T_w s + 1)$, where $T_w = 0.1$ s is the time constant of TF in the feedback speed loop. The reference speed equals to current speed of WT $\omega_0 = \omega$. The reference current signal i_{q0} is known from the electromagnetic torque equation: $i_{q0} = 2 / (3p) \cdot T_{em}^* / [(L_d - L_q) i_{d0} + \Phi]$, and the T_{WT} can be found like in OTC system [11] – $T_{WT} = K_T \omega^2$.

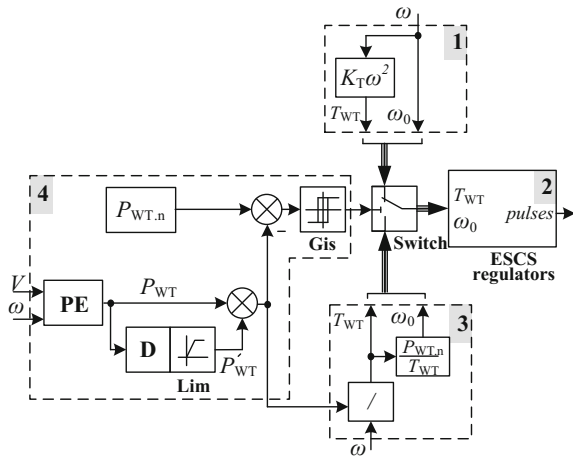
According to [24], ESCS with regulators (12) provides high static and dynamic performance of WECS without wind speed sensor, and also ensure the WECS operation in optimal response mode, which is meant to combine mechanical wind energy extraction by VAWT and electric energy losses in PMSG in such a way that the maximum of WECS output energy is obtained [24]. Such ESCS improves the WECS energy extraction, compared with the OTC, by 0.6–10% for different winds, WECS constructions, and ESCS settings. The maximum improvement of efficiency is ensured at turbulent winds with small average speed.

5.3 Power Limitation in ESCS

ESCS with regulators (12) are synthesized for optimal power extraction mode at partial-loading of WECS. In order to adapt it to operation in power limitation mode on high winds, we offer, depending on the operating mode, to change procedure of formation of the reference signal, in particular—speed ω_0 and torque T_{WT} .

Structural schema of adapted ESCS of WECS, with implemented possibility of stall regulation, is shown in Fig. 11. The system consists of four functional blocks.

Fig. 11 ESCS of WECS adapted for power limitation mode



Block 1 forms reference signals by described in Sect. 5.2 method, and will take effect in optimal power extraction mode. Block 2 represents ESCS regulators (12). Block 3 forms objective signals in power limitation mode. Block 4 implements the logic function, which is responsible for switching between optimal power extraction and power limitation modes.

Proposed adapted ESCS works as follows. In Block 4 power estimator PE, based on wind speed V and angular speed ω signals, calculates the current value of mechanical power. This value is compared to $P_{WT,n}$. The resulting difference ($P_{WT,n} - P_{WT}$) goes to hysteresis function G_{is} , which forms output «0» when $P_{WT} > 0.95 P_{WT,n}$, and «1» when $P_{WT} < P_{WT,n}$ (hysteresis is introduced to avoid frequent switching in case $P_{WT} \sim P_{WT,n}$). Output signal of G_{is} controls switcher Switch, which conduct ESCS connection of reference signal former from Block 1 or Block 3.

In order to implement proactive control, similar to PID controller, in Block 4 a differential component D is introduced. It performs proactive control that reduces overshoot of mechanical power P_{WT} . This allows you to consider not only the current value of the mechanical power P_{WT} while controlling, but the dynamics of its change P'_{WT} as well. Then switching between modes will be based on the comparison result of $P_{WT,n} > P_{WT} + P'_{WT}$. Time constant of differential link is 0.1 s, and the value of the differential part P'_{WT} is limited on $(0...0.25) P_{WT,n}$.

If $P_{WT} + P'_{WT} > P_{WT,n}$, then ESCS switches to power limitation mode, and reference signals begin to form from Block 3. Based on the estimated value of mechanical power $P_{WT} + P'_{WT}$ and angular speed ω the new value of the mechanical moment $T_{WT} = P_{WT}/\omega$ is calculated and then goes to ESCS regulators as a reference signal of PMSM electromagnetic torque. The presence of the mechanical power differential part P'_{WT} in calculating of the reference torque signal accelerates system response to disturbances (an increase of wind speed V). Based on the calculated signal T_{WT} and the desired nominal mechanical power $P_{WT,n}$ desired reference speed signal $\omega_0 = P_{WT,n}/T_{WT}$ is being calculated. Such signals formation provides automatic movement of the system to the point of acceptable power extraction $P_{WT,n}$.

The comparative studies of the proposed adapted ESCS and OTC with stall regulation on PID power controller designed in Sect. 3.1 were conducted on the same test wind profile with the following ESCS settings: $k = -100$, $r_3 = 100$.

The research results (Fig. 12) show a slight increase in mechanical power overshoot for ESCS compared to OTC, but smaller transition process time and absence of oscillation, similar to the results obtained in Sect. 4.2 with the fractional order PID controller.

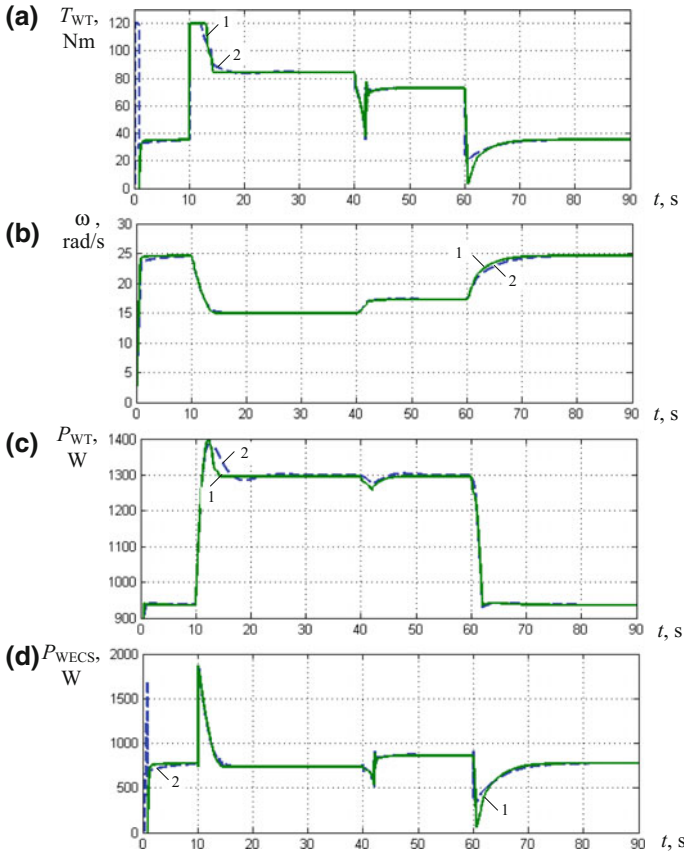


Fig. 12 Time dependencies of WECS operation with classical ACS (curve 2) and ESCS (curve 1): **a** PMSG electromagnetic torque, **b** VAWT angular velocity, **c** VAWT mechanical power, **d** electric power of WECS

6 Research of Developed System of VAWT Power Limitations in Turbulent Wind

To assess the effectiveness of the developed system of VAWT power limitation was held computer simulation research of WECS work at the wind with speeds close to real. For this used a computer model of turbulent wind, built on the Kaimal mathematical model [48]. The profile of average wind speed is set such that the instantaneous wind speed in certain intervals exceeds the rated value for research WECS of 10 m/s (Fig. 13a). The two control system's work was compared: the OTC with unlimited power and the OTS with power limitation through passive stall regulation with PID power controller. In the latter, an intermediate regarding the speed of regulation setting of power controller was applied—about halfway between PI and PID controllers studied in Sect. 3.1. To do this, the following coefficients of PID controller were applied: $-k_p = 0.35$, $k_i = 0.20$, $k_d = 0.30$.

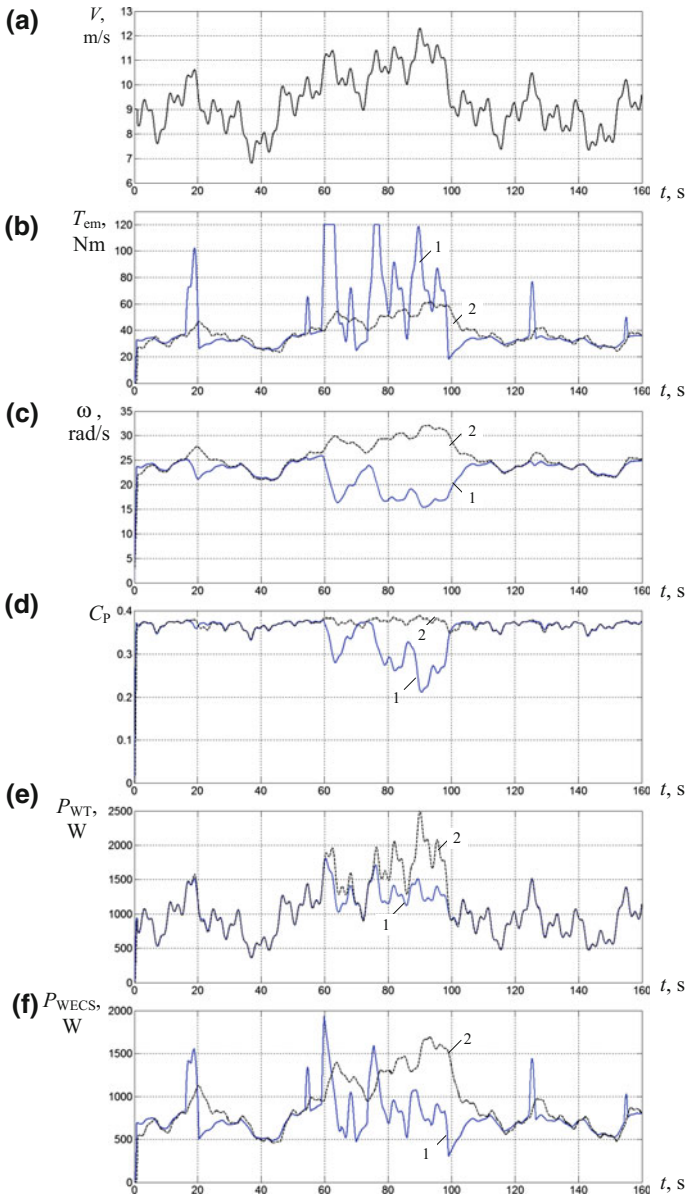


Fig. 13 Waveforms of main coordinates of WECS with different control systems at its work in turbulent wind: **a** wind speed, **b** PMSG electromagnetic torque, **c** VAWT angular velocity, **d** power coefficient, **e** VAWT mechanical power, **f** output electrical power of WECS (1—OTC with power limitation, 2—OTC without power limitation)

The results of the simulation are shown in Fig. 13a–f. They demonstrate the effectiveness of developed control system of mechanical power limitation. In the intervals when the wind speed exceeds the nominal value—59...98 s (Fig. 13a), due to the formation of the maximum values of PMSG electromagnetic torque (Fig. 13b), VAWT angular velocity decreases (Fig. 13c). This leads to lowering of power coefficient C_p (Fig. 13d), in resulting the mechanical power of VAWT has reduced (Fig. 13e)—carried out a stall regulation. Average output electrical power of WECS also has reduced (Fig. 13f)—made its overload protection.

7 Conclusion

This article reports the results of a study by computer simulation of the work of WECS with SB-VAWT at the wind speeds greater than nominal in operating modes of power limitation by the passive stall and feathering regulation. To ensure the reliability of the mechanical parts of VAWT, preference is given to stall regulation, which is characterized by the nonlinearity of the control object. The article demonstrates different approaches to the development of the control system of power limitation modes: the use of classical PI and PID power controllers, PID controller of fractional order and the implementation of additional structures for ESCS. All developed control systems showed the effective limit of VAWT power during its work in turbulent winds at different speeds. The obtained results make it possible to choose an effective implementation of the control system of power limitation for various VAWT designs.

Appendix

(a) Parameters of the VAWT

WECS	VAWT					
$P_{WECS,n}$ (kW)	$P_{WT,n}$ (kW)	A (m ²)	r (m)	ω_n (rad/s)	$T_{WT,n}$ (N m)	J_Σ (kg m ²)
1.0	1.214	5.29	1.4	26.8	45.3	19.0

(b) Parameters of the PMSG

PMSG			
p	Φ , Wb	R , Ω	$L_d = L_q$, H
20	0.13	0.75	0.004

References

1. Harrison, R., Hau, E., Snel, H.: *Large Wind Turbines: Design and Economics*. Wiley, Chichester (2000)
2. Simic, Z., Havelka, J., Vrhovcak, M.: Small wind turbines—a unique segment of the wind power market. *Renew. Energy* **50**, 1027–1036 (2014)
3. Klymko, V.I.: *Wind-solar systems for power supply of low power consumers* (in Ukrainian). Ph.D. thesis, Lviv (2016)
4. Akello, P., Ochieng, F., Kamau, J.: Performance analysis of a direct drive permanent magnet generator for small wind energy applications. *J. Sustain. Res. Eng.* **1**(3), 1–9 (2014)
5. Bhutta, M., Hayat, N., Farooq, A., Ali, Z., Jamil, S., Hussain, Z.: Vertical axis wind turbine—a review of various configurations and design techniques. *Renew. Sustain. Energy Rev.* **16**, 1926–1939 (2012)
6. NACA profile coordinates—Airfoil tools. <http://airfoiltools.com/airfoil/details?airfoil>
7. Shchur, I.: Estimation of electromagnetic compatibility and efficiency of the adjustable load systems of PMSG in wind turbines. *Przegląd Elektrotechniczny* **1**, 85–90 (2011)
8. Stiebler, M.: *Wind Energy Systems for Electric Power Generation*. Springer, London (2008)
9. Alaimo, A., Esposito, A., Messineo, A., Orlando, C., Tumino, D.: 3D CFD analysis of a vertical axis wind turbine. *Energies* **8**, 3013–3033 (2015)
10. Tian-Pau, C., Feng-Jiao, L., Hong-His, K., Shih-Ping, C., Li-Chung, S., Shye-Chorng, K.: Comparative analysis on power curve models of wind turbine generator in estimating capacity factor. *Energy* **73**, 88–95 (2014)
11. Abdullah, M., Yatim, A., Tan, C., Saidur, R.: A review of maximum power point tracking algorithms for wind energy systems. *Renew. Sustain. Energy Rev.* **16**, 3220–3227 (2012)
12. Marimoto, S., Nakayama, H., Sanada, M.: Sensorless output maximization control for variable-speed wind generation system using IPMSG. *IEEE Trans. Ind. Electron.* **41**(1), 60–67 (2005)
13. Anders, G., Fredrik, B.: Robust VAWT control system evaluation by coupled aerodynamic and electrical simulations. *Renew. Energy* **59**, 193–201 (2013)
14. Sareni, B., Abdelli, A., Roboam, X., Tran, D.: Model simplification and optimization of a passive wind turbine generator. *Renew. Energy* **34**, 2640–2650 (2009)
15. Ming, C., Ying, Z.: The state of the art of wind energy conversion systems and technologies. *Energy Convers. Manag.* **88**, 332–347 (2014)
16. Shchur, I., Rusek, A., Klymko, V., Gastolek, A., Sosnowski, J.: Analysis of methods of electrical load of permanent magnet synchronous generator for small wind turbines. *Maszyny Elektryczne, Zeszyty Problemowe* **105**(1), 75–81 (2015)
17. Wang, Q., Chang, L.: An intelligent maximum power extraction algorithm for inverter-based variable speed wind turbine systems. *IEEE Trans. Power Electron.* **19**(5), 1242–1249 (2006)
18. Whei-Min, L., Chih-Ming, H.: Intelligent approach to maximum power point tracking control strategy for variable-speed wind turbine generation system. *Energy* **35**, 2440–2447 (2010)
19. Ying-Yi, H., Shiue-Der, L., Ching-Sheng, C.: MPPT for PM wind generator using gradient approximation. *Energy Convers. Manag.* **50**, 82–89 (2009)
20. Eftichios, K., Kostas, K.: Design of a maximum power tracking system for wind-energy-conversion applications. *IEEE Trans. Ind. Electron.* **2**, 486–494 (2006)
21. Iigo, K., Jon, A., Iigo, M., Jaime, J., Jos, I., Eider, R.: A novel adaptative maximum power point tracking algorithm for small wind turbines. *Renew. Energy* **63**, 785–796 (2014)
22. Brice, B., Tarek, A., Mohamed, E.: Sliding mode power control of variable-speed wind energy conversion systems. *IEEE Trans. Energy Convers.* **23**(2), 551–558 (2008)
23. Changliang, X., Qiang, G., Xin, G., Tingna, S., Zhanfeng, S.: Input–output feedback linearization and speed control of a surface permanent-magnet synchronous wind generator with the boost-chopper converter. *IEEE Trans. Ind. Electron.* **59**(9), 967–974 (2012)

24. Shchur, I., Rusek, A., Biletskyi, Y.: Energy-shaping optimal load control of PMSG in a stand-alone wind turbine as a port-controlled Hamiltonian system. *Przegląd Elektrotechniczny* **5**, 50–55 (2014)
25. Muteanu, I., Bratcu, A., Cutululis, N., Ceangă, E.: *Optimal Control of Wind Energy Systems*. Springer, London (2008)
26. Serban, I., Marinescu, C.: A sensorless control method for variable-speed small wind turbines. *Renew. Energy* **43**, 256–266 (2012)
27. Andriollo, M., De Bortoli, M., Martinelli, G., Morini, A., Tortella, A.: Control strategies for a VAWT driven PM synchronous generator. *Int. Symp. Power Electron. Electrical Drives Autom. Motion SPEEDAM* **2008**, 804–809 (2008)
28. Potspov, A.A., Chernykh, V.A.: Fractional calculation of A. Letnikova, fractal and scaling theory (in Russian). *Phizmatlit*, Moscow (2010)
29. Schafer, I., Kruger, K.: Modelling of lossy coils using fractional derivatives. *J. Phys. D Appl. Phys.* **41**, 1–8 (2008)
30. Freeborn, T., Maundy, B., Elwakil, A.: Fractional-order models of supercapacitors, batteries and fuel cells. *Mater. Renew. Sustain. Energy* **4**, 1–7 (2015)
31. Tijera, M., Maqueda, G., Yague, C., Cano, J.: Analysis of fractal dimension of the wind speed and its relationships with turbulent and stability parameters. In: Ouadfeul, S.-A. (eds.) *Fractal Analysis and Chaos in Geosciences* (2012). <http://cdn.intechopen.com/pdfs/40877/InTech->
32. Vaikundaselvan, B.: Dynamic model of wind energy conversion systems with fractional order controllers for the variable-speed operation of wind turbine. *Int. J. Eng. Sci. Adv. Technol.* **2** (4), 1115–1121 (2012)
33. Asrom, K., Hagglund, T.: The future of PID control. *Control Eng. Pract.* **9**, 1163–1175 (2001)
34. Chen, Y., Moore, K.: Help working with abstracts relay feedback tuning of robust PID controllers with iso-damping property. *IEEE Trans. Syst Man Cybernet. Part B (Cybernetics)* **35**(1), 23–31 (2005)
35. Burceva, Y.S.: No searching method for calculating of controller settings on minimum quadratic criterion (in Russian). Ph.D. thesis, Moscow (2014)
36. Rotach, V.Y.: *Automatic Control Theory*. MEI, Moscow (2004). (in Russian)
37. Kopchak, B.L.: Approximation transition functions of fractional order polynomials (in Ukrainian). In: Odessa National Polytechnic University, Scientific and technical journal “*Elektrotekhichni ta komputerni systemy*” **14**, 20–27 (2014)
38. Ortega, R., van der Schaft, A., Mareels, I., Maschke, B.: Putting energy back in control. *IEEE Control Syst. Mag.* **21**(2), 18–33 (2001)
39. Ortega, R., van der Schaft, A., Escobar, G., Maschke, B.: Interconnection and damping assignment passivity-based control of port-controlled Hamiltonian systems. *Automatica* **38**, 585–596 (2002)
40. Ortega, R., van der Schaft, A., Castanos, F., Astolfi, A.: Control by interconnection and standard passivity-based control of port-Hamiltonian systems. *IEEE Trans. Autom. Control* **53**(11), 2527–2542 (2008)
41. Zou, Z., Yu, H., Tang, Y.: Maximum output power of PMSM based on energy-shaping and PWM control principle. In: *IEEE International Conference on Automation and Logistics*, Qingdao, China, pp. 1556–1560 (2008)
42. Li, J., Liu, Y., Wu, H., Chu, B.: Passivity-based robust control of permanent magnet synchronous motors. *J. Comput. Inf. Syst.* **12**(9), 4965–4972 (2013)
43. Tang, Y., Yu, H., Zou, Z.: Hamiltonian modeling and energy-shaping control of three-phase AC/DC voltage-source converters. In: *IEEE International Conference on Automation and Logistics*, Qingdao, China, pp. 591–595 (2008)
44. De Battista, H., Mantz, R., Christiansen, C.: Energy-based approach to the output feedback control of wind energy systems. *Int. J. Control* **76**(3), 299–308 (2003)
45. Wang, C., Zhou, J.: Hamiltonian control stabilization for grid-side converters in doubly-fed wind turbines. In: *Chinese Automation Congress*, Wuhan, China, pp. 1252–1257 (2015)

46. Pahlevani, M., Pan, S., Mash, J., Jain, P.: Port-Controlled Hamiltonian (PCH)-based control approach for wind energy conversion systems. In: IEEE 5th International Symposium on Power Electronics for Distributed Generation Systems, Wuhan, Galway, pp. 1–5 (2014)
47. Bose, B., Eisenhut, C., Krug, F.: Modern Power Electronics and AC Drives. Prentice-Hall, Upper Saddle River (2002)
48. Eisenhut, C., Krug, F.: Wind-turbine model for system simulations near cut-in wind speed. IEEE Trans. Energy Convers. **22**(2), 414–420 (2007)

Multithreading Analysis of Properties and Electromagnetic Interference in Inductive Contactless Power Supply System with Bidirectional Energy Flow— Part 1: Topology System for Electric Vehicles

R.M. Miśkiewicz, A.J. Moradewicz, P. Chudzik and D. Stando

Abstract Inductive Contactless Energy Transfer systems (ICET) are becoming commonplace in electrical and electronics equipment. Increased growth of interest in electric vehicles (EV) and renewable energy sources, significantly changed the approach to vehicle. EV battery pack is no longer just a vehicle for the drive tank, but it is also a distributed storage for energy from the power grid. To ensure the automation of the flow of energy best fits is inductive contactless power supply system with bidirectional energy flow. These systems are based on inductively coupled resonant circuits and offer many properties that affect the high-efficiency energy transfer. The paper presents selection and simulation studies ICET system in use for EV with power $P = 100$ kW.

Keywords Contactless charging · Air transformer · Electric vehicles

1 Introduction

Inductive Contactless Energy Transfer systems (ICET), are becoming an everyday reality in electrical and consumer electronics. A wide range of applications and transmitted power in many areas by medicine to the vehicles and transport

R.M. Miśkiewicz (✉) · A.J. Moradewicz · P. Chudzik · D. Stando
Department of Electrical Drivers, Electrotechnical Institute, Warsaw, Poland
e-mail: r.miskiewicz@iel.waw.pl

A.J. Moradewicz
e-mail: a.moradewicz@iel.waw.pl

P. Chudzik
e-mail: p.chudzik@iel.waw.pl

D. Stando
e-mail: d.stando@iel.waw.pl

equipment [1, 3], causes the design of the system is selected for a particular application. One of the concepts of applying the ICET system is battery chargers for electric vehicles (EV). The idea of a fully automated battery charging is one of the important technical problems since the resumption of work on the vehicles EV. The current trend in European countries, promoting EV and renewable energy from the renewable energy sources has created a new concept of contactless power supply system. Assuming that the battery EV during his stopover can provide energy storage for the power grid, and the energy produced from RES is unevenly over time, then these batteries can become distributed storage for energy extracted from RES.

For this application perfectly fit ICET systems with bidirectional energy flow.

The most important advantage of this system is to automate the process flow of energy charge and return it to the grid. Block diagram of the inductive contactless energy transfer system with bidirectional energy flow is shown in Fig. 1.

The ICET system consists of two main parts: the stationary-located at the charging station and the mobile part associated with energy receiver. The main elements of the stationary part are the primary winding of the transformer, the compensation circuit elements, and the inverter responsible for the power system or to enable the return of energy to the grid. The work of the components of the system controls the master controller responsible for the maintenance and billing functions with the operator of the electricity system. The movable part, similar to the stationary, comprises a secondary coil system, the compensation circuit elements, and converters. The main task of controllers of lower and higher levels is to ensure optimal charging process or the return energy to the grid and maintain the longest possible battery life. In the process control ICET system with bidirectional energy transfer, the information about currents, voltages and the direction of energy flow are exchanged between drivers using wireless communication modules, Bluetooth or others. The CET systems based on inductive coupling require selection of multiple elements, such as construction of a transformer, resonant compensating circuits, and power supply converter, etc. The article presents the genesis of contactless energy transfer systems, selection, and description of the properties the transformer circuit with a resonant compensation circuit in the application for EV.

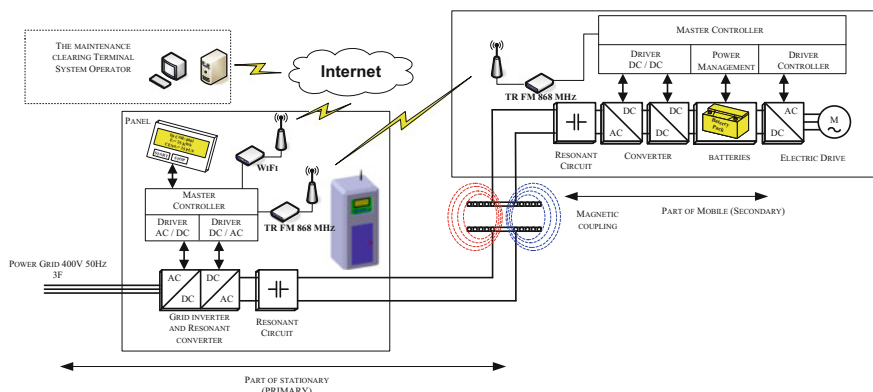


Fig. 1 Block diagram of the inductive contactless energy transfer system with bidirectional energy flow

Presents the methodology of ICET with bidirectional energy flow control converters and the results of simulation for a system with rated power $P = 100 \text{ kW}$.

2 Inductive Coupling: The Genesis of Contactless Energy Transfer

The inductive coupling (transformer air) is a phenomenon that occurs when you have two or more coils coupled magnetically. A characteristic feature of such a circuit is low, magnetic coupling factor k . The flow of alternating current in the coil produces an alternating magnetic field and thus the magnetic flux. The only part of this flow mediates in energy transfer. The rest of the stream called dissipation or leakage flux causes the induction voltage opposite to the voltage forcing, which strongly limits the energy transfer. A simplified equivalent circuit of the ICET transformer and vector diagram are shown in Figs. 2 and 3.

When L_p, L_s —the windings self-inductances, L_{rp}, L_{rs} —leakage inductances, L_m —mutual inductance, N_p, N_s —number of the windings coils.

The equation for output voltage is as follows:

$$u_s(t) = u_p(t) - u_{L_{rp}}(t) - u_{L_{rs}}(t) \tag{1}$$

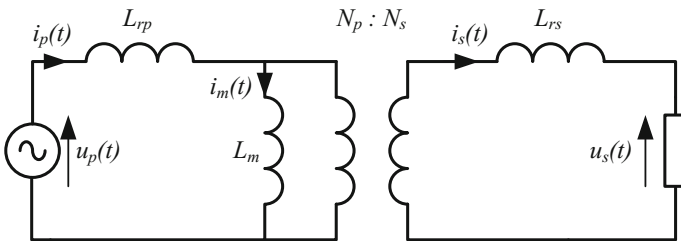
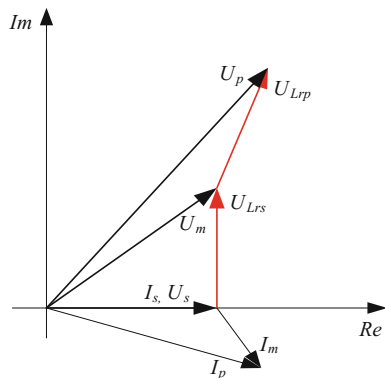


Fig. 2 Equivalent circuit of the ICET transformer

Fig. 3 Vector diagram in the ICET transformer



In order to make energy transfer in ICET transformer possible with high efficiency, you need to compensate for voltage drops in the leakage inductances. For this purpose to primary and secondary terminals of both transformer sides, capacitors are included. Figure 4 shown the general case as it looks like a compensation voltage drop on the leakage inductance. Blue indicator shows the system after compensation.

Then the output voltage u_s is almost equal the supply forcing voltage u_p taking into account the voltage drops on the resistances of passive components. Additionally, satisfying a condition of $R < \omega L_m$ the currents and voltages in the circuit are in phase. This case makes the efficiency of energy transfer grows with increasing load. The distribution of magnetic field strength for this state is shown in Fig. 5.

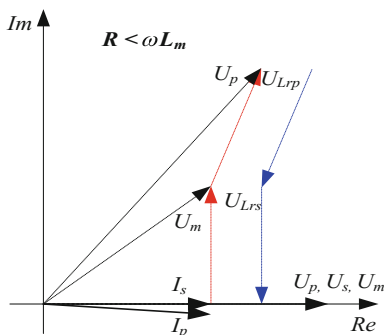


Fig. 4 Vector diagram of the compensated ICET system

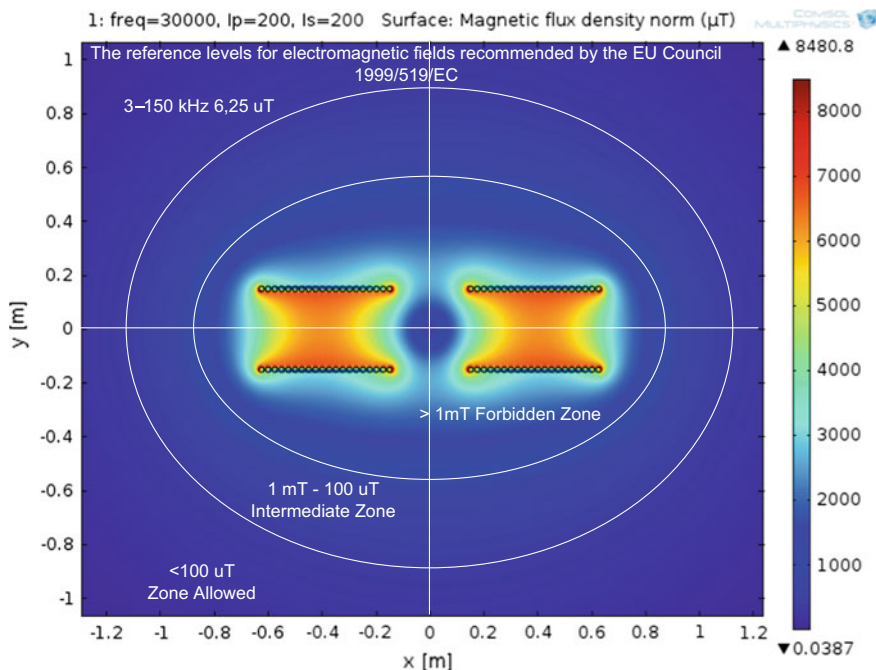


Fig. 5 The distribution of magnetic field strength

The distribution of magnetic field strength shown in Fig. 5, proves that shaping/control of the phase shifts voltage (voltage resonance) by a resonant circuit, brings together the main stream within the working field coils to minimize its leakage dispersion, despite the absence of the magnetic core (the magnetic core of the transformer). ICET systems allow to the construction of any structure or require a transformer. In the use of EV best fits the design of transformer windings flat (planar). This is because of less sensitivity to the windings displacement relative to each other and the flat structure which allows easy installation on the vehicle, etc.

3 Compensating Circuit Topologies and their Properties

Hig-efficiency ICET systems require the use of resonant circuits compensating voltage drops on leakage inductances [2, 4]. Their distribution is shown in Fig. 6.

They are divided into two groups: simple and complex. Nomenclature of individual circuits has adopted the method of connecting the capacitors to the transformer terminals. The second division is the possibility of bidirectional energy flow. For ICET systems with bidirectional energy flow check up a few circuits compensation methods.

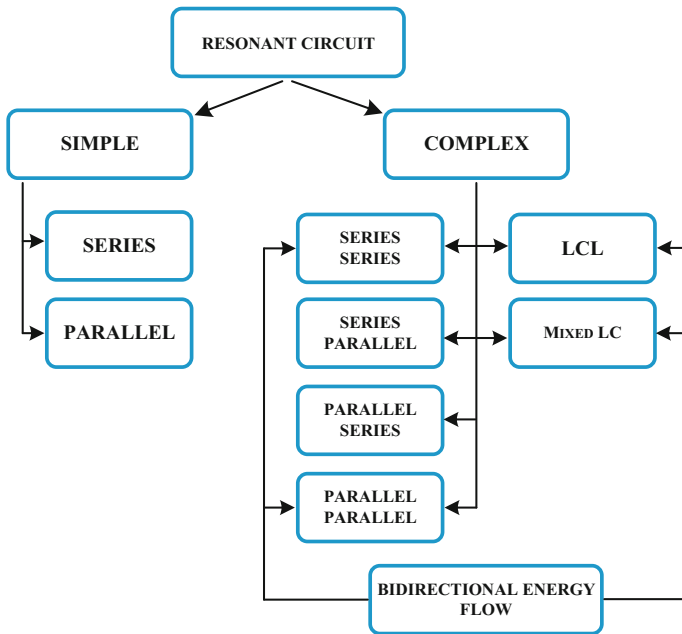


Fig. 6 Division of resonance compensation circuit

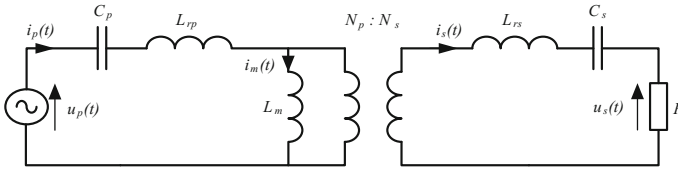


Fig. 7 Equivalent circuit with series–series compensation

The basic criteria for the selection of the compensation circuit are type of power supply—voltage or current inverter, the acceptable sensitivity of the system to changes in magnetic coupling factor, and also on the parameters of the circuit, allowable susceptibility to a change load. For systems with parallel–parallel compensation and fed up from the current inverter, the system shows a high sensitivity to change of the load parameter, and each time required the selection of the LC elements according to magnetic coupling coefficient.

The systems with mixed and LCL compensation circuits supply from voltage inverter, operating in a limited range of changing magnetic coupling coefficients. The basic characteristics of serial–serial compensation circuit are: fed up from voltage inverter, low sensitivity to changes in the magnetic coupling, and a single choice of LC elements. This feature mainly determines the use of series compensated ICET system with bidirectional energy flow for EV. The equivalent circuit is shown in Fig. 7.

Solving the system of equations created on the basis of the equivalent circuit diagram, Fig. 7, we can determine the three basic characteristics, which are complex numbers defining the properties and behavior of the system.

The input impedance Z_{we} , current gain G_i and voltage gain G_v can be expressed by following equations:

$$z_{we} = \frac{U_p}{I_p} = j\omega L_{rp} - j\frac{1}{\omega C_p} + \frac{\frac{L_m}{C_s} - \omega^2 L_{rs} L_m + j\omega L_m R}{R + j\left(\omega L_{rs} - \frac{1}{\omega C_s} + \omega L_m\right)} \quad (2)$$

$$G_i = \frac{I_s}{I_p} = \frac{\omega L_m C_s}{\omega^2 C_s (L_m + L_{rs}) - 1 - j\omega C_s R} \quad (3)$$

$$G_v = \frac{U_s}{U_p} = R \frac{G_i}{Z_{we}} \quad (4)$$

From the above equations, we can determine the frequency characteristics of the module and phase. In order to the presentation of the properties of series–series compensation system is sufficient: the module voltage gain $|G_v|$, phase impedance and phase current gain. The characteristics shown in Figs. 8, 9 and 10 presenting the behavior of the circuit to changes in the magnetic coupling factor and the load resistance changes.

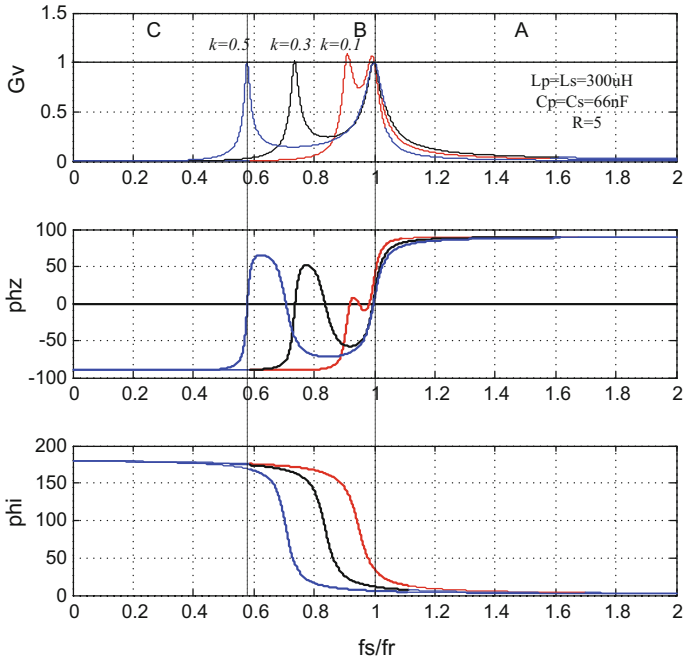


Fig. 8 Frequency characteristics of series-series compensation circuit as a function of changes in the magnetic coupling coefficient k

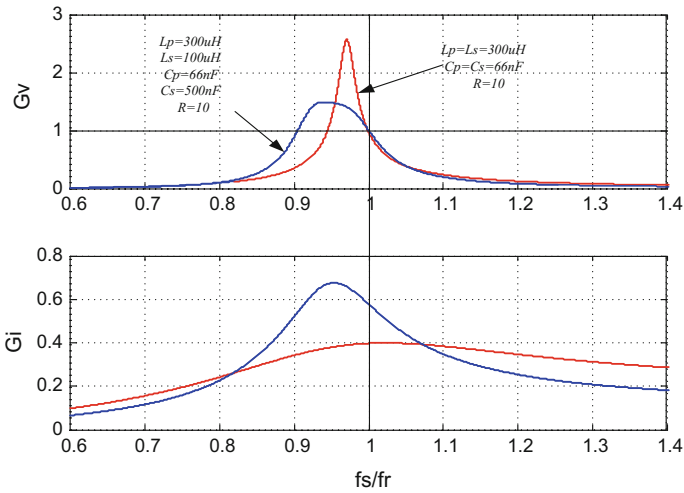


Fig. 9 Frequency characteristics of series-series compensation circuit as a function of changes in the inductance of the windings

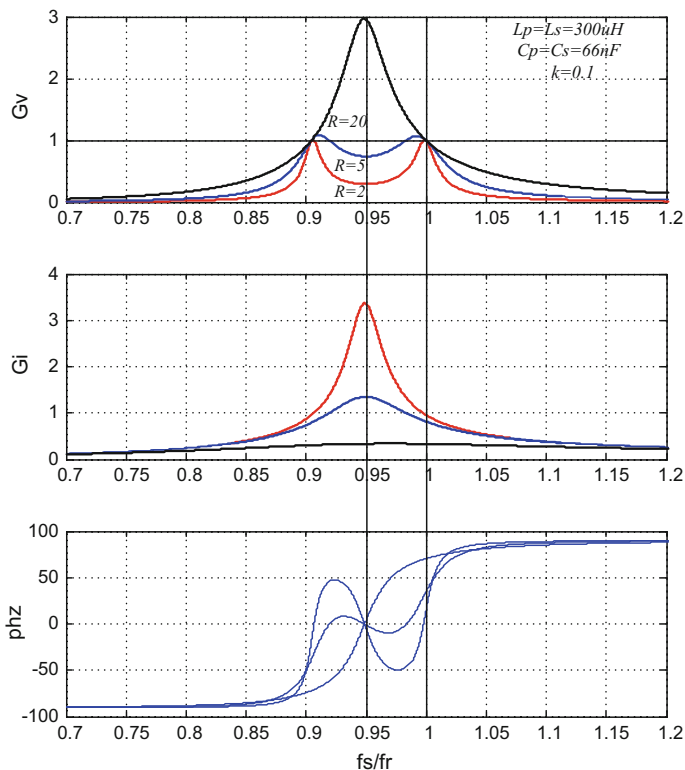


Fig. 10 Frequency characteristics of series-series compensation circuit as a function of load resistance changes

On the basis of the above characteristics can be specified many properties of the above circuit. The first feature is the elimination of the concept of helical gears by the resonant circuit. When the system operated at the resonant frequency regardless of changes in the number of coils (the self-inductance) or the capacitance $C_s = (L_p/L_s) C_p$ the voltage gain is a unit, this state is shown in Fig. 9.

If the resistance $R < \omega L_m$, we can distinguish three frequency operating ranges A, B, and C. Zone A and C are characterized by a monotonic decrease in gain. Zone B is unstable as a function of changes in the resistance. Zero phase shift and separate voltage gain are obtained for the resonant frequency of a particular relationship according to Eq. (6).

$$f_r = \frac{1}{2\pi\sqrt{L_{rp}C_p}} \quad (6)$$

In case of $R > \omega L_m$ the zero phase shift is obtained for frequencies (7)

$$f_r = \frac{1}{2\pi\sqrt{L_p C_p}} \quad (7)$$

and a discussed system has a voltage boost.

Higher load resistance causes greater voltage gain. The frequency characteristics illustrate the output voltage regulation. The first method is to tune and maintenance the system operation at the resonant frequency. The adjustment is made by changing the amplitude of supply voltage. The second method is to change the frequency of the supply voltage, regulate the output voltage by changing the frequency of the supply voltage. The third method is not directly resulting from the above analysis, it is the integration method [1]. It involves zero voltage switching vector forcing for a period equal to a multiple of the current half-cycles whose amplitude exceeds the set point. It uses here the phenomenon of attenuation of current amplitude. Then the output voltage varies in amplitude by a number of $\{U_p, U_p/2, U_p/3, \dots, U_p/n\}$.

4 The Simulation Model of the ICET System with Bidirectional Energy Flow for Electric Vehicle

The system is based on the planar transformer with series-series compensation circuit voltage drops across the leakage inductances. To control the inverter it uses a method which combines the integration with the phase shift method. The main aim of this type of control is to stabilize the output voltage regardless of the direction of energy flow. Rated power of the analyzed system is $P = 100$ kW. The parameters of the simulation model of ICET system are presented in Table 1.

Because the system operates as a symmetric, voltage and current waveforms are shown only for one of the directions of energy transfer, Figs. 11, 12 and 13. The study was carried out for the magnetic coupling coefficient $k = 0.1$.

Table 1 The parameters of the simulation model

Parameter	Value	Unit
$L_p = L_s$	300	uH
$C_p = C_s$	66	nF
k	0.1	–
U_{in}	600	V
P_{max}	100	kW



Fig. 11 ICET system response for load jumps

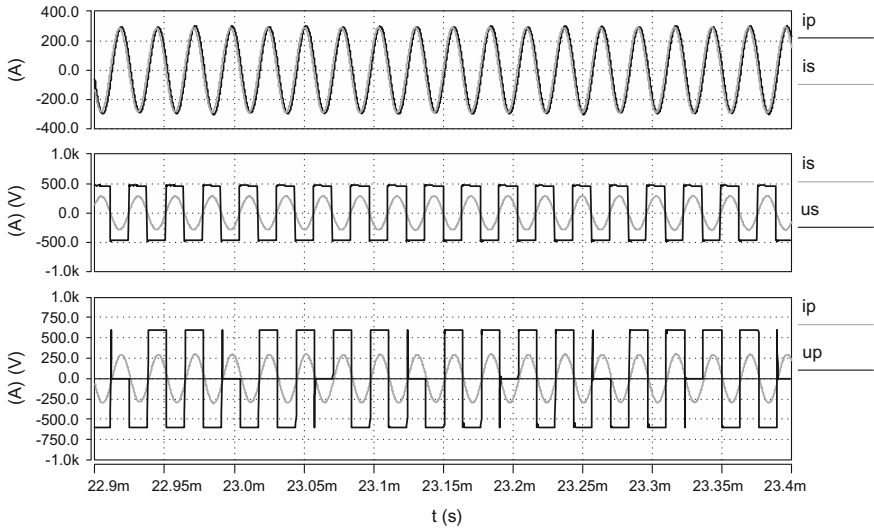


Fig. 12 AC waveforms for the maximum load power $P = 100$ kW

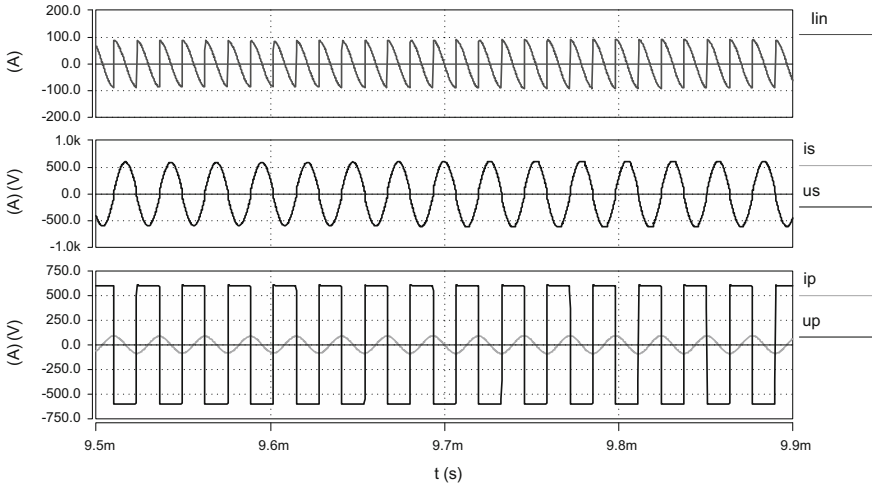


Fig. 13 AC waveforms for minimum power load

5 Discussion and Conclusion

The article presents the contactless energy transfer system ensures:

- Bidirectional energy flow
- The high-efficiency energy transfer
- Universality of application

A wide range of applications ICET systems, their capabilities and value of energy transfer, contributes to their dissemination, together with the development of modern technology. Starting small medical applications ending with all kinds of transport vehicles.

Publication funded by NCN no. decision DEC-2012/07/N/ST7/03487

6 Discussion and Conclusions

A conclusion section is not required. Although a conclusion may review the main points of the paper, do not replicate the abstract as the conclusion. A conclusion might elaborate on the importance of the work or suggest applications and extensions.

References

1. Kaźmierkowski, M.P., Moradewicz, A.J.: Unplugged but connected review of contactless energy transfer systems. *IEEE Ind. Mag.* **6**, 47–55 (2014)
2. Kaźmierkowski, M.P., Moradewicz, A.J.: Contactless energy transfer (CEET) systems—a review, conference proceedings, EPE, 3-1-3-6 (2013)
3. Kshy, A., Swain, K., Devarakonda, S., Madawala, U.K.: Modeling, sensitivity analysis and controller synthesis of multipickup bidirectional inductive power transfer system. *IEEE Trans. Ind. Inf.* **10**(2), 1372–1380 (2014)
4. Twiname, R.P., Thrimawithan, D.J., Madawala, U.K.: A new resonant bi-directional DC–DC converter topology. *IEEE Trans. Power Electron.* **9**, 4733–4740 (2014)

Review of Structural Solutions in High-Voltage Overhead Power Lines and Possibilities of Reducing Emission of Electromagnetic Fields

Zbigniew Wróblewski, Dariusz Szafrowski and Jacek Gumiela

Abstract This article compares the electromagnetic field distribution in the environment of overhead power lines built based on typical constructions of poles to be built as pipe-poles. On the basis of the distribution of digital simulation of the electric fields and magnetic fields specified range of the impact on the environment of overhead power lines. In conclusion, a proposed structure which the areas management under overhead power lines is optimal.

Keywords Electromagnetic fields · Digital simulations · Overhead power lines

1 Introduction

Power stations and power lines during their operation produce electromagnetic fields of 50 Hz, which can be considered as two separate components: electric and magnetic.

Electric fields occur due to the occurrence of the difference of potential, while magnetic fields are generated by the flowing current [1]. The electromagnetic field intensity achieved in the vicinity of high-voltage overhead power lines is mainly affected by the following parameters [1–4]:

- transmission line voltage,
- current intensity in phase wires,
- distance between phase wires and earth,
- distance between different phase wires or groups of wires, if the line uses bundle wires,

Z. Wróblewski (✉) · D. Szafrowski · J. Gumiela
Faculty of Electrical Engineering, Wrocław University of Technology, Wrocław, Poland
e-mail: zbigniew.wroblewski@pwr.edu.pl

D. Szafrowski
e-mail: dariusz.szafrowski@pwr.edu.pl

J. Gumiela
e-mail: jacek.gumiela@pwr.edu.pl

- geometric arrangement of the phase wires and their mutual position cables or bundles of the same phase,
- area of wire cross section.

Identification of the distribution of electromagnetic fields around power lines can be performed using either the measurement method or calculation method [3, 5, 6]. Analytical methods commonly used for computational assessment of electromagnetic field intensity due to the applied simplification of the object or some of its electrical parameters yield results slightly different from the actual results [4]. In the case of numerical methods, obtaining an approximated result is a natural feature and calculations are finished after achieving the desired accuracy. A separate group consists of measuring methods which are subject to cumulative error of the measuring instrument and other errors resulting, among others, from irregularities of terrain, difficulty in identifying the perpendicular and rectilinear direction during the measurement process, and finally changes in the voltage and current during the measurement process [2, 3, 5].

The paper presents the results of digital simulation of the distribution of fields for several designs of single-circuit and double-circuit transmission lines installed on supporting truss or tube pylons. The obtained maximum values of electromagnetic fields generated under transmission lines and widths of technology strips for the example objects were compared.

2 Analysis of Distributions of Electromagnetic Fields Under High-Voltage Transmission Lines

Transmission of electricity over long distances is an integral part of modern civilization. The fact that electrical losses vastly depend on the transmission voltage, make it economically viable to construct higher voltage overhead lines. In practice, however, typical technical support structure solutions are commonly used for both single-circuit and multiple-circuit transmission systems.

At the design stage of every overhead transmission power line, it is necessary to specify the size of the exclusion zone and establishment of land easement in the whole zone. Then, to minimize the costs of purchase or lease of the land, it is important to accurately assess the impact of the line on the environment already at the stage of creating the technical–economic feasibility study and to ensure optimal management of land resources [5–7]. Such relatively simple measures usually yield significant cost savings [8] (Fig. 2).

While the power, voltage, and current are in this case predetermined, careful consideration of the spatial geometric arrangement of wires is highly recommended. This way, at low cost and through proper selection of supporting structures, the mutual positioning of the phase wires or the use of multi-lane systems [8–10] can help reduce the environmental impact of electromagnetic fields.

For the purpose of this study the author analyzed several variants of double-circuit transmission lines with rated voltages of 220 and 400 kV, installed on truss popular structures type M52, R220 in the case of the 220 kV line, and type Z52, E33P in the case of the 400 kV line (Fig. 4).

For double-circuit lines, an analysis of the distribution of electromagnetic field at both extremely favorable and extremely unfavorable positioning of phase wires was performed (Figs. 1 and 2), which produced significant differences in maximum intensity of electric and magnetic fields, as well as change of width of exclusion zone under the line [4, 8–10]. Numerical analysis of field distribution was performed using EMFields application to support simulation of complex multi-circuit and multi-voltage overhead transmission systems.

For comparison purposes, a number of general assumptions regarding the parameters of the analyzed power lines were adopted:

- rated voltage of the line $U = 220$ kV,
- full symmetry of voltages and currents,
- width of the zone for which the calculations were performed $X = \pm 50$ m from the axis of the line,
- calculation step delta $X = 0.2$ m,
- measuring height $h = 2.0$ m.

Fig. 1 Geometry of the phase wires for type M52 truss pylon

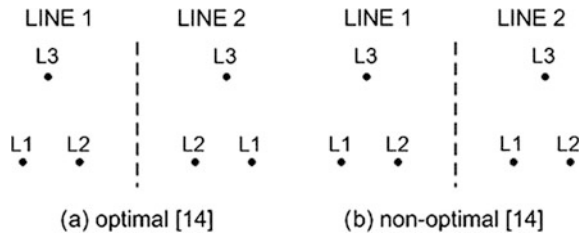
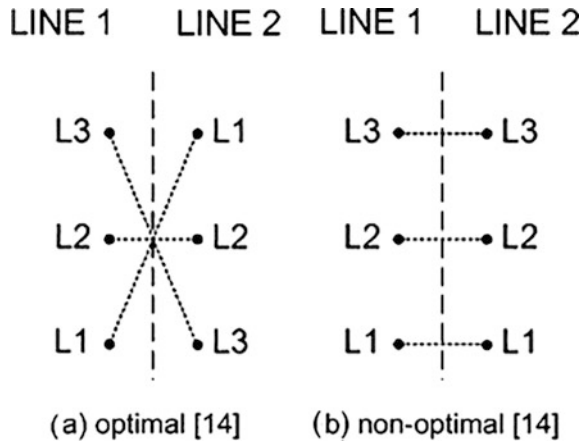


Fig. 2 Geometry of the phase wires for type R220, Z52, E33P pylon



2.1 Electromagnetic Field Under 220 kV Lines

Figure 3 shows the supporting structures, and Table 1 lists distances characterizing the arrangement of cables on truss pylons type M52 and R220 tubular type. The proposed geometric configuration of the double-circuit transmission line wires proves to be the most favorable in terms of the maximum intensity of the electromagnetic field [8]. For the purposes of determining the magnetic component of the field, it is assumed that the phase wires of the line carry operating currents of 600 A.

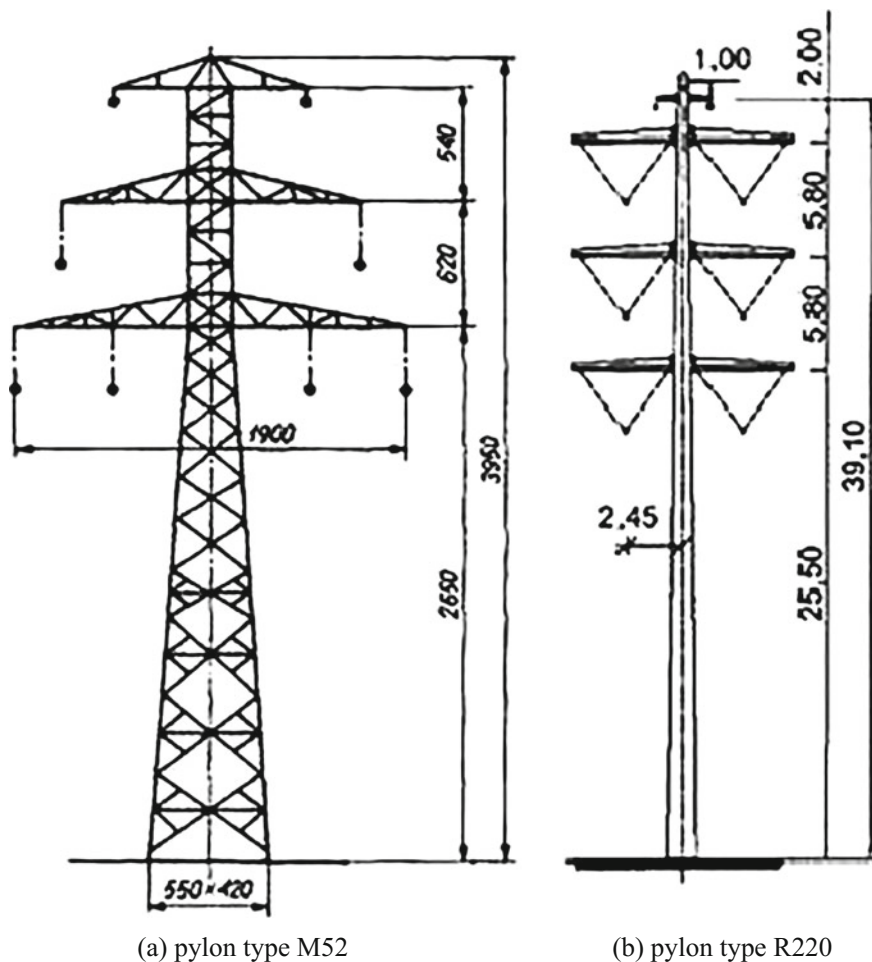


Fig. 3 Shapes of dual circuit 220 kV transmission line pylons. [Source <http://www.elektroinstalacje.info>]

Table 1 Geometrical configuration of wires for the two-circuit 220 kV transmission line

	Pylon type M52 (truss)						Pylon type R220 (pipe)					
	LINE 1			LINE 2			LINE 1			LINE 2		
	L1	L2	L3	L1	L2	L3	L1	L2	L3	L1	L2	L3
X (m)	-4.9	-9.5	-7.2	9.5	4.9	7.2	-2.45	-2.45	2.45	2.45	2.45	2.45
Y (m)	13.0	13.0	19.2	13.0	13.0	19.2	12.0	17.8	23.6	12.0	17.8	23.6

A double-circuit overhead transmission line installed on the type M52 truss pylons generates an electric field with the maximum intensity about 46% smaller in the case of the optimal configuration of wires ($EM52_{(1)} = 1.43$ kV/m against $EM52_{(2)} = 2.09$ kV/m) (Fig. 4).

A double-circuit overhead line built on the M220 tube pylons generates an electric field with the maximum intensity about 300% smaller in the case of the optimal configuration of wires ($ER220_{(1)} = 0.90$ kV/m against $ER220_{(2)} = 3.55$ kV/m) (Fig. 5).

Smaller maximum intensity of both the electric component and a magnetic variant can be observed in R220 type pylons. It clearly shows that in the optimal configuration the electric field hardly reaches 1 kV/m (Fig. 5).

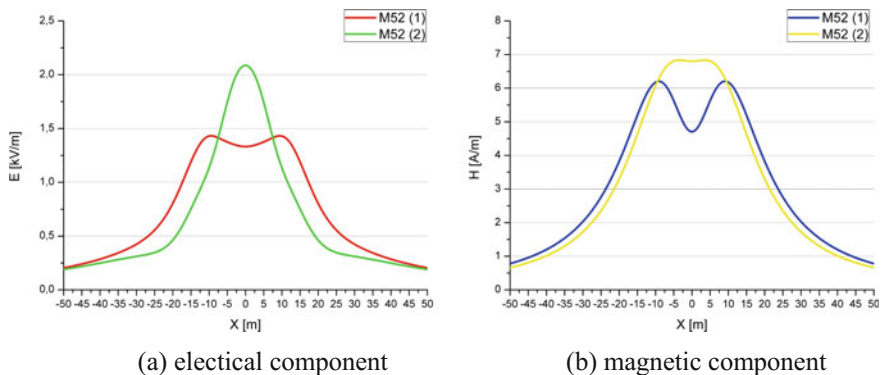


Fig. 4 Electromagnetic field under 220 kV double-circuit transmission line installed on type M52 truss pylons

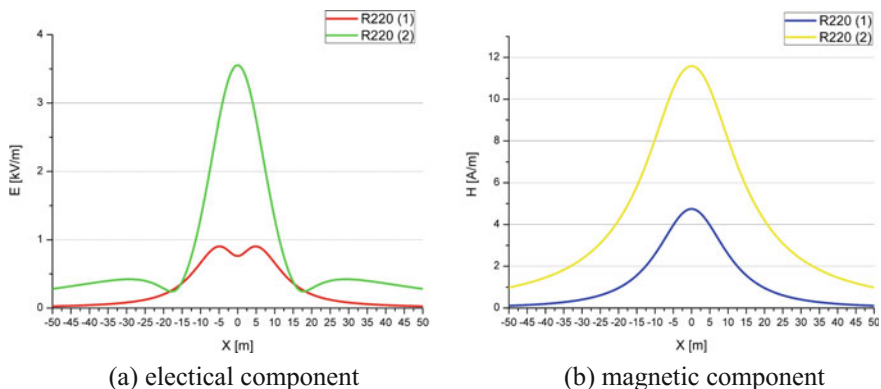


Fig. 5 Electromagnetic field under 220 kV double-circuit transmission line installed on type R220 pipe pylons

2.2 Electromagnetic Fields Under 400 kV Lines

Figure 6 shows the column structures, and Table 2 lists distances characterizing the arrangement of cables on straight-line support pylons type Z52 and E33P over-forest type. The proposed geometric configuration of the double-circuit line wires is the most favorable in terms of the maximum intensity of the electromagnetic field [8]. For the purposes of determining the magnetic component of the field, it is assumed that the phase wires of the line carry operating currents of 900 A.

Double-circuit overhead line built on the type Z52 truss pylons generates an electric field with a maximum intensity about 24% smaller in the case of the optimal configuration of wires ($EZ52_{(1)} = 3.226$ kV/m against $EZ52_{(2)} = 4.010$ kV/m) (Fig. 7).

Double-circuit overhead line built on the E33P over-forest pylons generates an electric field with a maximum intensity about 97% smaller in the case of the optimal configuration of wires ($EE33P_{(1)} = 1.542$ kV/m against $EE33P_{(2)} = 3.045$ kV/m) (Fig. 8).

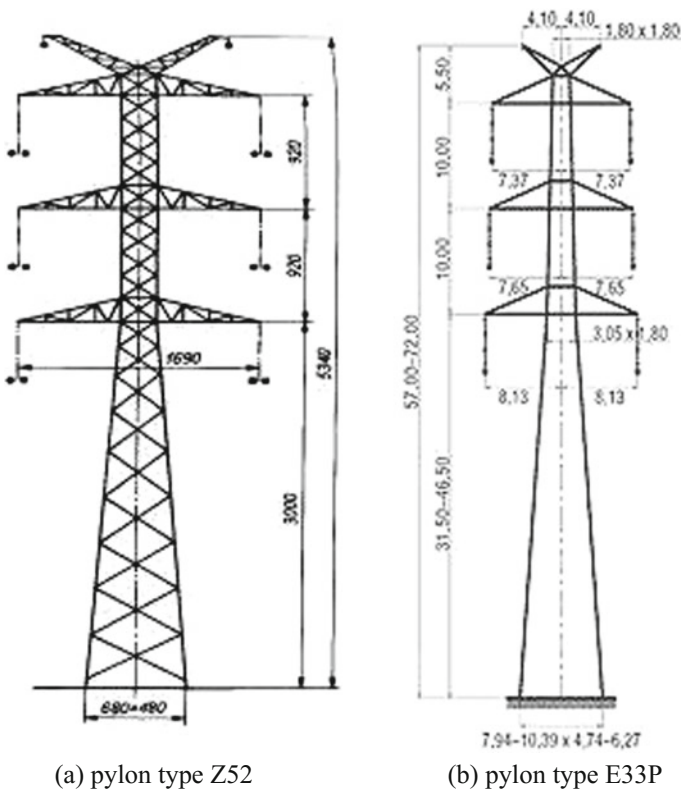


Fig. 6 Shapes of dual circuit 220 kV transmission line pylons. [Source: <http://www.elektroinstalacje.info>]

Table 2 Geometrical configuration of wires for the two-circuit 400 kV transmission line

	Pylon type Z52						Pylon type E33P					
	Line 1			Line 2			Line 1			Line 2		
	L1	L2	L3	L1	L2	L3	L1	L2	L3	L1	L2	L3
X (m)	-8.45			8.45			-8.13			7.37		
Y (m)	32.4	23.2	14.0	14.0	23.2	32.4	20.5	30.5	40.5	40.5	30.5	20.5

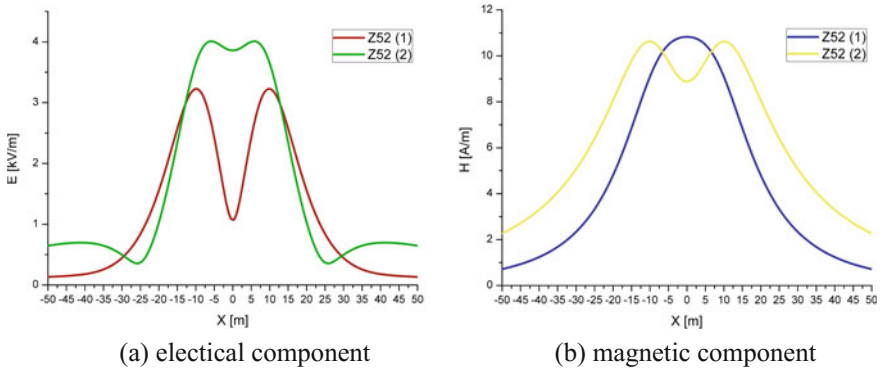


Fig. 7 Electromagnetic field under 400 kV double-circuit transmission line installed on type Z52 truss pylons

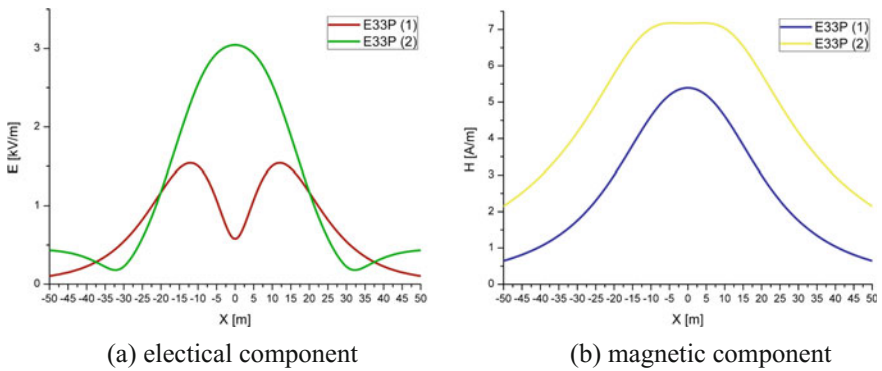


Fig. 8 Electromagnetic field under 400 kV double-circuit transmission line installed on type E33P pylons

Smaller maximum intensity of both the electric and magnetic components can be observed in the variant with E33P type pylons.

In addition, for both examined 400 kV pylons the electric component of the field decreases with distance from the axis of the line, and then, at a distance of several meters, there is a slight increase in the value of electric field intensity to a local maximum, beyond which it again reduces its value with the distance from the power line (Figs. 7 and 8).

2.3 Summary of Results

Tables 3 and 4 present results of the digital simulation conducted to analyze the electromagnetic field distribution in the space underneath the line wires.

Table 3 Comparison of maximum intensity of electric and magnetic fields and the width of the exclusion zone below the line in which the field intensity is exceeded

Dual circuit 220 kV transmission line				
Construction	E (kV/m)	$d_{E>1 \text{ kV/m}}$ (m)	H (A/m)	$d_{H>60 \text{ A/m}}$ (m)
R220 (O)	0.90	–	6.21	–
R220 (N)	3.55	–11.2 to +11.2	6.84	–
M52 (O)	1.43	–17.2 to +17.2	4.74	–
M52 (N)	2.09	–11.6 to +11.6	11.59	–

Table 4 Comparison of maximum intensity of electric and magnetic fields and the width of the exclusion zone below the line in which the field intensity is exceeded

Dual circuit 400 kV transmission line				
Construction	E (kV/m)	$d_{E>1 \text{ kV/m}}$ [m]	H (A/m)	$d_{H>60 \text{ A/m}}$ (m)
E33P (O)	1.542	–22.2 to +22.2	5.394	–
E33P (N)	3.045	–21.2 to +21.2	7.181	–
Z52 (O)	3.226	–23.6 to +23.6	10.829	–
Z52 (N)	4.010	–20.0 to +20.0	10.624	–

It is worth noting that all the examined varieties of double-circuit lines share a common relationship that lower maximum electric field intensity comes at the expense of wider zone in which it may exceed the maximum permissible value of 1 kV/m [11]. The magnetic component does not exceed the limit of 60 A/m in any of the measurement points [11]. Electric power lines are the source of electromagnetic field which, for safety reasons, should not exceed the values set out in relevant legislation [11–13].

In the design phase of new infrastructure these objects are located far from human settlements. However, there is often intensive development near existing overhead power lines. The impact zone designed according to the old criteria that are not in effect today may no longer meet the current permissible values of electric field intensity at various locations inhabited by people [13, 14]. Reconstruction of the power line in order to remove the conflict is, for many reasons, not always feasible. Such alteration may also be very expensive.

Multiple-circuit lines, with a particular arrangement of electrical circuits, demonstrate the effect of field compensation and consequently, the resultant electric field generated by two electrical circuits may be lower than the electric field generated individually by either of these circuits.

3 Conclusions

1. Specialized support structures, through the use of a different geometry, allow reducing electromagnetic fields generated in the vicinity of high-voltage lines.
2. In the case of double-circuit lines, the geometric configuration of cables is especially important, as in extreme cases, the intensity of electromagnetic fields generated by wires can be reduced several times due to compensation of the influence of individual wires or entire electric circuit.
3. It is possible to achieve the effect of reducing the maximum intensity of the electromagnetic field without changing the transmission capacity of the overhead line or reduce the width of the exclusion zone exposed to certain intensity through the appropriate spatial arrangement of cables on the supporting structures.
4. When designing an overhead multi-circuit power line typically a choice must be made about one of the available solutions to strike the right balance between the maximum value of the intensity of the electromagnetic field and the width of the strip of land where the electromagnetic field strength decreases relatively slowly with the distance from the axis of the line.

References

1. Kiessling, F., Nefzger, P., Nolasco, J.F., Kaintzyk, U.: Overhead Power Lines Planning, Design, Construction. Springer: Berlin. ISBN-13:978-3-642-05556-0 (2003)
2. Filippopoulos, G., Tsanakas, D.: Analytical calculation of the magnetic field produced by electric power lines. *IEEE Trans. Power Deliv.* (2005). doi:[10.1109/TPWRD.2004.839184](https://doi.org/10.1109/TPWRD.2004.839184)
3. Dawalibi, F.P., Southey, R.D.: Analysis of electrical interference from power lines to gas pipelines I, computation methods. *IEEE Trans. Power Deliv.* (2002). doi:[10.1109/6132680](https://doi.org/10.1109/6132680)
4. Polk, Ch.: Physical Mechanisms for Biological Effects of Low Field Intensity ELF Magnetic Fields; Shoogo Ueno, University of Tokyo; ISBN 978-0-306-45292-5; Springer US; 3–4 September 1993
5. Portier, Ch.J., Wolfe, M.S.: Assessment of Health Effects from Exposure to Power-Line Frequency Electric and Magnetic Fields; NIEHS Working Group Report; National Institute of Environmental Health Sciences of the National Institutes of Health; Minnesota 16–24 June 1998
6. Zeńiczak, M.: Estimation of electric and magnetic field intensities under power transmission lines in real country conditions, *Przegląd Elektrotechniczny* Nr 7; 2008
7. Linder, S.H.: Contending discourses in the electric and magnetic fields controversy: the social construction of EMF risk as a public problem. *Policy Sci.* (1995). doi:[10.1007/BF00999676](https://doi.org/10.1007/BF00999676)
8. Stewart, J.R., Dale, S.J., Klein, K.W.: Magnetic field reduction using high phase order lines. *IEEE Trans. Power Delivery* (2002). doi:[10.1109/61.216869](https://doi.org/10.1109/61.216869)
9. Memari, A.R., Janischewskyj, W.: Migration of magnetic field near power lines. *IEEE Trans. Power Delivery* (2002). doi:[10.1109/61.517519](https://doi.org/10.1109/61.517519)
10. Olsen, R.G., James, D.C., Chartier, V.L.: The performance of reduced magnetic fields power lines: theory and measurements on an operating line. *IEEE Trans. Power Deliv.* (2002). doi:[10.1109/61.252670](https://doi.org/10.1109/61.252670)

11. Rozporządzenie Ministra Środowiska z dnia 30 października 2003r. w sprawie dopuszczalnych poziomów pól elektromagnetycznych w środowisku oraz sposobów sprawdzania dotrzymania tych poziomów. Dz. U. nr 192, poz. 1883 (2003)
12. Zmyslony, M., Kubacki, R., Angolczyk, H., Kieliszek, J., Trzaska, H., Bienkowski, P., Krawczyk, A., Szmigielski, S.: Verification of Polish regulations of maximum permissible intensities In: Electromagnetic Fields by the Commission for Bioelectromagnetics Issues of the Polish Radiation Society. *Medycyna Pracy* **56** (2005)
13. Vulević, B., Osmokrovic, P.: Survey of ELF magnetic field levels in households near overhead power lines in Serbia. *Radiat. Prot. Dosim.* **145**, 385–388 (2011)
14. Vulević, B., Predrag, O.: Evaluation of uncertainty in the measurement of environmental electromagnetic fields. *Radiat. Prot. Dosim.* **141**(2), 173–177 (2010)

Active Power Flow Control on Cross-Border Connections

L. Beňa, K. Buczek, P. Rydz and H. Wachta

Abstract Occurrence of unscheduled electric power flows is one of the most important issues challenging safety of any electric power system. To prevent failures related to the phenomenon, power flows in the system are controlled. This paper contains a review of the causes for which power flow control in a system is necessary, methods used to make flow adjustments, and devices used to control power flows in networks. The practical portion of the presented study includes development of a simulation model for the network with the use of PowerWorld software. Presented are also results of measurements of active power and its losses in the states of equilibrium, increased demand for energy, and with phase shift transformer (PST) and thyristor-controlled series capacitor (TCSC) installed in the system. On the grounds of the obtained measurements it was demonstrated how harmful is the effect of unscheduled active power flows on stability of an electric power system. Moreover, the effect of PST and TCSC on active power flows in the system is discussed including advantages and disadvantages of both device types.

Keywords Power flow control · Phase shift transformer · Thyristor-controlled series capacitor · PowerWorld

L. Beňa (✉) · K. Buczek · P. Rydz · H. Wachta

The Faculty of Electrical and Computer Engineering, Rzeszow University of Technology,
Rzeszow, Poland

e-mail: lbena@prz.edu.pl

K. Buczek

e-mail: kbuczek@prz.edu.pl

P. Rydz

e-mail: 19paula92r@wp.pl

H. Wachta

e-mail: hwachta@prz.edu.pl

© Springer International Publishing AG 2018

D. Mazur et al. (eds.), *Analysis and Simulation of Electrical and Computer Systems*, Lecture Notes in Electrical Engineering 452,
https://doi.org/10.1007/978-3-319-63949-9_11

1 Introduction

In recent years, the electric power industry was subject to numerous changes encompassing its technological, economical, and legal aspects. Currently, the main goal of EU countries is to create a common and integrated market of electric energy. Such market is expected to guarantee stable and reliable operation of the common electric power system with security of supplies to all consumers being maintained at the same time. Establishment of the integrated market for electric energy in Europe poses a significant challenge to the whole electric power industry. The necessity to transmit energy over large distances (from sources to consumers) and continuously increasing demand exert pressure on further expansion of infrastructure. Additionally, transactions concluded on the liberalised energy market result in unscheduled flows, i.e. deviations between actual and planned flows occurring on cross-border connections. This is a result of insufficient links between rules governing trade on modern markets and principles of physic ruling power flows. Occurrence of unscheduled flows is one of the most important issues posing threat to any electric power system. To prevent failures related to the phenomenon, power flow control is implemented in the system. For this purpose, Flexible Alternating Current Transmission Systems (FACTS) devices are used. TCSC and PST are the solutions selected most frequently, of which the transformer with controlled load angle (PST) turns out to be one of technically most effective choices as far as power flow control is concerned.

2 The Phenomenon of Unscheduled Power Flows

Building up large electric power systems offers better utilisation of production potential and transmission capability of the network. This, however, gives rise to difficulties with maintaining stability of operation of the system. In large complex systems integrating a number of smaller networks, energy transmission paths can lengthen and increased power flows arise affecting security of supplies. An electric power system can lose its stability even under seemingly normal conditions. The so-called unscheduled flows are among the most dangerous and difficult to predict phenomena which can turn out to be a source of serious failures.

Unscheduled power flows can be defined as deviations between physical flows and scheduled flows occurring on a given cross-border connection at a given time. They follow from the absence of appropriate links between rules of trade adopted on the energy market and laws of physic which govern actual operation of large electric power systems. Unscheduled flows mean uncontrolled exchange of power which remained unwittingly unreported to the transmission network operator (in the form of a schedule of cross-border transactions) and was not taken into account in the market-driven allocation mechanism of cross-border transfer capabilities. Therefore, formation of unscheduled flows within the transmission network area

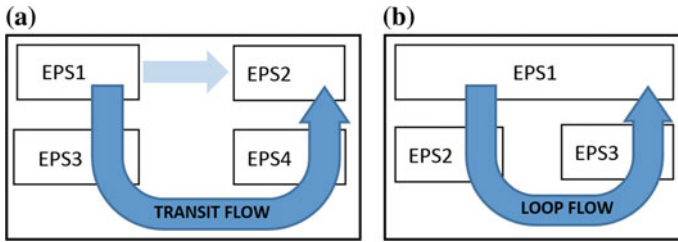


Fig. 1 Unscheduled **a** transit and **b** loop flows

administered by a given operator is a result of a flawed system of supervision of commercial transactions concluded in neighbouring systems [1].

The phenomenon of unscheduled flows poses a significant challenge to the electric power industry in the process of establishing a common and integrated market for electric energy, as it can be the cause of numerous failures which pose a risk to stability of supplies and safety of the system. Additionally, unscheduled flows deteriorate effectiveness of cross-border exchange transactions [2].

One can distinguish between two main causes of occurrence of unscheduled flows

- Transit flows, which result from neglecting the effect of transactions concluded between large market areas (countries) on energy flows in neighbouring zones (countries). A visualisation of the phenomenon is presented in Fig. 1a, where power flow from the area EPS1–EPS2 does not occur directly but instead via the neighbouring areas EPS3 and EPS4.
- Loop flows, which arise as a result of uncoordinated energy trading transactions inside specific market zones (countries) and affect power flows in neighbouring systems (countries). The phenomenon is illustrated in Fig. 1b—the power flow in area EPS1 does not occur internally but instead via neighbouring areas EPS2 and EPS3 [1].

To prevent adverse effect related to unscheduled flows, power flow controlling devices can be installed in an electric power system.

3 Active Power Flow Control

Active power flow control consists in changing individual power flows with the total generated power being maintained. The control can be exercised according to the relationship determining active energy flow in a single line with inductive nature, which can be written in the form

$$P = \frac{U_1 \cdot U_2}{X_1} \cdot \sin \delta \quad (1)$$

where P is the active power flowing out from the analysed branch; U_1 , U_2 are voltage module at the beginning and end of branch, respectively; X_1 is the line's reactance; and δ is the load angle (the difference between arguments of node voltages at the beginning and end of branch, $\delta = \delta_1 - \delta_2$) [2].

3.1 *Reasons Behind Active Power Control*

Control of the active power flow in transmission lines is exercised in view of the three following aspects:

- Technical
 - increasing stability of the system by protecting transmission lines against overloading and reduction of occurrence of unscheduled power flows on inter-system connections;
 - improving electric power quality by controlling values of: voltage, power oscillations (swings) and flows, and reduction of losses on transmission routes;
 - increasing capacity of lines with highest voltage rating.
- Economic
 - reducing operating costs related to failures, overloads and losses of the transmitted power;
 - stimulating development of the energy market;
 - increasing potential for cross-area transactions thanks to optimal utilisation of cross-border connections.
- Political
 - possibility to fulfil international obligations concerning electric power quality;
 - expansion of the integrated power market covering the whole Europe [2].

3.2 *Active Power Flow Control Methods*

It follows from formula (1) that the active power flow in a network line can be controlled by

- Changing node voltage levels at the beginning and the end of a selected line of the network. However, this method is not used as a means of controlling active

power flows in view of the necessity to maintain voltages U_1 and U_2 within the limits of admissible changes.

- Series compensation, or a change of reactance of the transmission line. The method offers the possibility to control power flow by artificial reduction of the inductive reactance value characterising a network line. This is obtained by connecting a bank of capacitors in series with properly selected reactance value.
- Controlling the load angle δ . Such active power flow control method allows to change values of the power flow in the line in a wide range and even reverse direction of the flow [2].

4 Power Flow Control Devices

The devices aiding failure-free operation of electric power systems are known as Flexible Alternating Current Transmission Systems (FACTS). Most advantageous features of FACTS devices are the speed and flexibility at which they are capable to control voltages as well as reactive and active power, and thus control power flows in transmission networks. FACTS devices are used to improve quality and effectiveness of energy transmission by controlling active and reactive power flows and node voltages. The use of FACTS improves also stability of the whole electric power system by damping power swings. The devices can be connected to power transmission lines: in series, in parallel, or in combinations of these two methods.

Basic FACTS devices used in electric power systems include [3–6]

- Series compensators: Static Synchronous Series Compensator (SSSC) and Thyristor-Controlled Series Capacitor (TCSC);
- Parallel compensators: Static Synchronous Compensator (STATCOM) and Static VAR Compensator (SVC);
- Unified Power Flow Controller (UPFC);
- Phase Shifting Transformer (PST).

In the following, PST and TCSC devices will be discussed in greater detail.

4.1 Phase Shifting Transformer

The Phase Shifting Transformer is a transformer device of a special design. The principle of operation of PST consists in controlling the angle of phase shift between voltages on both ends of a transformer. PSTs find their application in controlling actual flows of active power in electric power systems. Power flow control after installing a PST should offer the possibility to either “block” or “enhance” transmission of power, if the need arises.

Operation of transformer phase shifters on cross-border connections improves stability and security of electric energy supplies and protects network structure components, i.e. transformers and lines, against thermal overloads. Because of development of unscheduled flows on cross-border connections, a higher value of the power transmission safety margin needs to be established. Installation of phase shifting transformers restricts occurrences of this undesired phenomenon (unscheduled flows). As a result, safety margins can be reduced and capability of cross-border transmissions can be increased accordingly. Additionally, phase shifting transformers allow to use the existing infrastructure of power transmission lines more effectively in the age of increasing demand for electric power.

A phase shifting transformer is a device comprising two transformers, i.e. a booster transformer and a regulation transformer. Such phase shifter is connected in series to a power transmission line. Schematic diagram of a line with PST installed is shown in Fig. 2.

Principle of operation of the Phase Shifting Transformer consists in controlling the electric energy flow through a transmission line. This is achieved by adjusting the angle of phase shift between voltages on two ends of the transformer. The control angle is varied very slowly, therefore correct operation of the device is possible only when the system is stable [2].

After connecting PST to a line, the active power flow changes according to the formula

$$P_{12} = \frac{U_1 \cdot U_2}{X_1 + X_{PST}} \cdot \sin(\delta_1 - \delta_2 + \vartheta), \quad (2)$$

where X_{PST} is the additional reactance introduced by the phase shifting transformer and ϑ is PST control angle.

Active power flow through the line is increased by adding angle ϑ to angle δ . Moreover, reactance of the line is increased by the transformer reactance X_{PST} . In a specific situation, when there is no phase shift in PST between input voltage and output voltage ($\vartheta = 0$), the phase shifting transformer restricts flow of active power through the line only by increasing reactance of the line by X_{PST} .

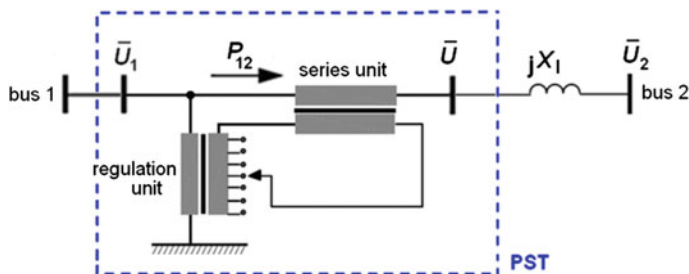


Fig. 2 Schematic diagram of a line with PST mounted

Operation of the powers shifting transformer can be analysed based on a schematic diagram of two parallel lines shown in Fig. 3. The PST is built into the first branch of the system which offers the possibility to control the degree to which both lines are loaded.

After installing PST in the system, a booster voltage appears in the system value of which can be calculated according to formula

$$\Delta U_d = U'_1 - U_1 \quad (3)$$

Voltage ΔU_d results in appearance of current ΔI_d which can be expressed as

$$\Delta I_d = \frac{U'_1 - U_1}{j(X_1 + X_2)} = -j \frac{\Delta U_d}{X_1 + X_2} \quad (4)$$

The current ΔI_d adds to the initial current in the first line,

$$I'_1 = I_1 + \Delta I_d \quad (5)$$

and subtracts from the current in the second line,

$$I'_2 = I_2 - \Delta I_d \quad (6)$$

One may distinguish between the two fundamental transformer regulation types:

- Direct-axis control which allows to add up in-phase voltages. When the angle between primary voltage U_1 and booster voltage ΔU_d is $\varphi = 0^\circ$ or $\varphi = 180^\circ$, then voltages in the system are in phase. In such situation, the transformer affects only the reactive power flow. Moreover, the additional current ΔI_d which arises together with installing the transformer, has an inductive nature and lags with respect to voltage by the angle of 90° . The direct-axis control method is illustrated by means of a phasor diagram in Fig. 4.
- Quadrature control where voltages can be added vectors of which are shifted with respect to each other by the angle of 90° . When $\varphi = 90^\circ$, one deals with the right-angled or the quadrature control method. In such case, the phase shifting transformer contributes to active power flow in the system. The quadrature control method is illustrated with the use of a phasor diagram shown in Fig. 5 [2].

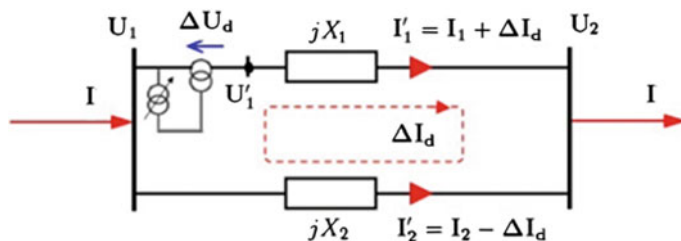


Fig. 3 A schematic diagram depicting the principle of operation of PST

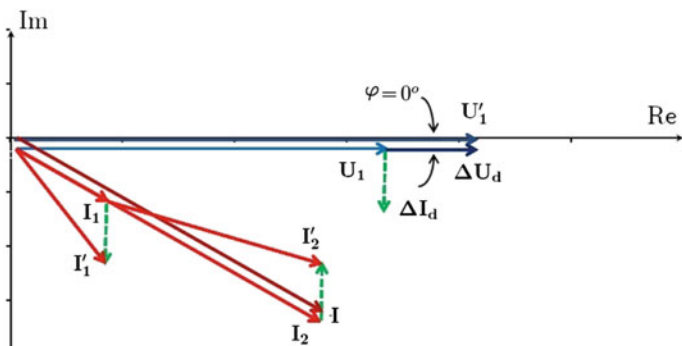


Fig. 4 Phasor diagram for direct-axis of PST

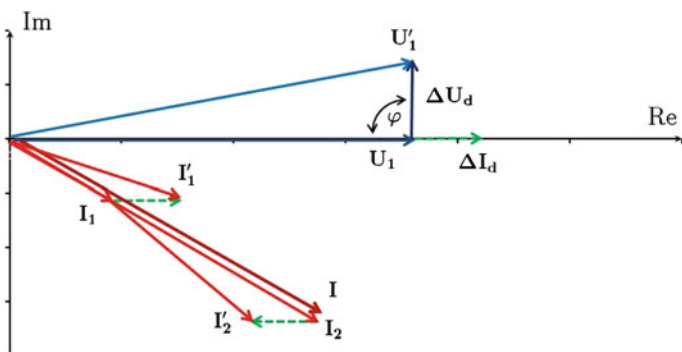


Fig. 5 Phasor diagram representing quadrature control of PST

4.2 Thyristor-Controlled Series Capacitor

TCSC is a device used to control power flows in electric power systems. TCSC comprises a bank of capacitors connected in series to which a thyristor-controlled reactor (TCR) is connected in parallel. The device is built in series into a power transmission line. Such solution offers the possibility to control power flow by changing reactance of the device in a continuous way. Additionally, properties of TCSC allow to increase transmission capacity of the line, as a result of which effectiveness and stability of the system improve. A schematic diagram of the TCSC device is shown in Fig. 6 [2].

Impedance of TCSC device is adjusted by varying reactance of an inductor which is controlled by thyristors (TCR) according to formula

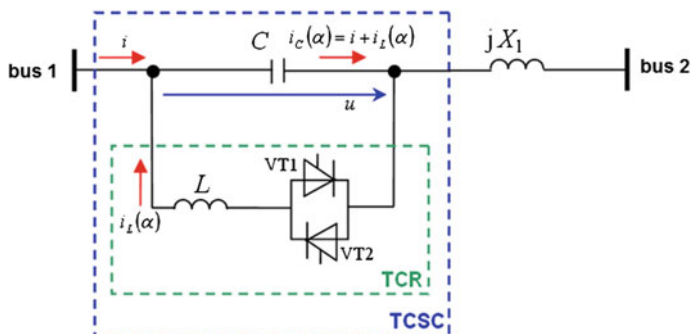


Fig. 6 Schematic diagram of a line with TCSC

$$X_{TCR}(\alpha) = X_L \cdot \frac{\pi}{\pi - 2\alpha - \sin 2\alpha}, \quad (7)$$

where X_L is the inductive reactance of the reactor and α is thyristors firing angle.

The quantity on which the inductive reactance value depends is the thyristors firing angle α . Theoretically, by varying the angle it is possible to obtain reactance varying within a range from the minimum value ($\alpha = 0^\circ \rightarrow X_{TCR} = X_L$) to infinity ($\alpha = 90^\circ \rightarrow X_{TCR} = \infty$). Ultimately, one obtains the control range $X_L \leq X_{TCR}(\alpha) \leq \infty$ [2].

A TCSC is a device composed of capacitors which are connected in parallel with a thyristor-controlled reactor. Hence, reactance of TCSC can be expressed by means of the formula

$$X_{TCSC}(\alpha) = \frac{X_C \cdot X_{TCR}(\alpha)}{X_C - X_{TCR}(\alpha)}, \quad (8)$$

where X_C is the reactance of the capacitor.

At the value of reactance of the induction coil sufficiently small with respect to reactance of capacitors ($X_L < X_C$), operation of TCSC covers both inductive and capacitive operating regime—a resonance interval is being created. Such situation must be considered unfavourable as in the interval in which the resonance occurs, the TCSC device is useless.

Figure 7 shows the three operation regimes characterising a TCSC: capacitive, resonant (operation inhibited) and inductive.

Consider a single-circuit line in which a TCSC device is installed (Fig. 6). To facilitate analysis of the system, the following simplifying assumptions are adopted: both resistance and susceptance of the transmission line are neglected ($R = 0$ and $B = 0$). The power transmitted through the line with installed TCSC is expressed by the following formula:

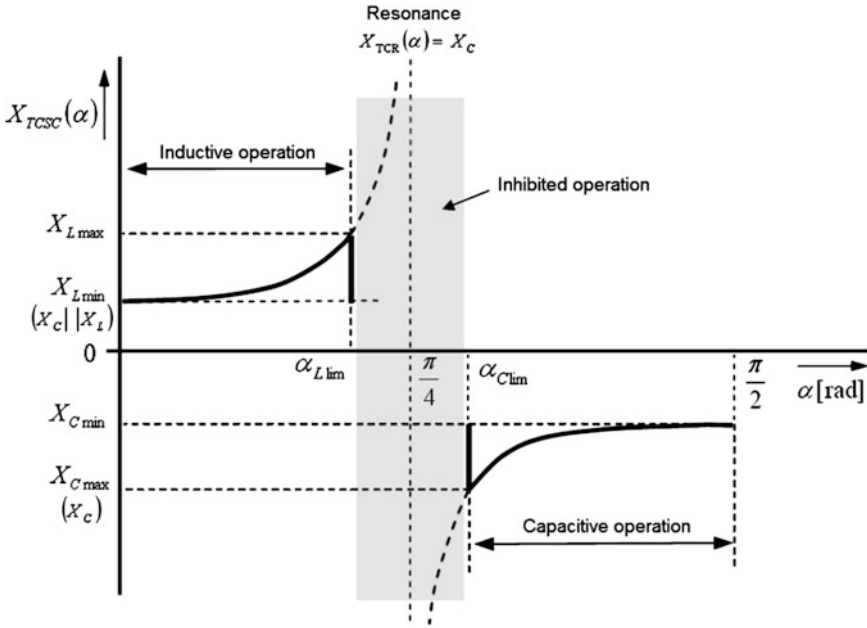


Fig. 7 A graph showing operation regimes of TCSC device

$$P'_{12} = P_{12} \pm \Delta P = \frac{U_1 \cdot (U_2 \pm \Delta U)}{X_1 \pm \Delta X} \cdot \sin(\delta_1 - \delta_2 \pm \Delta\delta), \tag{9}$$

where P_{12} is the active power in the analysed line (without TCSC); ΔX is the line reactance change following from operation of TCSC ($\pm j X_{TCSC}$); ΔU is the voltage change in node 2 attributable to the line reactance change; and $\Delta\delta$ is the load angle change resulting from the transmission line reactance change.

Figures 8, 9, and 10 show phasor diagrams for a line without TCSC, a line with TCSC in inductive operating regime, and a line with TCSC in capacitive regime, respectively.

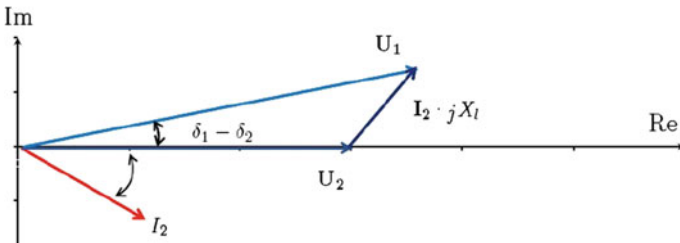


Fig. 8 Phasor diagram for the system's basic operating mode—line without TCSC

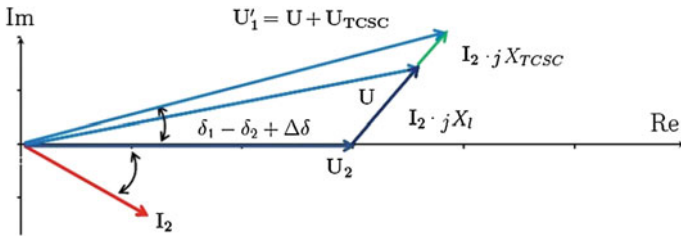


Fig. 9 Phasor diagram for a line with TCSC operating in inductive regime

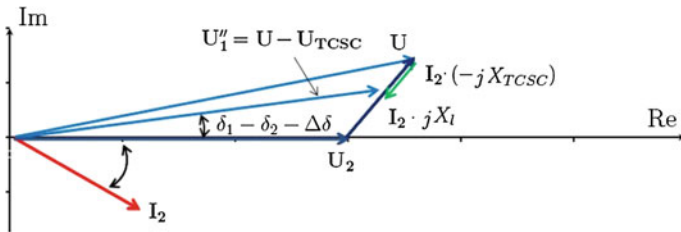


Fig. 10 Phasor diagram for a line with TCSC operating in capacitive regime

The basic benefit from installing TCSC devices in transmission lines is the possibility to control the power flow in an electric power system by means of changing reactance of the line.

Operation of TCSC devices suppresses the phenomenon of unscheduled flows on inter-system connections. Additionally, TCSC devices improve stability of the system also by damping power swings in power systems, minimising system losses, eliminating overloads and facilitating optimisation of power distribution between individual lines [3–6].

5 Development of a Power Flow Regulation Model with PST and TCSC in the PowerWorld Programming Environment

Figure 11 shows a schematic diagram of the developed basic model of an electric power network operating at 400 kV. The modelled electric power system comprises 11 buses which are interconnected with the use of 29 lines. Additionally, power generators and loads are connected to individual system buses. The model was coded using PowerWorld software [7].

The network includes into the following four component systems or sub-networks:

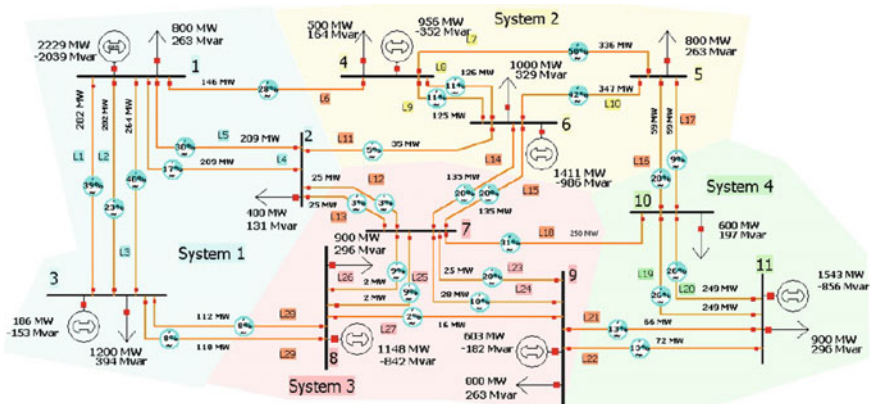


Fig. 11 Schematic diagram of the network model used to examine the power flow control

- System 1, comprising buses 1, 2, and 3 interconnected with lines L1, L2, L3, L4 and L5;
- System 2, comprising buses 4, 5, and 6 interconnected with lines L7, L8, L9 and L10;
- System 3, comprising buses 7, 8, and 9 interconnected with lines L23, L24, L25, L26 and L27;
- System 4 comprising buses 10 and 11 interconnected with lines L19 and L20.

Moreover, L6, L11, L12, L13, L14, L15, L16, L17, L18, L21, L22, L28 and L29 are cross-border lines which integrate all the above-defined component systems into a single large electric power network.

Values of loads and powers generated in individual nodes of the network are presented in Table 1.

Next, simulation of stable operation of the system at constant load values was carried out. The obtained results are presented in Fig. 11 and Table 2.

Table 1 Values of loads and powers generated in network nodes

Load			Generation		
Bus no.	P (MW)	Q (MVar)	Bus no.	P (MW)	Q (MVar)
2	400	131	1 (slack-bus)	2229	-2039
4	500	164	3	186	-153
10	600	197	4	956	-352
1, 5, 9	800	263	6	1411	-986
8, 11	900	296	8	1148	-842
6	1000	329	9	603	-182
3	1200	394	11	1543	-856

Table 2 Power balance in the modelled electric power system

	System 1	System 2	System 3	System 4
Power generated (MW)	2415.37	2367	1751	1543
Power consumed (MW)	2400	2300	1700	1500
Power loss (MW)	74.33	34.04	28.88	39.13
Balance (MW)	-58.96	32.96	22.12	3.87

5.1 System Operation in Conditions of Increased Demand for Energy

To examine how the system behaves in situations when demand for energy is increased, a hypothetical commercial transaction scenario was considered. In System 3, specifically on Bus 9, an increase of electric power consumption by 1800 MW was simulated. The missing energy was transferred from System 1—energy generation on Bus 1 increased.

In the course of analysis of simulation results (Fig. 12; Table 3), the phenomenon of unscheduled flows was observed in the system. The purchased power was not transmitted directly from System 1 to System 3, but in an indirect way by means of using System 2. System 1 was unloaded at the expense of System 2 in which increased power flow occurred. Consequences of unscheduled flows include also an increased transfer of active power on cross-border connections. Line L6 interconnecting System 1 and System 2 is utilised only in 81% which must be considered a serious waste of its transmission capability.

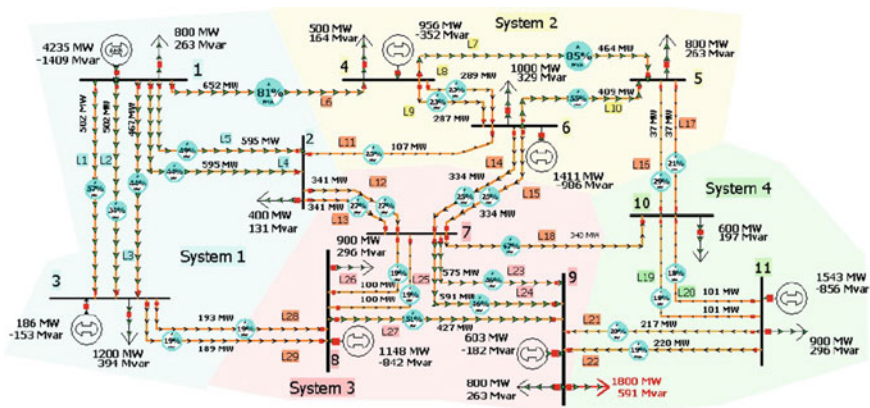


Fig. 12 Schematic diagram of the developed network model—a commercial transaction from System 1 to System 3

Table 3 Power balance in the integrated power system—a commercial transaction from System 1 to System 3

	System 1	System 2	System 3	System 4
Power generated (MW)	4421.43	2367	1751	1543
Power consumed (MW)	2400	2300	3500	1500
Power losses (MW)	192.82	92.72	67.12	29.78
Balance (MW)	1828.61	-25.72	-1816.12	13.22

5.2 A Model of Network with PST

To curb occurrence of the phenomenon of unscheduled flows, a phase shifting transformer was installed in one of cross-border lines. Table 4 summarises basic parameters of the used PST which are given in the device’s catalogue card. The data were used to calculate necessary values of X_{PST} , R_{PST} , B_{PST} and G_{PST} which were then entered to the Power World program in order to configure the simulation correctly.

Figure 13 shows the basic model of the network with PST installed in line L6 connecting System 1 and System 2.

The phase shifter operating range was $\vartheta = \pm 30^\circ$, with angle ϑ being changed in 5° steps.

The results of calculations were then used to draw plots representing active power losses versus PST control angle for individual systems and totalled (Figs. 14, 15).

Table 4 Selected catalogue data of the used PST

Rated power (MVA)	Rated voltage (kV)	Short circuit voltage (%)	No load current (%)	Short circuit losses (kW)
800	400	10	0.06	220

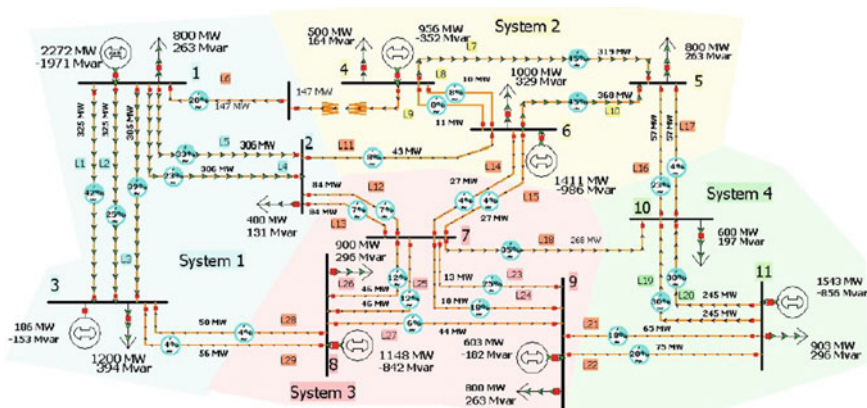


Fig. 13 Schematic diagram of the network model with PST installed in L6

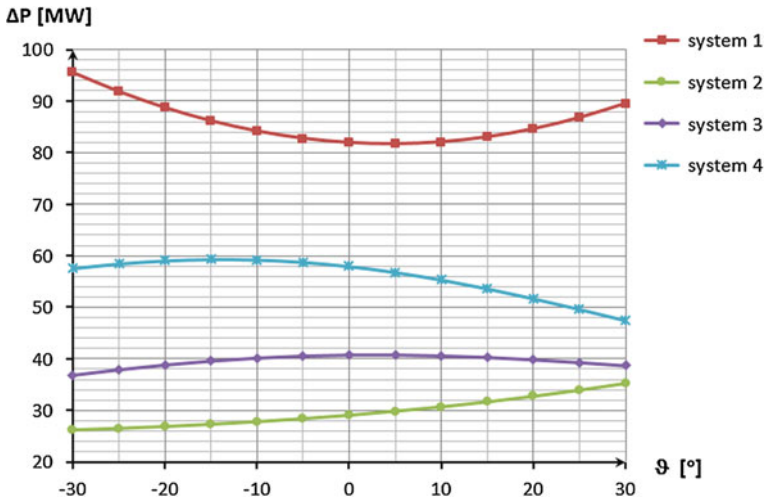


Fig. 14 Active power losses in individual systems—network model with PST

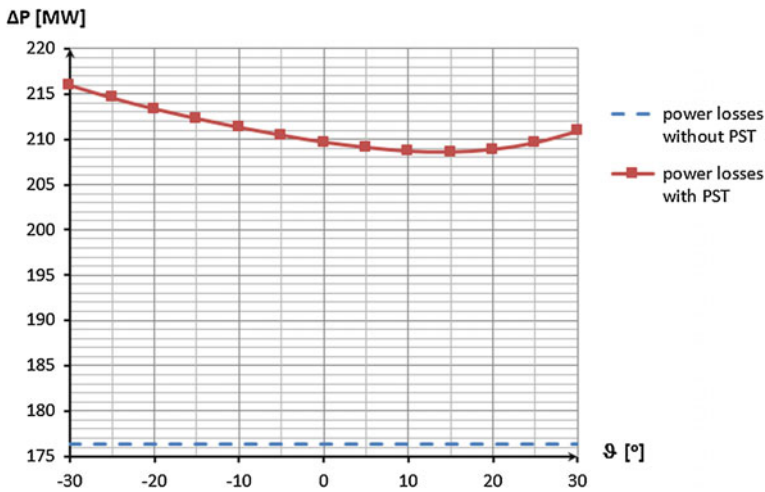


Fig. 15 Total active power losses—network model with PST

Additionally, the obtained values were compared with results of simulation of network with PST not installed. The resulting differences are summarised in Table 5.

After installing PST in line L6, an increase of active power losses were observed in the whole integrated system (Fig. 15). In the system without PST, diagram of which is presented in Fig. 11, there is a free power flow, not restricted in any way. The energy flows are such that total active power losses in the whole system are the

Table 5 Active power losses in individual systems before installing PST

	System 1	System 2	System 3	System 4	Total
ΔP (MW)	74.33	34.04	28.88	39.13	176.38

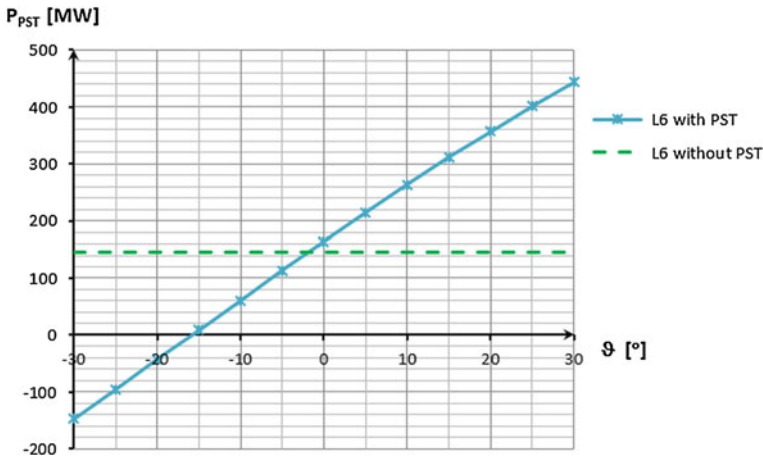


Fig. 16 Active power flow in line L6 with PST installed

least possible. Installing PST in the system results in reduction of active power losses in System 2. However, this is related to an increase of losses in the other systems. It can be said that the phase shifting transformer constitutes a specific protection measure for System 2 against undesired effects connected with unscheduled flows, which is an increase of active power losses.

Based on the simulation model (Fig. 13), the effect of phase shifter installed in line L6 on power transmission in lines of the integrated electric power system was analysed.

Figure 16 shows the quantities of power transmitted through the line in which the phase shifting transformer was installed, as a function of the control angle ϑ .

To get a full picture of results obtained from simulation of the system with installed PST, power flows in transmission lines interconnecting the component systems were measured. The results of the measurements are presented in the form of characteristics plotted in Fig. 17.

It was observed when analysing results of the simulation that installing the phase shifter in the system produces a very significant effect on quantities of power transmitted through cross-border lines. The effect of PST on power transmitted via such connection is different, depending on the value set for the control angle ϑ . The situation is depicted with particular clearness in Fig. 17. It follows from the graph shown in the figure that the phase shifting transformer installed in line L6 has an effect not only on active power transmission lines connecting Systems 1 and 2 (L6, L11), but also on connections between Systems 1 and 3 (L12, L13, L28, L29)

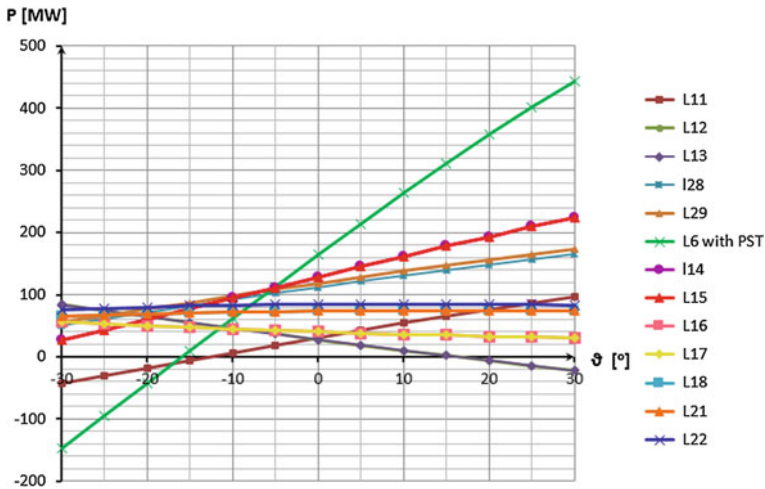


Fig. 17 Active power flow control on connections between the component systems—a model with PST

and Systems 2 and 3 (L14, L15). Apart from that, the phase shifter has a limited effect on energy transfers through the remaining inter-system connections.

Line L6, in which the phase shifter was installed, has an essential effect on power flows in the system. Figure 16 illustrates lucidly what is the dependence of active power flow in the line on value of the control angle set for PST. When value of the control angle ϑ increases, an increase of flow occurs. On the other hand, when value of angle ϑ decreases, a decrease of active power flow in the line is observed. Moreover, for $\vartheta < -15^\circ$, direction of power flow reverses. It is worth noting that when the control angle on PST is set to $\vartheta = 0^\circ$, the absolute value of power transmitted through lines is comparable to this which flows in the system without phase shifter.

5.3 Network Model with TCSC

The basic network model was extended by installing a TCSC in a selected cross-border line in order to curb the effect of unscheduled power flows. Based on formulas (7) and (8), calculations were performed for a TCSC device characterised with the following parameters: $L = 7$ mH and $C = 210$ μ F.

With the use of the obtained results, a characteristic of reactance of the TCSC device X_{TCSC} was plotted as a function of the thyristors firing angle α . In the characteristic, one can distinguish between the following different operating regimes of TCSC device: inductive, resonant and capacitive (Fig. 18).

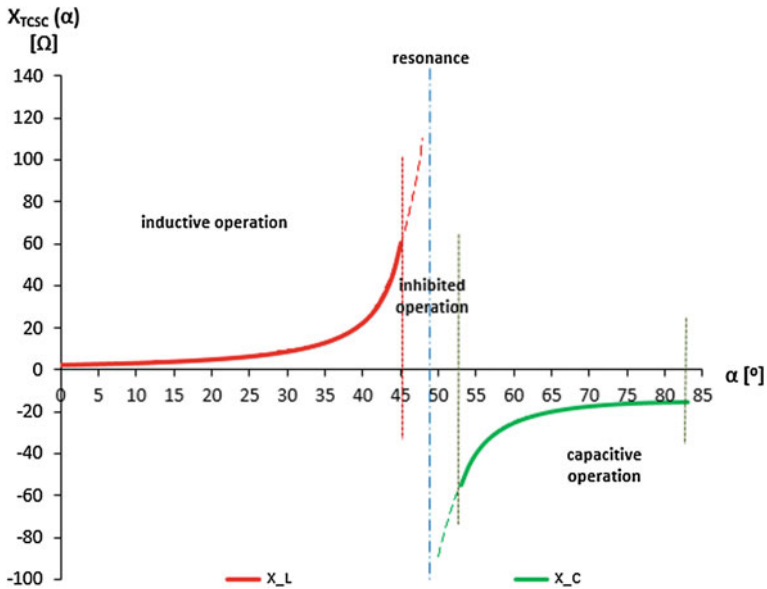


Fig. 18 Reactance X_{TCSC} as a function of the thyristors firing angle α

A simulation of operation of the network (Fig. 11) with TCSC installed in line L6 connecting Systems 1 and 2 was then carried out. In the course of the simulation, the value of TCSC reactance X_{TCSC} was changed while all load values were kept constant.

Results of calculations were then used to draw plots representing active power losses as functions of $X_{TCSC}(\alpha)$ for individual systems and for the whole integrated network (Figs. 19, 20).

Analysis of the obtained results revealed that the combined active power losses were small compared to values measured in the course of simulation without TCSC device. In case of the device operating in the capacitive regime the losses are higher, while in the inductive operating mode the losses are lower compared to those observed before installing TCSC in L6 (Fig. 20). It should be however emphasised that within the TCSC device's safe operating regime, active power losses increase with increasing reactance X_{TCSC} only in System 1, decreasing in the other systems. This situation is represented by the graph shown in Fig. 19.

With the use of results of the simulation, the effect of installing TCSC in line L6 on power flows in the system was analysed. Figure 21 is a graph representing values of power transmitted through line L6 in which TCSC device is installed.

To get a full picture of the results obtained from simulation of the system with installed TCSC, power flows in transmission lines interconnecting the component systems were measured. The results of the measurements are presented in the form of characteristics plotted in Fig. 22.

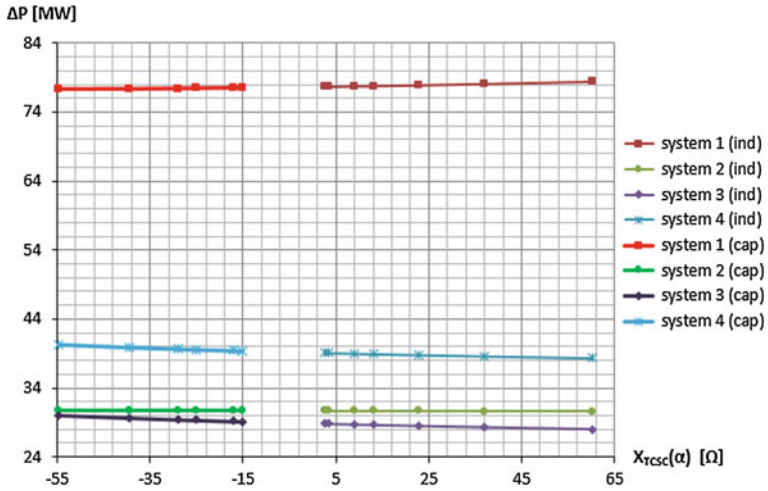


Fig. 19 Active power losses in individual systems—network model with TCSC

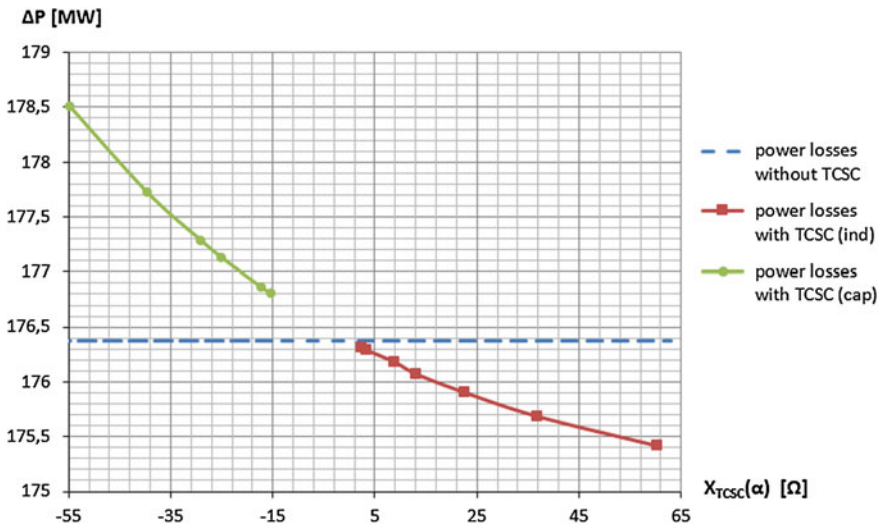


Fig. 20 Total active power losses—network model with TCSC

From graphs presented in Fig. 22 it can be concluded that TCSC installed in line L6 has an effect not only transmission of active power lines connecting Systems 1 and 2 (L6, L11) but also on connections between Systems 1 and 3 (L12, L13, L28, L29) and Systems 2 and 3 (L14, L15). Apart from that, TCSC affects to some small extent the energy quantities transmitted on remaining cross-border connections. The

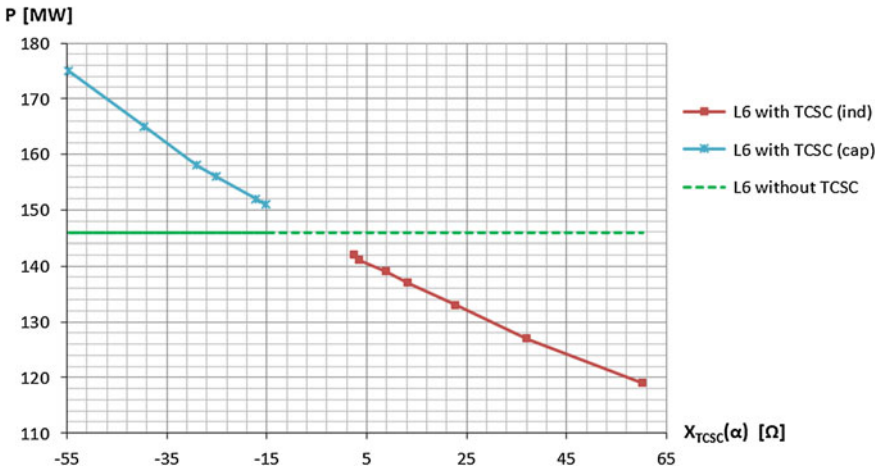


Fig. 21 Active power flow in line L6 with TCSC device

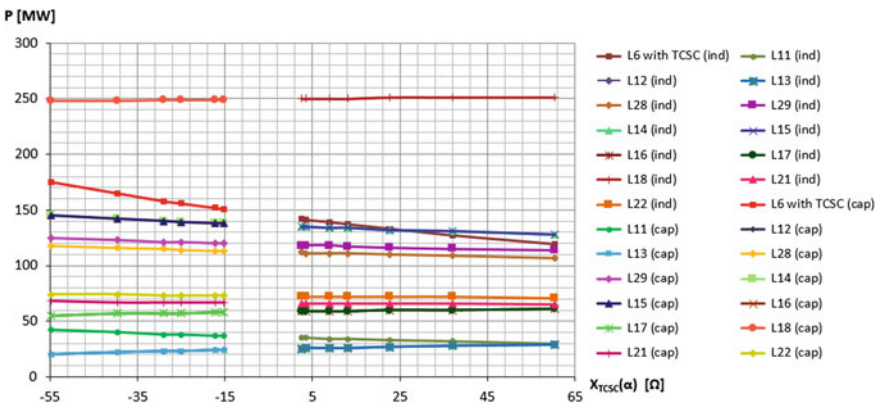


Fig. 22 Control of active power flow on inter-system connections—model with TCSC

most significant effect on power flows in the system is produced by line L6 in which the thyristor-controlled capacitor was installed.

Figure 21 illustrates clearly what is dependence of active power flow in the line on the value of reactance X_{TCSC} .

A comparison of simulation models with PST and TCSC is presented in the form of Table 6. Model features presented in the table refer to the basic simulation model [8].

Table 6 Properties of network models with PST and TCSC installed

	Model with PST	Model with TCSC
Control method in PowerWorld program	Changing the phase shifter's control angle ϑ	Changing reactance X_{TCSC} by setting thyristors firing angle α
Active power losses in the whole system	<ul style="list-style-type: none"> • Variable losses depending on angle ϑ values; • Increase of total loss by 18.3–22.5% 	<ul style="list-style-type: none"> • Variable losses depending on X_{TCSC}; • Capacitive regime = higher total losses 0.2–1.2%; • Inductive regime = lower total losses 0.1–0.5%
Power transmitted in individual systems	With increasing angle ϑ : <ul style="list-style-type: none"> • In System 1, transmission of power decreases, • In System 2, power transmission increases, • Strong links between power quantities transmitted between Systems 1 and 2 • In Systems 3 and 4, small changes of transmitted energy [8] 	With increasing reactance X_{TCSC} : <ul style="list-style-type: none"> • In System 1, power transmission increases; • In System 2, transmission of power decreases; • Moderate links between power quantities transmitted between Systems 1 and 2; • In Systems 3 and 4, small changes of transmitted energy [8]
Power transmitted through cross-border line L6	<ul style="list-style-type: none"> • Power transmitted through the line varies and depends on angle ϑ; • Load on line L6 varies in wide range; • Option to change direction of energy flow 	<ul style="list-style-type: none"> • Power flow on the line varies and depends on reactance X_{TCSC}; • Narrow range of load changes in line L6; • No option to change direction of energy flow
Capability to block power flow	Is possible by proper setting the PST control angle ϑ	No such option
Additional advantages	<ul style="list-style-type: none"> • Network components protected against thermal overloads • Increased number of inter-area transactions 	<ul style="list-style-type: none"> • Reduction of short-circuit currents • Damping of oscillations • Voltage stability improvement

6 Conclusion

The paper is focused on the issue of unscheduled power flows. In particular, possible ways to counteract the phenomenon by means of controlling power flows on cross-border connections were analysed. To this end, PowerWorld software package was used to reproduce a fragment of electric power network utilised then to simulate different operating states of the system. To analyse the phenomenon of unscheduled power flows, a basis network model was created. Further, by adding blocks representing PST and TCSC to the system, models of networks with power flow control devices were developed. Comparing the effect of installing the transformer- and capacitor-based compensators on formation of power flow patterns it was found that devices of both types provided protection against negative effects

pertaining to occurrence of unscheduled flows. Active power losses in the system were larger compared to those observed in the model with phase shifting transformer. However, as far as the power flow control range is considered, it turned out to be much larger in case of installing PST than the control range available with TCSC. What is more, PST allows to “block” and change direction of flow through a cross-border line. On the other hand, TCSC performs well as a device damping oscillations in the system. Making a decision on selection of proper solution for active power flow control in a power network it is necessary to consider the existing needs and tasks to be realised by the device.

References

1. Loop flows—final advice. (2016, April 20) Retrieved from https://ec.europa.eu/energy/sites/ener/files/documents/201310_loop-flows_study.pdf
2. Kolcun, M., Beňa, L.: Using of Specialised Devices for Power Flow Control in Electric Power Systems. Technical University of Kosice, Kosice (2011). (in Slovak). ISBN 978-80-553-0767-1
3. Hingorani, G.N., Gyugyi, L.: Understanding FACTS. Concepts and Technology of Flexible AC Transmission Systems. IEEE Press, New York (2000). ISBN 0-7803-3455-8
4. Song, Y.H., Johns, T.A.: Flexible ac Transmission Systems (FACTS). IEEE Press, London (1999). ISBN 0-85296-771-3
5. Mathur, R.M., Varma, K.R.: Thyristor-based FACTS controllers for electrical transmission systems. IEEE Press, USA (2002). ISBN 0-471-20643-1
6. Zhang, X., Rehtanz, Ch., Pal, B.: Flexible AC Transmission System: Modelling and Control. Springer, Berlin (2006). ISBN 3-540-30606-4
7. The visual approach to electric power systems. (2016, April 15) Retrieved from <http://www.powerworld.com/>
8. Rydz, P.: Active power flow control in cross-border lines. Diploma work. Rzeszow University of Technology, 2016 (in Polish)

Wind Farm Fluctuation Suppression Using Energy Storage

Bartosz Wańkiewicz

Abstract Because of constant technological advancement, lowering costs and different law and regulations this paper deals with reducing the negative influence of the wind farms on the power grid, enabling higher renewable power penetration. The chosen way of achieving this is incorporating energy storage systems in wind farms. A control algorithm has been proposed along with sizing method based on said control method.

Keywords Renewable energy · Wind power · Power quality · Energy storage · Monte Carlo

1 Introduction

In the last half of century, there has been a steady increase of energy consumption coupled with increasing environmental concerns. This makes modernizing the energy grid a necessity [1]. Modern energy grids produce more energy and are more efficient thanks to higher renewable energy penetration. They put less emphasis on fossil fuels and incorporate more distributed generating units.

This makes maintaining high power quality indices and system stability much harder because of higher number of generating stations. Many of which have greater variation in output power levels than traditional fossil power plants [1]. It is possible, however, to make renewable generating stations more stable by adding energy storage systems. The type, characteristics, and capacity depend on the role of the storage.

Local law and legal regulations often enforce certain parameters to be met for the far to be connected to the energy grid. According to Polish power traffic regulations [2, 3], a wind farm

B. Wańkiewicz (✉)

Institute of Electrical Engineering, University of Zielona Góra, Zielona Góra, Poland
e-mail: b.waskowicz@iee.uz.zgora.pl

- Cannot output sudden spikes or dips exceeding 3% of reference power level
- Must have a short-term flicker factor below 0.35.

2 Control Method

2.1 Method Types

There is no generally accepted framework and many methods exist and are being used for determining the required storage size. However two of those are most prevalent, the deterministic and stochastic approach.

Other methods include genetic algorithms [4], artificial neural networks [5], applying low-pass filter methodology [6], and using inventory models [7].

Deterministic methods [8–11] rely on a complicated mathematical models to analyze the system with numerous parameters that require determining and variables. They are most often used for making a day-ahead forecast. To make a day-ahead forecast it is impossible to do so based on statistical data alone [9]. Therefore they often incorporate meteorological data, historical data, which often are uncertain which makes it difficult to implement and determine the expected accuracy, because there are no widespread forecast tools [10]. Also the forecast error greatly impacts the required storage capacity [9, 10]. Although wind farms are proven to function making a day-ahead forecast using this method [11] they involve very large capacities.

Stochastic approach [1, 12, 13] may appear more intuitive when dealing with such unpredictable elements as the weather without any meteorological data. It is best suited for short-term prediction although there are instances where a stochastic algorithm using weather data has been used to make a day-ahead forecast [1, 10]. Using statistical methods is convenient because it does not require determining numerous parameters and it is possible to get an accurate confidence level using a cumulative distribution. Stochastic methods are also easier to implement, are capable of short-term forecast, which potentially may cause it to be widely used in the future.

2.2 Proposed Method

The aim of the proposed method is to reduce the negative wind farm influence on the power grid, by using as small energy storage capacity as possible. For minimizing storage size a prediction part of algorithm was created. Its task is to identify a trend of power generation for 1 min ahead, determining the next interval's static power level. This method uses Monte Carlo simulation in setting a prediction and is stochastic in nature. The algorithm tests were run also on 10 min intervals. Unlike

complicated deterministic forecast methods, proposed method does not require determining numerous parameters, nor does it need current and historical meteorological data.

3 Wind Data

Wind data used in this paper consist of the measurements of power outputs of two wind farms

- Location A Wind Farm ($12 \times 3.3 \text{ MW} = 39.6 \text{ MW}$) measurement span over the period of 31 months.
- Location B Wind Farm ($12 \times 2.5 \text{ MW} + 2 \times 3.3 \text{ MW} = 36.6 \text{ MW}$) measurement over period of 37 months

It is important to point out that the above-mentioned data do not allow for in-depth analysis of output power level short-term dynamics, they do allow however, for active power output estimation over long periods of time (months/years). Knowledge of short-term (minute and below) power fluctuations is necessary in power prediction and regulation. Figure 1 illustrates the averaged values of active power. The values obtained for different wind speeds are presented with histograms.

A power curve was estimated based on those power levels. Power curve obtained from this analysis was used for further study.

Having solid information of short-term fluctuations is vital for simulating power distribution and the state of charge for one-minute intervals. Information about 10 min power variation will be the starting point for further calculations. It is important to point out that used data do not allow for in-depth analysis of power level dynamics, they do allow however, for active power output estimation over long periods of time (months/years). Knowledge of short-term (minute and below) power fluctuations is necessary in short-term power prediction and regulation.

Distribution of averaged 10-min power increases is symmetrical with respect to 0. This means that in every next interval increase or decrease in power is equally likely. As presented in Table 1, the changes are in the range of -39.6 – 39.6 MW . Furthermore around 99% of changes are in the range of -11 – 11 MW . Analysis of 99% of cases is especially important in accordance to the Polish power traffic regulations. Those regulations demand that the power quality indices to be above a certain level 99% of the time in a period of one week [2]. Table 1 shows how selection of a storage for 99% cases of power changes allow for significant reduction of storage capacity.

Identical analysis was carried out for Location B wind farm and very similar results were achieved.

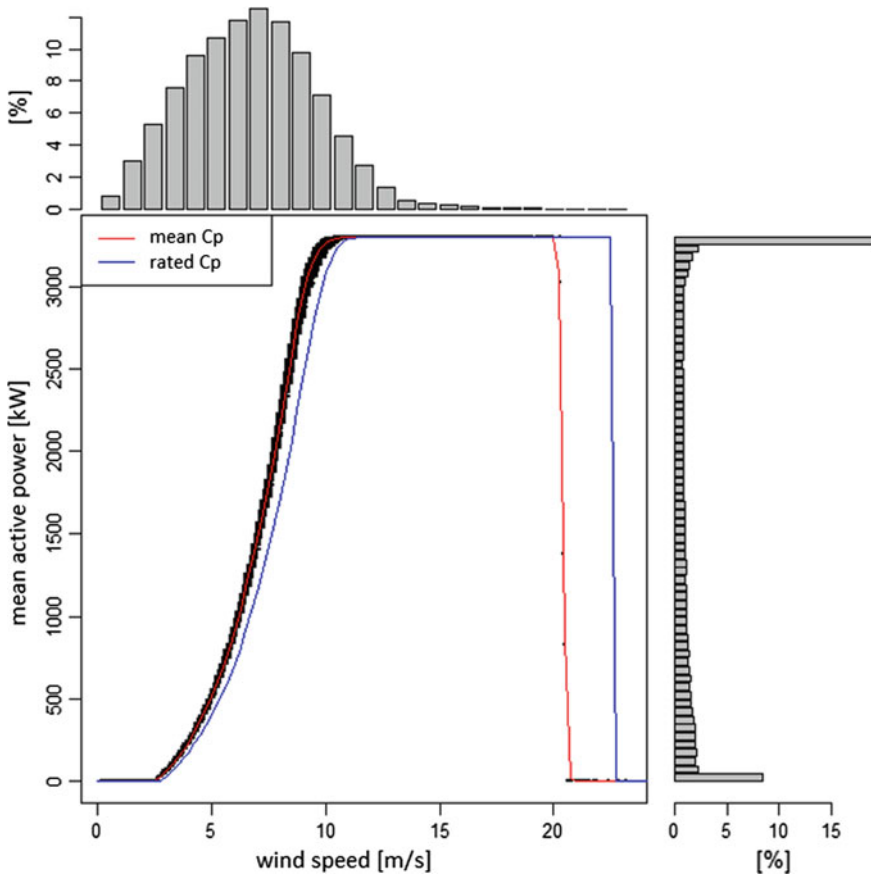


Fig. 1 Power curves and histograms of wind farm at location A

Table 1 Ranges of generated wind farm power changes

Quantile of power change (kW/10 min)						
Min	0.5%	25%	50%	75%	99.5%	Max
-39,600	-11,313	-875	0.0	846	11,858	39,600

4 Statistical Analysis

The reason of the simulation is the selection of power storage to achieve a constant level of output power in one-min intervals. Reference power level for the *i*-th cycle is determined by the average value wind farm output power *P_{wf}* in previous cycle and the state of charge of the storage system according to the formula:

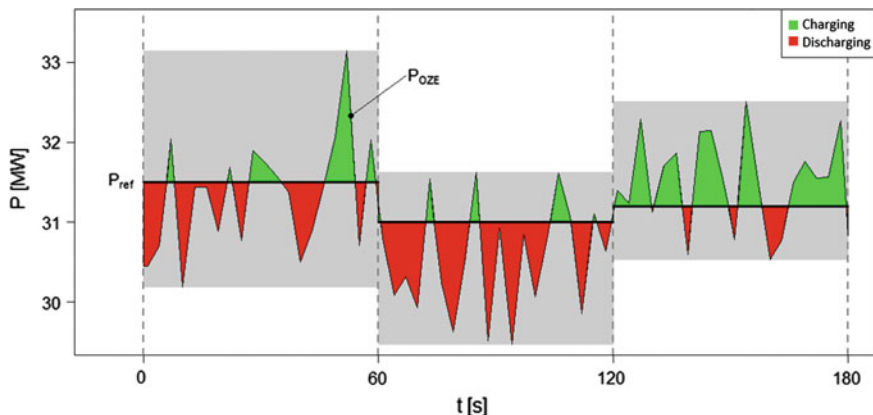


Fig. 2 Fluctuations of the active power without magazine (P_{wf}) and with energy storage (P_{ref}) [16]

$$P_{ref,i} = \frac{1}{n} \sum_{j=1}^n P_{wf,i-1}(t_j) + A_{i-t}(t_0) \tag{1}$$

This model allows to control the state charge of the storage system by making a prediction of active power in following one-minute intervals shown on Fig. 2. Amount of power required to compensate the power fluctuations and calculated power prediction values are the basis for determining the energy storage capacity. For this analysis it is assumed that the base state of charge is 50%. The capacity calculated from this simulation is the required minimum usable capacity. If chosen battery technology do not allow for total discharge, it is necessary to increase the capacity of the energy storage accordingly. The changes of wind farm power output without and with storage are illustrated on Fig. 2 in the form of a graph. Power output with the storage system is identical to the predicted power values (P_{ref}).

5 Simulation Assumptions

Set reference power levels, thanks to energy storage, allow for elimination of short-term power fluctuations.

1. Simulation only involves power changes from ranges between starting speed and rated rotational speed or the rotor.
2. Short-term fluctuation have been simulated from experimental results of the study published in “Wind farms in the power system” monograph by Zbigniew Lubośny, WNT publishing house, Warsaw [14]. Used power curve was estimated on the basis of provided data.

3. Multiple possible types of trends were considered
 - (a) large–medium frequency of changes of trend direction every 10 min,
 - (b) medium–medium frequency of changes of trend direction every 1–2 min.
4. Trend slope was set in two variants
 - (a) Large—in the range from 0.9 to 11 MW/10 min,
 - (b) Small—in the range from 0 to 0.9 MW/10 min

Ranges mentioned above result from the distribution of power changes calculated from provided data simulation (10-min changes).

5. Received simulation data only contained information about power fluctuations every 10 min. Additional data about short-term changes were injected, which are required for analysis of wind farms with storage. Said data were adjusted in accordance with the data found in the literature, so the variation of power in the 10 min intervals is consistent with the simulation data provided.

Simulation analysis were conducted for two wind farms in four variants: (Table 2).

6 Simulation Results

All simulation results are listed in Table 3. Results show strong dependence of required capacity on the trend of power fluctuation slope.

All current energy storage technologies can be divided into roughly three kinds according to their application based on their parameters and characteristics.

Long-term storage (hours-months)

- Pumped hydro storage (PHS)
- Compressed Air Energy Storage (CAES)
- Hydrogen-based Energy Storage System (HESS)

Medium-term storage (minutes-hours)

- Battery Energy Storage System (BESS)
 - Lead-Acid battery (LA)
 - Nickel–cadmium battery (Ni–Cd)
 - Sodium–sulfur battery (NaS)

Table 2 Symulation variants

	Slope (MW/10 min)	Trend (min)
Simulation 1	0.9–11	10
Simulation 2	0.9–11	1
Simulation 3	0–0.9	10
Simulation 4	0–0.9	1

Table 3 Full list of estimates of the minimum usable capacity (C_{min}) based on 99% power change reference (P_{ref}) for all the analyzed cases

	Reference power (kW)		Energy storage (kWh)				
	Max	99%	Max	Min	99% range	C_{min}	
<i>Location A wind farm</i>							
S. 1.	3420.7	2079.2	-44.1	46.4	-26.4	25.8	52.8
S. 2.	3404.7	1980.5	-43.0	49.5	-25.1	25.1	50.1
S. 3.	2270.6	1538.3	-35.2	36.4	-19.8	19.6	39.7
S. 4.	2409.5	1532.3	-35.0	36.5	-19.7	19.8	39.6
<i>Location B wind farm</i>							
S. 1.	3252.8	1697.0	-36.5	39.6	-23.0	21.2	45.9
S. 2.	2526.3	1704.0	-36.0	36.4	-21.1	21.2	42.4
S. 3.	1969.7	1137.6	-27.8	29.4	-15.0	14.9	30.1
S. 4.	1730.1	1148.6	-28.5	27.9	-14.7	15.0	30.1

– Lithium-ion battery (Li-ion)

- Flow Battery Energy Storage System (FBESS)

Short-term storage (seconds-minutes)

- Flywheel Energy Storage System (FESS)
- Superconducting magnetic energy storage (SMES)
- Supercapacitor energy storage system (SCESS)

Although all above-mentioned technologies have their uses. Long-term energy storage is used for peak shaving and time shifting. Because this paper deals with reducing the high-frequency power variation, the short-term storage will be the main focus.

Expected cycle time while fluctuation suppression is around 1 min. Additionally, smoothing the power output does not require large capacities of the storage system. It is interesting that, when considering technologies with almost unlimited cycles, short cycles while smoothing are actually beneficial as it reduces the required storage capacity even further. However, this task requires the storage system to be able to inject or absorb power for less than a minute for power smoothing of wind turbines. To achieve that it is necessary to use an energy storage technology that allows for near-instantaneous reaction, and can input or output energy with little to no delay.

Electrochemical batteries are not optimal for power smoothing due to limited cycle life not exceeding few thousand cycles and lower specific power.

6.1 FESS

A Flywheel Energy Storage System is an electromechanical device that converts electrical energy into kinetic energy and stores it using a rotating mass. The mass is placed in a vacuum and mounted on two magnetic bearings in order to decrease

friction at high speed. The mass is coupled with an electric machine. Energy is transferred to the flywheel when the machine operates as a motor, charging the energy storage device. Similarly the energy is discharged when the electric machine operates as a generator. FESS presents a wide array of helpful features for this specific application like, long cycling life, wide operating temperature range, high power and high energy density, and depth-of-discharge effects do not apply here. Other features like self-discharge rates around 20% of the stored capacity per hour do not impact the system significantly.

6.2 *SCESS*

Supercapacitors, also known as ultracapacitors, store charge on the interface between the surfaces of the electrolyte and the two conductor electrodes. The energy stored in the capacitors is directly proportional to their capacity and the square of the voltage between the terminals. The capacity is proportional to the surface area of the electrodes and inversely proportional to the distance between them [15]. Because the voltage and capacity of a single cell is low, it is necessary to connect cells in series and parallel to achieve the desired parameters of the supercapacitor. Short time constants, short response times, high number of cycles, long life and high power makes supercapacitors a good choice for fluctuation suppression. When selecting ESS technology low supercapacitor's energy and high price have to be taken into account.

6.3 *SMES*

SMES stores energy in a magnetic field created by a DC current through a superconducting coil maintained at constant cryogenic temperature. The characterization of the coil has a main role in the system specification. Superconducting coils can be divided to: High Temperature Coils, and Low Temperature Coils depending on the system operating temperature. Because of the low operating temperatures, a cooling system must be considered as an element of fundamental role obtaining a superconducting state of the coil. However, the energy, the system requires to maintain proper temperature is much smaller than energy stored in the system. Most important feature of SMES systems for power smoothing is ability to inject or absorb large amounts of energy in a very short amount of time. The power of these systems ranges from 100 kW to 100 MW. Additionally energy densities are higher than those of flywheels and supercapacitors [15].

Table 4 Selected parameters of chosen storage technologies [15]

Type	Power output (MW)	Energy stored (kWh)	Capital cost (PLN/kWh)
FESS	0.1–10	5–15	40,000
SCESS	0.001–0.1	0.1–10	80,000
SMES	0.1–100	1–15	60,000–120,000

6.4 Costs

Energy efficiency of all above-mentioned technologies are around 85%, lifetime over 20 years and around 1,000,000 cycles, additionally all three technologies have self-discharge rates that render them unsuitable for long-term storage [15]. For short-term storage their self-discharge rates are irrelevant (Table 4).

7 Conclusions

In modern times, it becomes necessary to steadily increase the power grid penetration of renewable energy generation. Because they are less stable and have larger variation of output power, the aim of this article is an efficient method of dimensioning energy storage using developed control algorithm used in conjunction with before-mentioned wind farms, decreasing their output power variation. Wind data is analyzed and used to draw cumulative distributions that are calculated for capacity to confidence level relation assessment. The developed control method is stochastic in nature and is based on 1 and 10 min forecasts and set constant power levels in those intervals. This way, this method reduces power variation and helps to minimize the needed storage capacity. The predictive part of the algorithm allows for even further minimization of storage capacity in reference to non-predictive methods.

The capacities received from the analysis using the developed algorithm are quite small in comparison to other methods and applications found in the literature. Using proposed method resulted in using 52.8 kWh for 39.6 MW wind farm which makes 1.3 kWh/MW and 45.9 kWh for 36.6 MW which makes 1.25 kWh/MW. Also the P_{ST} factor has been significantly reduced from 0.5 to 0.17, which is a 68% reduction. For instance in [6] a storage capacity of 5 kWh/MW reduces the standard deviation of generated power by 10% and storage capacity of 25 kWh/MW reduces the standard deviation by 50% in most cases. Using energy storage to improve power indices is relatively cheap but, at the same time is an essential and required under certain local law and regulations for a wind farm to take part in energy exchange in the power grid.

Storage technologies suitable for fluctuation suppression present high ramp power rates and high cycling capability, since fast power modulation and

continuous operation are required. With that in mind supercapacitors, flywheels and SMES are best suited for fluctuation suppression.

Further studies can be based on hybrid energy storage especially focusing on the economic aspect of storage devices. Hybrid storage systems contain storage of multiple types and technologies. Typically smaller one but with high power output to reduce high-frequency power variation and with much larger capacity to minimize cost while meeting power output requirements in specific situations. Building a hybrid is a complicated task with multiple factors to consider, the role of the whole system, and what tasks should it be capable of doing. It all makes every hybrid storage system a tailored project for a specific application. Economics may play the most important role in the design process because of the different prices of each component storage and the proportions of the component storage.

References

1. Shokrzadeh, S., Jozani, M.J., Bibeau, E., Molinski, T.: A statistical algorithm for predicting the energy storage capacity for baseload wind power generation in the future electric grids. *Energy* (2015)
2. Instrukcja ruchu i eksploatacji sieci przesyłowej. Warunki korzystania, prowadzenia ruchu, eksploatacji i planowania rozwoju sieci. Wersja 2.1 Tekst jednolity po Karcie aktualizacji CK/1/2012 zatwierdzonej decyzją Prezesa URE nr DPK-4320-2(16)/2010÷2013/LK z dnia 29 stycznia 2013 r
3. Norma PN-EN 50160: 2002. Parametry napięcia zasilającego w publicznych sieciach rozdzielczych
4. Luo, Y., Shi, L., Tu, G.: Optimal sizing and control strategy of isolated grid with wind power and energy storage system. *Energy Conversion Manage.* **80**, 407–415 (2014)
5. Zhang, Y., Tang, X., Qi, Z., Liu, Z.: The Ragone plots guided sizing of hybrid storage system for taming the wind power. *Electr. Power Energy Syst.* **65**, 246–253 (2015)
6. Paatero, J.V., Lund, P.D.: Effect of energy storage on variations in wind power. *Wind Energy* **8**(4), 421–441 (2005)
7. Schneidera, M., Bielh, K., Pfallera, S., Schaede, H., Rinderknechta, S., Glock, C.H.: Optimal sizing of electrical energy storage systems using inventory models. *Energy Procedia* **73**, 48–58 (2015)
8. Singh, R., Xie, L., Kumar, P.R.: On storage and renewables: a theory of sizing and uncertainty. *IEEE Power and Energy Society General Meeting, Denver, July 26–30* (2015)
9. Jaworsky, C., Turitsyn, K., Backhaus, S.: The effect of forecasting accuracy on the sizing of energy storage. In: *ASME 2014 Dynamic Systems and Control Conference*
10. Haessig, P., Multon, B., Ahmed, H.B., Lascaud, S., Bondon, P.: Energy storage sizing for wind power: impact of the autocorrelation of day-ahead forecast errors. *HAL* 2013
11. Korpaasa, M., Holena, A.T., Hildrumb, R.: Operation and sizing of energy storage for wind power plants in a market system. *Electr. Power Energy Syst.* (2003)
12. Pinson, P., Papaefthymiou, G., Klockl, B., Verboomen, J.: Dynamic sizing of energy storage for hedging wind PowerForecast uncertainty. In: *Power and Energy Society General Meeting, 2009. PES '09. IEEE*
13. Musolino, V., Pievatolo, A., Tironi, E.: A statistical approach to electrical storage sizing with application to the recovery of braking energy. *Energy* (2011)
14. Lubośny, Zbigniew: “Wind farms in the power system” monograph. WNT Publishing House, Warsaw (2013)

15. Díaz-González, F., Sumpera, A., Gomis-Bellmunta, O., Villafáfila-Robles, R.: A review of energy storage technologies for wind power applications. *Renew. Sustain. Energy Rev.* **16**, 2154–2171 (2012)
16. Bojarski, Jacek., Smoleński, Robert., Kaniewski, Jacek.: Analysis in terms of power storage dimensioning. University of Zielona Góra, Zielona Góra (2015)

Simulations and Experimental Investigations of an Impulse System for Battery Charging in Electric Bike

Krzysztof Ludwinek, Jan Staszak, Roman Nadolski,
Zbigniew Gawecki, Jaroslaw Kurkiewicz and Tomasz Bekier

Abstract The paper presents simulation results of a push–pull converter allowing energy recovery back to two Sealed Lead-Acid 7 Ah, 12 V serially connected batteries. The converter is powered by three phases of induced voltage from a BLDC motor mounted in the front wheel hub of an electric bike. In a steady state, computed current and voltage waveforms were verified experimentally in the measurement stand on the basis of registered waveforms.

Keywords BLDCM · Generator · Battery charging · Electric bike · Control system

1 Introduction

Utilization of electric bicycles as means of personal transportation, especially in cities, is of great importance from the point of view of ecology and health benefits [1–5]. Replacing internal combustion powered vehicles by classic or electric bikes utilizing maintenance-free batteries reduces greenhouse gas emissions.

K. Ludwinek (✉) · J. Staszak · R. Nadolski · Z. Gawecki · J. Kurkiewicz · T. Bekier
Faculty of Electrical Engineering, Automatic Control and Computer Science,
Kielce University of Technology, Kielce, Poland
e-mail: k.ludwinek@tu.kielce.pl

J. Staszak
e-mail: j.staszak@tu.kielce.pl

R. Nadolski
e-mail: r.nadolski@tu.kielce.pl

Z. Gawecki
e-mail: zgaw@tu.kielce.pl

J. Kurkiewicz
e-mail: jkurkiewicz@tu.kielce.pl

T. Bekier
e-mail: tbekier@tu.kielce.pl

Electrically powered vehicles can, for example, be topped-up when there is an oversupply in the power grid. At the same time, electric bikes can be considered a form of distributed energy storage [6–8].

Most imported electric bikes in Poland lack advanced control system able to efficiently charge the batteries during generative operation of the electric motor [2]. Such systems in electric bicycles could be used in a variety of situations such as riding through the terrain with varying levels of elevation, during braking or pushing the bike while dismounted.

This article describes an attempt by the authors to develop a control system for a $P_N = 125$ W and 24 V brushless direct current motor (BLDCM) placed in the electric bike's front wheel hub. During generative operation of the BLDC motor, the control system allows to charge a set of two serially connected HV7, 12 V and 7 Ah Seal Lead-Acid (SLA) batteries. The article also presents a simulation study in MATLAB-Simulink and experimental investigations of the BLDC motor performed on a measurement stand.

2 Simulation Model

The most important part, both during charging and discharging, of the BLDCM control system analyzed in this paper are batteries. Batteries' parameters during charging and discharging change nonlinearly. The most important parameters used to model batteries are the effective internal resistance (influenced by electrolyte and electrode type) and voltage. A method of modeling the battery's behavior during operation is quite complex, as it requires to determine a number of coefficients [9–12]. Battery manufacturers provide only the most basic parameters such as: voltage, capacity, or start-up current. Internal resistance or supply voltage characteristics as a function of current and charge are omitted.

Creation of an appropriate simulation model of a BLDC motor during generative operation makes it possible to determine the optimal value of the charging current, instantaneous current, and voltage waveforms and power losses in the individual components of the system consisting of the BLDC motor, rectifier, push–pull converter, and the battery pack. Therefore, in this article, the model of the battery's behavior in MATLAB-Simulink utilizing SimPowerSystem toolbox, during BLDCM's generative operation, is presented. SimPowerSystem toolbox provides multiple battery models such as (for 2010b version): Lead-Acid, Lithium-Ion, Nickel-Cadmium, and Nickel-Metal-Hydride. Figure 1 shows a system schematic which allows one to simulate the process of battery charging from a voltage source—BLDC motor during generative operation.

In order to carry out simulation tests of the charging process in the system as in Fig. 1, it is necessary to know the source voltage and internal resistance of the tested batteries. The article assumes that the battery is 90% charged and it is modeled by defining a nonlinear internal resistance and the nonlinear voltage source, which depend only on the value of current. Figure 2 shows the

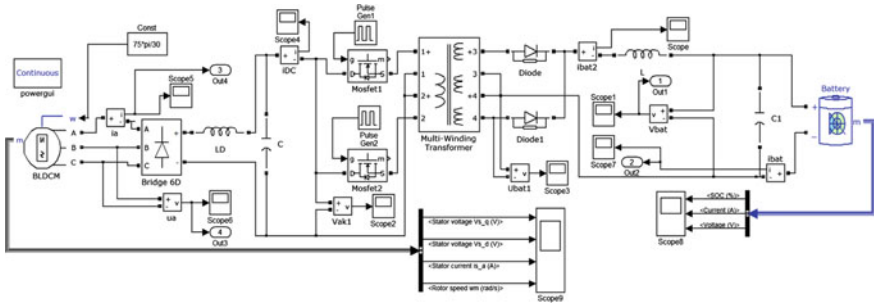


Fig. 1 Schematic of a system used for simulation of a battery charging process

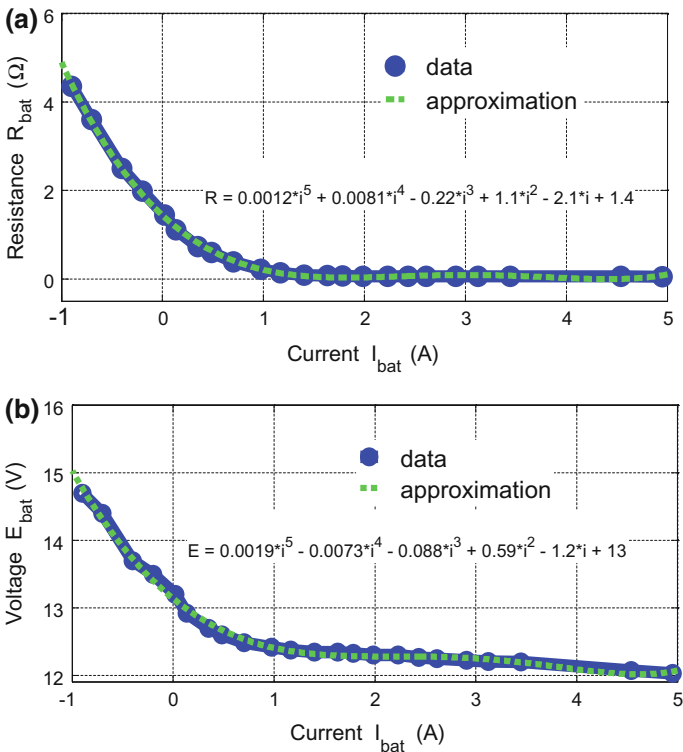


Fig. 2 a internal resistance and b source voltage characteristics of the 7 Ah, 12 V battery as a function of load current

characteristics of changes in the internal resistance of a Sealed Lead-Acid 7 Ah, 12 V (90% charged battery).

The characteristics shown in Fig. 2 were obtained experimentally by performing a very short load current measurements using a differential method. The study was

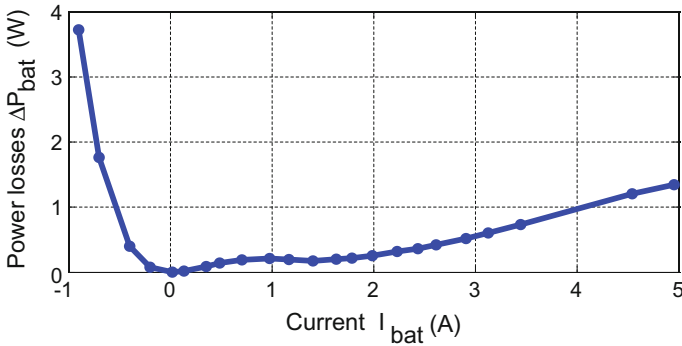


Fig. 3 Power losses ΔP_{bat} of a single battery

performed for small current increments around the base currents shown in Fig. 2 (data points). After each voltage and current measurement, the battery was disconnected for a time needed for the source voltage E_{bat} to return to the initial state E_{bat0} .

A similar procedure was used for determination of the characteristics during battery charging. Positive current in Fig. 2 indicates that the BLDC motor is being supplied from the battery, while negative current indicates the charging process. From the characteristics presented in Fig. 2, it is possible to determine power losses ΔP_{bat} , which occur during the battery charging process (negative current) or while the motor is being supplied (positive current).

From the power loss characteristics in Fig. 3, it follows that during the battery charging process, as a result of an increase in its internal resistance, applying current greater than 0.1 Q (where Q is the battery's capacity—7 Ah) results in greater power losses than for the same current when motoring.

3 Simulation Results

Figures 4 and 5 show waveforms of i_{bat} charging current, u_{bat} battery voltage as well as u_a phase voltage and i_a phase current of the BLDCM, while charging two batteries in a set, calculated from the model shown in Fig. 2.

The generative operation model of the BLDC motor consisting of a push-pull converter and battery set makes it possible to determine instantaneous values of voltage and current waveforms.

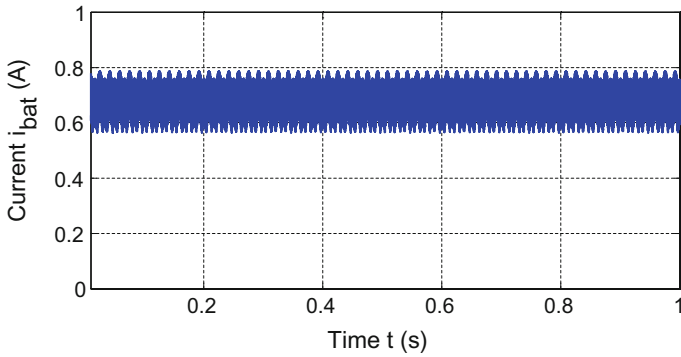


Fig. 4 Waveforms calculated on the basis of the model from Fig. 2 of battery charging current i_{bat}

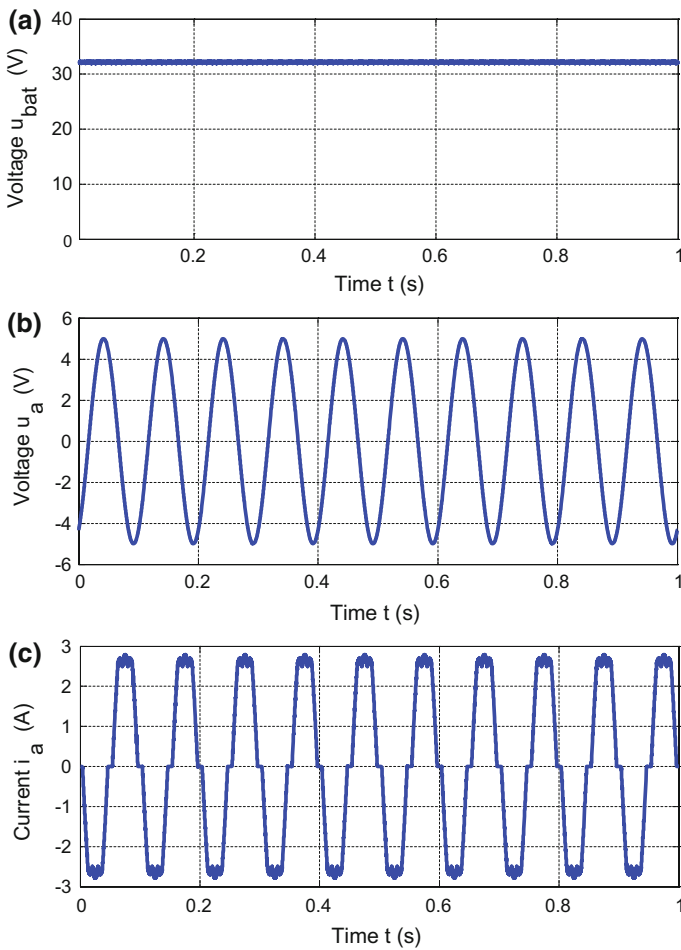


Fig. 5 Waveforms calculated on the basis of the model from Fig. 2 of **a** battery voltage u_{bat} , **b** u_a motor phase voltage and **c** i_a phase current of the BLDC motor

4 Results of Experimental Investigations

Figure 6 presents a simplified schematic of the power and control parts of the impulse circuit used for energy recovery from BLDC motor’s phase winding induced voltages.

The converter presented in Fig. 6 operates in push–pull configuration and is used to boost the voltage in order to charge two 7 Ah, 12 V serially connected batteries. The charging process starts when BLDC motor’s induced phase voltages reach 1.6 V. The charging current values are regulated by potentiometers and PWM circuit in the range between 0 and 0.7 A and set to reach 0.1 Q value in the finishing part of the charging process. The charging current can be arbitrarily changed depending on the rotational speed of the BLDC which corresponds to induced voltage values. The control part of the impulse circuit was implemented using Silicon SG2525A integrated circuit [13].

Figure 7 presents an overview of examined BLDC motor (operating as a generator) and other important devices incorporated into the measurement stand.

The measurement stand (Fig. 7) consists of the following:

- BLDC motor rated at 125 W, $U_N = 24$ V, $n_N = 120$ rpm, mounted in the electric bike’s front wheel hub;

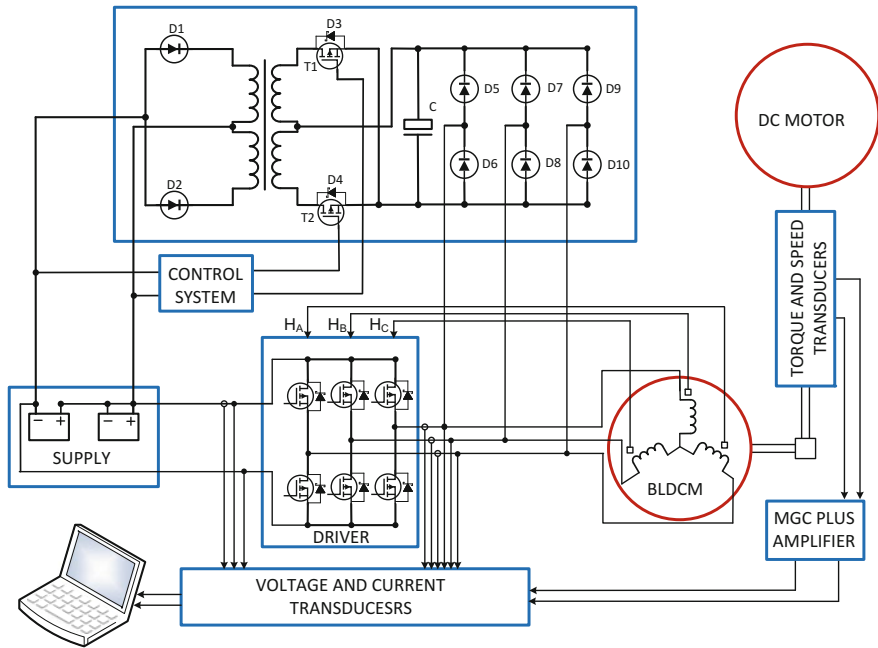


Fig. 6 Simplified schematic of the power and control parts of the impulse circuit used for energy recovery

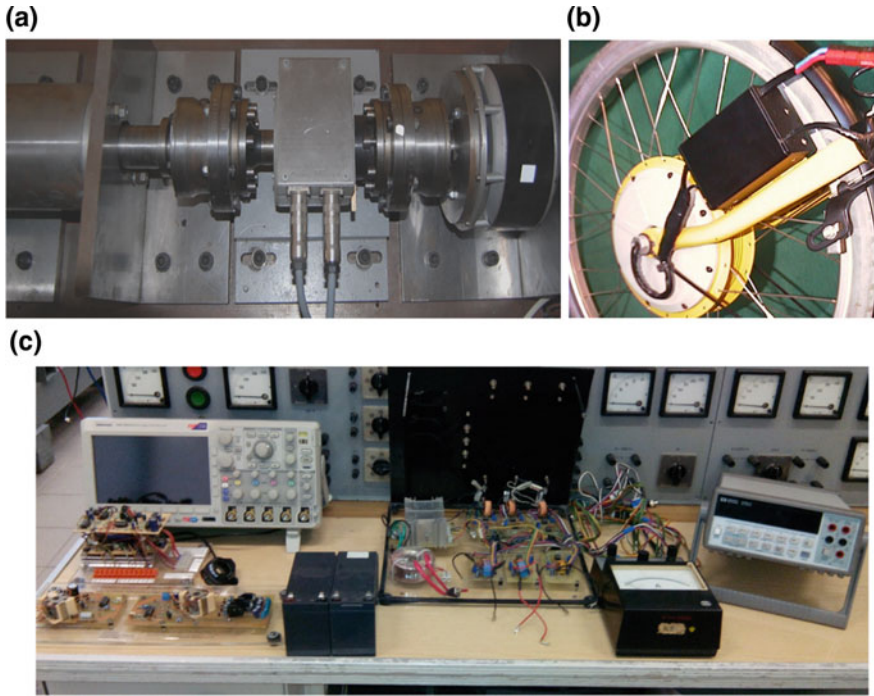


Fig. 7 An overview of **a** examined BLDC motor operating as a generator, **b** BLDC motor mounted in the front wheel hub, **c** the most important tools utilized in the measurement stand

- DC motor driving the BLDC motor via a torque measuring shaft made by Hottinger Baldwin Mesttechnik;
- Six transducers set used for instantaneous value measurement of voltages and currents, utilizing A3515LUA Hall-effect sensor described in [14, 15];
- Digital mixed signal oscilloscope MSO 3014;
- Two SLA gel batteries KOBÉ HV7 12 V, 7 Ah;
- BLDC motor control system (with utilization of PICAXE microcontroller) and push-pull converter used for energy recovery (with utilization of SG3525 Pulse Width Modulator Control Circuit [13]).

The registered waveforms (with utilization of the voltage and current transducers set) of the charging current i_{bat} and u_{bat} battery voltage are shown in Fig. 8. The phase voltage u_a and i_a phase current of the BLDC motor during the charging process are presented in Fig. 9. The last one second of the registered waveforms (Figs. 8 and 9) correspond to the simulation tests presented in Fig. 4.

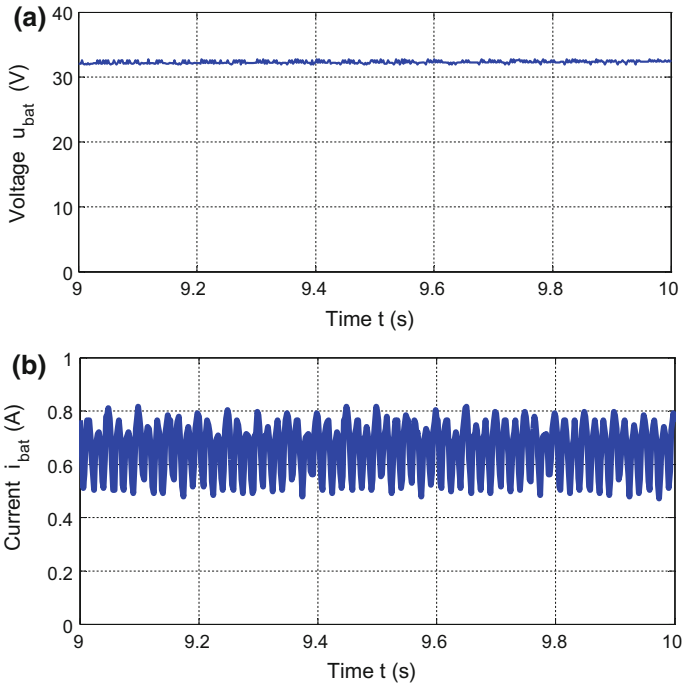


Fig. 8 Registered waveforms of **a** battery charging current i_{bat} , **b** battery voltage u_{bat}

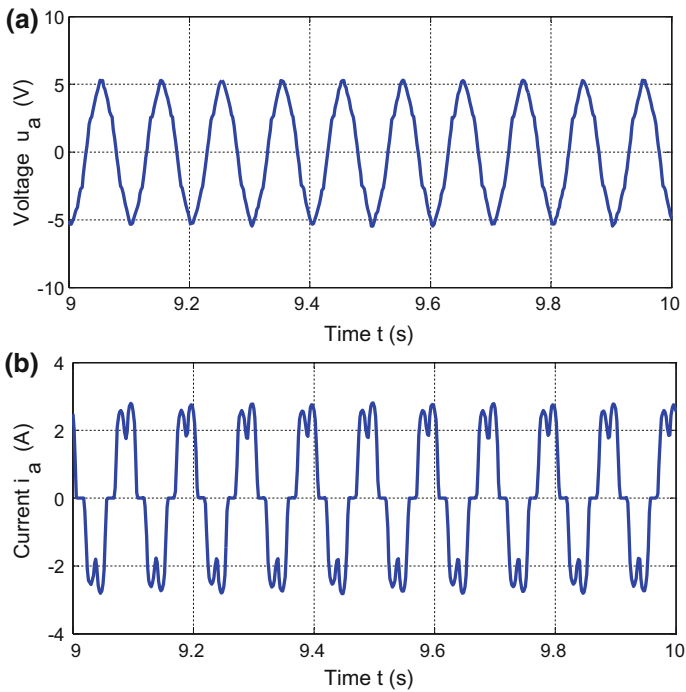


Fig. 9 Registered waveforms of BLDC motor's **a** phase voltage, **b** phase current

5 Conclusion

The paper presents a simple model of the impulse system for battery charging in electric bike powered by a BLDC motor during the generative operation. The model employs the calculation of internal resistance and source voltage characteristics obtained experimentally by performing a very short load current measurements using a differential method. The presented system makes it possible to conduct simulations of instantaneous values of voltages and currents during Sealed Lead-Acid battery charging. During the generative operation the direction of power transfer changes. The power produced by the BLDC motor constitutes an input power.

Results from the presented simulation model correlate favorably with experimental investigation.

Future research focus could shift to include a system for fully regenerative braking, different battery technologies such as Li-ion or even fuel cell technology [16].

References

1. Thiagarajan, V., Sekar, V.: Controlling of brushless dc motors in electric bicycles using electronic based circuit with 8-bit microcontroller. *Int. J. Eng. Sci. Emerg. Technol. (IJESET)* **4**(1), 26–34 (2012)
2. Nadolski, R., Ludwinek, K., Staszak, J., Jaskiewicz, M.: Utilization of BLDC motor in electrical vehicles. *Electr. Rev.* **4**, 180–186 (2012)
3. Zahedi, A.: Electric vehicle as distributed energy storage resource for future smart grid. In: 22nd Australasian Universities Power Engineering Conference (AUPEC), pp. 1–4, September 2012
4. Spagnol, P., et al.: A full hybrid electric bike: how to increase human efficiency. In: Proceedings of IEEE American Control Conference, pp. 2761–2766, June 2012
5. Como, M., Berretta, D., Spagnol, P., Savaresi, S.M.: Design, control, and validation of a charge-sustaining parallel hybrid bicycle. *IEEE Trans. Control. Syst. Technol.* **24**(3), 817–829 (2016)
6. Muetze, A., Tan, Y.C.: Electric bicycles—a performance evaluation. *IEEE Ind. Appl. Mag.* **13**(4), 12–21 (2007)
7. Heydt, G.T.: The next generation of power distribution systems. *IEEE Trans. Smart Grid* **1**(3), 225–235 (2010)
8. Taylor, J., Maitra, A., Alexander, M., Brooks, D., Duvall, M.: Evaluation of the impact of plug-in electric vehicle loading in distribution system operations. In: Proceedings of IEEE Power and Energy Society General Meeting, pp. 1–6, July 2009
9. Barsali, S., Ceraolo, M.: Dynamical models of lead–acid batteries: implementation issues. *IEEE Trans. Energy Convers.* **17**(1), 16–23 (2002)
10. Schweighofer, B., Raab, K.M., Brasseur, G.: Modeling of high power automotive batteries by the use of an automated test system. *IEEE Trans. Instrum. Meas.* **52**(4), 1087–1091 (2003)
11. Tian, S., Hong, M., Ouyang, M.: An experimental study and nonlinear modeling of discharge I-V behavior of valve-regulated lead-acid batteries. *IEEE Trans. Energy Convers.* **24**(2), 452–458 (2009)

12. Ceraolo, M.: New dynamical models of lead–acid batteries. *IEEE Trans. Power Syst.* **15**(4), 1184–1190 (2000)
13. SG3525 Pulse Width Modulator Control Circuit. Datasheet, January 2005, Rev. 5
14. Ludwinek, K.: Measurement of momentary currents by Hall linear sensor. *Prz. Elektroteh.* **10**, 182–187 (2009)
15. Ludwinek, K.: Practical application of a linear Hall-effect sensor in contactless measuring of current temporary values. *Int. Rev. Electr. Eng.* **8**(5), 1631–1640 (2013)
16. Chang, Y.T., Chen, P.C., Liu, Y.C., Chang, S.B.: The development of the PEM fuel cell power system for the electric bike. In: 9th World Congress on Intelligent Control and Automation (WCICA), pp. 1041–1046, June 2011

Powers Balances in the AC Circuit with Nonlinear Load and Reactive Power Compensation

M. Wciślik

Abstract The paper deals with analysis of definitions of reactive power. Properties of reactive power described as proportional to the product of the instantaneous values of voltage and current time derivative are presented. The analysis of the active and reactive power propagation in the circuit with nonlinear load, which the voltage is proportional to the signum function of the current and supplied by means of R, L elements from sinusoidal voltage source with reactive power compensation were made. A mathematical model circuit, with dimensionless variables and operational diagram of the circuit in Simulink were created. An analysis of nonlinear load equivalent circuit and balances of active and reactive power of the fundamental and higher harmonics were performed.

Keywords Nonlinear load · AC circuit · Reactive power compensation · Simulation · Equivalent diagram

1 Introduction

Nonlinear loads disturb the flow of electricity from the producer to the consumer. The energy is transferred from the producer to the consumer through mains in the form of fundamental harmonic energy. If the load is nonlinear, the energy is converted to higher harmonics energy and is returned to the mains. The harmonics spreading depends on the impedance of other consumers connected to the system node, transmitting line impedances and capacitors of reactive power compensation units. The consumers, which generate higher harmonics, can transmit it to other customers.

In control of power distribution in the power system, the reactive power is applied. Financial settlements between the supplier and the consumer are regulated on the basis of indications of the counters integrating powers (active and reactive). The active power has determined commonly used definition and measuring

M. Wciślik (✉)

Department of Automatic Control Systems, Kielce University of Technology, Kielce, Poland
e-mail: wcislik@tu.kielce.pl

© Springer International Publishing AG 2018

D. Mazur et al. (eds.), *Analysis and Simulation of Electrical and Computer Systems*, Lecture Notes in Electrical Engineering 452,
https://doi.org/10.1007/978-3-319-63949-9_14

229

systems. This definition also applies to nonlinear load. For that load the definition of reactive power is still unresolved. There is known a few definitions. An analysis of the basic definition of reactive power and reactive power calculation algorithms were presented. In the [1, 2], the presentation of different definitions for nonsinusoidal currents and voltages in the circuits most often containing linear elements can be found. But which definition gives the right results is not described. There is also lack of the balances of the powers. The balances are the base of engineering economics. Therefore, it is important to answer the questions: “Are known definitions of reactive power allowed reactive power balancing in a circuit with nonlinear receiver and with reactive power compensation system? What are the possibilities for the implementation of power measurements by modern electronic measuring systems?”.

In order to answer these questions, in the paper the following are presented: basic definitions of reactive power and conclusions results from analytic (symbolic) solutions of ac circuit containing inductance, resistance and nonlinear load; algorithms for reactive power determining and analysis of the reactive power balance in the model of the circuit with the nonlinear load and with the reactive power compensation

2 Basic Definitions of Reactive Power

In the second half of the nineteenth century, the basic quantities characterizing circuit sinusoidal current were current and voltage rms values I_{rms} , U_{rms} and active power P , measured as an average of the values of the product of the instantaneous values of current and voltage on the receiver. The presence of inductance in such circuit causes the active power was less than the product of the rms values of current and voltage. That product is called an apparent power S . The quotient P/S is called the power factor and mated with the current waveform phase shiftment angle with account to the supply voltage waveform. Hence for sine waves, the active power definition resulted in form

$$P = U_{\text{rms}} \cdot I_{\text{rms}} \cdot \cos \varphi \quad (1)$$

Reactive power, saved by the formula

$$Q = U_{\text{rms}} \cdot I_{\text{rms}} \cdot \sin \varphi \quad (2)$$

after rising to the square completed the active power square to the apparent power square in the power equation

$$S^2 = P^2 + Q^2 \quad (3)$$

At the end of the nineteenth century, Ch.P. Steinmetz [1], while examining the ac circuit with the electric arc stated that

$$S^2 > P^2 + Q^2 \quad (4)$$

Thus, in the beginning of the twentieth century, there began research of such definition of reactive power, which allowed to describe the circuit with nonsinusoidal current and voltage waveforms by the power equation as for the sinusoidal ones. The earliest reactive power definitions were presented by Illović, Budeanu, and Fryze. The process of formation can be traced in [1, 2].

In 1925, M.A. Illović offered two variants to the definition of the reactive power

– capacitive

$$Q_C = \sum_{n=1}^{\infty} n \cdot U_{\text{rmsn}} \cdot I_{\text{rmsn}} \cdot \sin \varphi_n \quad (5)$$

– inductive

$$Q_L = \sum_{n=1}^{\infty} \frac{1}{n} \cdot U_{\text{rmsn}} \cdot I_{\text{rmsn}} \cdot \sin \varphi_n \quad (6)$$

and proposed to designate its using electrodynamic wattmeter, which in the voltage circuit has incorporated respectively capacitor or inductor [1].

In 1927, Budeanu published the work in which the active power for nonsinusoidal waveforms is in form

$$P = \sum_{n=1}^{\infty} P_n = \sum_{n=1}^{\infty} U_{\text{rmsn}} \cdot I_{\text{rmsn}} \cdot \cos \varphi_n \quad (7)$$

analogically describes reactive power

$$Q_B = \sum_{n=1}^{\infty} Q_{Bn} = \sum_{n=1}^{\infty} U_{\text{rmsn}} \cdot I_{\text{rmsn}} \cdot \sin \varphi_n \quad (8)$$

and introduces distortion power, the square of which is equal to

$$D^2 = S^2 - (P^2 + Q^2) \quad (9)$$

Budeanu assumed a priori, that each harmonic reactive power is described as for the first harmonic, and does not depend directly on the harmonic frequency [1, 2].

Another approach to the power equation was proposed by Fryze in 1931. He introduced the load current decomposition in the time domain to the orthogonal components: active and passive i_a and i_F without use of Fourier series

$$i(t) = i_a(t) + i_F(t) \quad (10)$$

The active component of the current flows through the equivalent conductance

$$G_e = P \cdot U_{\text{rms}}^2 \quad (11)$$

and has the instantaneous value of the shape such as the load voltage

$$i_a(t) = G_e \cdot u(t) \quad (12)$$

Fryze reactive component is calculated as

$$i_F(t) = i(t) - i_a(t) \quad (13)$$

The defined components are mutually orthogonal and their values effectively satisfy the condition equation

$$I_{\text{rms}}^2 = I_{\text{rmsa}}^2 + I_{\text{rmsF}}^2 \quad (14)$$

which, multiplied by the square of the RMS voltage power equation becomes power equation with active and reactive powers defined as follows:

$$P = U_{\text{rms}} \cdot I_{\text{rmsa}}, \quad Q = U_{\text{rms}} \cdot I_{\text{rmsF}} \quad (15)$$

This approach is very convenient for problems of reactive power compensation, power factor correction, etc. However, this means that in nodes with different shape of the voltages can be used different algorithms for the reactive power calculation.

It should be noted that the above definitions of reactive power refers to the node of the circuit and do not determine the direction of flow of reactive power. The definition should refer to the circuit and allow reactive power balance in the circuit. To examine the phenomenon of supply power conversion for power higher harmonics, a single-phase ac circuit containing resistance, inductance, and a nonlinear element is considered in [8]. This circuit provides a convenient basis for discussing the definition of reactive power. There is presented symbolic analysis of waveforms in the quasistatic state. The resulting characteristics of the circuit are in the form of analytical equations. It facilitates the interpretation of phenomena in the circuit and allows a new look at the definition of reactive power.

The influence of nonlinearity and phenomena occurring in the circuit with nonlinear load are visible when the circuit is compared to the circuit containing a linear, resistive load. This comparison shows that the nonlinearity even with single-valued current–voltage characteristics can cause

- an increase in the circuit reactance, seen from the power source terminals,
- lowering of maximum of the active power circuit
- decrease energy efficiency of the circuit,
- decrease of power factor.

In [8], it was found that in the analyzed circuit with nonlinear load, reactive power defined for the n -th harmonic of the relationship

$$Q_n = n \cdot U_{\text{skn}} \cdot I_{\text{skn}} \cdot \sin \varphi_n \quad (16)$$

can be balanced similarly as active power. This definition has the form proposed by Illović [1], for the capacitive reactive power (5). For reactive power specified by (16) in [8] it was found that, although the equivalent circuit of the nonlinear load includes resistance and inductance, the total reactive power of the receiver equals zero.

Adopted at work, the definition form of reactive power is related to the circuit equations and describes the energy flow in the circuit. For a periodic waveform with a period T the value of reactive power, averaged for the period can be determined using the expression

$$Q = \frac{1}{2} \frac{1}{\omega T} \int_0^T U(t) \cdot \left(\frac{dI(t)}{dt} \right) \cdot dt \quad (17)$$

which is easily implemented physically. The time derivative of the current can be measured directly using a Rogowski coil or may be calculated numerically. In the steady state (quasistatic state), when no changes of magnetic energy occur, the reactive power associated with the inductance is given by

$$Q = L \cdot \frac{1}{2} \frac{1}{\omega T} \int_0^T \left(\frac{dI(t)}{dt} \right)^2 \cdot dt \quad (18)$$

When the current is interpreted as the product of the charge and its speed, the time derivative of the current can be understood as the product of the load and its acceleration. Therefore it can be concluded that the relation (18) is “similar” to the Larmor formula, describing the radiation power of the oscillating electric dipole, proportional to the square of the product of the charge q and its acceleration a [4, p 489]:

$$P_{\text{rad}} = \frac{\mu_o \cdot q^2 \cdot a^2}{6 \cdot \pi \cdot c} \quad (19)$$

where c is the speed of light, μ_o —the coefficient of magnetic permeability of vacuum. Hence, it may be argued that the reactive power (18) corresponds to the radiation power of the inductance and the current flowing through it.

3 Algorithms for Determining Reactive Power

Despite the long-standing debate, IEEE has not selected a definition of reactive power, which would force financial settlements. As a result, applications used by manufacturers of measuring systems usually implements one of the four algorithms, sometimes leaving the choice to the user. These algorithms are as follows [3]:

1. Determination of reactive power from the power equation on the basis of apparent power and active power,
2. Designation as the imaginary part of the Fourier transform power spectrum,
3. Timeshifting of the current corresponding to 90° phase shift of the fundamental harmonic current,
4. Calculation of active power with the harmonic shift's equal 90° according to the proposal Budeanu (8).

The first of the algorithms does not distinguish the sign of reactive power. The sign of the power have is determined on the basis of other information. The algorithm uses the RMS values, which is associated with a certain delay, caused by the calculation and filtering procedures.

In the second algorithm, the Fast Fourier Transform algorithm for voltage and current is used. It is associated with a fairly complex numerical calculations and also some delay.

The third algorithm is easily implementable. The time delay may be accomplished digitally using a FIFO shift register. Therefore, this algorithm is often used. But in that case, the reactive power harmonic components of according to [2 str.251] for the even harmonics correspond to Budeanu active power (7) and for the odd harmonics to reactive power (8). Algebraic summation of the components representing the active power and reactive power of harmonics as components of total reactive power reactive power has no physical meaning. Therefore, this algorithm should be skipped.

The latter method calculation of reactive power requires the implementation of 90° phase shiftment angle for each harmonic, while maintaining constant magnitude gain for each harmonic. It would mean that each separate harmonic has the phase shifter. In [3], was proposed the implementation of the phase angle shift through the use of differentiation or integration operator. Differential operator was previously used in [6] to determine the inductance with formula similar to (18).

As it was previously mentioned, when the operator of differentiation is applied for the current and it is multiplied by voltage, the expression for the determination of reactive power corresponds to the Illovići capacitive power formula (5). In [8], the analysis of the AC circuit of the nonlinear load was performed. Based on this analysis, it was found that reactive power determined using differentiation operator allows balancing the reactive power in the circuit and that it explains the phenomena observed in the supply of electric arc furnaces [5].

For the currently accepted powers definitions, energy consumer, with nonlinear load is not responsible for the increase losses of active and reactive circuit powers.

Energy supplier or other customers are charged economically for that. To avoid that phenomenon, the economic accounts should be made using active and reactive power of the fundamental harmonic.

The flow of harmonics in the power system depends on the impedance of the power supply. Reactive power compensation systems are used mainly to improve energy efficiency, but they can disrupt the flow of currents harmonics in the circuit. Hence the question arises: Does reactive power with definition as (17) be balanced in the circuit with compensation of reactive power?

4 Diagram and Model of Analyzed Circuit

Symbolic analysis of circuit with nonlinear load and reactive power compensation is difficult and often impossible. But it may be done using simulation methods. The diagram of considered system is shown in Fig. 1

The system is powered by a sinusoidal voltage with angular frequency ω . The load is nonlinear. Its voltage is proportional to signum function of current. The system equations are as follows:

$$L_2 \frac{dI_2}{dt} = E_m \cdot \sin(\omega \cdot t) - R_2 \cdot I_2 - U_c \tag{20}$$

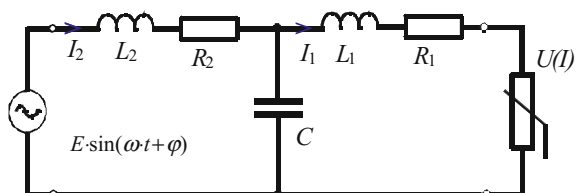
$$L_1 \frac{dI_1}{dt} = U_c - R_1 \cdot I_1 - U_a \cdot \text{sign}(I_1) \tag{21}$$

$$C \frac{dU_c}{dt} = I_2 - I_1 \tag{22}$$

In these equations were used indications: I_1, I_2 instantaneous values of currents flowing respectively through inductances L_1, L_2 and resistances R_1, R_2 . Inductance L_2 represents the power supply system inductance. Its reactance value is much greater than the resistance of R_2 . Similarly, the reactance value of the inductance L_1 representing the inductance of the load system is much higher than the resistance value R_1 of the system. The inductance value L_1 is considerably larger than the inductance L_2 . These relationships can be represented in the asymptotic notation

$$R_1 = o(\omega L_1) \quad R_2 = o(\omega L_2) \quad L_2 = o(L_1) \tag{23}$$

Fig. 1 Diagram of analyzed circuit



In order to simplify the organization of simulation experiment in the equations, the time scaling and reference variables were used

$$\tau = \omega t, X_1 = \omega L_1, E_m, I_m = E_m/X_1, Y = \omega C \tag{24}$$

Then after transformation (20–22) the equation were received in the form of

$$x_2 \frac{di_2}{d\tau} = \sin(\tau) - r_2 i_2 - u_c \tag{25}$$

$$\frac{di_1}{d\tau} = u_c - r_1 i_1 - u_a \cdot \text{sign}(i_1) \tag{26}$$

$$y \cdot \frac{du_c}{d\tau} = i_2 - i_1 \tag{27}$$

In the notation, the following dimensionless variables and parameters were used

$$i_2 = I_2/I_m, \quad i_1 = I_1/I_m, \quad u_c = U_c/E_m, \quad u_a = U_a/E_m \tag{28}$$

$$x_2 = X_2/X_1, \quad r_2 = R_2/X_1, \quad r_1 = R_1/X_1, \quad y = Y \cdot X_1 \tag{29}$$

Based on Eqs. (25–27) the operating diagram shown in Fig. 2 was created. Signum function was performed by amplifying a thousand times the input signal and then using the saturation module. For the determination of reactive power of capacitor, the time derivative of capacitor current was calculated.

Waveforms of dimensionless currents and voltages [described in (28)], calculated for $x_2 = 0.05, r_2 = 0.2, r_1 = 0.1, u_a = 0.45, y = 0.6$ after switching on the circuit supply for zero initial conditions are shown in Fig. 3.

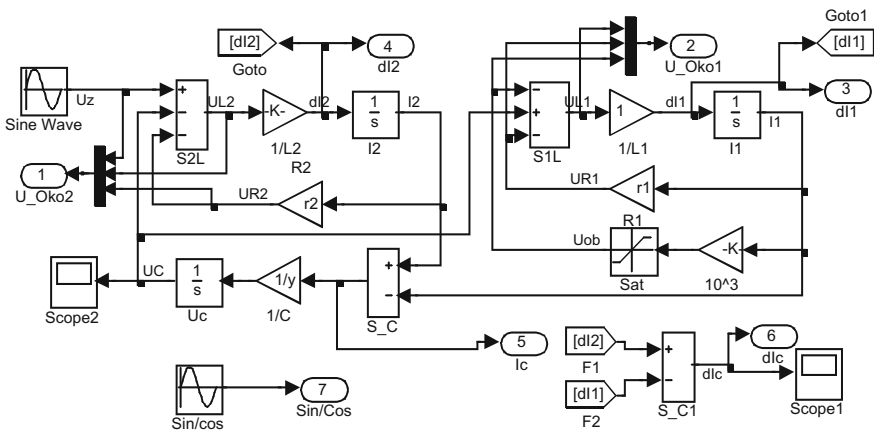


Fig. 2 Circuit model in Simulink

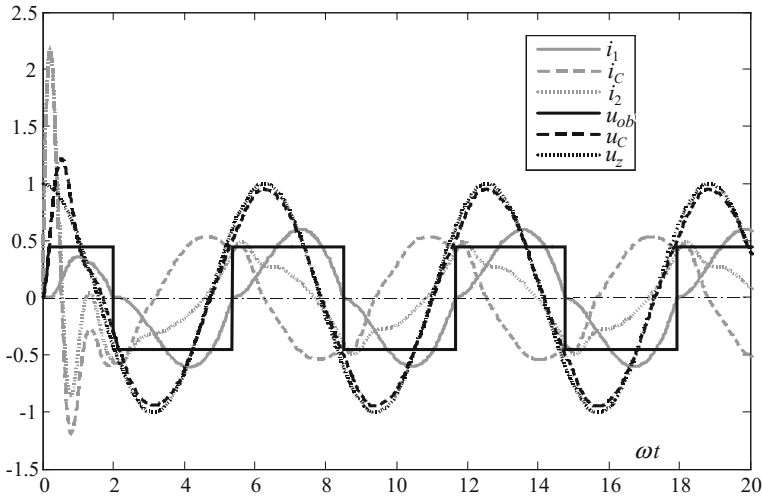


Fig. 3 Waveforms of dimensionless currents and voltages of the circuit model during switching on process, u_{ob} and u_z denotes voltages waveforms of load and supply respectively

On the basis of the figure, it can be concluded that the currents distortion are correlated with the time derivative of the voltage. Inrush current oscillations with increased amplitude and frequency are also visible.

The voltages, currents, and its derivatives which are analyzed in the balances of active and reactive powers are connected to the output ports. Voltage drops vector in the power source mesh elements and the vector of voltage drops on the elements of the load mesh were formulated. Reactive power compensation capacitor is treated separately.

After multiplying these voltages, vectors and the capacitor voltage by corresponding currents and current derivatives, instantaneous values of active and reactive powers of individual elements are obtained. The powers are averaged for the period and presented in the displays. Powers shown in the displays are dimensionless and related to E_n^2/X_1 . Block diagram of determining the averaged powers is shown in Fig. 4.

Exemplary active and reactive powers were determined for: $x_2=0.05$, $r_2=0.2$, $r_1=0.1$, $u_a=0.45$, $y=0.6$. Part of the results was written in the floating-point notation and have negative exponents, less than -5 . Their values result from the declared calculation error in parameters of ordinary differential equation solver. Calculations were carried out with relative accuracy equals 10^{-3} and an absolute accuracy equals 10^{-6} . Modified Rosenbrock algorithm with variable step (ode23s) was applied.

Some of the calculated values should be equal to zero, as they relate to inductor or capacitor active power or resistor reactive power. The nonlinear load reactive power value close to zero related to that the current–voltage characteristics of the load are single valued.

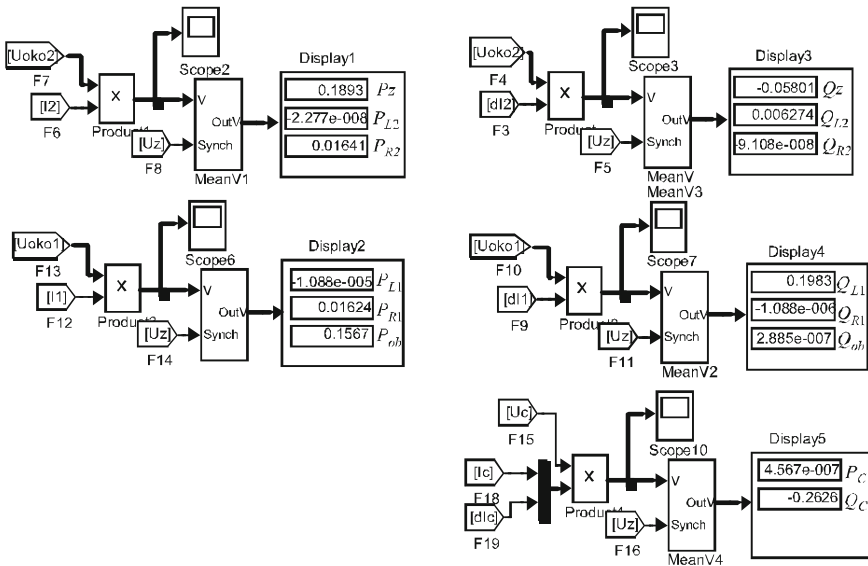


Fig. 4 Diagram of powers measurement system in Simulink

Analysis of the balance of reactive power and active power was performed for several different values of the variables x_2 , r_2 , r_1 , u_a , and y . The values of the BP, BQ, BQ_{ob} variables, which denote respectively: relative balance of active power circuit, relative balance of reactive power circuit, and relative total reactive power of nonlinear load, were checked

$$BP = (P_{ob} + P_{r1} + P_{r2} - P_z) / P_z \quad (30)$$

$$BQ = (Q_{ob} + Q_{x1} + Q_c + Q_{x2} - Q_z) / (Q_{ob} + Q_{x1}) \quad (31)$$

$$BQ_{ob} = Q_{ob} / Q_{x1} \quad (32)$$

For that selected values of input variables (x_2 , r_2 , r_1 , u_a , y) it was found that the value of BP, BQ, BQ_{ob} equal zero with an accuracy respectively of 0.01, 0.001, and 0.4%. The last value is closely related to the integration step and the values of tolerances of variable step procedure of differential equations solver.

On the basis of the BP, BQ errors, it can be assumed that the for proposed definition of reactive power the balance of reactive power in the circuit is valid similarly as active power balance of active power. Zero value of BQ_{ob} means that for single-valued current–voltage load characteristic, the total reactive power according to (17) ought to be equal to zero.

5 Conclusions

Reactive power balance equation may be obtained as sum of products of the circuit elements voltages by the scaled time derivative of the currents flowing through these elements.

Reactive power defined in (17) is time-averaged for the supply voltage period instantaneous reactive power, like in active power. Reactive power can be interpreted as the power of radiation. It is positive for the inductance and elements of nonlinear processing power of the fundamental harmonic into the power of higher harmonics. It is negative for capacitors and power sources.

Reactive power of the capacitor may be calculated similarly as inductor power, the product of voltage, and the capacitor current derivative (with respect to the scaled time). That is to say that definition of reactive power proposal in (17) is universal and is in force for the inductances and reactive for the capacitances.

As the nonlinear load which current–voltage characteristics is single valued (without the “hysteresis”), such determined reactive power is equal to zero and the reactive power of fundamental harmonic and higher harmonics have the same absolute value but different signs.

Nonlinear load causes increase of the reactive power of the fundamental harmonic observed at the terminals of the power supply source, as the increase of powered circuit reactance.

It is possible to measure the reactive and active powers distinguishing between fundamental harmonic powers and higher harmonics powers. The system implementing such measurement is presented in [7]. The measurement algorithm implementing definition (17) may be implemented in energy parameters measurement systems.

References

1. Czarnecki, L.S.: Powers in electric circuits with nonsinusoidal waveforms of currents and voltages. *Oficyna Wydawnicza. Politechniki Warszawskiej, Warszawa* (2005). (in Polish)
2. Emanuel, A.E.: Summary of IEEE Standart 1459: definitions for the measurement of electric power quantities under sinusoidal, nonsinusoidal, balanced or unbalanced conditions. *IEEE Trans. Ind. Appl.* **40**(3), 869–874 (2004)
3. Emanuel, A.E.: *Power Definitions and the Physical Mechanism of Power Flow*. IEEE Press, John Wiley & Sons Ltd, Hoboken (2010)
4. Griffiths, D.J.: *Introduction to Electrodynamics*. PWN, Warszawa (2005). (in Polish)
5. Köhle, S.: Linear equivalent diagram of high current threephase arc furnace. *Elektrowärme Int.* **43**(B1), B314–B324 (1985). (in German)
6. Wciślik, M.: Estimation method of electric circuit parameters of arc furnace for steelmaking process automatic control. *ZN Politechniki Swietokrzyskiej*, E28, Kielce, Poland (1992). (in Polish)
7. Wciślik, M., et al.: Node power quality monitoring system. *Int. J. Commun. Antenna Propag.* **2**(2), 133–139 (2011)
8. Wciślik, M.: Power balances in AC circuit with nonlinear load. *Prz. Elektrotch.* **90**(2), 5–8 (2014). (in Polish)

The Analysis of Wind Turbine with Horizontal Rotation Axis with the Use of Numerical Fluid Mechanics

Damian Mazur, Mariusz Trojnar and Andrzej Smoleń

Abstract The analysis of horizontal rotation axis wind turbine of type H-rotor is presented in this article. The calculation has been made using a 3D model of horizontal rotation axis turbine for three wind flow speeds: 5, 10, 15 m/s, with the stable rotational speed of the rotor of 200 rotations per minute. The analysis of wind turbines requires building a 3D calculation model. The building of such a model is very time-consuming and the calculations involving numerical fluid mechanics require substantial calculation power. The article presents 3D CAD model of horizontal rotation axis wind turbine in ANSYS calculation environment, discrete net, and boundary conditions and the results of calculating horizontal rotation axis wind turbine with the use of numeric fluid mechanics.

Keywords Wind turbine · Horizontal rotation axis · CFD analysis · Turbine-generated power

1 Introduction

The article describes the analysis of horizontal rotation axis wind turbine of type H-rotor. The calculation has been made of horizontal rotation axis wind turbine using a 3D model of horizontal rotation axis turbine for three wind flow speeds: 5, 10, 15 m/s, with the stable rotational speed of the rotor of 200 rotations per minute.

This analysis has been made to illustrate and follow the turbine behavior and to present the calculation opportunities of horizontal rotation axis turbines.

D. Mazur (✉) · M. Trojnar · A. Smoleń
Department of Electrical and Computer Engineering Fundamentals,
Rzeszow University of Technology, ul. Wincentego Pola 2, 35-959 Rzeszow, Poland
e-mail: mazur@prz.edu.pl

M. Trojnar
e-mail: trojnar@prz.edu.pl

A. Smoleń
e-mail: smolen@prz.edu.pl

The analysis of wind turbines with horizontal axis rotation requires building a 3D calculation model. The building of such a model is very time-consuming and the calculations involving numerical fluid mechanics require substantial calculation power [1].

It is necessary to create geometrical models of turbine rotor elements to be able to conduct CFD analysis. In order to enable horizontal turbine to work properly, it is necessary to choose the right geometrical dimensions of the rotor blade. This requires great knowledge concerning horizontal rotation axis turbine, because from the very stage of designing the blade certain requirements need to be made, such as optimum work at given wind speed or wind conditions. The CFD analysis of the turbine has been conducted with the use of movable net for 3D model [2].

2 CAD 3D Model of Horizontal Rotation Axis Wind Turbine in ANSYS Calculation Environment and Boundary Conditions

The wind turbine blade is one of the most important elements of horizontal rotation axis turbine. The blade geometrical parameters, which have been used to establish the CAD calculation model for the turbine have been presented in Table 1.

Table 1 The blade geometrical parameters for different values of radius

R (m)	Chord profile (m)	Angle of rotation Θ_p (°)
Hub	Hub	Hub
Fixing element—cylinder $\phi = 0.1$	Fixing element	Fixing element
0.29	0.1	0
0.34	0.2	9.9
0.37	0.25	13.4
0.43	0.33	18.07
0.49	0.33	14.29
0.53	0.32	11.91
0.63	0.31	7.98
0.76	0.29	4.72
0.83	0.28	3.42
0.93	0.26	2.08
1.03	0.25	1.12
1.12	0.23	0.49
1.22	0.22	-0.01
1.32	0.21	-0.47
1.42	0.19	-0.92
1.52	0.18	-1.35
1.69	0.16	-1.77

The CAD wind turbine calculation model is presented in Fig. 1.

Numerical modeling of external flow requires establishing finite range/zone [3]. The range/area accepted for calculations must be big enough for established boundary conditions on the boundaries of calculation area not to disturb flow phenomenon near rotor and to present properly the conditions in infinity. A cylinder containing wind turbine has been modeled in order to simulate the rotation of turbine rotor. Figure 2 presents 3D calculation model of the turbine together with external finite area and a cylinder modeling the area near rotor created using ANSYS program [4].

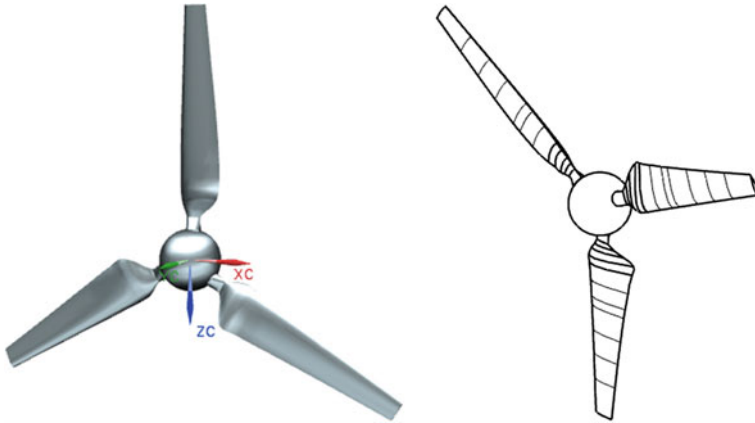


Fig. 1 CAD turbine model of horizontal rotation axis and its view with segment division



Fig. 2 CAD 3D calculation model of turbine with external finite area

3 Discrete Net and Boundary Conditions

Finite area has been modeled in form of a cylinder 6 m in diameter and 20 m long. The movable/mobile AREA/ZONE created in a form of a cylinder 3.6 m in diameter and 0.48 long has a more thickened net compared with the finite area. A set of turbine blades along with turbine hub has been placed inside movable/mobile AREA/ZONE. Moreover, the area near the blades is additionally thickened in order to simulate the behavior of parietal/boundary layer. Figure 3 shows discrete net of calculation model CAD together with the rotor [5].

The boundary conditions assigned to the surfaces limiting the analysis areas have been presented in Fig. 4.

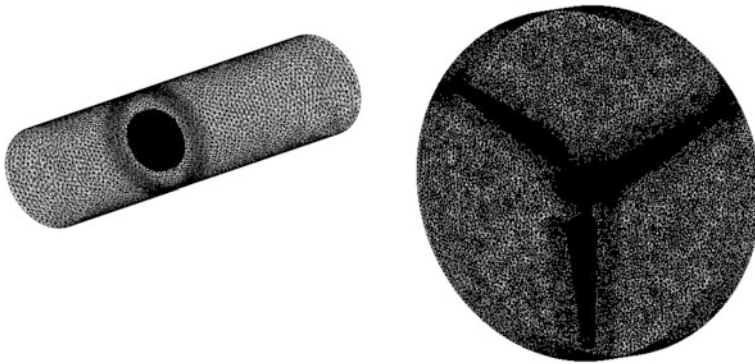


Fig. 3 Discrete net CAD 3D model together with the rotor

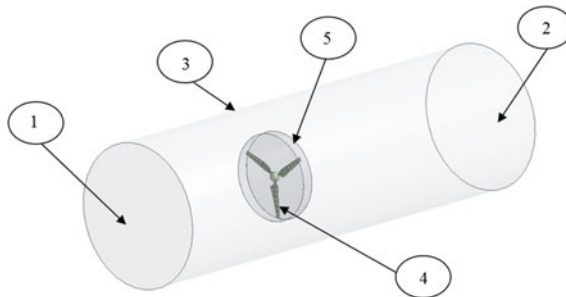


Fig. 4 Boundary conditions assigned to surface; 1 left surface of the cylinder defining condition at the inlet of *finite area/zone*, 2 right surface of the cylinder defining condition at the outlet of *finite area/zone*, 3 the outer surface of *finite area/zone* defined as wall, 4 turbine surface—the conditions of impenetrability, 5 the surface of outer cylinder circle imitating motion and the inner surface of the *finite area/zone*

Additionally, the following assumptions have been adopted for calculations:

- working pressure 101,325 Pa,
- speed/velocity at inlet 5, 10, 15 m/s,
- viscosity 17.08×10^{-6} kg/ms,
- density 1.225 kg/m^3 ,
- turbine rotation velocity 200 rpm,
- intensity of turbulence at inlet 1%,
- turbulence mode $k-\varepsilon$ - standard.

4 The Results of Calculating Horizontal Rotation Axis Wind Turbine with the Use of Numeric Fluid Mechanics

Figures 5 and 6 present the results of calculations in the form of power lines for the chosen positions of turbine rotor existing in a defined area for flow velocity of 5 and 10 m/s.

Figure 7 presents the calculations results in the form of pressure areas in chosen cutting planes of one of the wind turbine blades at the distance from the middle of coordinate system 0.4; 1; 1.6 m for the inflow velocity of 5, 10 m/s (Fig. 8).

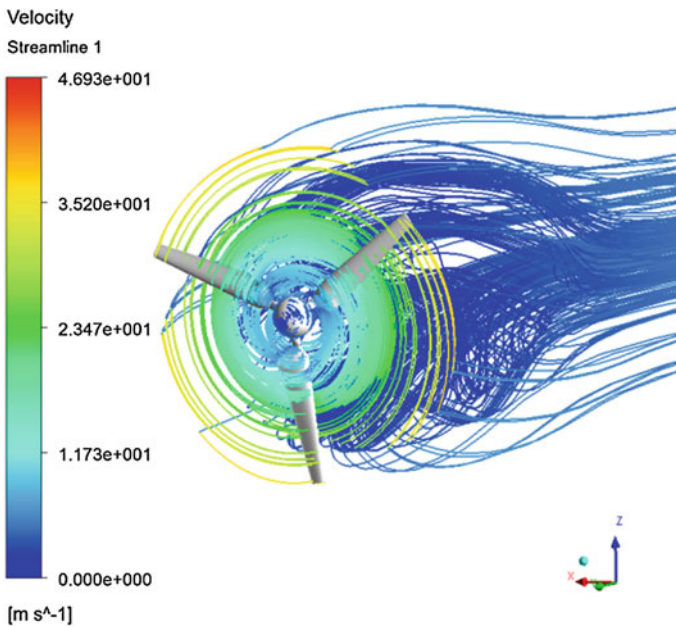


Fig. 5 Power lines in the rotor area for the chosen position of wind turbine rotor at inflow velocity of 5 m/s

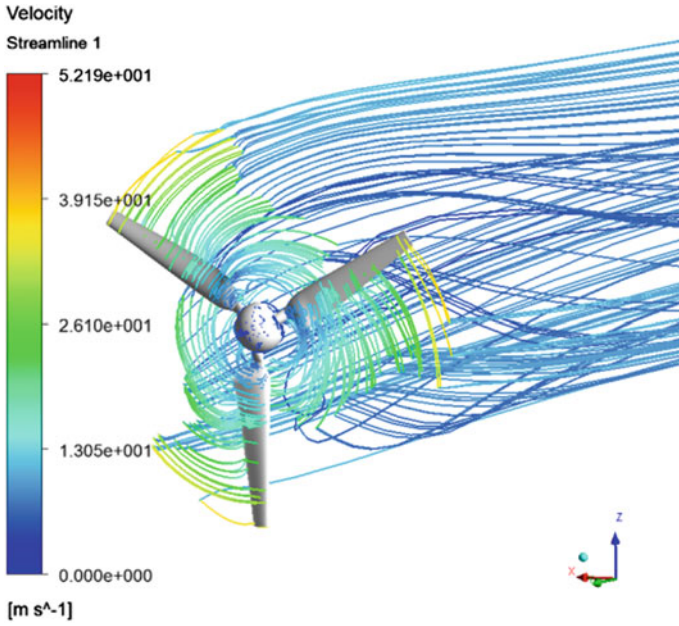


Fig. 6 Power lines in the rotor area for the chosen position of wind turbine rotor at inflow velocity of 10 m/s

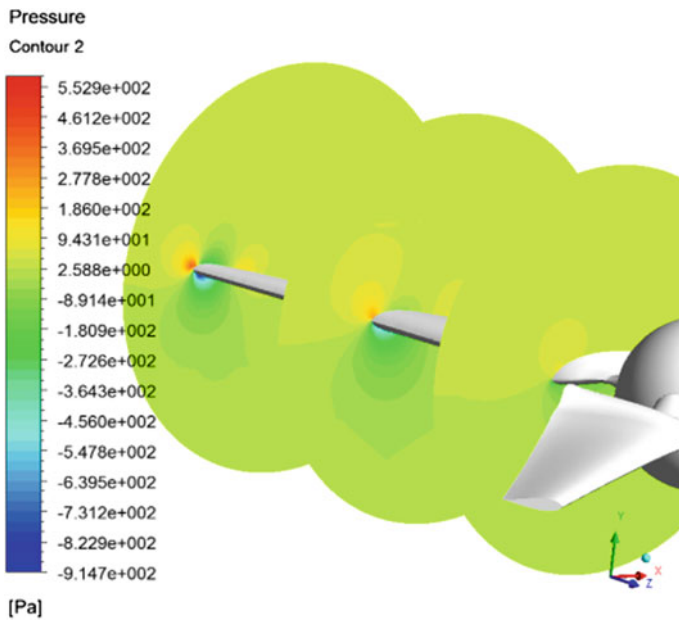


Fig. 7 Pressure areas in cutting planes of a blade for the inflow velocity of 5 m/s

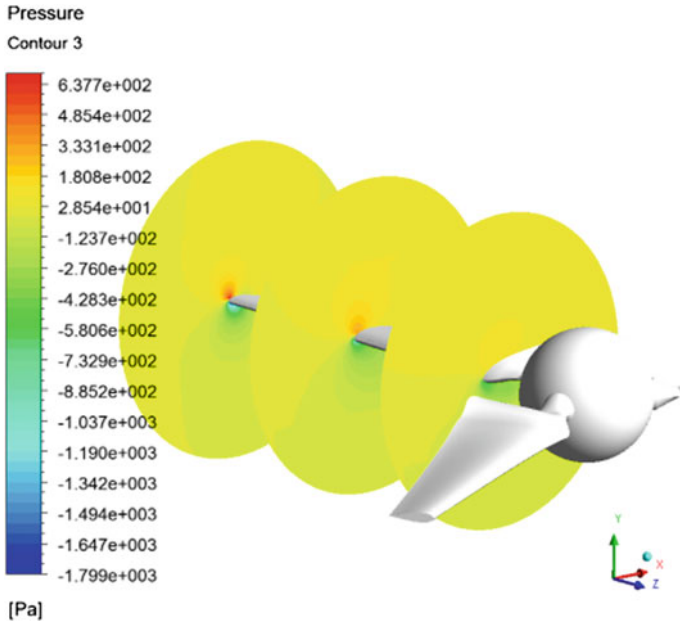


Fig. 8 Pressure areas in cutting planes of a blade for the inflow velocity of 10 m/s

Figures 9 and 10 present the calculations results of the distribution of global velocity on the surface of turbine blades for the chosen positions of turbine rotor and the inflow velocity of 5; 10 m/s.

On the basis of the conducted analysis CFD in Fluent environment, the momentum has been also determined, which consequently allowed the power generated by the wind turbine to be determined. Moreover, analysis has been made for comparative purposes using QBlade environment and BEM method [6].

Figure 11 presents the comparative characteristics of generated power determined using the two methods.

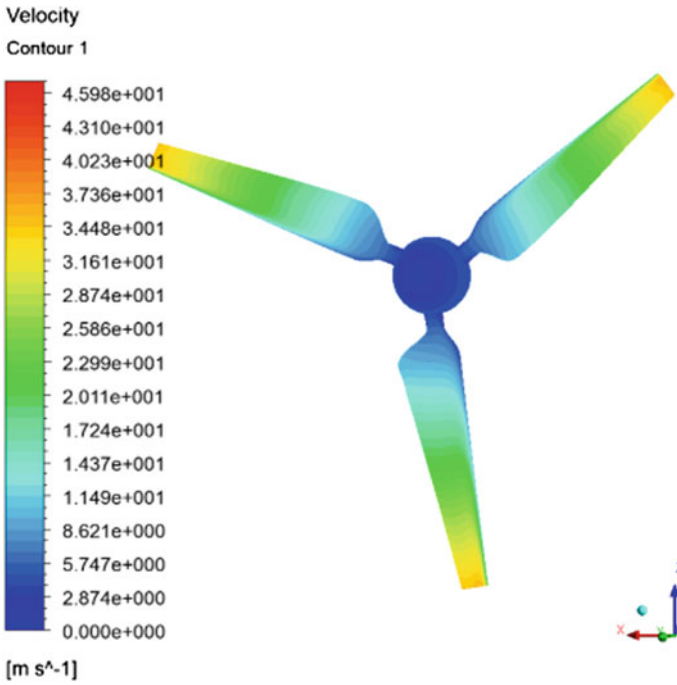


Fig. 9 The distribution of global velocities on the surface of turbine blades for the inflow velocity of 5 m/s

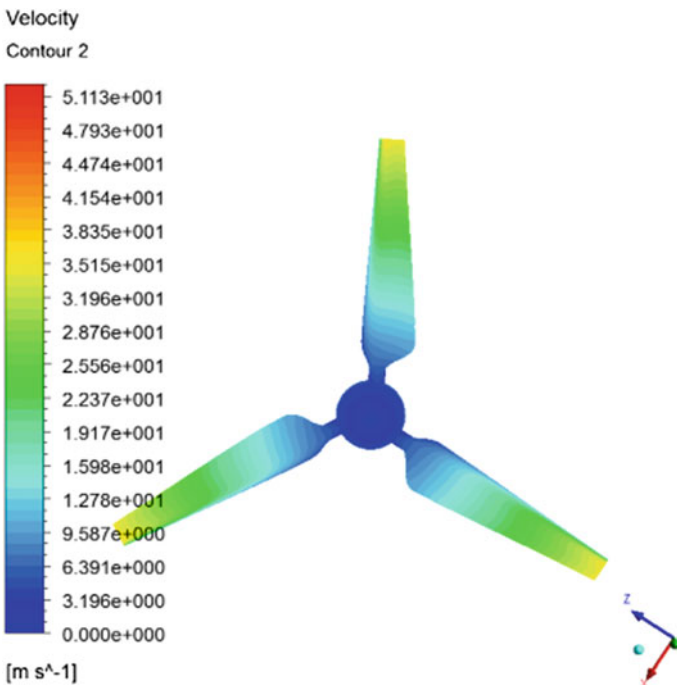
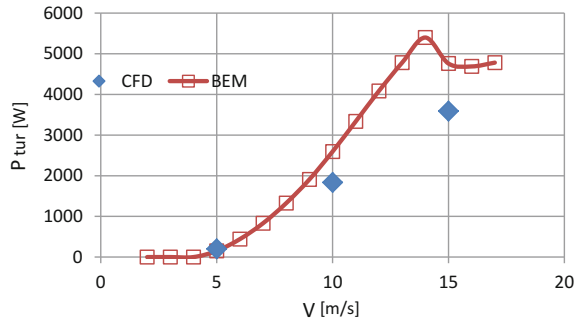


Fig. 10 The distribution of global velocities on the surface of turbine blades for the inflow velocity of 10 m/s

Fig. 11 The comparison of turbine generated power in QBlade program BEM method with that of CFD using numerical fluid mechanics



5 Conclusions

The power values determined by BEM method in QBlade environment for speed over 5 m/s are higher than those determined by CFD method. Exemplary power difference for the velocity of 15 m/s is 32%. CFD method provides complex information concerning the distribution of pressure velocity on the turbine [7]. It is, however, more work consuming and therefore the analysis has been conducted for three velocity values.

References

1. Chi-Jeng, B., Wei-Cheng, W.: Review of computational and experimental approaches to analysis of aerodynamic performance in horizontal-axis wind turbines (HAWTs). *Renew. Sustain. Energy Rev.* **63**, 506–519 (2016)
2. Fischer, G.R., Kipouros, G.T., Savi, A.M.: Multi-objective optimisation of horizontal axis wind turbine structure and energy production using aerofoil and blade properties as design variables. *Renew. Energy* **62**, 506–515 (2014)
3. Liu, X., Lu, C., Liang, S., Godbole, A., Chen, Y.: Vibration-induced aerodynamic loads on large horizontal axis wind turbine blades. *Appl. Energy* **185**(2), 1109–1119 (2017)
4. Nicholls-Lee, R.F., Turnock, S.R., Boyd, S.W.: Application of bend-twist coupled blades for horizontal axis tidal turbines. *Renew. Energy* **50**, 541–550 (2013)
5. Luo, K., Zhang, S., Gao, Z., Wang, J., Zhan, L., Yuan, R., Fan, J., Cen, K.: Large-eddy simulation and wind-tunnel measurement of aerodynamics and aeroacoustics of a horizontal-axis wind turbine. *Renew. Energy* **77**, 351–362 (2015)
6. Abdelrahman, M.A., Abdellatif, O.E., Moawed, M., Eliwa, A., Mišák, S.: The CFD performance analysis for horizontal axis wind turbine with different blade shapes and tower effect. In: 16th International Scientific Conference on Electric Power Engineering (EPE) (2015)
7. Abedi, H., Davidson, L., Voutsinas, S.: Numerical studies of the upstream flow field around a horizontal axis wind turbine. In: 33rd Wind Energy Symposium, AIAA SciTech Forum

Electrical Circuits of Non-integer Order: Introduction to an Emerging Interdisciplinary Area with Examples

Jordan Hristov

Abstract The chapter is an attempt to collate the basics of fractional electric circuits involving fractional time derivatives in the sense of Riemann–Liouville, Caputo and Caputo–Fabrizio. The examples analysed use mainly Caputo time-fractional derivative but comparative analyses with derivative based on different relaxation kernels are provided, too.

Keywords Time-fractional derivative · Electric circuits · Transient regimes

1 Introduction

Fractional calculus (FC), involving integrals and derivatives of non-integer order, is the natural generalization of the classical calculus allowing better modelling and control of processes in various areas of science and engineering [1–6]. A broad range of physical phenomena can be deeply analysed by applications of models involving fractional integral and derivatives [6] thus providing accurate information of the physical systems employing the memory mechanisms and hereditary effects in various materials and processes [7] where dissipations take place.

In this chapter, we focus on fractional calculus applications on simple electric circuits involving resistors, capacitors and inductors under transient conditions. The non-local character of the transient processes in the electric circuits is directly related to the dissipative processes in their elements such as the Ohmic resistance, the capacitor charge–discharge process, dissipation of charge transfer in dielectrics [8] or energy accumulation by inductors.

Fractional calculus is a well-known tool for the investigation of nonlinear time-dependent process in electrochemistry for surface concentration determination [1] and impedance spectroscopy [9].

J. Hristov (✉)

Department of Chemical Engineering, University of Chemical Technology
and Metallurgy, 8 Kl. Ohridsky Blvd., 1756 Sofia, Bulgaria
e-mail: jordan.hristov@mail.bg

The purpose of this chapter is to demonstrate the mathematical formalism in analyses of transient process of simple RLC circuits by the tools of fractional calculus and to focus on the fact that the real resistors, capacitors and inductors are nonlinear by nature with sensible dissipative processes in their work. The text collates research results from various sources and tries to present them in a straightforward manner, thus allowing an easy step from the conventional integer-order models to one with fractional derivatives.

2 Time-Fractional Derivatives to Transient Electric Circuit Analysis: The Reason to Use

The linear approach to model RLC circuits by integer-order derivatives and integrals are idealizations which do not take into account the fractality in time and the inherent nonlinearities of the electric components. The principle questions prior to some detailed analyses of fractional electric circuits are as follows: Why this modelling technique should be applied and what are the advantages of it beyond the well-known integer-order models?

We will try to answer these principle questions in view of the basic knowledge of relaxation phenomena and how this philosophy works when transients in electric circuits should be analysed.

Let us start with the well-known constitutive equations associated with the three basic elements of RLC electric circuits as follows[10]:

The voltage drop across an inductor

$$U_L(t) = L \frac{d}{dt} I(t). \quad (1)$$

The voltage drop across a resistor

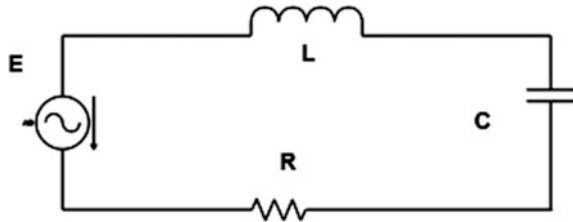
$$U_R = RI(t). \quad (2)$$

The voltage drop across a capacitor

$$U_c = \frac{1}{C} \int_0^t I(z) dz. \quad (3)$$

Applying the Kirchhoff voltage law and the above constitutive equations we can express the homogeneous integer-order differential equation expressed through the voltage drop across the capacitor (3) or alternatively non-homogenous equation about the current $i_C(t)$ (2) corresponding to RLC circuit (see Fig. 1):

Fig. 1 Basic RLC circuit used in the analysis



$$L \frac{d^2}{dt^2} U_c(t) + R \frac{d}{dt} U_c(t) + \frac{1}{C} U_c(t) = \frac{d}{dt} u(t), \tag{4}$$

where $u(t)$ is the unit step of the voltage (Heaviside function).

Let consider only a resistive medium (only Ohmic resistance) and that the current between points with a gradient of the electric potential $\partial\varphi/\partial x$ depends on its history over time, namely

$$I(t) = -\frac{1}{R} \int_0^t S_z(t-z) \frac{\partial\varphi}{\partial x} dt. \tag{5a}$$

We may simplify the problem and consider a homogeneous resistor as element of a circuit where accordingly $\partial\varphi/\partial x$ is equal to the voltage drop applied to its ends. Let us consider the voltage drop as a unit step $u(t)$ and therefore the memory integral (5a) can be expressed as (omitting the negative sign as unnecessary since the equation becomes expressed in scalar values) in contrast to (5a) where $\partial\varphi/\partial x$ is a vector.

$$I(t) = \frac{1}{R} \int_0^t S_z(t-z) u(t) dt. \tag{5b}$$

In these equations z is a dummy variable, while the negative sign in front of the history integral simply indicates that the current flow direction is opposite to the change in the potential gradient.

Moreover, (5a) and (5b) are constitutive equations which simply state *natural processes with infinite speed of change do not exist and therefore the relaxation in time should be taken into account*. In the heat conduction area, this is the well-known Cattaneo–Maxwell postulate of heat transfer across a homogeneous rigid conductor [11–15], namely

$$q_H(x, t) = - \int_{-\infty}^t S_H(x, t) \nabla T(x, t-z) dz. \tag{6}$$

In terms of the present chapter the heat flux $q_H(x, t)$ is analogue of the electric $i(x, t)$ current, while $\nabla T(x, t)$ corresponds to the electric tension (potential $\partial\varphi/\partial x$) applied to the resistor. As in the spatially homogeneous heat conductors, the current passing through a simple resistor, the relaxation kernel, should be space-independent, that is $S_R(t)$ is a function only of the time.

If we consider the relaxation kernel as an exponential function $S_H(t) = \exp(-(t - z)/\tau_z)$, where the relaxation time τ_z is finite, i.e. $\tau_z = \text{const.}$; then for $\tau_z \rightarrow 0$ the limit of Eq. (5a) is the Ohm law (2). However, in the first-order approximation of the current $i(t)$, in τ_z we have

$$i(t + \tau) \approx i(t) + \tau_z \frac{\partial i(t)}{\partial t}. \quad (7)$$

This leads to a first-order differential equation

$$\frac{1}{\tau_z} i(t) + \frac{\partial i(t)}{\partial t} = -\frac{k_1}{\tau_z} \frac{\partial \theta(x, t)}{\partial t}. \quad (8)$$

The integration of (8) leads to the constitutive Eq. (5a) which is an analogue of the Cattaneo constitutive equation and considers only *linear elastic effects* in the transient of the passing electric current.

However, if the relaxation kernel is presented as a linear combination [16]

$$S_{\text{ex}} = k_1 \delta(z) + (k_2/\tau_z) \exp(-z/\tau_z), \quad (9)$$

where $k_1 = 1/R$ and $k_2 = 1/R_2$ are the *effective resistance* and the *elastic resistance* of the resistor. $\delta(z)$ is the Dirac delta function. If the relaxation kernel is presented only by $\delta(z)$, that is $S_z(t) = \delta(t)$, then Eq. (5a) reduces to the classic Ohm law.

In case the relaxation function is expressed as S_{ex} , then the modified Ohm law leads to a current defined as

$$i(t) = \frac{1}{R_1} U(t) - \frac{1}{R_2} \frac{1}{\tau_z} \int_{-\infty}^t e^{-\frac{(t-z)}{\tau_z}} \frac{\partial U(z)}{\partial z} dz. \quad (10)$$

Hence, when τ_z is infinite, the history of the current evolution process presented by the memory integral [the second term in (10)] is zero and we get the classical Ohm law. The consequent step in integration of (10), with a finite value of τ_z , leads to the well-known Kirchhoff's telegraph equation [16] (see [16] and the reference therein for more details).

Now, the natural question is: what happens if the relation function in (5a) is defined not by an exponential (Jeffrey's kernel $S_H(t)$) but with a power-law function $S_s(t, \mu) = t^{-\mu}$? In this case, we get a new form of the history integral

$$I(t) = \frac{1}{R} \int_0^t (t-z)^{-\mu} U(z) dz, \quad 0 < \mu < 1. \quad (11)$$

As we will see in the next section, the fractional integral with singular power-law kernel $S_s(t, \mu) = t^{-\mu}$ is the basis of the widely used Riemann–Liouville and Caputo fractional derivatives. Otherwise, when the relaxation kernel is of the Jeffrey’s type we get a history integral with non-singular kernel [17, 18] resulting in the Caputo–Fabrizio time-fractional derivative [15, 17, 18].

With these introductory notes, we try to explain why fractional integrals and derivatives are used to describe relaxation processes in electric circuits. The reason is simple and physically motivated: *There are no physical phenomena with infinite speed of change and the correct description should take into account relaxation processes.* If the relaxation process is rapid and the relaxation time is negligible with respect to the entire observation time at issue, then we get the well-known constitutive equation (5a). However, when the processes at issue are with time-scales comparable to the relaxation times, the histories (the memories) should be taken into account that leads to use of the memory formalism (history integrals) and the fractional calculus approach.

3 Preliminaries: Necessary Mathematical Background

We start with the mathematical background necessary to demonstrate the solution and modelling approaches. The fractional integral and derivatives of Riemann–Liouville and Caputo with singular (power-law) kernels are the principles ones used in the literature devoted to the problems discussed in this chapter. In addition, the basis of the newly defined Caputo–Fabrizio derivative with a non-singular (Jeffrey) kernel is briefly outlined.

3.1 Time-Fractional Integral and Derivatives with Singular Kernels

3.1.1 Fractional Integral

In accordance with the Riemann–Liouville approach, the fractional integral of order $\mu > 0$ is a natural result of the Cauchy’s formula reducing calculations of the m -fold primitive of a function $f(t)$: the result is a single integral of convolution type [19] for arbitrary positive number $\mu > 0$, namely

$${}_0I^\mu f(t) := \frac{1}{\Gamma(\mu)} \int_0^t (t - \tau)^{\mu-1} f(\tau) d\tau, \quad t > 0, \quad n \in \mathbb{R}^+ \tag{12}$$

where $\Gamma(\cdot)$ is the gamma function.

For the sake of convenience, we will use also the notation ${}_0D^{-\mu}f(t)$ for ${}_0I^\mu f(t)$. Further, the law of exponents for fractional integrals means ${}_0D^{-\mu}{}_0D^{-\nu}f(t) = {}_0D^{-\mu-\nu}f(t) = {}_0D^{-\nu}{}_0D^{-\mu}f(t)$.

The Laplace transform of the fractional integral is defined by the convolution theorem as

$$\text{Laplace} [{}_0D_t^{-\mu}f(t)] = \text{Laplace} \left[\frac{t^{\mu-1}}{\Gamma(\mu)} \right] \text{Laplace}[f(t); s] = s^{-\mu}F(s), \tag{13}$$

where $\Re(s) > 0$, $\Re(\mu) > 0$ and $F(s)$ is the Laplace transform of $f(t)$.

3.1.2 Riemann–Liouville Fractional Derivative

Therefore, we may define the fractional derivative $D^\mu f(t)$ with $n \in \mathbb{N}^+$ by the relations [19] as ${}_0D^\mu{}_0I^\mu = I$ but ${}_0I^\mu{}_0D^\mu \neq I$. Therefore, D^μ is the left-inverse, but not right-inverse, to the integral operator I^μ . Hence, introducing a positive integer m such that $m - 1 < \mu \leq m$ the natural definition of the Riemann–Liouville (left-sided) fractional derivative of order $\mu > 0$ is

$${}_0D^\mu f(t) := {}_0D^m{}_0I^{m-\mu}f(t) = \frac{1}{\Gamma(m - \mu)} \frac{d^m}{dt^m} \int_0^t \frac{f(\tau)}{(t - \tau)^{\mu+1-m}} d\tau, \tag{14}$$

$$m - 1 < \mu \leq m, \quad m \in \mathbb{N}$$

$${}_0D^\mu f(t) = \frac{d}{dt} f(t), \quad \text{for } \mu = 1. \tag{15}$$

Thus, we have $D^0 = I^0 = I$, that is $D^\mu I^\mu = I$ for $\mu \geq 0$. Additionally, the fractional derivative of power-law function and a constant, frequently used in this chapter, is

$${}_0D^\mu t^\beta = \frac{\Gamma(\beta + 1)}{\Gamma(\beta + 1 - \mu)} t^{\beta-\mu} \quad \text{and} \quad {}_0D^\mu C = C \frac{t^{-\mu}}{\Gamma(1 - \mu)} \mu > 0, \quad \beta > -1, \tag{16}$$

$t > 0.$

Similarly, the fractional integrals of the power-law function and a constant are

$${}_0D^{-\mu}t^\beta = \frac{\Gamma(\beta + 1)}{\Gamma(\beta + 1 + \mu)}t^{\mu + \beta}, \quad {}_0D^{-\mu}C = \frac{C}{\Gamma(1 + \mu)}t^\mu, \quad \mu \neq 1, 2, \dots \quad (17a, b)$$

The Laplace transform of the Riemann–Liouville fractional derivative for $m \in N$ is

$$\begin{aligned} \text{Laplace} \left[\frac{d^m}{dt^m} f(t); s \right] &= s^m F(s) - \sum_{k=0}^{m-1} s^{m-k-1} f^{(k)}(0+) \\ &= s^m F(s) - \sum_{k=1}^m s^{k-1} D_t^{\mu-k} f(0+), \end{aligned} \quad (18)$$

where $\Re(s) > 0$, $\Re(\mu) > 0$ and $m - 1 \leq \mu < m$.

3.1.3 Caputo Fractional Derivative

The Caputo derivative of a casual function $f(t)$, i.e. $f(t) = 0$ for $t < 0$, is defined [19, 20] as

$$\begin{aligned} {}_cD_t^\mu f(t) &= {}_0I^{m-\mu} \frac{d^m}{dt^m} f(t) = {}_0D_t^{-(m-\mu)} f^{(m)}(t) \\ &= \frac{1}{\Gamma(m - \mu)} \int_0^t \frac{f^{(m)}(\tau)}{(\tau - t)^{\mu+1-m}} d\tau, \end{aligned} \quad (19a)$$

where $m \in N$ and $m - 1 < \mu < m$

$${}_cD_t^\mu f(t) = \frac{d}{dt} f(t), \quad \text{for } \mu = 1. \quad (19b)$$

The Laplace transform of Caputo derivative is

$$\text{Laplace} [{}_cD_t^\mu f(t); s] = s^\mu F(s) - \sum_{k=0}^{m-1} f^{(k)}(0) s^{\mu-k-1}. \quad (20)$$

The Caputo derivative of a constant is zero, i.e. ${}_cD_t^\mu C = 0$ that matches the common knowledge we have from the integer-order calculus; and because of that the Riemann–Liouville derivative is the preferred fractional derivative among mathematicians, while Caputo fractional derivative is the preferred one among engineers [3].

If $f(0) = f'(0) = f''(0) = \dots = f^{(m-1)}(0) = 0$, then both Riemann–Liouville and Caputo derivatives coincide. In particular for $\mu \in (0, 1)$ and $f(0) = 0$ one has

${}_C D_t^\mu f(t) = {}_{RL} D_t^\mu f(t)$. Further, in this chapter we will use the notations ${}_{RL} D_t^\mu f(t)$ and ${}_C D_t^\mu f(t)$ to discriminate the effects of the solutions when both derivatives are used. In addition in some situations, we will use also the notation $\partial^\mu f(t)/\partial t^\mu$ meaning a time-fractional derivative without specification of the type.

Further, for simplicity, we will assume that all expressions are with the Caputo time-fractional derivative. For the sake of coherence with the existing practice describing transient regimes in electrical circuits, we will use the notation ${}_C D_t^\mu = d^\mu/dt^\mu$.

3.1.4 Mittag–Leffler Function

Generally, the fractional-order differential equation has the form

$$\sum_{k=0}^n a_k D_t^{\mu_k} f(t) = g(t). \quad (21)$$

After application of the Laplace transform and successful solution on the s -space, the inverse transform with $0 < \mu < 1$ requires a special function, namely the Mittag–Leffler function defined as [19, 21]

$$E_\mu(t) = \sum_{k=0}^{\infty} \frac{t^k}{\Gamma(\mu k + 1)}, \quad \mu > 0. \quad (22)$$

For example with $\mu = 1$ we have $E_1(t) = \sum_{k=0}^{\infty} \frac{t^k}{\Gamma(k+1)} = e^t$ since the Mittag–Leffler function is a generalization of the exponential function and widely used for describing dissipative processes.

3.1.5 Alternative Representation of the Fractional Derivative with Singular Kernels

In order to facilitate the understanding of the transition from the classical integer-order models to the ones involving time-fractional derivatives, we will present this step as [22]

$$\frac{d}{dt} \rightarrow \frac{1}{\sigma^{1-\mu}} \frac{d^\mu}{dt^\mu}. \quad (23)$$

Here the parameter σ (with a dimension in seconds) plays a role of normalizing function, and when $\mu = 1$ we get the ordinary fractional derivative. This presentation is more intuitive rather than mathematically correct but for people not involved in fractional calculus, it would be the more acceptable approach.

3.2 Fractional Derivatives with Non-singular Kernel

The hot topic in modelling of dissipative phenomena involves fractional derivatives by the application of fractional derivatives. As it is stated in the seminal work of Caputo and Fabrizio [17] many classical constitutive equations (see the comments in [15] and the references therein) cannot model some transport dissipative process with advanced characteristics. To satisfy these requirements a new time-fractional derivative with a non-singular smooth exponential kernel was conceived by Caputo and Fabrizio [17], namely

$${}_{CF}D_t^\mu f(t) = \frac{M(\mu)}{1-\mu} \int_0^t \exp\left[-\frac{\mu(t-z)}{1-\mu}\right] \frac{df(z)}{dz} dz \quad (24)$$

$${}_{CF}D_t^\mu f(t) = \frac{1}{1-\mu} \int_0^t \exp\left[-\frac{\mu(t-z)}{1-\mu}\right] \frac{df(z)}{dz} dz, \quad (25)$$

where $M(\mu)$ in Eq. (24) is a normalization function such that $M(0) = M(1) = 1$. With $M(\mu) = 1$ suggested for convenience in [17] we get the final definition of the Caputo–Fabrizio time-fractional derivative in the form of Eq. (25). The derivative of a constant is zero as in the classical Caputo derivative [19, 20], but now the exponential (Jeffrey’s) kernel has no singularity. An application to transients in RC circuit is demonstrated in this chapter.

The Laplace transform of Caputo–Fabrizio derivative is [17]

$$\begin{aligned} \text{Laplace} [{}_{CF}D_t^\mu f(t)] &= \frac{1}{1-\mu} \text{Laplace}[f(t)] \text{Laplace}\left(\exp - \frac{\mu}{1-\mu} t\right) \\ &= \frac{s \text{Laplace}[f(t)] - f(0)}{s + \mu(1-s)}. \end{aligned} \quad (26)$$

Similar to the alternative and intuitive presentation of the transition from fractional to integer-order derivative we have the following [24, 25]:

- Fractional in time

$$\frac{d}{dt} \rightarrow \frac{1}{\exp\left[-\frac{(1-\mu)}{2-\mu}\right] \sigma_t} {}_{CF}D_t^\mu f(t) \quad (27)$$

- Fractional in space

$$\frac{d}{dt} \rightarrow \frac{1}{\exp\left[-\frac{(1-\mu)}{2-\mu}\right] \sigma_x} {}_{\text{CF}}D_x^\mu f(t), \quad (28)$$

where for $\mu = 1$ we recover the ordinary (integer-order) derivatives

4 Transients in Fractional Electric Circuits: Analyses by Examples

4.1 Fractional RC Circuit

The conventional integer-order differential equation for the RC circuit is given by

$$E(t) = R \frac{dq(t)}{dt} + \frac{q(t)}{C}. \quad (29)$$

We will investigate two simple cases: capacitor discharge and transient due to unit step of the voltage.

4.1.1 Capacitor Discharge

In case of capacitor discharge through the resistor R we have $E(t) = 0$

$$C \frac{dU_c}{dt} + \frac{1}{R} U_c(t) = 0 \quad (30)$$

and in this case the solution of (30) classic solution is [25]

$$U_c = U_0 \exp\left(-\frac{t}{RC}\right), \quad U_c(t=0) = U_0. \quad (31)$$

With Riemann–Liouville time-fractional derivative the analogue of (31) is

$${}_0D^\mu U_c(t) + \frac{1}{R} U_c(t) = 0. \quad (32)$$

Then, the solution is [26]

$$U_c^{\text{RL}}(t) = U_0 E_\mu\left(-\frac{1}{RC} t^\mu\right) - U_0 \frac{\mu}{\Gamma(1-\mu)} \int_0^t (t-z)^{-\mu} z^{\mu-1} E_\mu\left(-\frac{1}{RC} z^\mu\right) dz \quad (33)$$

or equivalently in a dimensionless form

$$\frac{U_c^{\text{RL}}(t)}{U_0} = E_\mu\left(-\frac{1}{\text{RC}}t^\mu\right) - \frac{\mu}{\Gamma(1-\mu)} \int_0^t (t-z)^{-\mu} z^{\mu-1} E_\mu\left(-\frac{1}{\text{RC}}z^\mu\right) dz. \quad (34)$$

With Caputo derivative the alternative equation of the capacitor discharge is

$${}_c D_t^\mu U_c(t) + \frac{1}{R} U_c(t) = 0'. \quad (35)$$

Then, the solution is

$$U_c^C(t) = U_0 E_\mu\left(-\frac{1}{\text{RC}}t^\mu\right) \quad (36)$$

or equivalently in a dimensionless form

$$\frac{U_c^C(t)}{U_0} = E_\mu\left(-\frac{1}{\text{RC}}t^\mu\right). \quad (37)$$

We can see that the only difference between (33) and (36) is the last term in (RC-1d) due to the fact that the Riemann–Liouville derivative of a constant is not zero (see 17b).

With the Caputo–Fabrizio derivative, the same problem has a model resembling (35), namely

$${}_{\text{CF}} D_t^\mu U_c(t) + \frac{1}{R} U_c(t) = 0. \quad (38)$$

The simple solutions through the Laplace transform yield

$$U_c^{\text{CF}}(t) = U_0 \exp\left(-\frac{2\mu}{2\text{RC} + 2(1-\mu)}t\right) \quad (39)$$

or equivalently in a dimensionless form

$$\frac{U_c^{\text{CF}}(t)}{U_0} = \exp\left(-\frac{2\mu}{2\text{RC} + 2(1-\mu)}t\right). \quad (40)$$

4.1.2 Transient Due to Unit Step of the Voltage

Assuming the transient analysis, that $E(t) = u(t)$ is a unit step function, we may express (29) in a dimensionless form [23]

$$\frac{d\eta_c(\tau)}{d\tau} + \eta_c(\tau) = u(\tau), \quad \eta_c(\tau) = \frac{q(t)}{C}, \quad \tau = \frac{t}{RC}. \quad (41a, b)$$

The time-fractional counterpart of (41a) (assuming Caputo derivatives) is

$$\frac{d^\mu \eta_c(\tau)}{d\tau^\mu} + \eta_c(\tau) = u(\tau), \quad 0 < \mu < 1. \quad (42)$$

Solution in the Time Domain

With the Laplace transform of the Caputo derivative (in the alternative form expressed by Eq. 20) we have from (42) that

$$V_c(\bar{s}) = \frac{1}{\bar{s}(\bar{s}^\mu + 1)}, \quad V_c(\bar{s}) = L[\eta_c(\tau)] \quad \text{and} \quad \bar{s} = (RC)s. \quad (43a, b, c)$$

The inverse Laplace transform of (43a) yields a solution in the time domain [23] :

$$\eta_c(t) = u(t) \left[1 - \sum_{k=0}^{\infty} (-1)^k \frac{\left(\frac{t}{RC}\right)^{k\mu}}{\Gamma(k\mu + 1)} \right] = u(t) [1 - E_{\mu,1}(\tau)] \quad (44a, b)$$

or equivalently in a dimensionless form

$$\frac{\eta_c(t)}{u(t)} = 1 - E_{\mu,1}(\tau). \quad (44c)$$

For $\mu = 1$ we have $E_{1,1} = e^{-\tau} = e^{-t/RC}$ and $\eta_c(t)/u(t) = 1 - e^{-t/RC}$.

The solution was tested by a simple example [23] calculating the times required the response to attain 10% of its initial value and the 90% value of the final (saturation) level. The answers are straightforward because from (44a) we have [23], for instance

$$0.99 = 1 - \sum_{k=0}^{\infty} (-1)^k \frac{(\tau_{ss})^{k\mu}}{\Gamma(k\mu + 1)} = 1 - E_{\mu,1}(\tau_{ss}). \quad (45a)$$

This allows to find a solution with respect to the dimensionless settling time defined as $\tau_{ss} = t_{ss}/RC$. From (45a) we have

$$f(\tau_{ss}) = \sum_{k=0}^{\infty} (-1)^k \frac{(\tau_{ss})^{k\mu}}{\Gamma(k\mu + 1)} - 0.01 = 0. \quad (45b)$$

The dimensionless settling time t_{ss}/RC can be determined by the Newton-Raphson method, where the m th iteration of solution of (45b) can be expressed as [23]

$$\tau_{ss}^{(m+1)} = \tau_{ss}^{(m)} - \frac{f[\tau_{ss}^{(m)}]}{f'[\tau_{ss}^{(m)}]}. \tag{46}$$

The plot of $\tau_{ss} = t_{ss}/RC$ as a function of the fractional-order μ demonstrates strong decaying behaviour (see Fig. 2).

Solution in the Frequency Domain

Starting from the Laplace transform (44) and multiplying both sides by $\bar{s} = (RC)s$ we get [23]

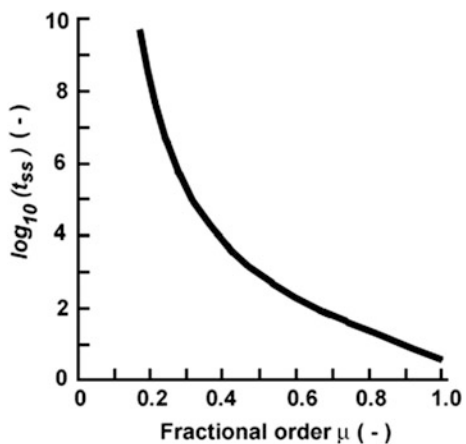
$$H(\bar{s}) = \frac{1}{\bar{s}^\mu + 1}. \tag{47}$$

Now we may construct the Bode plot from the relation $H(j\omega)|_{\bar{s}=j\omega}$ resulting in two equations:

$$|H(j\omega)|_{dB} = 20 \log_{10}(|H(j\omega)|) \tag{48a}$$

$$\arg H(j\omega) = \frac{180 \arg H(j\omega)}{\pi}. \tag{48b}$$

Fig. 2 Semi-logarithmic relationship of the settling time and the fractional order μ
Adapted from [23]



4.2 Fractional RL Circuit

With only resistor and inductor charged by a voltage source $U(t)$, the integer-order model is

$$L \frac{d}{dt} I(t) + RI(t) = E(t). \quad (49)$$

We will consider some sub-examples of (49) and the solutions of their time-fractional analogues.

4.2.1 Constant Electromotive Force

With initial condition $I(t=0) = I_0 \neq 0$ and $E(t) = E_0$, the solution of (49) is [27]

$$I(t) = \left[I_0 - \frac{E_0 L}{R} \right] \exp\left(-\frac{R}{L} t\right) + \frac{E_0 L}{R} \quad (50a)$$

or equivalently

$$\frac{I(t)}{I_0} = \left[1 - L \frac{I_{R0}}{I_0} \right] \exp\left(-\frac{R}{L} t\right) + L \frac{I_{R0}}{I_0}, \quad I_{R0} = \frac{E_0}{R}. \quad (50b)$$

With Riemann–Liouville time-fractional derivative the analogue of (49) is [26, 27]

$${}_0 D^\mu I(t) + \frac{R}{L} I(t) = \frac{E_0}{L}. \quad (51a)$$

With a dimensionless solution

$$\frac{I(t)}{I_0} = E_\mu\left(-\frac{R}{L} t^\mu\right) + \mu \int_0^t \left[\frac{U_0}{I_0 L} - \frac{(t-z)^\mu}{\Gamma(1-\mu)} \right] z^{\mu-1} E'_\mu\left(-\frac{R}{L} z^\mu\right) dz. \quad (51b)$$

Now, with Caputo derivative the equivalent of (49) and (51a) is [26]

$${}_C D_t^\mu I(t) + \frac{R}{L} I(t) = \frac{E_0}{L}. \quad (52a)$$

Then, the dimensionless solution is

$$\frac{I(t)}{I_0} = \left(1 - \mu \frac{I_{R0}}{I_0} \right) E_\mu\left(-\frac{R}{L} t^\mu\right) + \mu \frac{I_{R0}}{I_0}, \quad I_{R0} = \frac{E_0}{R}. \quad (52b)$$

With the Caputo–Fabrizio derivative the same transient process is modelled as

$${}_{CF}D_t^\mu I(t) + \frac{R}{L}I(t) = \frac{E_0}{L}, \tag{53a}$$

and therefore the solution is

$$\frac{I(t)}{I_0} = \frac{I_{R0}}{I_0} - \left(\frac{I_{R0}}{I_0} - 1\right) \exp\left[-2\mu \frac{1}{L/R + (1 - \mu)t}\right], \quad I_{R0} = \frac{E_0}{R}. \tag{53b}$$

The plots in Fig. 3 show the graphical representations of the developed solutions, as it was reported by [26] for $\mu = 0.5$; there is no similarity between the developed solutions. However, when $\mu \rightarrow 1$, particularly for $\mu = 0.999$, solutions with the classical ($\mu = 1$) and the Caputo–Fabrizio derivative coincide matching in the exponential current increase and the steady-state value that is easy to check from the developed dimensionless solutions (see Fig. 4 in the original work).

4.2.2 Absence of Electromotive Force

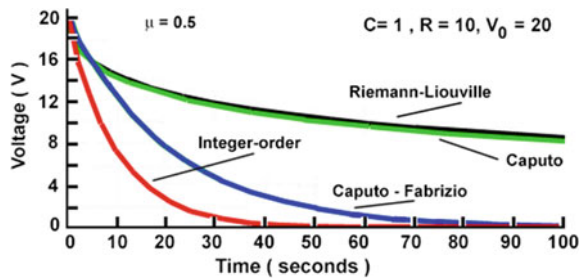
Hence with $E(t) = 0$ we may rewrite (49) in terms of Caputo time-fractional derivative as

$${}_CD_t^\mu I(t) + \frac{R}{L}I(t) = 0. \tag{54}$$

Then, the solution through the Laplace transform of (54) yields [27]

$$I(s) = I_0 \frac{s^{\mu-1}}{(s^\mu + R/L)} \Rightarrow I(t) = I_0 E_\mu\left(-\frac{R}{L}t^\mu\right). \tag{55}$$

Fig. 3 Time evolution of the voltage calculated by different fractional derivatives in the case $\mu = 0.5$. Adapted from [26]



4.2.3 Electromotive Force as a Unit Step Function

With an electromotive force as a unit step, i.e. $E(t) = u(t) = 1$ we have with the Caputo derivative

$${}_c D_t^\mu I(t) + \frac{R}{L} I(t) = \frac{u(t)}{L}. \quad (56)$$

With the initial conditions $I(t=0) = I_0 > 0$ taking into account that $\mu \rightarrow 1$ ${}_c D_t^\mu I(t) \rightarrow dI/dt$ we may express (56) as

$${}_c D_t^\mu I(t) = \frac{1}{L} u(t) - \frac{R}{L} I(t). \quad (57)$$

The Laplace transform of (57) is

$$I(s) = \frac{1}{L s(s^\mu + R/L)} + I_0 \frac{s^{\mu-1}}{(s^\mu + R/L)}. \quad (58)$$

Then, the time domain solution is

$$I(t) = \left(I_0 - \frac{1}{R} \right) E_\mu \left(-\frac{R}{L} t^\mu \right) + \frac{1}{R}. \quad (59)$$

4.3 Fractional RLC Circuit

The integer-order equation of an RLC circuit is

$$L \frac{d^2}{dt^2} q(t) + R \frac{d}{dt} q(t) + \frac{q(t)}{C} = 0. \quad (60)$$

The last term $q(t)/C$ is crucial for the oscillatory behaviour of the circuit since the RL circuit only exhibits a decaying transient behaviour.

4.3.1 Analysis Through the Caputo Derivative

Since the transformation of the integer-order equations to the fractional time counterparts could be considered as a formal replacement of the integer-order derivatives by fractional ones, which might cast some doubts what really needs this step, we will use the alternative approach to explain intuitively the requirement to use fractional derivatives. With the expression (23) we may present (60) as [22]

$$\frac{1}{\sigma^{1(1-\mu)}} L \frac{d^{2\mu}}{dt^{2\mu}} q(t) + R \frac{d^\mu}{dt^\mu} q(t) + \frac{q(t)}{C} = 0, \quad (61)$$

where $\frac{d^\mu}{dt^\mu}$ is the Caputo derivative, assumed by default.

The solution of (61) by the Laplace transform is [22]

$$q_{\mu(\text{RLC})}(t) = q_0 E_\mu \left[-\frac{R\sigma^{1-\mu}}{2L} t^\mu \right] \cdot E_{2\mu} \left\{ -\left[\frac{1}{LC} - \frac{R^2}{4L^2} \right] \sigma^{2(1-\mu)} t^{2\mu} \right\}. \quad (62)$$

In the undamped case when $R < 2\sqrt{L/C}$ and $q_{\mu(\text{RLC})}(t=0) = q_0$ the natural frequency is defined as $\omega_0 = \sqrt{1/LC}$.

In the limiting situation with $\mu = 1$ the solution (62) reduces to the classical solution defining the time constant $\tau_{RL} = 2L/R$:

$$q_{(\text{RLC})}(t) = q_0 \exp\left(-\frac{R}{2L}t\right) \cos(\Omega t), \quad \Omega = \sqrt{\omega_0^2 - \frac{R^2}{4L^2}}. \quad (63a, b)$$

The solution (63a) allows demonstrating the functional relationship between the normalizing parameter σ and the fractional order μ [22]

$$\mu = \sigma \sqrt{\frac{1}{LC} - \frac{R^2}{4L^2}}, \quad 0 < \sigma \leq \frac{1}{\sqrt{\frac{1}{LC} - \frac{R^2}{4L^2}}}. \quad (64a, b)$$

When the *undamped case*, $R < 2\sqrt{L/C}$ and the damping factor is defined as $\alpha = \sqrt{R/2L}$. With the condition $\alpha < \omega_0$ solution reduces to [22]

$$q_{\mu(\text{RLC})}(t_1)_{\text{under}} = q_0 E_\mu \left[-\frac{R}{2L\sqrt{\frac{1}{LC} - \frac{R^2}{4L^2}}} \mu^{(1-\mu)} t_1^\mu \right] \cdot E_{2\mu} \left\{ -\mu^{2(1-\mu)} t_1^{2\mu} \right\} \quad (65a)$$

$$\frac{t_1}{t} = \sqrt{\frac{1}{LC} - \frac{R^2}{4L^2}}. \quad (65b)$$

When the *overdamped case* is at issue where $\alpha > \omega_0$ and $R > 2\sqrt{L/C}$ the solution (62) reduces to [22]

$$q_{\mu(\text{RLC})}(t)_{\text{over}} = \bar{q}_0 E_\mu \left[-\sigma^{1-\mu} \frac{R}{2L} t^\mu \right] \cdot E_{2\mu} \left\{ -\sigma^{(1-\mu)} t^\mu \sqrt{\frac{R^2}{4L^2} - \frac{1}{LC}} \right\}. \quad (66)$$

For $\mu = 1$ the solution (66) reduces to the well-known aperiodic solution of the capacitor discharge

$$q_{\mu=1(\text{RLC})}(t)_{\text{over}} = \bar{q}_0 \exp\left[-\frac{t}{t_{\mu=1}}\right], \quad t_{\mu=1} = \frac{2L}{R\left[1 + \sqrt{1 - \frac{4L}{R^2C}}\right]}, \quad (67a, b)$$

where \bar{q}_0 is the charge of the capacitor at $t = 0$

4.3.2 Analysis Through the Caputo–Fabrizio Derivative

Case with Voltage Drop Dependent on Space and Time

For this analysis, we will use the model of Riaza [28] and the results of Atangana and Nieto [24]

$$\frac{\partial^2 U(x, t)}{\partial x^2} - LC \frac{\partial^2 U(x, t)}{\partial t^2} - (RC + GL) \quad (68a)$$

$$\frac{\partial U(x, t)}{\partial x} - GRU(x, t), \quad (68b)$$

where G denotes the electric resistance of the materials connecting the resistors (conductors) in the circuits.

Their fractional analogues of (68a, b) are [24]

$$\begin{aligned} & \frac{{}_{\text{CF}}D_x^\beta U(x, t)}{\exp\left(-\frac{\beta}{1-\beta}\sigma_x\right)} - LC \frac{{}_{\text{CF}}D_t^\beta U(x, t)}{\exp\left(-\frac{\beta}{1-\beta}\sigma_t\right)} \\ & - \frac{(RC + GL)}{\exp\left(-\frac{1-\mu}{2-\beta}\sigma_t\right)} [{}_{\text{CF}}D_t^\mu U(x, t)] - GRU(x, t) = 0 \end{aligned} \quad (69)$$

with $1 < \beta < 2$ and $0 < \mu < 1$.

This model has no analytical solution and only numerical approaches are possible. Atangana and Nieto [24] used finite-difference approximations in time and space of the Caputo–Fabrizio derivatives and the Crank–Nicolson solution scheme. More details about the numerical solution and the stability analysis are available in the original work [24]. We will skip the mentioned problems which are beyond the scope of the present chapter.

Solution in Time Domain Only

In this case the analogue of (60) is [25]

$$L \frac{{}_{\text{CF}}D_t^{2\mu} q(t)}{\exp\left(-\frac{1-\mu}{2-\mu}\sigma_t\right)} + R \frac{{}_{\text{CF}}D_t^\mu q(t)}{\exp\left(-\frac{1-\mu}{2-\mu}\sigma_t\right)} + \frac{q(t)}{C} = 0. \quad (70)$$

In this model the second fractional derivative is considered as a sequential one, namely

$${}_{CF}D_t^{2\mu}q(t) = {}_{CF}D_t^\mu [{}_{CF}D_t^\mu q(t)]. \tag{71}$$

The Laplace transform of (70) is [25]

$$L \frac{\text{Laplace} [{}_{CF}D_t^{2\mu}q(t)]}{\exp\left(-\frac{1-\mu}{2-\mu}\sigma_t^2\right)} + R \frac{1}{\exp\left(-\frac{1-\mu}{2-\mu}\sigma_t\right)} \frac{sQ(s) - q(0)}{s + \mu(1-s)} + \frac{Q(s)}{C} = 0. \tag{72}$$

With

$$\text{Laplace} [{}_{CF}D_t^{2\mu}q(t)] = s \frac{\{s\text{Laplace}[q(t) - q(0)]\}}{s + \mu(1-s)}. \tag{73}$$

The solution becomes

$$Q(s) = q(0) \frac{[a(s) + 1]}{sa(s) + b(s) + \frac{1}{C}} \tag{74a}$$

$$a(s) = \frac{1}{\exp\left(-\frac{1-\mu}{2-\mu}\sigma_t^2\right)} \frac{s}{[s + \mu(1-s)]^2} \tag{74b}$$

$$b(s) = \frac{1}{\exp\left(-\frac{1-\mu}{2-\mu}\sigma_t\right)} \frac{R}{[s + \mu(1-s)]}. \tag{74c}$$

The exact solution can be obtained by the inverse Laplace transform, namely

$$q(t) = \text{Laplace}^{-1} \left\{ \frac{q(0)[a(s) + 1]}{sa(s) + b(s) + \frac{1}{C}} \right\}. \tag{75}$$

More details concerning numerical simulations are available in the original work [25].

5 Electrical Impedance Spectroscopy to RC Circuits: An Example

The electric impedance spectroscopy is wide and well-developed scientific area [9] and the fractional-order analysis allows deeper understanding of the physical problems at issue. With this short example taken from [29], we demonstrate how the fractional-order analysis of RC circuit works.

The electrical impedance spectroscopy applies a potential difference between two electrodes attached to a sample by passing a low power alternating electric current. This input is then compared to the corresponding output voltage and current. The impedance is defined by the simple relation

$$Z(s) = \frac{U(s)}{I(s)}. \quad (76)$$

From the Kirchoff law of a simple RC circuit, we have that

$$u = R_p i + U_{C_p} \quad \text{and} \quad i = i_R + i_c = \frac{U_{C_p}}{R_p} + C_p \frac{dU_{C_p}}{dt}. \quad (77a, b)$$

In term of time-fractional derivatives the fractional versions of (77a,b) are

$$i_R = \frac{U_{C_p}}{R_p} \quad \text{and} \quad i_c = C_p \frac{d^\mu U_{C_p}}{dt^\mu}. \quad (78a, b)$$

Hence, we have

$$i = \frac{U_{C_p}}{R_p} + C_p \frac{d^\mu U_{C_p}}{dt^\mu} \quad \text{and} \quad u = R_s i + U_{C_p}. \quad (79a, b)$$

In this model the time-fractional derivative will be considered in its alternative form $(1/\sigma^{1-\mu})(d^\mu/dt^\mu)$. Further, the Laplace transforms of (79a,b) are

$$I(s) = \frac{U_{C_p}(s)}{R_p} + \frac{C_p}{\sigma^{1-\mu}} s^\mu U_{C_p}(s) \quad \text{and} \quad U(s) = R_s I(s) + U_{C_p}(s). \quad (80a, b)$$

Therefore, from the definition of the impedance (76) we have [30]

$$Z(s^\mu) = R_s + \frac{R_p}{1 + \frac{R_p C_p}{\sigma^{1-\mu}} s^\mu} \Rightarrow Z(j\omega)^\mu = R_s + \frac{R_p}{1 + \frac{R_p C_p}{\sigma^{1-\mu}} (j\omega)^\mu}. \quad (81a, b)$$

Since the normalizing function, σ needs justification that the simplest approach applicable to the RC circuit is the choice $\sigma = R_p C_p$ which allows to reduce the Cole model [29]. In the case when $\mu = 1$ we obtain an ideal RC circuit.

6 Further Commentaries

Fractional calculus is attractive not only for electrical engineers but also for any scientist applying the equivalent electric circuit approach to model biomedical problems derivatives (assume the Caputo derivative); it is possible to define a generalized in [31, 32] because of the application of the Laplace transform to the fractional impedance of a fractional in time device with a proportionality to s^μ [33–35]. In this case the well-known general devices with $\mu = -1$ (capacitor), $\mu = 0$ (resistor) and $\mu = 1$ (inductor) are special cases. In this direction the Cole–Cole impedance [29, 34, 36] with fractional developed on the basis of equivalent fractional-order circuits is a powerful tool in the bioimpedance measurements [22, 23, 34, 37].

Further, the diffuse layer capacitances at micro- and nanoelectrodes are well described by simple RC circuits [38]. The anomalous diffusion in ionic solutions, especially in the low-frequency limit where the systems may be a present anomalous electrical response, are well described by anomalous diffusion and equivalent RC circuits of fractional order [39]. In this context, the development of supercapacitors [40] is more accurately described by fractional order in their transient processes of charging and discharging [37].

Systems process with equivalent RLC circuit models which allow deep analysis by the fractional calculus approach for a hot research area with a continuously number of publication on various applications which are hard to encompass in a single chapter. For more complex cases, some literature sources are highly recommended [31, 41–43].

References

1. Oldham, K.B., Spanier, J.: *The Fractional Calculus*. Academic Press, New York (1974)
2. Samko, S.G., Kilbas, A.A., Marichev, O.I.: *Fractional Integrals and Derivatives, Theory and Applications*. Gordon and Breach Science Publishers, Langhorne (1993)
3. Podlubny, I.: *Fractional Differential Equations*. Academic Press, New York (1999)
4. Baleanu, D., Diethelm, K., Scalas, E., Trujillo, J.J.: *Fractional Calculus Models and Numerical Methods*. World Scientific Publishing Company, New York (2012)
5. Nigmatullin, R.R.: The realization of the generalized transfer equation in a medium with fractal geometry. *Phys. Status Solidi (B) Basic Res.* **133**, 425–430 (1986)
6. Petras, I.: *Fractional Order Nonlinear Systems: Modelling, Analysis and Simulation*. Springer, London (2011)
7. Uchaikin, V.: *Fractional Derivatives for Physicists and Engineers*. Springer, Berlin (2013)
8. Jonsche, A.K.: *Dielectric Relaxation in Solids*. Chelsea Dielectric Press, London (1993)
9. Brasoukov, E., Macdonald, J.R. (eds.): *Impedance Spectroscopy, Theory, Experiment and Applications*. Wiley, New York (2005)
10. Krantz, S.G., Simmons, G.F.: *Differential Equations: Theory, Technique and Practice*, 2nd edn. McGraw-Hill, Boston (2007)
11. Cattaneo, C.: On the conduction of heat (In Italian). *Atti Sem. Mat. Fis. Università Modena* **31**, 83–101 (1948)

12. Curtin, M.E., Pipkin, A.C.: A general theory of heat conduction with finite wave speeds. *Arch. Ration. Math. Anal.* **31**, 313–332 (1968)
13. Carillo, S.: Some remarks on materials with memory: heat conduction and viscoelasticity. *J. Nonlinear Math. Phys.* **12**(Suppl. 1), 163–178 (2005)
14. Ferreira, J.A., de Oliveira, P.: Qualitative analysis of a delayed non-Fickian model. *Appl. Anal.* **87**, 873–886 (2008)
15. Hristov, J.: Transient heat diffusion with a non-singular fading memory: from the Cattaneo constitutive equation with Jeffrey's kernel to the Caputo–Fabrizio time-fractional derivative. *Therm. Sci.* **20**, 765–770 (2016)
16. Joseph, D.D., Preziosi, L.: Heat waves. *Rev. Mod. Phys.* **61**, 41–73 (1989)
17. Caputo, M., Fabrizio, M.: Applications of new time and spatial fractional derivatives with exponential kernels. *Progr. Fract. Differ. Appl.* **2**, 1–11 (2016)
18. Losada, J., Nieto, J.J.: Properties of a new fractional derivative without singular kernel. *Progr. Fract. Differ. Appl.* **1**, 87–92 (2015)
19. Gorenflo, R., Mainardi, F.: Fractional calculus. Integral and differential equations of fractional order. In: Carpinteri, A., Mainardi, F. (eds.) *Fractals and fractional calculus in continuum mechanics*, 223–276. Springer, Wien (1997)
20. Caputo, M.: *Elasticità e dissipazione*. Zanichelli, Bologna (1969)
21. Gorenflo, R., Loutchko, J., Luchko, Y.: Computation of the Mittag–Leffler function and its derivatives. *Fract. Calc. Appl. Anal.* **5**, 491–518 (2002)
22. Gomez, F., Rosales, J., Guia, M.: RLC electrical circuit of non-integer order. *Cent. Eur. J. Phys.* **11**, 1361–1365 (2013)
23. Guia, M., Gomez, F., Rosales, J.: Analysis of the time and frequency domain for the RC electric circuit of fractional order. *Cent. Eur. J. Phys.* **11**, 1366–1371 (2013)
24. Atangana, A., Nieto, J.J.: Numerical solution for the model of RLC circuit via the fractional derivative without singular kernel. *Adv. Mech. Eng.* **7**, 1–7 (2015). doi:[10.1177/1687814015613758](https://doi.org/10.1177/1687814015613758)
25. Atangana, A., Badr, S.T.A.: Extension of the RLC electrical circuit to fractional derivative without singular kernel. *Adv. Mech. Eng.* **7**, 1–6 (2015). doi:[10.1177/1687814015591937](https://doi.org/10.1177/1687814015591937)
26. Alsaedi, A., Nieto, J.J., Vencatesh, V.: Fractional electric circuits. *Mech. Eng. Adv.* (2015). doi:[10.1177/1687814015618127](https://doi.org/10.1177/1687814015618127)
27. Shah, P.V., Patel, A.D., Salehbbhai, I.A., Shukla, A.K.: Analytic solution for the RLC electric circuit model in fractional order. *Abstr. Appl. Anal.* **24**, Article ID 343814, doi [10.1155/2014/343814](https://doi.org/10.1155/2014/343814)
28. Riaza, R.: Time-domain properties of reactive dual circuits. *Int. J. Circ. Theor. Appl.* **34**, 317–340 (2006)
29. Gomez-Aguiolar, J.F., Rosales-Garcia, J., Rzaio-Hernandez, J.R., Guiia-Calderon, M.: Fractional RC and LC electric circuits. *Ing. Inv. Technol. (Mexico)* **15**, 311–319 (2014)
30. Cole, K.S., Cole, R.H.: Dispersion and absorption in dielectrics I. Alternating current characteristics. *J. Chem. Phys.* **9**, 341–351 (1941)
31. Magin, R., Ortigueira, M.D., Podlubni, I., Trujillo, J.: On the fractional signals and systems. *Signal Process.* **91**, 350–371 (2011)
32. Hilfer, R. (ed.): *Application of fractional calculus in physics*. World Scientific, Singapore (2000)
33. Nakagawa, M., Sorimachi, K.: Basic characteristics of a fractance device. *IEICE Trans. Fundam. Electron. Commun. Comput. Sci.* **75**, 1814–1819 (1992)
34. Freeborn, T.J.: A survey of fractional-order circuit models for biology and biomedicine. *IEEE J. Emerg. Sel. Top. Circ. Syst.* (2013). doi:[10.1109/JETCAS.2013.2265797](https://doi.org/10.1109/JETCAS.2013.2265797)
35. Inaba, A., Manabe, T., Tsuji, H., Iwamoto, T.: Electrical impedance analysis of tissue properties associated with ethylene induction by electric circuit in cucumber. *Plant Physiol.* **77**, 195–205 (2005)
36. Cole, K.S.: Permeability and impermeability of cell membranes for ions. In: *Cold Spring Harbor Symposia on Quantitative Biology*, vol. 8, pp. 110–122 (1940)

37. Freeborn, T.J., Elwakil, A.S.: Measurement of supercapacitor fractional-order parameters from voltage-excited step response. *IEEE J. Emerg. Top. CAS.* **3**, 367–376 (2013)
38. Dickinson, E.J.F., Compton, R.G.: How ell does simple RC circuit analysis describe diffuse double layer capacitance at smooth micro-and nanoelectrodes? *J. Electroanal. Chem.* **655**, 23–31 (2011)
39. Silva, F.R.G.B., Ribeiro, H.V., Lenzi, M.K., Petrucci, T., Michels, F.S., Lenzi, E.K.: Fractional diffusion equations and equivalent circuits applied to ionic solutions. *Int. J. Electrochem. Sci.* **9**, 1892–1901 (2014)
40. Rousan, A.A., Ayoub, N.Y., Alzoubi, F.Y., Khateeb, H., Al-Qadi, M., Hasan (Qaseer), M.K., Albis, B.A.: A fractional LC–RC circuit. *Fract. Calc. Appl. Anal.* **9**, 33–41 (2006)
41. Agarwal, O.P., Sabatier, J., Macahado, J.A.T. (eds.): *Advances in fractional calculus: theoretical developments and applications in physics and engineering*. Springer, Berlin (2007)
42. Kaczorek, T., Rogowski, K.: *Fractional linear systems and electric circuits*. Springer, London (2007)
43. Elwakil, S.A.: Fractional-order circuits and systems: an emerging interdisciplinary research area. *IEEE Circuit Syst. Mag.* **10**, 40–50 (2010)

The Electromagnetic Compatibility in Researches of Railway Traffic Control Devices

Zofia Wróbel

Abstract Using modern electronic devices in the railway extorts the necessity of complying the rules of coexistence of these devices in an electromagnetic environment in compliance with rules of the electromagnetic compatibility. Performing researches of railway devices in the range of electromagnetic compatibility is essential not only because of the negative influence on the railway traffic controlling devices, but also there can be an influence on the safety of devices and systems of public use. This results from the mutual coexistence of public objects like individual houses or huge commercial galleries full with systems and electronic devices. They are often found in the zone of the rolling stock influence. In the report, main sources of electromagnetic disturbances in the railway area and ways of their measurement are represented.

Keywords Electromagnetic compatibility · Radioelectric disturbances · Electromagnetic disturbances · Measurements

1 Introduction

The electromagnetic compatibility (EMC—often used shortening) can be defined as the ability of given apparatus, an equipment set or a system of an activity in an electromagnetic environment in a satisfying way and without producing disturbances which are not tolerated by everything found in this environment [1].

The term apparatus qualifies all electric and electronic devices along with their equipment and installations containing electric and/or electronic elements [1].

Z. Wróbel (✉)

PKP Polish Railway Lines JSC, Railway Lines Establishment in Rzeszów,
Rzeszów, Poland

e-mail: zwrobel@prz.edu.pl

© Springer International Publishing AG 2018

D. Mazur et al. (eds.), *Analysis and Simulation of Electrical and Computer Systems*, Lecture Notes in Electrical Engineering 452,
https://doi.org/10.1007/978-3-319-63949-9_17

275

At first, when mechanical devices were used in the railway traffic control (rtc), the electromagnetic compatibility in PKP (Polish Railways) was connected mostly with the emissivity from the electric traction. The using of electric, electronic and microprocessor devices caused the enlargement of requirements concerning compatibilities for these devices.

In this range the compatibility can be divided into internal compatibility including all railway devices: electric traction, feed systems, rtc devices, telecommunication and informatic devices and external including disturbances originated from different industrial environments and natural disturbances.

The internal compatibility qualifies the interaction of elements in their own environment. For example, in the railway environment, this is the interaction of the electric traction and the devices of the railway traffic control.

The external compatibility refers to influences among different environments. These are industrial environments and the natural environment. The influence of railway devices outside is qualified as the emission, and the extent of other disturbances influence from outside on railway devices is their resistance.

2 The Railway Environment in the Area EMC

The complexity of the electromagnetic compatibility problems in the railway environment is conditioned by

- considerable area extensiveness;
- interaction of circuits and devices of high and low voltage at different systems of power supply;
- common conduct of feeding, signal, control and telecommunication cables;
- complexity and the interrelationship of subsystems including devices of different generations; and
- possibility of simultaneous influence of disturbances from many sources.

3 The Formation and the Transfer of Disturbances

Disturbances are electromagnetic occurments appear simultaneously with a useful signal (desirable) and they are the reason of the irregular work of the given system. In the literature, different methods of classification the disturbances can be found [1].

From the regard in time durations of the disturbance, it is can be divided into

- prolonged, when the duration is greater than 0.2 s (above 1 s—the buzz), and
- short duration, called switching noise (the duration to 0.2 s and the break-time above 0.2 s).

Taking into account the partition from the regard of the transferred energy, we can distinguish the following:

- -Lowenergetic (to 100 mJ) of high frequency. They belong to them bursts, that is to say, disturbances qualified by the name of quick electric temporary states. They are the most frequent and most dangerous source of disturbances arise in joining processes in which the interruptions of the circuit happen in other moments than the passing of the current through the zero-value. Especially strong disturbances of this type can arise, when inductive charges appear in the system. The specificity of the railway environment connected with the common conduct of various cables in considerable distances is propitious to the penetration of this type of disturbances to neighbouring circuits and systems, even if as a result of the capacity coupling. On account of the not large energy most often it does not go as far to permanent damages, but disturbances caused by it can be even more dangerous in results, than in the case of strokes of high energy.
- High-energy courses of a large energy (from 100 mJ to 40 J), that is to say, atmospheric discharges are most often a source of electric strokes. They arise also during short circuits in the elektroenergetic power supply circuits and as a result of joining processes. Endangerments of a single high-frequency strokes character having considerable voltages amplitudes and a large energy in spite of they are relatively rare; however, they are especially dangerous for rtc devices and telecommunication systems working in the railway environment. As a result of their influence, it goes as far not only to disturbances in the systems work but also to their physical extensive damages.

Electromagnetic disturbances occurring in railway devices can be caused by the following:

- The electric coupling happening by mutual capacities of different parts of devices or circuits being found in different potentials. These occurrences appear at quick changes of high potentials (du/dt) in the range of the internal compatibility in devices found in close relation to itself distance.
- The galvanic coupling, occurring in common sections of two or more electric circuits, in the area which follows an overlap of currents and the influence of voltages falls in circuits compound. A characteristic example is track circuits and the occurrence of stray currents.
- The inductive coupling caused by inducing conjugate by the mutual inductance circuits of strange voltages to the disturbed circuit. This occurrence is characteristic for cables of rtc devices led parallel to tracks.
- The coupling by the electromagnetic field, emitted across circuits and devices which produce quickly variable electric and magnetical field. It appears in devices working at a high frequency, containing components of high frequency and in the case, when temporary states happen with large abruptnesses of voltages or currents changes (ergoelectronic converters installed in vehicles and connected to them installations and circuits).

4 The Classification of the Railway Traffic Controlling Devices

For these devices we ought to accept all devices installed in stations and railway tracks:

- jointless track circuits and overlaid electronic track circuits,
- metres of the axis,
- the electronic control panel for rtc devices,
- interlocking computer devices,
- automatics electronic devices of the gravity shunting on hump,
- devices of automatic line block system,
- the diagnostic system of automatic line block system,
- devices of the train controlling of the railway traffic operations (e.g. the train brake controlling) and
- devices of the automatic level crossing.

5 The State of Normalization

Problems of the electromagnetic compatibility in the railway environment are qualified in the group of norms [2]. These norms are compatible to the Directive 89/366/EEC of the European Community Council concerning EMC. They systematized problems of the electromagnetic compatibility in the railway environment, because they approach to the problem in a systematic manner and open to further progress in the EMC sphere. They characterize and qualify requirements of the railway system as a whole and of its each (individual) subsystems, keeping among them the electromagnetic compatibility. The realization, by the device, of requirements of each norm means only this, that the article is conforming to these requirements and is more probable that it will be, in real exploitation conditions, more compatible electromagnetically than a product which does not realize these requirements.

Those group of norms contains six parts:

- 50121-1 Railway applications. Electromagnetic compatibility. General.
- 50121-2 Railway applications. Electromagnetic compatibility. Emission of the whole railway system to the outside world.
- 50121-3-1 Railway applications. Electromagnetic compatibility. Rolling stock. Train and complete vehicle.
- 50121-3-2 Railway applications. Electromagnetic compatibility. Rolling stock. Apparatus.
- 50121-4 Railway applications. Electromagnetic compatibility. Emission and immunity of the signalling and telecommunications apparatus.

- 50121-5 Railway applications. Electromagnetic compatibility. Emission and immunity of fixed power supply installations and apparatus.

The specificity of the railway environment demands also usages of other groups of norms, concerning among others things like the lightning protection [3]. In this range a radical change of normalization rules took place. The issue of these norms does not close the process of changes. Qualified teams, so-called maintenances of norms, have the job of estimating after 5 years of the running of a given norm, its usefulness and the necessity of possible changes. Simultaneously, we ought to underline that the resignation of a given norm does not forbid using it and because of the lack of norms usage obligatoriness, it is legally admissible.

The meaning of mentioned norms in the range of the lightning and surges protection is undeniable. Besides, the mentioned norms studies of committees interested in related spheres can be useful.

6 Radioelectric Disturbances in the Railway Area

Most characteristic sources of radioelectric disturbances belong to the following:

- the electric and internal-combustion electric railway rolling stock,
- feeding substations,
- catenary and
- control devices.

The harmonical research generated to the trolley wires takes place in real conditions on the line of the railway into the speed range from 0 to V_{max} of the traction vehicle. Measurements are made simultaneously: on the engine, the traction substation and in the track. Radioelectric disturbances produced by electric traction vehicles are not, however, an essential threat for electronic devices working in the railway area, that is to say mostly for devices of the railway traffic controlling. Electronic devices of the railway traffic controlling containing transmitters and receivers of signals work in a lower frequency range.

Norms [2, 4, 5] determining admissible levels of radioelectric disturbances originating from the electric traction devices contain also devices of the railway traffic controlling. The electric devices rtc contain relays situated in relay rooms and by-tracks wardrobes. Part of transmitters works in a definite unit of time, which diminishes the quantity of disturbances of an impulse character. Disturbances emitted by these devices do not exceed values given in the norm [4].

Below is represented an example—results from the research of the disturbances influence generated by the locomotive Vectron DC on wheel's sensors used in axis metres [6]. These researches were performed on the experimental railway district in Żmigród. The research consisted of the registration and estimation of the voltage stability (considering the reaction on the axis of the vehicle) on the wheel sensor exists during rides (movements) of the above-mentioned vehicle.

Measurements of the magnetic fields influence generated by the locomotive Vectron DC performed according to recommendations contained in standing norms [4]. The Research consisted of the registration and estimation of measurement results in three magnetic field surfaces X , Y , Z , using the measuring—set MFMS during rides of the above-mentioned vehicle over installed measuring—sensors for the frequency range of 10 kHz–13 MHz.

During the ride of the engine type X4-E-Loco-C on the track equipped with wheel sensor, it was ascertained that the influence of the examined vehicle is conforming to expectations, i.e. detected are axis; however, there is no other influence on these sensors.

For example, registration for the sensor type ELS-93 is shown in Fig. 1.

Offences of magnetic fields limiting values generated by the locomotive type X4-E-Loco-C were not ascertained. For example, registrations for magnetic field surfaces X , Y , Z represented properly in Figs. 2, 3 and 4.

Knowing the occurrent levels of undesirable signals in the feeding net makes possible the use of suitable resources at the construction or projection of systems. Represented in this work [7] results of research referred to levels of radioelectric disturbances in the strand from 0.15 to 30 MHz as well as of amplitudes and frequencies of the surges occurrence in a low-voltage net feeding chosen railway objects. It is known that the course of the alternating voltage in energy nets of low voltage, only approximately, can be acknowledged as sinusoidal [7]. The coefficient of nonlinear distortion (the coefficient of harmonical contents), in most of cases, has not, however, a very essential meaning for needs of this energy receivers.

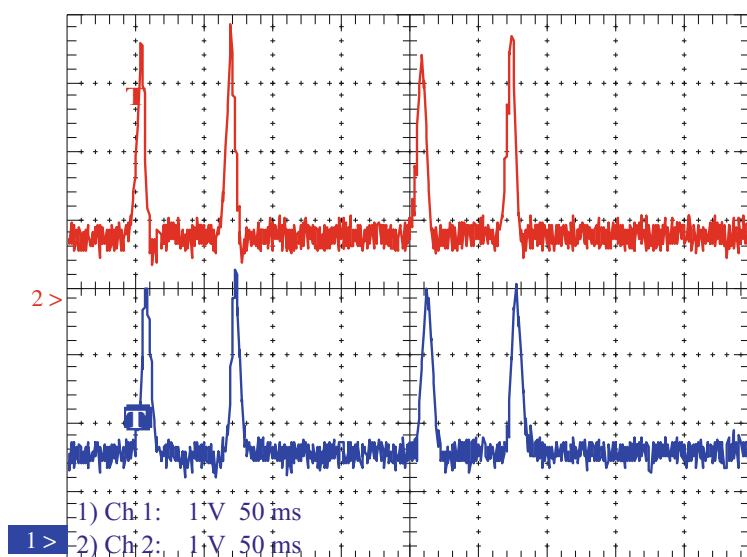


Fig. 1 F1 Level and F2 Level signals of the sensor ELS-93—at the ride of the locomotive type X4-E-Loco-C (the registered ride of *four* axes vehicle)

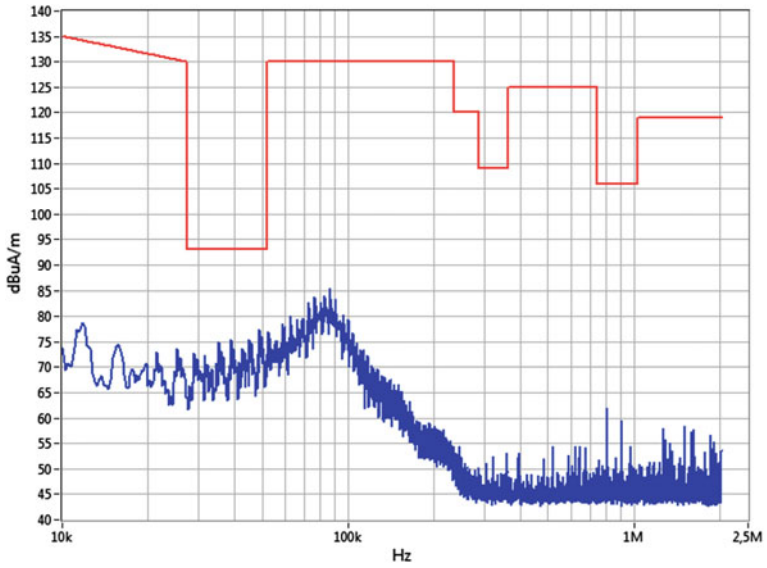


Fig. 2 The magnetic field intensity generated by the locomotive type X4-E-LoCo-C in surface X

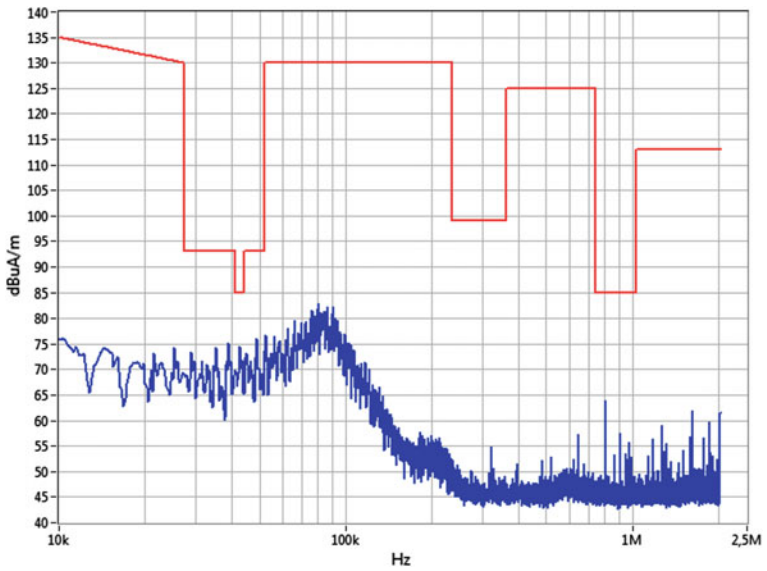


Fig. 3 The magnetic field intensity of generated by the locomotive type X4-E-LoCo-C in surface Y

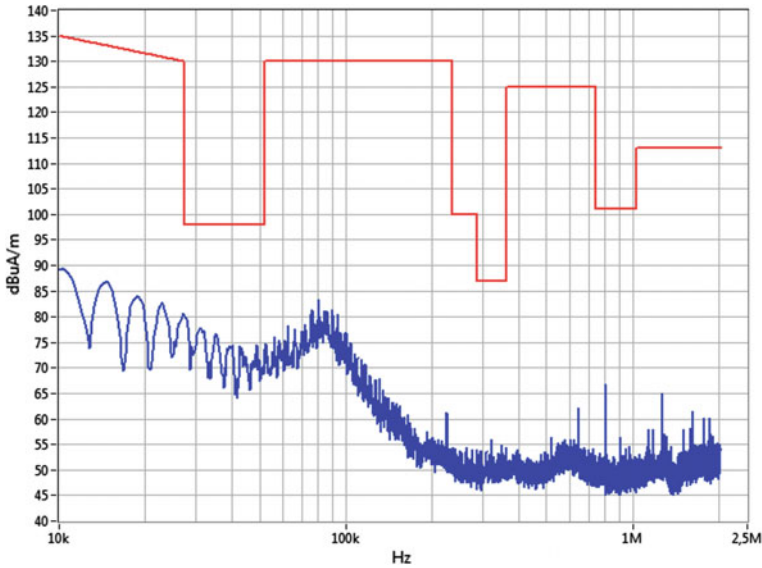


Fig. 4 The magnetic field intensity of generated by the locomotive type X4-E-Loco-C in surface Z

Considerably more harmful, from the point of view of safety and correct working of devices, are electromagnetic disturbances of a large energy (surges) which have a very differential character. Reasons of surges occurrence, disappearances and voltage fluctuations in the feeding net are natural occurrences, as well as occurrences resulted from the activity of humans. Particularly, main reasons of surges in an energy net can be connecting and disconnecting of charges (especially of reactance character), the commutation in electric circuits (especially of a large power consumption), statics and certain weather conditions having the influence on the quality of sent electrical energy, the state of the transmission line and the manner of the energy distribution to each receiver. To assure a correct work of railway devices supplied from an energy net, it is indispensable to guarantee deliveries of the electrical energy in a suitable qualitative level.

7 Electrostatic Discharges

The source of a given device electrostatic discharge can be another working device into his vicinity or a human touching the given device. The phenomenon depends on inducing in the given device currents and voltages not only perturbative (disturbing) its work, but also liable to cause damage. Electrostatic discharges caused by devices are usually low-voltage discharges. Considerably more dangerous are discharges originating from human because they call out large changes of

the electromagnetic field intensity [8]. The researches of the resistance on the influence suchlike of discharges depend on the reduction of current impulses led to examined device in the most exposed place. Distinguished are direct discharges (devices in metal cases) and indirect (devices in plastic cases).

8 Purposely Produced Electromagnetic Field About the Sinusoidal Character

The source of these disturbances is a different kind of practical transmitters to send the information in wireless communication systems. An agreed upon signal testing is the sinusoidal amplitude–frequency modulated signal of the modulation 1 kHz of the modulation depth 80% into a frequency range of 80 MHz–1 GHz.

9 The Influence of Electromagnetic Disturbances on Electronic Devices Installed on the Railway Area

The most essential threat for electronic devices working in the railway area are electromagnetic impulse disturbances (Fig. 5) originating from the following:

- the lightning threat in the nearby objects,
- discharges inducing a surge in power supply circuits and transmissions of the devices information,
- direct discharges into the installation lightning rod of the object and
- surges, arising in the network as result of joining processes or short circuit.

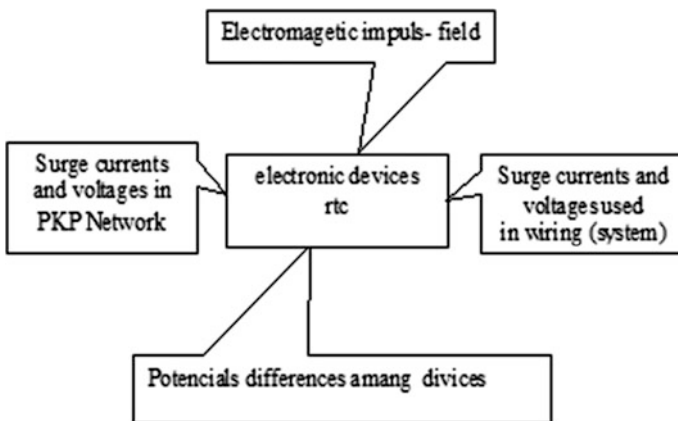


Fig. 5 Impulse endangerments of rtc electronic devices

Table 1 Maximum values of lightning parameters according to LPL—parameters of the first positive impulse [3]

First positive impulse	LPL—lightning protection levels		
	I	II	III–I
Current parameters			
Peak current/(kA)	200	150	100
Impulse charge Q_{SHORT} (C)	100	75	50
Specific energy W/R (MJ/fi)	10	5.6	2.5

Table 2 Maximum values of lightning parameters according to LPL—parameters of the long stroke [3]

Lang stroke	LPL—lightning protection levels		
	I	II	III–IV
Current parameter:			
Long stroke charge Q_{LONG} (C)	200	150	100
Time parameter T_{LONG} (s)	0.5	0.5	0.5

In compliance with the norm [3], shapes of atmospheric discharges used to image temporary courses are marked on the ground of real registrations of managed conditions. Norms concerning protections against the lightning electromagnetic impulse LEMP contain recommended values of basic parameters characterizing shapes of lightning to earth currents. Parameters of strokes are presented in Tables 1 and 2.

For example, given for the first level of protection in the norm of the amplitude and courses shapes of the current carry out for

- the prolonged component of the discharge: 400 A; 0.5 s
- the first component of the discharge: 200 kA; 10/350 μ s
- following components of the discharge: 50 kA; 0.25/100 μ s.

On their subject affected are devices or construction elements of the object into which can follow a direct discharge or if they are found in circuits of lightning currents flow.

10 The Nuclear Explosion

Called out of a nuclear explosion, the electromagnetic impulse can go over for considerable distances from a dozen or so to several thousands of kilometres, depending on the place of explosive powers and the kind of explosion [9]. Produced electromagnetic field affects power lines, signal tracks, antennas and joint to them electronic devices. Penetrating by walls and windows, it can influence also the devices themselves.

11 Measurement of Percussive Extortions in Laboratory —Research

In the range of lightning and surge protection, the performed measurements are often a laboratory research, targeting check of the activity efficiency of projected protection system. Research of the rtc devices electromagnetic compatibility targeting verifying of the resistance range is qualified in the norm [2]: by denominative norms of the research method [8].

In this type of research (Fig. 6), the stroke generator combined with the stroke voltage 1.2/50 μ s, with the current 8/20 μ s and the characteristic impedance 2 Ω [8] is used.

In research of telecommunication devices, the generator of the stroke voltage 10/700 μ s [8] is used.

Research of the resistance on series of quick temporary states at a suitable maximum value of the stroke for the given device is performed with the stroke 5/50 ns [8].

Detailed parameters of strokes, kinds of exposures and suitable criteria estimations are placed in the mentioned norms.

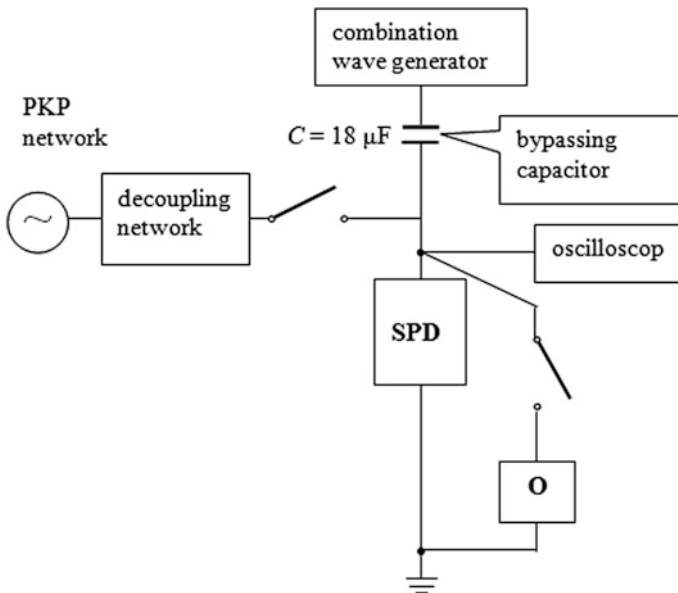


Fig. 6 The block-measuring—practical schema in research of protection system devices rtc SPD —examined surge protective, O—loading (according to [8]), [10]

12 Discussion and Conclusions

The introduction to norms of the series [2] arranged the problems of the electromagnetic compatibility in the Polish railways. The realization of requirements of these norms is possible at the use of standardized methods of research conditioned of a full repeatability and comparabilities of received results of research and measurement. It allows the explanation of unexpected events, the exclusion of the relationship of existing events with EMC and limiting the disturbing effects at offenses of limiting values. That gives the possibility of the influence on settled requirements by the limitation of consequential costs from disturbance occurrences.

The problem of the electromagnetic compatibility refers not only to existing devices but also to all newly brought in devices which should be examined absolutely, considering the resistance against impulse electromagnetic disturbances. The problems of compatibility ought to be considered already in the stage of devices projection. The realization of its requirements in building the device is a difficult and expensive undertaking.

References

1. Council Directive 89/336/EEC of 3 MAY 1989 on the approximation of the laws of the Member States relating to electromagnetic compatibility
2. PN-EN 50121 Railway applications. Electromagnetic compatibility
3. PN-EN 62305: Protection against lightning.—Part 1: General principles. Part 2: Risk management. Part 3: Physical damage to structures and life hazard. Part 4: Electrical and electronic systems within structures
4. PN-EN 50238 Railway applications—Compatibility between rolling stock and train detection systems—Part 2: Compatibility with track circuits., Part 3: Compatibility with axle counters. + CLC/TS 50238-3:2010 corr (September 2010)
5. PN-EN 50617 Railway Applications—Technical parameters of train detection systems for the interoperability of the trans-European railway system—Part 1: Track circuits, Part 2: Axle counters
6. Adamski, D., Białoń, A., Furman, J., Kazimierczak, A., Ortel K., Zawadka, Ł.: Badania lokomotywy typu X4-E-Loco-C (Vectron DC) z oprogramowaniem C.1 – badania zakłóceń generowanych do sieci trakcyjnej i ich wpływu na urządzenia srk. Instytut Kolejnictwa Zakład Sterowania Ruchem i Teleinformatyki. Praca nr 10/5269.03/21. Warszawa, marzec 2015 r
7. Laskowski, M., Malesa, R., Wróbel Z. et al.: *Określenie istniejących poziomów zakłóceń elektromagnetycznych w ruchomych i stacjonarnych obiektach kolejowych*. Praca CNTK nr 1049/24. Warszawa 1997r
8. PN-EN 61000-4: Kompatybilność elektromagnetyczna (EMC)—Część 4-2: Metody badań i pomiarów – Badanie odporności na wyładowania elektrostatyczne.; Część 4-4: Badanie odporności na serie szybkich elektrycznych stanów przejściowych.; Część 4-5: Badanie odporności na udary.; Część 4-6: Odporność na zaburzenia przewodzone, indukowane przez pola o częstotliwości radiowej.; Część 4-8: Badanie odporności na pole magnetyczne o częstotliwości sieci elektroenergetycznej. Część 4-9: Badanie odporności na pole magnetyczne o częstotliwości sieci elektroenergetycznej

9. PN-IEC 61312-1:2001. Ochrona przed impulsem elektromagnetycznym. Zasady ogólne. Część 2: Ekranowanie obiektów połączenia wewnątrz obiektów i uziemienia. Część 3: Wymagania dotyczące urządzeń do ograniczanie przepięć (SPD)
10. Wróbel, Z.: Possibility of the modelling of combination waves generators (2010). Przegląd Elektrotechniczny, PL ISSN 0033-2097, R. 86 NR 9/2010, pp. 289–292

The Horn Gap Arresters Modelling in a Lightning Discharge Analysis

Zofia Wróbel

Abstract The large differentiation in the quality of the electrotraction devices insulation causes the advisability of using another kind of surge protection for every type of these devices. This also permits the independent working out of the catenary protection problems, the substation or the rolling stock. In the present situation to the relation of the installation of new computer devices in the railway which often are subjected to damage caused by atmospherical surges, the analysis of the catenary protection against surges is advisable. In the report, chosen results of the horn gap arresters modelling implemented into the circuit taking into account the real section model of the track containing models of towers, insulators, contact line, rail return, rails and stroke sources are represented. In the analysis, the results are collected for this purpose for many years—exploitation research and measurements were taken into account.

Keyword Horn gap arrester · Catenary · Lightning discharge analysis · Numerical modelling · Simulations

1 Introduction

Surges of atmospherical origin in the catenary can be caused either by the direct shock of a thunderbolt into the catenary or have the character of surges induced by the shock of a thunderbolt some distance away from the network (indirect).

Aside from the installed kind of protection, the direct shock always causes a spark gap on the insulation of the network. Afterward, the gap between the network lines and the rails appears a surge resulting in the fall of voltage from the discharge current on the resistance and inductances of the tower and connections. When the value of the voltage will exceed the percussive endurance of the network insulation, other spark gaps in the insulation of neighbouring towers will take place.

Z. Wróbel (✉)

PKP Polish Railway Lines JSC, Railway Lines Establishment in Rzeszów, Rzeszów, Poland
e-mail: zwrobel@prz.edu.pl

Induced surges cause spark gaps only then, when the place of the thunderbolt shock is found in a comparatively near distance from the network.

The problem of the network statics protection from was the object of many elaborations performed in the years 1955–1964 of research [1–6] and in the years 1962–1970 of works of the Committee of Experts ORE (Office of Research and Experiments), which was an International Railways Relationship UIC (International Union of Railways) Question A-50 [7–9].

2 Rules of the Catenary Protection Activity

The low insulation level and the lack of a lightning rod line cause that every discharge into the line induces spark gaps in the insulators in the area of the thunderbolt shock. The number of towers on which a gap appears depends—first of all—on the value of the lightning current. Considering large energies of surges, usually as a result of a direct shock of the thunderbolt into the network, a damage of the catenary follows.

Spark gaps in insulators resulting in induced surges, connected with an accompanying of the stroke (transient) current (due to the short time of this current flow), usually do not cause damage to insulators. This damage is caused by a thermal activity of a direct current arc which arises after the spark gap and is held up by the voltage of the catenary (Fig. 1). An arc remaining longer on insulators can cause their permanent damage such as metal melting, heating of the glaze, the

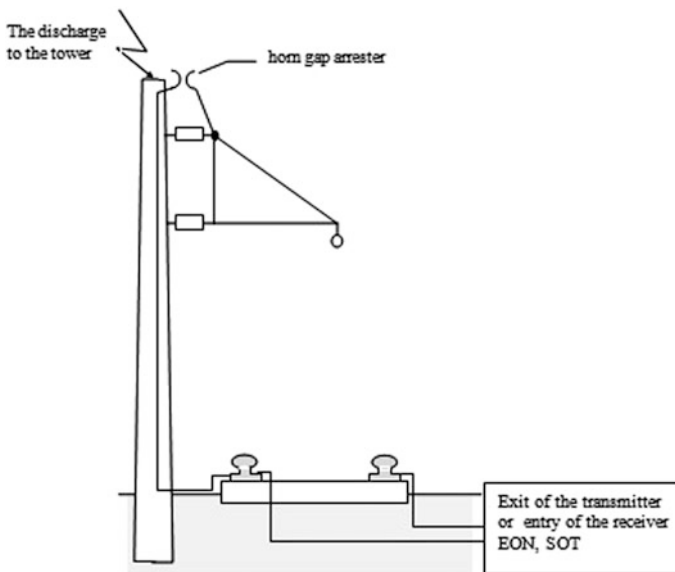


Fig. 1 The underthreat catenary: the connection diagram of the track circuit. EON—the electronic sewn on circuit SOT—the station-track circuit [10]

crack of the insulator porcelain, etc. To eliminate this damage, we endeavor to limit the time of the arc burning.

Researches [1–9] showed that at a considerable limitation of the arc burning time in the insulator to about tens ms, in most cases, insulators in which an arc appeared were not damaged. This condition is realised by using the protection of the catenary horn gap arresters. As the exploitation tests showed Research [1–9], spark gaps do not appear as a result of surges of atmospherical origin on insulators of networks being near the lightning conductors. On neighbouring towers insulators, these gaps appear, but the arc of the direct current after the spark gap lasts very short and does not cause damage to the insulators. The arc is put out as at the first moment of the arc length of the lightning conductor horns is so little that the voltage of this arc is not enough to hold up the discharge on the insulators. From exploitation research, it is concluded [8, 9] that the acceleration of the arc extinction (putting out) on insulators appears even then, when the horn gap arresters are installed at a distance above 1 km from the place of the spark gap.

Since 1957, horn gap arresters OR-3/56 have been used for the protection of the PKP catenary.

As a result of the use of modern devices for controlling railway traffic and their resultant damage resulting from atmospherical origin surges in PKP, works (aiming among other things) to view the estimation of horn gap arresters activity are being performed.

3 Horn Gap Arresters—Surge Tests

The tests began in 1956. The results from tests, which lasted 2 years, were put in document No. 1 (A50 Committee of Experts) ORE A-50 [6].

Table 1 presents the electrical characteristics of OR-3/56 as a function of the different length gaps. After preliminary tests the length of the arc gap was fixed at 10 ± 1 mm. When mounting the arresters, the distance of 1200 m was adopted. In the case of section especially exposed to atmospheric over voltages, these distances were reduced to 600 m, where $\frac{U_{pmax}}{U_{sparkover}}$ or $\frac{U_{St}}{U_{sparkover}}$ — the relation between statistic or impulse sparkover voltage and sparkover voltage of a gap formed by spherical electrodes with the diameter 62.5 mm at the same distance of electrodes; $K_{St} = \frac{U_{St}}{U_{pmax}} = \frac{U_{St}}{U_p \sqrt{2}}$ — the coefficient shock.

4 Schemes Model

The complexity of the electromagnetic compatibility issue in the railway environment is conditioned by [10–12]:

Table 1 Electrical characteristics of horn type arrester OR-3/56 [6]

Distance between electrodes (mm)	Static test		
	Sparkover voltage U_p rms value (kV)	Sparkover voltage U_{pmax} peak value (kV)	$\frac{U_{pmax}}{U_{sparkover}}$
10	22.5	31.9	1.00
15	29.7	42.0	0.92
20	36.6	51.8	0.89
25	40.3	57.0	0.82
30	43.7	61.9	0.78
Distance between electrodes (mm)	Surge test (St) with positive polarity		
	50% of sparkover voltage U_{St} (kV)	Co efficient of shock K_{St}	$\frac{U_{St}}{U_{sparkover}}$
10	31.9	1.00	1.000
15	44.6	1.06	0.970
20	55.1	1.07	0.920
25	61.9	1.08	0.855
30	66.9	1.08	0.800
Distance between electrodes (mm)	Surge test (St) with negative polarity		
	50% of sparkover voltage U_{St} (kV)	Coefficient of shock K_{St}	$\frac{U_{St}}{U_{sparkover}}$
10	31.9	1.00	1.000
15	44.1	1.05	0.965
20	52.6	1.02	0.905
25	58.2	1.03	0.840
30	65.1	1.05	0.820

- a significant vastness of the area;
- mutual interaction of the circuits low- and high-voltage devices with different supply systems;
- joint running of the supply, signalling and telecommunication cables;
- the complexity and common connection of subsystems, including devices of different generations; and
- the possibility of simultaneous interference interaction from many sources.

4.1 Traction System

The simulation of risks caused by electromagnetic impulse interferences requires creating a model considering R , L , C parameters and their variability in the frequency function [12]; therefore, in the analysis it should be taken into consideration

that it is a circuit with the transmission model of the coupled lines parameters. The general scheme of the model railway supply network and rail return model accepted for the testing is presented in Fig. 2 [13], and for the purpose of simplification it has been accepted for the analysis that the velocity of wave spreading is equal to the light velocity and the reflection of current waves from the peak of the initial stroke has not been taken into account.

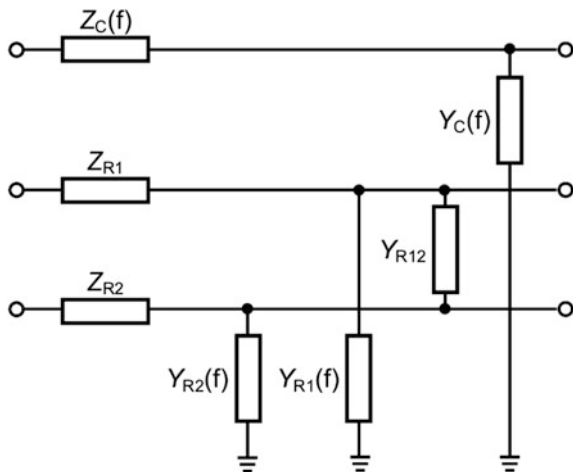
For the frequency band regarded in this types of analyses, equalling a few kHz, the traction system has the length of a quarter wave responding the section length between substations, and according to the data presented in paper [14], on the basis of the literature included in the paper, if the length of the overhead system section replaced with a four-terminal network does not exceed the wave length by 3%, then the mistake of such a model is smaller than 2.5%; so for the frequency accepted for the analysis equal 10 kHz the length of the four-terminal network fulfilling this condition is 900 m, and in the developed calculation model, the length of the four-terminal network responds to the distance between two towers of overhead system.

The parameters calculated from the measurements included in the paper, for the $l = 72$ m overhead system section, as shown in Fig. 3, regarding the frequency-dependent characteristics of the electric traction and the suggested section parameters were $R_1 = 5.04$ m Ω , $L_1 = 97.35$ μ H, $R_2 = 16.45$ m Ω , $L_2 = 12.39$ μ H, $R_3 = 118.34$ m Ω , $L_3 = 4.19$ μ H, $C_0 = 2.32$ nF [13, 14].

A simple but exact solution of the transmission line equations for lossless, coupled lines that are implementable in the SPICE circuit analysis programme and the multiconductor transmission line equations can be written in matrix form [15].

To solve these equations we have to decouple them; that is, reduce the coupled pairs of lines to a set of three-conductor lines that do not interact, and in order to do

Fig. 2 Rail track line impedance and admittance model [13, 14]



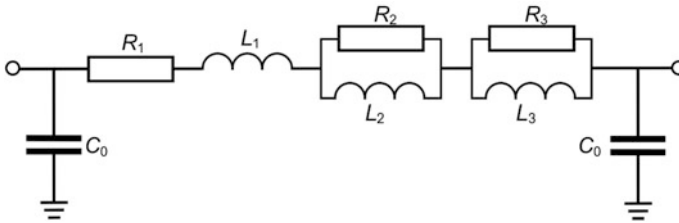


Fig. 3 Frequency-dependent PI section of the traction system model [13, 14]

this, we must define transformations that convert these desired line voltages and currents to mode voltages and currents.

These uncoupled mode lines can be modelled in the SPICE programme using the exact, three-conductor line model, so the SPICE model for the mode voltages and currents along the line is solved, and the mode currents and voltages at the end-points of the line can be converted to the actual line currents and voltages by implementing the transformations.

This can be implemented with voltage-controlled voltage sources and by using current-controlled current sources as shown in Fig. 4, zero-volt voltage sources are necessary for SPICE to sample the controlling current for current-controlled sources.

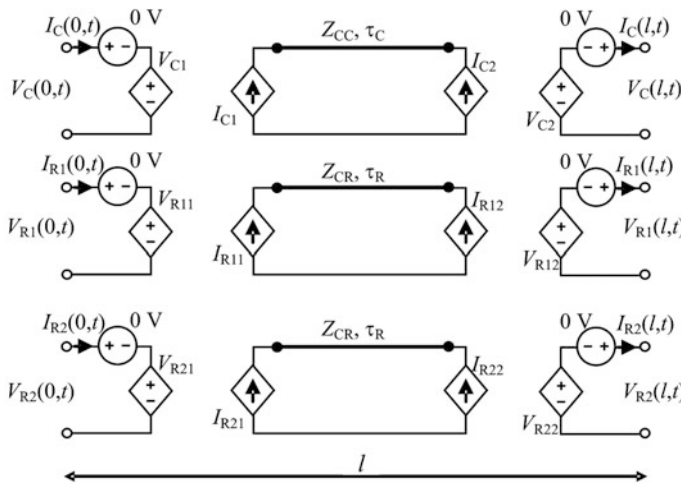


Fig. 4 The complete SPICE model for a three-conductor line [15]

4.2 Rail Network and Electrical Track Parameters

The rail parameters calculated on the basis of measurement results included in [13, 14] for the length of the 72-m four-terminal network equalled (Fig. 5): $R_1 = 0.576 \Omega$, $L_1 = 0.0576 \text{ mH}$, $G_{12} = 0.115 \text{ S}$, $C_{12} = 1.44 \mu\text{F}$, and in a similar way the substitute parameters of the four-terminal network describing a rail network section while taking into account their changeability in the frequency function (rail 1): $G_1 = 6.24 \text{ mS}$, $C_1 = 3.98 \mu\text{F}$, $G_2 = 6.07 \text{ mS}$, $C_2 = 0.37 \text{ mF}$, $G_3 = 13.3 \text{ mS}$, $C_3 = 5.94 \mu\text{F}$, $G_4 = 0.305 \text{ S}$, $C_4 = 3.06 \mu\text{F}$ were determined, there for the same values were accepted for the second four-terminal network connected with rail 2, but the cross-tying of rails by around 300 m were taken into account.

For the analysis in LTSPICE programme the traction system section accepted was composed of 178 four-terminal networks of 72 m length, and the impulse wave was applied to tower number 87.

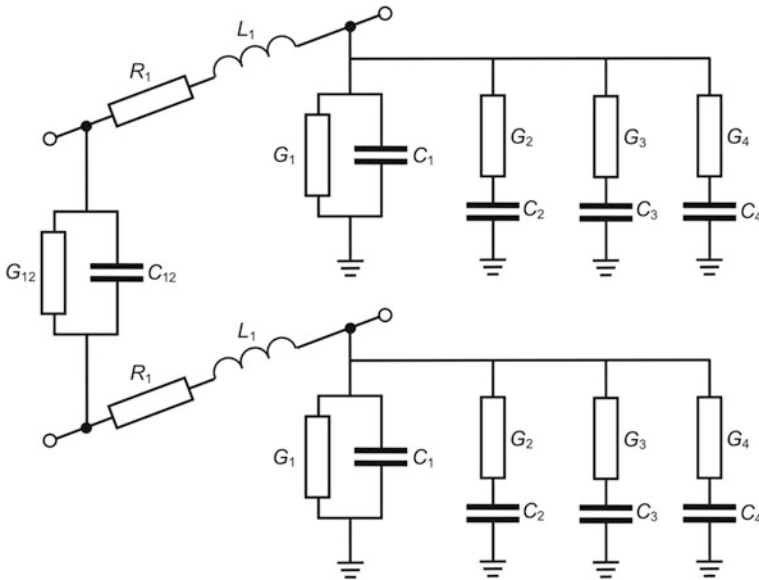


Fig. 5 The scheme of railway track section regarding the influence of the ground [13, 14]

4.3 A Substation Model

As a substation model the parameters regarding substation voltage $U_p = 3450$ V, substation inductance and the supply system $L_p = 4.774$ mH [16] have been accepted (Fig. 6).

The parameters of the return and supply cable have been accepted according to the measurement results included in the paper [16] for the frequency 10 kHz and the length of the cable equal 200 m as $R_{Kz} = R_{Kp} = 3\Omega$, $L_{Kz} = L_{Kp} = 0.3$ mH and $C_{Kz} = C_{Kp} = 0.4$ μ F. This model is introduced into calculations as a four-terminal network may be expanded in further simulations.

4.4 Towers

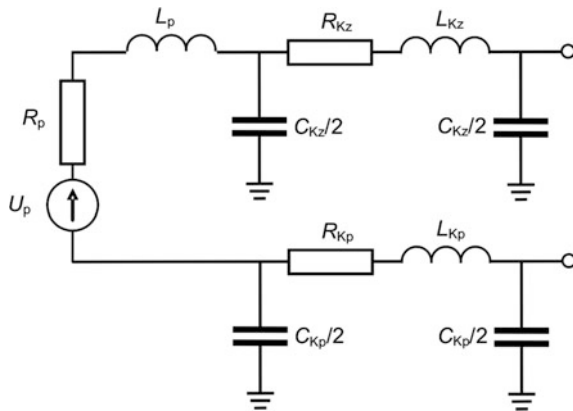
In the analysis of atmospheric discharges a tower model may be realised as a row connection of inductance and resistance, so assuming the unit inductivity $L_0 = 1.67$ μ H/km calculated using the following formula:

$$L_0 = 0.2 \mu_r \ln \frac{2h}{r} \quad [\mu\text{H}/\text{km}], \tag{1}$$

where

- μ_r the relative magnetic permeability (for air $\mu_r = 1$);
- h height of the tower;
- r cable radius. The tower inductance was accepted as $L = 20.28$ μ H, and the tower impedance as $R = 10$ Ω , and as for the connection to the rail of the tower inductance as $L = 5$ μ H was accepted [14].

Fig. 6 The scheme of the substations and connections cable [14, 16]



4.5 Horn Gap Arresters and Insulators

The model of the horn gap arrester is introduced as a switch. In the analysis as a model of the insulator was taken into account (in the model of the tower) the switch voltage-controlled 90 kV of a spark gap for different voltage values and a spark gap of the resistance 100 MΩ. Applied to the protection of the catenary, horn gap arresters are installed for every 1200 or 600 m (for terrains of large stormy intensity, more than 30 days in a year). In the analysis distance of 600 m was taken into account [17–19].

5 Declaration of Current Sources 5/320 μs

In the CDEGS™ we can work out temporal forms of surge currents in the form of formulas [20]; therefore, the 5/320 μs current surge of $U_m = 1$ kV lightning surge declaration was chosen.

5/320 μs current surge parameters were determined by the following formula:

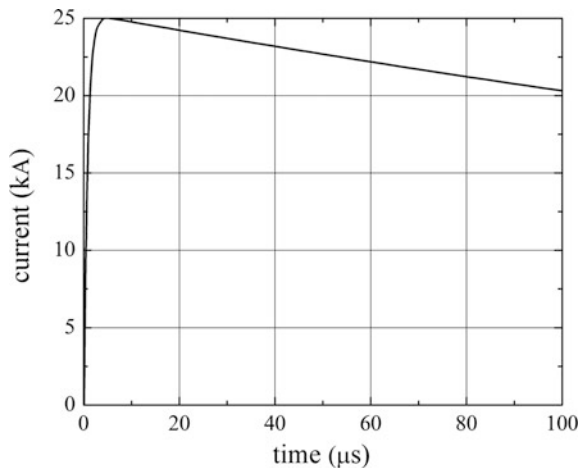
In the CDEGS™ we can work out temporal forms of surge currents in the form of formulas [20]. For the 5/320 μs current surge of $U_m = 1$ kV lightning surge declaration was chosen.

5/320 μs current surge parameters were determined by the following formula:

$$i(t) = 1.012845 I_m [\exp(-2205.969t) - \exp(-1273948 t)]. \tag{2}$$

Its analysis in the article was subjected to the scheme of contact wires with the input current waveform maximum values $I_m = 25$ kA and shapes 5/320 μs shown in Fig. 7.

Fig. 7 Current surge 5/320 μs for $I_m = 25$ kA



6 Chosen Modelling Results

The elements of the analysed system presented above were grouped in the form of four-terminal networks of the type II, creating a three-wire model containing a section of the catenary and a track of 72 m length:

1. a tower with an insulator,
2. a tower with horn gap arrester, and
3. a tower to which a stroke was led.

It has been considered in the analysis that at first the spark gap of horn gap arrester OR-3/56 was set at 15 mm. In further research, it was diminished to $10 \pm \text{mm}$.

For the analysis a section of catenary wires containing 174 four-terminal networks was accepted. In the middle of the distance among substations, a four-terminal network with a modelled stroke was introduced. A metallic short circuit on the switch of the tower was installed to make it easier. For example, for the analysis of the current stroke model (Fig. 7), the value 25 kA was accepted. In the modelling, chosen results from the included measurements in Table 1 for stroke tests (surge test with positive polarity) for the spark gap of the values 10, 15 and 20 (mm) were taken into account. The stroke was led to the tower previous with installed horn gap arresters. Additionally, calculations for a lower value of the spark gap were done leading a stroke of 10, 15, 20, and 25 kV.

To determine the influence of the spark gap on the work of catenary, in Figs. 8, 9, 10, 11, 12, 13, and 14, the modelling results of the voltage courses were placed and established for different voltage values on the horn gap arrester.

For determining influence of spark gap on the work of catenary, in Figs. 8, 9, 10, 11, 12, 13 and 14 the modelling results of the courses were placed, at the establishment of different voltage values on the horn gap arrester.

Fig. 8 Courses of voltages on three following towers with installed horn gap arresters (1 the full line, 2 the dashed line, 3 dotted–dashed line) for $U_{\text{max}} = 31.9 \text{ kV}$. The current extortion $5/320 \mu\text{s}$ led to tower 2, the previous central tower with a horn gap arresters

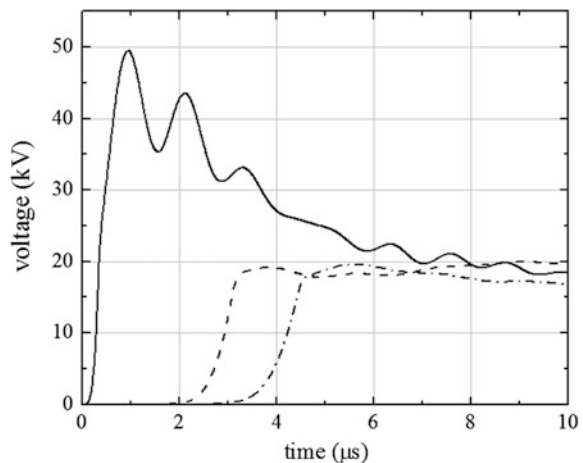


Fig. 9 Courses of voltages for Fig. 8 for the voltage of $U_{max} = 44.6$ kV on the horn gap arresters

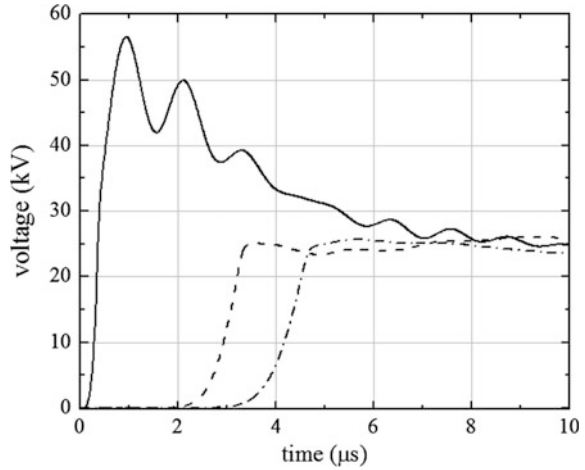
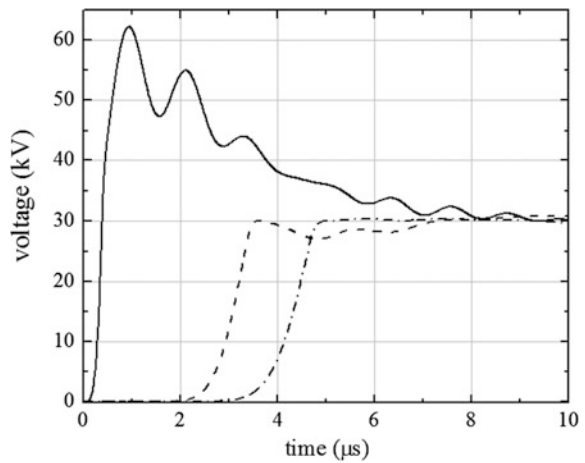


Fig. 10 Courses of voltages for Fig. 8 for the voltage of $U_{max} = 55.1$ kV on the horn gap arresters



The estimation of threats of catenary caused by statics demands exact analyses of the lightning current run and of falls of voltages in structural elements and analysed devices installations.

The presented model of the circuit which was complemented by installing elements railway traffic control (rtc) may be useful in the analysis of overvoltage threats of these installations.

The results that were received have been compared with calculations of LtSpice programme and of the programme elaborated in FORTRAN 77. The received

Fig. 11 Courses of voltages for Fig. 8 for the voltage of $U_{max} = 10$ kV on the horn gap arresters

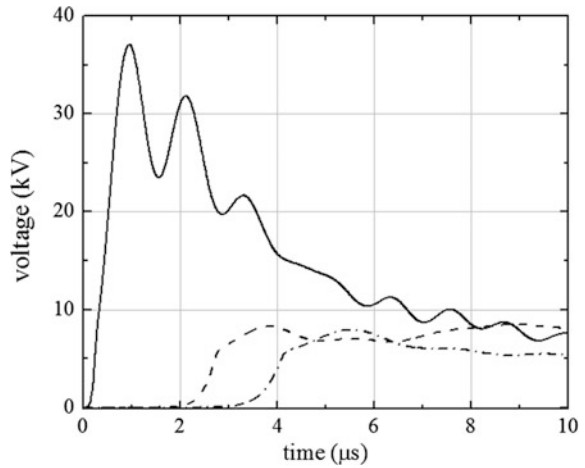
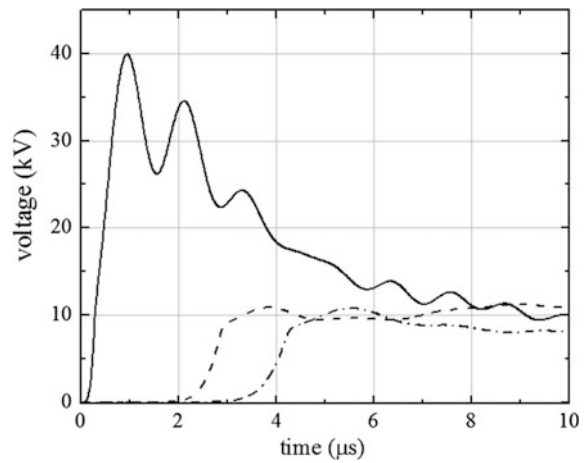


Fig. 12 Courses of voltages for Fig. 8 for the voltage of $U_{max} = 15$ kV on the horn gap arresters



results and recognised possibilities of programme LTSpice will be utilised in further works about estimation independency of the supplying system for the railway traffic control equipments. The distinguished possibilities of the programme have the cognitive character and can be useful in the threats estimation of the power supply elements of railway devices caused by surges of atmospherical origin.

Fig. 13 Courses of voltages for Fig. 8 for the voltage of $U_{max} = 20$ kV on the horn gap arresters

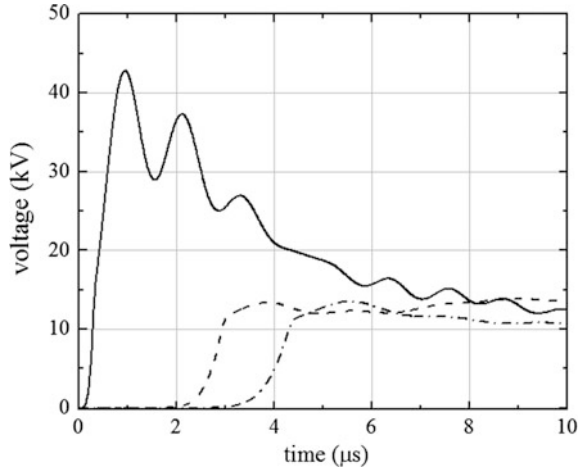
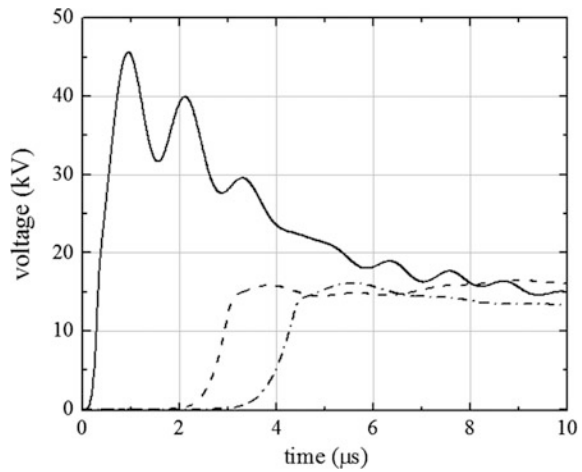


Fig. 14 Courses of voltages for Fig. 8 for the voltage of $U_{max} = 25$ kV on the horn gap arresters



7 Discussion and Conclusions

The efficient external lightning rod protection and internal lightning rod protection (surge protection) should assure an unflinching work of devices. The selection of parameters of surge limiters should be preceded by a scrupulous analysis of their threat rank. One of the methods can be also the analytic estimation. In the report, data concerning the existing damaging problem of catenaries caused by statics were represented. Chosen results of research from the performed works concerning the introduction of the horn gap arresters exploitation were presented. These materials will be used for the comparative analytic estimation of the horn gap arresters activity with reference to performed measurements.

References

1. Figurzyński, Z., Zugaj, Z.: Zabezpieczenia i automatyka urządzeń elektrotrakcyjnych na PKP—Temat nr IE-504/56 Część IV A: Zabezpieczenia przeciw napięciowe sieci 3 kV, Instytut Naukowo Badawczy Kolejnictwa, Zakład Trakcji Elektrycznej, Poland, Warsaw (1956)
2. Figurzyński, Z., Zugaj, Z., Czerepiński, J.: Dokumentacja techniczna odgromnika różkowego dla sieci trakcyjnej PKP 3 kV, Temat IE- 504/56, Poland, Warsaw (1956)
3. Figurzyński, Z.: Ochrona sieci trakcyjnej prądu stałego 3000 V od przepięć atmosferycznych za pomocą odgromników różkowych, Praca COBiRTK, z3, Poland, Warsaw (1960)
4. Centralny Ośrodek Badań i Rozwoju Techniki Kolejnictwa: Zakład Trakcji Elektrycznej, Badania zabezpieczeń przeciwprzepięciowych w urządzeniach zasilających elektrotrakcyjnych oraz w taborze el. Temat E-328/60, Poland, Warsaw (1961)
5. Centralny Ośrodek Badań i Rozwoju Techniki Kolejnictwa: Zakład Trakcji Elektrycznej, Badania układów zabezpieczających od przepięć sieć, podstacje i tabor, Temat E-20 Czxś II, Poland, Warsaw (1963)
6. Centralny Ośrodek Badań i Rozwoju Techniki Kolejnictwa: Zakład Trakcji Elektrycznej, Badanie układów zabezpieczających od przepięć sieci, podstacje i tabor. Temat E-20/65, Poland, Warsaw (1965)
7. International Union of Railways: Office for research and experiments, question A-50. Protection of traction installations against over-voltage. Interim Report, No. 1, Testes made with horn type lightning arresters in direct current overhead contact systems, Netherlands, Utrecht (March 1962)
8. International Union of Railways: Office for research and experiments, question A-50. Protection of installations and electric motive power units against the effects of over-voltages. Interim Report, No. 4, Tests in services on surge diverters and horn gap arresters (3000 V direct current) General survey of the different solutions for protection. Future trends and questions not yet resolved, Netherlands, Utrecht (March 1964)
9. International Union of Railways: Office for research and experiments, question A-50. Protection of the traction installations and electric motive power units against the effects of over-voltages. Report (Final Report), No. 12, General survey of the different solutions for protection. Future trends and questions not yet resolved, Netherlands, Utrecht (April 1970).
10. Wróbel, Z.: Horn gap arresters in the 3 kV catenaries protection in PKP (Polish railways). In: 12th International Conference Modern Electrified Transport. Croatia, Trogir (2015)
11. Laskowski, M., Wróbel, Z.: Levels of electromagnetic interferences in the low voltage circuits of traction vehicles and coaches. Problemy Kolejnictwa, Railway Scientific and Technical Centre in Warsaw, no. 143, Poland, Warsaw (2006)
12. Laskowski, M., Wróbel, Z.: The levels of radio noises and electromagnetic interferences in the low-voltage power system supplying railway permanent installations, Problemy Kolejnictwa, Railway Scientific and Technical Centre in Warsaw, no. 145, Poland, Warsaw (2007)
13. Szela, A.: Zagadnienia analizy i projektowania systemu trakcji elektrycznej prądu stałego z zastosowaniem technik modelowania i symulacji. Prace Naukowe, Elektryka z. 123, Oficyna Wydawnicza Politechniki Warszawskiej, Poland, Warsaw (2002)
14. Wróbel, Z.: Computer modelling of lightning discharge threat to railway installations, Modern Electric Traction. Power Supply. In: Karwowski, K., Szela, A., (eds.) Gdansk University of Technology, Faculty of Electrical and Control Engineering, Gdańsk (2009)
15. Paul, C.R.: Introduction to Electromagnetic Compatibility. Wiley, Hoboken (2006)

16. Białoń, A., Kaźmierczak, A., Zając, W.: Opracowanie dopuszczalnych parametrów zakłóceń dla urządzeń srk, łączności i pojazdów trakcyjnych. Sprawozdanie końcowe. Praca 6915/23, CNTK, Poland, Warsaw (1999)
17. Centralny Ośrodek Badań i Rozwoju Techniki Kolejnictwa: Zakład Trakcji Elektrycznej, Badania pełne odgromników różkowych wg projektu normy branżowej BN-87/9317 Zakład Trakcji Temat 53020 -7-300-wrzesień 1987 r. (zleceniodawca—producent odgromników różkowych Spółdzielnia Pracy Produkcyjno-Usługowej Bałtyk, Poland, Słupsk (1987)
18. Łoboda, M., Sobolewski, K.: Lightning deaths and injuries in Poland, European COST Action P 18 International Symposium on Lightning Physics and Effects, Austria, Vienna (2009)
19. Głowacki, K., Onderka, E.: Sieci trakcyjne EMTRAK s.c (2002)
20. FFTSES User's Manual, Fast Fourier Transforms: Safe Engineering Services & Technologies Ltd, Canada, Montreal (1997)

Evaluating the Level of Waveform Distortion

Jacek Bartman

Abstract The paper presents a multi-parametric evaluation of voltage waveform distortion, briefly discusses the methods of analysing distorted waveforms and specifies the factors for evaluating the level of distortion. The experimental part illustrates the changes in values of the selected indices depending on waveform distortion. The investigation that was carried out involved the output voltage of frequency inverter.

Keywords Distorted waveforms · Spectral analysis · THD · Harmonics · RMS

1 Introduction

The waveform distortion of electric signals is present in most electric networks. The occurrence of this negative phenomenon [1–3] is caused by greater and more common use of electric appliances (electric energy receivers) of nonlinear characteristics [4, 5]. Devices of this type are widely used in industry, but more often appear in other sectors such as lighting technology, variable speed drives and office technology (computers, UPS, etc.). In the case of electric drives, the systems with their basic part in the form of frequency inverter-fed induction motor became a practical and common solution. It allows to adjust the speed in induction motors which in turn enables to construct cheap and reliable electric drives and broaden the scope of applications of induction motor [6, 7]. Nonlinearity in the unit frequency inverter–induction motor results from a distorted waveform of the inverter’s output voltage that is not only distorted [1, 8, 9] but also nonstationary [8, 10].

Voltage measurements and analysis of its distortion are very often applied to evaluate the quality of energy [10–14]. For this reason, most authors in their works reduce distortion analysis to examining the value of the THD coefficient [5, 11–14] and the spectrum of harmonics [9–11, 13–15]. The spectrum of interharmonics

J. Bartman (✉)

Department of Computer Engineering, University of Rzeszow, Rzeszow, Poland
e-mail: jbartman@ur.edu.pl

[9, 10, 14, 15] is more and more often involved in the analysis. Complying with the directives of the norm IEC 61000-4-7 [16] the analysed spectra are reduced to first 40 components. The approach presented in the paper [9] fails to guarantee the right reflection of signal waveform. Moreover, the way the effective value of voltage and THD coefficient with the measurement devices used is based on the harmonic analysis (cf. the formulas 2b, 4a) that is why reducing the spectrum causes more limitations.

As very few works include other parameters, which are useful in evaluating waveform distortion, they are going to be presented in the current paper.

2 Analysis of Distorted Waveforms

The evaluation of distorted waveforms is a complex question. The analysis of harmonics is its primary element, aiming to obtain a spectrum of waveform, more precisely the amplitudes A_k and the angles of phase shift φ_k of particular harmonics. Most popular methods for spectral analysis are conducted on the basis of Discrete Fourier Transform—DFT [1, 8–11, 13–16]. DFT requires that the examined waveform $y(t)$ with the period T meets Dirichlet conditions:

- be absolutely integrable, i.e.

$$\int_0^T |y(t)| dt < \infty, \quad (1)$$

- have, within one period, finite number of local maxima and minima;
- have, within one period, finite number of points of first kind discontinuity.

What is more, a primary assumption of Fourier analysis is to ensure that the sampling period is a total multiple of the period of the examined waveform. It means that determining the waveform period is the first problem to be solved in order to conduct the harmonic analysis. In the case of distorted waveforms, which next to harmonics also involve interharmonics (particularly subharmonics) assuring this condition may mean that the sampling period needs to be significantly extended. If the waveform additionally involves fast-changing signals, it is necessary to maintain high sampling frequency in order to meet the conditions resulting from the Nyquist criterion. As a result, a discrete description of the waveform can include a lot of samples.

A lot of works have been devoted to the question of determining the waveform frequency and a lot of methods designed using various algorithms in order to estimate the waveform period quickly and precisely [8, 15]. However, in reality because of the frequency drift of analysed waveform, its period is not stable, and the selected values are only its approximation. Consequently, it is impossible to avoid a little spectral leakage. Moreover, in real Fourier transformations, an analysed signal

has a limited length to N -samples which is synonymous with multiplying discrete signal $y(i)$ by the function describing the measurement window. The factors mentioned here cause that DFT has limited accuracy [15, 17]. That is why the wrong selection of the parameters of measurements and analyses can distort the obtained results. Selecting the primary signal frequency, the amount of samples, sampling time and analysis window [1, 8, 17] needs to be done very carefully. The examination of signal distortion becomes complicated when the signal has harmonics and also interharmonics [1, 8–10]. Signal nonstationarity entails additional complications connected with determining and selecting the parameters and methods that were mentioned before [8].

In the literature, one can find the algorithms that improve the precision of Fourier-based methods [12, 15]; however, they are not very popular and most of the analysers are based on DFT.

There are multiple parametric and nonparametric methods that can be an alternative to DFT. Among the group of linear nonparametric methods, the discrete wavelet transform (DWT) is worth mentioning [18]. Among the parametric methods, the most popular is the Prony's method [19]. Methods that use artificial intelligence, e.g. artificial neural networks [20] or hybrid methods, are becoming more and more popular [21].

Wavelet transform enables to analyse time and frequency of signals with changeable window. A variety of wavelet functions allows for an easier matching of particular wavelet with the signal character. It allows to obtain high-frequency definition for the components with low frequencies and precise localization in time for high frequencies which is very crucial in nonstationary signal analyses.

The Prony's method involves extraction from a signal exponentially damped sinusoids. Owing to this, apart from the information about amplitudes, phases and component frequencies in the signal, the information about damping coefficients of particular sinusoids that create a signal is also returned. The Prony's method allows for a precise estimation of component frequencies and for using short analysis windows. Computational complexity and lack of localization in time of particular components seem to be disadvantages of this method.

Despite these drawbacks and limitations, and in spite of the existence of many other alternative methods, DFT is still one of the most frequently used methods for the analysis of distorted waveforms [1, 8–11, 13–15, 17]; it results from its simplicity and easy implementation.

3 Waveform Distortion Indices

In practice, the evaluation of the level of distortion in periodic waveforms needs to be multi-criterial using the indicators carrying various information. The necessity of such evaluation entails different influences of particular harmonics on the operation of network and devices. Below, the selected indices are compared describing periodic waveforms which can be used in the evaluation of waveform distortion.

A. Effective value

An effective value of periodic electric voltage is the value that equals to direct voltage applied to particular resistance, which results in emitting of the same energy on this resistance as in the case of alternating voltage:

$$X_{\text{RMS}} = \sqrt{\frac{1}{T} \int_{t_0}^{t_0+T} f^2(t) dt} = \sqrt{\sum_{k=1}^{\infty} X_k^2}. \quad (2a)$$

For the purpose of analyses, a lot of measuring apparatuses determine an effective value based on the dependency:

$$X_{\text{RMS}} = \sqrt{\sum_{k=1}^N X_k^2}. \quad (2b)$$

B. Coefficient of k -th harmonic content

The coefficient of harmonic content determines the contribution of each harmonic in the output signal. The higher the value of index for a particular harmonic, the greater contribution it has in the signal waveform:

$$w_k = \frac{x(k)}{x(1)} \times 100\%. \quad (3)$$

C. Coefficient of higher harmonics content

THD coefficient reflects the ratio of higher harmonics effective value to the effective value of primary component (4a):

$$\text{THD}_F = \text{THD} = \frac{\sqrt{\sum_{k=2}^n x_{(k)}^2}}{x_{(1)}} \quad (4a)$$

$$\text{THD}_R = \frac{\sqrt{\sum_{k=2}^n x_{(k)}^2}}{\sqrt{\sum_{k=1}^n x_{(k)}^2}}. \quad (4b)$$

Historically, THD coefficient was defined in two ways, in accordance with the dependency (4a) and (4b). In the paper [22] the author demonstrated that better results can be obtained when using THD_F coefficient (4a). The use of THD_R coefficient, defined according to (4b), may lead to huge errors, when determining the power coefficient or distortion coefficient [23]. Modern energy analysers determine the THD coefficient in accordance with the dependency (4a) and such a definition has been used in the current paper.

D. Peak coefficient

The peak coefficient informs about the level of waveform distortion and is defined as a quotient of the peak value to the effective value:

$$CF = \frac{\max|f(t)|}{X_{RMS}}. \quad (5)$$

For an ideal sinusoid the peak coefficient equals $\sqrt{2}$ and the more the distorted waveform, the higher peak coefficient is.

E. Absolute average value

The absolute average value corresponds to the value of ideally straight signal:

$$X_{AV} = \frac{1}{T} \int_{t_0}^{t_0+T} |f(t)| dt. \quad (6)$$

F. Shape coefficient

The shape coefficient determines the shape of periodic waveform and is defined as the ratio of effective value to the value of absolute average:

$$FF = \frac{X_{RMS}}{X_{AV}}. \quad (7)$$

For an ideal sinusoid, this coefficient equals $\pi\sqrt{2}/4$. The value of this coefficient is used to determine the measurement conditions of power losses in magnetically soft materials.

G. Coefficient of k -th interharmonic content

The coefficient of interharmonic determines the contribution of particular interharmonics in the output signal. The higher value of index for a particular component, the higher is its contribution in the signal waveform:

$$wi_k = \frac{V_{(k)}}{X_{(1)}} \times 100\%. \quad (8)$$

H. Coefficient of interharmonics content

This coefficient is analogous to the THD coefficient and reflects the ratio of interharmonics effective value to the effective value of primary component:

$$\text{TIHD} = \frac{\sqrt{\sum_{k=1}^n V_{(k)}^2}}{X_{(1)}}. \quad (9)$$

I. Deformation coefficient

The coefficient of deformation, also called a nonsinusoidal coefficient, is

$$h_D = \frac{X_{AV(1)}}{X_{AV}}. \quad (10)$$

J. Relative deviation value

The relative deviation value determines the ratio of maximum exceeding in signal momentary value over the momentary effective value of basic component

$$w_H = \frac{\max|f(t) - X_{(1)} \sin(\omega t + \varphi)|}{X_{(1)}}, \quad (11)$$

where

- $f(t)$ signal momentary waveform;
- $X_{(k)}$ k -th harmonic of signal spectrum;
- $V_{(k)}$ k -th interharmonic of signal spectrum

4 Lab Research Area

In order to conduct measurements, the lab research has been prepared comprising Emerson Commander SK frequency inverter supplying Temal 3Sg90L-4-IE2 induction motor, which was loaded by Delta ECMA-E21315GS servomotor (Fig. 1). The measurements were done using Elspec Blackbox G4500 current quality analyser. The measurement results were transferred to MS SQL server using PQScada software. For the analyses, in turn, there were used PQInvestigator, Matlab environment and spreadsheet. The PQScada and PQInvestigator softwares are provided by the manufacturer together with Elspec G4500 analyser.

Commander SK inverter through the change of power frequency enables to adjust the rotational speed of induction motor. The control is performed in the open loop of reverse coupling in accordance with a sensorless, actual field vector orientation. By an automatic compensation of torque and lost motion, it allows for full torque and speed control [23].

Elspec Blackbox G4500 power quality analyser class A was used in the measurements. It allows for making 1024 samples in the voltage period that allows to

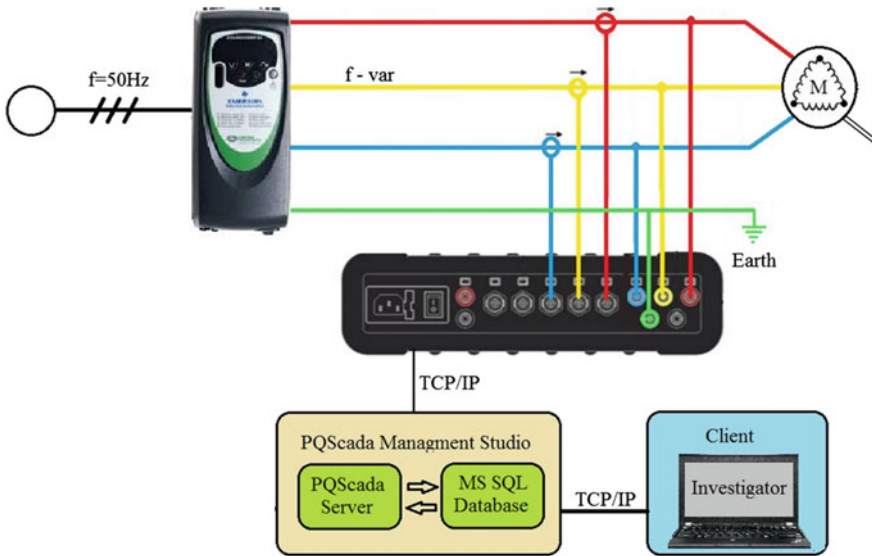


Fig. 1 Schematic of the measuring system

analyse 511 harmonic components. The device allows to analyse the measured voltage in accordance with the norms EN 50160 [24] and IEC 61000-4-30 [25] or also including a wider spectrum of harmonics [26]. According to the research [9], widening the analysed spectrum of harmonics provides a better knowledge about the signal distortion. Additionally, the device enables to analyse interharmonics which can be the source of further knowledge concerning the signal distortion [26].

5 Results

The analysis of all the indices mentioned in part III is too broad to present it in the current paper. That is why, below there are presented studies of a few indices, conducted in three ways:

- cycle by cycle, including all components (index CpC in the tables).
- according to the norm PN-EN 61000-4-30 [25] within the time of 10 periods (index 10 in the tables) and
- according to the norm PN-EN 61000-4-30 [25] within the time of 150 periods (index 150 in the tables).

A. Effective value (RMS)

The voltage-effective value is an extremely important parameter in the evaluation of waveform that determines the energetic signal potential.

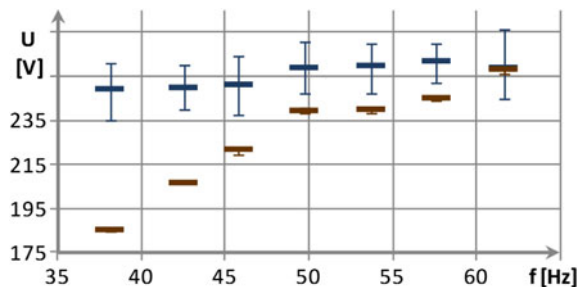
The analysis of the results presented in Table 1 shows that the effective value increases together with the output voltage frequency. In case of the measurement using cycle by cycle, this increase is not significant, but in case of the measurement done in accordance with the norms [16, 25] and averaging in 150 periods, the increase is very clear (Table 1). Characteristic is the fact that together with the increase of frequency, the difference between the values is determined by cycle by cycle and the value obtained from averaging in 150 waveform periods (Fig. 2). This is probably caused by the analysis method of the effective value (2a) including only harmonics to the row resulting from the norm and the fact that the spectrum includes the harmonics that occur outside the analysed range (Fig. 5).

A single value measured in the cycle-by-cycle mode can be unrepresentative for the whole waveform because of its quasi-periodicity and nonstationarity [8, 9]. That is why, the variety of the values, presented in Table and in Fig. 1, is much higher than the variety of the values averaged in 150 periods. However, the values measured cycle by cycle have broader spectrum of harmonics than the values averaged in 150 periods (according to the norm they have only 40 components). That is why, the voltage-effective value measured in the cycle-by-cycle mode seems to be more accurate than the value measured according to the norm [16], as the second measurement contains a big error when higher harmonics are involved.

Table 1 The changes in RMS voltage-effective value depending on the output voltage frequency

f (Hz)	RMS ₁₀ (V)			RMS ₁₅₀ (V)			RMS _{CPC} (V)		
	Min	Avg	Min	Min	Avg	Max	Min	Avg	Max
38.1	182.8	182.8	235.2	235.2	235.2	187.2	185.1	185.2	185.4
42.5	205.3	205.3	239.5	239.5	239.5	207.8	206.3	206.6	206.8
45.8	219.9	219.9	237.7	237.7	237.7	223.1	213.6	221.5	221.7
49.7	231.0	231.0	247.0	247.0	247.0	247.2	238.2	239.1	240.3
53.7	238.5	238.5	247.3	247.3	247.3	240.6	238.6	239.7	239.9
57.6	242.8	242.8	252.1	252.1	252.1	246.9	244.0	244.9	245.8
61.6	236.6	236.6	244.4	244.4	244.4	262.9	239.5	258.0	258.8

Fig. 2 Dependence of voltage-effective value from frequency. *Blue colour* cycle by cycle including all components, *brown colour* averaged value in the time of 150 periods according to [25]



B. Coefficient of harmonics content (THD)

In accordance with the definition (4a) the coefficient of harmonics content determines a relative contribution of higher harmonics in the signal in relation to the primary component. It is commonly considered as the basic component of waveform distortion.

On the basis of data analyses presented in Table 2, it can be noted that the THD value, determined through the averaging of values in 150 periods, ranges from 10% to almost 30% and it is difficult to state if it depends on the output voltage frequency. In the case of measurements and analyses of cycle by cycle, it can be noticed for the frequencies lower than 50 Hz, THD together with the decrease in frequency has increasingly higher values, but for the frequencies higher than 50 Hz practically remains stable (Fig. 2).

It is necessary to emphasise that the value of THD for the measurements and analyses of cycle by cycle is significantly higher than the value obtained by averaging of 150 periods—according to the norm [25].

C. Crest factor

The dependence of the value of crest factor (CF) from the output voltage of frequency inverter is presented in Table 3 and shown in Fig. 3. The more the output

Table 2 The changes in value of harmonics content coefficient THD depending on the output voltage frequency

<i>f</i> (Hz)	THD ₁₀ (%)			THD ₁₅₀ (%)			THD _{CpC} (%)		
	Min	Avg	Max	Min	Avg	Max	Min	Avg	Max
38.1	7.98	10.22	13.1	9.93	10.25	10.68	90.18	98.41	100
42.5	19.72	21.03	21.16	20.87	21.04	21.16	67.55	76.32	84.57
45.8	17.77	20.04	22.44	19.86	20.07	20.87	49.56	61.83	72.97
49.7	2.09	24.20	37.56	24.67	26.04	27.68	35.93	50.07	61.19
53.7	16.69	18.03	19.6	17.89	18.09	19.43	36.40	49.64	59.00
57.6	17.73	27.05	30.63	26.21	27.08	30.62	43.00	51.73	58.97
61.6	16.52	19.13	21.4	18.67	19.13	21.31	41.81	49.21	57.32

Table 3 The changes in values of crest factor CF depending on the output voltage frequency

<i>f</i> (Hz)	CF ₁₀ (%)			CF ₁₅₀ (%)			CF _{CpC} (%)		
	Min	Avg	Max	Min	Avg	Max	Min	Avg	Max
38.1	1.573	1.714	1.842	1.694	1.714	1.727	1.576	1.889	2.353
42.5	1.499	1.611	1.724	1.578	1.611	1.632	1.582	1.911	2.594
45.8	1.467	1.519	1.597	1.506	1.52	1.538	1.529	1.816	2.308
49.7	1.293	1.467	1.631	1.449	1.47	1.498	1.429	1.664	1.982
53.7	1.443	1.496	1.57	1.482	1.496	1.51	1.37	1.637	2.017
57.6	1.576	1.738	1.918	1.711	1.738	1.773	1.391	1.658	2.047
61.6	1.589	1.771	2.014	1.738	1.772	1.8	1.46	1.684	2.01

Fig. 3 Dependence of THD value from frequency. *Blue colour* cycle by cycle including all components, *brown colour* averaged value in the time of 150 periods according to [25]

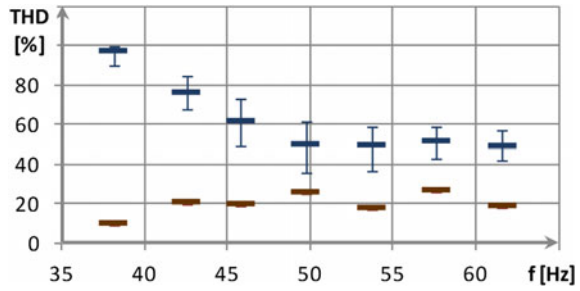
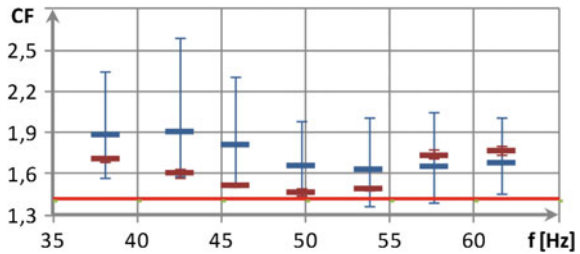


Fig. 4 Dependence of CF value from frequency. *Blue colour* cycle by cycle including all components, *brown colour* averaged value in the time of 150 periods according to [25], *red line* value of CF for ideal sinusoid



frequency diverges from 50 Hz, the higher value the shape coefficient obtains. For an ideal sinusoidal waveform, the value of crest factor is $\sqrt{2}$, while in the analysed examples it changes from the value of 1.47 for 50 Hz to the value of 1.714 (38.1 Hz) and 1.772 (for 61.6 Hz).

The coefficient value is different for particular signal periods (cycle-by-cycle measurements); however, it is characteristic that it practically fails to decrease below the value of $\sqrt{2}$ (Fig. 4).

D. Harmonics content

The content coefficient of the k -th harmonic determines its contribution in the shape of waveform. In the case of waveforms distorted with multiple components, and such is the output voltage of frequency inverter, a wide range of harmonics spectrum occurs. That is why, further figures (Fig. 5a–g) show the spectrum of output voltage for various frequencies in relation to the basic component—the respective bars are determined according to the dependency (3).

All the waveforms contain the third harmonic and a group of harmonics that represent the frequency of around 2800 Hz. In the waveforms with the frequencies below 50 Hz, other groups appear which are multiple of 2800–5600, 8400 Hz.

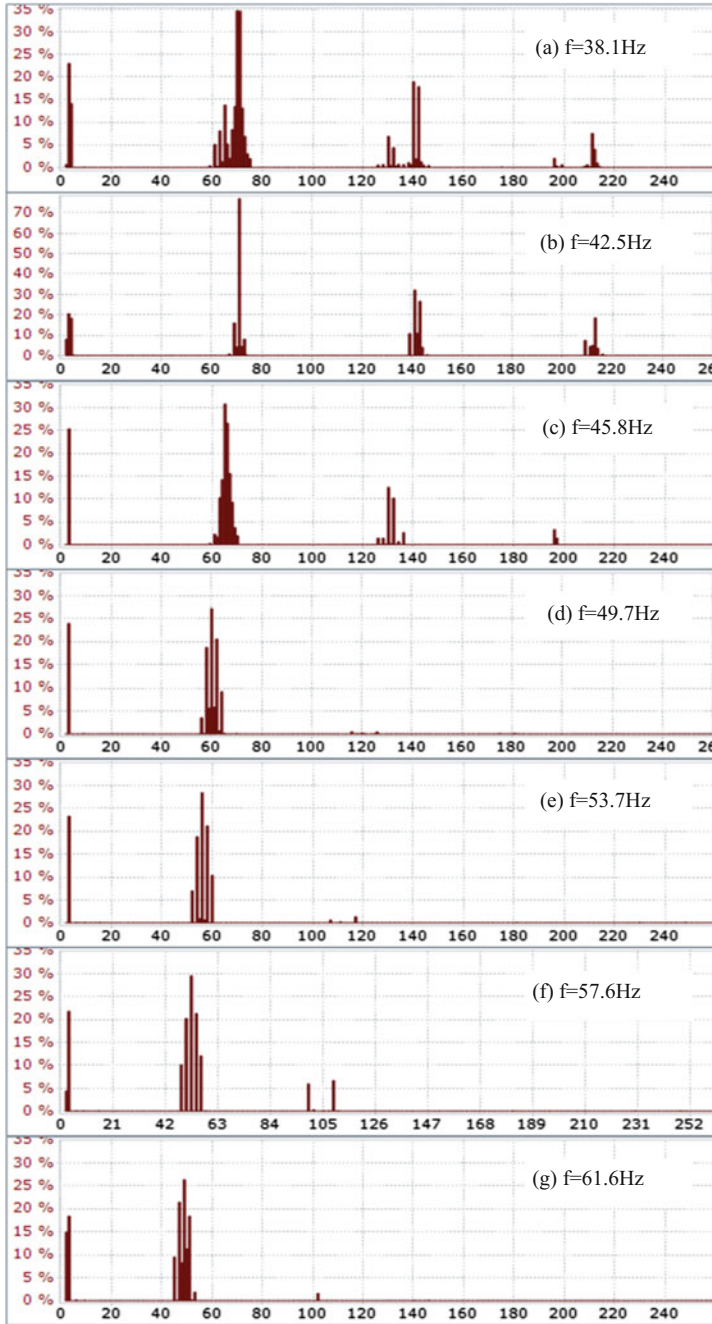


Fig. 5 The spectrums of the output voltage for different frequencies

6 Conclusions

Evaluating the voltage and current waveform distortion is the need of the hour. There are various devices on the market that allow to perform the evaluation accurately. However, the methodology of measurements (e.g. of effective value or THD) may lead to wrong results caused by reducing the spectrum or averaging of value (in accordance with the norms [16, 25]).

The analysed waveform—output voltage of frequency inverter—is considered as a significantly distorted waveform that is indicated by the values of THD coefficient and the analysis of particular harmonics. However, the values of shape coefficient (CF) fail to diverge significantly from the ideal value and indicate that the spectrum should be considered as slightly distorted. Only the understanding of THD and CF allows to provide a diagnosis: the waveform includes a wide spectrum of harmonics but maintains University of Rzeszow a sinusoidal shape. That is why, it is crucial that the evaluation of waveform distortion is performed on the basis of multiple coefficients determined in various ways.

The term ‘distorted waveforms’ is not precise as it implies that the waveform has a stable period and each has identical distortion. In fact, the analyses most often cover the waveforms with drifting period and a different spectrum of particular periods; that is why, it is more appropriate to call them quasiperiodic waveforms.

References

1. Hanzelka, Z., Bień, A.: Harmonics, Interharmonics, Power Quality Application Guide (2004)
2. Chapman, D.: Harmonics Causes and Effects, Power Quality Application Guide (2001)
3. Bednarek, K.: Jakość, pewność i właściwa konstrukcja układu zasilania, a bezpieczeństwo urządzeń elektrycznych, *Elektro.info*, no. 12, pp. 26–31 (2012)
4. Shmilovitz, D., Duan, J., Czarkowski, D., Zabar, Z., Lee, S.: Characteristics of modern nonlinear loads and their influence on systems with distributed generation. *Int. J. Energy Technol. Policy* **5**(2), 219–240 (2007)
5. Kamuda, K., Klepacki, D., Kuryło, K., Sabat, W.: Analiza statystyczna wpływu odbiorników nieliniowych małej mocy na odkształcenie napięcia zasilającego. *Przegląd Elektrotechniczny* **91**(8), 19–22 (2015)
6. Binkowski, T.: Universal High Speed Induction Motor Driver. *Lecture Notes in Electrical Engineering*, pp. 149–162. Springer, Berlin (2015)
7. Sobczynski, D.: A concept of a power electronic converter for a BLDC motor drive system in aviation. *Aviation* **19**(1), 36–39 (2015). doi:[10.3846/16487788.2015.1015294](https://doi.org/10.3846/16487788.2015.1015294)
8. Rezmer, J., Leonowicz, Z., Gono, R.: Analysis of distorted waveform in power concrete systems. *Przegląd Elektrotechniczny* **87**(1), 254–257 (2011)
9. Bartman, J.: Accuracy of reflecting the waveforms of current and voltage through their spectrum determined by the standards regulating measurements. *Revue Roumaine des sciences techniques—Serie Electrotechnique et Energetique* **61**(4), 355–360 (2016)
10. Bartman, J., Sobczyński, D.: The analysis of the voltage and current waveforms of frequency inverter fed induction motor. *Computing in Science and Technology*, pp. 5–18 (2016)

11. Koziorowska, A., Bartman, J.: The influence of reactive power compensation on the content of higher harmonics in the voltage and current waveforms. *Przegląd Elektrotechniczny* **90**(1), 136–140 (2014)
12. Antić, B.M., Mitrović, Z.L., Vujičić, V.V.: A method for harmonic measurement of real power grid signals with frequency drift using instruments with internally generated reference frequency. *Meas Sci Rev* **12**(6), 277–285 (2012)
13. Bartman, J., Koziorowska, A., Kuryło, K., Malska, W.: Analiza rzeczywistych parametrów sygnałów elektrycznych zasilających układy napędowe pomp wodociągowych. *Przegląd Elektrotechniczny* **87**(8), 8–11 (2011)
14. Koziorowska, A., Kuryło, K., Bartman, J.: Harmoniczne napięcia i prądu generowane przez nowoczesne napędy stosowane w kopalniach kruszywa. *Przegląd Elektrotechniczny* **86**(6), 279–284 (2010)
15. Lin, H.C.: Current harmonics and interharmonics measurement using recursive group-harmonic current minimizing algorithm. *IEEE Trans. Ind. Electron.* **59**(2), 1184–1193 (2012)
16. IEC 61000-4-7: Testing and measurement techniques—General guide for harmonics and interharmonics measurements and instrumentations for current supply systems
17. Pawłowski, M.: Podstawy analizy harmonicznej odkształconych przebiegów prądów i napięć w sieciach zasilających. *Mechanizacja i Automatykacja Górnictwa* **7**(473), 17–23 (2010)
18. Taranenko, I., Pawełek, R., Gorpynych, O.: Zastosowanie transformaty falkowej do analizy przebiegów napięć zasilających napędy z częstotliwościową regulacją prędkości obrotowej. *Przegląd Elektrotechniczny* **91**(11), 69–73 (2015)
19. Zygariłcki, J., Mrocza, J.: Prony's method with reduced sampling—numerical aspects. *Metrol. Meas. Syst.* **21**(3), 521–534 (2014)
20. Valtierra-Rodriguez, M., de Jesus Romero-Troncoso, R., Osornio-Rios, R.A., Garcia-Perez, A.: Detection and classification of single and combined power quality disturbances using neural networks. *IEEE Trans. Ind. Electron.* **61**(5), 2473–2482 (2014)
21. Zadeh, R.A., Ghosh, A., Ledwich, G.: Combination of Kalman filter and least-error square techniques in power system. *IEEE Trans. Power Deliv.* **25**(4), 2868–2880 (2010)
22. Shmilovitz, D.: On the definition of total harmonic distortion and its effect on measurement interpretation. *IEEE Trans. Power Deliv.* **20**(1), 526–528 (2005)
23. Advanced User Guide Commander SK (2015), <http://www.emersonindustrial.com>
24. EN 50160: Voltage characteristics of electricity supplied by public distribution systems
25. IEC61000-4-30: Electromagnetic compatibility. Testing and measurement techniques—Current quality measurement methods
26. User and Installation Guide G4500/G3500: Black Box Portable Power Quality Analyzer (2014). <http://www.elspec-ltd.com>

Digital Processing of Frequency–Pulse Signal in Measurement System

D. Świsulski, E. Pawłowski and M. Dorozhovets

Abstract The work presents the issue of the use of multichannel measurement systems of sensors processing input value to impulse signal frequency. The frequency impulse signal obtained from such sensors is often required to be processed at the same time with a voltage signal which is obtained from other sensors used in the same measurement system. In such case, it is usually necessary to sample the output signals from all sensors in the same, predetermined points in time. Sampling voltage signal by means of A/D converters is practically possible in any selected time points, and the sampling frequency–pulse signal FPS requires special algorithms. The authors present the algorithms of digital signal processing pulse frequency offline and online modes, providing the acquisition of samples at certain evenly distributed points over time.

Keywords Multi-channel measurements system • Converter with frequency output • Frequency-pulse signal • Analog-to-digital conversion • Instantaneous frequency • Signal reconstruction

D. Świsulski (✉)

Faculty of Electrical and Control Engineering, Gdańsk University of Technology,
Gdańsk, Poland

e-mail: dariusz.swisulski@pg.gda.pl

E. Pawłowski

Faculty of Electrical Engineering and Computer Science, Lublin University
of Technology, Lublin, Poland

e-mail: e.pawlowski@pollub.pl

M. Dorozhovets

Department of Information and Measuring Technology, National University
Lviv Polytechnic, Lviv, Ukraine

e-mail: dorozhovets@polynet.lviv.ua

© Springer International Publishing AG 2018

D. Mazur et al. (eds.), *Analysis and Simulation of Electrical and Computer Systems*, Lecture Notes in Electrical Engineering 452,
https://doi.org/10.1007/978-3-319-63949-9_20

1 Introduction

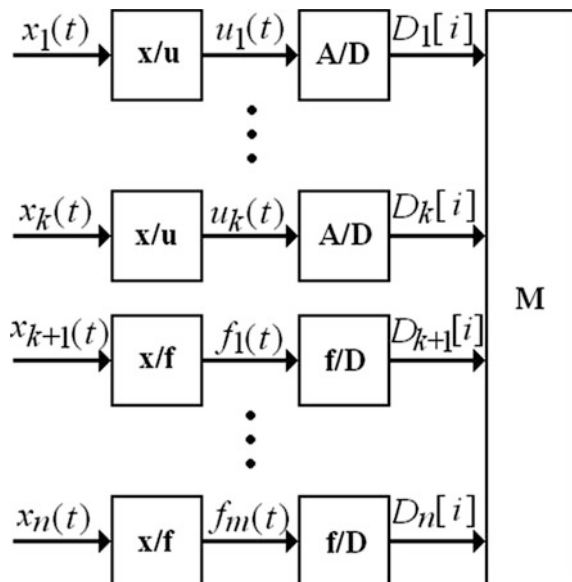
Modern measurement systems use various digital signal processing algorithms. For this purpose, all the measured values of the input system must be converted to their digital representations by suitable sensors and A/D converters, for which the most commonly used is an indirect voltage signal. This is due to the fact that now commonly available are integrated A/D converters processing only analogue voltage signal.

Often used instead of the voltage signal is the frequency signal [1, 2], which is easily and accurately processed into the digital form by means of metering systems and has a high resistance to interference, which greatly facilitates the transmission over long distances. The frequency signal can be obtained using integrated voltage-to-frequency converters VFC [3] or using sensors with frequency output [4, 5]. In multichannel measurement systems, both types of signals are often used simultaneously: voltage and frequency [6]. The structure of the measurement system under consideration is shown in Fig. 1.

During the acquisition of analogue signals $x(t)$, defined at any time in the time interval of observation, they are processed on the next channel on the N strings of numbers $\{D_k[0], D_k[1], D_k[2], \dots, D_k[N-1]\}$. They represent, respectively, the instantaneous values of analogue signals at regular intervals and are placed in the memory M of the measurement system. To maintain proper timing relationship between all the input quantities, analogue-to-digital processing in each channel should be carried out at the same time instants, typically evenly spaced in time, as required by DSP algorithms currently used (e.g. FFT, Hilbert transform, etc.).

If the signal is an intermediate voltage $u(t)$ produced by sensor type x/u , then the processing to digital form is implemented as standard in the A/D converter, and the

Fig. 1 Multichannel measuring system with tracks that use voltage signals u_1, \dots, u_k and frequency signal f_1, \dots, f_m



moment sampling can be chosen almost arbitrarily. A significant problem occurs when the intermediate signal is a variable in time frequency $f(t)$, since the pulses of the output frequency signal of the sensor type x/f are generated with a different time interval. This time depends on the mean value of the input $x(t)$ at the time of the previous pulse [7]. Therefore, to obtain the frequency signal, samples uniformly distributed at certain time instants require special methods other than voltage circuit.

2 Frequency–Pulse Signal

The sensor frequency output is a converter of the instant value of the measured quantity $x(t)$ to the instantaneous value of the frequency $f(t)$ with a coefficient of proportionality known as sensitivity of the sensor S :

$$f(t) = Sx(t). \quad (1)$$

The frequency f is a parameter of periodic signal $y(t)$ present at the output of the sensor. In practice, it is usually a voltage signal, which may be of any shape: sinusoidal, triangular, rectangular, etc. [7]. In such case, the instantaneous values of the signal $y(t)$ do not reflect the actual values of the measured value $x(t)$, but they are a particular form of a periodic-input function $F(\varphi)$, describing the shape of the signal $y(t)$. The argument of the function $F(\varphi)$ is a variable during the phase $\varphi(t)$ of the signal $y(t)$:

$$y(t) = F(\varphi(t)). \quad (2)$$

If the frequency of the output of the sensor is constant $f = \text{const}$, then the phase $\varphi(t)$ of this signal is a linear function of time:

$$\varphi(t) = 2\pi ft + \theta, \quad (3)$$

where θ is the initial phase. Otherwise, when the frequency $f(t)$ of the signal changes, the phase signal $\varphi(t)$ is described by an integral relationship:

$$\varphi(t) = 2\pi \int_0^t f(t) dt + \theta. \quad (4)$$

Regardless of the actual shape of the signal $y(t)$ described by Eq. (2), in measuring systems, processing frequency to form a numerical includes only the selected characteristic of the states of this signal, usually timely rising or falling slope, which is marked by periods of the signal. Therefore, in practice, the signal $y(t)$ can be considered as a series of pulses Dirac δ shown in Fig. 2, appearing at moments t_i separated from each other by intervals T_i , corresponding to the following equal increments of the signal phase $\Delta\varphi$ equal to the period of 2π :

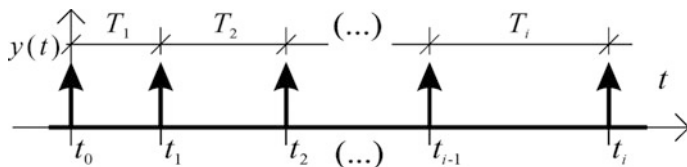


Fig. 2 The idealised frequency-pulse signal

$$y(t) = \sum_{i=-\infty}^{+\infty} \delta(t - t_i), \quad t_i - t_{i-1} = T_i. \tag{5}$$

The signal $y(t)$ shown in Fig. 2, described by the relation (5), whose instantaneous frequency $f(t)$ is proportional to the value of the processed $x(t)$ according to Eq. (1), will be called as the frequency-pulse signal FPS. The fundamental problem is to convert instantaneous frequency $f(t)$ of the signal FPS $y(t)$ (5) to its digital representation of $D[i]$ (Fig. 1). In measurement technique, having respectively taken into account the transformed Eq. (4), the instantaneous frequency $f(t)$ of the signal is determined by the derivative of the phase φ of this signal with respect to time t [8]:

$$f(t) = \frac{1}{2\pi} \frac{d\varphi}{dt}. \tag{6}$$

Phase $\varphi(t)$ for a frequency-pulse signal FPS (5) is a continuous function of time, but the function F describing the shape of the signal $y(t)$ (2) is not a one to one: different values of the phase $\varphi(t)$ correspond to the same signal values $y(t)$. In the present signal, FPS (5) information is not accessible about the increase of the phase φ of the signal between the successive pulses. For such a signal, one cannot determine arbitrarily small increments of phase φ , and so one cannot also determine the frequency f on the basis of the derivative (6) for any time t . It is also clear that for the frequency-pulse signal FPS (5) we can determine only the increases of phase equal to a multiple of the period 2π . So in order to determine the frequency f of the pulse signal (5) the derivative (6) should be replaced by the quotient of the growth of phase $\Delta\varphi$ and time gain Δt [9]:

$$f(t) = \frac{1}{2\pi} \frac{\Delta\varphi}{\Delta t}. \tag{7}$$

Pulse at time t_i (rys. 2) is the incremental phase of the signal FPS (5) by an angle $\Delta\varphi = 2\pi$ relative to the pulse at time t_{i-1} , in block f/D implementing sampling pulse frequency signal $f(t)$ (Fig. 1); successive time intervals T_i are measured digitally via filling them with impulses T_{ref} of reference frequency f_{ref} , which allows to determine the next sampling frequency f_i :

$$f_i = \frac{1}{2\pi} \frac{\Delta\varphi}{\Delta t} = \frac{1}{2\pi} \frac{2\pi}{t_i - t_{i-1}} = \frac{1}{T_i} = \frac{1}{K_i T_{\text{ref}}} = \frac{f_{\text{ref}}}{K_i}, \quad (8)$$

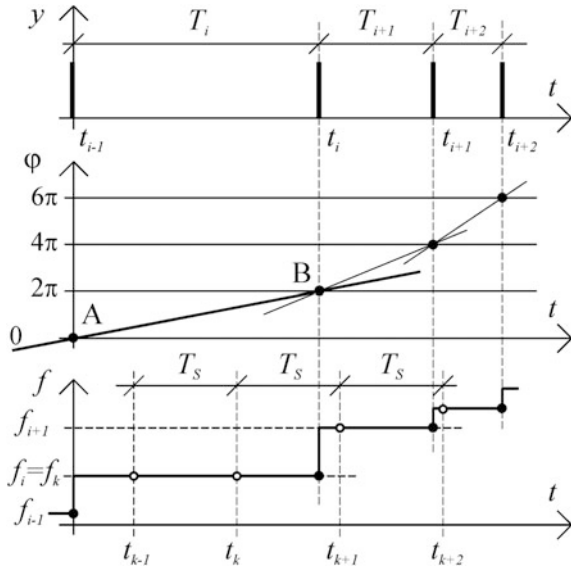
where K_i is the number of impulses of reference frequency f_{ref} , which have been counted in time T_i . The resultant quantization error can be analysed by simulation methods [9]. If the input value $x(t)$ varies with time, the more frequencies f_i are obtained at times t_i and unevenly distributed over time (Fig. 2). Besides, the frequency value f_i is not an instantaneous value, being an average value for the time T_i , and therefore does not assign it to the time t_i , but properly chosen time t_i^* being within the interval T_i [9]. For an unknown form of $x(t)$ it is not known where the moments of time t_i^* can be reasonably attributed to the value of f_i . Since the location of points (t_i^*, f_i) is not known, it is impossible unfortunately to approximate the value of $f(t)$ for any time t . The frequency–pulse signal FPS has, however, the additional advantageous property: all the pulses occur exactly at those moments t_i , in which the phase angle of the signal growth $\Delta\varphi = 2\pi$ is equal to the period of the signal $y(t)$. As a result, points $(t_i, 2\pi i)$ allow clearly to approximate the course of the instantaneous phase $\varphi(t)$ of the signal (5), and after calculation of the derivative (6) also the course of the instantaneous frequency $f(t)$.

The methods of processing a frequency–pulse signal FPS can be divided into two groups, depending on the position of the time for which the measurement result is determined. When measuring in offline mode, first time t_i of all pulses are remembered and then one determines the value measured in moments of measurement adopted by the position of the pulse of both preceding and occurring after the moment of the measurement. In online test, the measured value is determined only on the basis of the position of the pulse preceding the moment of measurement.

3 Offline Processing

While converting the frequency–pulse signal FPS in offline mode in M system memory (Fig. 1), the location of all subsequent pulses at times t_i , distant in time o T_i , has been remembered, which allows approximating the course of instantaneous values of the phase $\varphi(t)$ of the signal and after differentiation (6), reconstituting the instantaneous frequency $f(t)$ [10]. For extremely low-frequency signals, it is often sufficient to assume that the frequency $f(t)$ is constant in successive time intervals T_i ; according to the formula (3), the phase of the signal $\varphi(t)$ can be interpolated in this range with a straight line. The procedure is shown in Fig. 3. Two points A and B define a straight line $\varphi(t) = a_0 + a_1 t$ approximating phase of the signal in the time interval of (t_{i-1}, t_i) , in which the signal phase growth occurred $\Delta\varphi = 2\pi$. After simple transformations, we calculate $a_0 = 0$ and $a_1 = 2\pi/T_i$, and taking into account (6) after setting the derivative we get $f(t) = f_i = 1/T_i$ for $t \in (t_{i-1}, t_i)$. Following an analogous procedure to the next interval T_i we get a line approximating the course

Fig. 3 The phase linear approximation of the frequency-pulse signal



of $f(t)$ in accordance with accepted at the beginning of assumptions, which will determine the frequency f_k at times $t_k = kT_S$ evenly distributed dug the period T_S of evenly sampling:

$$f_k = f(t_k) = f(kT_S) = 1/T_i, \quad t_k \in (t_{i-1}, t_i). \tag{9}$$

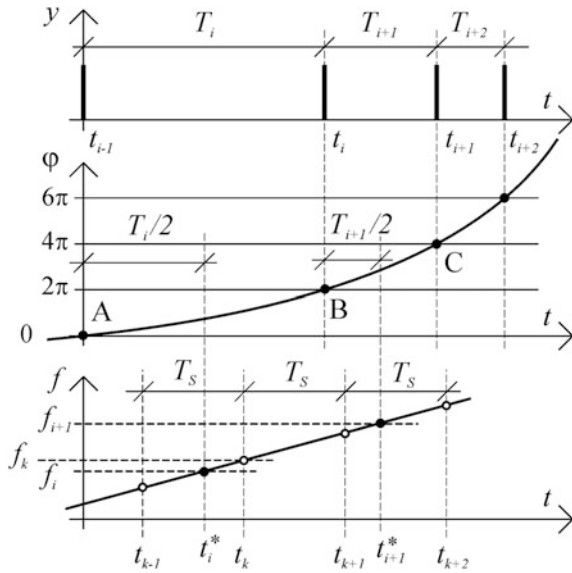
For signals changing faster, one can assume a linear change in frequency as a function of $f(t)$, and then one should approximate the course of the signal phase with a polynomial of the second degree $\varphi(t) = a_0 + a_1t + a_2t^2$. This requires determination of the coordinates of three points A, B and C (Fig. 4) corresponding to the phase increments $\varphi(t)$ of the signal by further multiple 2π at times t_{i-1}, t_i, t_{i+1} . The three moments of time determine the position of three successive signal pulses $y(t)$, away from each other by times T_i and T_{i+1} .

Points $(0, 0)$, $(T_i, 2\pi)$ and $(T_i + T_{i-1}, 4\pi)$ enable the arrangement of a system of three equations with three unknowns a_0, a_1 and a_2 . After solving this system of equations one receives dependency of the instantaneous phase value $\varphi(t)$, and after differentiation (6) we obtain the polynomial interpolating instantaneous frequency $f(t)$ (1) of the signal $y(t)$ in the time interval of (t_{i-1}, t_{i+1}) , based on the two neighbouring inter-pulse times T_i, T_{i+1} :

$$f(t) = \frac{1}{T_i + T_{i+1}} \left[\frac{T_{i+1}}{T_i} - \frac{T_i}{T_{i+1}} + 2 + 2 \left(\frac{1}{T_{i+1}} - \frac{1}{T_i} \right) t \right]. \tag{10}$$

Substituting Eq. (10) $f(t_i^* = 1/T_i)$ one can show that for the linear frequency change its mean value is equal to the instantaneous value of exactly half of the time

Fig. 4 The second degree phase approximation of the frequency–pulse signal



interval T_i . Therefore, it is reasonable to interpolate in the time interval from the time $t_i^* = t_{i-1} + T_i/2$ to time $t_{i+1}^* = t_i + T_{i+1}/2$, for which the instantaneous frequency takes appropriate values $f_i = 1/T_i$ and $f_{i+1} = 1/T_{i+1}$. Following points t_i^*, f_i :

$$t_i^* = t_{i-1} + T_i/2 = \sum_{j=1}^{i-1} T_j + T_i/2 \tag{11}$$

$$f_i = 1/T_i$$

mark the following sections of a broken line, which allows the download of frequency f_k at times $t_k = kT_S$ equally distant in even time sampling period T_S :

$$f_k = f(t_k) = \frac{(t_k - t_i^*)f_{i+1} + (t_{i+1}^* - t_k)f_i}{t_{i+1}^* - t_i^*} \tag{12}$$

$$t_k = kT_S, \quad t_k \in (t_i^*, t_{i+1}^*).$$

In justified cases, one can also approximate the phase $\varphi(t)$ of the pulse signal FPS with a higher order polynomial.

4 Online Processing

During online mode, to determine the value of the measured value at and time t_k on the basis of the pulse signal FPS, one can use only the position of the use preceding the moment t_k , which requires the use of extrapolation instead of interpolation used in offline mode. The easiest way of processing the pulse frequency signal lies in the fact that the value of the signal $f_k = f_i$ at any time t_k is calculated (8) from the length of the last inter-pulse range T_i preceding time t_k (Fig. 5).

If the value of the processed signal $x(t)$ changes during the measurement, it also changes the interval T_i between pulses FPS. Thus, for a longer period T_i of pulse signal FPS, the longer is the time between the time $t_i^* = t_{i-1} + T_i/2$ which is assigned to the frequency $f_i = 1/T_i$, and time t_k for which one should extrapolate the values of the signal f_k . This means that the value obtained by extrapolating f_k may differ significantly from that which was actually sampled at the time t_k . In such case, the value of f_k at any time t_k can be calculated from the formula (13) using extrapolation of two adjacent inter-pulse ranges T_{i-1} , T_i preceding the time t_k , assuming a linear variation in frequency and given that the frequency f_i resulting from the measurement interval T_i is equal to the instantaneous frequency at the middle point of the interval t_i^* (11) (Fig. 6):

$$\begin{aligned}
 f_k &= f_{i-1} + \frac{(f_i - f_{i-1}) \left(t_k - \left(\sum_{j=1}^{i-2} T_j + \frac{1}{2} T_{i-1} \right) \right)}{\left(\sum_{j=1}^{i-1} T_j + \frac{1}{2} T_i \right) - \left(\sum_{j=1}^{i-2} T_j + \frac{1}{2} T_{i-1} \right)} \\
 &= \frac{1}{T_{i-1}} + \frac{2 \left(\frac{1}{T_i} - \frac{1}{T_{i-1}} \right) \left(t_k - \sum_{j=1}^{i-2} T_j - \frac{1}{2} T_{i-1} \right)}{T_{i-1} + T_i}.
 \end{aligned}
 \tag{13}$$

The frequency determined on the basis of the last two periods may differ materially from its current value. Figure 7 shows the error distribution of the

Fig. 5 Online frequency determination in interval between the last inter-pulse range

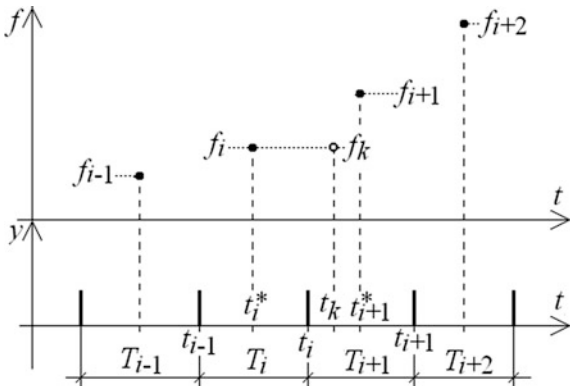


Fig. 6 Online frequency extrapolation of the last two inter-pulse ranges T_{i-1} and T_i

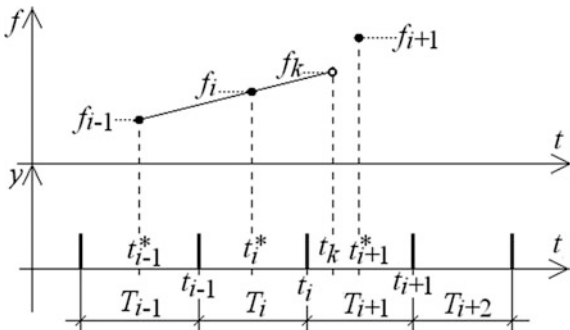
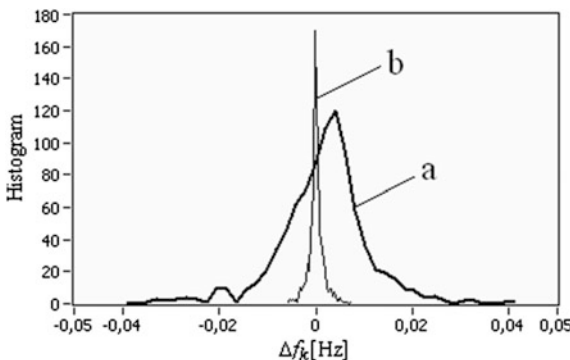


Fig. 7 Histograms of errors Δf_k for $f_0 = 20$ Hz, $a = 2$ Hz/s, $s_{\max} = 0.001$ Hz and $T_S = 100$ ms; **a** frequency determination from last period, **b** frequency determination from two last periods



measured frequency, assuming a linear change of frequency $f = f_0 + a \cdot t + s$ for $f_0 = 20$ Hz, $a = 2$ Hz/s, $s_{\max} = 0.001$ Hz and the even sampling period $T_S = 100$ ms, where s is the noise (s simulates the noise of the measured signal, but also processing errors). Error values were calculated as the difference between the frequency f'_k obtained from the measurement and value f_k accepted as true at the time t_k : $\Delta f_k = f'_k - f_k$.

If the noise level will be greater, errors measured using an extrapolation based on the last two periods may be even greater than a single measurement period. As an example, Fig. 8 shows the distributions of errors obtained for the same parameters as in Fig. 7, but with a noise value of $s_{\max} = 0.1$ Hz.

A similar analysis as for the linear frequency changes can be made to change the sine. Assuming that during measurement of the measured quantity changes as a function of time in a sinusoidal manner with frequency f_s , with the superimposed noise s :

$$f(t) = f_0 + f_m \cdot \sin(2\pi f_s t) + s, \tag{14}$$

Fig. 8 Histograms of errors Δf_k for $f_0 = 20$ Hz, $a = 2$ Hz/s, $s_{\max} = 0.1$ Hz and $T_S = 100$ ms; **a** frequency determination from last period, **b** frequency determination from two last periods

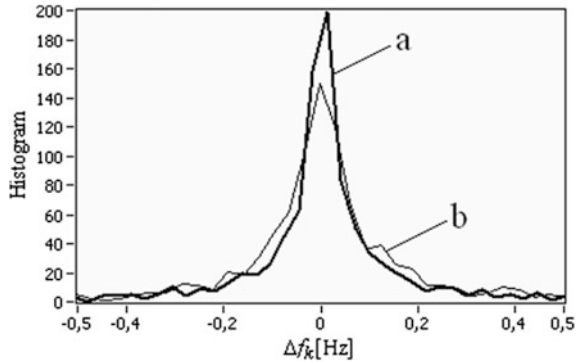
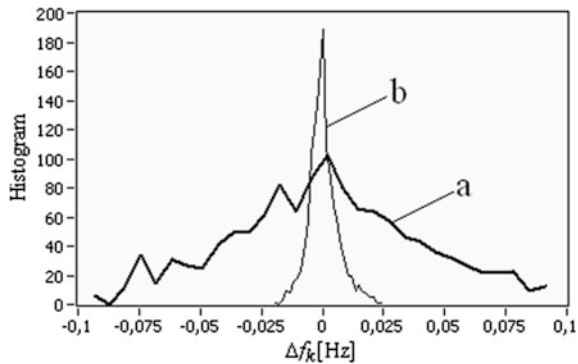


Fig. 9 Histograms of errors Δf_k distribution for $f_0 = 20$ Hz, $f_m = 2$ Hz, $f_s = 0.3$ Hz, $s_{\max} = 0.001$ Hz and $T_S = 20$ ms; **a** frequency determination from last period, **b** frequency determination from two last periods



where

- f_0 the constant pulse signal frequency $f(t)$ and
- f_m amplitude changes in the frequency of the pulse signal $f(t)$.

Figure 9 shows a distribution of errors with the sinusoidal pulse signal frequency change for $f_0 = 20$ Hz, $f_m = 2$ Hz, $f_s = 0.3$ Hz, $s_{\max} = 0.001$ Hz and an even sampling period of $T_S = 20$ ms.

Figure 10 shows the error distribution obtained for the same parameters as in Fig. 9, but for $s_{\max} = 0.1$ Hz.

The frequency f_k determined based on the last two ranges T_{i-1} , T_i (13) may also differ significantly from its current level if it does not vary in a manner similar to a linear, but in a random manner. In such case, a more favourable method may be the one in which another earlier interval T_{i-2} is used. The additional frequency f_{i-2} is used to determine the difference (see Figs. 11 and 12):

$$\Delta f_{i-2} = |f_{i-2} - f'_{i-2}|, \tag{15}$$

Fig. 10 Histograms of errors Δf_k distribution for $f_0 = 20$ Hz, $f_m = 2$ Hz, $f_s = 0.3$ Hz, $s_{\max} = 0.1$ Hz and $T_S = 20$ ms; **a** frequency determination from last period, **b** frequency determination from two last periods

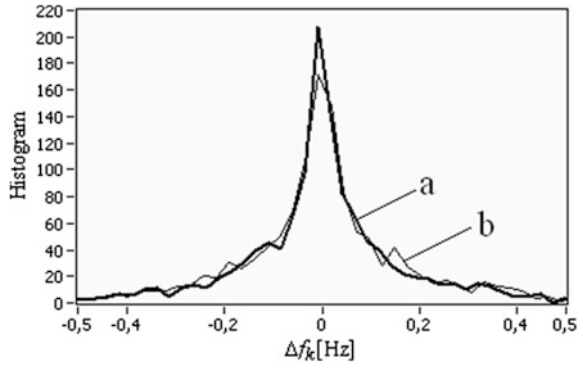


Fig. 11 Online frequency determination of the last three ranges for $\Delta f_{i-2} \leq \Delta f_{gr}$

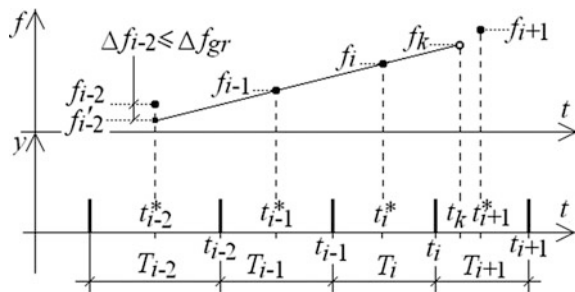
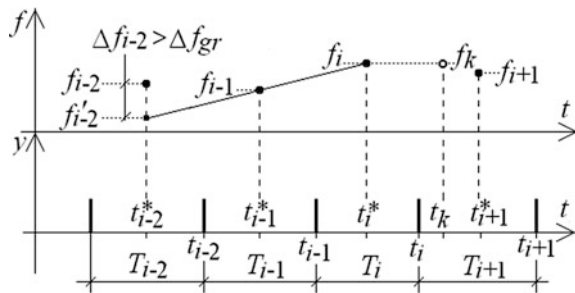


Fig. 12 Online frequency determination of the last three ranges for $\Delta f_{i-2} > \Delta f_{gr}$



where

- f_{i-2} frequency value determined from the interval T_{i-2} ,
- f'_{i-2} frequency value in the middle of the range of T_{i-2} determined by extrapolation of the ranges T_{i-1} and T_i .

Obtained from the formula (15) value Δf_{i-2} is compared with the established experimentally limit value Δf_{gr} . For $\Delta f_{i-2} \leq \Delta f_{gr}$ as a result of the measurement is taken the frequency f_k determined by extrapolation of the intervals T_{i-1} and T_i (Fig. 11). If $\Delta f_{i-2} > \Delta f_{gr}$ as a result of the measurement, the frequency f_i value is assumed to be determined from the interval T_i (Fig. 12).

For the conditions shown in Figs. 7, 8, 9 and 10 measurement simulations were repeated. For the proposed method, the error distributions were obtained corresponding to the distribution b in Figs. 7 and 9 and a distribution similar to that in Figs. 8 and 10. This confirms the validity of the adopted considerations. For the measured signal with a small change dynamics and low noise, frequency is determined by extrapolating on the basis of the last two periods. With high content of noise frequency, value is determined from the last period. The simulations performed adopted experimentally determined limit value of $\Delta f_{gr}/f_{i-2} = 0.2\%$. It has been obtained by determining the error values as a function of limit value.

5 Practical Application

For the practical verification of the algorithms, combined were the single-phase electric motor of low power with incremental rotary pulse encoder generating 512 pulses per revolution of the shaft. For measuring and recording the times T_i a measuring card was used (CTM-PER, company KEITHLEY) co-working with an IBM PC class computer. The measuring card has a 28-bit counter that counts the reference signal of 10 MHz, the FIFO memory provides meter reading “on the fly”, and for measuring the next time T_i in the range from 0.1 ms to 26.8 s and a transfer of results into the computer memory. Figure 13 shows the value of 512 times T_i recorded in one revolution of the motor shaft, which is then converted to the rotation speed and assigned in accordance with (11) times t_i^* lying in the middle of T_i giving a sample distributed unevenly over time. For greater clarity, Fig. 14 only shows the position of the selected part of pulses for $i = 234, \dots, 268$, covering part of the graph in Fig. 13 for the times $t_i = 19.9, \dots, 22.9$ ms. The total measurement time was 47.3 ms (one full rotation of the motor shaft). Uniform sampling period $T_s = 92.6$ ms (sampling rate approx. 10,800 samples/s) was adopted in such a way, so as to obtain the same number of 512 samples. Using the algorithm for offline (12) 512 signal values were calculated at times $t_k = kT_s$ evenly distributed over time

Fig. 13 Intervals T_i for one revolution of the motor shaft

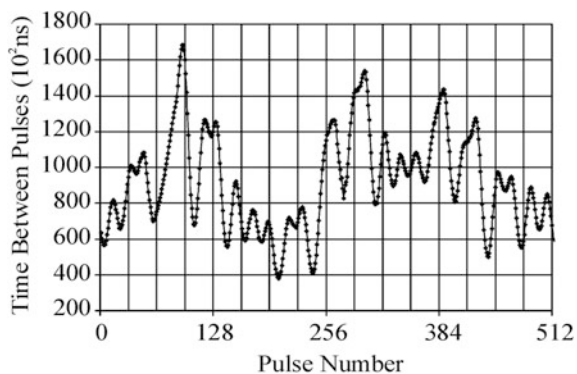


Fig. 14 Rotation speed unevenly sampled converted from a pulse scale into a timescale (pulse from 234 to 268 in Fig. 13)

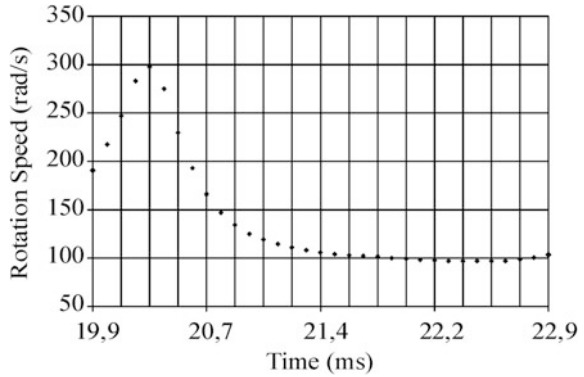


Fig. 15 Rotation speed evenly sampled converted from Fig. 14 using offline mode method (12)

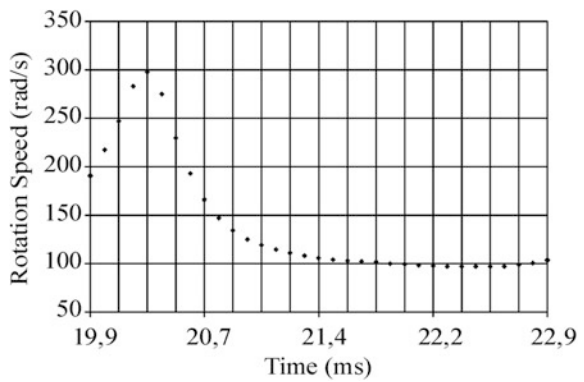
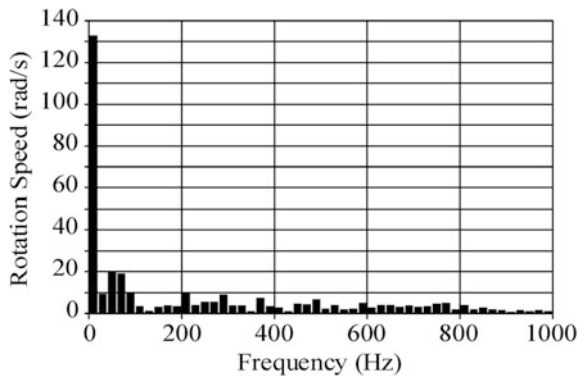


Fig. 16 Frequency spectrum rotation speed calculated for one rotation of the motor shaft after the application of a uniform sampling FPS



(Fig. 15), and then set a frequency spectrum signal speed of the motor shaft (Fig. 16) with a visible component of a constant value of 133 rad/s and a 50 Hz component of the value of 20 rad/s.

6 Conclusions

The presented review of the methods of acquisition of the pulse signal at specific sampling instants shows that the choice of method depends on the measurement mode (online or offline) and on the nature of the change of the measured value. The simplest solution is to determine the value measured on the basis of a single inter-pulse interval, more complex methods using two or more time intervals. The presented methods allow to obtain information on the measured value at the same time for the voltage and frequency of the channel, and the samples obtained from the frequency channels can be processed by methods requiring a constant sampling frequency (e.g. The FFT, Hilbert transform). An additional advantage is the possibility to determine the resolution in the same way for both types of channels, using the effective number of bits.

References

1. Yurish, S.Y.: Sensors and transducers: frequency output vs voltage output. *Sens. Transducers Mag.* **49**(11), 302–305 (2004)
2. Świsulski, D.: Digital registration of pulse signals with frequency data carrier. Wydawnictwo Politechniki Gdańskiej, Gdańsk (2006). (in Polish)
3. Murillo, C.A., Lopez, B.C., Pueyo, S.C.: *Voltage-to-Frequency Converters, CMOS Design and Implementation*. Springer, New York (2013)
4. Mejer, G. (ed.): *Smart Sensor Systems*. Wiley, Hoboken (2008)
5. Pawłowski, E., Świsulski, D.: Problems with microprocessor voltage to-frequency and frequency-to-voltage converters implementation. *Przegląd Elektrotechniczny* **91**(8), 46–49 (2015)
6. Świsulski, D.: Methods of simultaneous acquisition in systems with voltage and frequency channels. *Przegląd Elektrotechniczny* **88**(10a), 29–31 (2012)
7. Pawłowski, E.: Simulation of sensor signal with frequency output. *Przegląd Elektrotechniczny* **88**(10b), 78–81 (2012). (in Polish)
8. Boashash, B.: Estimating and interpreting the instantaneous frequency of a signal-part 1: fundamentals. *Proc. IEEE* **80**(4), 520–538 (1992)
9. Pawłowski, E.: Reconstruction of input signal of sensor with frequency output. In: *20th International Conference on Methods and Models in Automation and Robotics (MMAR), Miedzyzdroje 2015*, IEEE Explore, pp. 909–914 (2015)
10. Pawłowski, E.: Digital processing of pulse signal from light-to-frequency converter under dynamic condition. In: *Proceedings of the SPIE*, vol. 9291, pp. 929102/1–929102/6 (2014)

Time Analysis of Data Exchange in Distributed Control Systems Based on Wireless Network Model

B. Twaróg, Z. Gomółka and E. Żesławska

Abstract The paper presents studies concerning time analysis of data exchange in distributed control based on Ethernet wireless network model and relevant Modbus protocol. Presented control system operated in a real-time system that was responsible for continuous-time and periodic event processing. The events appeared at the input of system which had to generate answers (events) at the output. External event response time is closely conditioned by time which means that such systems have to ensure that response time is not exceeded, regardless of the sequence of object events. It is essential to keep the time determinism in the functioning of all real-time, regardless of whether it is a single PLC driver or their group of distributed control system.

Keywords Microprocessor controllers · Distributed wireless networks · Data transmission

1 Introduction

Distributed control systems may exist when all devices are connected to the computer network that enables communication and data transfer between them. Communication in distributed control system is used both for the exchange of essential process data (discrete and analogous) between control devices and actuators and for the exchange of data between control apparatus and measuring-control sta-

B. Twaróg (✉) · Z. Gomółka

Department of Computer Engineering, Faculty of Mathematics and Natural Sciences,
University of Rzeszow, ul. Pigonia 1, 35-959 Rzeszow, Poland
e-mail: btwarog@ur.edu.pl

Z. Gomółka

e-mail: zgomolka@ur.edu.pl

E. Żesławska

Department of Applied Information, Faculty of Applied Informatics,
University of Information Technology and Management in Rzeszow,
ul. Sucharskiego 2, 35-225 Rzeszow, Poland
e-mail: ezeslawska@wsiz.rzeszow.pl

© Springer International Publishing AG 2018

D. Mazur et al. (eds.), *Analysis and Simulation of Electrical and Computer Systems*, Lecture Notes in Electrical Engineering 452,
https://doi.org/10.1007/978-3-319-63949-9_21

333

tions. Locally placed signal conditioning and data acquisition are the basis of this architecture. In addition, it is necessary to consider the features like synchronized measurement, environmental resistance and the selection of bus and communications protocol with their speed, functionality, capacity and determinism that have to meet particular requirements. Sometimes, it is not required to use intelligent units in distributed control systems. However, this solution is beneficial when some of the logic is directly placed in the measuring nodes. It enables local data analysis and nondependent subsystems control reducing the central processor load. Pre-processing of information reduces the amount of transferred data. Instead of transferring full packages of downloaded samples, only the measurement results are sent, as they are needed for decision-making and saving processes and for further analysis. It is always possible to transfer the whole package of data if necessary. Implementation of the above features suggests the selection of real-time operating system (RTOS) due to its reliability and deterministic nature. By having the execution of commands and measurements in particular time-guaranteed, real-time systems are a suitable solution for the projects that require precise definition of the moment of operation execution and high level of reliability. Synchronization in centralized measurement systems is relatively easy to be executed, as its particular elements are located in common housing. Synchronization in distributed control system, in turn, involves significant impediments which often result from large distances between devices. This problem may be resolved, for example, by time synchronization which provides all the system elements with an access to a common reference source of information on time. It can be used for generating the event, trigger pulses and clock signals. When the distance between units is significant, it is popular to apply currently available techniques that provide information about the running time, such as GPS, IEEE 1588 or IRIG-B. Time synchronization is used most often in order to avoid problematic physical connections, replacing them with existing network infrastructure or wireless communication [1–4]. The network which links particular parts of distributed control system is an equally evaluative element as the applied measurement equipment. The solution should be selected after the analysis of basic parameters of the system, such as the distance between nodes, network capability, synchronization technique and transmission speed. The applied Modbus is a nondeterministic protocol with basic client-server architecture and TCP/IP layer. It is an ideal solution for the applications that work with a large number of devices from different suppliers. Moreover, it is well adapted to critical data transfer as it caches information and implements the process which controls the correctness of received data between the sender and the recipient, the so-called handshake.

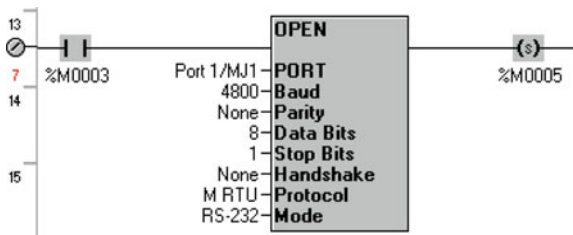
2 System Components and Configuration

The system elements used for the flagship research solution were installed and run in the laboratory of Interdisciplinary Centre for Computational Modelling at the University of Rzeszow.

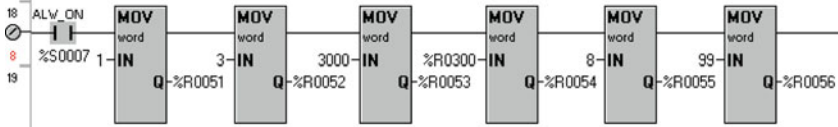
- The control units HEXT251C112 (an integrated whole driver’s function and operator touch panel, equipped with 12 discrete inputs (four inputs can be configured so that they can work as high-frequency counters), six relay outputs max. load of 2A and four analogous inputs operating in current standard (0–20, 4–20 mA) or voltage standard (0–10 V), ports RS232 and RS485, USB, Ethernet, CAN).

The central unit has 1 MB of memory for software and powerful processor that executes algorithms with the speed of 0.013 ms/kB. The 3.5" operator touch screen supports resolution of 320 × 240 pixels and 32,000 colours depth. The applied LED backlight technology ensures high contrast ratios and light display. The screen is equipped with five keys where four of them are freely programmable function keys. 130 MB of memory is dedicated to visualization application which allows creating 1024 operator panels. A driver is programmed from a professional level device C-scape which allows the device configuration, control algorithm creation, operator panel’s creation and configuration of communication and extension modules. Creating sophisticated control algorithms is possible thanks to a rich selection of ready function blocks. In order to facilitate driver’s configuration, one can use ready wizards which organize the procedure of the ports’, protocols’ and communication networks’ configuration. Additional tools that the module for driver’s programming is equipped with enable verification of the correctness of the written application in debug mode, a status display of controller’s operation or saving current records in a file. Driver’s configuration to operate in Modbus RTU master mode allows cyclic polling of devices operating as slaves and can be executed in two ways: from the level of wizard and a drop down list of available protocols in the menu *Program/Protocol Configuration*, or from the level of ladder language using available function blocks. Ladder program configuration enables the replacement of communication ports’ parameters during operation of the driver and closing of communication from the level of control program [5, 6].

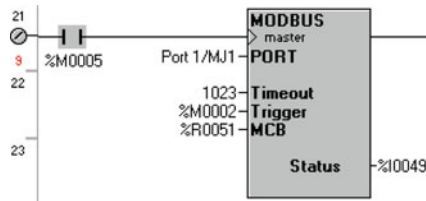
When selecting the block **Open Communication Port** from the menu *Comm operation* it is possible to create a channel for the demanded communication port. Channel’s operating parameters can be set by this element. The channel remains open until it is closed by the *Close Port* element, or it is closed when a controller disables the RUN mode.



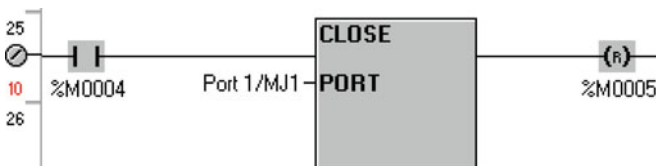
Data block for the Master device is a group of six words, configured for each RTU command. All the *Master Control Blocks* are stored in a programmable controller’s memory. A word MCB is created using *Data Move* blocks that consist of six successive records where information about saving and reading of variables is stored.



- Word 1—ID Slave address we want to establish communication
- Word 2—Performed function
- Word 3—Offset Slave
- Word 4—Length of block being read
- Word 5—Type of read variables
- Word 6—Destination address of the read variables



We close communication with the block *Close Communication Port* and close the open channel.



- The network switches Korenix JetNet 2005 (5-port 10/100 TX Compact Fast Ethernet, 3.2 Gbps Switch Fabric with excellent data exchange performance, support 1.5 kV Hi-Pot isolation protection, dual mode for power input, AC18-27V/DC18-32V, fault relay alarm).

Industrial Astraada Net switches are the elements which allow data exchange between the devices that communicate via Ethernet. Unmanageable switches are the compact solutions which have to ensure stable and efficient communication in demanding industrial environment. Additionally, to increase the efficiency of data transfer and using the full capacity of all ports (without their blocking and losing packages), the devices use the filtering—Broadcast Storm, prioritizing of packages—Quality of Service and the Flow Control function [7–9].

- Radiomodems SATELLINE-1870 (band 868–870 MHz, transmission speed 1200–9600 bps, 80 channels, channel spacing 25 kHz, output power 100 mW, coverage up to 2 km, RS232)

Radiomodems replace cable connections (depending on the topography and output power) up to the distance of tens of kilometres. It is possible to increase transmission coverage by using signal transmitters (any modem can be used as a transmitter). Popular applications of radiomodems are telemetry, as well as remote control and monitoring. For the range of frequency 868–870 MHz, wireless devices can operate without special permits and extra costs. This band is divided into the ranges depending on the output power and the operating cycle of the transmitter. For industrial applications the band excerpt from 869,400 to 869, 650 MHz is most interesting as it enables data transfer with max. power up to 500 mW. The applied omnidirectional antennas in the discussed model are characterized by the fact that the waves they create disperse in each direction with the same strength. In the case of small systems and mobile applications, it is advised that quarter-wave and half-wave antennas should be installed vertically, at the height of at least 0.5 m above the surrounding objects.

In order to change the determined options of radiomodems a terminal configuration application SaTerm.exe was used, to allow modelling of characteristic values by selecting a relevant number in the menu. The frequency of 869.6375 MHz has been set for all the radiomodems (Fig. 1).

In the case of transferring data via radiomodem there are some delays caused by a radio link and by the circuits of radiomodem itself. Such delays appear during switching from standby mode to data transfer mode and also when data is received and transmitted. In the data transfer mode, the radiomodem monitors both the radio channel and the serial port. A synchronization signal is sent at the beginning of every transmission. When the signal is detected by radiomodem, the mode switches to data receiving. When radiomodem synchronization signal is being transmitted, radiomodem caches data in memory. Transmission is closed after the cache is emptied and break in data sent by the terminal is detected. If the speed of serial port is the same or lower than the speed of radio link, it is impossible to overfill internal transmit cache (Table 1).

Delay from the time the transmission was completed to the time the reception on the serial link was finished is presented in Fig. 2 (Table 2).


```

-----
***** SATEL, SATELLINE - 1870 *****

SW Version 2.12 HW Version uCTC8L.f0 Serial no. no entry
-----
Current settings
-----
1) Radio frequency      869.6375 MHz, Band 6 (869.4000-869.6500, 500 mW)
2) Radio settings      TX power 100 mW, RSSI-threshold -113 dBm, TX delay 0 ms
3) Addressing          RX address OFF/0000/0000, TX address OFF/0000/0000
                       Protocol 1: OFF, Start char. 00, Offset 0, 1 BYTE
                       Protocol 2: OFF, Start char. 00, Offset 0, 1 BYTE
                       Hop-count 15, TX address bitmapping OFF
                       RX address masking OFF, Repeater address bypassing OFF
                       Subnet mask 1 0000, Subnet mask 2 0000
4) Serial port         9600 bit/s, 8 bit data, Even parity, 1 stop bit
                       Pause length 3
5) Handshaking         CTS Clear to send, RTS Ignored
6) Additional setup    Repeater OFF, SL OFF, Block-CRC OFF, TX priority ON,
                       Power save OFF, Frame limit OFF, SL Extended OFF
                       Full frame CRC - OFF
7) Tests               Test mode Inactive
8) Restore factory settings

```

Fig. 1 Values of configuration options for the modem SATEL1870

Table 1 Time of delays

Functions	Delay (ms)	Comment
Time of moving from standby time to activation state (switching controlled by DTR line)	700	Activation state, radiomodem is ready to receive data
Time of moving from deactivation state (economical) to activation state (switching controlled by SHDN line)	120	
Time of moving from activation time to economical mode (switching controlled by SHDN line)	1000	
Time of delay of the RS serial connector	0	
Delay between characters	Max. 6–7 characters	Speed of data transfer using a communication link is 9600 bps or less

- The Astraada Drive GD10 inverter (input voltage $1 \times 230\text{VAC} \pm 15\%$ or $3 \times 400\text{VAC} \pm 15\%$, port RS485, Modbus RTU communication, LED panel, integrated brake module up to 15 kW, integrated PID controller).

Astraada Drive GD10 is a series of frequency converters that have a separate LED control panel with a potentiometer (can be at a distance of 20 m), enabling drive system control, with the power between 0.2 and 2.2 kW for the single-phase power supply and between 0.75 and 2.2 kW for the three-phase power supply [10, 11].

Fig. 2 Delay in data transfer via radiomodem

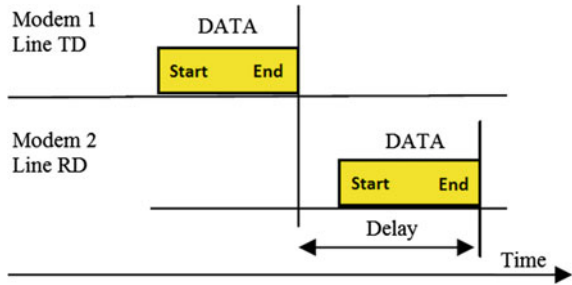


Table 2 Delay [in (MS)] of transmission for the radio channel 25 kHz numbers of the transferred bytes

Bps	1	10	100	500	1000
1200	70	70	70	70	70
4800	70	70	70	70	70
9600	70	70	86	120	160
19200	70	75	126	370	670

3 Master Communication—Modbus Protocol

Master/Slave networks, which allow direct information exchange between Master and Slave stations, have two basic types of triggered exchanges:

- *request—response* information exchange with a selected Slave subscriber station; in this case, if the exchange includes command, the response must follow,
- *publishing—no response* Master unit sends a publishing frame to all subscribers.

Realization of all configuration exchanges occurs in Master station, which is a significant feature of the network with Master/Slave access. The so-called exchange scenario, created in the station, is then realized by the coprocessor. It can be assumed that the duration of data exchange is calculated in the dependence as follows:

$$D_{E_{qr}} = D_{NM} + D_{AM} + 2(D_{PF} + D_{TF} + D_{DF} + D_{AF}) + D_{AS} \tag{1}$$

where:

- $D_{E_{qr}}$ duration of request—response exchange execution
- D_{NM} time measured from the moment of reporting the exchange during cycle phase to the moment of communication phase start
- D_{AS} duration of Slave station cycle
- D_{AM} time from the moment of decoding of information by Master station processor to the moment of receiving and using it in the Master station application
- D_{PF} duration of frame preparation

- D_{TF} duration of frame transmission
- D_{DF} duration of frame detection
- D_{AF} duration of frame analysis

Modbus/TCP protocol is based on TCP protocol stacks and Modbus/RTU protocol frame is included in TCP/IP frame. This protocol works in the client-server architecture where the Client station (Master from the serial networks) is the one that initializes communication. The implementation of Modbus/TCP protocol discussed here includes split operations of recording and reading since the moment of starting the port. Each open port command is triggered from the application level and includes information about the device the transaction will be executed with. All messages are triggered from the level of PLC driver's application. In order to connect with another device it is necessary to open the port for communication, trigger a read or record functions, and when the communication is over, use the close connection function.

$$D_{EM} = \sum_i^n D_{MOP_i} + \sum_j^m D_{MWR_j} + \sum_k^w D_{MCP_k} \quad (2)$$

where:

- D_{EM} duration of exchanges in Modbus/TCP protocol over a certain time period
- D_{MOP} duration of open port operation
- D_{MWR} duration of exchange, record or read
- D_{MCP} duration of close port operation
- n number of open port operations
- m number of record and read operations
- w number of close port operations

The final time evaluation should also include delays that result from the application of radiomodems as a communication link.

4 Time Dependencies in the Process of Data Exchange

The presented measurements were executed with the use of devices equipped exclusively with communication interface after RS-485 in Modbus/RTU protocol, and further measurements were done using devices that enable communication in the Ethernet standard with Modbus/TCP protocol via radiomodems. In the experimental verification of the duration of data exchange for distributed communication nodes, there was use of the developed software which initiated communication between the system's nodes and then realized the measurement of data exchange duration. This software uses embedded time read functions from PLC driver. The time is measured from the moment of starting central supply unit to the moment of measurement. Starting and ending the measurement of the duration of a particular

Table 3 Duration of the request–response exchange for Modbus RTU protocol

Number of read registers	Initial register	Min. time (ms)	Max. time (ms)	Number of tests
1	100	33	51	200
32	100	67	83	200
64	100	105	121	200

Table 4 Duration of the request–response exchange for Modbus/TCP protocol via SATEL radiomodem link

Number of read registers	Min. time (ms)	Max. time (ms)	Number of tests
1	225	272	300
32	227	268	300
64	230	271	300

exchange is a substantial problem. In the study, Master station individually queried Slave station—triggered by bit. The read number of registers is 1, 32, 64 (Table 3).

Basic research area for Modbus/TCP comprised two stations. Each node had a unique IP number. With regard to the measurement of data exchange duration in the system of a deterministic access to the link, only one node served as client station and sent data only through one communication channel. The read number of registers is 1, 32, 64 (Table 4).

The executed measurements for Modbus/TCP protocol show that maximum time of sending a small data package lasts longer than in Modbus/RTU network. However, increasing data package fails to cause a significant increase in transaction duration. These results may suggest that this standard suits very well when larger amounts of information are sent.

5 Conclusions

The first part of the studies involved the analysis of Modbus/RTU protocol where the time between reporting the demand of executing the exchange and its termination was measured. The exchange is defined as an order to read or record a certain amount of information given in 16-bit or 32-bit words. The read information block had a size of 1–64 words for Modbus/RTU protocol and 128 words for Modbus/TCP protocol. The obtained minimum and maximum transaction durations are the results of the measurement. For the real-time systems, the worst case seems to be the most significant. It can be assumed that the worst case of read or record for the studied area would be the situation where there would be no common data area and the communication system would have to read every register through separate transactions. The obtained results show that the selection of devices working in

particular network loops is a very important element of the system. Transaction scenario has the greatest impact on the duration of network cycle and the system reaction time depends on it. That is why it is crucial to separate groups of devices during the designing of the system. Application of the Ethernet technology in the low-level communication gave an opportunity to send larger blocks of information at a minimum time when compared to a smaller amount of data. The executed measurements show that the system which sends information blocks larger than 32 words should use Modbus/TCP protocol. This technology is faster especially in the case of monitoring the status of multiple parameters of the control device. When small data package exchange is concerned, communication is faster with the use of the RS-485 interface. Delays connected with the radiomodems had a significant influence on the times of Modbus/TCP transmissions. It was concluded that it is better to employ communication in Modbus/RTU when there is need to manage controlling devices or security devices in Modbus/RTU, especially when the size of data block does not exceed a few registers.

Acknowledgements This work has been supported by the National Science Centre, Poland, based on decision DEC-2012/05/B/ST7/01183.

References

1. Bolanowski, M., Paszkiewicz, A.: The use of statistical signatures to detect anomalies in computer network, Analysis and simulation of electrical and computer systems. Lecture Notes in Electrical Engineering, vol. 324, pp. 251–260. Springer (2015)
2. Grabowski, F., Paszkiewicz, A., Bolanowski, M.: Wireless networks environment and complex networks, analysis and simulation of electrical and computer systems. Lecture Notes in Electrical Engineering, vol. 324, pp. 261–270. Springer (2015)
3. Flaga, S.: Programowanie sterowników PLC w języku drabinkowym. BTC, Warszawa (2014)
4. Mackay, S., Wright, E., Reynders, D., Park, J.: Practical Industrial Data Networks: Design, Installation and Troubleshooting. Elsevier, Great Britain (2004)
5. Kasprzyk, J.: Programowanie sterowników przemysłowych. WNT, Warszawa (2012)
6. Sacha, K.: Systemy czasu rzeczywistego. Politechnika Warszawska, Warszawa (2006)
7. Rinaldi, J.: Modbus: The Everyman's Guide to Modbus. John S Rinaldi, Mechanicville (2015)
8. Gaj, P.: Zastosowanie protokołu TCP/IP do transmisji informacji dla potrzeb przemysłowych systemów kontrolno-nadzorczych. Rozprawa doktorska, Gliwice (2003)
9. Sidzina, M., Kwiecień, A.: Systemy czasu rzeczywistego: projektowanie i aplikacje/ praca zbiorowa pod red. Piotra Gaja, WKiŁ, Warszawa (2005)
10. Cupek, R., Gaj, P., Kwiecień, A.: Współczesne problemy systemów czasu rzeczywistego. Praca zbiorowa, WNT, Warszawa (2004)
11. Reynders, D., Wright, E.: Practical TCP/IP and Ethernet Networking for Industry. Elsevier, Great Britain (2003)

Non-Invasive Thermal Methods for the Research and Diagnosis of Electromechanical Objects

B. Twaróg, Z. Gomółka, E. Żesławska and A. Lewicki

Abstract The paper discusses the issues connected with noninvasive thermal methods for the research and diagnosis of electromechanical objects. It covers the issues of thermovision and its application, as well as the most important techniques of thermovision measurements. Moreover, the paper presents the results of comparative analysis for several examined objects, i.e. commutator motor with heating spiral, alternating current commutator motor and asynchronous three-phase motor.

Keywords Thermovision measurements · Emissivity · Objects diagnosis

1 Introduction

Thermovision is one of the methods of objects diagnosis, designed to measure radiation in the infrared band. The measurement result is a visible image of temperature distribution on the measured object's surface, called thermogram. The basic keystone of this way of imaging is the so-called infrared, that is light band invisible to the naked eye or the so-called "mid infrared", i.e. the light wave of the length from about 0.9 to 14 μm . Thanks to this phenomenon and devices used

B. Twaróg (✉) · Z. Gomółka
Department of Computer Engineering, Faculty of Mathematics and Natural Sciences, University of Rzeszow, ul. Pigońia 1, 35-959 Rzeszow, Poland
e-mail: btwarog@ur.edu.pl

Z. Gomółka
e-mail: zgomolka@ur.edu.pl

E. Żesławska · A. Lewicki
Department of Applied Information, Faculty of Applied Informatics, University of Information Technology and Management in Rzeszow, ul. Sucharskiego 2, 35-225 Rzeszow, Poland
e-mail: ezeslawska@wsiz.rzeszow.pl

A. Lewicki
e-mail: alewicki@wsiz.rzeszow.pl

to detect and display, it is possible to observe thermal radiation emitted by physical bodies on their surface, that is the temperature they emit. The results obtained in this way may significantly help to diagnose electric circuits, buildings or mechanical and electromechanical devices and detecting potential risks may prove to be much simpler, faster and more effective.

Thermovision devices are designed to capture and detect electromagnetic radiation that occurs in nature in a few forms, is divided depending on the length of wave X into:

- cosmic radiation and gamma radiation ($\lambda < 10^{-5} \mu\text{m}$),
- X radiation ($10^{-5} < \lambda < 10^{-2} \mu\text{m}$),
- ultraviolet radiation ($10^{-2} < \lambda < 0.35 \mu\text{m}$),
- visible radiation ($0.3 < \lambda < 0,75 \mu\text{m}$),
- infrared radiation ($0.75 < \lambda < 103 \mu\text{m}$),
- micro waves and radio waves ($\lambda > 103 \mu\text{m}$).

It may happen that the infrared radiation given above and the range of wavelength are sometimes divided into smaller bands that are as follows:

- near infrared radiation ($0.78 \div 3 \mu\text{m}$),
- mid infrared radiation ($3 \div 6 \mu\text{m}$),
- far infrared radiation ($6 \div 15 \mu\text{m}$),
- very far infrared radiation (above $15 \mu\text{m}$) [1–4].

2 Thermovision Measurement Techniques

Thermovision camera measures and displays infrared radiation that comes from an object. Radiation value is the feature of the temperature of object's surface that enables the camera to do measurements and display temperatures. The energy carried by the camera is not only dependant on the object's temperature, but it is also the emissivity's feature [5–8]. Radiation also comes from the ambience, and it is reflected by the object. Object's radiation and reflected radiation are also affected by atmospheric absorption. In order to carry out precise measurement of temperature, it is necessary to determine the influence of various sources of radiation. It is automatically performed by the camera after entering the following parameters of the object:

- object emissivity coefficient,
- ambient temperature,
- atmosphere temperature,
- distance between object and camera,
- relative humidity.

Emissivity is the most important and key parameter input in the thermovision camera during measurements. It determines a particular body's ability to emit thermal radiation and depending on the kind of material the object was made, it is given in the form of a number from about 0.1 to 0.95. Emissivity coefficient may vary depending on the object's type and the temperatures it achieves. In order to measure the object's temperature, it is necessary to know its emissivity and this parameter is a key factor for correct evaluation of the obtained result. If the coefficient is unknown and temperature of an object is different than ambient temperature, then determining the coefficient is necessary [9–13]. This process can be performed in various ways but is not an easy one.

In order to measure the emissivity of particular material, one can use one of the commonly applied methods. Limitation connected with them concerns reflection of the examined surface and its emissivity. Bodies usually radiate to the whole half-space and the reflection is diffusive, thanks to which the radiation is distributed in all directions. However, when it comes to emissivity and its multiple features, some measurements involve only its particular type (e.g. directional emissivity, normal, total, spectral, to the half-space). The methods of determining the emissivity are as follows:

- contact method,
- emissivity or reference body method,
- reflection method,
- calorimetric method.

The contact method consists of selecting the emissivity values in the camera for an object being measured of unknown emissivity so that the temperature would be the same as the results of its contact measurement for the material of known emissivity. The temperature of the object with known emissivity is defined as the reference temperature.

In the calorimetric method, the temperature of the object being measured and of exitance must be known $M(\text{W}/\text{m}^2)$. There are two ways of determining the material's emissivity. First is based on using the camera to measure spectral exitance in order to select the material's emissivity so that the result is the same as the body temperature measured with a different method. The second way of determining the material's emissivity is based on determining the spectral exitance emitted by the object being measured and background using the following formula:

$$M(T) = \varepsilon_0 M_c(T_0) + (1 - \varepsilon_0) M_a(T_a) \quad (1)$$

where ε —stands emissivity of the object being measured, $M_c(T_0)$, $M_a(T_a)$ —black body exitance value with the temperature of the object being measured T_0 and background with the temperature T_a .

According to Boltzmann laws, the exitance value can be determined when the temperature values of the object being measured and ambience are known as follows:

$$M_c(T_0) = \sigma T_0^4 \tag{2}$$

$$M_{ot}(T_a) = \sigma T_a^4 \tag{3}$$

Based on the above, the material’s emissivity can be determined by the following:

$$\varepsilon_0 = \frac{T^4 - T_a^4}{T_0^4 - T_a^4} \tag{4}$$

where T is the radiation temperature indicated by a thermovision camera.

The reflection method is based on a double lighting of an object by two thermal sources with different temperature, as shown in Fig. 1.

The camera receives radiation from both radiation sources that is reflected from the object $(1 - \varepsilon_0)M_{Z1}$ or $(1 - \varepsilon_0)M_{Z2}$ and reflector M_{Z1} or M_{Z2} , as well as own radiation of the object being measured $\varepsilon_0 M_c(T_0)$ that can be determined by the dependencies given below:

$$M_1 = \varepsilon_0 M_c(T_0) + (1 - \varepsilon_0)M_{Z1} + (1 - \varepsilon_0)M_a \tag{5}$$

$$M_2 = \varepsilon_0 M_c(T_0) + (1 - \varepsilon_0)M_{Z2} + (1 - \varepsilon_0)M_a \tag{6}$$

Based on these formulas, the material’s emissivity can be determined as follows:

$$\varepsilon_0 = 1 - \frac{M_1 - M_2}{M_{Z1} - M_{Z2}} \tag{7}$$

During determining the emissivity by the method with the reference body, we have a body with known emissivity ε_r . During the measurement, both the object

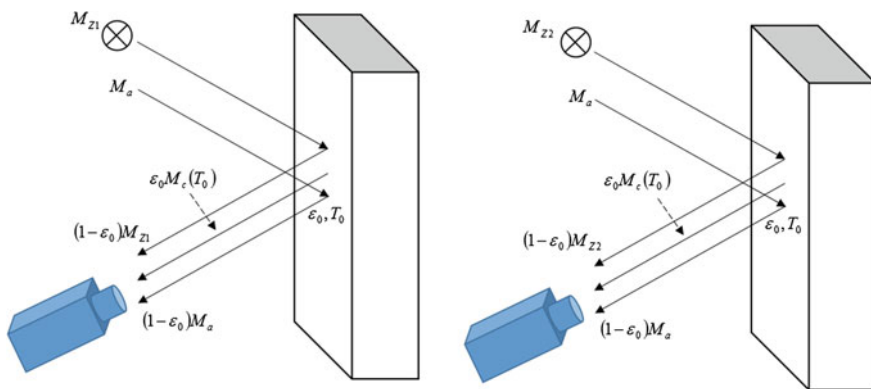
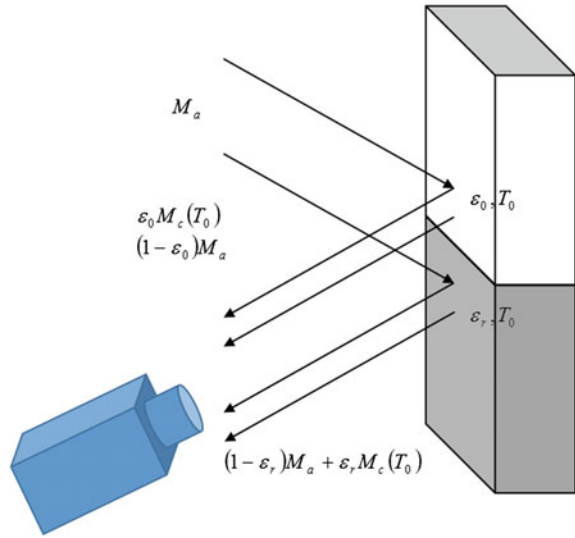


Fig. 1 Emissivity measurement by the reflection method

Fig. 2 Emissivity measurement by the method with reference body



being measured and the reference object have the same temperature T_0 (Fig. 2). Moreover, both objects must be close to each other and are measured at the same time so that the background radiation influences them equally.

The radiation exitance may be described as follows:

$$M_1 = \epsilon_0 M_c(T_0) + (1 - \epsilon_0)M_a \tag{8}$$

$$M_2 = \epsilon_r M_c(T_0) + (1 - \epsilon_r)M_a \tag{9}$$

Based on (8) and (9) the emissivity may be determined in the form as follows:

$$\epsilon_0 = \epsilon_r - \frac{M_1 - M_a}{M_2 - M_a} \tag{10}$$

The following radiation energy of background M_a can be determined by replacing the materials during measurement with a reflector of reflection coefficient for infrared waves $\rho \approx 1$.

The ambient temperature—this parameter is necessary to customise thermovision camera settings during experimental works. It significantly influences the results, especially when the object’s emissivity is low and its temperature similar to the ambient temperature. Its value may be identified with the value of room temperature in which the measurements are conducted or with the temperature outside when objects being measured are outside the building. This parameter, similarly to the object’s emissivity value, is entered in the camera settings before the operation, and its proper estimation will be reflected in results of the object’s temperature being measured.

The relative humidity—the transmission quality can be customised with the thermovision camera and the entered ambience relative humidity parameter. In order to do it, the correct value of relative humidity needs to be set. For short distance and normal humidity, it can be set to the default value of relative humidity of 50%.

The distance—it is the distance between an object and the front of camera lens. This parameter is used for redeeming the influence of the following phenomena:

- Absorption of an object's radiation by the atmosphere between object and camera,
- Detecting radiation of atmosphere by camera [9, 14–19].

3 Comparative Thermovision Analysis of the Objects Being Measured

Within the experimental work, the studies on the selected electromechanical objects were carried out. Their results provided information about the temperatures achieved by these devices during operation. In the first part of experiments, the thermal observation involved a commutator motor with heating spiral (Fig. 3a, b) and the camera FLIR T620. The temperature distribution during the operation of the device, both in the heating unit and on the motor showed areas where these elements are faced with greatest thermal loads.

The emissivity of 0.95 is a default value recommended by a camera producer when a user is unsure about its range. The increase of temperature in the heating unit, as opposed to the motor, was dynamic (see Fig. 4b), and a heater's temperature being out of temperature scale was read using the colour temperature scale which turned out to be a basic element in their verification.

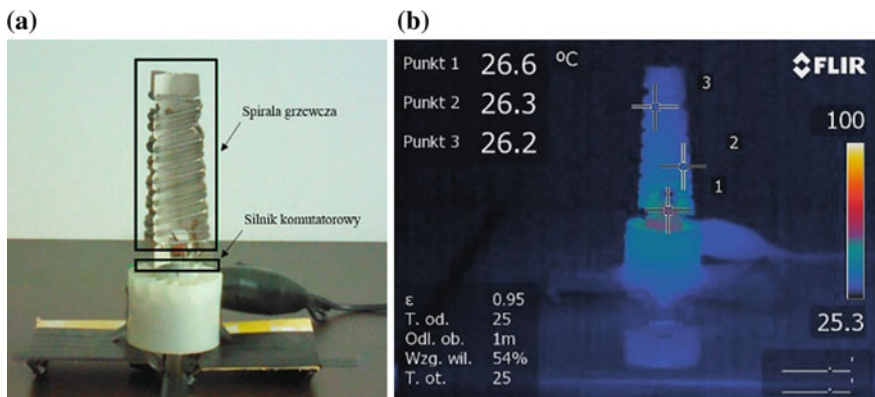


Fig. 3 Commutator motor (a) and thermogram with temperature distribution before the start-up (b)

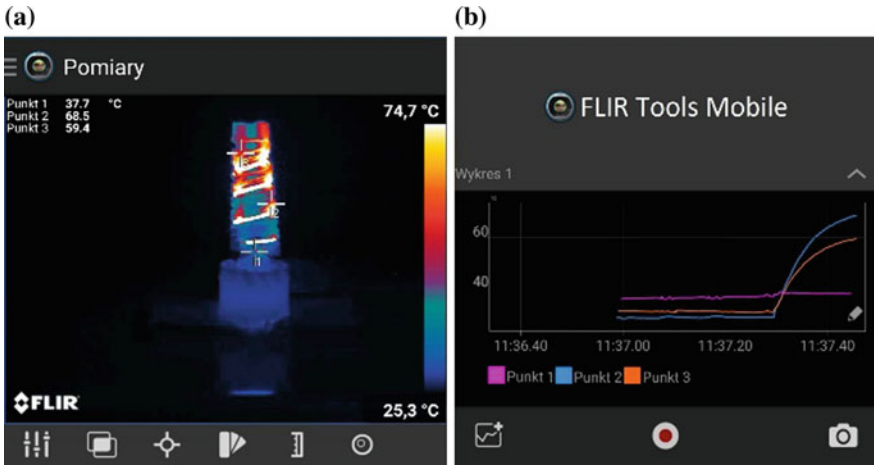


Fig. 4 Thermogram (a) and temperature distribution of the object being measured in time (b)

The differences between the initial and the last measurement were significant in a very short period of time and were caused by the lack of spiral’s cover which in the original device had a huge influence on the decrease in the pace of thermal changes. The cooling turbine sucked and blew out the air along the heating unit while after the modifications this air is dispersed in various directions causing heating.

Table 1 presents the results for the three points selected on the object being measured at various times of device’s operation. In the first point determined on the commutator motor, after 60 s the temperature changed from a nominal value of 26.6–41.7 °C showing temperature increase being in all the norms characteristic of this type of devices. The measurement points selected on the heating spiral showed, in turn, a rapid and immediate growth in the temperature of this unit. In point 2 the initial temperature of 26.3 °C rose to 160.2+ °C while in point 3 it was 80.2 °C when compared to the initial value of 26.2 °C. The verification by the colour temperature scale mentioned above concerned point 2 where the spiral achieved the colour corresponding to the temperature between 600 and 800 °C.

Alternating current commutator motor was another object measured, and its thermal diagnosis was directed to the impeller—to be more precise—on its end and on the stator with its winding (Fig. 5a–c). The selected units provided valuable information during the experiment, in the form of measurements that are important guidelines useful in formulating the conclusions related to the thermal diagnosis of

Table 1 Comparison of the results over time

	Initial temp. (°C)	Temp. after 20 s (°C)	Temp. after 60 s (°C)
Point 1	26.6	37.7	41.7
Point 2	26.3	68.5	~ 600–800
Point 3	26.2	59.4	80.2

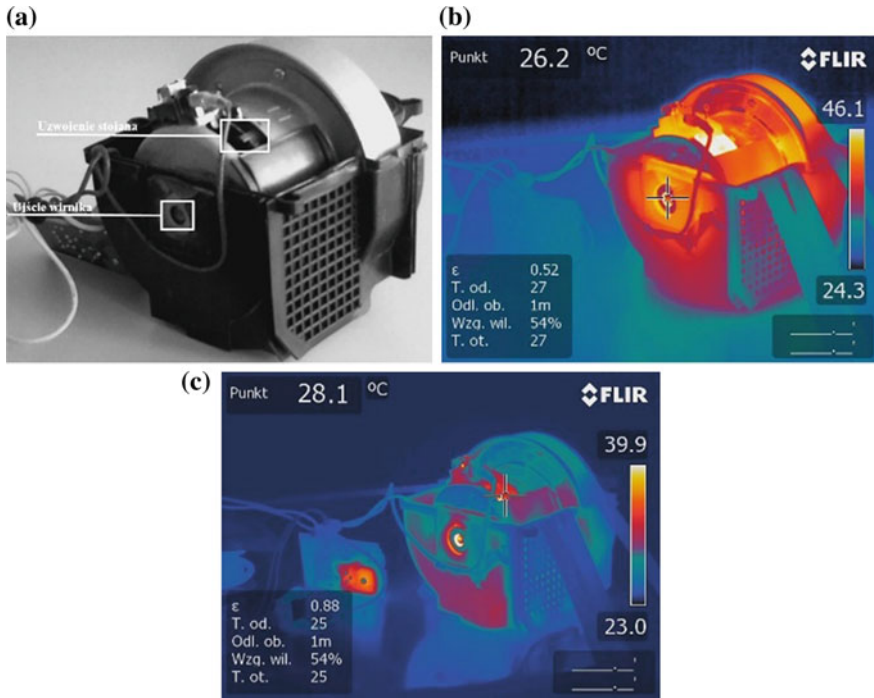


Fig. 5 Alternating current motor (a) and thermograms with temperature distribution before starting the motor (b, c)

more complex electromechanical machines. Accurate determination of the emissivity of each unit was a key element, without which the conducted measurements could result in errors. These values were, respectively, $\epsilon = 0.52$ for the impeller and $\epsilon = 0.88$ for the stator's windings.

The initial temperature of both modules fluctuated similarly, for the impeller's influx it was 26.2 °C, while for the stator's winding 28.1 °C. Their growth in both cases was similar in the initial phase of experiment and occurred at a uniform pace. The device operation time and dynamism of device's heating process until achieving highest reached temperatures were significantly different depending on the unit being measured. After first 2 min, the impeller's temperature was 60.7 °C while the temperature of the winding achieved the value of 41.4 °C. Further 5-min operation of the machine resulted in an increase in temperatures up to 85 °C (Fig. 6a) and 54.4 °C. It was the last measurement when it comes to the motor shaft. The final reading of the point determined on the winding occurred in the 12th minute from the motor starting and amounted to 69.6 °C (Fig. 6b). Table 2 presents the obtained measurements in time.

The third object which underwent diagnosis was a three-phase motor with its stator was submitted for modifications (part of stator was removed) to have more convenient conditions for observations of the machine's inside. Stator's winding,

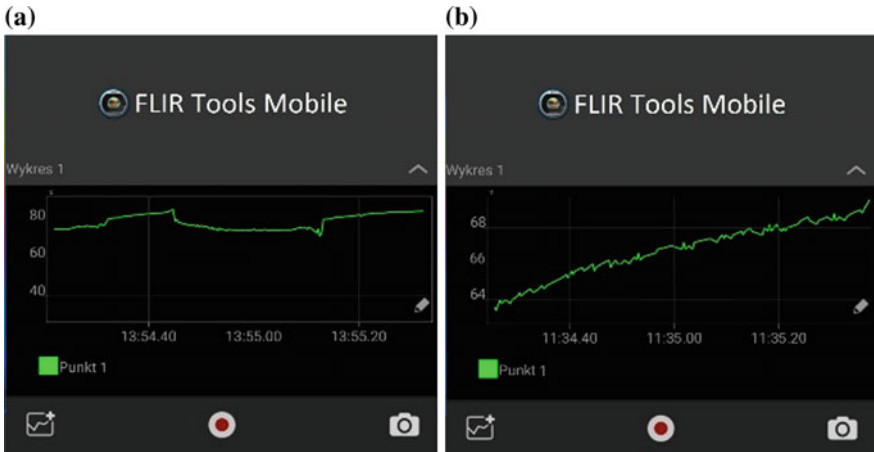


Fig. 6 The graph of time at temperature since the time on the impeller's influx (a) and stator's winding (b)

Table 2 Comparison of the obtained measurements over time

Object	Initial temp. (°C)	Temp. (°C) after 2 min	Temp. (°C) after 5 min	Temp. (°C) after 12 min
Impeller's influx	26.2	60.7	85.0	–
Stator's winding	28.1	41.4	54.4	69.6

shaft and impeller's core were the machine's units that underwent study in terms of thermal emission (Fig. 7). Initial temperatures at the moment the measurements started with the emissivity values were presented in Table 3.

Dynamism of the heating process was varied according to individual parts of the engine. This was related to the functionality of each of them and the type of material they are made of. The time from the beginning to the end of all the measurements amounted to 8 min, and the final measurements and their

Fig. 7 Modified asynchronous three-phase motor (1 Stator's winding, 2 Shaft, 3 Impeller's core)

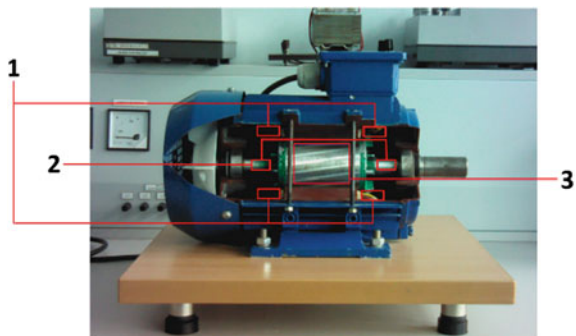


Table 3 Comparison of the obtained measurements over time

Object		Initial temp. (°C)	Temp. (°C) after 1–2 min	Temp. (°C) after 8 min
Stator’s winding $\varepsilon = 0.88$	Point 1	25.3	38.1	53.6
	Point 2	25.3	37.6	53.9
	Point 3	25.3	145.8	152.4
	Point 4	25.4	131.9	144.6
Shaft $\varepsilon = 0.20$	Point 1	26.0	42.1	80.5
	Point 2	26.2	41.7	75.1
Impeller’s core $\varepsilon = 0.31$	Rectangle average	29.1	51.7	62.9

contrastivity with relation to their initial values were visible. Respectively, the pictures 8, 9, 10 present thermograms for the winding of stator, shaft and impeller’s core and, respectively, the courses of temperature in time for particular points (Figs. 8, 9 and 10).

The time of motor’s operation of merely 8 min since its starting was conditioned by its high heating dynamics, instability and shaft’s vibrations escalating in direct proportion to the temperature increase of each unit being submitted for diagnosis. Comparison of the selected measurements of the asynchronous three-phase motor was presented in Table 3.

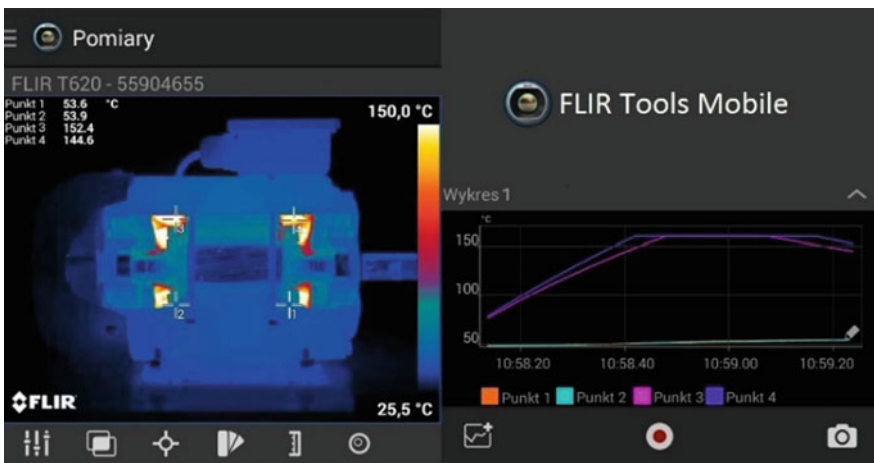


Fig. 8 Thermogram for the stator’s winding and the temperature changes for the indicated points

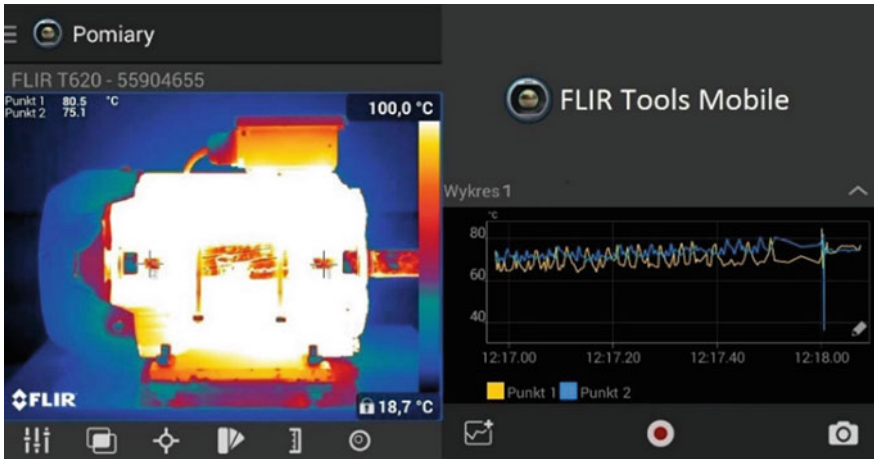


Fig. 9 Thermogram for the shaft and the changes of temperature for the indicated objects

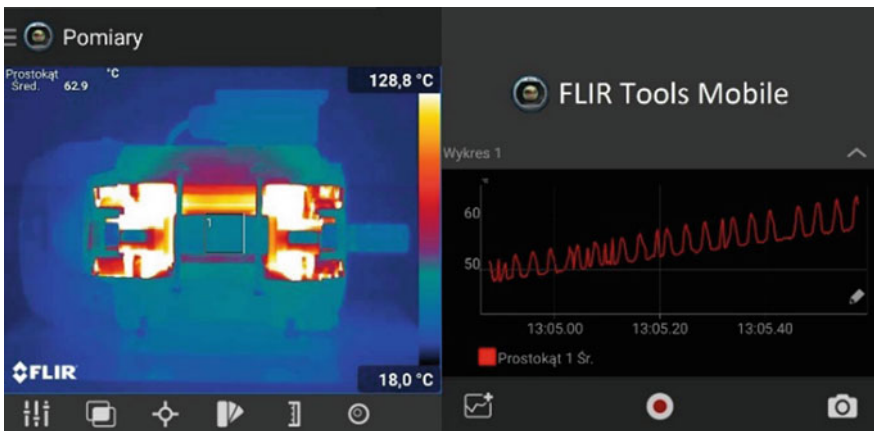


Fig. 10 Thermogram for the impeller's core and the changes of temperature for the indicated points

4 Conclusions

The experiment conducted on the selected electromechanical objects in the form of a low direct current motor, alternating current commutator motor and modified asynchronous three-phase motor adapted to observe thermal changes their particular units were submitted for. Using the gained knowledge for the third type of devices enables more precise thermal analysis and determining the critical areas in order to decrease to a minimum risk of failure, extend their life, improve their design that includes the cooling system or changes of material used for making particular units.

Thermovision studies are very precise and have a wide range of use. Thermovision cameras were proved in the analysis of the achieved results to be useful in the area of studies and diagnosis of electromechanical objects.

Acknowledgements This work has been supported by the National Science Centre, Poland, based on decision DEC-2012/05/B/ST7/01183.

References

1. Rudowski, G.: Termowizja i jej zastosowanie. Wydawnictwo WNT, Warszawa (2004)
2. FLUKE: Wprowadzenie do termografii. American Technical Publishers, Orland Parkway (2009)
3. Fokaides, P., Kalogirou, S.: Application of infrared thermography for the determination of the overall heat transfer coefficient (U-Value) in building envelopes. *Appl. Energy* **88**(12), 4358–4365 (2011)
4. Gomółka, Z., Żesławska, E., Twaróg, B., Bolanowski, M.: Restitution of 3D scenery with coherent and structured light scanner technologies. *MAM* **09**, 430–433 (2015)
5. Herve, P., Cedelle, J., Negreanu, I.: Infrared technique for simultaneous determination of temperature and emissivity. *Infrared Phys. Technol.* **55**(1), 1–10 (2012)
6. Jura, J., Adamus, J.: Politechnika Częstochowska. Zastosowanie termografii do oceny izolacyjności cieplnej budynku. *Budownictwo o zoptymalizowanym potencjale energetycznym* **2**(12), 31–39 (2013)
7. Molin, A., Rohdin, P., Moshfegh, B.: Investigation of energy performance of newly built lowenergy buildings in Sweden. *Energy Build* **43**(10), 2822–2831 (2011)
8. Mukosiej, J.: Problem dokładności badań cieplnych maszyn elektrycznych. *Zeszyty problemowe – Maszyny Elektryczne* **100**(1), 67 (2013)
9. Kaczmarek, J.: Using a thermovision method for measuring temperatures of a workpiece during abrasive cut-off operation. *Adv. Manuf. Sci. Technol.* **35**(4), 85 (2011)
10. Ronkowski, M.: (red.), *Maszyny elektryczne wokół nas*, Wyd. Politechniki Gdańska Gdańsk, p. 220 (2011)
11. Michalski, L., Kuźmiński, K., Sadowski, J.: Regulacja temperatury Urządzenia elektrotermicznych. WNT, Warszawa (1991)
12. Teodorescu, R., Liserre, M., Rodriguez, P.: *Grid Converters for Photovoltaic and Wind Power Systems*. Wiley, London (2011)
13. Wittchen, W., Niesler, M., Borecki, M., Zdonek, B.: Application of thermovision method in analysing metallurgical processes. In: *9th International Conference on Quantitative InfraRed Thermography*, Krakow (2008)
14. Bareła, J., Firmanty, K., Kastek, M., Polakowski, H.: Wzorce promieniowania podczerwonego używane do kalibracji urządzeń termowizyjnych. *Biuletyn, WAT LX I*(2), 81–91 (2012)
15. Minkina, W.: *Pomiary termowizyjne - przyrządy i metody*, p. 243. Wydawnictwo Politechniki Częstochowskiej, Częstochowskiej (2004)
16. Mynarek, P.: *Analiza systemów cieplnych w silnikach małej mocy*, Politechnika Opolska, Wydział Elektrotechniki, Automatyki i Informatyki, Opole (2014)
17. Nowak, H.: *Zastosowanie badań termowizyjnych w budownictwie*. Oficyna Wydawnictwo Politechniki Wrocławskiej, Wrocław (2012)
18. Więcek, B., De Mey, G.: *Termowizja w podczerwieni. Podstawy i zastosowania*. Wydawnictwo PAK, Warszawa (2011)
19. Pękala, Robert, Kwater, Tadeusz, Kwiatkowski, Bogdan: Calculations of conjugated fields in the ferromagnetic medium. *Anal. Simul. Electr. Comput. Syst.* **324**, 1100–1876 (2015)

Mutual Forces Acting on Chains of Particles

Eugeniusz Kurgan and Piotr Gas

Abstract This paper describes a method to determine mutual forces acting between dielectric particles, which form chains. The Maxwell stress tensor method together with finite element method are used. It is shown that particles placed in inhomogeneous field, because of dielectrophoretic forces acting between them, have a tendency to collect one by one giving in effect even long particles chains. In this article, Maxwell stress tensors are integrated over particle surfaces to give total mutual forces interacting between molecules.

Keywords Dielectrophoresis · Maxwell stress tensor · Forces · Particle chains · Finite element method

1 Introduction

Dielectrophoresis (DEP) phenomenon is increasingly used in a variety of cheap fabricated devices, where micro-scale fluid flow is observed. Such small apparatus may easily interact with larger electronic devices, which results in a great reduction for complex and expensive methods of macro-fluid manipulations by mechanical valves and complex pumps. DEP techniques are also very useful in purifying, enriching and characterizing a large amount of various biological, clinical, environmental and industrial ingredients. Recently, significant development of these and many accompanied technologies have been made [1]. It should be emphasized that dielectrophoretic phenomenon enables voltage trapping, concentrating, translating as well as fractionating of minerals, biological and chemical molecules of suspending liquid medium. Dielectrophoretic forces make possible to investigate

E. Kurgan · P. Gas (✉)

Department of Electrical and Power Engineering, AGH University of Science and Technology, al. Mickiewicza 30, 30-059 Krakow, Poland
e-mail: piotr.gas@agh.edu.pl

E. Kurgan

e-mail: kurgan@agh.edu.pl

© Springer International Publishing AG 2018

D. Mazur et al. (eds.), *Analysis and Simulation of Electrical and Computer Systems*, Lecture Notes in Electrical Engineering 452,
https://doi.org/10.1007/978-3-319-63949-9_23

different fluid properties including dielectric and conducting properties of individual particles since they depend not only on frequency of the exciting source, but also on both its structure and composition. Many different effects appear when dielectric particles such as, for example, biological cells are subjected to an electric field generated in dielectric fluid. In practice, dielectrophoresis occurs in micropatterned electrodes immersed in dielectric fluid. When the electrodes are subjected to applied external voltages, they generate nonuniform electric field, which next produces dielectrophoretic forces [2]. Next, such forces induce effective dipole moment and force resulting in specific molecule movement. What is important, the magnitude of dielectrophoretic force depends mainly on the gradient of the square of the magnitude of electric field strength produced around the interdigitated electrodes.

The dielectrophoretic force calculations are essential during the modelling of complex electrical and mechanical systems. In the case of stiff materials, only the total effective force is necessary, while for non-rigid system with deformable structure the local force distribution is required. This is especially important during separation processes of various biological particles, such as bacteria, cells, proteins and so on. Usually, to calculate DEP force one uses equivalent dipole method, which is computationally very effective because there is no need to consider particles together with surrounding medium [3]. It is enough to compute electric field strength distribution in points of particle's positions and by adequate equations compute force acting on the particle. In the case of one or two particles, this method can be without difficulties applied; but in multi-particles structures, it gives force values with unacceptable error levels. This is caused by mutual interaction of particles placed between two distant particles. Moreover, this method does not permits force density calculations on particle boundary. This is especially important when particles are made from little coherent material, which by high field gradient can undergo total destruction. Another important approach for evaluating DEP forces is based on so-called Maxwell stress tensor (MST) method [4]. It should be stressed that such tensor is calculated by integration over whole molecule surface. Moreover, this method is the most general approach to calculate DEP forces acting on particles.

The methodology presented in this paper is similar to that described by other authors [5]. In this work, two different techniques are used to calculate the same force on both sides of surrounding particle surface. Theoretically, both forces should be equal but often some unexpected differences can occur. At the beginning, in order to estimate the electric potential distribution within the fluid and particles, the Laplace equation is solved. In the next step, the electric field strength is determined. All calculations are based on analysis with the finite element method [6]. MST method allows fast computing of the electromagnetic field around electrodes with complex geometries as well as the DEP forces acting on particles immersed in fluid with inhomogeneous electric properties. However, many papers have reported that both force and torque values obtained from FEM analysis could be not precise in the case of particularly complex models, including DEP traps with multiple molecules [7].

In the Maxwell’s stress method, the total force, which acts on particle, is computed by surrounding an object by closed surface and integrating Maxwell stress tensor over the entire surface. In application of the ordinary Maxwell stress method, the integration surface should be closed, and located completely in the linear part of the material. Inhomogeneous domains should be treated with special care. In this paper [8], the authors discuss particle chain formation using a reaction-diffusion approach. Jones [5] extensively has been considered different interaction collections of various particles. In article [9], the authors describe known DC dielectrophoretic particle interactions as well as their mutual motions through equivalent dipole method. In papers [10–12], the authors propose a new method based on iterative moment method for computing dielectrophoretic forces, which does not need to solve electromagnetic field by the finite element method. In the current paper, the authors have successfully shown in which way the particles immersed in fluid and placed in the strongly inhomogeneous field can collect to form chains. Some important application of particle manipulation can be found in similar numerous publications [13–20].

2 Main Equations

Let us consider longitudinal cross section of the flow channel with two electrodes and two particles, as in the following Fig. 1.

There are two electrodes: one connecting to ground potential and another to potential U_z , which is equal usually several volts. Because distance between electrodes is very small, thus the gradient of the electric field can attain very big value. This results, as consequence, with very high mutual forces acting between particles. In order to derive surface force density, we assume that unit vector is normal to given surface. Maxwell stress tensor T_{ij} for electric field \mathbf{E} has the following formula [3]:

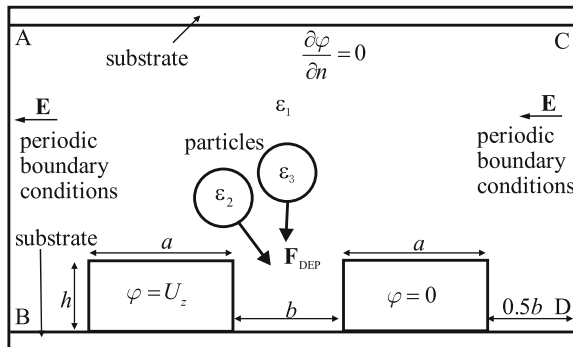


Fig. 1 Schematic representation of the electrode arrangement with one pair of electrodes and moving biological particle (periodic boundary conditions mean that the potentials at the inlet and outlet of the subsequent periodic computational cells are the same, e.g. $\varphi_{A-B} = \varphi_{C-D}$)

$$T_{ij} = \varepsilon \left(E_i E_j - \frac{1}{2} E^2 \delta_{ij} \right) \quad (1)$$

The surface force density \mathbf{f} can be computed by

$$\mathbf{f} = \vec{\mathbf{T}} \cdot \mathbf{n} = \sum_{j=1}^3 \sum_{k=1}^3 \sum_{r=1}^3 T_{jk} n_r \mathbf{a}_j (\mathbf{a}_k \cdot \mathbf{a}_r) \quad (2)$$

In this formula, the indexes $i, j, k = 1, 2, 3$ should be replaced, conveniently, by coordinates x, y and z . Only these terms under summation signs remain nonzero, where scalar product $(\mathbf{a}_k \cdot \mathbf{a}_r)$ is nonzero. This will occur for $r = k$, thus, we have [3]:

$$\mathbf{f} = \varepsilon \sum_{j=1}^3 \sum_{k=1}^3 E_j E_k n_k \mathbf{a}_j - \frac{1}{2} \varepsilon \sum_{j=1}^3 \sum_{k=1}^3 E^2 \delta_{jk} n_k \mathbf{a}_j \quad (3)$$

In the last expression only these terms are nonzero, when $k = j$, but in our case:

$$\mathbf{E} = \sum_{j=1}^3 E_j \mathbf{a}_j \quad \text{and} \quad \mathbf{n} = \sum_{j=1}^3 n_j \mathbf{a}_j \quad (4)$$

gives

$$\mathbf{f} = \varepsilon \left(\sum_{k=1}^3 E_k n_k \right) \mathbf{E} - \frac{1}{2} \varepsilon E^2 \mathbf{n} \quad (5)$$

The terms in parenthesis are identical to scalar product \mathbf{E} and \mathbf{n} , therefore:

$$\mathbf{f} = \varepsilon (\mathbf{E} \cdot \mathbf{n}) \mathbf{E} - \frac{1}{2} \varepsilon E^2 \mathbf{n} \quad (6)$$

This is the fundamental equation, which enables us to compute force densities on particle surfaces. Because dielectric in fluid and particles undergo mutual polarization, force densities will occur on both sides of the boundaries. When we assume that liquid has number 1 and particle has number 2, then formula (6) on both sides of the boundary give us suitable force densities values [7]:

$$\mathbf{f}_1 = \varepsilon_1 (\mathbf{E}_1 \cdot \mathbf{n}_1) \mathbf{E}_1 - \frac{1}{2} \varepsilon_1 E_1^2 \mathbf{n}_1 \quad (7)$$

$$\mathbf{f}_2 = \varepsilon_2 (\mathbf{E}_2 \cdot \mathbf{n}_2) \mathbf{E}_2 - \frac{1}{2} \varepsilon_2 E_2^2 \mathbf{n}_2 \quad (8)$$

External field induces surface charge density which can be integrated to obtain total force acting on the particle. One can assume that we have no free electric charges in particle. The resulting force density is equal to the sum of both components:

$$\mathbf{f} = \mathbf{f}_1 + \mathbf{f}_2 \quad (9)$$

Let us now relate force densities with normal and tangential components of electric field strength acting on boundaries of the particle. On both sides of the suspension-particle boundary, unit vectors have opposite sign. In this way: $\mathbf{n}_1 = \mathbf{n}$ and $\mathbf{n}_2 = -\mathbf{n}$, therefore in end effect we get:

$$\mathbf{f}^{(2)} = \varepsilon_1(\mathbf{E}_1 \cdot \mathbf{n})\mathbf{E}_1 - \varepsilon_2(\mathbf{E}_2 \cdot \mathbf{n})\mathbf{E}_2 - \frac{1}{2}(\varepsilon_1 E_1^2 - \varepsilon_2 E_2^2)\mathbf{n} \quad (10)$$

Now both vectors \mathbf{E}_1 and \mathbf{E}_2 can be split into two components: one perpendicular and another tangential to the surface:

$$\mathbf{E}_1 = E_{1n}\mathbf{n} + E_{1t}\mathbf{t} \quad (11)$$

$$\mathbf{E}_2 = E_{2n}\mathbf{n} + E_{2t}\mathbf{t} \quad (12)$$

and after some further manipulation we obtain:

$$\begin{aligned} \mathbf{f}^{(2)} = & \left(\frac{1}{2}\varepsilon_1 E_{1n}^2 - \frac{1}{2}\varepsilon_2 E_{2n}^2 - \frac{1}{2}\varepsilon_1 E_{1t}^2 + \frac{1}{2}\varepsilon_2 E_{2t}^2 \right) \mathbf{n} \\ & + (\varepsilon_1 E_{1n} E_{1t} - \varepsilon_2 E_{2n} E_{2t}) \mathbf{t} \end{aligned} \quad (13)$$

Boundary conditions on both sides of the particle surface give:

$$E_{1t} = E_{2t} \quad (14)$$

$$\varepsilon_1 E_{1n} = \varepsilon_2 E_{2n} \quad (15)$$

or finally

$$\mathbf{f}^{(2)} = \frac{1}{2}(\varepsilon_2 - \varepsilon_1) \left(\frac{\varepsilon_2}{\varepsilon_1} E_{2n}^2 + E_{2t}^2 \right) \mathbf{n} \quad (16)$$

This is the force density acting between fluid and particle. After calculation of the electric field \mathbf{E} inside of the particle, the total force acting on the whole particle can be computed by following formula:

$$\mathbf{F}^{(2)} = \frac{1}{2}(\varepsilon_2 - \varepsilon_1) \oint_S \left(\frac{\varepsilon_2}{\varepsilon_1} E_{2n}^2 + E_{2t}^2 \right) \mathbf{n} ds \quad (17)$$

In quite analogous, we can derive similar relation using fields from fluid side. The boundary condition gives:

$$E_{2n} = \frac{\varepsilon_1}{\varepsilon_2} E_{1n} \quad (18)$$

and after introduction (18) into (16) we have [14]:

$$\mathbf{f}^{(1)} = \frac{1}{2}(\varepsilon_1 - \varepsilon_2) \left(\frac{\varepsilon_1}{\varepsilon_2} E_{1n}^2 + E_{1t}^2 \right) \mathbf{n} \quad (19)$$

When we use electric field in suspension to calculate force acting on particle and integrate it over whole boundary, we get

$$\mathbf{F}^{(1)} = \frac{1}{2}(\varepsilon_1 - \varepsilon_2) \oint_S \left(\frac{\varepsilon_1}{\varepsilon_2} E_{1n}^2 + E_{1t}^2 \right) \mathbf{n} ds \quad (20)$$

In accordance with the Newton's third law, both forces $\mathbf{F}^{(1)}$ and $\mathbf{F}^{(2)}$ acting on particle should have the same value. It should be emphasized, that this form of equations can be used both in two and three-dimensional problems.

3 Illustrative Example

One section of the separating structure in two dimensions can be modelled by one electrode with voltage $U_z = 4$ V and one the electrode with zero potential. The presence of another parts of the interdigitated electrode array outside the analyzed region can be taken into account using periodic boundary conditions on both sides of the given section. The periodic boundary condition relates potential and electric field values on these parts of the boundary, which are neighbouring with left and right sections with the same field distribution. In our, case it was assumed that

$$\varphi(a, y) = \varphi(a + d_{A-C}, y) \text{ and } \frac{\partial \varphi(a, y)}{\partial n} = \frac{\partial \varphi(a + d_{A-C}, y)}{\partial n} \quad (21)$$

In Fig. 1, we can see cross section, which consists of the isolating base and channel covering, the interdigitated electrodes and a suspension. The finite element has been used to calculate field in geometry given by: $d_{A-B} = 60$ μm , $d_{A-C} = 160$ μm , $a = 40$ μm , $b = 40$ μm and $h = 4$ μm . Dielectric cylindrical particles have radiuses $r_2 = r_3 = 5$ μm and relative permittivity $\varepsilon_2 = \varepsilon_3 = 80$. The suspension with the particle, has relative permittivity $\varepsilon_1 = 5$. On the bottom and top of the substrate, we have the Neumann's conditions. We also have periodic boundary conditions on the left and right sides of boundary parts: A–B and C–D. Moreover, the Laplace equation $\text{div}(\varepsilon \text{ grad } \varphi) = 0$, for electric potential φ , where ε

is dielectric permittivity, should be solved to obtain the electric field strength \mathbf{E} in simulated chamber section. In Fig. 1 two particles are shown and our goal is to compute Maxwell tensor, force densities and total forces acting on particles by means of Eqs. (16) and (19). Let us now consider two particles as depicted in Fig. 1 and compute Maxwell tensor, force densities as well as total forces acting on particles using Eqs. (17) and (20). Force densities acting between two particles are given in Fig. 2.

One can easily see that we have greatest forces in the neighborhood of both particles. Figure 3 shows the real values of force density calculated along each particle perimeter.

Let us now compute total forces acting on both particles by means of Eqs. (17) and (20), namely:

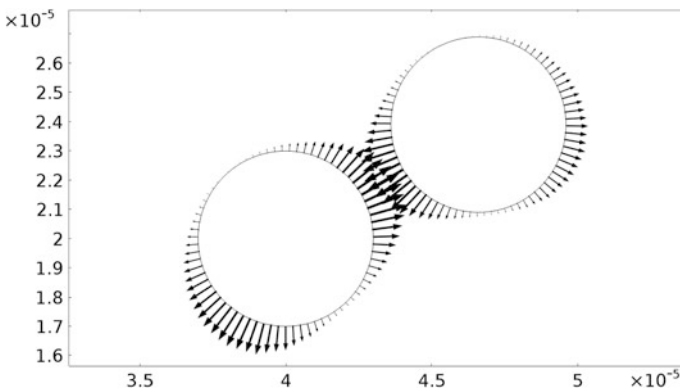
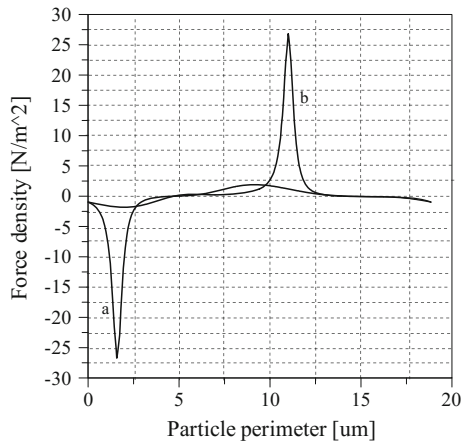


Fig. 2 Force densities distribution on particle-fluid boundaries

Fig. 3 Force densities on particle perimeters: **a** particle on the *right* side and **b** particle on the *left* side as depicted in Fig. 1



$$\begin{aligned}\mathbf{F}^{(1)} &= 3.144\mathbf{a}_x - 2.600\mathbf{a}_y \quad (\mu \text{ N/m}^2) \\ \mathbf{F}^{(2)} &= -1.561\mathbf{a}_x - 4.415\mathbf{a}_y \quad (\mu \text{ N/m}^2)\end{aligned}\quad (22)$$

It is easy to see that both forces are directed towards electric trap occurring between electrodes. This force can be calculated by simple projection forces $\mathbf{F}^{(1)}$ and $\mathbf{F}^{(2)}$ on the stride line connecting centers of both particles and labelled as $\mathbf{F}_s^{(1)}$ and $\mathbf{F}_s^{(2)}$. From geometrical relations, required angles can be calculated. After some manipulations we finally get the following values:

$$\begin{aligned}\mathbf{F}_s^{(1)} &= 1.3938 \quad (\mu \text{ N/m}^2) \\ \mathbf{F}_s^{(2)} &= 3.5944 \quad (\mu \text{ N/m}^2)\end{aligned}\quad (23)$$

They are not equal because additional force resulting from electrodes influences both forces. In Fig. 4, we can see the example when two particles touch each other. Maxwell stress tensor assumes substantial values in the vicinity of both particles. Mutual forces acting between both particles also assume much greater values than in the previous case.

$$\begin{aligned}\mathbf{F}^{(1)} &= 17.663\mathbf{a}_x + 5.168\mathbf{a}_y \quad (\mu \text{ N/m}^2) \\ \mathbf{F}^{(2)} &= -15.537\mathbf{a}_x - 13.830\mathbf{a}_y \quad (\mu \text{ N/m}^2)\end{aligned}\quad (24)$$

One can easily see that now forces acting between particles are almost on order greater and directed almost parallel each other. In Figs. 5, 6 and 7, collections of four particles are shown. It can be observed that distribution of Maxwell stress tensor given as resultant forces which attract each other. This process leads to the formation of specific particle chains. This was confirmed experimentally by several authors [8, 9, 20].

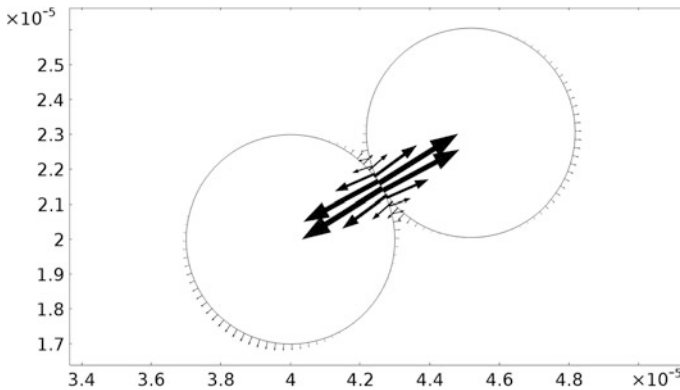


Fig. 4 Force densities on particle perimeters for two contacting particles

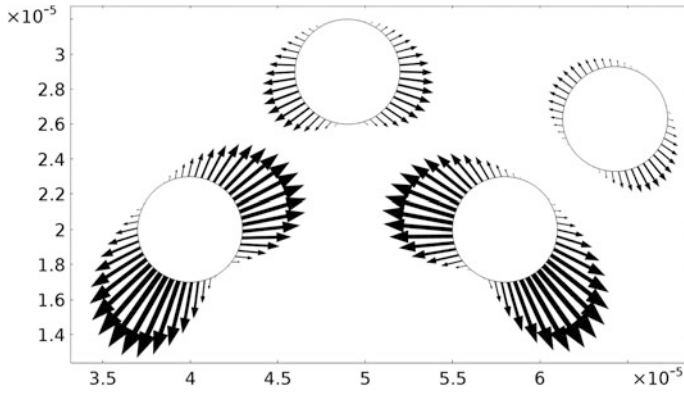


Fig. 5 Force densities on particle perimeters for distant particles

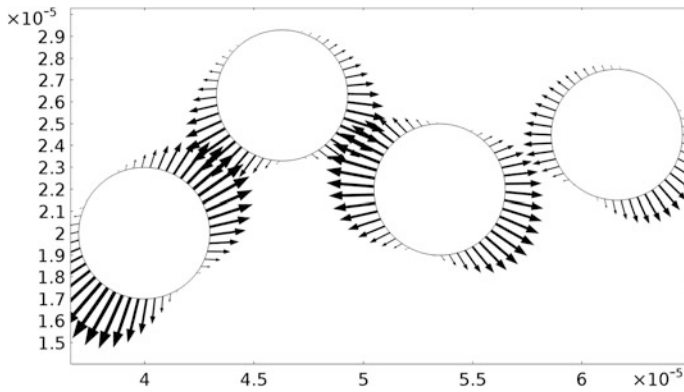


Fig. 6 Force densities on particle perimeters for molecules at shorter distances than in Fig. 5 (the acting forces are much higher than in Fig. 5)

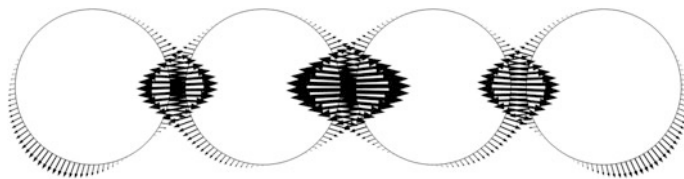


Fig. 7 Force densities on particle perimeters for molecules connected in one chain as a result of acting DEP forces

4 Conclusions

Various dielectrophoretic techniques are greatly useful in enriching, purifying and describing of various environmental, biological, industrial and clinical ingredients. In this paper, it has been demonstrated that with an appropriate electrode array and a suitable electric field, separation of particles can be accomplished. Unfortunately, this phenomenon of mutual force interaction has negative influence on particle separation process. Because dielectrophoresis is mainly utilized to separate different micro-particles, aggregation of particles can substantially hinder separation process of various molecules. The mutual interaction of particles by surface densities forces can be minimalised by according selection suspension permittivity and interdigitated electrode potentials. Therefore, any theoretical considerations, leading to better understanding of this phenomenon, have great practical value.

References

1. Mahaworasilpa, T.L., Goster, H.G.L., George, E.P.: Forces on biological cells due to applied alternating (AC) electric fields. 1. Dielectrophoresis. *Biochim. Biophys. Acta Biomembr.* **1193**(1), 118–126 (1994)
2. Gutierrez, M.A., Khanbareh, H., van der Zwaag, S.: Computational modeling of structure formation during dielectrophoresis in particulate composites. *Comput. Mater. Sci.* **112**(A), 139–146 (2016)
3. Kurgan, E.: Comparison of different force calculation methods in DC dielectrophoresis. *Prz. Elektrotechniczn.* **88**(8), 11–14 (2012)
4. Kurgan, E., Gas, P.: An influence of electrode geometry on particle forces in AC dielectrophoresis. *Prz. Elektrotechniczn.* **86**(1), 103–105 (2010)
5. Jones, T.B.: *Electromechanics of Particles*. Cambridge University Press, Cambridge (2005)
6. Kurgan, E., Gas, P.: Calculation of forces imposed on particles in AC dielectrophoresis. *Prz. Elektrotechniczn.* **85**(12), 100–103 (2009)
7. Kurgan, E.: Stress calculation in two-dimensional DC dielectrophoresis. *Prz. Elektrotechniczn.* **87**(12B), 107–110 (2011)
8. Nicotra, O.E., La Magna, A., Coffa, S.: Particle-chain formation in a DC dielectrophoretic trap; a reaction-diffusion approach. *Appl. Phys. Lett.* **95**(7), 073702 (2009)
9. Ai, Y., Qian, S.Z.: DC dielectrophoretic particle–particle interactions and their relative motions. *J. Colloid Interface Sci.* **346**(2), 448–454 (2010)
10. Liu, L., Xie, C., Chen, B., Wu, J.K.: Iterative dipole moment method for calculating dielectrophoretic forces of particle–particle electric field interactions. *Appl. Math. Mech. Engl. Ed.* **36**(11), 1499–1512 (2015)
11. Xie, C., Chen, B., Liu, L., Chen, H., Wu, J.: Iterative dipole moment method for the interaction of multiple dielectrophoretic particles in an AC electrical field. *Eur. J. Mech. B Fluids* **58**, 50–58 (2016)
12. Liu, L., Xie, C., Chen, B., Chiu-On, N., Wu, J.: A new method for the interaction between multiple DEP particles: iterative dipole moment method. *Microsyst. Technol.* **22**(9), 2223–2232 (2016)
13. Kurgan, E.: Forces acting on multilayer dielectric particle in DC dielectrophoresis. *Prz. Elektrotechniczn.* **87**(5), 92–95 (2011)

14. Kurgan, E.: Numerical computation of mutual force acting between two particles in DC dielectrophoresis. *Prz. Elektrotechniczn.* **88**(12B), 213–216 (2012)
15. Kurgan, E.: Dipole moment calculation in two-dimensional DC dielectrophoresis. *Prz. Elektrotechniczn.* **86**(12), 192–195 (2010)
16. Ciesla, A., Kraszewski, W., Skowron, M., Surowiak, A., Syrek, P.: Application of electrodynamic drum separator to electronic wastes separation. *Gospod. Surow. Miner. Miner. Resourc. Manag.* **32**(1), 155–174 (2016)
17. Mathew, B., Alazzam, A., Destgeer, G., Sung, H.J.: Dielectrophoresis based cell switching in continuous flow microfluidic devices. *J. Electrostat.* **84**, 63–72 (2016)
18. Mhatre, S.: Dielectrophoretic motion and deformation of a liquid drop in an axisymmetric non-uniform AC electric field. *Sens. Actuators B Chem.* **239**, 1098–1108 (2017)
19. Ali, H., Park, C.W.: Numerical study on the complete blood cell sorting using particle tracing and dielectrophoresis in a microfluidic device. *Korea Aust. Rheol. J.* **28**(4), 327–339 (2016)
20. Hossan, M.R., Gopmandal, P.P., Dillon, R., Dutta, P.: A comprehensive numerical investigation of DC dielectrophoretic particle–particle interactions and assembly. *Colloids Surf. A* **506**, 127–137 (2016)

The S_{11} -parameter Analysis of Multi-slot Coaxial Antenna with Periodic Slots

Piotr Gas

Abstract The motivation behind this study is specifying the proper arrangement of periodic air slots within the multi-slot coaxial antenna with $50\text{-}\Omega$ feeding load operating at 2.45 GHz to provide the conformal microwave thermotherapy. The desired temperature profile of the liver tissue was numerically evaluated for coupled electromagnetic and thermal problems by the finite element method. Considering the growing number of radiating apertures within the thin microwave needle applicator requires some unique optimization approach based on the S_{11} -parameter characteristics to guarantee the best antenna–tissue impedance matching. Moreover, the proposed multi-step iterative numerical procedure allows effective modelling of optimal placement of the periodic slots of microwave antenna, required limit levels of the antenna power input and thus conformal cancer treatment for both interstitial microwave hyperthermia and thermal ablation.

Keywords Scattering parameters · Multi-slot coaxial antenna · Periodic slots · Interstitial microwave hyperthermia · Cancer ablation · Finite element method

1 Introduction

Over the last several decades, more and more extensive usage of electromagnetic fields (EMFs) has been observed in different branches of science, technology and medicine [1]. Beneficial operation of EMFs at various frequencies can be recognized in many radio-communication systems, wireless data transmission as well as in some therapeutic purposes [2–6]. An excellent example for electromagnetic (EM) localized treatment of cancer may be interstitial techniques, including both microwave hyperthermia (40–45 °C) and thermal ablation (50–110 °C) [7, 8]. Such treatment modalities rely on tumor heating to supraphysiological temperatures

P. Gas (✉)

Department of Electrical and Power Engineering, AGH University of Science and Technology, al. Mickiewicza 30, 30-059 Krakow, Poland
e-mail: piotr.gas@agh.edu.pl

above 40 °C to induce irreversible destructions of malignant cells involving apoptosis, necrosis, denaturation or even tissue burning [7, 9]. Minimally invasive techniques are mainly intended for hepatic tumors which, due to deep location in human body and strong tissue vascularisation, cannot be easily removed in a surgical way [10–12]. These procedures rely on insertion of the thin needle antenna radiator into the target tissue. The position of the applicator can be typically controlled by the magnetic resonance imaging (MRI) or computed tomography (CT) guidance during the cancer treatment [10]. Such therapy usually lasts from a few to 10 min, depending on the kind of tumor, therapeutic temperatures, the input power of the antenna as well as its operating frequency [10, 13]. The coaxial antennas have been commonly applied in medical treatment for many years due to uncomplicated construction, low production cost and ease in application [11, 13, 14]. The interstitial techniques are very popular because they offer desired temperature profile of human tissue both for hyperthermia and ablation procedures [9, 9]. Importantly, such methods enhance the effectiveness of other cancer treatment modalities such as radio-, chemo-, immunotherapy and gene therapy [7, 10]. Recently, also other techniques utilizing magnetic nanoparticles subjected to external radiofrequency fields have been widely tested in research centres all around the world [15, 16].

A multi-slot coaxial antenna was proposed for the first time in 2014 [17] and improved in the following years [12, 13]. This paper describes the S_{11} -parameter analysis of such microwave needle applicator with some radiating periodic air gaps. Previously, coaxial cables with periodic slots were explored as leaky antennas [18]. The main research problem presented in the current paper is such arrangement of the periodic slots within the microwave applicator that leads to proper antenna performance and the heating efficiency of the target tissue. The proposed multi-step iterative procedure of estimating the reflection coefficient at the feeding point of the multi-slot coaxial antenna allows fast determining the resonant frequencies of the applicator, and thus the best impedance matching of analyzed antenna–tissue system. The author’s preliminary considerations on this subject can be found in [19] and the full version of this article will be published in [8]. The unique methodology described in this paper could be highly relevant for computerized planning of cancer treatment as well as looking for new directions in thermotherapy.

2 Model Definition

The representation of the considered model of multi-slot coaxial antenna with periodic air slots has been outlined in Fig. 1. The microwave applicator includes two cylindrical conductors separated by the coaxial dielectric with a 50 Ω feeding load. These elements are enclosed within the plastic catheter that protects internal antenna components. Initially, coaxial slots with dimensions of $d_1 = 1.21$ mm, $d_2 = d_3 = 1$ mm are positioned within the outer conductor at equal distances of $l_1 = l_2 = 1$ mm. Importantly, the length between the first periodic slot and the

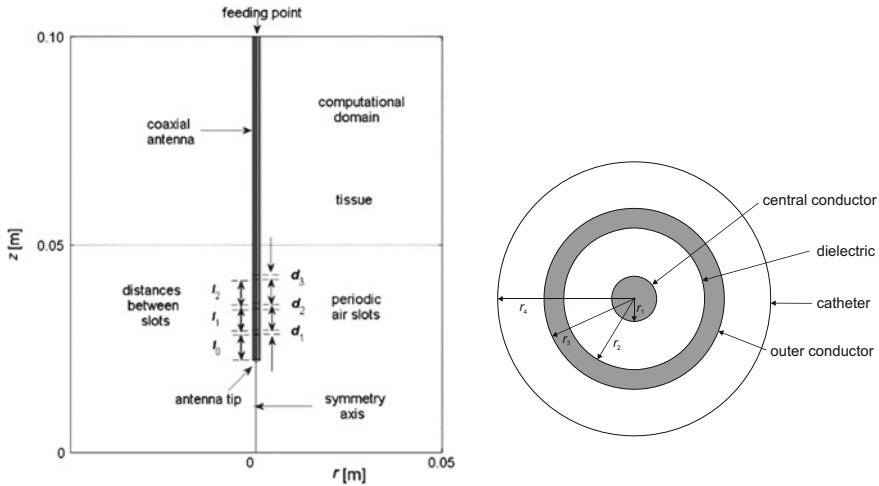


Fig. 1 Model of the multi-slot coaxial antenna with periodic slots

antenna tip is a critical parameter which has a value of $l_0 = 6.13$ mm as established for liver tissue in [19]. The other dimensions of the multi-slot coaxial antenna have been taken from related articles about this topic [11, 13, 14].

From the mathematical point of view, the presented issue of microwave heating of human tissue contains the coupling of electromagnetic wave equation under harmonic conditions with the transitory bio-heat transfer equation. Due to axial symmetry, the 2D model with cylindrical coordinates (r, ϕ, z) and transverse magnetic (TM) waves has been employed. That is why, the magnetic field strength has only one component $\mathbf{H} = H_\phi \mathbf{e}_\phi$, and the electric field strength is equal to $\mathbf{E} = E_r \mathbf{e}_r + E_z \mathbf{e}_z$. In terms of magnetic field, the wave equation takes the scalar formulation as follows [17]:

$$\nabla \times [(\epsilon_0 \underline{\epsilon}_r)^{-1} \nabla \times H_\phi] - \mu_0 \mu_r \omega^2 H_\phi = 0 \tag{1}$$

Knowing the magnetic field \mathbf{H} , the electric field \mathbf{E} could be computed effectively using the Faraday’s law. The frequency-dependent complex relative permittivity of biological objects can be calculated using the Cole–Cole model [20]:

$$\underline{\epsilon}_r(\omega) = \epsilon'_r - j\epsilon''_r = \epsilon_\infty + \frac{\epsilon_s - \epsilon_\infty}{1 + (j\omega\tau_0)^{1-\alpha}} - j \frac{\sigma_s}{\omega\epsilon_0} \tag{2}$$

It should be stressed that the imaginary part of this parameter ϵ''_r is responsible for power losses in dielectric medium [7]. Additionally, the effective electrical conductivity of tissue (S/m) can be established by

$$\sigma_{\text{eff}} = -\text{Im}[\underline{\epsilon}_r] \omega \epsilon_0 = \omega \epsilon_0 \epsilon_r'' \quad (3)$$

The bio-heat transfer inside living human tissues could be effectively modelled by the transitory Pennes equation [21]:

$$\rho C \frac{\partial T}{\partial t} + \nabla \cdot (-k \nabla T) = \rho_b C_b \omega_b (T_b - T) + Q_{\text{ext}} + Q_{\text{met}} \quad (4)$$

Importantly, the tissue dielectric properties impact on the EM energy dissipation as well as the heat generation inside the human tissue. On the other hand, the tissue thermal parameters influence the heat transfer in the target human tissue [7]. A coupling element for both fields is so-called external heat source produced by the thin antenna $Q_{\text{ext}} = \sigma_{\text{eff}} |E|^2$ (W/m³). Other important parameters are blood perfusion rate ω_b (1/s) and metabolic heat generation rate Q_{met} (W/m³) [13]. Detailed description and full derivation of the governed equations can be widely found in the current literature [11, 12, 17].

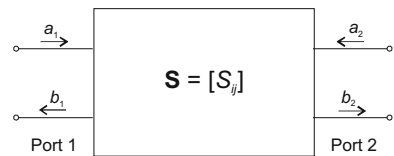
3 Scattering Parameters

In general, devices equipped with n -port transmission line can be fully expressed by so-called scattering parameters forming together the S -parameter matrix: $\mathbf{S} = [S_{ij}]$ [19, 22]. The complex-valued elements of such matrix S_{ij} denote the transmission ($i \neq j$) or reflection ($i = j$) coefficients of the electromagnetic wave at individual paired points ($i, j = 1, \dots, n$) i.e. ports. The generalized two-port device is outlined in Fig. 2 where a_1 is incident signal at the port 1, and b_1 is reflected signal at the port 1, etc. ($S_{11} = b_1/a_1|_{a_2=0}$, $S_{12} = b_1/a_2|_{a_1=0}$, $S_{21} = b_2/a_1|_{a_2=0}$, $S_{22} = b_2/a_2|_{a_1=0}$).

For analyzed multi-slot coaxial antenna with only one port, the S_{11} -parameter is identical to voltage reflection coefficient Γ that describes the dependable antenna working within the external environment [19]. In relation to electric field, the S_{11} -parameter can be analytically evaluated by [23]:

$$S_{11} = \Gamma = \frac{\int_{\text{port1}} (\mathbf{E} - \mathbf{E}_1) \cdot \mathbf{E}_1^* dA_1}{\int_{\text{port1}} \mathbf{E}_1 \cdot \mathbf{E}_1^* dA_1} \quad (5)$$

Fig. 2 Schematic view of two-port line device



where the designation “port 1” corresponds to the multi-slot coaxial antenna input at the feeding point. Additionally, A_1 represents the surface area of port 1 and E_1 is the electric field strength at this port. In terms of microwave power flow, the voltage reflection coefficient is proportional to the dimensionless ratio of reflected power P_r to incident power P_{in} at the antenna port as follows [23]:

$$|\Gamma|^2 = \frac{P_r}{P_{in}} \quad (6)$$

It indicates the antenna attenuation at the feeding point. Very often, the voltage reflection coefficient is expressed in decibels (dB) by the S_{11} -parameter describing the return loss with a negative sign in port 1 as indicated below [14, 19]:

$$S_{11,\text{dB}} = 20 \log_{10}(|\Gamma|) = 20 \log_{10} \sqrt{\frac{P_r}{P_{in}}} = 10 \log_{10} \left(\frac{P_r}{P_{in}} \right) \quad (7)$$

Moreover, the effective wavelength within the biological materials is expressed by the formula [8]:

$$\lambda_{\text{eff}} = \frac{\lambda_0}{\sqrt{\epsilon'_r}} = \frac{c_0}{f \sqrt{\epsilon'_r}} \quad (8)$$

where λ_0 represents the wavelength of light in free-space (m), c_0 denotes a speed of the light in vacuum (m/s) and f means the electromagnetic wave frequency (Hz). According to the above equation, any changes in the dimensions of the microwave applicator and the tissue dielectric properties could strongly influence the antenna resonant frequency (f_r) and thus matching or mismatching of analyzed antenna to the 50Ω coaxial feeding load [24].

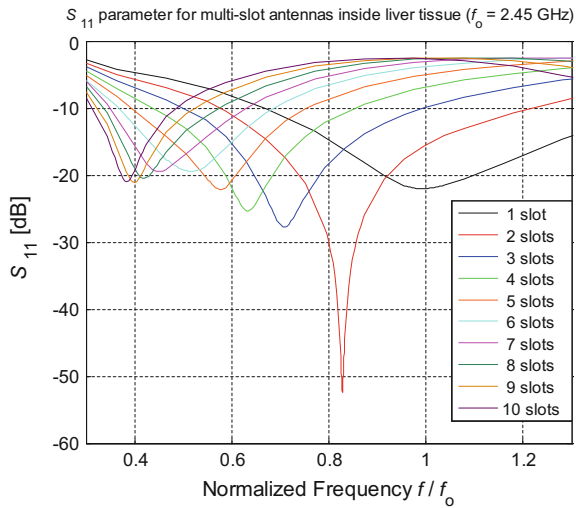
4 Simulation Results

The coupled analysis of interdisciplinary electro-thermal problem was solved for the antenna operating frequency of 2.45 GHz. It was assumed that microwave needle applicator was invasively entered into human liver tissue. The presented paper incorporates the material data for hepatic tissue based on the experiments available in the literature [11, 13, 20]. The antenna dielectric properties were taken from the previously published data for related models [11, 14, 17]. All necessary data have been listed in Table 1. The previously discussed scalar formulas (1)–(8) were solved together with the proper initial-boundary conditions [12, 14, 17] in Comsol Multiphysics software. On the external border of the computational area, the absorbing boundary conditions have been employed to prevent any reflections of EM waves back to the target human tissue and thus improve return loss.

Table 1 Electro-thermal parameters of hepatic tissue for frequency of 2.45 GHz [13]

ϵ_r (-)	σ_{eff} (S/m)	ω_b (1/s)	k (W/(m K))	ρ (kg/m ³)	C (J/(kg K))	Q_{met} (W/m ³)
43.03–12.37j	1.686	0.015466	0.52	1079	3540	5301

Fig. 3 Impact of various number of multiple slots within the coaxial microwave applicator structure on antenna reflection coefficient



In the numerical implementation, the finite element method has been used. The simulation results for the liver tissue are shown in the following Figs. 3, 4 and 5.

Ensuring the satisfactory scattering parameters of the actual antenna–tissue system can be achieved by modifying the dimensions of the analyzed multi-slot coaxial antenna with periodic apertures. The parameter that strongly impacts on the needle applicator performance is the length between the first periodic slot and the antenna tip, depicted as l_0 in Fig. 1. The numerical routine for evaluating the return loss against of l_0 -parameter of single-slot coaxial antenna was fully described in the author’s previous paper [19].

Now, to such antenna with pre-defined dimensions of $l_0 = 6.13$ mm and $d_1 = 1.21$ mm, some new radiating slots have been successfully added with equal lengths and distances between them ($l_i = d_{i-1} = 1$ mm, where $i = 1, 2, \dots, N - 1$). It should be emphasized that it is possible to include up to $N = 10$ air gaps in the multi-slot coaxial antenna due to its finite length. Figure 3 compares all computed characteristics of S_{11} -parameter valid in such case. For various multi-slot coaxial antennas, significant differences in the obtained resonant frequencies have been observed. The increase of slots number within the microwave applicator structure results in a reduction of the antenna resonant frequency and growth in return loss ranging from double-slot antenna where the resonance occurs. For this purpose, the procedure described in [19] should be repeated and thus new elevations of

Fig. 4 The S_{11} -parameter distributions against normalized frequency for the microwave antenna with periodic slots after optimization procedure

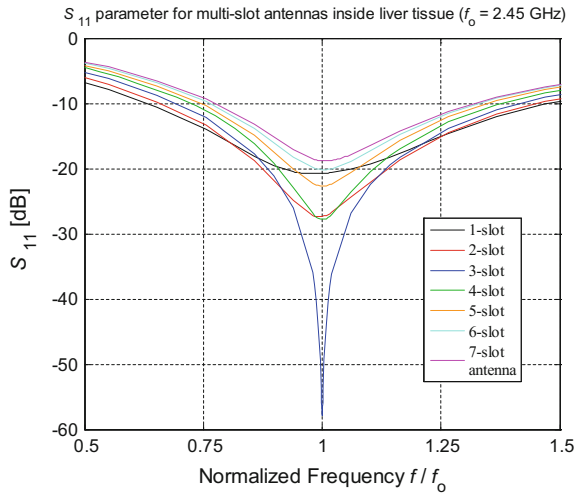
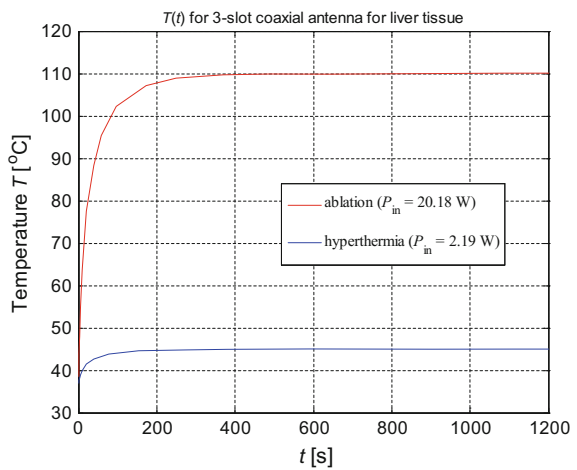


Fig. 5 Transient-temperature distributions for optimal hyperthermia and ablation treatments derived from the 3-slot antenna working at $f_0 = 2.45$ GHz



l_0 -parameter for multi-slot coaxial antenna with periodic air slots ($l_i = d_i = 1$ mm where $i = 1, 2, \dots, N$) should be established. In this case, the antenna can include no more than $N = 7$ radiating gaps as outlined in Fig. 4. As a result of the proposed procedure, the desired the S_{11} -parameter characteristics devoid of shifting between the antenna working and resonant frequencies of 2.45 GHz have been obtained.

Table 2 compares the numerical assessments for various parameters of the analyzed multi-slot-coaxial antennas placed inside the liver tissue. According to the performed numerical analysis, the growing number of periodic slots within the antenna structure is closely connected with the decrease in the l_0 -length from the needle tip. Importantly, the characteristic resonance has appeared in the distribution of S_{11} -parameter for microwave applicator with three periodic air slots,

Table 2 Optimal parameters of the multi-slot coaxial antennas with periodic slots operating at 2.45 GHz

Number of periodic slots	Antenna parameters for liver tissue				
	l_0 (mm)	S_{11} (dB)	f_r (GHz)	P_{in} (W) $T = 45$ °C	P_{in} (W) $T = 110$ °C
1-slot antenna	6.13	-20.78	2.40	2.13	19.62
2-slot antenna	4.62	-27.38	2.43	2.15	19.84
3-slot antenna	3.34	-57.80	2.45	2.19	20.18
4-slot antenna	2.33	-27.77	2.45	2.25	20.74
5-slot antenna	1.53	-22.64	2.45	2.33	21.48
6-slot antenna	0.88	-20.14	2.46	2.41	22.24
7-slot antenna	0.35	-18.81	2.46	2.48	22.85

which is equivalent to the smallest possible value of the reflection coefficient. What is more, the conducted simulations reveal that interstitial antennas including 3, 4 and 5 radiating slots considerably resulted in levelling the resonant frequency of the applicator with its operating frequency $f_o = 2.45$ GHz. For the remaining antennas, small deviations within the ISM band of 2.40–2.50 GHz are observed. It should be stressed that the desired temperature profile of the liver tissue was controlled by adjusting the antenna microwave input power (P_{in}) to the treated tissue not to exceed the therapeutic elevations for conformal interstitial microwave hyperthermia (up to 45 °C) and ablation (up to 110 °C) treatment modalities. What is more, the multi-step iterative approach, as presented in [13], has been successfully implemented to specify the limit levels of P_{in} parameter. The last Fig. 5 illustrates the examples of the obtained transient temperature curves that correspond to the three-slot antenna working conditions with the total input power P_{in} set to 2.19 and 20.80 W in the case of analyzed interstitial thermal therapies.

5 Conclusions

Minimally invasive thermal therapies such as microwave interstitial hyperthermia and thermal ablation have emerged as advanced modalities of cancer treatment. The proposed multi-step iterative numerical procedure allows effective modelling of such conformal tumor therapies. It was successfully proved that the increasing number of periodic apertures within the multi-slot coaxial antenna strongly impact on the antenna impedance matching to the hepatic tissue and thus resulting efficiency in microwave liver tissue heating. Importantly, the best performance of analyzed multi-slot coaxial antenna has been noticed for needle applicator including three radiating gaps. Moreover, the increasing number of periodic slots provides the l_0 -length reduction while growing of P_{in} parameter to achieve optimal cancer treatments. The presented methodology could be highly relevant for the computerized planning of cancer treatment and could help in looking for new directions in modern heat therapy.

References

1. Bienkowski, P., Cala, P., Zubrzak, B.: Optimization of measurement methods for a multi-frequency electromagnetic field from mobile phone base station using broadband EMF meter. *Med. Pr.* **66**(5), 701–712 (2015)
2. Michalowska-Samonek, J., Miaskowski, A., Wac-Wlodarczyk, A.: The distribution of electromagnetic field of high frequency in breast gland. *Prz. Elektrotechniczn.* **86**(12), 106–108 (2010)
3. Miaskowski, A., Gas, P., Krawczyk, A.: SAR calculations for titanium bar-implant subjected to microwave radiation. In: 2016 17th International Conference Computational Problems of Electrical Engineering (CPEE), 14–17 September 2016, Sandomierz, Article No. 7738726, pp. 1–4. IEEE (2016). doi: [10.1109/CPEE.2016.7738726](https://doi.org/10.1109/CPEE.2016.7738726)
4. Syrek, P., Skowron, M., Ciesla, A.: Therapy's individualization of bone injuries with the magnetic field applicators. In: 2016 International Conference and Exposition on Electrical and Power Engineering (EPE), Iasi, 20–22 October 2016, art. no. 7781378, pp. 435–438. IEEE (2016)
5. Glowacz, A., Glowacz, Z.: Recognition of images of finger skin with application of histogram, image filtration and K-NN classifier. *Biocybern. Biomed. Eng.* **36**(1), 95–101 (2016)
6. Rhein, S., Graichen, K.: Coupled actuator placement and controller design for electromagnetic heating by means of dynamic optimization. In: 2016 IEEE 55th Conference on Decision and Control (CDC), 12–14 December 2016, Las Vegas, pp. 4809–4814. IEEE (2016)
7. Rossmann, C., Haemmerich, D.: Review of temperature dependence of thermal properties, dielectric properties, and perfusion of biological tissues at hyperthermic and ablation temperatures. *Crit. Rev. Biomed. Eng.* **42**(6), 467–492 (2014)
8. Gas, P.: Optimization of multi-slot coaxial antennas for microwave thermotherapy based on the S_{11} -parameter analysis. *Biocybern. Biomed. Eng.* **37**, 78–93 (2017). doi:[10.1016/j.bbe.2016.10.001](https://doi.org/10.1016/j.bbe.2016.10.001)
9. Majchrzak, E., Paruch, M., Dziewoński, M., Freus, S., Freus, K.: Sensitivity analysis of temperature field and parameter identification in burned and healthy skin tissue. In: Munoz-Rojas, P.A. (ed.) *Computational Modeling, Optimization and Manufacturing Simulation of Advanced Engineering Materials*. Book Series: Advanced Structured Materials, chapter 5, vol. 49, pp. 89–112. Springer, Berlin (2016)
10. Hernandez, J.I., Cepeda, M.F., Valdes, F., Guerrero, G.D.: Microwave ablation: state-of-the-art review. *OncoTargets Ther.* **8**, 1627–1632 (2015)
11. Zafar, J., Zafar, T., Zafar, H., Sharif, F.: Design, development and microwave inter-comparison of dual slot antenna configurations for localized hepatic tumor management. *Australas. Phys. Eng. Sci. Med.* **38**(4), 593–601 (2015)
12. Wang, T., Zhao, G., Qiu, B.: Theoretical evaluation of the treatment effectiveness of a novel coaxial multi-slot antenna for conformal microwave ablation of tumors. *Int. J. Heat Mass Transf.* **90**, 81–91 (2015)
13. Gas, P.: Multi-frequency analysis for interstitial microwave hyperthermia using multi-slot coaxial antenna. *J. Electric. Eng. Elektrotech. Cas.* **66**(1), 26–33 (2015). doi:[10.1515/jee-2015-0004](https://doi.org/10.1515/jee-2015-0004)
14. Rubio, M.F.J.C., Lopez, G.D.G., Perezgasa, F.V., Garcia, F.F., Hernandez, A.V., Salas, L. L.: Computer modeling for microwave ablation in breast cancer using a coaxial slot antenna. *Int. J. Thermophys.* **36**(10), 2687–2704 (2015)
15. Kurgan, E., Gas, P.: Analysis of electromagnetic heating in magnetic fluid deep hyperthermia. In: 2016 17th International Conference Computational Problems of Electrical Engineering (CPEE), 14–17 September 2016, Sandomierz, art. no. 7738756, pp. 1–4. IEEE (2016). doi: [10.1109/CPEE.2016.7738756](https://doi.org/10.1109/CPEE.2016.7738756)

16. Varon, L.A.B., Orlande, H.R.B., Elicabe, G.E.: Combined parameter and state estimation problem in a complex domain: RF hyperthermia treatment using nanoparticles. In: *Journal of Physics: Conference Series*, vol. 745, no. 3, art. no. 032014, pp. 1–8 (2016)
17. Gas, P.: Study on interstitial microwave hyperthermia with multi-slot coaxial antenna. *Rev Roum. Sci. Tech. Ser. Electrotech. Energ.* **59**(2), 215–224 (2014). <http://revue.elth.pub.ro/index.php?action=details&id=453>
18. Wang, J.H., Mei, K.K.: Theory and analysis of leaky coaxial cables with periodic slots. *IEEE Trans. Antennas Propag.* **49**(12), 1723–1732 (2001)
19. Gas, P.: Determination of the optimal multi-slot coaxial antenna sizes based on the microwave antenna reflection coefficient characteristics. In: *2015 Selected Problems of Electrical Engineering and Electronics (WZEE)*, 17–19 September 2015, Kielce, art. no. 7394015, pp. 1–4. IEEE (2015). doi: [10.1109/WZEE.2015.7394015](https://doi.org/10.1109/WZEE.2015.7394015)
20. Peyman, A., Holden, S., Gabriel, C.: Measurement of the dielectric properties of biological tissues in vivo at microwave frequencies. In: *Mobile Telecommunications and Health Research Programme, RUM3, Final Report* (2005)
21. Pennes, H.H.: Analysis of tissue and arterial blood temperatures in the resting human forearm. *J. Appl. Physiol.* **85**(1), 5–34 (1998)
22. Komarov, V.V.: Estimation of heating rate in the near zone of interstitial microwave applicator. *IEEE Microw. Wirel. Compon. Lett.* **24**(9), 640–642 (2014)
23. Nowakowska, H., Jasinski, M., Debicki, P.S., Mizeraczyk, J.: Numerical analysis and optimization of power coupling efficiency in waveguide-based microwave plasma source. *IEEE Trans. Plasma Sci.* **39**(10), 1935–1942 (2011)
24. Katrich, V.A., Lyashchenko, V.A., Medvedev, N.V.: Coaxial-slot antenna array with different lengths of radiators. In: *2016 International Conference in Radio Electronics & Info Communications (UkrMiCo)*, 11–16 September 2016, Kiev, art. no. 7739607, pp. 1–4. IEEE (2016)

The Reliability of Critical Systems in Railway Transport Based on the Track Rail Circuit

Ryszard Mielnik, Maciej Sulowicz, Krzysztof Ludwinek and Marek Jaskiewicz

Abstract This paper presents a system for monitoring and control of unoccupied railway track of automatic railway crossing signaling devices. The most important task of this system is to ensure the safety of rail and road traffic. This solution belongs to the class of critical systems, and is particularly important not only for safety reasons to prevent the collision of railway vehicles and road wheeled, but also entails various economic aspects. The first part of the article raises issues related to the safety of rail transport process. It then discusses the possibilities of using rail circuit to determine unoccupied section of the approach and the distance of the rail vehicle from the railroad crossing. Structure and functionality of automatic railway crossing signaling devices on a level crossing were defined. The synthesis of safe measurement control digital system is based on a dynamic model using Petri net. Factors of reliability and discusses the advantages of the proposed system solutions were estimated.

Keywords Track rail circuit · Wave impedance · Measuring system · Critical systems · Railway traffic safety · Railway control systems · Discrete event system · Petri nets · Realtime systems

R. Mielnik (✉) · M. Sulowicz
Institute of Electromechanical Energy Conversion, Cracow University of Technology,
Cracow, Poland
e-mail: rmiel@pk.edu.pl

M. Sulowicz
e-mail: msulowicz@pk.edu.pl

K. Ludwinek
Faculty of Electrical Engineering, Automatic Control and Computer Science,
Kielce University of Technology, Kielce, Poland
e-mail: k.ludwinek@tu.kielce.pl

M. Jaskiewicz
Faculty of Mechatronics and Mechanical, Kielce University of Technology, Kielce, Poland
e-mail: m.jaskiewicz@tu.kielce.pl

1 Introduction

Speed, comfort, and safety of movement of people and goods in the rail transport is a very important issue for the economic development in each country. The result is therefore the requirement of rolling stock, railway traffic control equipment and track infrastructure, which will ensure a high level of reliability and the required safety level of the transport process.

Currently used railway traffic control systems belong to the class of computer control systems used in critical processes [22]. This type of systems is particularly important in preventing railway accidents in which people die and there are large material losses. In critical industrial processes measuring control digital systems (MCD systems) are commonly used [22]. These systems are built on the basis of hardware platforms such as PLCs, industrial computers, and embedded systems [22]. They owe their rich functionality to implemented software utility. The quality of work MCD systems is affected by the hardware platform used and software of MCD systems applied [8, 9, 19, 24]. A major problem in the implementation of MCD systems is not only writing of the design, construction, and testing, but also testing the system as a whole. Ensuring high reliability of the software and the reliability of the entire MCD systems is required especially in critical applications. Improper function or failure of the system during its operation can lead to malfunctioning of the controlled process. The effect of this may be human and material losses. One of the critical processes is rail transport [3, 5, 14, 24]. In this process, the basic requirement is to ensure the safety of the shipping process. The second essential requirement in this process is to ensure adequate reliability of the process, i.e., that trains and all kinds of rail vehicles move in accordance with the approved mining plan-timetable [5, 18, 24]. Any defect traffic control devices (which provide the planned course of the transport process) influences the movement disorder plan-timetable. Smooth and trouble-free transport process is affected by many factors related to the rolling stock [6, 12, 13, 16, 19], traction, track infrastructure [7], and railway traffic control equipment [1, 5, 14, 15, 17, 24].

The purpose of this article is to present the possibilities of using the system of monitoring and control approaching section of the automatic railway crossing signaling devices (ARCD devices). These devices are built over at the one-level crossings so that the devices MCD systems generate appropriate signals to warn drivers of impending rail vehicle. The present system provides security by closing the passage in the event of damage to the MCD systems and information to the railway driver to reduce the speed of the vehicle so as to avoid a train crash.

According to the station from 11 February 2015 Poland has 15,403 crossings and only 1316 railway crossings are secured by automatic railway crossing signaling devices. Among them, there are practically none constant-time automatic crossing devices, which provide constant-time warning drivers of closing of the passage. Therefore, it seems reasonable to develop and implement such system solutions.

2 The Process of Rail Transport

The process of rail transport takes place on a network of Polish Railway Lines (PLK), and it allows the movement of passengers and goods in Poland. It also allows the implementation of transport services in terms of their transit areas of Europe. Traffic on the railway lines must be properly planned, controlled, and implemented. The implementation of these requirements provides a process for railway traffic control [5]. This process not only provides timely and reliable realization of the planned rail traffic on the roads driving trains and warehouses maneuvering, but must first and foremost ensure the safety of the movement. The main factors for the preparation of a safe road driving for rail vehicles are [5]:

- correct setting organization, setting, and releasing waveform driving,
- reliable implementation conditions guaranteeing safety.

Control of the fulfillment of conditions for the implementation of safe driving trains can be implemented in a way that is not dependent on or addicted to [5, 18]. The method is not dependent when the realization of the conditions driving safety rests with the personnel, while in the addicted method implementation of these conditions is carried out by means of railway traffic control devices (RTC devices) [5]. This entails that the damage to components of RTC devices does not result in their transition endangering the safety of traffic. Addicted way to control the implementation of safety RTC devices shows greater reliability of repeated action than when done by people. In addition, the control method depending on the security conditions is more reliable than not implementation [5]. Therefore, the larger the scope of the addict how to implement the safety requirements included in the technical solutions of the RTC devices while providing reliable their implementation the greater safety signaling system can provide [5].

Currently, designed and built RTC devices and systems must meet appropriate levels of safety and reliability; and as devices based on the platform of the computer and the PLC should be considered an appropriate choice of features of the system for both the underlying hardware and software of a system. The Technical Committee of the Organization of Engineers Rail Signaling (TC-IRSE) developed levels of security RTC systems depending on the effects of potential failures and errors resulting in the system, system functions, security level, and intensity of damage λ for one piece of the system (e.g., driver switch-point) [5]. According to TC-IRSE fourth, a very high level of security (Fail-safe) is required for security systems railway traffic, and the effect of potential damage or system errors is the loss of human life or health, or very large material losses and the failure intensity λ element (module) system cannot be greater than 10^{-11} [5, 18]. This level of security is required, e.g., For devices setting the police station of train traffic, monitoring, and control systems unoccupied tracks and switches or automatic signaling device are spared [5, 18].

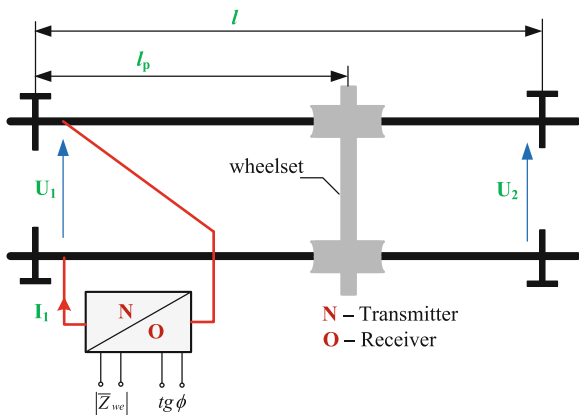
3 Monitoring and Control System for Unoccupied Tracks

The basic condition for ensuring the safety of rail traffic is that at any given time on the road only one rail vehicle moves, and that in this way there is no other rolling stock or other obstacles. Track provides checking this condition Track circuit is an electrical system designed to monitor the condition of a particular section of railway track, which is part of a route or rail vehicles [5]. Checking the track circuit section concern the seizing of the rolling stock and is realized on the basis of the transformation of external criteria for designating finding rolling stock into electrical signals that can be used in MCD systems, information or other [5]. Most of the track circuits also allow continuous monitoring of cross level covered by the system of electrical track circuit, and also the principle of being on the track other obstacles than the rolling stock. Such monitoring can detect, e.g., rail fracture. Then, an electric track circuit will lead to the generation of the busy signal of the segment which is safe for the traffic situation. For measuring the following distance of the rail vehicle from the end section of the track, you can use the rail track circuit, which is part of devices interaction relationship track-vehicle of automatic railway crossing devices on railroad crossing. The general track rail circuit is shown in Fig. 1 [11, 14].

Shown in Fig. 1 the track circuit is supplied with a sinusoidal AC voltage U_1 [5, 11]. Entry of a rail vehicle (rolling stock) on the circuit section of rail with a length l results in short-circuiting the set of circular cross level on a variable-length l_p . This alters the input impedance of the circuit. To determine the input impedance of the binding equation used voltages and currents at the ends of the circuit, by the means of the transmission line equation [2]. Because in the circuit, $\bar{U}_2 = 0$ so that the input impedance of the circuit rail is [5, 11]:

$$\bar{Z}_{we} = \bar{Z}_f \cdot \text{th}\bar{\gamma} \cdot l_p \tag{1}$$

Fig. 1 A basic block diagram of track rail circuit



where \bar{Z}_f —wave impedance circuit, $\bar{\gamma}$ —propagation constant.

The results of the analysis of the function of impact given in the work [11]:

$$|\bar{Z}_{we}| = f(l_p) \tag{2}$$

$$tg \phi = Arg \bar{Z}_{we} = g(l_p) \tag{3}$$

The results of the analysis of the function of impact in work [11] were obtained on the assumption that:

- a section of the track is separated from the track by means of insulated connectors on both ends and moving rolling stock takes place from the end of the track circuit to railway pass,
- a place of measuring the change in the module $|\bar{Z}_{we}|$ and $tg\phi$ the input impedance of the track circuit is the beginning of a variable-length l_p ,
- examination of variations module and an argument input impedance $|\bar{Z}_{we}|$ were carried out in the state of fixed operating circuit for sinusoidal signal supply circuit with a frequency that ensures the uniqueness of changes in the studied parameters input circuit,
- a circuit rail is perfectly contained within a l_p of passing the first axle of a vehicle,
- the mathematical model of circuit rail describes the symmetrical long line with distributed parameters uniformly along a section of length l ,
- a rail circuit is powered from an ideal AC voltage source,
- a net traction does not effect on the analyzed rail circuit.

Figures 2 and 3 show the relationship between modulus and argument of input impedance for typical parameters of track subgrade and for two different input signal frequency. Simulation of rail circuit operation was carried out for the typical parameters of the track subgrade for two power frequency: 500 and 1000 Hz. The resulting waveforms are shown in Figs. 2 and 3. The red color is a graph of the input signal $f = 500$ Hz, and the blue color for $f = 1000$ Hz.

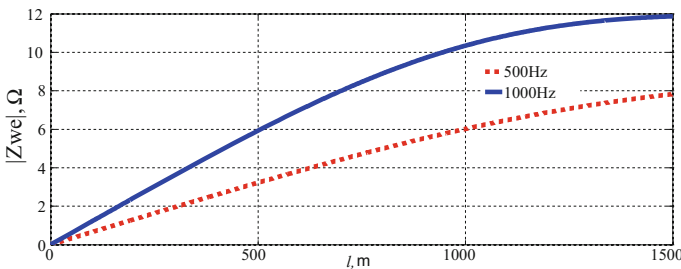


Fig. 2 $|\bar{Z}_{we}|$ impedance modulus change as a function of distance l

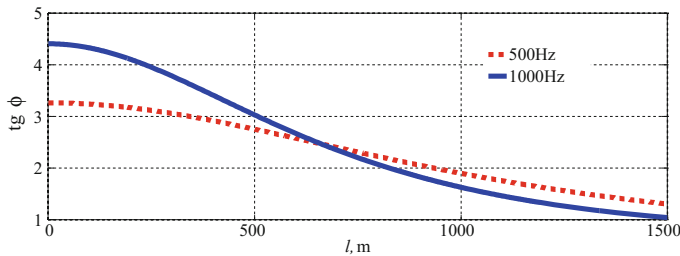


Fig. 3 $tg\phi$ change as a function of distance l

In a real system, a frequency signal should be chosen so that the operation of the measuring system was the best, i.e., to obtain uniqueness impedance measurement. To ensure the safe operation of the monitoring section of track, one channel of measuring system measures the module of impedance, and the second phase shift. Only two correct signals obtained from the measurement of impedance modulus and shift, informing about the whereabouts of the vehicle (basically the first axis) and served on a secure, two-channel measuring and control system helps ensure the correct and actual value of the distance of the rail vehicle from the beginning of the rail circuit.

The conducted simulation analysis [11] runs a function module $|\bar{Z}_{we}|$ and $tg\phi$ of input impedance showed that:

- for track circuits, you can get a clear run function impact $|\bar{Z}_{we}| = f(l_p)$ and $tg\phi = \text{Arg}\bar{Z}_{we} = g(l_p)$ on approaching sections length 1500 m, provided the selection of the frequency of the power supply circuit, according to the border conductance track subgrade,
- for a given parameter, which is the argument of input impedance, designated effective length of the track circuit is greater than for the module of the input impedance (under the same conditions track subgrade). A similar relationship exists for the argument and the module of the wave impedance,
- in the case of simultaneous use of both functions influence should be the frequency of the power supply circuit to choose in order to ensure the uniqueness of changes in impedance modulus, as this parameter is achieved shorter useful length of the track section.

The above results of the research function of the impact $|\bar{Z}_{we}| = f(l_p)$ and $tg\phi = \text{Arg}\bar{Z}_{we} = g(l_p)$ point to the possibility of using the circuit rail, as part of the impact relationship track—a vehicle for self-crossing signaling devices. Another issue that needs separate study is selecting the frequency of the signal power. This is because changes of amplitude and phase angle from changes parameter pf track and the effect of interfering signals from other devices SRK and electric rolling stock.

4 Equipment of Automatic Railway Crossing Signaling Devices

Traffic safety at a level crossing is provided by automatic signaling light with dams of the road, called automatic railway crossing signaling devices (ARCS devices). These devices operate automatically, i.e., without human intervention.

Figure 4a shows a typical layout of equipment ARCS devices on level crossing category B of double-track line. These are [14, 15]:

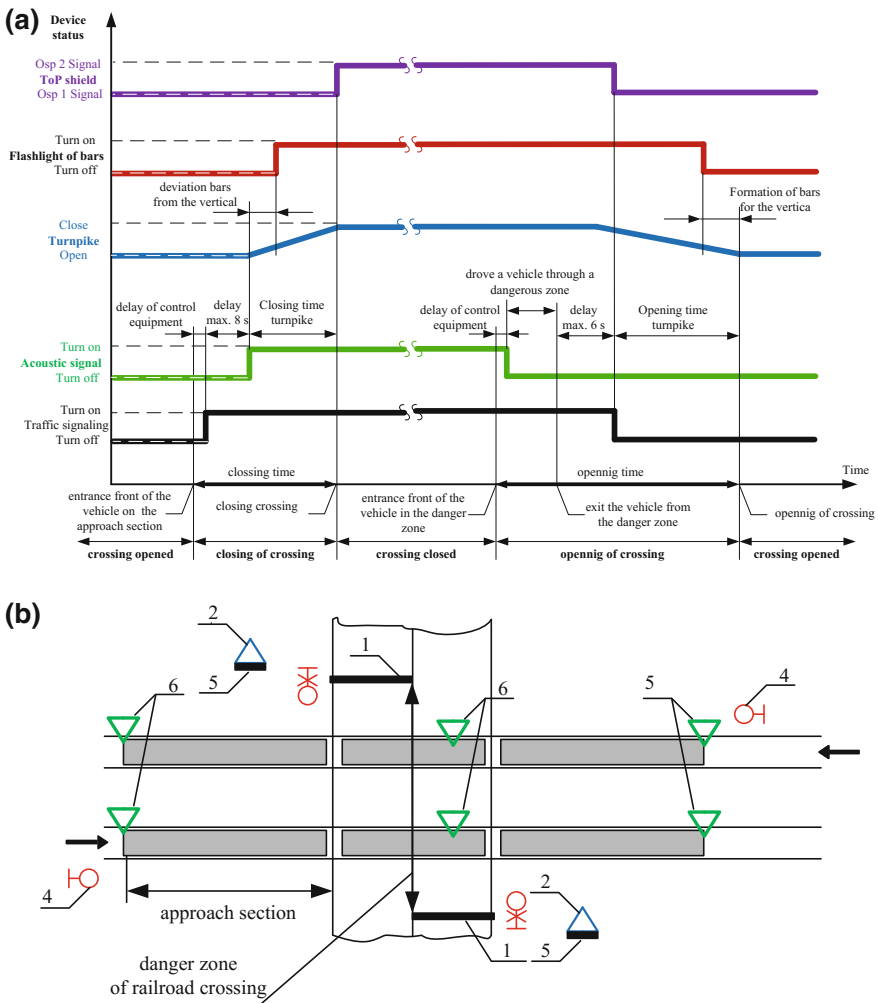


Fig. 4 Equipment of automatic railway crossing signaling devices: **a** time diagram of operation devices, **b** layout of level crossing devices

- dams of road—(1),
- acoustic indication warning drivers—(2),
- optical indication warning drivers—(3),
- track sensors, which detect entry of a rail vehicle on a approaching section—(5),
- sensors track stating occupation and leave the danger zone of a railway crossing through a railway vehicle—(6),
- optical indication warning drivers of rail vehicle, ToP—(4).

With this equipment of one-level railroad crossing in the device shown in Fig. 4, it is possible to provide a warning road users (drivers) before approaching rail vehicle.

4.1 *Warning Users of Roads*

Warning road users are done from the moment of entering of the front of a rail vehicle in the approach section, until the moment when the whole rail vehicle crosses the danger zone. This process consists of following phases [3, 15, 18]:

The process of closing the crossing:

- rail vehicle approaching the crossing, crashing into sensors track approach section, will launch controller of MCD system, resulting in the inclusion of red light on the road signals and turning on sirens sound signal,
- after 8 s delay electric drives that leave the bars dams are activated,
- the deviation of bars dams from the vertical position results in turning on the lights of lighthouse on bars,
- positive verification: closure of the dams in the horizontal position, shining lights on the road signaling, and lighthouse on bars will turn on the signal OSP2 on the signaling ToP.
- If during the warning process a rail vehicle on the second track is detected, the closure process will be continued.

The process of opening of the crossing:

- after max. 6 s from the exit of the rail vehicle from the sensor track of the crossing danger zone, lights on the road signaling are switched off and lifting of bars dams begins,
- turning off lights lanterns on drums takes place when they reach the vertical position,
- a change is also a signal to the Top signaling,
- positive verification: the state of dams in the vertical position, turning off the lights on the road signaling and lighthouse on drums, causes turning on the signal OSP2 on the signaling ToP.

From the point of view of ensuring the safety of road users starting the warning process and closing of the crossing must be made with the appropriate lead time.

This time is defined as pre-warning time t_0 [5, 18]. When calculating this time, it is assumed that the rail vehicle is running at the maximum permissible speed of force on the route of the railway and road vehicles leaving the danger zone passing move at the minimum speed. In [5, 18], it is assumed that the pre-warning time t_0 is

$$t_0 = t_n + t_{zp} + t_{0p} \quad (4)$$

where t_n [s]—the time classes of danger zone of railway crossing, t_{0p} [s]—the delay time to be paid by the MCD controller, for electronic devices shall be 1 s, t_{zp} [s]—the constant value of inventories time, shall be 10 s.

This t_0 time for the station's conditions, according to the decree of the Ministry of Communications [18], cannot be less than 30 s and because of practical reasons not more than 90 s. Thus, the time should be included in the range:

$$30 \text{ s} < t_0 < 90 \text{ s} \quad (5)$$

The general structure of the block diagram under consideration automatic railway crossing devices is shown in Fig. 5a [14, 15]. Figure 5b, c shows the action rule (in the form of conditional expressions *IF the condition THEN is action*) of linguistic model of the closing (Fig. 5b) and the opening (Fig. 5c) process of railway crossing.

4.2 The Dynamic Model of an Automation Railway Crossing Signaling Devices

Modeling of dynamic behavior of discrete event system requires the use of tools for modeling time constraints. One class of Petri nets allowing such modeling is a class of simple time, Petri net [4, 10, 21]. Using the knowledge and experience of the development of reduced net an automatic railway crossing devices, using the methodology of the construction of hierarchical nets—from the particular to the general (bottom-up) [20]—a simple time net for these devices is developed. This net, (Fig. 6), highlights two fundamental processes: the process of moving rail vehicle and the control—supervising process of an automation railway crossing signaling devices.

Symbols of time Petri net structure is shown in Fig. 6, means:

Places:

- p1—away from the station of rail vehicle on the track,
- p2—the rail vehicle is before approaching section,
- p3—the rail vehicle is on approaching section,
- p4—the rail vehicle is on approaching section,
- p5—message “close” crossing devices,
- p6—status of crossing devices is “open”,

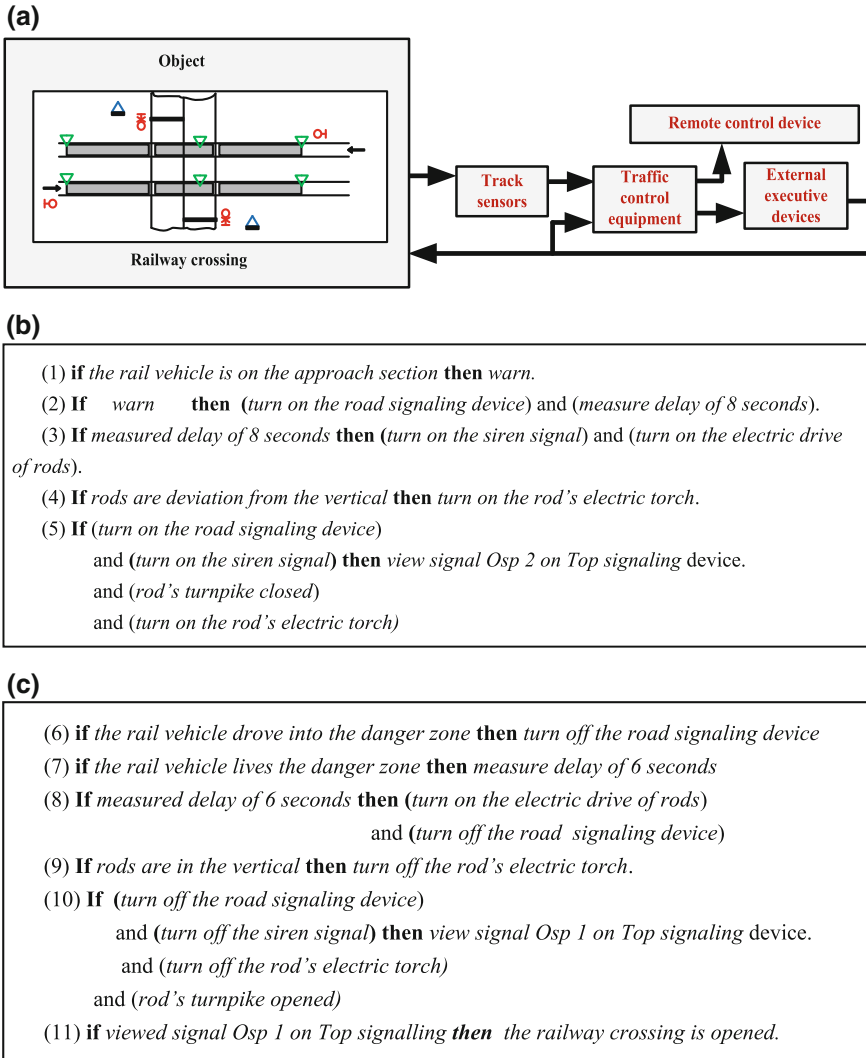


Fig. 5 **a** The block diagram of an automatic railway crossing devices, **b** rules of the process of closing the crossing, **c** rules of the process of opening of the crossing

- p7—entry rail vehicle from the track to the station.
 p8—the rail vehicle is before the danger zone of crossing devices,
 p9—status of crossing devices is “close”,
 p10—the rail vehicle on the track,
 p11—the rail vehicle exit from the danger zone of crossing devices,
 p12—message “open” crossing devices,
 p13—track is free (no rail vehicle on the track).

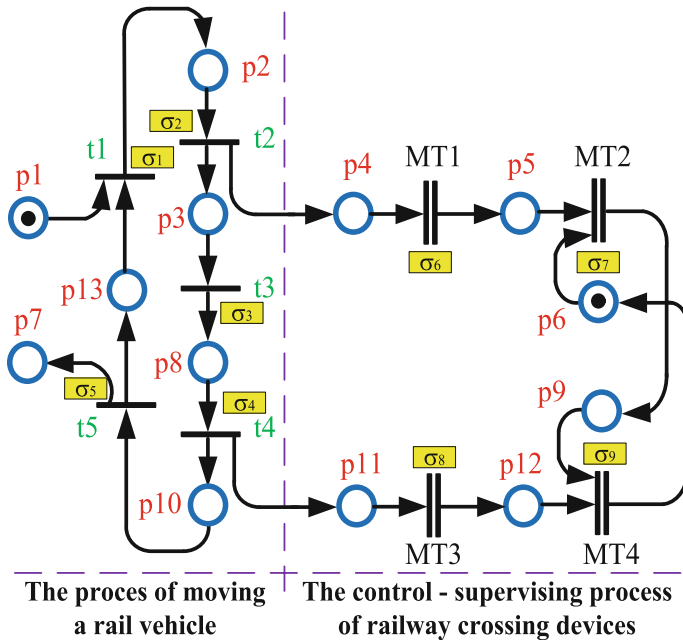


Fig. 6 Simple time Petri net of an automation crossing devices

Transition:

- t1—ride a rail vehicle by track to approaching section,
- t2—moving the front of rail vehicle approaching section,
- t3—drove a rail vehicle through a approaching section,
- t4—drove a rail vehicle through the danger zone of crossing devices,
- t5—leaving the track by a rail vehicle.

Microtransition:

- MT1—detected by measuring system entry rail vehicle to the approaching section,
- MT2—making process of closing,
- MT3—detected by measuring system exit rail vehicle from the danger zone of crossing,
- MT4—making process of opening.

The process of movement of the rail vehicle corresponds to the place p1, p2, p3 and p7, p8, p10 of simple net time—Fig. 6, which is associated with the entry vehicle to the approaching section from trial, entry, and exit from the danger zone of crossing and travel and leaving trail. Places p4, p5, p6 and p9, p11, p12 correspond to the control—executive process of an automation crossing devices. Macrotransitions MT1 and MT3 model subprocesses of acquisition of measurement signals from the sensors track section approaching and passing the danger zone.

Macrotransition MT2 is responsible for closing the passage subprocess and macrotransition MT4 for subprocess of opening run. For transition and macrotransition of this simple time net appropriate static times σ_n are assigned. After these times, transition and macrotransitions are performed [21]. These times are modeling delay times associated with the processing of signals and data.

5 The Hardware and Software Structure of the System

In the case of small MCD systems, which could include controller of ARCS devices, allowance for the detection of a single error, which is the result of damage to the structure of the system, is required. To implement this requirement, the structure of the hardware system with a “vote” and working in the structure of “ k of n ” [14, 15] is adopted. The practical realization of this layer was applied by redundant, dual-channel hardware structure of voting “2 of 2”, as shown in Fig. 7.

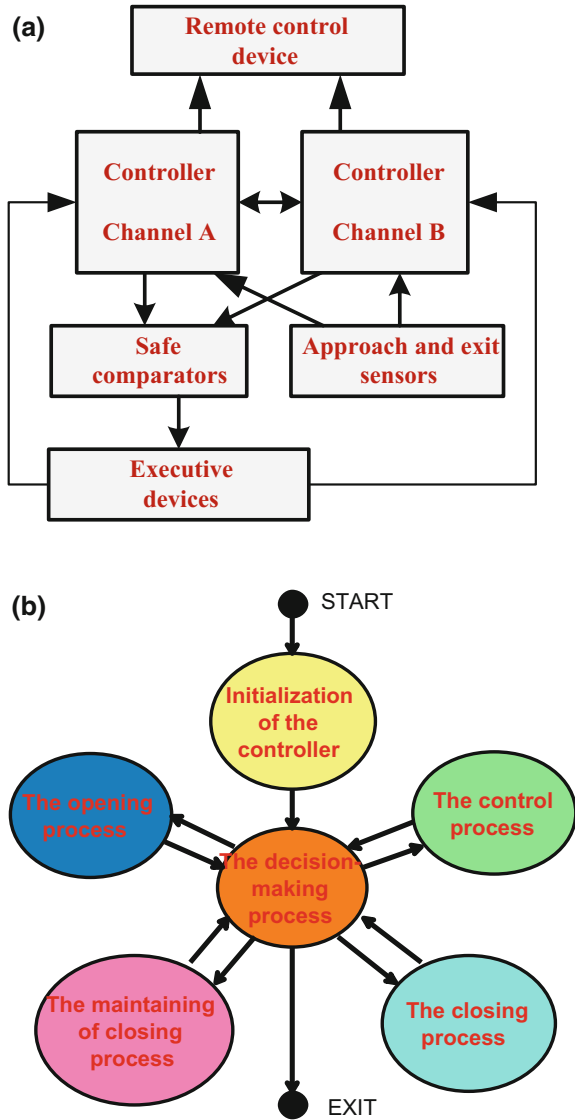
Figure 7a in the illustrated layer structure hardware controller of ARCS devices distinguished:

- two independent sensors of approaching rail vehicle, measuring the time of its directions to pass,
- two independent sensors of stating leave the danger zone for a rail vehicle,
- two modules of independent MCD controllers, performing making decision and executive functions,
- external actuators, warning road users,
- safe comparators of output signals,
- monitoring computer (remote control).

The use of transmission interfaces between modules driver channel A and B can synchronize the work of both channels, and compare internal transition states of variables and time stamps. As illustrated, the hardware structure mirrored all inputs and outputs. Outside control signals of the external equipment of warning road users are generated by the safe comparators. The above hardware structure also allows you to use functions of the remote control system. Overall equipment of controllers of ARCS devices may be implemented in hardware using single-chip microcontrollers, PLCs, or industrial modular computers. The general functional structure of software for the control unit to ARCS devices is shown in Fig. 7b in the form of a diagram of states. As this diagram shows, software highlights the following states: initialization of the controller, the process of decision-making processes and support the closing process control. In the work, [15] provides the possibility of using equipment and methodology state of the encoding process described above in a state diagram graphical programming environment.

For metering and control in critical applications, not only functional implementation of the tasks set is important, but also providing the required level of reliability and safe operation. This requires, therefore, estimating numerical markers of reliability and safety.

Fig. 7 a The hardware structure of MCD system of ARCS devices, **b** the state diagram of the decision-making and executive ARCS devices



6 Reliability Factors of the System

The basic parameter determining the level of reliability and security is the intensity factor λ of the system [5]. At the stage of development of technical guidelines system for critical uses, a minimum of requirements for the reliability and security of the system and its components (modules) should be set. For this purpose, a procedure to estimate factors reliability and safety are used. It involves

decomposition of system on subsystems (modules or devices) consisting of serial-parallel structures. A simplified method of forecasting reliability is also used, which is used for newly designed systems [5]. The analysis of the reliability-developed SPS-dual-channel hardware structure MCD system of ARCS devices was performed with an accuracy of modules, which are autonomous functional blocks. General expression for the reliability of the device or module has the form [5]:

$$\lambda_U = \sum_{i=1}^N N_i \lambda_i \tag{6}$$

where λ_U —intensity factor damage the module or device, N_i —the number of elements i -type, λ_i —the average intensity factor damage of elements i -type.

Reliability structure is presented in Fig. 8.

The estimated intensity factor damage λ_U of the individual modules MCD system of ARCS devices are summarized in Table 1 [14, 15].

Estimated total intensity factor damage λ MCD system of ARCS devices is $3.8 \times 10^{-5} \text{ h}^{-1}$. In the operating phase of MCD systems in addition to the states work correctly states may be referred to as functional states of dangerous and threatening the safety of railway traffic. Security at the system level is defined as an event opposite to the event stay the system in the states of dangerous [5].

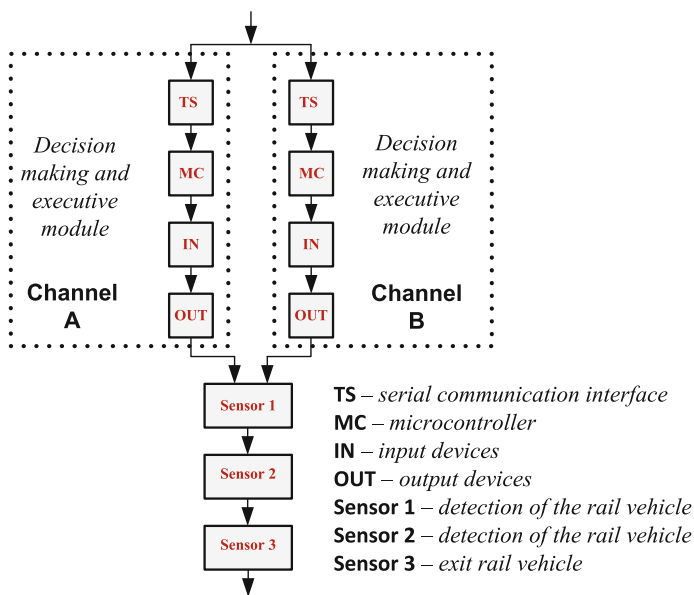


Fig. 8 MCD system reliability structure of ARCS devices

Table 1 Intensity factor damage λ_U of the individual modules MCD system of ARCS devices

Lp.	Name of module	Intensity factor damage λ_U (h ⁻¹)
1	TS	9.20×10^{-6}
2	MK	5.58×10^{-6}
3	IN	6.58×10^{-6}
4	OUT	2.31×10^{-6}
5	Sensor 1	3.58×10^{-6}
6	Sensor 2	3.58×10^{-6}
7	Sensor 3	3.61×10^{-6}

Assuming that the sum of the events stays in the states of the system safe and hazardous exhausts the whole set of events, the safety value S defined by the formula [5]:

$$S = 1 - P_{NB} = 1 - \lim_{t \rightarrow \infty} \left\{ \sum_{i=1}^n P_i(t) \right\} \tag{7}$$

where P_{NB} —the probability of system stay in the set unsafe conditions, $P_i(t)$ —the probability of system stay in a state of threatening security dangerous.

The probability of presence in the set of states of the system secure, and therefore the safety of S can be determined as a function of intensity factor damage λ and response time t for the detection of an error [5]:

$$S = 1 - \lambda t \tag{8}$$

Assuming that the response time of the system to detect an error in damage equal to 0.000278 s and the estimated total intensity factor damage λ developed MCD system is 3.8×10^{-5} , the estimated value of the projected MCD system of ATCS devices security is at $S \approx 1 - 1 \times 10^{-9}$. Due to remaining after testing errors (logical, compiling, and side effects) [5, 23] it is extremely difficult for the software to analyze the reliability. In control systems, one undetected error software in 1000–10,000 lines of source code can be presumed, according to the [5, 23]:

- quality (qualifications and experience) development team,
- quality-possessed computer equipment,
- quality held compiler, and other utilities used to test and run the software,
- quality of the testing process.

Assuming that the disclosure of error during normal operation of the program may appear in the range from 1 month to 1 year, it was assumed that the estimated intensity factor damage λ_S of software is [5] from

$$\lambda_S = \frac{n}{1000 \cdot 0.083 \cdot 8760} \text{ to } \lambda_S = \frac{n}{10,000 \cdot 8760}$$

where n is the number of program lines. Assuming that the software program modules is approximately 1000 lines of source code in assembler language, the

estimated intensity factor damage λ_s of software ranges from $\lambda_s = 1.3 \times 10^{-6}$ to $\lambda_s = 1.1 \times 10^{-5} h^{-1}$.

7 Conclusion

This article presents a modern solution of monitoring approach section of automatic traffic crossing signaling devices mounted on a single-level crossing of roads with the railway. This solution allows the simultaneous measurement of two independent parameters of the rail circuit of approach section. This ensures safe operation of ATCS devices. The effect of continuous measurement of changes parameters of the tail circuit of approach section is the continuous measurement of the distance of the rail vehicle from the danger zone railroad crossing. This affects the stabilization time warning drivers of railroad crossing, which may result in increasing the safety and comfort of level crossing users. You can then talk about constant-time crossing signaling that practically is not yet used in Poland. The second important aspect tackled in the article is the ability to dynamically modeling work these ATCS devices. The primary way this modeling starting from a linguistic model is a dynamic model based on simple time Petri nets. This model not only allows testing of rail vehicles passing on the railway line, but also functional testing ATCS devices. Moreover, on the basis of simple time Petri nets, it was possible to modeling the basic structure of software MCD system resistant bugs. This article proposes a general structure of hardware MCD system to ensure the required level of reliability and safety of these devices. The proposed structure enables the analysis of reliability assurance of the ATCS devices. The most important achievement presented in the article is to present the possibilities of interdisciplinary integration models reflecting aspects: rail traffic on the approach section, functionality and reliability of railway traffic control devices, which are combined into a single model. The integration of these different models allows for a universal approach to a comprehensive analysis of the entire system, not only in the design phase but also during the operation. In addition, such a process modeling enables its easy expansion with new elements for a variety of critical applications that require simultaneous analysis of functionality, reliability, and safety of operation.

References

1. Ali Nur Oz, M., Sener, I., Kaymakci, O.T., Ustoglu, I., Cansever, G.: A tool for automatic formal modeling of railway interlocking systems. In: EUROCON 2015—International Conference on Computer as a Tool (EUROCON), IEEE, pp. 1–4, 8–11 Sept 2015
2. Bolkowski, S.: Teoria obwodów elektrycznych. WNT, Warszawa (2012)
3. CENELEC EN 50128. Railway applications—communication, signaling and processing systems. Software for Railway Control and Protection Systems (2011)
4. David, R., Alla, H.: Discrete, Continuous, and Hybrid Petri Nets. Springer, Berlin (2005)

5. Dąbrowa-Bajon, M.: Podstawy sterowania ruchem kolejowym. Oficyna Wydawnicza Politechniki Warszawskiej, Warszawa (2002)
6. Duda, S.: Modelowanie i symulacja dynamiczna oddziaływań dynamicznych w układzie napędowym elektrycznych pojazdów szynowych. *Eksplatacja i Niezawodność Maintenance and Reliability* **15**(4), 343–348 (2013)
7. Guzowski, S., Michnej, M.: Influence of technological methods increasing surface layer durability on axles fretting wear in railway wheel sets. *Eksplatacja i Niezawodność Maintenance and Reliability* **18**(1), 1–9 (2016)
8. Hei, X., et al.: Modeling and analyzing component-based distributed railway interlocking system with Petri nets. *IEEE Trans. Ind.* **129**(5), 455–461 (2009)
9. Hruz, B., Zhou, M.C.: Modeling and Control of Discrete-event Dynamic Systems with Petri Nets and other Tool. Springer, Berlin (2007)
10. Jacobsen, L., Jacobsen, M., Moller, M.H., Srba, J.: Verification of timed arc Petri nets. *Lect. Notes Comput. Sci.* **6543**, 46–72 (2011)
11. Jakubas, W., Zajac, W.: Indukcyjne oddziaływania zakłócające pojazdów szynowych na obwody torowe. Praca zbiorowa pod redakcją A. St. Jagiełły *Elektrotechnika w zastosowaniach trakcyjnych*, Monografia nr 450, Politechnika Krakowska, s. 167–177 (2014)
12. Lebedevas, S., Dailyka, S., Jastremskas, V., Vaičiūnas, G.: Research of the rational operational load of diesel locomotives. *Eksplatacja i Niezawodność Maintenance and Reliability* **16**(4), 545–553 (2014)
13. Lin, J., Asplund, M.: Comparison study of heavy haul locomotive wheels' running surfaces wearing. *Eksplatacja i Niezawodność Maintenance and Reliability* **16**(2), 276–287 (2014)
14. Mielnik, R.: Petri nets in the engineering project of measurement-control systems in critical applications. Praca zbiorowa pod redakcją A. St. Jagiełły – *Elektrotechnika w zastosowaniach trakcyjnych*, Monografia nr 450, Politechnika Krakowska, s. 295–308 (2014)
15. Mielnik, R.: Synteza sterownika urządzeń sygnalizacji przejazdowej z wykorzystaniem sieci Petriego oraz modułu Statecharts środowiska LabVIEW. Materiały konferencyjne XVI Ogólnopolskiej Konferencji Naukowej Trakcji Elektrycznej, SEMTRAK 2014, Zakopane, październik 2014, Wydaw. PiT, s. 409–418 (2014)
16. Płaczek, M., Buchacz, A., Wróbel, A.: Use of piezoelectric foils as tools for structural health monitoring of freight cars during exploitation. *Eksplatacja i Niezawodność Maintenance and Reliability* **17**(3), 443–449 (2015)
17. Qiang, W., Xin, Z., Yan, W., Naizhang, F., Yi, S., Rail defect detection based on vibration acceleration signals. In: *Instrumentation and Measurement Technology Conference (I2MTC), 2013 IEEE International*, pp. 1194–1199, 6–9 May 2013
18. Rozporządzenie Ministra Transportu i Gospodarki Morskiej z dnia 26 lutego 1996 r. w sprawie warunków technicznych, jakimi powinny odpowiadać skrzyżowania linii kolejowych z drogami publicznymi i ich usytuowanie. *Dz. U.* Nr 33, poz. 144
19. Szkoła, M.: Assessment of reliability, availability and maintainability of rail gauge change systems. *Eksplatacja i Niezawodność Maintenance and Reliability* **16**(3), 422–432 (2014)
20. Szmuc, T., Szpyrka M.: Formal methods—support or scientific decoration in software development? In: *Mixed Design of Integrated Circuits & Systems (MIXDES), 2015 22nd International Conference*, pp. 24–31, 25–27 June 2015
21. Szpyrka, M.: Sieci Petriego w modelowaniu i analizie systemów współbieżnych. WNT Warszawa (2008)
22. Winiecki, W.: Organizacja komputerowych systemów pomiarowych. Oficyna Wydawnicza Politechniki Warszawskiej, Warszawa (2006)
23. Xinhong, H., Lining, C., Weigang, M., Jinli, G., Guo, X., Automatic transformation from UML statechart to Petri nets for safety analysis and verification. In: *Quality, Reliability, Risk, Maintenance, and Safety Engineering (ICQR2MSE), 2011 International Conference on*, pp. 948–951, 17–19 June 2011
24. Xiukun, W., Hai, L., Yong, Q.: Fault diagnosis of rail vehicle suspension systems aby using GLRT. In: *Control and Decision Conference (CCDC), 2011 Chinese*, pp. 1932–1936, 23–25 May 2011

Research of Cohesion Principle in Illuminations of Monumental Objects

D. Mazur, H. Wachta and K. Leśko

Abstract The article presents the analysis of the possibilities for fulfilling the cohesion principle of images in architectural sites illuminations. Computer simulation was done on the basis of the Azkuna Zentora culture centre in Bilbao; the simulation involved imaging the building geometry in the 3 ds Max graphical programme. A proposed illumination concept was designed, for which visualisations showing concept effects and illumination distribution were done, on the basis of which the possibility of acquiring cohesion between day and night images was analysed for the given object.

Keywords Illumination objects · 3 ds Max · Architectural objects · LED light

1 Introduction

Illumination of architectural objects [1, 2] aims to expose the play of light and shadows that are interesting from the perspective of architectural elements—ledges, columns, tympanums, avant-corps, etc., that are characteristic for particular styles in architecture over different centuries. Due to this fact, illuminations are most often made for historic sites, in order to distinguish them among other buildings. In order for illumination to comprise an actual embellishment of an object that does not interfere in admiring architecture, certain rules of illumination [1] need to be followed. The principle of illuminated object cohesion may be considered as a guiding principle.

D. Mazur (✉)

Department of Electrical and Computer Engineering Fundamentals,
Rzeszow University of Technology, Rzeszow, Poland
e-mail: mazur@prz.rzeszow.pl

H. Wachta · K. Leśko

Department of Power Electronics, Power Engineering and Complex Systems,
Rzeszow University of Technology, Rzeszow, Poland
e-mail: hwachta@prz.edu.pl

© Springer International Publishing AG 2018

D. Mazur et al. (eds.), *Analysis and Simulation of Electrical and Computer Systems*, Lecture Notes in Electrical Engineering 452,
https://doi.org/10.1007/978-3-319-63949-9_26

Illuminated object cohesion is understood as the possibility to view and perceive an object from a given direction of observation [1] as a whole. This definition implies that an object can be seen without unclear or confusing areas, which could seemingly alter the real architectural layout that appears during the daytime.

The cohesion principle is a fundamental principle of illumination. Following this principle comprises a basic condition determining whether an image will be viewed positively by an observer. The main aim of this principle is to find such illumination concept that would provide the possibility of perceiving night view of the whole object or its illuminated facades regardless of the assumed illumination method [1], so that the image would be most similar to the one seen at daytime.

The flood method of illuminations by its definition meets the conditions of the cohesion principle—even illumination of the whole elevation implies that the image is almost identical with the daytime image; the only difference is dark sky.

The problem of the cohesion of daytime and night images is definitely easier to encounter when doing illuminations by means of the point or point-flood methods. The whole image of an object consists of single elements as well as light emphases. It is possible, for such layout of light spots, that they are too distant and there will not be cohesion between them. This problem can be solved by selecting and arranging frames in such a way that a light spot has a bigger size than the distance between spots.

There are many examples of fulfilling this principle; one of them is the illumination of the building of Wanda Siemaszkowa Theatre in Rzeszów (Fig. 1).

Illumination of this object is made with the flood method, and thus cohesion between object images occurs by default. Roof of the building is also lighted, which is often omitted in illuminations.



Fig. 1 An example of fulfilling the cohesion principle in object illumination—Wanda Siemaszkowa Theatre in Rzeszów

Fig. 2 An example of the cohesion principle violation in illumination—Rzeszow Castle



There are also illuminations in which the element of image cohesion was omitted. It happens, for example, because of choosing the point illumination method, but often also because of intentional choice not to lighten the whole object, but only its part. An example of this is the illumination of the Rzeszow Castle, which relies on exposing only the tower before the front wall of the building, which remains unlit. Location of the building causes that by greater observation distance one can see only the tower, which from the observer's perspective may comprise a separate object (Fig. 2).

2 Application of the Cohesion Principle with Reference to the Concept of Real Object Illumination

A suggested illumination for the object of the culture centre in Bilbao was developed in the work. The building does not currently have illumination and negligible amounts of light that fall on the building elevation come from street lights. Due to large size of the structure, one may speak of cohesion from two perspectives: macro and micro. The first one implies illumination of the elevation in such a way that every level of the building is well seen at night so that the observer could specify



Fig. 3 Immission light—view on the front of the building

general dimensions and sizes of the structure. The micro-perspective aims to light more the decorative elements (small columns, reliefs, etc.)

Figure 3 shows the front of the culture centre building. One can see that the structure is poorly visible, especially its upper parts—details above the windows of the second floor are so dark that an observer cannot see clearly those elements, which would occur at daytime. The highest level of the building is not visible from this perspective, which causes that one can receive incomplete image of the structure, which shows a lack of cohesion of day and night images in the macro perspective.



Fig. 4 Immission light of the building—view on the south-east corner of the building

The view of the building from the south-west side, presented in Fig. 4, clearly shows the influence of the lack of building illumination on the possibility of structure image reception. On the western side, negligible amounts of light on the elevation at ground floor level come from park fittings located on the pavement; lack of street lights causes that upper parts of the building are poorly visible or not visible at all—especially to the highest levels of the structure. On the south side, in contrast, darkened glass level with completely switched off interior light makes the impression that the taller level does not comprise integrity of one structure with lower levels.

Such an analysis enables to state that by applying only street lights the building of the culture centre is not fully visible at night—there is no cohesion with the daytime image of this structure, which in case of such an important and architecturally intriguing building, is important. In order to see the whole range of aesthetic values of the building proper illumination that shows undistorted, real shapes and dimensions of the building together with its details, needs to be done.

3 Development of Architectural Structure Special Model

A computer model, that reflects geometry of a given architectural structure, was designed in 3 ds Max graphical programme. On the basis of photographs and materials available on the Internet, general dimensions of the structure and details were determined, and then the process of computer modelling was initiated by using functions available in the programme [3, 4]. Elevations of selected walls of the building computer model were presented in Figs. 5 and 6.

Due to large size, the structure is distinguished by regularity and recurrence of elements. In every corner of the building there are large, identical towers. The front side of the building has a form of a concave arch located in the north-eastern corner. Above the three basic levels, there emerges a glazed superstructure, in which there are brick rooms protruding from inside the building.

When comparing Figs. 5 and 6 one can notice differences between particular levels of the structure on particular walls. The ground floor level is distinguished by

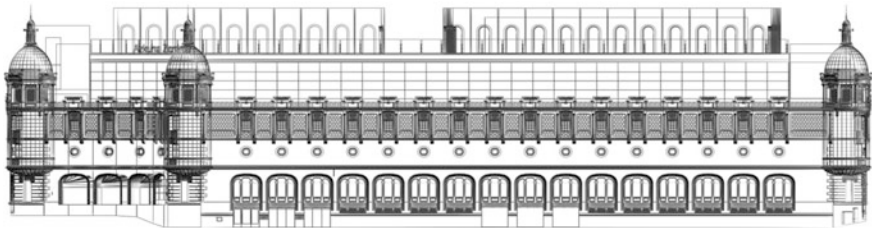


Fig. 5 Computer projection of the structure geometry—north side elevation

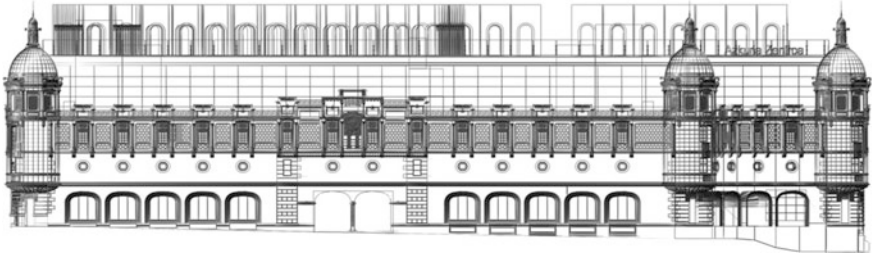
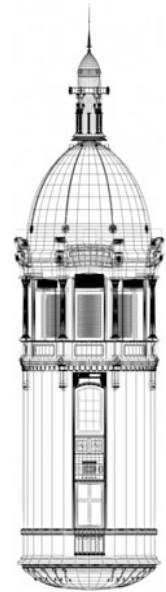


Fig. 6 Computer projection of the structure geometry—eastern side elevation

Fig. 7 Computer projection of the tower geometry



a variety of windows on each wall as well as height due to the topography. The level of the first floor on each side is almost identical, on the elevation brick sheathing there are small round windows in different number and on each wall. In the middle of the eastern and western walls, there are longitudinal windows in the concrete background. There also occurs similarity on the height of the second floor.

The towers in the corners that rise from the level of the first floor are important elements of the structure. The tower is distinguished by round shapes and a large amount of small, recurring elements. Projection of the geometry was presented in Fig. 7.



Fig. 8 Division of the building form into levels on the stage of creating structure form in graphical environment

4 Elements Comprising the Cohesion Principle

In terms of architecture, the building may be divided into levels, as shown in Fig. 8. This division can be used in the process of creating illumination from the perspective of fulfilling the cohesion principle, considering, namely, which elements are so important that their lack in the night view would cause that the image would not present the same elements as the day view.

In the night image, it is the most difficult to see upper parts of the building, marked in Fig. 8 as level P5. Due to their remoteness from the brink of the level P4 they often become not visible, depending on the observation perspective, therefore their proper illumination is significantly important so that the night view would be a real view. The possibility to view the building as a whole implies cohesion in the macro perspective. More intense lighting of all the details is equally important so as to provide cohesion between images in the micro-perspective. On the basis of the analysed structure, it is especially important in the case of details of the building lower levels. The level P4 is distinguished by the greatest amount and variety of details, but due to their high location and small sizes some details (small reliefs etc.) are difficult to recognise even at the daytime.

5 Visualisation of the Assumed Illumination

After projecting the geometry of structures in the computer model and attributing real materials with their characteristic coefficients of reflection [5], development of the illumination project was begun. The illumination for Azkana Zentroa makes use



Fig. 9 Visualisation of the illumination concept—view on the building frontside

of both point and flood method elements. For the assumed concept, renders were made in order to visualise the illumination effects.

When analysing Fig. 9, one may notice that each building level is clearly visible, which proves fulfillment of the cohesion principle in the macro perspective. In the micro-perspective, one can see the difference between facades of ‘roofs’ above windows of the level P4. In the assumed concept, they are darker than other elements of this level.



Fig. 10 Illumination concept visualisation—view on the south-eastern corner of the building

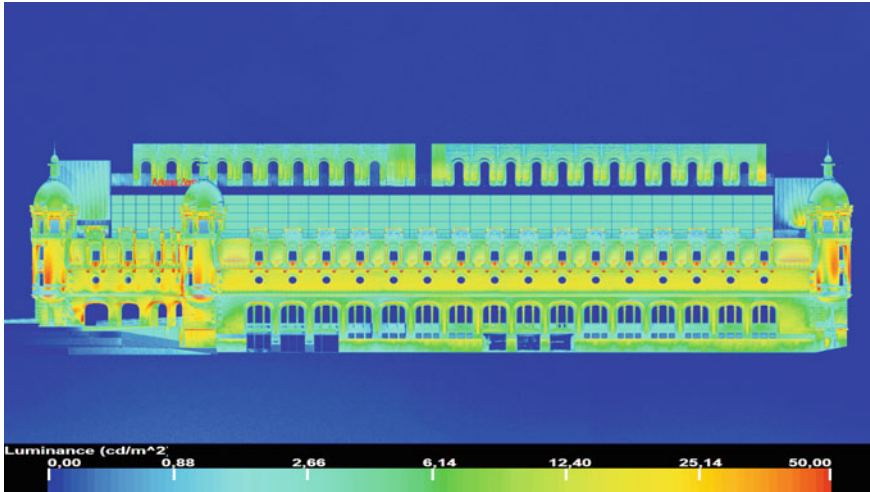


Fig. 11 Exemplary illumination distribution for the presented illumination concept—the northern wall of the building

In corner views, one can notice the influence of lighting columns placed in front of the elevation. When viewing, under low angle, the southern wall (Fig. 10) the view of the P4 level comprises of frequently recurring, brightly lit columns, which in result makes an impression of more intensively lit elevation than the perpendicular wall.

For the suggested concept renders were also made, in order to acquire illumination distributions on the building elevations; illumination levels of particular floors of the building are kept on each wall on the same level and according to the guidelines [6]. An exemplary illumination distribution is presented in Fig. 11.

When analysing illumination distribution in Fig. 11 one may notice the difference in illumination levels between the building floors. Elevations of particular levels of the building are distinguished by illumination of a lower level than the occurring details and their more intensive lighting introduces elements of the point method. One can also notice that the walls are evenly lit by means of the flood method; therefore, there occurs cohesion between night and day views of the illuminated structure.

6 Equipment Specification

Several types of lighting fittings were used for the presented illumination concept, depending on the mounting location of the equipment, as well as the aimed lit elements. All the fittings that were used are LED light sources. Vast majority of the applied fittings are linear fittings used (Figs. 12, 13) both to light the building

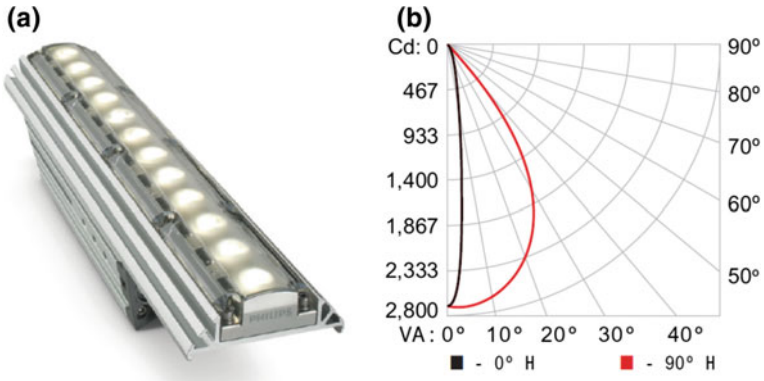


Fig. 12 Philips eW Graze MX Powercore lighting fitting **a** fitting view, **b** curve of intensity distribution [8]

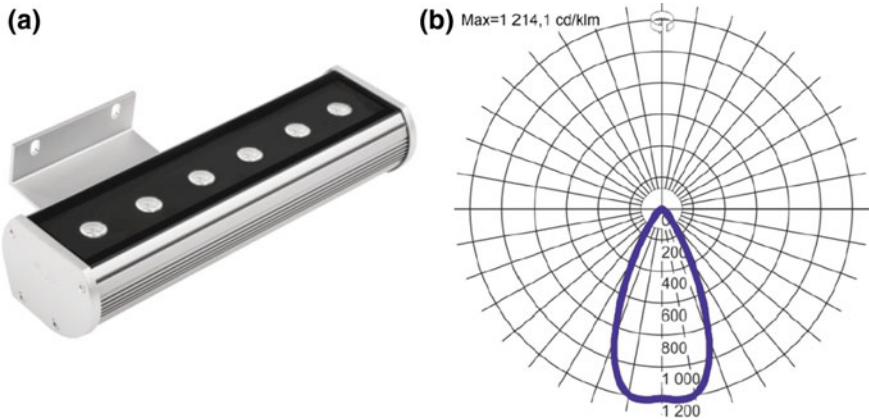


Fig. 13 Lighting fitting used to light the P4 level—LUG Modena LED **a** fitting view, **b** curve of intensity distribution [9]

elevation (fittings with wide light intensity distribution) as well as to emphasise light features (feature with narrow light intensity distribution). Point fittings for lighting the towers were also used. The superstructure of the building as well as the tower dome are lit by compact floodlights.

Because the aim of the illumination concept was to use fittings close to elevations (ledges, windowsills, etc.), in order to avoid the phenomenon of light immission [7], the sizes were an important element regarding the choice of fittings. The liner Philips eW Graze fittings are characterised by compact sizes. An additional advantage of this model is the possibility to use them as earth fittings. Basic technical and photometric parameters are presented in Table 1.

Table 1 Parameters of Philips eW Graze MX Powercore [8]

Parameter		Value	
Beam angle	–	10 × 60	°
Luminaire power	<i>P</i>	15	W
Colour temperature	<i>T_c</i>	2700	K
Luminous flux	<i>φ</i>	645	lm
Dimensions			
<i>Height</i>	<i>h</i>	69	mm
<i>Width</i>	<i>w</i>	305	mm
<i>Depth</i>	<i>d</i>	71	mm
Weight	<i>m</i>	1	kg

An important role in the presented illumination concept is also played by another linear fitting—LUG Modena LED. Its task is to light decorations on the P4 level. The fitting power is 28 W, and the luminous flux is 2260 lm. The mounting method of the fitting enables to attach it to the wall and ensures its shift from target lit elevation, which in this case eliminates the problem of mounting fittings on ledges.

The proposed illumination makes use of altogether 1520 lighting fittings, the total input power of which equals 37,534 kW, which gives an average fitting power of about 25 W. Light sources in the applied fittings have influence on the total amount of the input power. Application of only the fittings that make use of the LED technology enabled to significantly decrease the value of power, which is of great importance when considering how many fittings the proposed concept uses.

7 Conclusions

Cohesion of illuminated structure night view with its day view is greatly important from the perspective of a viewer. At daytime, the structure is fully and evenly lit with sunlight; therefore, illumination should be chosen in such a way that the night image would resemble the day image as much as possible and that the image would present the real image of a structure without any distortions and dark areas. Frequently, however, this aspect is omitted in the existing illuminations by, e.g. lighting only certain part, and not the whole object, or by placing impressive lighting over regularity of structure illumination.

The created illumination shows the possibility to meet requirements of the main illumination principle—the principle of image cohesion for a high and large area building with numerous protruding, interesting architectural elements. The presented concept was made by means of the mixed method—linear fittings placed in close proximity from elevation lit it evenly, not causing light immission, as well as minimising the risk of discomfort glare occurrence. All decorations were additionally lit, and because of their large number and regularity of occurrence there appears a certain sort of a ‘rhythm’. Lighting only those elements (e.g. columns)

would cause lack of cohesion, because their width, and, therefore, light spot, would have smaller size than the distance between the elements.

When talking about cohesion in the micro scale one may notice a slight discrepancy between facades of elements above windows of the second floor. All elements that protrude before the facade are lit, and thus general shapes and sizes are clearly visible; and therefore, there is not a big influence on image reception. When wanted to lit the façade one should add an additional fitting, but the problem would be the issue of its location as well as the fact that more visible protruding elements would be distinguished by even greater illumination level, which would lead to exceeding recommended values [7].

An additional problem, considering day and night time image cohesion, are large glazed areas. Lighting such areas from outside is pointless, and on the other hand, leaving such elements not lit implies lack of cohesion. The proposed illumination concept implies soft lighting of the glass area from inside, with the interior utility lighting turned off, because incidental switching on the light might cause disharmony, which leads to neglecting conditions set by the principle of image ordering [1]. The aim of such illumination method is to separate sheets of glass from metal frames, and, therefore, to avoid perception of the structure as one big glazed area.

References

1. Żagan W.: Iluminacja obiektów. Oficyna Wydawnicza Politechniki Warszawskiej (2003)
2. Ratajczak J.: Oświetlenie iluminacyjne obiektów architektonicznych. Wydawnictwo Politechniki Poznańskiej (2009)
3. Krupiński R.: Modelowanie 3D dla potrzeb iluminacji obiektów. Oficyna Wydawnicza Politechniki Warszawskiej (2011)
4. Murdock K.L.: Autodesk 3ds Max 2014 Bible. Wiley (2013)
5. PN-90/E-01005.: Technika świetlna. Terminologia. Wydawnictwa normalizacyjne Warszawa (1991)
6. Raport CIE 094-1993, Guide for Floodlighting
7. Leszczyńska H.: Zanieczyszczenie - imisja światłem. Technika świetlna'09 (2013)
8. Koroglu, M.T., Passino, K.M.: Illumination balancing algorithm for smart lights. IEEE Trans. Control Syst. Technol. **22**(2), 557–567 (2014)
9. Bimber, O.: Projector-Based Illumination and Display Techniques. Technical University of Munich (2007)

Analysis and Simulation of Internal Transport in the High Storage Warehouse

J. Krystek and S. Alszer

Abstract The transport plays a growing role in the integrated logistics management of semifinished products and components flow. For manufacturing companies, it is important to maximize the use of production resources and optimize the process in terms of both production costs and time. The use of specific means of transport and correct organization of material flow are fundamental in order to assure continuity of production. The exemplary means of transport, their characteristics, and purpose are presented in this article. One of the elements included in the production systems and used to reduce the number of unplanned downtimes are warehouses. They may be small structures placed near workstations, storage buffers along the supply chain, or the separate buildings with a height up to several tens of meters. The choice of storage solution depends on both the profile of the industrial company and the destination of goods storage area. Due to highly complicated processes of warehouses design and management, the computer systems are currently used. These systems support the processes and allow to carry out necessary simulations. An example of using a support application, a discussion of the conducted simulations and analysis of result are presented in the final part of this paper.

Keywords Internal transport · External transport · High storage warehouse · Transport resource

J. Krystek (✉) · S. Alszer
Institute of Automatic Control, Faculty of Automatic Control,
Electronics and Computer Science, Silesian University of Technology,
Gliwice, Poland
e-mail: jolanta.krystek@polsl.pl

S. Alszer
e-mail: sara.alszer@polsl.pl

1 Introduction

Growing customer demand and sublime orders force volatility of production assortment; therefore, production currently is a highly specialized production. The purpose of manufacturing plants is to produce in the shortest possible time high-quality products, assuring the company the highest income. This is the reason, why companies are constantly evolving; also they are looking for methods that allow for better capacity utilization in order to increase the productivity of the system. In this connection, it has to be considered aspects directly related to the production system, such as limited efficiency of machines and equipment, sequence restrictions associated with process route and selected manufacturing technology. There should be also taken into account requirements imposed by customers: execution of orders in time, high quality and appropriate prices of the final products. Therefore, the problem of material flow planning in the system is one of the basic tasks of company management. The reason is that shortening the path, needed to provide the semifinished products in the right place, has a direct impact on the shortening delivery times and reducing manufacturing costs. Thus, in recent years a transport area has become an important point considered while formulating a strategy for companies. The transport issues and a shipping strategy should be thoroughly analyzed before production. In addition, found solutions should meet both technical and organizational constraints.

2 Transport System in Manufacturing Plants

From the perspective of companies, it is important to provide just in time the final product to customers, to fulfill the obligations of the agreement and to meet customers' expectations. For this purpose, it is necessary to ensure an efficient system of external transport, which takes place by means of long-distance transport with unlimited range. On the other hand, in order to achieve high production efficiency and to reduce production costs and time, also the organization of internal transport should be considered.

Transport, which is directly associated with production, provides the flow of raw materials and semifinished products between workstations, sections and departments situated close to each other and within these different production shops. In turn, the second branch of internal transport concerns the following issues: storage, warehousing, and service of warehouses with raw materials, semifinished, and finished products. This branch of transport is also associated with external transport. The classification of transport is presented in the Fig. 1.

The detailed characterization of the internal and external transport with examples use of transport resources will be presented in the following sections.

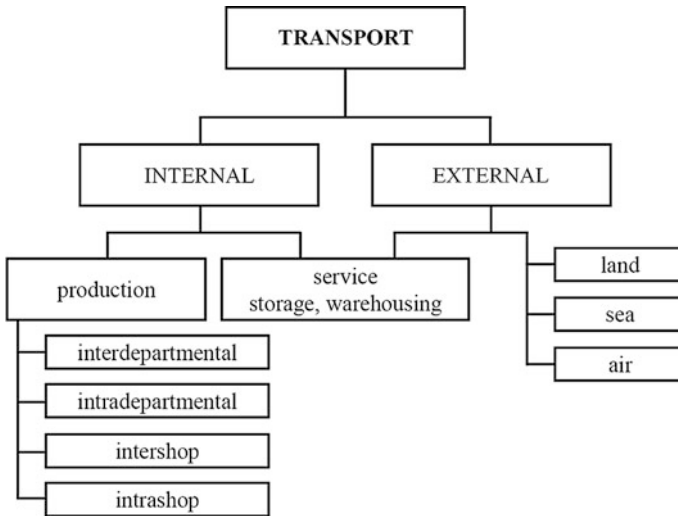


Fig. 1 The classification of transport

2.1 *The External Transport*

Products delivery on the domestic or global market forces company to develop an external transport system. This type of transport can be carried out both by its own means of transport and by transport providers or forwarding services. Regardless of the type of transport resources, it is important to optimize the use of vehicles working time, mileage, and payload and to protect products during transport. Below are presented the possibilities and limitations of each branch of external transport [1]:

- rail transport—advantages: possibility of mass transport, vast rail network, high spatial accessibility, regular and rhythmic connection, profitable transport time, disadvantages: products, which are sensitive to high levels of vibration and shock, are not suitable for carriage by rail, because there are not guaranteed safe conditions for transport, there is also a high risk of transported products theft;
- road transport—advantages: the highest density and coherence of car network, profitable transportation time, the ability to deliver goods directly to customers, disadvantages: high transport costs;
- maritime transport—advantages: ability to mass transport, worldwide coverage of sea routes, disadvantages: low operating speed of ships, problem with frequency and punctuality of connections, products sensitive to moisture are not properly secured, long travel time;
- inland waterways—advantages: possibility of mass transport, disadvantages: problems with the regularity of transport, delivery times, availability of space and safety assurance of products;

- air transport—advantages: ability to transport small production batches, requiring specific conditions during transport, the relatively short transport time, high security of transported products, disadvantages: need to ensure the delivery means of transport, high transport costs.

The aspects mentioned above, characteristic to the external transport resources, illustrate some of the possible advantages and disadvantages of use of these means of transport. The choice of a particular branch of transport, used in the company, is largely determined by a thorough analysis of transport costs and profits calculation. As mentioned earlier, the external transport system ensures the distribution of manufactured goods, but reaching the final stage of production requires prior planning of the internal transport system.

2.2 The Internal Transport

The term internal transport stands for all activities related to the movement of products within the area of the manufacturing plant or company [2]. Each of the materials is valuable only if it is available at the right time and in the place, where it is currently needed [3]. This is the reason, why the issues of internal transport are mainly important for distribution and production rationalization.

The internal transport infrastructure determines the general means of technological transport and auxiliary transport resources. These resources allow the movement of products during the manufacturing processes and storage, which are executed as a part of logistic processes [4]. The means of technological transport are used during the movement and distribution of materials, semifinished, and finished products. These include: hoist operating, cranes, trolley trucks, conveyors, chargers, manipulators, industrial robots, palletizes, and depalletizes.

The most popular and the most commonly used means of internal transport are industrial trolley trucks. This is due to their high flexibility, low occupation of the surface, and the relatively low investment costs [5].

In turn, the auxiliary devices allow efficient movement of cargo, using the resources of technological transport. These devices can be generally used repeatedly and enable mechanization and automation of ongoing operations. They also provide adequate security of products, as well as the preservation of safe working conditions [6]. Among the auxiliary devices can be distinguished: freight containers, pallets, pallet collars, transport and storage boxes/containers, bridges and loading platforms, warehouses-feeders empty pallets, devices for securing cargo units.

Optimization of the production is not possible without proper organization of internal transport, which should be adapted to the type of the executed processes. By efficient managing of materials and semifinished products flow, it can be understood, among other things, moving the right amount of these elements on the shortest possible routes, while making maximum use of means of transport. At the same time, the least possible consumption should be ensured. The next section will present some principles regarding the organization of internal transport.

2.3 The Principles of Internal Transport Organization

The development and organization of internal transport in a company should be carried out simultaneously with the design of the entire manufacturing plant. It should take into account also the size of this plant and the type of process. Proper organization of internal transport aims to provide continuous, unidirectional flow of materials and other components by all workstations, as well as storage and control stations [4].

It lists several important aspects related to the preparation of transport infrastructure and affects subsequent the capacity of the system:

- avoid crossing of transport routes on one level;
- use gravity to transport from a higher to a lower level;
- striving to the shorten transport routes;
- adaptation of loading units to the possibility of transport resources.

The rapid growth of production, high volatility of orders, and the scope and number of provided services require the company systematically improve the organization of internal transport and modernization of existing infrastructure. Usually, this is connected with the desire to reduce or eliminate manual operations of means of transport by partial or complete automation of activities performed by machinery and devices. But it is necessary to bear in mind that, in some cases, use of simple and inexpensive manual transport resources can bring greater benefits than automated solutions. The issue of organization of internal transport infrastructure will be discussed in more detail in the next section.

3 Storage in System Production

The storage, according to information contained in [7], is defined as a functional and organization unit, which is designed to store materials and goods in a separate building storage space for use in the future. The storage process, in accordance with polish norm [8] is meant in turn a set of activities that are related to temporary: intake, storage, completing, migration, maintenance, keeping a record, controlling, and issuing of material goods. The diversity of listed activities also points out how the warehouse is organized. However, regardless of the adopted definition of storage, storage is an important link in the logistics of production. A storage space can be both a place of delivery, receipt, or goods distribution, as well as a kind of buffer, ensuring continuity of process. Managing the storage process may favorably affect the profits of the company, provided that it ensures proper management of goods flow in the warehouse. It is important to take into account that reducing the cost of storage leads to lowering logistics costs. In the absence of transparent and clear organization of material flow and warehouse management, the company is exposed to additional costs. These costs are related, inter alia, to part-filling the

storage space or slow search for the desired storage space. Therefore, even during production planning, structure, and organization of warehouses should be considered.

3.1 The Structure and Organization of the Warehouses

In order to operate warehouses, various types of transport resources and equipment for the mechanization of warehouse operations are very often used. This is to avoid high costs of operating the warehouses, on the way to make the best use of storage area. In turn, organization and management of warehouses are based on modern management tools to support the activities of storage. Information systems play an important role in warehouses management, decision making and supervising work of stationary and mobile installation, devices, handling equipment, and other elements of the warehouse.

The organization of warehouses should be enough thought to get a maximum storage efficiency, determined in relation to the surface. The measure of this efficiency is generally square meter, based on which all calculations of storage costs are conducted. Thus, it appears advisable to use all three dimensions of space, to ensure the best effects of goods managing. Resource efficiency is generally recognized to one of the spatial dimensions—height. It gives the ability to store goods at high altitudes. Simultaneously maximum filling of storage space at different levels is provided. If the height of storage warehouse is between 7.6 and 40 m, then a storage warehouse is called a high storage warehouse [9].

The definition of high storage warehouse has not yet been legally regulated, but the term of this type of warehouse refers to a warehouse, where shelves create supporting structure for housing components (walls and roof). If additional storage area is supported by automatic stacker cranes, the storage is called automatic high storage warehouse. The products are stored on or in special transport units, for example, on pallets or in containers, on shelves of specialized racks. The storage area is coupled to individual storage zones by means of the conveyor system. A warehousing process usually consists of a number of subprocesses, including following zones [10]:

- receiving—space of a warehouse system for incoming material flows [11], includes the physical unloading of incoming transport, checking and updating the inventory record and also unpacking, repacking, preparing of loading units for storage and so on;
- storing—the largest surface area of warehouse for storing goods on shelves, equipped with handling road, allowing the movement of products, storage is concerned with organization of materials, held in a warehouse in order to achieve high space utilization and facilitate efficient material handling [11];
- picking—intended for the preparation of orders strictly according to customers requirements, picking products to fill customer orders is one of the most

important activities in the warehouse, due to its high contribution (about 55%) to the total warehouse operating cost [12]. It involves the process of clustering and scheduling the customer orders, assigning stock on locations to order lines, releasing orders to the floor, picking the articles from storage locations, and disposing of the picked articles [13];

- packing—separate function within logistics, where a shipping material can be entered in a packaging dialog at any time and a handling unit can be subsequently created. All packing functions are available to pack, repack, or unpack a handling unit. A handling unit can itself manually be packaged or automatically generated upon goods receipt or in the packing zone of a warehouse and then represents a new handling unit shipping [14];
- shipping—space of a warehouse system for outgoing material flows [11], in which the transfer of control from warehouse to customers or carrier of the merchandise take place. If these transfers of control are not accomplished efficiently, safely, and accurately, the warehouse cannot possibly meet its objective of satisfying customers requirements, regardless of the quality of the other aspects of the warehouse [12].

The characteristics of each warehouse zones indicate that virtually in every part of storage area there is a movement of the stored goods. It requires the use of various transport resources. Some simulation studies were carried out for different numbers of means of transport and for the exemplary structure of high storage warehouse. The aim of these simulations was to draw attention to the importance of ensuring proper transport infrastructure in a production system. A detailed description of researchers, together with the obtained results will be presented in this paper.

4 Simulation Researches

The organization of tasks in warehouses depends on the factors, which continually change, such as: changing the number of assortments, the number of orders, whether requirement shorter the time for order completion. On the other hand, it is important to continuously reduce costs of both production and storage and accelerating production process. Therefore, development of warehouse structure should be a properly thought-out process, supported by simulations of designed construction and based on the expected or possessed input data. Thus, warehouse management is now supported by IT systems, due to high complexity of the management and design processes.

For a defined structure of warehouse, some simulations are conducted, based on a sample system, supporting design and management of a high storage warehouse. These tests were aimed to show the impact of the number of transport resources for average time of execution, average, and maximum waiting time of orders in the system.

4.1 Simulation Parameters

A simulated warehouse is a “bag” storage system (Fig. 2), that is, with a horizontal arrangement of particular zones and with a separate receiving, storing and shipping zones. The receiving and shipping zones are adjacent to each other, but have other functions. Thus, they cannot be regarded as one receiving-shipping zone.

The analyzed warehouse consists of 480 slots, arranged in 10 shelves, each of which is composed of 6 rows and 8 levels (Fig. 3). The orders executed by the warehouse are admissions and release of the goods in full containers and each of the goods has an assigned zone (A, B, C) and a priority in the range of 1–10.

The assumed number of goods types is 6. The designation of warehouse zones was based on the ABC method with two criteria—number of orders and frequency of orders.

The goods were assigned right priorities, based on the assumption that the order of goods unloading from the warehouse must take place before loading products, in order to assure the best customer service, and based on the analysis of ABC

Fig. 2 A “bag” storage system

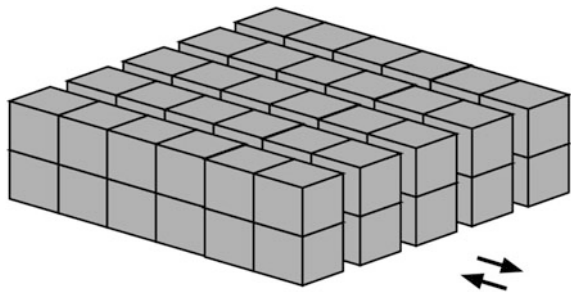


Fig. 3 The rack storage system with marked zones

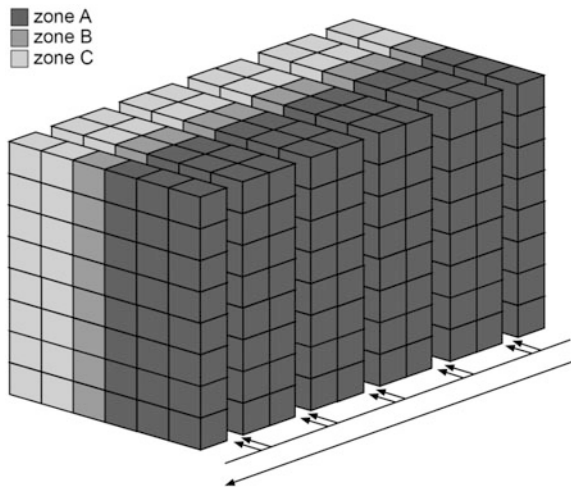


Table 1 Summary of orders' priorities

Code of product	Priority of order	
	Loading	Unloading
1	6	2
2	5	1
3	5	1
4	7	3
5	5	1
6	7	3

method. Table 1 presents a summary of priorities assigned to particular types of goods. The details of the analysis will not be considered in this article.

During simulations as transport resource a forklift is adopted, because it is the most commonly used mean of transport. A forklift, after completing its assigned order, remains in place and is waiting for the next job assignment.

Below other simulation parameters are presented and they relate to the access time of forklifts to warehouse locations, times are contractual units of time [c.u.t]:

- access time to the shelves between two consecutive shelves: $12 \times \text{No. shelves}$;
- access time to the row, specifying time it takes to go the way between adjacent rows: $3 \times \text{No. row}$;
- access time to the level, specifying time needed to overcome a distance of lifting the loading units between levels: $4 \times \text{No. level}$;
- time of loading/unloading, so the manipulation time of postponed and down-loaded good from the slot: 2.

The time needed to transport goods between loading and unloading zone is 35 [c.u.t].

There are adopted four following criteria (in a hierarchy according to the shown order), allowing to select the method that defines the order of orders execution and location in warehouse:

- minimum time of order execution;
- minimum priority order—it is assumed that the lower the priority, the more important is the order;
- minimum waiting time of order;
- maximum waiting time of forklift.

The simulation was performed for 333 jobs, the first order falls on 28.10.2016, at 7.00 a.m. and the last on 10.30.2016 r., at 6.45 a.m. It was assumed a work carried out 24-h a day and three shift arrangements. The number of the forklift, used in this simulations, is varied in the range of 1–15.

4.2 The Results of Researches

For the adopted structure of high storage warehouse and set of simulation parameters several tests were conducted. Those researches were aimed to select the effective number of means of transport.

The simulation results carried out with a different number of transport, are shown in Table 2.

The data contained in Table 2 are also presented in the form of three following charts and a chart, presenting a comparison of all received data.

4.3 The Analyzes of Results

As it to be expected, the increase in the number of transport resources significantly influences reduction of average waiting time of order (Fig. 4)—using maximum available number of forklifts, it can be observed more than 56 times reduction of average waiting time of order in relation to use only one mean of transport. Based on Fig. 5, it can be concluded that in most cases maximum waiting time of order decreases with increasing of the number of used transport resources, but this decline is not as gradual as in the case of average waiting time of order—there is no characteristic trend. When changing the number of forklifts with 1, the largest differences in time are for the number of resources equal to 9 and 10, and 12 and 13. The maximum waiting time of order for 10 forklifts is reduced by 381 [c.u.t] in

Table 2 Summary of simulation results for a particular number of transport resources

Number of transport resources	Average execution time (c.u.t)	Average waiting time (c.u.t)	Maximum waiting time (c.u.t)
1	60.71	534.69	1411.00
2	55.68	392.19	1422.00
3	57.66	295.00	1315.00
4	58.97	237.94	1316.00
5	60.47	194.71	1317.00
6	61.61	154.26	1301.00
7	64.55	121.65	1287.00
8	66.26	88.96	1222.00
9	68.65	61.33	1047.00
10	70.04	45.57	666.00
11	70.41	33.32	578.00
12	71.19	25.66	505.00
13	71.80	17.20	229.00
14	71.46	12.10	197.00
15	71.31	9.42	197.00

Fig. 4 The average waiting time of order for a particular number of used forklifts

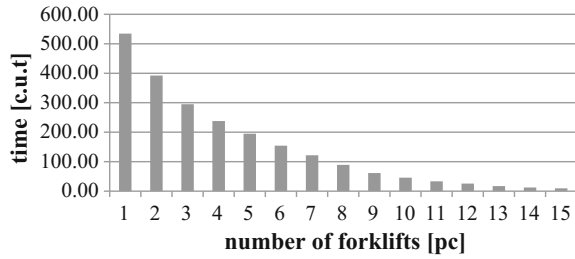
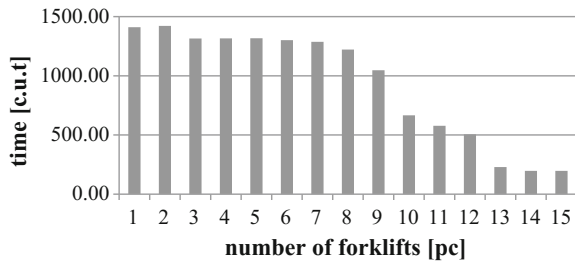


Fig. 5 The maximum waiting time of order for a particular number of used forklifts



relation to the time for 9 forklifts. In contrast, for 13 resources maximum waiting time, compared to the time for 12 resources, is shorter by 276 [c.u.t]. For 13 and more forklifts, there are none or small changes in maximum waiting time of orders. On the other hand, Fig. 6 represents a general upward trend in average time of orders executions with an increase of the number of forklifts. By average execution time is understood time elapsed, since the emergency of order in the system until completion of the order.

The summary of the results, presented in the Fig. 7, can thus be used to predict that the most effective number of forklifts for analyzed high storage warehouse is 13. This number was chosen due to several important observations. Namely, differences in average waiting times of orders and average times of execution of orders for the number of resources greater than 13 are definitely smaller, and in turn, maximum waiting time is significantly smaller than in the case of a smaller number of forklifts. It should be however noted that in the conducted tests the focus was mainly on the relationship between the number of used forklifts and the time

Fig. 6 The average execution time of order for a particular number of used forklifts

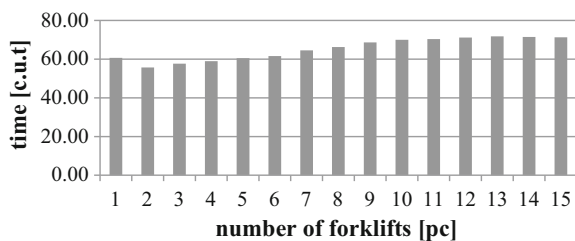
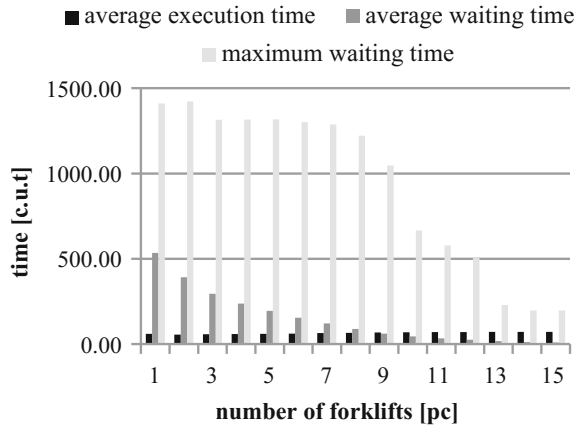


Fig. 7 A summary of the results



parameters. If the carried out analysis would be completed by additional analysis of purchase and maintenance costs, the most effective number of forklifts should be reduced to 10. This choice was made in view of the fact that average execution time for 13 resources is slightly different in relation to average time occurring for the 10 forklifts. While Fig. 5 demonstrates that reducing the number of forklifts below 10 significantly increases maximum waiting time of orders.

The chosen fragments of the Gantt charts for 10 and 13 forklifts, showing when these means of transport were occupied, are presented in Figs. 8 and 9. The Figs. 10 and 11. show the percentage occupancy of this warehouse for 10 and 13 forklifts.

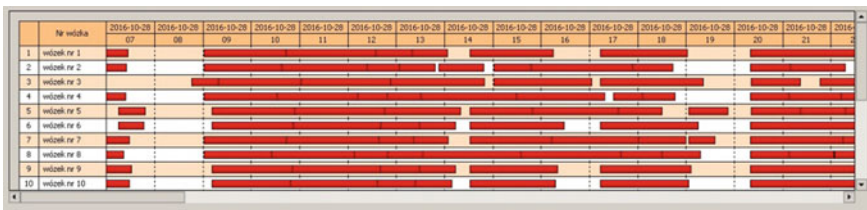


Fig. 8 Fragment of the Gantt chart for 10 forklifts

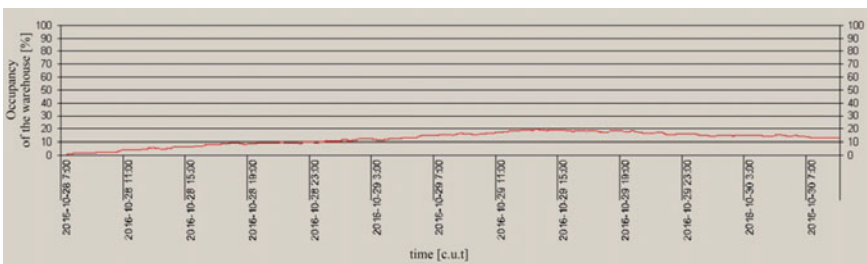


Fig. 9 Percentage occupancy of the warehouse for 10 forklifts

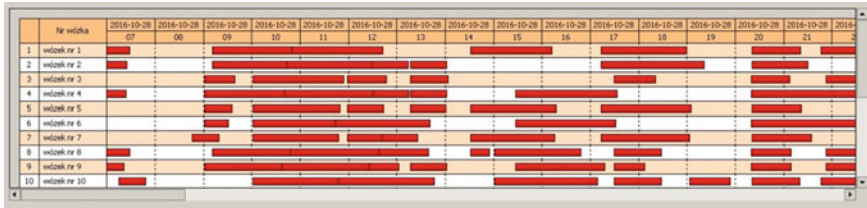


Fig. 10 Fragment of the Gantt chart for 13 forklifts

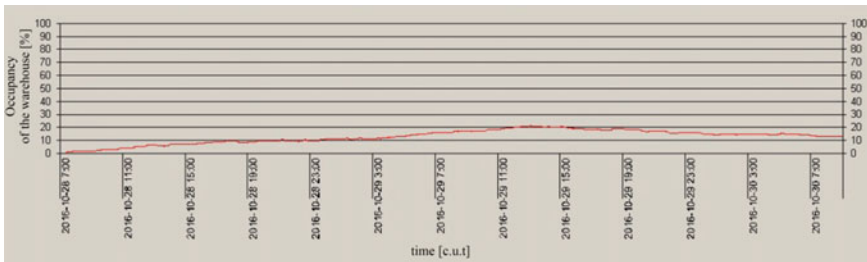


Fig. 11 Percentage occupancy of the warehouse for 10 forklifts

5 Conclusions

The development of material flow in the manufacturing system is one of the most important stages of production planning. The analysis should be submitted to both transport path occurring within factories and external transport infrastructure, ensuring the distribution of finished goods and deliver them to the customer in a timely manner. The use of applications and systems supporting design flow of goods, organization, and management of storage space are an essential convenience for the qualified personnel. In addition, it reduces the likelihood of errors already at the stage of emerging prototypes. The possibilities of an exemplary supporting system designed to simulate the operation of a user-defined high storage warehouse and the benefits of its use were presented in this paper. The results of the investigations were subjected to statistical analysis in order to select the most effective number of transport resources. The increase in the number of forklifts is associated with an increase in the cost of transport resources purchase and their subsequent operation. It has been taken into account in the considered analysis. At the time of determining the number of means of transport, one more aspect should be also included. Namely, more resources require appropriate organization of transport paths so as to avoid crossing paths and ensure collision-free transport. This indicates that use of systems and applications, designed to simulate, only support decision making, so this decision should be supported by additional analysis of the results obtained from these systems.

Acknowledgements This work has been supported by Polish Ministry of Science and Higher Education under internal Grants BK-213/RAu1/2016 for Institute of Automatic Control, Silesian University of Technology, Gliwice, Poland.

References

1. Bowersox, D.J., Closs, D.J., Cooper, M.B.: *Supply Chain Logistics Management*, pp. 166–190. McGraw-Hill, New York (2002)
2. de Koster, R., Le Anh, T.: Vehicle online dispatching rules in practice. In: Fleischmann, B., Klose, A. (eds.) *Distribution Logistics: Advanced Solutions to Practical Problems*, p. 160. Springer, Berlin (2005)
3. Barman, D., Kushwaha, G.S., Das, D.: Impact of supply chain quality management on competitive advantage and organizational performance. In: Kersten, W., Blecker, T., Flamig, H. (eds.) *Global Logistics Management: Sustainability, Quality, Risks*, pp. 171–186. Erich Schmidt Verlag, Berlin (2008)
4. Schroeder A.K., Nebl T., Mainzinger C.: Theoretical foundations of efficiently organizing production processes: using the example of combining organizational forms of component manufacture and internal transport. *J. Ind. Eng.* **2014**, (2014)
5. Kosacka, M., Kudelska, I.: Storage method for parts from end of life vehicles' dismantling process according to sustainable development requirements: polish case study. *World Acad. Sci. Eng. Technol. Int. J. Econ. Manag. Eng.* **3**(7), 2378–2385 (2016)
6. Wiendahl, H.P., Reichardt, J., Nyhuis, P.: *Handbook Factory Planning and Design*, pp. 158–160. Springer, Berlin (2015)
7. Definition of storage, www.dictionary.cambridge.org/dictionary/english/storage. Accessed 28 Nov 2016
8. Technical Committee KT No. 162 of Logistics, Barcode and Warehouse Management, PN-N-01800:1984 Stock management—Basic terminology, Standards Publishing Alfa (1984) **(in Polish)**
9. Williams C.E.: *The Costing of Handling and Storage in Warehouses. Part 2. High-bay Warehouses*, Her Majesty's Stationery Office, London, p. 16 (1972)
10. Bidgoli, H.: *The Handbook of Technology Management. Supply Chain Management, Marketing and Advertising, and Global Management (Distribution and Warehousing in Supply Chains)*, vol. II, pp. 163–175. Wiley, Hoboken (2010)
11. Gu, J., Goetschalck, M., McGinnis, L.: Research on warehouse operation: a comprehensive review. *Eur. J. Oper. Res.* **177**(1), 1–21 (2007)
12. Tompkins, J.A., Smith, J.D.: *The Warehouse Management Handbook*, p. 231. Tompkins Press, Raleigh (1998)
13. de Koster, R., Le-Duc, T., Roodbergen, K.J.: Design and control of warehouse order picking: a literature review. *Eur. J. Oper. Res.* **182**(2), 418–501 (2007)
14. Kappauf, J., Lauterbach, B., Koch, M.: *Logistic Core Operations with SAP. Inventory Management, Warehousing, Transportation, and Compliance*, p. 127. Springer, Berlin (2012)

Effectiveness Analysis of Small Hybrid Power Plant with Energy Storage

Andrzej Smolen and Marek Golebiowski

Abstract The objective of this paper is to investigate and compare the expected yield of small renewable energy power plants. The method of determining configuration of photovoltaic system, able to work autonomously under the given load conditions, has been presented. The impact of support such systems by a wind turbine has been investigated in case of minimal demanded battery capacity and the total energy yield. The simulation study has been performed using data describing the typical climatic conditions in 61 locations on Polish territory. The results showed that minimal demand battery capacity depends mostly on daily character of system load and cannot be noticeable decrease owing to wind turbine support.

Keywords Hybrid power plants · PV installations · Renewable energy sources

1 Introduction

In recent years a lot of efforts were made for develop and popularisation of small and medium size renewable energy power plants. In view of EU regulation in case of buildings energy efficiency it is expected that many of such installations will be created to satisfy the demanding norms. In purpose of analyse the potential of using the energy of sun and wind to supply power for a small recipients the presented simulation study has been performed. The calculation has been made for three

Please note that the LNCS Editorial assumes that all authors have used the western naming convention, with given names preceding surnames. This determines the structure of the names in the running heads and the author index.

A. Smolen (✉) · M. Golebiowski
Department of Electrical and Computer Engineering Fundamentals,
Rzeszów Ul. W. Pola 2, Rzeszów, Poland
e-mail: andrzej.kroscienko@gmail.com

M. Golebiowski
e-mail: yegolebi@prz.edu.pl

different types of daily load profiles. The minimum energy storage capacity needed in case of system autonomous work has been determined. Possibilities of decreasing this parameter by supporting the system with micro wind turbine has been analysed for a various rated power. The amount of energy potentially lost during the year cycle, in case of system autonomy, has been estimated. The main components of considered system are: photovoltaic modules (PV), energy storage consist of lead-acid batteries and the micro wind turbine (MWT). The quasi-static mathematical models of each component were used to simulate the system energy flows. Such an approach require input data in form of time series average values of solar irradiance, ambient temperature and wind speed. Taking into account that the placement of system can be forced by external circumstances such as currently available location, the calculations were based on data describing the typical climatic conditions (TCC) in 61 locations on Polish territory [1].

1.1 Preliminary Calculations

The purpose of presented method is to obtain the configuration of photovoltaic system being able to work autonomously and satisfy the energy load, which is given as a expected series of hourly averages. According to conception presented in [2] the PSH is used for a rough calculation of system energy balance. Firstly the minimum needed value of PV generator power is calculate as:

$$P_{\text{gen}} = \frac{2L}{\overline{\text{PSH}}}$$

Multiplying the minimum value of generator nominal power by 2 is caused by substantial differences of solar irradiance occurring at considered latitude in course of the year. Because of this changes it can be assumed that total energy storage capacity necessary to system autonomy, depends on yearly cycle energy deficit which is calculated as:

$$E_{\text{def}} = \min(P_{\text{gen}} \overline{\text{PSH}}_{\text{month}} - \overline{L}_{\text{month}})$$

To estimate a needed battery capacity, the efficiency of energy conversion and minimum admissible battery state of charge are taken into account.

$$Q_{\text{bat}} = \frac{E_{\text{def}}}{\eta_{\text{bat}} \zeta}$$

where: battery efficiency $\eta_{\text{bat}} = 0.8$ in accordance with [3] and minimum state of charge $\zeta = 0.4$ has been assumed.

This roughly calculated value has been used as a starting point in iterative calculations of optimal battery capacity for each load profile and location.

1.2 Quasi-Static PV Model

In order to calculate the expected energy yield of photovoltaic panel it is necessary to calculate the temperature of its modules for each simulation step. For this purpose the single layer PV thermal models described in [4, 5] has been used. In a first model the influence of forced convection is neglected and for this reason to increase the accuracy for simulation steps in which the wind speed exceed 1 m/s the second one is used. The values of forced and natural convection coefficients have been adopted in accordance with [6]. The influence of ambient temperature for an open circuit voltage was taken into account.

$$V_T = \frac{dV}{dT} T_{pv}$$

The temperature-caused change of module current has been calculated as:

$$I_T = \frac{dI}{dT} (T_{pv} - T_{STC})$$

Based on [2, 7] the quasi static PV model has been created. Method applied for calculating the hourly average value of generated power is presented below.

The current of module under the given conditions of solar radiation is given by:

$$I_{scm} = \frac{G_c}{G_{STC} (I_{scmr} + I_T)}$$

The value of open circuit voltage under corresponding conditions is given by:

$$V_{ocm} = V_{ocmr} + \frac{dV}{dT} (T - T_{STC}) n N_s V_T \log \left(\frac{I_{scm}}{I_{scmr}} \right)$$

The MPP current of module under given conditions is calculated as:

$$I_{mpp} = \frac{I_{mppSTC} G_c}{G_{STC} + I_T}$$

The value of module MPP voltage corresponding to the same conditions is given by:

$$V_{mpp} = n N_s V_T \log \left(\frac{1 + I_{scm} - I_{mpp}}{I_{scm} e^{\frac{V_{ocm}}{n N_s V_T}} - 1} \right) - I_{mpp} R_{sm}$$

The hourly average value of generated power is finally calculated as:

$$P_g = V_{\text{mpp}} I_{\text{mpp}} I_m$$

Furthermore the losses caused by wires and contacts resistance are about 5% of produced energy [7]. Module parameter values have been adopted in accordance with the note sheet of BP-Solar-380.

1.3 Expected Energy Yield of Micro Wind Turbine

Further part of presented study aims to investigate a possibility of decrease minimum value of energy storage capacity needed for system autonomy, by support it with micro wind turbine. Taking into account that the simulation has been performed based on averaged and statistically processed data, the probabilistic model has been applied to calculate the expected energy yield of MWT. According to [8] the distribution of time moments at with the wind is blowing as a function of wind velocity can be approximated by a Weibull and Rayleigh density function. The total amount of energy yield obtained at considered time period is, in this model, calculated as integral of this density function on the interval between minimum and maximum wind speed range at with the turbine is able to work. Applied method has been discussed minutely in [8]. For the further studies hourly resolution of power generation time series has been used.

1.4 Energy Storage

In order to simulate the power flows for the systems comprises the energy storage, the kinetic model of lead-acid battery has been developed in National Renewable Energy Laboratory (USA). This approach consider the limitations of available power stored in battery in case of rapid unloading as well as an access to free capacity during charging. The model was described fully in [7]. Model parameters has been adopted in accordance with Homer software database. Furthermore the charging and discharging losses are treated as constant and equal, the total efficiency coefficient of energy storage has been assumed as 0.8 in accordance with [3].

1.5 Simulation Process

In purpose of obtain the information about system configuration needed to satisfy a given energy consumption as well as to estimate the performance of supply system during course of the year, the models and methods presented above has been

implemented in Matlab and the consistent program has been developed. The simulation is based on energy conservation law, what ensure a cohesion. The process is quasi-static, means that all variables are constant during simulation step with is 1 h. According to [7] this resolution is sufficient to obtain accurate results when it comes to battery state of charge.

The calculations were carried out for three exemplary load profiles:

- nightly-the energy is consumed while PV generator do not work
- daily-the energy can be consumed and produced at the same time
- stable-average value of system load is constant during 24 h cycle

Additionally the random component of load with magnitude 10, 20 and 30% of hourly average value, has been implemented for each profile respectively. To improve clarity all of results will be presented as a daily averages (Fig. 1).

The first step of simulation process, comes to obtain a preliminary system configurations able to satisfy the loads and work autonomously, for each of 61 analysed locations. This roughly method has been presented in first section. Next based on TCC data the hourly average values of generated power and system energy balance are calculate for each configuration. On this basis the minimum battery capacity satisfying a minimum state of charge condition is computed iteratively. The maximal admissible depth of discharge is associated with a battery service life and the demanded system reliability. For further calculation the 0.4 has been adopted. In purpose of investigate the possibility of decreasing the needed battery capacity by supporting a system with micro wind turbines, the mentioned

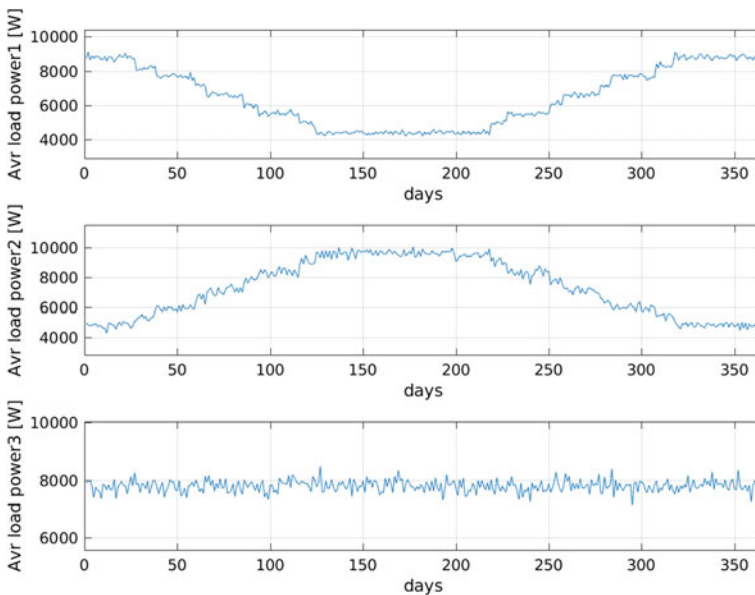


Fig. 1 Daily averages of system load

probabilistic method and TCC data has been used to compute expected hourly average values of MWT power generation. System energy balance and the procedure of battery capacity optimization were carried out for each instance separately.

2 Results

The system performance calculated for each locations were compared in terms of MWT efficiency. The results obtained in case of MWT rated power equal to half of PV installation nominal power for the best and worst location are presented below (Fig. 2).

In accordance with the expectations the turbine energy yield is much better in Leba with is located on the Baltic coast (North Poland) and PV installation are more efficient in Nowy Sacz. (South Poland) The configuration of the system obtained for 12 kW of nominal load power for daily and nightly load profile and 6 kW for the third one, in considered locations are presented below (Tables 1, 2).

The results showed that the nominal power of PV installations needed to satisfy the loads is higher in a north location. The total battery capacity necessary for system autonomy seems to be dependent only on load profile type. In purpose of investigate the possibilities of decreasing the needed battery capacity by supporting such systems with MWT the appropriate simulations has been carried out for each locations and load profile, for a various rated power of MWT. Afterwards the

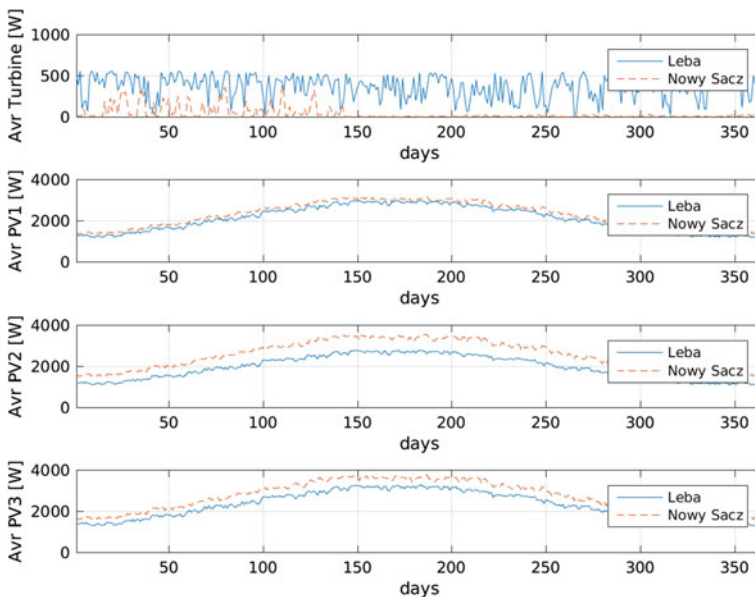


Fig. 2 Comparison of generated power

Table 1 Configuration of system obtained for Nowy Sacz

	PV nominal power (W)	Battery capacity (Wh)
Load profile 1	4720	2.7038e+04
Load profile 2	5280	2.4213e+04
Load profile 3	5600	1.7843e+04

Table 2 Configuration of system obtained for Leba

	PV nominal power (W)	Battery capacity (Wh)
Load profile 1	5920	2.7000e+04
Load profile 2	5520	2.4836e+04
Load profile 3	6480	1.7879e+04

change of demanded battery capacity, in relation to roughly estimated value, has been calculated. The averaged results are presented below (Fig. 3).

The results showed that this solution do not lead to decreasing a needed battery capacity, with remains dependent mostly on load profile type. Moreover in case of evenly distributed load the needed battery capacity increasing significantly. It is caused by increasing a loading speed what leads to decrease the total amount of energy the battery is able to receive during charging.

The average configurations of system able to work autonomously obtained for each load profile are presented in a table below (Table 3).

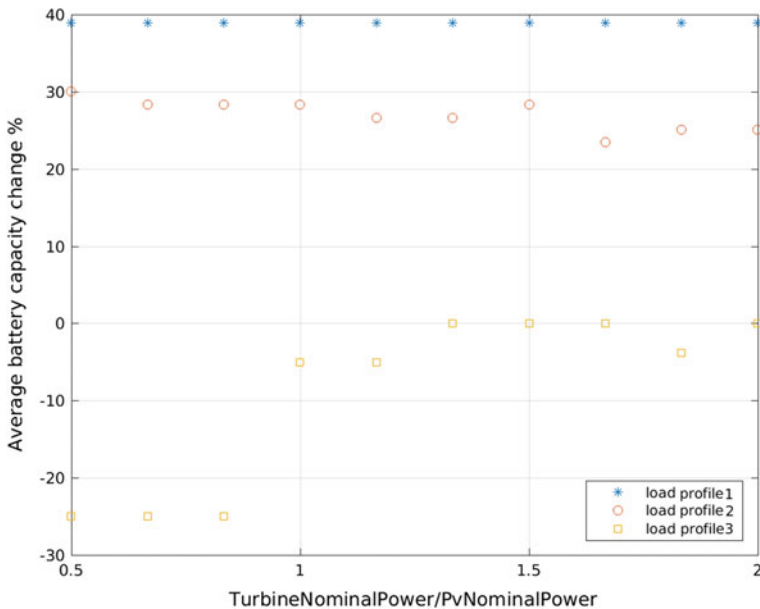


Fig. 3 Changes of needed battery capacity in case of supporting PV system by MWT

Table 3 Average values of system parameters

	AvrNmods	AvrBatterySize	MinBatterySize	MaxNmods	MinNmods
Load profile 1	64	27,028	2.674684e+04	76	53
Load profile 2	66	24,762	2.386708e+04	76	58
Load profile 3	74	16,365	1.200943e+04	84	63

Table 4 Average values of generated power

	PvGeneration	TurbineGeneration	ToGridPv	ToGridHybrid
Load profile 1	1.900946e+07	1.540754e+06	1.451663e+07	1.611444e+07
Load profile 2	1.961097e+07	1.558178e+06	1.391784e+07	1.569867e+07
Load profile 3	2.184663e+07	1.733588e+06	2.184498e+07	2.356512e+07

The average value of total yearly energy yield corresponding to each system configuration has been calculate for supporting MWT rated power equal to half of PV installation nominal power. The amount of energy which can be provide to the grid has also been calculated. All results are expressed in Wh (Table 4).

References

1. http://mib.gov.pl/2-Wskazniki_emisji_wartosci_opalowe_paliwa.htm
2. Castaner, L., Silvester, S.: *Modelling Photovoltaic Systems Using PSpice*. Wiley, Hoboken (2002)
3. Wills, R.G.A., Collins, J., Stratton-Campbell, D., Low, C.T.J., Pletcher, D., Walsh, F.C.: Developments in the soluble lead-acid flow battery. *J. Appl. Electrochem.* **40**(5), 955–965 (2010)
4. Bardhi, M., Grandi, G., Tina, G.M.: Comparison of PV cell temperature estimation by different thermal power exchange calculation methods. In: *International Conference on Renewable Energy and Power Quality (ICREPQ'12)*, pp. 28–30 (2012)
5. Notton, G., Mattei, M.: Calculation of the polycrystalline PV module temperature using a simple method of energy balance. *Renew. Energy* **3**(1), 553–567 (2006)
6. Feiman, D.: Assessing the outdoor operating temperature of photovoltaic modules. *Process. Photovolt. Res. Appl.* **16**, 307–315 (2008)
7. Manwell, J.: *HYBRID2—A Hybrid System Simulation Model—Theory Manual*. National Renewable Energy Laboratory (1997)
8. Mathew, S.: *Wind Energy: Fundamentals, Resource Analysis and Economics*. Springer, Berlin (2006)

Application for Contactless Objects' Identification by NFC Chips Embedded in Mobile Devices

Bartosz Pawłowicz and Anna Pitera

Abstract The aim of project was to design and implement application dedicated for contactless identification of fast-moving consumer goods (FMCG) using mobile devices. During the realization, application to reading and presentation of data from RFID tag was prepared. The whole work was preceded by thorough overview of protocol ISO/IEC15693 specifications and existing solutions. The concept of using of the RFID technique to storing products information was presented. The last step of the whole project was the performing of a series of tests.

Keywords RFID · NFC · Mobile device

1 RFID Technique

Barcodes are currently the most popular way to mark products. They initiated a revolution in identification systems and were a first step towards the full automation of process of cataloging and tracking products. Their appearance replaced human in a laborious, manual reading out of identification numbers which drastically accelerated the process of shopping. Unfortunately, they turn out to be insufficient these days due to a very limited amount of stored information, which also cannot be modified [1]. The main advantage of using the barcodes is its very low cost. Unfortunately, the most popular unidimensional codes are not able to store information describing marked objects in detail. During the identification process, only

B. Pawłowicz (✉)

Department of Electronic and Telecommunications Systems, Rzeszow University of Technology, Rzeszow, Poland
e-mail: barpaw@prz.edu.pl

A. Pitera

Students Scientific Circle of Electronics and Information Technology,
Department of Electronic and Telecommunications Systems, Rzeszow University of Technology, Rzeszow, Poland
e-mail: 123403@stud.prz.edu.pl

© Springer International Publishing AG 2018

D. Mazur et al. (eds.), *Analysis and Simulation of Electrical and Computer Systems*, Lecture Notes in Electrical Engineering 452,
https://doi.org/10.1007/978-3-319-63949-9_29

the encoded number is being read which is intended for searching information in a dedicated database. To a certain extent, appearance of two-dimensional codes having much more capacity improved this situation. They allow storing up to 2953 bits [2]. All graphic codes, according to the way they are read, have to be located in a visible non-covered place which exposes them to damages. Position of every label has to be determined on an object and label has to be scanned, which significantly hinders identification process automation [2]. A meaningful limitation of barcodes is lack of the possibility of dynamic modification of stored data.

Smart cards having built-in chips do not have such limitations, as they store data in a digital form inside the built-in non-volatile memory. Cards of this type are commonly used for cashless payments and people identification. Unfortunately, considering the readout process, they require placing in a special reader and therefore they are not suitable for products marking [1]. With a view to barcodes and smart cards limitations a method called Radio Frequency Identification (RFID) has been established. Similarly, just like in the case of the cards, data are stored inside a reprogrammable silicon chip. However, in case of RFID transponders, data transmission takes place without a physical connection. Instead, a magnetic field or electromagnetic waves are used [1]. RFID technique allows for using a RFID transponder not only for a quick identification, but also for storing and reading individual object's information. An example of using the RFID transponder for access control are contactless reusable tickets, which allow not only to check authorization to a particular service (e.g., storing a ticket's expiry date), but also their renewal [1, 3]. Currently, research is being conducted over new ways of transponders' usage. So far, they allow only to store and read previously saved information. One of the new ideas is usage of the RFID transponders to monitor marked objects' condition [3–5].

2 HF RFID System

2.1 *Obligatory Standards*

In the case of devices working in HF bandwidth, the most popular protocols were standardized in documents ISO/IEC 14443 and ISO/IEC 15693. The first one covers proximity coupling systems, characterized by a greater data bitrate and transmission safety. It consists of four documents

- ISO/IEC 14443-1: Physical characteristics—defines physical characteristics of Proximity Integrated Circuits Card (PICC) and basic terms;
- ISO/IEC 14443-2: Radio frequency power and signal interface—specifies characteristics of a radio interface used for energy transmission and communication between Proximity Coupling Devices (PCD) and PICC;
- ISO/IEC 14443-3: Initialization and anticollision—describes the way of transponder initialization, data format, time dependences during initialization, and methods of communication with many transponders (anticollision);

- ISO/IEC 14443-4: Transmission protocol—specifies half duplex communication protocol.

Transponders compatible with ISO/IEC 14443 standard exist in A and B variants, that differ by a method of modulation and coding. Furthermore, the ISO/IEC 18092 standard was created to describe systems of near field communication NFC [1].

ISO/IEC 15693 standard specifies contactless vicinity coupling systems which are characterized by a lower energy consumption, increased interrogation zone, easier and less secure communication, as it is present in proximity systems. It consists of three documents:

- ISO/IEC 15693-1: Physical characteristics—defines physical characteristics of Vicinity Integrated Circuits Card (VICC) and basic terms [6];
- ISO/IEC 15693-2: Air interface and initialization—specifies characteristics of a radio interface used for energy transmission and communication between Vicinity Coupling Devices (VCD) and VICC, as well as describes a manner of communication initialization [7];
- ISO/IEC 15693-3: Anticollision and transmission protocol describes a method of communication with many transponders, as well as used half duplex communication protocol [8].

Moreover, ISO/IEC 15693 standard is compatible with mode 1 described in ISO/IEC 18000-3 [6]. Additionally, the ISO/IEC 18000-3 standard defines mode 2 which is dedicated to simultaneous identification of a high number of transponders. Mode 2 is not compatible with previous standards, however it refers to EPC Class-1 HF RFID specification.

2.2 Energy and Data Transmission in RFID System Compatible with ISO/IEC 15693 Protocol

The unique feature of all RFID systems distinguishing it from Short Range Devices (SRD) is the lack of an internal power source in transponder. Instead, energy is transmitted to transponders through a magnetic or electromagnetic field produced by a Read/Write Device (RWD). The same field is used for data transmission in both directions [1]. A magnetic field used in HF RFID system is created between antennas. Transponder's antenna loop is designed in such a way to create, with a chip's input capacity, a parallel resonance system with central frequency corresponding to the frequency of the carrier wave i.e. 13.56 MHz [1, 7]:

$$f_0 = \frac{1}{2\pi\sqrt{L_{TA}C_{TC}}} \approx f_c, \quad (1)$$

where f_0 and f_c are accordingly resonance frequency of LC layout and carrier wave frequency, and also L_{TA} , C_{TC} correspond respectively to antenna's inductance and

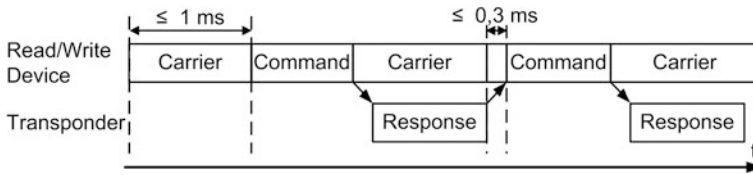


Fig. 1 Half duplex transmission in HF RFID system

input capacity of the chip. Transponder which is close to the antenna of a Read/Write Device couples with it creating an air transformer [1]. In the moment of moving the transponder closer to the RWD antenna, a process of charging a capacitor integrated in transponder [1] by field of the antenna occurs. After reaching a minimum voltage which enables to start of a chip, a process of communication begins. In HF RFID systems, compatible with ISO/IEC 15693 standard, Read/Write Device serves as a master device, whereas transponders are slave devices. It means that only RWD can start the communication process and send commands and transponders are only able to response to RWD commands. Transmission between them is held in half duplex mode according to command—response scheme (Fig. 1) [1].

During transmission of a command, the average value of energy transmitted to the transponder undergoes a slight decrease results from carrier wave amplitude's modulation. In case of transponder response transmission, a RWD creates a constant carrier wave which enables power supply to transponder. The amplitude of wave reflected from transponder is modulated by it [1]. It means that the most energy comes to the transponder before start of communication and during intervals between transmitted frames. ISO/IEC 15693-2 standard defines that the maximum time required for an transponder startup and its entering in the standby mode for receiving a command should be maximum of 1 ms. Maximum allowed time between the end of an response's transmission and entering in the standby mode for receiving another command was also defined [7] and should be no longer than 0.3 ms.

2.3 Communication Protocol in RFID System Compatible with ISO/IEC 15693 Protocol

Communication protocol described in ISO/IEC 15693-3 standard defines a mechanism of delivering instructions and data between a Read/Write Device and a transponder. The command sent by the RWD begins with a Start of Frame (SOF) and consists of 1 byte of flags, 1 byte command code, Unique Identifier (UID), (apart from command beginning inventory round) and one or a few bytes of parameters and data (Fig. 2a). Similarly, the transponder's response begins with SOF followed by 1 byte of flags and optional data (Fig. 2b) [8]. Every frame ends with two Cyclic Redundancy Code (CRC) bytes and End of Frame (EOF) symbol.

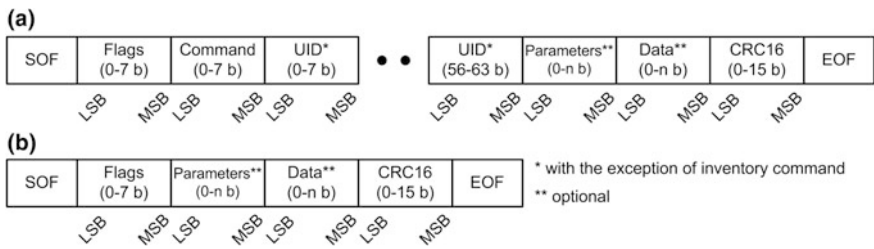


Fig. 2 The construction of the typical frame generated by: **a** read/write device, **b** transponder

During the interpretation of transferred data, one must remember that transmitted bytes are in order from the youngest to the oldest and each of them starts with the youngest bit [8]. Simple and short frames cause that transponders do not have to accumulate a huge amount of energy before establishing communication, thereby it is possible to identify a large amount of them in a short period of time.

In ISO/IEC 15693-3 standard there were defined four groups of commands. The first group consists of obligatory commands which every identifier compatible with this standard should perform. Second group includes optional commands defined in the standard but implemented optionally by a transponder manufacturer. The next group is created by customized commands which were not described in the standard but only a number of code numbers and general frame format were predicted for. In this case, the manufacturer has a full freedom as far as the commands functionality is concerned. The last group is commands reserved for manufacturers for test purpose. In their case the manufacturer can arbitrarily define frame format and the way of working of specified command [8].

The basic command beginning transponders readout sequence is *Inventory*. It consists of 4, 5, or 6 fields, according to *AFI_flag* byte settings and a mask length. It allows for the Data Storage Format Identification (DSFID), as well as UID number identification (Fig. 3) [8]. *Inventory* command begins with a flag field in which the *Inventory_flag* byte has to be set, whereas four oldest bytes have a different interpretation from the ones they have in other commands. Among them an *AFI_flag* occurs which indicates whether the AFI field occurs inside the frame

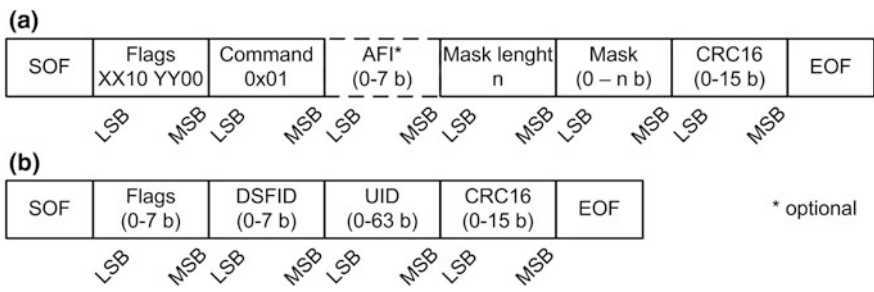


Fig. 3 Frame of **a** inventory command and **b** response

defining an Application Family Identifier. Afterward, a command's code and AFI's code are sent and, as a result, it is possible to decrease transponders' group responding to *Inventory* command. If anticollision protocol is used, the next field has a nonzero mask's length and later the mask itself is sent. It is designed to limit the responding transponders pool in a single inventory round through the UID number masking.

The last field includes two bytes of cyclic redundancy check designed to verify the correctness of a received frame by a transponder [8]. As a response, the transponder sends back an UID number (Fig. 4).

UID number is divided into 8 bytes and is sent from the youngest bit to the oldest one. In case when a transponder is compatible with ISO/IEC 15693, the oldest byte has 0xE0 value. Next byte identifies a chip's producer accordingly with the number given in ISO/IEC 7816-6AM1 standard. The last 6 bytes create a unique serial number.

Second basic command is *Stay_quiet*. It allows to keep transponders inactive which are jamming each other. It consists of a flag field, command's code, recipient UID number and CRC field (Fig. 5).

Stay_quiet command will be received properly only when it is sent in an address mode. It means a necessity of reset to zero *Inventory_flag* and *Select_flag* flags, as well as setting and *Address_flag* followed by the right UID number.

If a transponder has to serve as a marked object's data storage, a memory block write/read command support is necessary. However, before any write/read operation can be done, size and amount of memory blocks must be determined. *Get system information* command serves that. Command frame requires only giving the command code and the UID number in case of address mode (Fig. 6) [8].

The structure of the response frame depends on information in flags field content. Afterwards, an UID number is transmitted from transponder to RWD. It allows

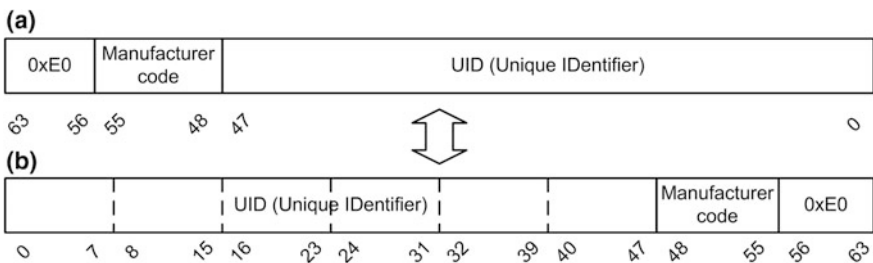


Fig. 4 UID number in a logic and b sent bytes form

Fig. 5 Stay_quiet frame command



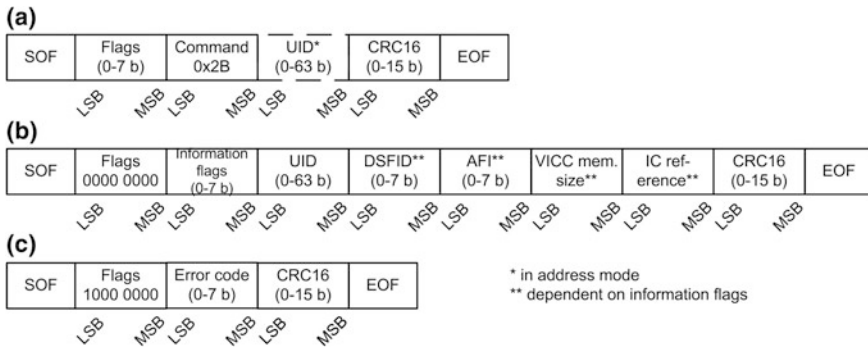


Fig. 6 Information read-out frame with an identifier: **a** command, **b** correct response, **c** response in case of an error

to check the unique identification number of a chip working in Select mode. Subsequently, optional fields are transmitted.

They include DSFID number, AFI, size and number of memory blocks and additional information about a chip coded by a producer. Field of memory size and amount consist of 16 bytes coding the size of blocks in the number of bytes and the amount of blocks. Due to information about the memory organization, a Read/Write Device can correctly address a desired block and decode received data.

In order to read a single memory block, a Read/Write Device has to determine UID of a transponder and send *Read single block* command frame with a given block address (Fig. 7). The content of an indicated memory block is sent back as the response. In case of a transmission error a frame including a fixed first flag and an error code is transmitted [8].

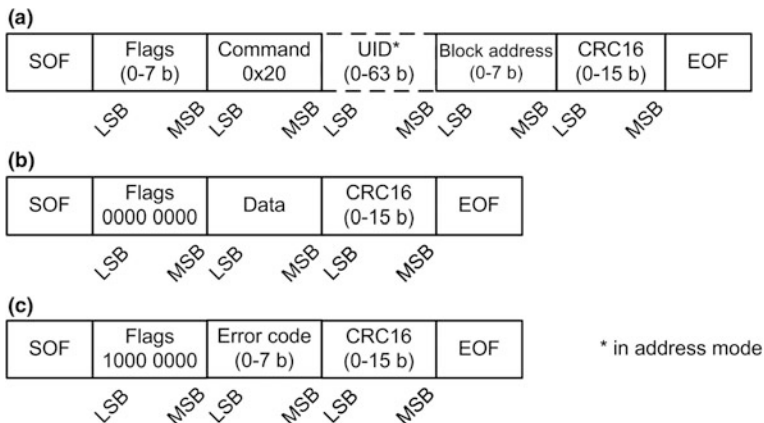


Fig. 7 Single-block read-out frame: **a** command, **b** correct response, **c** response in case of an error

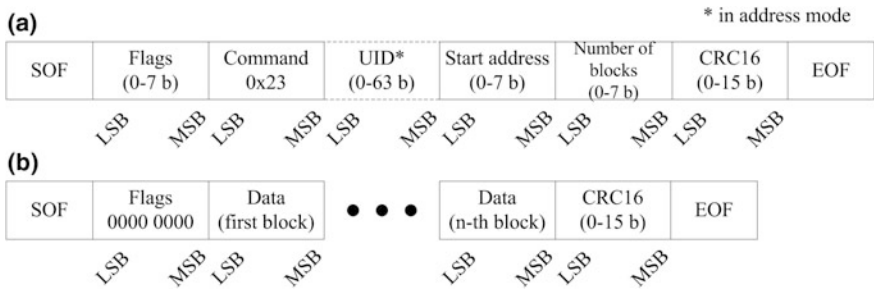


Fig. 8 Multiple blocks read-out frame: **a** command, **b** correct response

Readout of many blocks with *Read single block* command would be very ineffective due to a necessity of sending the command each time and waiting for response. Hence, the standard has a defined *Read multiple block* command by means of which it is possible to read up to 256 following memory blocks.

Only the address of the first block and the number of blocks to read have to be given (Fig. 8) [8]. In case of error, the response looks alike to single block readout.

A process of writing data into a transponder memory looks similarly to the readout. In this case, two separate commands for writing single or many blocks are determined. The difference in relation to the readout lies in data occurring in the command rather than in the response (Fig. 9).

The frame which informs about occurring errors looks similar as in the example of data read out attempt, that is why it was not presented in the figure above [8].

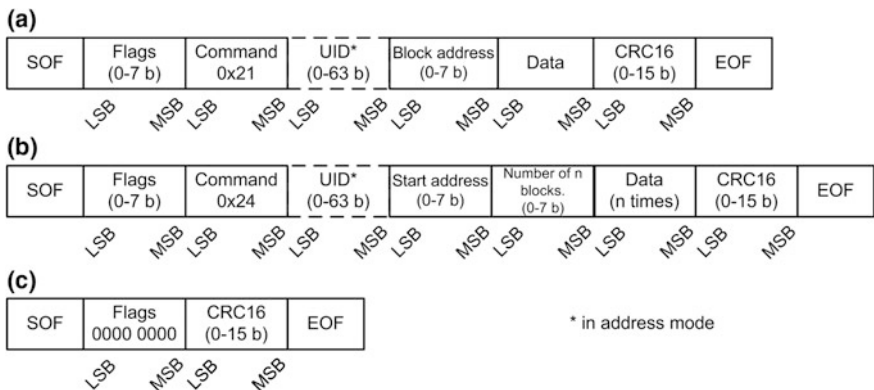


Fig. 9 Recording frame **a** one or **b**) multiple blocks and **c**) correct response

2.4 Transponder's Operation State in RFID System Compatible with ISO/IEC 15693 Protocol

Transponder software operation algorithm compatible with ISO/IEC 15693 standard is based on a simple state machine (Fig. 10). Default state of a transponder supplied from a Read/Write Device field is *Ready*. In this state the transponder awaits an incoming command. After receiving and recognizing a command, a response is sent. Next the transponder is set to standby mode.

The most common event that causes termination of all operation states of transponder occurs when it will come out of interrogation zone. It causes discharge of an internal capacitor and in result power-off of the transponder.

Another event causing change of present transponder's state is receiving the *Stay quiet* command with desired transponder UID number. It activates *Quiet* mode in which the transponder ignores all incoming inventory commands. Return to standby mode occurs in the moment of receiving *Reset to ready* command. Despite being in Quiet mode, contact with the transponder is possible due to commands addressed with UID number.

The last optional transponder's operation mode is *Select*. In order to select only one transponder a RWD should send the *Select* command including its proper UID

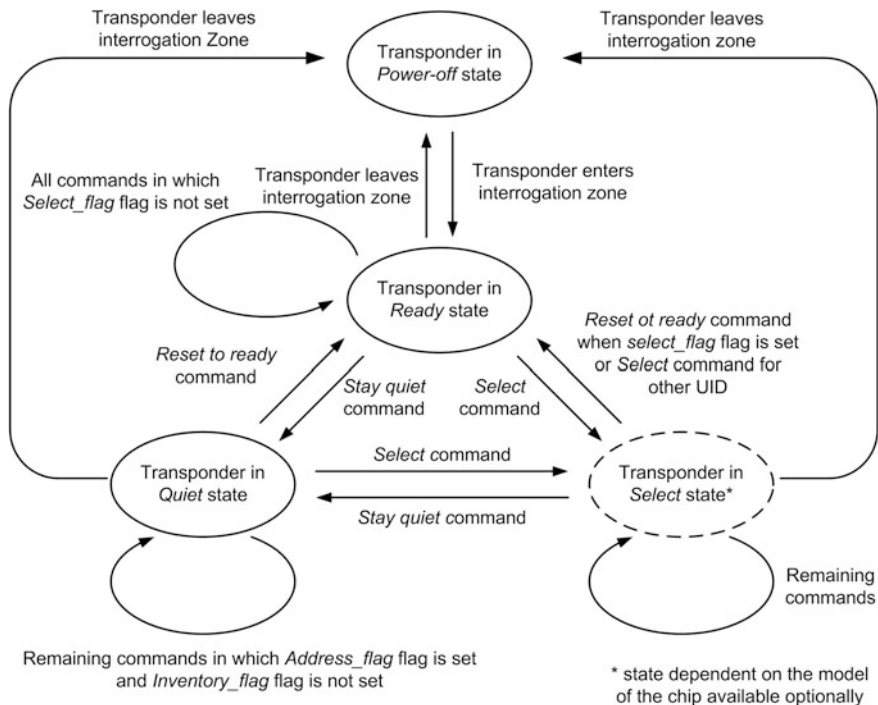


Fig. 10 Transponder's states diagram [8]

number. This condition allows sending different commands without the necessity of the receiver addressing each time. Only the usage of *Select_flag* flag is needed. Leaving from this mode is possible with *Reset to ready* command or by choosing a transponder with a different UID number [8].

3 Idea of Marking FMCG Products

Nowadays more and more advanced mobile devices, such as smartphones, smart-watches or tablets are equipped with an integrated NFC module by default. NFC technique gives a number of new possibilities, e.g., allows for fast establishing of a direct connection between devices, proximity payments [3] or reading out labels of marked products. In the last example utilization of available popular devices significantly affects reduction of migration costs from classic barcodes to RFID labels.

Replacement of barcodes by their electronic counterparts brings new possibilities. For example, with a dedicated application installed on smartphone, a consumer can read basic information from internal memory of transponder installed as label on product. Thanks to this fact, a connection with the local shop's database is unnecessary to show, e.g., price of a product. Manual products scanning allows for generation of a list of a virtual shopping cart which informs a customer online about total cost of products put into the cart. An application that implements mentioned functions can be used as a part of an innovative system of automatic products' recognition by shop checkouts (Fig. 11).

The objective of the system's user is to scan a chosen product with their own or borrowed mobile device and to make a decision about adding this particular product to the list of the virtual cart. Collecting of all desired products is followed by verification of created list (Fig. 12).

For this purpose, the user goes to the checkout equipped with RFID Read/Write Device, where an automatic readout of all transponders labeled on the products

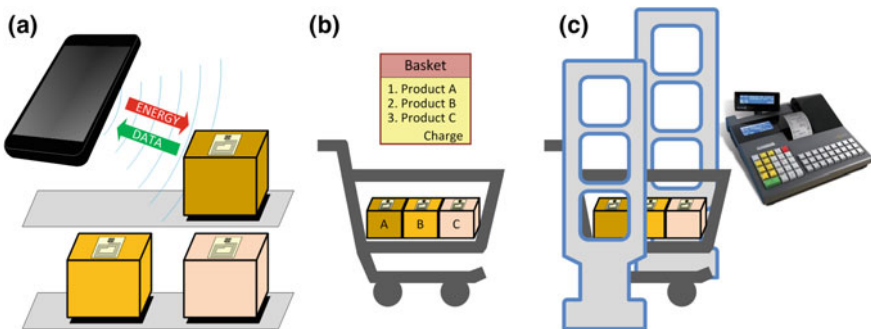


Fig. 11 Proposal of a buying process: **a** products' scanning, **b** adding products to a virtual cart's list, **c** list of products verification by a checkout

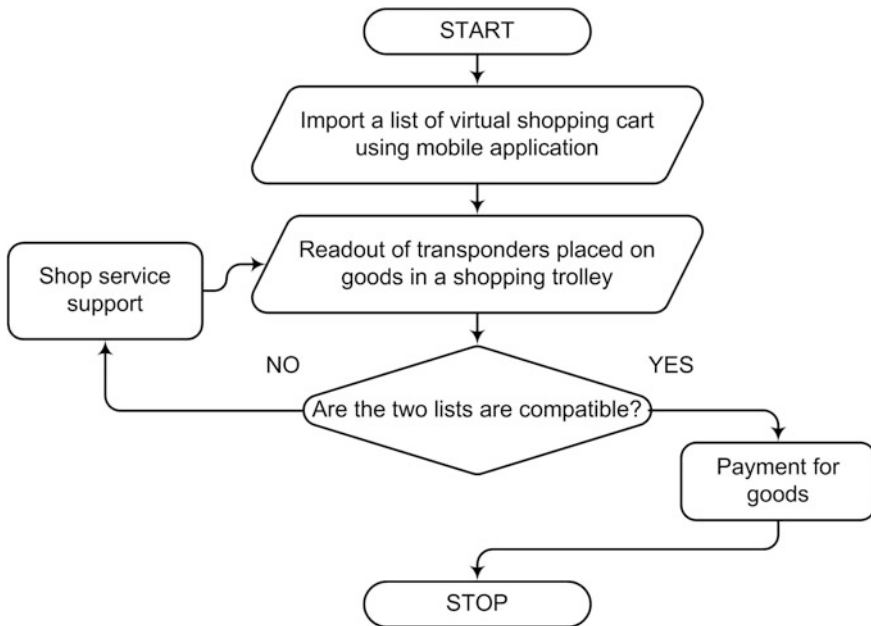


Fig. 12 List of products verification process by a checkout

occurs. During this process a second, independent list of products is created. Simultaneously the user should send (by other types of wireless connections) an information about the virtual cart's content from the mobile device to the checkout. Checkout's software compares contents of both the lists. In case of their consistency, it calls to settle a payment and take the products. However, if any problems occurred during products' identification, staff is called who helps to solve existing issue.

An advantage to this solution would be ability of a rapid reading out of all products without any need of putting them out from a trolley, which would be reflected in shortening checkouts' queues [9]. Moreover, a user would have information all the time about not just supposed, but actual payment. This will lead to the reduction of situations when customer resigns from buying of a certain product being at the checkout which additionally extends the payment process.

RFID transponders can store many other information besides the price. In the case of foodstuff, it can be, e.g., weight, calorific value, or expiry date. The application having such data can, for example, presents a normalized cost of a product per weight, calorific value in relation to overall daily energetic requirement, or count the amount of days before expiration.

Today, manufacturers more frequently describe their household products as "intelligent". Unfortunately, this term is widely abused for marketing purpose, in order to highlight the additional functionality, e.g., forwarding data to mobile devices. As an example, an advanced washing machine allows for monitoring the

washing state on a smartphone's or tablet's screen. Unfortunately, the user himself has to choose the washing program and its parameters because the machine is unable to recognize the laundry. If clothes had HF RFID transponders with information concerning fabric, color or maximum washing temperature and a machine was equipped with an appropriate RWD, this would allow to automate the whole process, and in case of detecting clothes which have to be washed separately, user would be informed about this fact (Fig. 13a). An intelligent refrigerator is another example (Fig. 13b).

Due to marked products, it would be able to recognize its own content and inform about their quantity. This would also enable creating an electronic shopping list, positions of which would be automatically transferred into a virtual cart. RFID systems utilization brings advantages not only for consumers, but foremost for sellers. For example, a producer is able to save information into transponder's memory about his own products, expiry dates and price tags. A wholesaler after receiving an order can identify the goods to add his profit margin and save new prices into the internal memory of chips. Similarly, goods reaching a shop can be verified paying special attention to the dates of expiration and then a retail price will be saved. At every write/read stage the data may be available by specific company systems, thus warehouses management may be automated (Fig. 14).

A wireless identification allows for logistical monitoring of products' flow, as well as quick finding of specified products [10]. Using the RFID transponders simplifies quality control, thereby caring for both producer and seller's image.

Currently, the biggest limitation to introducing RFID technique for marking products is transponder price. Unlike trade, RFID technique gained a significant popularity in details marking industry and more frequently in logistics where a label

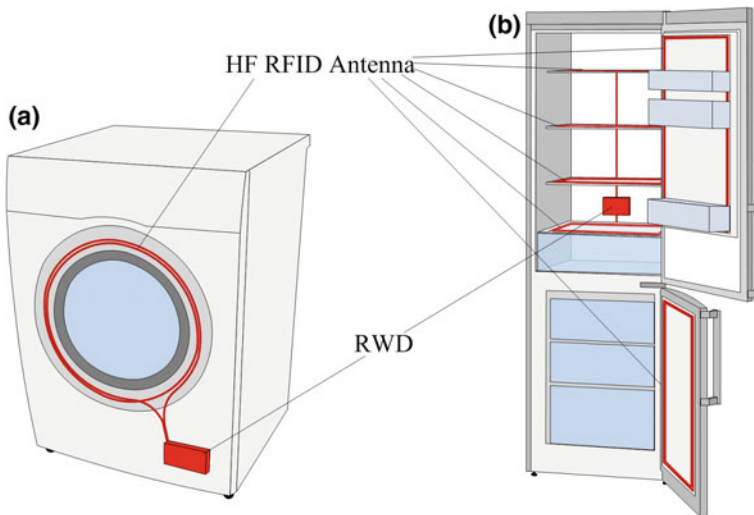


Fig. 13 Concept of **a** washing machine and **b** refrigerator with an integrated RFID reader

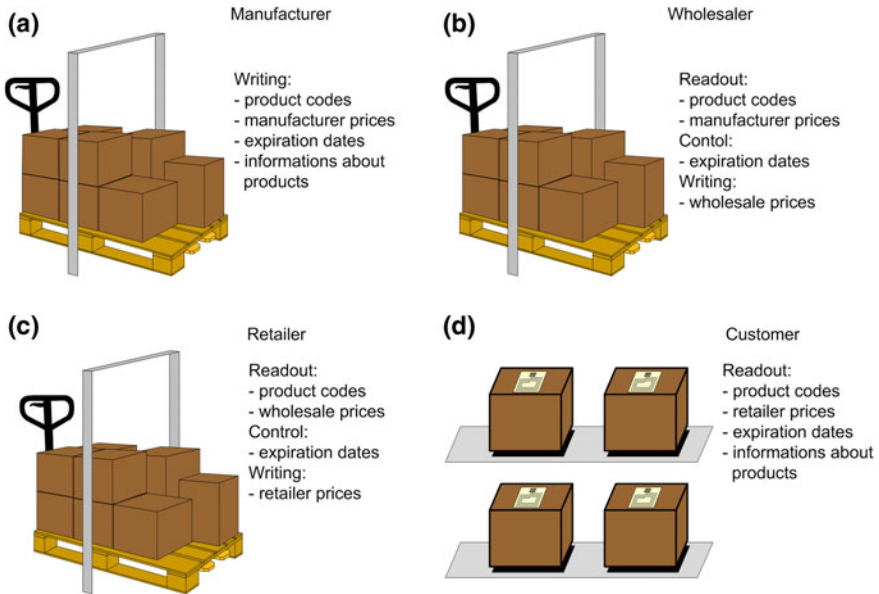


Fig. 14 RFID transponders utilization at various products distribution stages by **a** producers, **b** wholesalers, **c** salesmen, **d** consumers

cost is not a critical parameter. In the future, the price barriers overcoming will lead to a rapid increase in using RFID technique in everyday life.

4 Mobile Application for Contactless FMCG Identification

4.1 Data Readout

According to the main idea of the paper, an application called *FMCG Reader* was developed. It is dedicated to readout and visualize information about fast-moving products saved in memory of HF RFID transponders.

This is the first element of automatic products recognition system by shop checkouts. Thanks to it a user can add products that have been read out to a virtual cart and manage its content. Devices equipped in NFC module running on Android™ software are the application's target platform. All classes and methods used to read HF transponders and described below were developed to fulfill idea proposed in the paper.

Running the program initiates activity's life cycle *ReadsActivity*. Its operation consists in capturing transponder's detection occurrence, saving process realization and data decoding, as well as presenting them on a device's screen (Fig. 15).

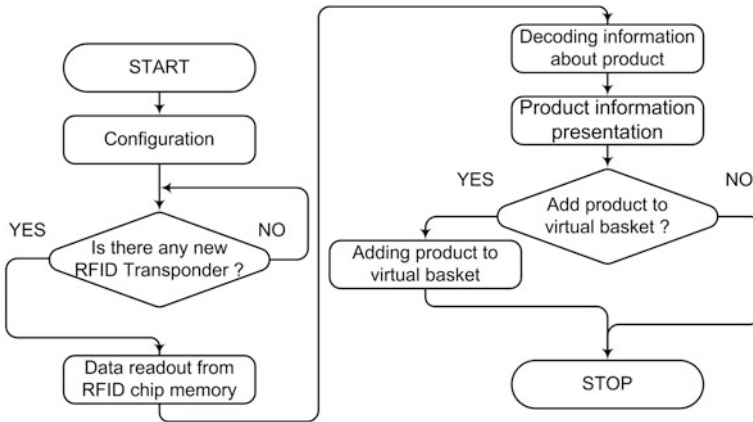


Fig. 15 Simplified algorithm of readout activity

Detection of the transponder starts of *intention's service* method *handleIntent()*. In this method, due to various intention sources, it needs to be checked whether an intention comes from NFC module. If everything is right, a process of communication with RFID chip begins. *ISO15693* and *MyTag* classes play the main roles in this process. The first includes static methods needed to a low-profile communication with a transponder, and the second allows for creating an object which stores an information about RFID chip.

Communication with a transponder begins with running inventory round. For this purpose, a method *ISO15693.SendInventoryCommand()* is used which receives as an argument, *MyTag's* class object. Thanks to that, the device is able to transfer a transponder's handle from intercepted intention and communication protocol settings, based on which a command frame flag byte is generated. In response, a transponder sends a frame saved in the *lastResponse* field of the same object. If response is finished successfully, then response's frame flag byte will be equal to 0x00. Otherwise communication failed and the program displays "BŁĄD ODCZYTU!" ("READOUT ERROR"). In the correct answer's frame to *Inventory* command an UID number of detected transponder is returned, based on which the producer and chip's model is recognized.

A successful finish of a inventory round allows to send *Get System Information* command by the use of *ISO15693.SendGetSystemInformationCommand()* method. As an argument, the same *MyTag* class object is given as the last time. The mechanism of this method is similar to *ISO15693.SendInventoryCommand()*, with the exception that earlier received UID number may be placed in the command frame. Thanks to this fact, an unambiguous addressee defining is possible. In the response such information as: chip's memory organization including the size and quantity of blocks are received. They are accordingly saved in *blockSize* and *blockNumber* fields of *MyTag* class object. These fields enable possibility of automatic read of the whole chip's memory.

Next step is a process of readout of the data about a product from the transponder memory. For this purpose the command *ReadMultipleBlocks* is used which enables single receiving up to 32 blocks [8]. If a chip capacity is larger, the command is sent multiple times in order to read all memory cells. Finally, an array is received which is saved in *tagMemory[]* field of *MyTag* class' object with a length corresponding to a chip memory capacity. It stores bytes string coding ASCII signs in CSV file form which include information about a marked product.

Depending on chip capacity, data read out process can last from several milliseconds to a few seconds. Executing time-consuming operations in the main thread may cause feeling of application crash, and indeed reduce the comfort of using it. Hence, the whole reading process was decided to be held in a separate, asynchronous thread—*ReadDataAsyncTask* realized as the subclass of *ReadsActivity*.

4.2 Data Decoding

In order to store information about marked product, *ProductInfo* class was made. It includes data fields into which chip UID number, exact readout time, currency, product and producer's names, www address and nutrients, as well as other data corresponding to AI codes described in GS1 specification are saved.

Having a table of readout bytes of data from a transponder application can proceed to decode them. Segmentation is being done, as a part of the first stage (Fig. 16). It is performed inside *setMapOfDataFromRawData()* method.

This process is preceded by change of every data table element for an adequate ASCII sign. A chain of signs created in this way is divided into substrings separated by commas (0x2c) or cursor return and transition into a new line (with two component code 0x0D 0x0A). In every loop's iteration two substrings are created. First one contains a potential key, whereas second has the key value. Afterwards, the potential key is compared to all supported key patterns. If whichever matches, value of chain is checked. In both cases, compatibility causes adding both key and a value to *mapOfData* set. It is followed by a new loop iteration. The process ends when the source string has no more substrings.

Second stage of readout data decoding is analysis of values assigned to keys and filling fields storing specific information about a product. This process is realized by *fillProductInfo()* method which as an argument takes a set of keys pairs—value. Filling next fields consists in searching in a set of previously defined keys. If any of them is found, a value signed to it is decoded and signed into respective object's field.

The last step is information presentation about a marked product. During this presentation text fields are filled which present RFID chip UID number, product and manufacturer name, price and other information (Fig. 17).

From this moment a user can decide whether to buy a product or to put it back on a shelf. If customer decides to buy it, he should press *Dodaj do koszyka* ("Add to

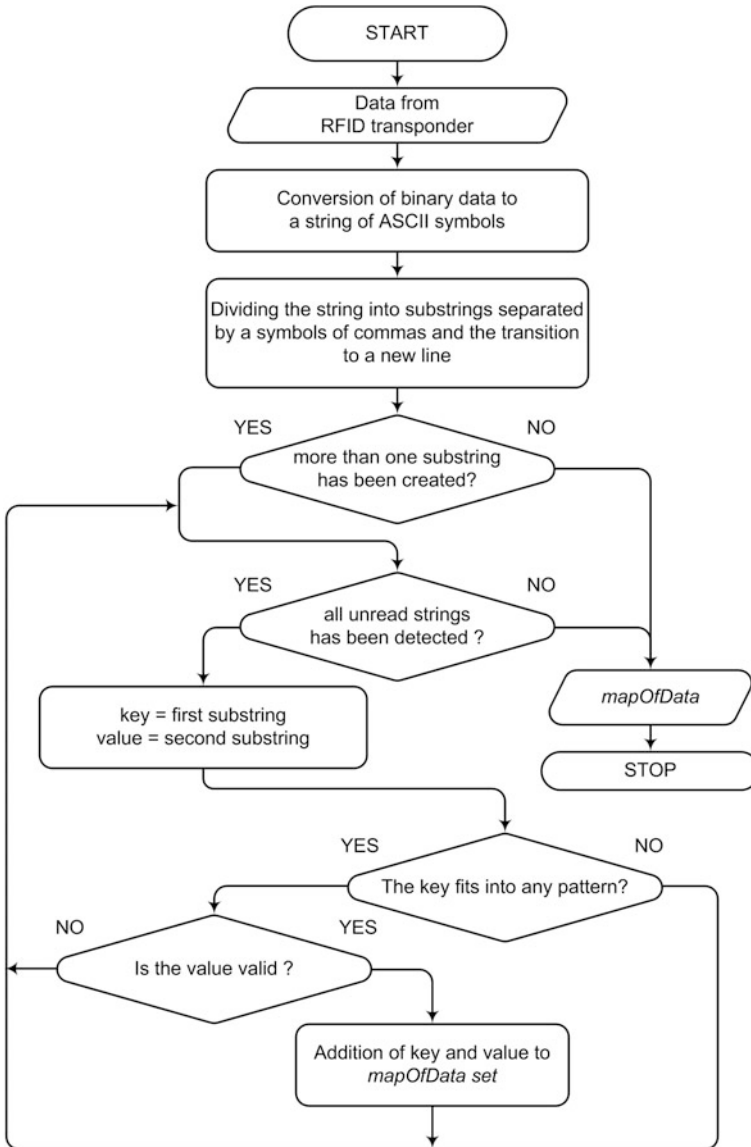


Fig. 16 Read-out and segmentation algorithm

the cart”) button. It will cause the object which stores information about the readout product to be added to current shopping cart (*currentShoppingCart*) which is stored in the application layer. Otherwise, the user can press *Wyczyść* (“Clean”) button or read another product’s identifier. This will lead to losing yet stored information and finally to replacing it with new one.



Fig. 17 Test product information readout

Adding a particular copy of a product to the virtual cart is possible only once. It may however occur that the user would want to buy more than one piece of a given product. That is why it was decided to differ objects based on RFID chips placed on UID numbers, instead of classic GTIN-13 numbers. Pressing *Dodaj do koszyka* button is followed by a list browsing *currentShoppingCart* and comparing current UID number to its successive positions. If the current number does not exist on the cart's list, the product can be added which causes increment of the appropriate counter at the same time. Otherwise, a dispatch is showed informing that this product is already on the list.

4.3 The Cart

A list of products is showed in the cart's activity which can be purchased by the application user. The whole process begins with generating an activity layout and creating handles for its elements. Subsequently, using *createData()* method, content is generated showing two layers, scrolled list *expandableListView* which presents data from *currentShoppingCart* object.

The two layers list is created as a list of objects which are lists themselves. For this purpose, a class *ShoppingCartGroup* was created which stores a header and sublist of a single line presenting a product inside the cart. After pressing it, a sublist is expanded, which presents detailed information about the product (Fig. 18). Additionally, every line of the list and the sublist has an icon for better clarity.

Adding at least one object to the shopping cart's list activates a bar showing the total value of shopping. Thanks to that a user can control its cost. Moreover, pressing and holding any position results in showing a dispatch asking to delete it.

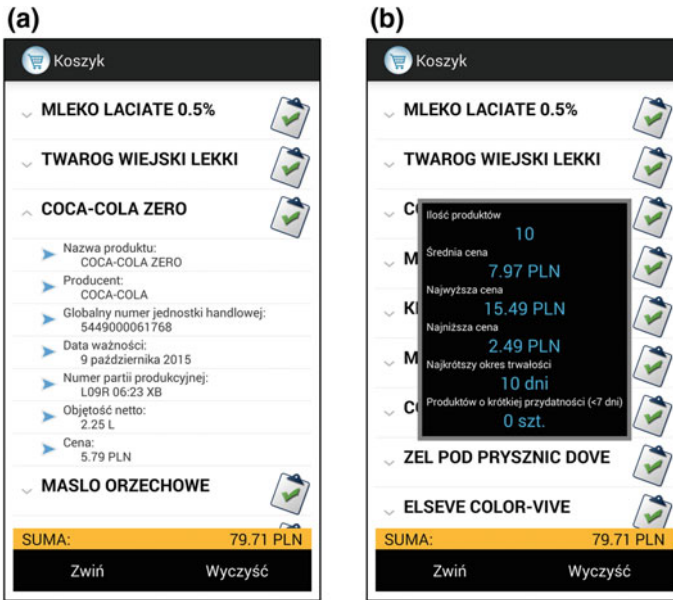


Fig. 18 Shopping cart: **a** product's details preview, **b** statistics window

This way one can throw an unwanted product or exchange it for a different one. Beneath the total price bar there are two buttons: *Zwiń* and *Wyczyść*. The former allows a rapid winding of all expanded lines, while the latter is used to delete all elements from the list. After pressing this button a dispatch asking to confirm one's decision appears on the screen.

5 Conclusions

The submitted research paper presents a conception of using objects radio identification technique in order to streamline shopping process, both on the consumer and the seller side. As part of it, popular mobile devices running on Android software were proposed in order to readout information directly from transponders placed on fast-moving products packages.

This idea required to develop a user-friendly application which realizes read out process and presents it in a clear way on a device's screen. The application allows for adding products to a virtual cart's list which gives information about, e.g., a total shopping cost, the shortest expiry date, and other statistics.

The created cart's list can also be used in a near future as a part of two-step system of products recognition by a checkout at a final shopping stage. Comparing a content of a virtual cart with a products list read out by the use of a stationary

reader/programmer can mitigate the amount of missed positions, therefore increasing the reliability of the whole system. Furthermore, the mechanism significantly shortens the time of being at the checkout which transfers into measurable savings.

The most difficulties were caused by implementation of low-profile ISO/IEC 15693 protocol functions, through which the process of communication with an identifier is performed. It turns out that not all mobile devices operate correctly in every defined mode.

To sum up, RFID technique can be successfully used to mark fast-moving objects, which, as a result, would bring many advantages for both producers and sellers, as well as consumers. A possibility of using existing mobile devices significantly reduces the cost of implementing such system and favors its popularization among the target customers.

Acknowledgements This work was partially supported by the Projects: “Synthesis of autonomous semi-passive transponder dedicated to operation in anticollision dynamic RFID systems”, grant of Polish National Centre for Research and Development, No PBS1/A3/3/2012, NCBR. The work was developed by using equipment purchased in the Operational Program Development of Eastern Poland 2007–2013 of the Priority Axis I Modern Economics of Activity I.3 Supporting Innovation under Grant No. POPW.01.03.00-18-012/09-00 and the Program of Development of Podkarpacie Province of The European Regional Development Fund under Grant No. UDA-RPPK.01.03.00-18-003/10-00.

References

1. Finkenzerler, K.: RFID handbook—fundamentals and applications in contactless smart cards and identification. Wiley, Hoboken (2003)
2. GS1: General Specifications. http://www.gs1.org/docs/gsm/barcodes/GS1_General_Specifications.pdf. Version 14, January 2014
3. Volpato Filho, O., Piva, F.: NFC-enabled decentralized checkout system. In: 2014 IEEE Brasil RFID, pp 35–37 (2014)
4. Jankowski-Miśkiewicz, P., Kalita, W., Skoczylas, M., Węglarski, M.: Modelling and design of HF RFID passive transponders with additional energy harvester. *Int. J. Antennas Propag.* **2013**, 1–10 (2013). doi:10.1155/2013/242840
5. Jankowski-Miśkiewicz, P., Tomaszewski, G., Węglarski, M.: RFID technique in remote control system. *Elektronika* **1**, 21–23 (2014). ISSN: 0033-2089
6. ISO/IEC: 15693-1:2010 Part 1: Physical characteristics. http://www.iso.org/iso/home/store/catalogue_tc/catalogue_detail.htm?csnumber=39694
7. ISO/IEC: 15693-2:2006 Part 2: Air interface and initialization. http://www.iso.org/iso/home/store/catalogue_tc/catalogue_detail.htm?csnumber=39695
8. ISO/IEC: 15693-3:2009 Part 3: Anticollision and transmission protocol. http://www.iso.org/iso/home/store/catalogue_tc/catalogue_detail.htm?csnumber=43467
9. Janakiraman, N., Meyer, R.J., Hoch, S.J.: The psychology of decisions to abandon waits for service. *J. Mark. Res.* **48**(6), 970–984 (2011)
10. Tyagi, S., Ansari, A.Q., Khan, M.A.: RFID Data Management. INTECH Open Access Publisher (2010). <http://cdn.intechweb.org/pdfs/8488.pdf>